Metal Oxides for High-Rate, High-Capacity Anodes for Li-ion Batteries

Evangeline Wheeler-Jones

March 2022

Thesis submitted to the University of Warwick in fulfilment of the requirements for the degree of Doctor of Philosophy

WMG, University of Warwick

Contents

List of Figures

List of Tables

Acknowledgements

I would like to thank all those who have supported me and given me invaluable advice during my studies. I would like to thank Mel for the opportunity to work with her and for her patience and wisdom over the past few years. I would like to thank Richard for his continued support since first arriving at Warwick and for his brilliant expertise he has imparted on me. I would like to thank everyone who has contributed to the smooth running of the labs and facilities, most importantly the team of technicians and lab managers who do endless work behind the scenes. Thank you to the microscopy team - Geoff, Sabrina, Fengzai and Tom - whose expertise was always on point and for the great conversations over hours sat at the microscopes. Thank you to the X-ray Platform managers, Dave and Steve, who have always been a friendly face and are always there to help with experiment set up and have brilliant ideas for future analysis. I would like to thank Helen for all her knowledge on PDFs and neutrons, it has been brilliant to have the opportunity to work with you again. I would like to thank my former supervisor Alex for giving me freedom to explore as a researcher. I would also like to thank John, my master's supervisor, for continued support and advice during my PhD.

Thank you to Phil and Margaret for supporting my public engagement endeavours and all those at the Institute of Engagement. I would like to thank the many friends I have gained through ChemSoc over the years and the brilliant Outreach opportunities that I have had alongside them. I would like to thank my fellow chemistry undergrad pal Alex who has supported me with various outreach projects over the years. I would also like to dedicate my journey to Nick Barker who inspired me to follow science and always give back to others.

I would like to thank the members of the Walton group for always being available to help me with any materials related questions. I would like to thank Katie, Jasmine, Aron, James and Will who have all helped me with various bits and understanding over the years. Specifically, I would like to shout from the roof how brilliant Aron has been, he is so selfless with his time and is a brilliant teacher. Thank you to Will, I only wished we had worked together sooner, you were always brightening up my day and making the experience a lot easier!

Thank you to my WMG crew – I'm sure that without each other, we all would have never made it this far! Thank you to Mike (aka Prof. Veg) for always being brilliantly creative and being resilience personified, you always make me feel like I could do anything. Thank you,

Sam, you never have stopped being the most ridiculously funny person and keeping a smile on my face. Thanks to Ben for being a great friend, always there when I need a boost or maybe more importantly a Pint. Thank you Sanghamitra for being the loveliest person in the room and showing me such kindness. Thanks to Craig for your continued friendship and genuine character. Thank you to Matt for all the glorious rants we have had over the years, I'm sure it has kept me saner. Thank you to Keiron for always being able to have a laugh with me. All of you were my backbone over my studies, I cannot thank you enough.

I would like to thank Zac for being here for me every single day, feeling my pain and my joy and always being there to hype me up and reminding me of who I am. Thank you to Phlan for your support and your quiet pride in me and what I have achieved. Thank you to my Mum and Dad who have never stopped believing in me, always continued to push me to my best and have given me endless love and support for years.

Declarations

This thesis is submitted to the University of Warwick in support of my application for the degree of Doctor of Philosophy. It has been composed by myself and has not been submitted in any previous application for any degree. The work presented (including data generated and data analysis) was carried out by the author except in the cases outlined below:

Thermal gravimetric analysis data were collected by Jasmine Clayton and Katie Everden in the Walton Group, Department of Chemistry, University of Warwick. XPS data were collected and processed by Dr Marc Walker at the XPS Research Technology Platform, University of Warwick.

Total neutron scattering data were collected by Dr Helen Playford and Dr Ron Smith at POLARIS at ISIS. Data processing, where scattering data was converted to pair distribution functions were also completed by Dr Helen Playford. High energy X-ray scattering data were collected by Dr Harry Geddes during block allocation group on the I15 beamline at the Diamond Light Source.

Results from Chapter 3 (Niobium Pentoxide as a High-Rate Li-Ion Anode Material) have already been published:

Evangeline C. Wheeler-Jones, Melanie J. Loveridge, Richard I. Walton, Investigating the influence of synthesis route on the crystallinity and rate capability of niobium pentoxide for energy storage, Electrochimica Acta, Volume 392, 2021, 138964.

Outcomes of Chapter 5 (Novel Niobium Pentoxide/Molybdenum Dioxide Composite Materials) are submitted for publication.

Abstract

This work synthesised a range of Nb_2O_5 and MoO_2 materials and produced a selection of novel composites through the combination of these oxides. These materials were characterised using a number of experimental techniques and their properties towards Li-ion storage were investigated to assess their use in Li-ion battery technology. All materials were produced via a simple hydrothermal preparation at 225 °C and in some cases, the use of a subsequent short heat-treatment step up to 1300 °C. The structure of the materials were characterised using X-ray diffraction and the particle properties were studied by microscopy, particle size analysis, thermal gravimetric analysis and N_2 adsorption analysis. All materials were cast into electrodes and tested against Li to establish their electrochemical abilities via cycling, cyclic voltammetry, and impedance spectroscopy.

Within the Nb_2O_5 family of materials an anisotropically crystalline, orthorhombic (T-) and monoclinic (H-) forms were produced. All materials show high-rate capability, although T-Nb_2O_5 has been favoured in the previous literature. This work presents H-Nb_2O_5 as a more capable high-rate anode, where long-term cycling at 100 C gave capacities of 50 $mAhg^{-1}$ after 400 cycles. As for MoO_2, the nature of the Li-ion storage mechanism is investigated using a range of electrochemical tests and *ex-situ* X-ray diffraction on cycled electrodes, where evidence of conversion, intercalation and pseudocapacitive mechanisms was apparent. Moreover, the activation process that MoO_2 exhibits was determined to be from a change in symmetry from monoclinic to tetragonal. The MoO_2 materials struggle to reach the high capacities expected from previous literature, yet significant knowledge is gained from their electrochemical characterisation. A range of composite oxides are synthesised with the ratios, 10:90, 20:80, 50:50, 80:20 and 90:10 of Nb_2O_5:MoO_2. The 50:50 composite shows the most promising electrochemical results, where heat-treatment was used to improve the electrochemical properties significantly. As such, capacities of 515 $mAhg^{-1}$ were achieved after low rates (200 cycles at 1C) and 105 $mAhg^{-1}$ at high rates (400 cycles at 100C). In summary, this thesis studies structural and electrochemical properties of Nb_2O_5 and MoO_2 and presents novel composite materials for high capacities and high charging rates in an anode material for potential use in Li-ion batteries.

Abbreviations

ANOH - ammonium niobate oxalate hydrate

AMTH - ammonium molybdate tetra hydrate

BET - Brunauer–Emmett–Teller

BJH - Barrett, Joyner, and Halenda

BVS - bond valance sum

CDC - carbide derived carbon

CNT - carbon nano tubes

CPE - constant phase element

CT - charge transfer

CV - cyclic voltammograms

DFT - density functional theory

DLS - dynamic light scattering

EDLC - electrochemical double layer capacitance

EDX - energy dispersive X-ray

EELS - electron energy loss spectroscopy

EIS - electrochemical impedance spectroscopy

EXAFS - extended X-ray adsorption fine structure

GITT - galvanostatic intermittent titration technique

GO- graphene oxide

ICSD - inorganic crystal structure database

IR - infra-red

LTO - $Li_4Ti_5O_{12}$, lithium titanium oxide

NMP - 1-methylpyrrolidin-2-one

NMR - nuclear magnetic resonance

OCP - open-circuit potential

OCV - open circuit voltage

PDF - pair distribution function

PSA - particle size analysis

SAED - selected area electron diffraction

SEI - solid electrolyte interphase

SEM - scanning electron microscopy

SPEIS - staircase potential EIS

STEM - scanning transmission electron microscopy

TEM - transmission electron microscopy

TGA - thermal gravimetric analysis

TNO - titanium niobium oxide

XANES - X-ray adsorption near edge spectroscopy

XPS - X-ray photoelectron spectroscopy

XRD - X-ray diffraction

XRF – X-ray fluorescence spectroscopy

1 Introduction

1.1 The Importance of the Li-ion Battery

In 2019, John Goodenough, Stanley Whittingham, and Akira Yoshino were recognised for their contribution to Li-ion batteries by awarding them a Nobel Prize.[1] Li-ion battery technologies have been explored for over 50 years, with Sony first commercialising the battery in 1991.[2] The Li-ion battery has driven the portable technological revolution and looks to also be key to the upcoming green revolution.[2,3] The Nobel prize noted that: "*They have laid the foundation of a wireless, fossil fuel-free society, and are of the greatest benefit to humankind*.".[1] The global push to a more sustainable future lies on general technological revolution, with implementation of renewable energy sources, new energy storage and the decarbonisation of transport. With this a reliance on batteries will be even more evident, and not only will an renewable energy grid rely on energy storage capabilities, but transport looks to electrification as a solution for decarbonising personal transport options.[4,5] To drive this change and to innovate the current battery systems governments and companies are investing in research and technology leading to a huge development over the last 30 years and more to come.

1.2 Inside the Li-ion Battery

The Li-ion battery is comprised of an anode (negative electrode), cathode (positive electrode), separator, and electrolyte. Typically, a graphite anode, a layered oxide cathode, polymeric separator and a Li salt in a carbonate-based electrolyte is used (Figure 1.1).[6,7] The Li-ion battery is a 'rocking chair' battery in which the Li-ions from the cathode can be pushed into and reversibly out of the anode repeatedly allowing it to be rechargeable.[8] In order to optimise the battery each individual component requires investigation and improvement. This leaves an extremely complex situation, as improvement of one component will call for changes in the others to allow for an efficient device. New materials are required for: electrodes, solid state electrolytes and to allow for movement away from a traditional Li based systems.[9] As such materials discovery, development and optimisation becomes a key part of improving batteries.[9–13] In the anode a departure from graphite looks to find materials with higher capacities, higher working voltages to reduce degradation and the ability to fast charge.[10] For the cathode, a move looks toward stable high capacity materials, ideally from sustainable and ethical materials.[14]

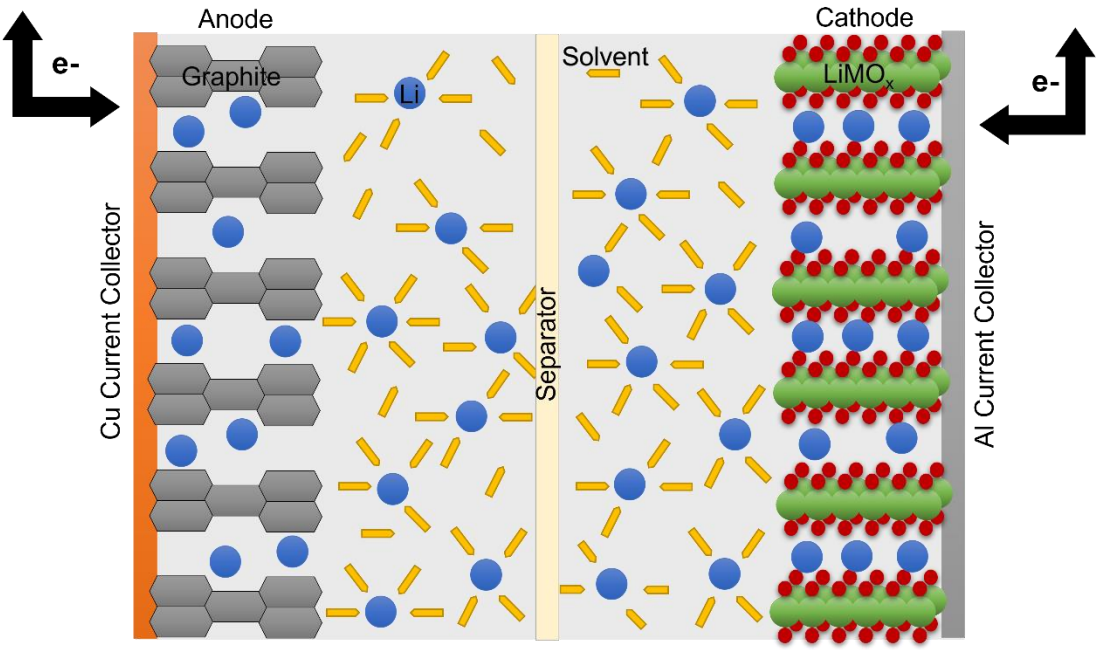

Figure 1.1 – General Li-ion Battery Schematic.

1.3 The Anode

This thesis focuses on the anode material and the push to improve the capacity and rate capability of the anode. Traditionally a graphite anode is used in the Li-on battery due to its reasonable theoretical capacity of 372 mAhg^{-1}, small expansion (~10 %) upon Li-ion insertion and low materials cost.[15,16] Yet graphite is limited due toa narrow working voltage and the continuous reformation of solid electrolyte interphase (SEI).[16] SEI is the passivating layer which forms from electrolyte degradation products upon the anode at low voltages and prevents further degradation of electrolyte and can contribute to the anodes stability.[17] Therefore, research has expanded to improve the anode via new materials discovery to replace graphite.[18]

1.4 Governing Equations for Li-Ion Batteries

Typically, in an electrode two charge storage processes take place: the storage of static charge in a double layer and storage via a redox reaction. The total capacitance of this system can be seen as:

$$C = C_{dl} + C_{pc}(E) \qquad [1]$$

where the sum of double layer capacitance (C_{dl}) and pseudocapacitance (C_{pc}) is a function of electrode potential (E).

A double layer is described as an interface between the electrode and electrolyte system (Figure 1.2). Where charge develops along the electrode interface the electrolyte balances this by accumulating charge at the electrode surface. When described by the Stern model there is an inner Helmholtz plane (IHP) – the distance of closest approach of an unsolvated ion adsorbed onto the surface, an outer Helmholtz plane (OHP) – the distance of closest approach for a solvated ion, and a diffuse layer- where ions are of a different concentration than in the bulk electrolyte because of the double layer.

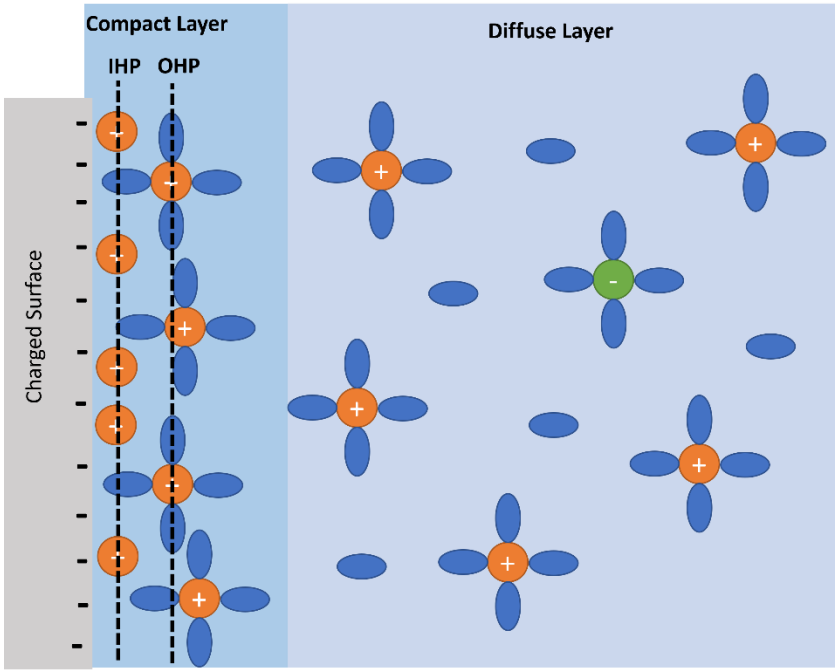

Figure 1.2 - Schematic of the Stern model of electrochemical double layer containing compact and diffuse layers.

The thickness of the diffuse layer can be changed by the concentration and dielectric constant of the electrolyte and temperature. Thus, it can be expressed using the Boltzmann distribution, at point x in the diffuse layer:

$$[ion]_x = [ion]_{bulk} e^{\left(-\frac{z_{ion} F \Psi_x}{RT}\right)} \quad [2]$$

where z_{ion} is the absolute charge of the ion, F is the faraday constant, Ψ_x is the potential at point x, R is the gas constant and T is temperature.

Many types of redox reactions contribute to the pseudocapacitance term in Equation [1]. If the redox material is insoluble in the electrolyte and distributed homogenously throughout the electrode, the redox reaction is described by:

$$Ox + ne^{-} \leftrightarrow Red \qquad [3]$$

where Ox is the oxidant, Red the reductant and n the number of electrons transferred for the reaction to take place. The Nernst equation helps to describe the thermodynamics involved within this process:

$$E = E^{0} + \frac{RT}{nF} Ln \frac{[Ox]}{[Red]} \qquad [4]$$

where E is the electrode potential, E^0 is the standard electrode potential, R the gas constant, T is temperature and F is the Faraday constant.

Above, the Nernst equation describes the potential of an electrochemical reaction as related to the species concentration, thus giving the position of the equilibrium within this reaction, yet this does not describe the speed at which the reaction may take place. Therefore, the electrochemical kinetics must be described too via a relationship between overpotential and current density.[19]

Overpotential (η) can be described as the potential difference between the actual (E) and equilibrium potentials (E_{eq}) :

$$\eta = E - E_{eq} \qquad [5]$$

The Tafel equation links the overpotential to current density for a single electrode:

$$Log\left(\frac{J}{J_0}\right) = \frac{\beta nF}{RT}\eta \qquad [6]$$

where J is current density, J_0 the exchange current density and β is the symmetry factor (from the Gibbs free energy barrier). The Tafel equation approximates the Butler-Volmer equation, where it assumes ion concentration at the surface is equal to that in bulk. Therefore, generally electrochemical kinetics for a reversible process is described by the Butler-Volmer equation:

$$J = J_0\left(e^{\left(\frac{\beta_a F\eta}{RT}\right)} - e^{\left(-\frac{\beta_c F\eta}{RT}\right)}\right) \qquad [7]$$

where there is a symmetry factor for both anode (β_a) and cathode (β_c). The Butler-Volmer equation states that anodic or cathodic current can flow with dependence on the sign and the magnitude of the overpotential.

1.5 Li-ion Storage Mechanisms

Intercalation materials are the popular choice for cathode and anode materials (e.g., graphite). Li-ion intercalation takes the form of reversible bulk insertion of ions into a lattice with minimal perturbation.[15] Typically intercalation materials undergo a phase change with insertion of ions and as such have clear peaks in the cyclic voltammograms (CV) and plateaus in charging profiles (Figure 1.3).[20,21]Although, where anodes are concerned, intercalation materials are favoured due to the high reversibility and thus efficiency, typically these materials have lower capacities as they can hold less ions than a conversion material due to the storage mechanism.[22] Therefore, conversion and alloy materials have been considered.[23] With conversion, the material undergoes a transition with ion insertion where new materials may be formed, typically a metal and a lithium compound (Equation 8):

$$M_aX_b + cLi^+ \rightarrow aM + bLi_cX \qquad [8]$$

where M is a transition metal X is an anion (O, P, N etc.).

The conversion mechanism allows for far higher capacities to be achieved yet this constant formation and reformation of material leads to instability in the electrode causing poor long-term performance.[24] Alloy type materials form intermetallic phases or alloys to store Li-ions. These materials are metal or semi metals, with Si being a promising choice due to its high abundance and high capacity of 3600 $mAhg^{-1}$. However, as with the conversion materials these materials suffer from electrode instability and pulverisation due to high expansion.

Alongside these storage mechanisms, one cannot dismiss capacitive mechanisms for ion storage. Typically, these are only exploited in supercapacitor devices, however with the introduction of the hybrid supercapacitor or 'supercapbatteries' the lines between batteries and supercapacitors have become blurred.[25–30] Furthermore, the pseudocapacitive storage route has been exploited in both battery and supercapacitor set ups. As such high-rate anodes use these mechanisms to achieve improved power densities. To further categorise the types of pseudocapacitive materials the terms intrinsic and extrinsic pseudocapacitance are used. Intrinsic pseudocapacitance manifests in a material with no dependence on size or morphology, whereas extrinsic pseudocapacitance can be engineered via nano-structuring

of a material. When a material is constrained to the nano scale the typical phase transition with ion intercalation is suppressed allowing for high-rate behaviour. This will be further discussed in the context of Nb_2O_5 in Section 1.7.4.[31]

To further explain these capacitive mechanisms, Figure 1.3 shows the difference in electrochemical response with different storage mechanism. Faradic versus double layer charging has been simply distinguished by the CV signatures in the past yet this has become more ambiguous with the introduction of pseudocapacitance.[32] Electrochemical double layer capacitance (EDLC) is a non-faradic storage method where ions form an interface at an electrode surface and forms a double layer through charge separation. The CV signature for this is quasi-rectangular and the current is proportional to scan rate (Figure 1.3a).[33,34] As this is surface reliant, EDLCs use high surface area carbons as the electrode materials. Pseudocapacitance can take many forms (Figure 1.3b-d), typically these rely on surface redox reactions which are not limited by diffusion.[32,35,36] Within the umbrella of pseudocapacitance is the phenomenon of intercalation pseudocapacitance.[37] Intercalation pseudocapacitance is when a material can store ions within the channels of the structure with no phase change and with fast ion diffusion pathways, hence a lack of bulk diffusion limitation. As such, the kinetics of this appear more like that of a capacitor than a battery, showing broad CV signatures and near linear charge profiles yet the presence of a redox change gives change in shape away from a purely rectangular CV (Figure 1.3b-d).

To distinguish between these different storage mechanisms, CV, galvanostatic charge/discharge (GCD) and electrochemical impedance spectroscopy (EIS) can be used to identify key features.[38] As well as understanding the typical shapes of CV signatures, discussed above, using CV to identify the different charge mechanism can also be achieved as a function of scan rate. The power law expresses the current (i) in a voltammetry sweep test:

$$i = av^b \qquad [9]$$

where a and b are arbitrary constants and *v* is the scan rate. A b-value of 0.5 indicates a diffusion-limited process (battery-like) and a b-value of 1.0 indicates surface controlled process (supercapacitor-like).[37,39] By plotting the log relationship between peak current and scan rate, the gradient of the line is equal to the b value. To further understand the ratios between the diffusion limited and surface controlled current, equation [9] can be separated out as:

$$i = k_1 v + k_2 v^{0.5} \qquad [10]$$

the surface controlled process can be described as $k_1 v$ as b = 1 and the diffusion controlled process is described as $k_2 v^{0.5}$ as b = 0.5.[40] When this is plotted as:

$$i v^{-0.5} = k_1 v^{0.5} + k_2 \qquad [11]$$

a linear fit can be used to calculate the k constants, which allow the calculation of the surface controlled current (capacitive contribution).

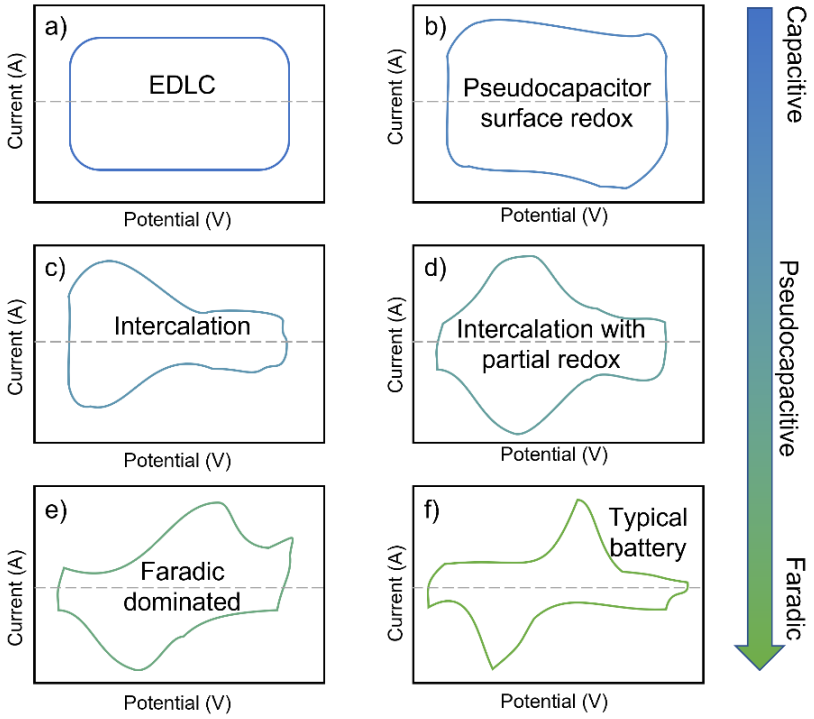

Figure 1.3 – Schematic cyclic voltammograms for various kinds of energy-storage materials. (a) EDLC (b) surface redox materials (c) intercalation-type materials or (d) intercalation-type materials with reversible redox peaks and (e–f) battery-like materials. Adapted with permission from ACS Nano 2018, 12, 3, 2081-2083. Copyright 2018 American Chemical Society.[20]

Further to uncovering the storage mechanism via CV, for identification via GCD, a EDLC will show a linear change in voltage with time, whereas a battery has a voltage plateau during GCD due to its phase transformation.[38] A pseudocapacitor is expected to also show a linear response, yet the slope is shallower compared to an EDLC. For EIS, one would expect a 90 ° response for a EDLC as it can be ideally modelled as an RC circuit. This is due to no contribution in the real axis as there are no faradic reactions nor limited ion diffusion. A

pseudocapacitor is ideally expected to also show a 90 ° diffusion tail due to lack of diffusion limitation but also show a small semi-circle in the high frequency region due to the fast redox reactions. Where a battery shows a larger semi-circle and 45 ° diffusion tail due to slower diffusion process and slower charge transfer.

Where the differences between charge storage mechanism may seem apparent through electrochemical analysis, in reality many of these mechanisms may be used concurrently and thus the true nature of the system may become very difficult to establish. This is further complicated by the hybrid devices which may combine a battery type and capacitive type electrode or a hybrid material which takes advantage of battery and capacitive mechanisms. Thus, there is now more room to design electrode materials for the application in mind. For anodes, the types of materials which may achieve a range of these storage abilities include metal oxides which is the focus of this work.

1.6 Metal Oxides for Anode Materials

Metal oxides are of interest for anode materials due to the diverse chemistry and breadth of properties which can be tapped into.[11,41–48] Titanium oxides have been widely explored as an anode in the form of $Li_4Ti_5O_{12}$ (LTO) and TiO_2 (in various polymorphs). LTO has been known particularly due to its good safety as compared to graphite and has been used in automotive batteries.[49] LTO has a spinel structure which can take on Li-ions with minimal expansion (<0.1 %) and operates in a 1-3 V range with a theoretical capacity of 175 $mAhg^{-1}$.[50] This is a lower capacity than graphite and LTO has poor conductivity, however, the higher working voltage prevents SEI issues, thus the material is known for excellent stability. Similar issues are seen in TiO_2, but this has a higher theoretical capacity of 336 $mAhg^{-1}$, although dependent on the polymorph used. Typically, the anatase and B-TiO_2 polymorphs have been studied.[51] Much research has been carried out to improve these Ti-oxides, this has included introduction of defects, doping and forming composites with carbon.[50–53]

Regarding other intercalation metal oxides, ternary oxides containing Ti have also been a well-researched area, with some of these being commercialised including titanium niobium oxides (TNO) by Toshiba.[41,54] Binary oxides which have been focused on include vanadium and niobium oxides, of which Nb_2O_5 is of particular interest due to its unique intercalation pseudocapacitive properties, hence this is a material focused on in this work.[40,55–58] Tin oxides are another binary oxide of interest, however these are for alloy-type storage. This is another highly researched material due to the high capacities achieved via an alloying mechanism.[59]

The tin oxides have been shown to be an improvement upon using pure tin via the improvement the electrochemical stability.[60,61] Due to the high interest in tin oxides, other mixed tin oxides, doped and composite materials have also been investigated.[41,61,62] In regards to metal oxides for conversion-type storage there is a large array to choose from, dioxides such as Mo, Mn or Ru, spinel materials in the form M_3O_4 and AB_2O_4, plus corundum A_2O_3 oxides of Fe, Cr and Mn. Reddy *et al*. have reviewed these in-depth.[41]

The work on metal oxides for anode materials is vast due to the different storage mechanism which may be exploited. This leaves much work to fully understand these materials and to explore their full electrochemical capability. As such, this work looks to investigate two oxides with particularly interesting properties. Nb_2O_5 looks to provide a key route to fast charging batteries, whereas MoO_2 is a rare oxide as it is both conductive and provides a high capacity. From here these materials are the focus of the discussion.

1.7 Niobium Pentoxide

1.7.1 The Structure of Nb_2O_5

The niobium oxygen system is vast with various stoichiometric and non-stoichiometric oxides, where niobium pentoxide (Nb_2O_5) is the most thermodynamically stable of the collection. Nb_2O_5 has a variety of polymorphs, built from six coordinated niobium-oxygen units (NbO_6 octahedra), which are organised into different forms and can have an array of distortions.[63] Essentially Nb_2O_5 contains Nb (V), the highest oxidation state for Nb, so has no remaining d electrons and hence the Fermi level lies between the filled O 2p band and empty Nb 4d band, thus Nb_2O_5 is a semiconductor and has a resultant low conductivity.[64] Nico *et al*. describes this system as complex due to the vast number and type of structures which can be formed.[65] The crystalline phases of Nb_2O_5 include: orthorhombic (T), monoclinic (B, H, N, Z and R), tetragonal (M and P) and also TT (pseudohexagonal or monoclinic). This uses the Brauer naming system (expanded by Schäfer *et al*.) to identify the phases.[66,67] The multiple nomenclatures used also adds to the confusion surrounding Nb_2O_5. Alongside these crystalline forms, many semi-crystalline and amorphous materials have also been produced.

The most thermodynamically stable phase of Nb_2O_5 is the H-, monoclinic structure, typically produced at high temperature. Alongside, this the T- orthorhombic phase is also well described by the literature. These structures are both displayed in Figure 1.4.[68,69] The orthorhombic phase is built from niobium-centred octahedra and pentagonal bipyramids,

linked by both corners and edges in the [001] plane, and connected via corner sharing in the c-direction. It should be noted that TT-Nb_2O_5 is a lower crystallinity phase of the T-Nb_2O_5 often with impurities or vacancies in the structure. The monoclinic phase is constructed of NbO_6 octahedra, connected by at the corners to form structural blocks, with edge-sharing joining the blocks to form an open structure.

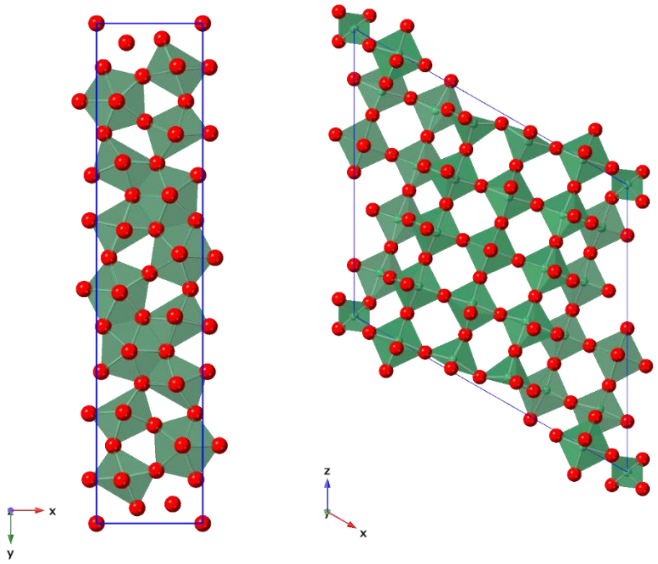

Figure 1.4 - Polyhedral views of the crystal structures of (left) orthorhombic (T-Nb_2O_5) and (right) monoclinic (H-Nb_2O_5).[68,69] The blue boxes in both cases show the unit cell, and the green polyhedra are the Nb units and the red spheres are oxygen atoms.

1.7.2 The Importance of Synthesis Method for Nb_2O_5

The physical properties of Nb_2O_5 are heavily based on the polymorph and the synthesis method.[70–73] Schäfer *et al*. reported extensively on the polymorphs of Nb_2O_5 and their properties.[67] They proposed the 'memory of solids' within Nb_2O_5 (originally described by Hüttig *et al*.)[74], where a material would have 'memory' of its synthesis condition and would behave differently due to this. This report showed that when Nb_2O_5 was prepared by three different methods upon heat treatment each of these would develop different polymorphs.

Raba *et al*. investigate the effect of synthesis on Nb_2O_5 and show a change in properties dependent on precursor and synthesis route.[75] This caused the different onset of crystalline phase formation with heat treatment. Furthermore, the materials have differences in particle size, morphology, and surface area, not only between synthesis routes, but with varied conditions within the same route. This property was also reported by Soares *et al*. where differences in physical properties have also been reported between the polymorphs

and within the same phases, which were synthesised via a different route (sintering or laser floating zone).[76] Not only did the synthesis route affect the lattice parameters but also the luminescence of the material. Furthermore, the heat treatment temperature also changed the dielectric constant, showing up to 4 times larger values with different temperatures even within the same crystallographic phase, this would be particularly notable for application in electrostatic capacitors a higher dielectric can lead to a higher charge storage.

The 'memory of solids' highlights the need to study the properties of different phases and synthesis conditions of Nb_2O_5. This makes Nb_2O_5 a particularly interesting case for practical applications as a targeted synthesis route could further improve properties.

1.7.3 Nb_2O_5 as an Energy Storage Material

The large variation in properties gained via different polymorphs or synthesis conditions allows Nb_2O_5 to have a large range of possible applications. Both crystalline and amorphous forms have been investigated for catalysis.[77–79] The TT-phase has been 'ranked amongst the best cathodic electrochromic films'.[80] The wide band gap allows for application in the realms of photo electrodes and gas sensing.[81,82] Regarding energy storage, Nb_2O_5 has been proposed for use in batteries (Li-ion and alternative ion technologies) and supercapacitor devices.[83–85] As a Na-ion anode, Nb_2O_5 has been explored due to the space in the structure capable of accommodating the large Na ion.[86–92] As Nb_2O_5 has a pseudocapacitive intercalation mechanism there is also much work in using this in supercapacitor devices, especially hybrid supercapacitors.[86,93–103] The literature on mixed niobium oxides is also vast and some materials have been recently commercialised.[54,104–112] The literature on Nb_2O_5 Li-ion batteries is heavily focused on T- Nb_2O_5 due to its unique high-rate capability. There are considerably less studies on the other Nb_2O_5 polymorphs for this application, but these should not be dismissed as similar properties may also be seen for these structures. Furthermore, due to the insulating nature of Nb_2O_5 a large amount of work looks at forming composites with carbon to improve this, and this will also be explored in this thesis.

1.7.4 Nb_2O_5 as an Anode for Li-ion Batteries

Niobium pentoxide was first used in an energy storage device by Reichman and Bard in the early 80's.[113] It is now generally accepted that Nb_2O_5 undergoes a two electron reaction (Equation 12) leading to a theoretical capacity of 200 $mAhg^{-1}$.[114,115]

$$Nb_2O_5 + xLi^+ + xe^- \leftrightarrow Li_xNb_2O_5 \qquad [12]$$

1.7.4.1 T-Nb_2O_5 and the Pseudocapacitive Intercalation Mechanism

After the initial study by Reichman and Bard, the mechanism of lithiation was explored by Kumagai *et al*. where the discharge of T-Nb_2O_5 was shown as a single step.[114] They used X-ray photoelectron spectroscopy (XPS) analysis to show that the Nb^{5+} was reduced to Nb^{4+} reversibly. X-ray diffraction (XRD) showed that upon lithiation the phase was unchanged, yet the disorder increased, they calculated a 50% disorder in the atomic arrangement. Upon delithiation the order was returned to the system. These researchers did further work on the Nb_2O_5 system, with study of the other phases (discussed below).[116] Nb_2O_5 was shown to be capable of lithiation with various electrolytes and it was confirmed that Li-ions would be expected to sit in the cavities in the structure. [117] Work by Ohzuku *et al*. at a similar time, was in agreement with the findings from Kumagai *et al*. where they described the T-Nb_2O_5 system as topotactic and suggested that the Li-ions would be accommodated into the vacant sites between the niobium sheets.[115] They also suggest that the Li-ions are likely to be mobile in the channels and from XRD they suggest the disorder caused by Li-ion intercalation comes in the [110] plane.

Kumagai *et al.* looked further into the Nb_2O_5 system by exploring the kinetics and further understanding the mechanism using extended X-ray adsorption fine structure (EXAFS).[116,118,119] T-Nb_2O_5 showed good capacity which faded over cycling in which the authors proposed was due to the poor conductivity of the material. T-Nb_2O_5 had small polarisation and shows a linear charge response with no plateaus in potential, suggesting that a solid-solution is maintained throughout cycling, in agreement with their previous works. Notably, they showed the TT-phase to follow the same mechanism. They calculated that the T-phase should be capable of undergoing up to two-electron reaction with no phase change. From the change in XRD peak intensities they proposed that the Li-ions would sit within the [001] plane vacancies, until x=1, in Equation 12. They suggested that further intercalation beyond this leads to niobium polyhedra parallel to [001] plane to distort due to the interaction between Li-ions and Nb metal centres. This increased disorder is further confirmed via quasi-open-circuit potential (OCP) temperature measurements, where the entropy of the system was calculated as a factor of the differential of temperature and potential, where entropy increased with lithiation. EXAFS studies showed a continuous valance variation upon lithiation from Nb^{5+} to Nb^{4+}, this helps to confirm the single phase process.[118] Further verification of these works was undertaken by Le Viet *et al*. where the T-

phase showed typical broad rectangular like CV signatures, and a linear charge profile.[120] Fast ion diffusion speeds expected of this type of mechanism were also confirmed via the galvanostatic intermittent titration technique (GITT) and electrochemical impedance spectroscopy (EIS).[121]

The Dunn group have become well known for their expertise on Nb_2O_5, with particular interest on the intricacies of the Li-ion storage mechanism. This group's work fired up interest on Nb_2O_5 as an energy storage material. This then led to a large development in knowledge on the intricacies of T-Nb_2O_5 and how to optimise it. Their first paper on this work looked at the different crystal structures of Nb_2O_5, (discussed later) where they conclude that the T-phase has superior performance compared to other crystalline and amorphous phases.[55] T-Nb_2O_5 exhibits extremely fast kinetics, where this was measured to be able to access 80 % of its capacity within 12s. In 2013, the Dunn group coined the term 'intercalation pseudocapacitance' to describe the Li-ion transport mechanism.[37] This study found that T-Nb_2O_5 does exhibit the kinetic properties of a pseudocapacitive material, where the kinetics are limited by surface transport rather than bulk diffusion. Yet, unusually they found that charge storage happens in bulk, not just at the surface, hence the term intercalation pseudocapacitance, as the material is showing both intercalation-like and pseudocapacitive-like properties. This study shows T-Nb_2O_5 as a superior high-rate anode material compared to a commercial material, LTO ($Li_4Ti_5O_{12}$). Furthermore, the electrochemical properties are noted to be due to the layered crystal structure where Li-ions could be stored along the [001] plane and allow for 2-dimensional ion transport, without a phase change. This was confirming what was previously shown by Komada *et al*. and Kumagai *et al*. [116,118]

Later, the Dunn group followed up their work alongside other researchers in the area, with further kinetic studies and *in-situ* XRD.[122] The *in-situ* XRD measurements confirmed what had already been found by Kumagai *et al*. This study showed a reversible lattice expansion to 4.02 Å at x= 1.8, ($Li_xNb_2O_5$) which returned to the resting state of the c-lattice parameter at 3.91 Å, suggesting that the [001] planes are the key Li-ion pathways. This work then was extended to a comparison of thick and thin electrodes, showing that Nb_2O_5 is a practical and scalable material and unlike many of the other pseudocapacitive materials as its properties are intrinsic to the structure, its unique properties allow it to be used in thick electrodes, which can be prepared by conventional slurry casting methods.

Griffith *et al.* presented a study on multiple Nb_2O_5 polymorphs.[123] They found that micro-sized Nb_2O_5 could achieve as good electrochemical performance when compared to the

nano-sized alternatives for the TT- and T-phases. They probed the Li-ion diffusion ability of the T-Nb_2O_5 using nuclear magnetic resonance (NMR) relaxation and exchange measurements, concluding that the fast ionic mobility translates into the larger particles and is not limited to nanostructures. Furthermore, bond valance sum (BVS) mapping shows a continuous 2 eV surface in T-Nb_2O_5 where the favourable storage sites are interconnected without obvious energy minima to trap Li-ions, hence the favourable kinetics. Similar was seen in a computational study by Lubimtsev *et al.*[124] When the Li-ion paths were computed they found Li-ions could move with low energy barriers between large voids found in the T-phase, which explains its high rates. Furthermore, long range diffusion was seen in the structure via 2D pathways and charge transfer could happen at all adsorption sites. *In operando* Raman studies by Chen *et al*. confirmed that T-Nb_2O_5 undergoes a reversible structural evolution during Li-ion cycling.[125] Its Raman spectrum is complex due to structural complexity, which could lead to over 150 vibration modes, yet the data allowed the system to be modelled. The Li-ions were found to sit in bridging O-Li-O sites, where the localised charge density sits around the oxygen atoms, as also seen in the study by Lubimtsev *et al*.[124] The Li-ion migration modelled appeared to follow two paths, both allowing free movement along passages that are 4 Å in size and the ions do not pass into any sterically hindered spaces leading to the materials high-rate ability.

A recent comprehensive study looked at analysing T-Nb_2O_5 over long term cycling, up to 10,000 cycles.[126] Using a combinatorial approach this study showed that T-Nb_2O_5 has a degradation in crystal structure over cycling which ultimately limits its long-term capability. They found this material initially shows inhomogeneous and incomplete lithiation, leading to trapping of the structure in irreversible states (Table 1.1). Transmission electron microscopy (TEM) image analysis shows that the lattice expansion needed for Li-ion accommodation is reversible initially, but the structural degradation leads to no expansion and hence limited ion diffusion. Furthermore, structural stress distorts the structure eventually leading to an amorphous form which in turn increases internal resistance and destroys the low energy diffusion pathways. These results were further confirmed by XRD and X-ray fluorescence (XRF) studies, and further imaging and energy dispersive X-ray (EDX) mapping also showed pitting and delaminating of the material with cycling.

Table 1.1 - Evolution of T-Nb_2O_5 crystal structure with cycling, from Andoni et al.[126]

Cycle	Lithiated	Delithiated
Pristine		Orthorhombic
1	Expanded orthorhombic	Orthorhombic
1000	Disorientated orthorhombic	Deformed orthorhombic
2000	Disorientated and deformed orthorhombic	Highly disorientated and deformed orthorhombic
10000	Amorphous	Amorphous

With understanding of the Li-ion storage mechanism the focus of the literature began to shift from mechanistic understanding to optimisation of T-Nb_2O_5. This led to many papers aiming to publish superior results compared to previous work, and further lead to the movement to compositing T-Nb_2O_5 to boost its conductivity. These materials and studies will be compared later in the text.

1.7.4.2 Understanding Li-ion Storage in Other Nb_2O_5 Polymorphs

Considering the complexity of Nb_2O_5 and the numbers of polymorphs that exist, the literature and understanding of these polymorphs as battery materials is lacking, due to the apparent superiority of the T-phase. Thus, the current literature covering the various crystal structures of Nb_2O_5 is discussed in detail here. More commonly the literature has focused on the TT-and H-phases. Where the TT-phase would be a good choice for an energy material due the expectation of this structure to be a similar to the T-phase, so assumedly it could lead to very similar properties.

Kumagai *et al*. looked at TT- and H-Nb_2O_5 as battery materials.[116] They reported high capacities from both phases with steady losses over cycles which they linked to the lack of conductivity. TT-Nb_2O_5 performed similarly to T-Nb_2O_5, with linear charge/discharge curves and thus, showed only 3 % lattice expansion at complete lithiation. Whereas H-Nb_2O_5 did show plateaus in cycling profiles as typically expected of a lithium intercalation material. XRD showed that although a monoclinic phase appeared to be maintained throughout lithiation, a new phase appeared to form alongside this. Cava *et al.* published on multiple Wadsley-Roth materials, including R- and H- Nb_2O_5.[127] These phases would react with n-BuLi and to accept up to 1.4 Li per transition metal. When tested electrochemically, voltage plateaus were observed during cycling suggesting a multi-phase insertion mechanism for these materials. H-Nb_2O_5 showed capacity fade due to resistance build up seen as hysteresis in the charge/discharge curves within 10 cycles in which the material was tested. Further study of the TT- and H-phases was completed by Le Viet *et al.*[120] The CV profile of TT-Nb_2O_5 shows a

single set of broad peaks confirming the maintained phase with Li-ion intercalation. Whereas, H-Nb_2O_5 materials show multiple sets of redox peaks within a 1.0 – 2.6 V range, which appear highly reversible. Furthermore, they found the higher temperature H-Nb_2O_5 produced improved reversibility, likely due to higher level of crystallinity, with the highest capacity of 249 $mAhg^{-1}$ were recorded at C/4. [121] Although, H-Nb_2O_5 appears to undertake a multi-step Li-ion storage mechanism this work showed that the diffusion coefficient is still high and should show superior diffusion compared to the other phases. Kim *et al.* studied Nb_2O_5 TT-, T- and an amorphous for pseudocapacitive response.[55] They found that the crystalline phases have much greater electrochemical storage ability. The study also looked at Na-ion capacitance, where a lack of capacity due to the inability for the larger ion to access the material was found, showing that the pseudocapacitive mechanism is size sensitive.

The TT-phase is generally seen to produce similar properties to the T phase but with some reduction in electrochemical ability e.g., specific capacity.[128] Yet it is suggested that differences in TT-phases arise via different heat-treatment steps.[129] As the TT- phase is seen as a disordered version of the T- phase due to impurities or lattice vacancies, the heat treatment is likely to lead to more order, which has been previously noted as a key feature for the fast Li-ion diffusion.[124] This may suggest that the synthesis method is particularly important in determining the properties of the material, as with the concept of memory of solids introduced earlier.[67] As such Li *et al*. presented the TT-phase to be better electrochemically than the T-phase due to the materials higher surface area and smaller crystallites.[130]

Griffith *et al*. studied TT-,T-, B- (monoclinic) and H-Nb_2O_5, where they found that the B-Nb_2O_5 had poor electrochemical performance, and the H-phase only had high capacities at low rates.[123] The TT- and T- Nb_2O_5 presented linear change and discharge as expected. BVS mapping revealed that H-Nb_2O_5 had local minima in the structure, where the Li-ions can be 'trapped' and would have to overcome a large energy barrier to allow for diffusion. There is also a size mismatch between the voids in H-Nb_2O_5 and the Li-ion, which can also lead to path obstruction. However, the large interlayer spacing gives way to a large amount of lithium storage hence the high-capacity results, yet poor rate capability. This study emphasises that crystal structure is a key factor in achieving good electrochemical properties.

The tetragonal phase (M-Nb_2O_5) was also explored by Kumagai *et al*., as discussed earlier.[118] The M-phase they present is actually a mix of M- and H-Nb_2O_5, which will be denoted as the M/H-Nb_2O_5 from here forward. This study concluded that the superior properties were due

to the M-phase within this material, as studies on a pure H-phase had shown poor results. The M/H-phase showed little lattice expansion upon insertion and XAFS revealed a linear relationship between valance and lithium content. This work confirms that not only the T-phase is capable of Li-ion insertion with no phase change but also the M- phase may be of interest. Little further interest had been taken into the M-phase until recently where Hu *et al*. studied it amongst the TT-, T-, M- and H- phases.[131] Notably the authors claim to have produced a pure M-Nb_2O_5, yet from the XRD pattern provided this is not obvious. They present electrochemical *in situ* XRD on M-Nb_2O_5 which appears to show no phase formation upon lithiation and only a lattice expansion. Ding *et al.* further studied the M-Nb_2O_5 only, in apparently a pure form.[132] They showed a combination of pseudocapacitive solid-solution and two-phase intercalation reaction when inserting Li-ions, with GITT studies showing that the two-phase reaction limits the Li-ion diffusion. As such, this study also presents the M-phase as a high-rate material due to the use of multiple storage mechanisms.

Other than the H-phase, another monoclinic form of Nb_2O_5 exists, this is the R-phase. The R-phase has ease of long-range diffusion due to the regularity of the crystal structure.[124] From modelling electrochemical behaviour with a simplified Nb_2O_5 structure and the calculated diffusion information the authors suggest that it is likely that the Nb_2O_5 family of materials should show pseudocapacitive capability. Lübke *et al.* reported also reported on monoclinic (*C*2/*m*) R-Nb_2O_5 but in a semi-crystalline form synthesised via a continuous hydrothermal process.[133] This work considered the as-synthesised material without further heat-treatment hence its semi-crystalline state, the first to explore electrochemical properties of a semi-crystalline form of Nb_2O_5. This material exhibits broad CV signatures, similar to what is typically seen in the T-phase. This aligns with the predictions of pseudocapacitive capability of R-Nb_2O_5 from the computational work of Lubimtsev *et al*.[124]

1.7.5 A Comparison of Nb_2O_5 Electrochemical Performance

The literature of T-Nb_2O_5 is about equivalent to that on all the other polymorphs put together, illustrated in Table 1.2 and Table 1.3. T-Nb_2O_5 generally shows higher capacities than the theoretical in its initial cycle, showing over lithiation of this material, yet this is not sustained to longer cycling, with a few exceptions.[134–136] This material is often reported to cycle at high rates of over 50C, with capacities as high as 127 $mAhg^{-1}$ at 50C and at the highest rate of 100 C, a capacity of 36 $mAhg^{-1}$.[137,138] This material has also shown its capability over long term cycling with multiple reports over 1000 cycles, notably a capacity of 120 $mAhg^{-1}$ is still achieved after 5000 cycles at 5C.[137] Regarding the other polymorphs, more recent studies

on TT-Nb_2O_5 begin to use similar test regimes as with T-Nb_2O_5; reporting at higher rate testing and longer cycling. As such TT- nano-pillars have achieved capacities of 55 $mAhg^{-1}$ at 20C, over a quarter of the theoretical, and 83 $mAhg^{-1}$ after 1000 cycles at 5C.[139] For H-Nb_2O_5 as already discussed the work is very contradictory, which is clear when looking at the high rate capability of these material in Table 1.2. Some reports do show great potential with capacities of 50 $mAhg^{-1}$ at 80C and 56 $mAhg^{-1}$ at 100C with others showing an inability to cycle over 10C.[123,138,140] This solidifies the physical properties dependence on preparative method, as all of these materials are H-Nb_2O_5, yet the electrochemical properties show large variation. When it comes to other polymorphs, semi crystalline and amorphous forms the literature is far too limited to make any overarching comments.

1.7.5.1 Comparison of Works on Pure T-Nb_2O_5

Table 1.2 - Comparison of literature on pure T-Nb_2O_5, where all rates were converted to C-rate, where 1C = 200 mAg^{-1}. Abbreviations are defined as: HT = heat-treatment, WC= wet chemistry, NP= nanoparticles, Solvo = Solvothermal, Hydro = Hydrothermal. '~' is used when values are estimated from the paper.

Synthesis	Morphology	Initial Capacity ($mAhg^{-1}$)	Initial rate (C)	Capacity at y rate ($mAhg^{-1}$)	y rate (C)	Capacity at x ($mAhg^{-1}$)	x (cycles)	Rate at x (C)	Ref/ Year
Hydro + HT	Nano-belts	250	0.5	50	50	180	50	0.5	[141]/2008
Hydro	Micro-spheres	391	0.25	39	4	219	200	0.25	[134]/2014
Electrospinning +HT	Nano-fibres	189	0.25	-	-	113	30	0.25	[120,121]/2010-14
Hydro + HT	Nano-sheets	184	1	90	5	70	200	5	[142]/2015
Hydro + HT	Nano-wires	209	0.5	160	25	-	-	-	[143]/2015
Hydro + HT	Nano-belts	300	2.5	250	25	300	500	2.5	[135]/2016
HT	Irregular micro-particles	160	1	85	60	160	100	1	[123]/2016
Sol-gel +HT	NP	140	0.05	75	2.5	110	120	0.5	[130]/2016
Hydro + HT	Urchins	175	1	90	25	131	1000	5	[144]/2016
Hydro + HT	Flower micro-spheres	191	0.25	90	25	147	1000	0.5	[145]/2017
Hydro + HT	Micro-spheres	184	0.5	119	10	126	150	2.5	[146]/2017
Electrospinning +HT	Nano-fibres	146	2.5	70	25	158	2000	2	[147]/2017
Template + HT	Porous network	210	0.1	77	50	124	100	10	[148]/2017
WC + HT	Nano-spheres	195	1	125	50	168	2000	1	[149]/2018
Solvo + HT	NP	270	0.25	140	5	175	100	0.25	[129]/2018
Electrospinning +HT	Nano-fibres	180	0.5	95	25	326	120	0.5	[136]/2019
Hydro + HT	Nano-capsules	360	0.5	107	25	86	100	0.5	[150]/2019
Solvo + HT	Nano-flake	224	0.1	117	20	100	5000	5	[151]/2019
WC + HT	NP	258	0.5	95	1	189	200	0.5	[152]/2019
Spray drying + HT	Yolk shell micro-spheres	205	0.5	118	25	175	200	0.5	[153]/2019
Drop drying + Oxidation	Microspheres	171	2.5	127	50	~120	5000	5	[137]/2019
Thermal Oxidation	Micro-spheres	117	0.5	33	25	~84	1000	1	[131]/2020
Solvo +HT	Flowers	289	0.1	~60	10	178	100	1	[154]/2021
Hydro+HT	Nano-wires	237	1	36	100	97	200	1	[138]/2021

1.7.5.2 Comparison of Works on Pure Nb_2O_5 of Other polymorphs.

Table 1.3 - Comparison of literature crystalline, semi-crystalline and amorphous forms of Nb_2O_5 (excluding T-), where all rates were converted to C-rate, where 1C = 200 mAg^{-1}. Abbreviations are defined as: HT = heat-treatment, WC= wet chemistry, NP= nanoparticles, Solvo = Solvothermal, Hydro = Hydrothermal, Semi-Cryst = Semi-Crystalline. '~' is used when values are estimated from figures or calculated from data in the paper.

Phase	Synthesis	Morphology	Initial Capacity ($mAhg^{-1}$)	Initial rate (C)	Capacity at y rate ($mAhg^{-1}$)	y rate (C)	Capacity at x ($mAhg^{-1}$)	x (cycles)	Rate at x (C)	Ref/ Year
TT-	Electrospinning +HT	Nano-fibres	152	0.25	-	-	118	30	0.25	[120,121]/2010-14
TT-	HT	Irregular micro-particles	165	1	120	10	165	100	1	[123]/2016
TT-	Sol-gel +HT	NP	190	0.05	114	2.5	170	120	0.5	[130]/2016
TT-	Hydro + HT	Nano-belts	209	0.5	104	10	96	200	5	[155]/2017
TT-	Solvo + HT	Urchin-microspheres	202	0.5	99	10	106	500	5	[156]/2017
TT-	Solvo + HT	NP	353	0.25	138	5	127	100	0.25	[129]/2018
TT-	Laser Ablation + HT	Nano-pillars	114	2	55	20	83	1000	5	[139]/2020
TT-	Thermal Oxidation	Micro-spheres	112	0.5	19	25	~74	1000	1	[131]/2020
TT-	Solid State	Hexagons	178	0.2	86	20	158	200	1	[157]/2020
H-	Electrospinning +HT	Nano-Nugget	242	0.25	227	2	198	300	0.25	[120,121]/2010-14
H-	HT	Irregular micro-particles	235	0.1	5	10	175	100	0.1	[123]/2016
H-	Sol-gel +HT	NP	185	0.05	120	0.5	-	-	-	[130]/2016
H-	Hydro	Urchins	406	0.25	-	-	390	200	0.25	[158]/2016
H-	Hydro + HT	Box implanted nano-rod	254	0.2	119	25	228	200	0.2	[159]/2017
H-	HT	Irregular micro-particles	266	0.05	~45	20	111	900	1	[160]/2019
H-	HT	Micro-particles	270	0.25	50	80	65	1000	10	[140]/2020
H-	Thermal Oxidation	Micro-spheres	151	0.5	68	25	~100	1000	1	[131]/2020
H-	Hydro +HT	Nano-cuboids	213	1	56	100	128	200	1	[138]/2021
B-	HT	Irregular micro-particles	20	0.1	10	10	20	100	0.1	[123]/2016
M-	Thermal Oxidation	Micro-spheres	162	0.5	121	25	~133	1000	1	[131]/2020
M-	Solvo +HT	Nano-particles	226	0.2	124	10	162	100	1	[132]/2021
T/M/H Mix-	Hydro+ HT	Nanosheets	206	1	47	50	174	800	5	[161]/2021
Semi-Cryst R-	Continuous Hydro	NP	145	2.5	43	50	143	800	2.5	[133]/2016
Semi-Cryst T-	Hydro	Nano-wires	225	1	19	100	61	200	1	[138]/2021
Amorphous	Sol-gel +HT	NP	150	0.05	50	2.5	~75	120	0.5	[130]/2016

1.7.6 Optimising Electrochemical Properties of Nb_2O_5

1.7.6.1 Nano-Structuring

To achieve pseudocapacitive properties nano-structuring is required to allow the material to perform as an extrinsic pseudocapacitor i.e., the particle size is key to achieving pseudocapacitive properties.[40] Yet in the case of Nb_2O_5, its pseudocapacitive properties are not dependant on sizes and morphology hence it is termed an intrinsic pseudocapacitor. In a way to prove Nb_2O_5 is an intrinsic pseudocapacitor Come *et al*. showed a lack of diffusion limitation for T-Nb_2O_5 in thick electrodes, prepared via a traditional slurry casting method.[122] The *in-situ* XRD measurements showed the expected continuous Li-ion insertion with no phase change, and a lattice expansion of only 3 % was measured. They concluded that there were no diffusion limitations in the bulk of the material, therefore nano-structuring is not required, and larger particles may be more appropriate for commercial use due to easier processability and likely improved material loading/packing. Griffith *et al*. also demonstrated this by reporting on micro-sized Nb_2O_5 as an alternative to the nano-sized particles.[123] They found that they could achieve as good electrochemical performance when compared to the nano-sized alternatives for the TT- and T- phases, with their NMR relaxation studies showing that the fast diffusion is available in the larger particles. This work confirms the categorisation of Nb_2O_5 as an intrinsic pseudocapacitor and hence nano structuring is not necessary for the desirable properties yet, the use of nano-structuring still appears to be favoured by researchers to further reach improved rates (Table 1.2 and Table 1.3).[63,81]

The type of nano-structuring should also be considered, where some nano structures have appeared to achieve better properties than others. Cheong *et al.* made a comparison between mesoporous T-Nb_2O_5 fibres and T-Nb_2O_5 nanoparticles.[147] They found that the fibres were superior due to high surface area, mesoporous active sites, nano-grains, and structural stability over large numbers of cycling. Whereas the nanoparticles sought stability via agglomeration with and in turn reduced lithium diffusion pathways. The authors emphasised that nano-structuring is not the key aspect to achieve the desired electrochemical properties, but nano material design is.

More recently an in-depth study on the pseudocapacitive ability of T-Nb_2O_5 in relation to its nanostructure was conducted by Van Den Bergh *et al.*[162] They conducted various tests to establish the surface limited and diffusion limited thresholds of mesoporous T-Nb_2O_5. The materials were made using a template method to carefully control porosity, pore size and

wall thickness of the materials. They revealed that the diffusion limited, and surface limited thresholds depend heavily on intercalation length. They note a moderated dependence on electron transport length and no dependence on electrolyte transport. Unlike previous works this has clarified the need for nanostructures.

1.7.6.2 Other methods

Preparative method, phase and nano-structure appear to be the key features that researchers look to optimise in Nb_2O_5 to create an application-ready material. Some work also suggests that further property dependence may be in oxygen vacancies, and highly oriented structures.

Zhang *et al.* noted that oxygen vacancies and low valence metal centres are the reason for variation in properties.[163] Indeed, this group think that the pseudocapacitive properties are due to niobium- oxygen chemistry rather than the specific crystal structure. As such, they found that the oxygen deficient Nb_2O_5 materials showed improvement in capacitive contribution, capacity at high rates and conductivity. Zhang *et al.* note that the oxygen vacancies serve as additional active sites, and an increase in donor density leads to these improved electrochemical properties. This is an interesting addition to the literature, as it was previously noted that an important part of Li-ion storage is the bridging oxygens in the structure.[124,125] Similar results were seen by Li *et al.* where a thermal reduction is also used to introduce oxygen vacancies.[164] Again, there were improvements in capacitive contribution, capacity and Li-ion diffusion coefficients. Here the authors suggest that the oxygen vacancies may also help to relieve structural strain upon Li-ion insertion. Amongst other nuances, Budak *et al.* also note oxygen vacancies as an important part of developing a superior electrochemical material. They note that with a low concentration or without oxygen vacancies, Nb_2O_5 will exhibit poor conductivity and lack of rate capability.[165] Other studies looking at creating oxygen vacancies in Nb_2O_5 found that this increased the number of active sites as seen by broadening of the redox peaks in the CV profile and improved capacities.[166,167]

Developing a highly oriented Nb_2O_5 structure is also seen as an opportunity to improve the electrochemical properties. Wu *et al*. aimed to exploit the fast Li-ion pathways via orienting the growth of T-Nb_2O_5 along the [001] plane.[150] They found higher crystallinity peaks in the [001] plane suggesting restricted growth in the other planes, with the [001] growth is along

the length of the nanowire. Their work shows that the ease of access to the [001] plane allows fast intercalation and complete insertion.

1.7.7 Nb_2O_5 Composites to Improve Electrochemical Properties for Li-ion Batteries

Composites are a simple way in which materials can be combined intimately to exploit properties of multiple materials. Carbon is highly explored as a composite material due to its ability to improve bulk conduction.[168–170] Yet combinations with other inorganic materials can be used to boost specific electrochemical properties too.

1.7.7.1 Nb_2O_5/Carbon Composites

Compositing the active material with carbon during synthesis can yield various improved properties due to the intimate connection between the carbon and the active material. Research has developed this in various ways, with carbon coatings and growth of active material from carbon structures. This pool of literature is vast as not only can various carbons be used, but synthesis conditions can yield different properties and a different Nb_2O_5 phase can also be developed within these composites compared to in the absence of carbon. Much of the literature in this area is detailed in Table 1.4, the key developments are discussed here. Many studies compare various Nb_2O_5/carbon composites with pure Nb_2O_5 to analyse the improvement given from the carbon content.[97,98,171] The improvements in electrochemistry can be seen as capacity increase, improved stability, better rate capability and reduced resistance. There have also been studies in which phase effects on electrochemistry have been the key outcome of the work.[128,140,153,165,172]

As has been reported for pure T-Nb_2O_5, carbon coated T-Nb_2O_5 also show intercalation pseudocapacitive mechanism with an expansion recorded here as 3.56 %.[153] Yet here this expansion is mainly in the [001] plane with limited 1.91 % expansion in the [180] plane. Similarly, Meng *et al.* found that in the carbon composites, T-phase only expands 3 % yet the H-phase expands 6.4 %.[172] Over 200 cycles at ~1C the T-phase showed the best capacity retention of 92 %, with 90 % for TT- and 78 % for H-Nb_2O_5. Furthermore, they believe the broad dispersive diffraction peaks seen in the time resolved *in-situ* XRD patterns in the T-phase are indicative of a quasi 2D network with random and continuous insertion, yet the H-phase has sharp peaks associated with the planes of ion insertion which may indicate limited pathways in the crystal lattice. This is confirmed by density functional theory (DFT) calculations. The H-phase underwent slow Li-ion diffusion due to 3D curved pathways, which is further hindered by higher migration energy of 1.14 eV (T-phase is 0.46 eV).

Alternatively, Song *et al*. showed diffusion kinetics from GITT in the H-Nb_2O_5/Carbon composite were faster than graphite and LTO.[140] Despite the fast kinetics they note that this material is limited by poor conductivity and inhomogeneous Li-ion intercalation into the bulk. The H-phase is shown to have drastic property improvements in a composite where a carbon coating is a critical factor in uniform Li-ion transport. The carbon shell allows for a uniform surface coating with good conductivity, measured at 0.38 Scm^{-2} compared to 10^{-11} Scm^{-2} for the pure material. They found that the H-phase undergoes a two-phase reaction with a solid solution mechanism. Both XRD and TEM showed lattice expansion along the [001] plane revealing that the lithiation is via the b-axis. *In operando* XRD patterns showed irreversible phase transformation in the pure H-Nb_2O_5 but not in the composite. In addition, *in operando* TEM also showed a larger expansion in the composite, which appear continuous with lithiation. They reveal that the fast Li-ion transport is like the T-phase due to the open tunnel structure and parallel structural expansion. To add to this work, Budak *et al.* prepared a riveting discussion on a carbide derived carbon (CDC) H/M- composite which outperformed the T-phase counterpart. [165] They conclude that the H/M- had superior performance due to particle size, surface area and distribution of CDC in the structure. Interestingly, they also mention oxygen vacancies as a key reason for improved electrochemical performance. These works add to the mix of literature on the H-Nb_2O_5 in which contradictory results have been seen.[116,118] Often this crystal structure is reported to have poor rate capability due to the hindered Li-ion pathways and local energy minima.[123,172] Yet other works report superior results, and suggest that H-Nb_2O_5 is capable of similar storage mechanism to T-Nb_2O_5.[138,140,165] A study by Sun *et al*. put emphasis on the carbon support changing the composites properties rather than Nb_2O_5.[173] They found that the more highly porous composite not only showed higher capacities over various rates but also showed a reduced ion resistance calculated from EIS of symmetric cells when fitting the diffusion tail. They showed that at 100C the holey graphene composite could achieve 75 $mAhg^{-1}$, which is nearly, double that of a Nb_2O_5/graphene composite.

When the wider literature is considered (Table 1.4), the choice of niobium oxide still mainly lies with T-Nb_2O_5, although there is a wide range of carbon materials explored. Coatings appear most favourable, likely due to them being a transferable to a variety of materials. Some studies show initial capacities far exceeding that of the theoretical capacity, with capacities of over 1000 $mAhg^{-1}$.[174,175] Yet these appear to be anomalous, with the majority of studies showing capacities in the expected range. Extremely high rate performance (>10,000 mAg^{-1}) was recorded by a few studies, with Nb_2O_5/Carbon composites achieving capacities

such as 150 $mAhg^{-1}$ at 30,000 mAg^{-1}.[140,165,174,176] These capacities are far higher than results from pure Nb_2O_5 (assuming 200 Ag^{-1} = 1C) showing the need for a conductive network to achieve the higher rate capacities.

1.7.7.2 Wider comparison of Nb_2O_5/Carbon composites in Li-ion half cells within the literature

*Table 1.4 - Comparison of literature Nb2O5/ Carbon. Abbreviations are defined as: RGO = reduced graphene oxide, CNT =carbon nano tubes, HT = heat-treatment, WC= wet chemistry, NP= nanoparticles, Solvo = Solvothermal, Hydro = Hydrothermal, NS= not specified. '~' is used when values are estimated from figures or calculated from data in the paper. * Unless stated otherwise.*

Phase	Carbon Type	Morphology of Nb_2O_5	Synthesis	C %	Initial Capacity ($mAhg^{-1}$)	Current Density (mAg^{-1})*	Capacity at y ($mAhg^{-1}$)	y (mAg^{-1})*	Capacity at x cycles ($mAhg^{-1}$)	x cycles	Current density at x (mAg^{-1}) *	Ref/ Year
T-	Coating	NP	WC +HT	11	170	10	115	5000	~110	4000	2000	[177]/2014
T-	Graphene	NP	Hydro + HT	33	162	100	120	2000	115	50	2000	[178]/2014
T-	Coating	NP	WC +HT	7	180	50	90	5000	-	-	-	[179]/2015
T-	CNT	NP	Hydro + HT	23	232	0.25 C	65	50C	80	1000	10C	[180]/2015
T-	Coating	Nano-wires	Hydro + HT	9	187	0.5C	140	25C	~150	1000	5C	[143]/2015
T-	Graphene	NP	Solvo + HT	25	195	C/10	115	10C	192	50	C/10	[181]/2015
T-	Amorphous	Nano-sheet	Solvo+ HT	8	563	100	250	1000	396	100	100	[182]/2015
T-	Porous nano-webs	NPs	WC+HT	60	125	500	82	10,000	~88	70,000	NS	[183]/2016
T-	Graphite	NP	Hydro + HT	60	1060	60	150	30,000	125	500	60,000	[174]/2017
T-	CNT	NP	Hydro + HT	5	207	500	130	5000	~125	2000	5000	[184]/2017
T-	Sheets	NP	WC +HT	19	409	50	160	1000	150	100	500	[185]/2017
T-	Coating	Nanowires	Microwave + HT	4	188	100	55	5000	~140	1000	100	[186]/2017
T -	Graphene	NP	WC +HT	15	~175	1C	75	100C	-	-	-	[173]/2017
T-	RGO	NP	WC	26	603	0.2C	221	5C	~450	100	NS	[175]/2018
T-	3D network	NP	WC	39	1052	0.2C	519	5C	~1000	100	NS	[175]/2018
T-	Graphene	NPs	Hydro + HT	10	163	0.5 C	110	50 C	~77	20000	50C	[187]/2018
T-	QDs	NP	Hydro + HT	26	391	100	134	5000	240	600	1000	[171]/2018
T-	Sheets	NP	WC +HT	28	170	100	50	10 000	~80	500	2000	[188]/2019
T-	CNT	Nano-peapods	WC +HT	78	207	100	108	10 000	170	1000	100	[176]/2019

T-	Coating	Nano-rods	Hydro + HT	25	478	100	143	5000	200	1000	5000	[150]/2019
T-	RGO	NP	Microwave	15	~125	1C	~100	10C	~140	1000	5C	[189]/2019
T-	Coating	NP	Solvo + HT	14	205	100	177	6000	181	200	200	[172]/2019
T-	NS	Shell micro-spheres	Spray drying + HT	-	205	0.5C	118	25C	175	200	0.5C	[153]/2019
T-	Carbon core shell	Shell micro-spheres	Drop drying +selenization	-	181	1000	~75	10,000	~80	5000	1000	[137]/2020
T-	Coating	NP	Solvo +HT	7	475	100	165	5000	512	100	100	[97]/2019
T-	RGO	NP	Hydro +HT	6	221	100	143	5C	189	100	100	[98]/2019
T-	N-doped tubes	NP	Hydro + HT	21	194	0.25C	87	25C	~130	1000	2.5C	[190]/2020
T-	Coating	Micro-particles	Chlorooxidation	2.6	300	10	~100	1000	~198	500	100	[165]/2020
T-	Coating	Micro-spheres	Solvo +HT	39	182	100	111	5000	~100	200	1000	[191]/2020
T-	CNT	Coating	ALD + HT	53	325	200	~180	3000	170	4000	3000	[192]/2020
TT-	CNT	Nano-peapods	WC +HT	78	~190	100	80	10,000	-	-	-	[176]/2019
TT-	Coating	NP	Solvo + HT	14	187	100	129	6000	153	200	200	[172]/2019
H -	CNT	Nano-cables	WC +Hydro	18	450	40	185	5000	441	100	40	[193]/2017
H-	Graphene	Urchins	Hydro + HT	8	412	40	345	400	404	100	40	[194]/2017
H-	Coating	NP	Solvo + HT	14	231	100	136	6000	179	200	200	[172]/2019
H-	N-doped coating	Micro-particles	HT	3	250	50	120	16,000	170	1000	2000	[140]/2020
H/M-	Coating	Micro-particles	Thermal decomposition	5.7	300	10	100	10,000	~215	500	100	[165]/2020

1.7.7.3 Beyond Nb_2O_5/Carbon Composites for Li-ion Battery Anodes

Although Nb_2O_5/carbon composites have often shown superior electrochemistry due to an overall conductivity boost, it should be considered that addition of carbons would bring down the overall loading of the material due to the low density of the material, hence limiting the achievable gravimetric capacity. Therefore, work has also looked at boosting the capacity and reducing resistance of Nb_2O_5 by developing composites with other materials. Other niobium oxides are an obvious choice, but this section also looks at various oxides.

Park *et al.* created a Nb_2O_5/NbO_2 composite via thermal reduction of Nb_2O_5, the material created was a mix of H-Nb_2O_5 and tetragonal NbO_2.[160] It is noted that the NbO_2 has been shown to have pseudocapacitive properties thus this material should be suitable for anode materials. This composite achieves initial lithiation capacity of 214 $mAhg^{-1}$ (at 0.05C) which is a large improvement compared to the NbO_2 electrode yet doesn't achieve the high capacity of 266 $mAhg^{-1}$ seen in H-Nb_2O_5. However, the electrode stability was vastly improved with the addition of NbO_2 to the material, showing a capacity retention of 81 % over 900 cycles at 1C Vs 62 % achieved by H-Nb_2O_5. The authors note that the addition of NbO_2 helps to improve properties by increasing conduction (NbO_2 is semi-conducting) and reduces the strain on H-Nb_2O_5 when charging. Similar results were found via compositing H-Nb_2O_5 with $KNb_6O_{15}F$ where the conductivity was improved, and strain reduced.[195] $KNb_6O_{15}F$ is presented as a pseudocapacitive material but with poor capacity. The composite produced 80 $mAhg^{-1}$ at 20C compared to 30 $mAhg^{-1}$ from H-Nb_2O_5, at lower rates both these materials perform similarly. However, the composite does have far improved stability due to strain reduction as $KNb_6O_{15}F$ is more structurally robust and undertakes less expansion on lithiation. To add to this Chen *et al.* looked to dope Nb_2O_5 with nitrogen but formed a NbN coating on T-Nb_2O_5 instead.[196] Their material showed capacities of 113 $mAhg^{-1}$ at 16C and could retain 86% of its capacity over 1000 cycles at 4C. Critically the NbN layer is conductive and acts to improve the rate capability.

Further oxides have been considered as suitable composite materials for Nb_2O_5. Kim *et al.* developed a nano-clusters made of Nb_2O_5 and Ge/GeO_2, where Ge- materials were used to boost the conductivity.[197] In addition, the alloying mechanism at play in Ge, involves expansion of the material, thus the pairing with T-Nb_2O_5 may allow expansion buffering. Within this composite a broad CV is still recorded with both materials in the composite showing broad redox peaks within the signature. This study compared the composite electrochemically to a physically mixed version of Nb_2O_5 and Ge/GeO_2, where the composite

showed higher capacities, thus the intergrowth between these materials is important to achieve desired electrochemical properties. This study seems to show great success for this combination of complementary materials where a composite is presented as a stable, high-capacity material with good rate capability.

Niobium vanadium oxide nanocomposites were presented by Li *et al*. with vanadium content of 2, 10, 20 and 30 %.[198] At 10 and 20 % a composite between $Nb_{18}V_4O_{35}$ and Nb_2O_5 was formed, when the vanadium content was increased to 30 %, a mixed oxide was formed ($NbVO_5$). Where at 2 % it is unclear whether a composite is made as the characterisation suggests a doped material. This work sits between the realms of compositing and forming mixed oxides. All composites showed improved capacity compared to Nb_2O_5 until 30 % material which showed large capacity losses, this is likely because at this level the material is no longer a composite and the $NbVO_5$ may not provide high Li ion accommodation.

1.8 Molybdenum Dioxide

1.8.1 The Structure of MoO_2.

There is a variety of molybdenum oxides, stoichiometric and non-stoichiometric, with the formula MoO_x where x can be between 2-3.[199] Crystalline molybdenum oxides are built from MoO_6 octahedra arranged in a variety of ways to give different phases. Both pure MoO_x and MMo_xO_y, where M is another metal, have application in both catalysis and energy storage.[200] The MoO_2 structure is a disordered rutile, where Mo is coordinated to six oxygen atoms.[201,202] The octahedra are joined by edges to form a string and share corners to form a 3D structure (Figure 1.5). The Mo-Mo distance alternates, giving a tilt in the [100] plane of the rutile cell, leading to monoclinic symmetry, instead of tetragonal as would be the case for the usual rutile structure.[203] The alternating Mo-Mo pairs have relatively short distances; 2.51 and 3.02 Å and the distances are correlated with the number of valance electrons in the Mo atoms. There is an extra electron per metal ion, compared to a d^1 oxide, i.e. VO_2 or NbO_2, which can populate t_{2g} bands,[204,205] which leads to the Mo-Mo bonding and metallic-like conductivity (MoO_2 has a resistivity of 10^{-4} Ωcm at 300 K.) [203,206] It is even suggested that the Mo-Mo bonds are of higher order than a single bond due to the number of d electrons Mo has available.[203]

1.8.2 MoO_2 as an Energy Storage Material.

Both MoO_3 and MoO_2 have been investigated particularly due to their high theoretical capacity in a Li-ion battery (1117 and 838 $mAhg^{-1}$ respectively).[207] There has been much interest in MoO_3 for energy storage applications with particular interest as a potential pseudocapacitive material.[208–210] However, the more unusual properties seen in MoO_2 i.e. its metal-like conductivity, makes it a particularly interesting subject for potential energy storage applications. MoO_2 has been reported in the literature as a suitable material for Li-ion and Na-ion batteries, and supercapacitor devices. For Na-ion batteries MoO_2 has drawn interest due to its 1111 $mAhg^{-1}$ theoretical capacity.[207] Where practically it has shown both good capacities and brilliant long term cyclability as a Na-ion anode.[200,207,211–215] There is also a large amount of work on MoO_2 in supercapacitors due to the material's extrinsic pseudocapacitive properties.[216–224]

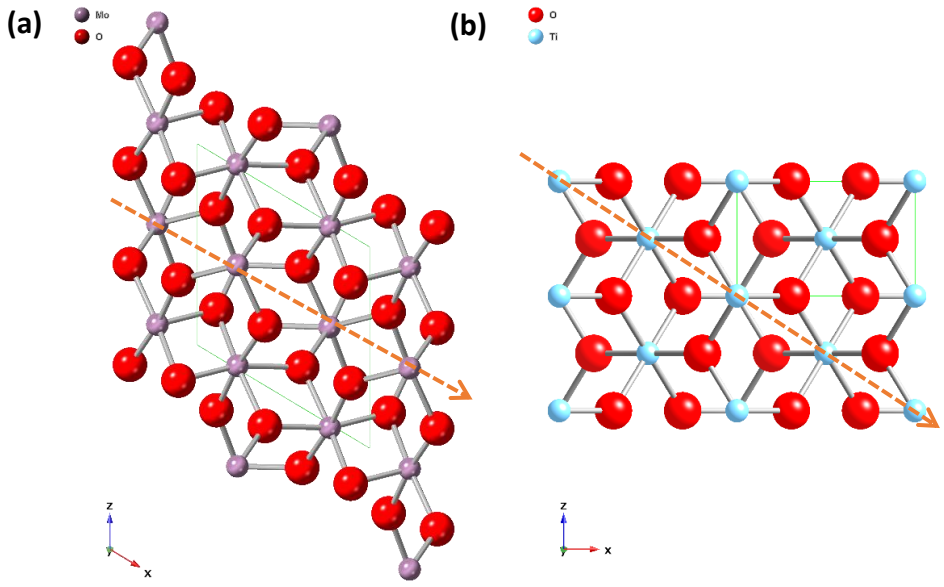

Figure 1.5 – (a) Monoclinic MoO_2 crystal structure (ICSD: 80830) from b-direction [225], (b) Rutile TiO_2 for comparison from b-direction (ICSD:16636).[226] Orange arrow is a guide along metal-metal distances.

1.8.3 Li-ion Storage in MoO_2 for Application as a Li-ion Battery Anode.

MoO_2 is prized for its high capacity of 838 $mAhg^{-1}$ for a four-electron Li-ion intercalation. It is generally accepted that the Li-ion storage is via two mechanisms, intercalation, and

conversion. The intercalation mechanism takes place at >1.0 V and is responsible for a theoretical capacity of 209 $mAhg^{-1}$ for the insertion up to x=1 as denoted below.

$$MoO_2 + xLi^+ \rightarrow Li_xMoO_2 \qquad [13]$$

The conversion reaction is responsible for storage of three Li-ions and takes place <1.0 V and corresponds to the remaining part of the theoretical capacity:

$$Li_xMoO_2 + (4 - \mathrm{x})\mathrm{Li}^+ \rightarrow Mo + 2Li_2O \qquad [14]$$

MoO_2 has potential to directly replace LTO as an intercalation anode, due to having similar working voltage and capacity, yet with the extra benefit of high volumetric capacity and good conductivity.[227] However, in practise MoO_2 has struggled to live up to expectations due to the intricacies of the Li-ion storage mechanisms and electrode degradation.

1.8.3.1 Lithium-Ion Intercalation Mechanism of MoO_2 at >1.0 V

It appears that the first mention of MoO_2 as a Li-ion storage material was by Murphy *et al.* in 1978.[228] They investigated topochemical reactions with Li for a variety of rutile related structures via a reaction with n-butyl lithium. They show the lithiated structure $Li_{1.0}MoO_2$ maintained the rutile structure and had an expanded unit cell compared to MoO_2. For the various rutile structures, a 10-18% expansion was recorded. They also showed proof-of-concept of MoO_2 as an electrochemical material with 30 cycles of MoO_2 in a Li-half cell set up. Cox *et al*. also created lithiated MoO_2 via a reaction with n-butyl lithium and used neutron diffraction to determine the structure of the material.[229] They found that at the diffraction pattern of $LiMoO_2$ was very similar to that of MoO_2, with the key rutile reflections, however there were small extra peaks and the monoclinic peak splitting was not clear. This suggested that the $LiMoO_2$ may also be monoclinic but with the ion storage being more complex than an expansion and Li-ion substitution. They found that when the Li-ions are inserted there is an expansion of the octahedra in the MoO_2 structure, and displacement of the oxygen atoms. They note that here the Mo-Mo pairs are at a short distance of 2.46 Å and that the structure is considerably less distorted from a rutile structure. They note that the $LiMoO_2$ structure is more similar to that of a distorted NiAs (Figure 1.6). This study shows that the Li-ion insertion between x=0-1 into Li_xMoO_2 must be a two-phase process, which start and end with a monoclinic structure, but of different types.

A study from Dahn and McKinnon in 1987 is well known to be the beginning of understanding the structure changes during the lithiation of MoO_2 in an electrochemical cell, rather than

via a chemical reaction with a lithium reagent.[230] They found that when the cell was cycled between 1.0 and 2.0 V it has a hysteresis in the charging profile, yet, when cycled between 1.5 and 2.0 V this was not observed. In this narrow voltage range, the MoO_2 structure expands by 5.6 % to accommodate Li-ions but does not change phase. When cycled to 1.0 V, a two-phase transition to orthorhombic then monoclinic phase was observed, with various transitionary regions (Figure 1.7). Within the same year, the first full cell with a MoO_2 negative electrode was proposed by Auborn and Barberio,[231] who demonstrated MoO_2 as a feasible reversible electrode when cycled between 1.0 and 2.0 V vs Li/Li^+. An irreversible inflection point at Li_xMoO_2 at x=0.5 was observed, which corresponds to an exothermic peak in a microcalorimetry profile thus a loss in capacity. These results reflect the study by Dahn and McKinnon, where similar capacity losses and irreversible reactions were observed.[230] Following this, Huang *et al.* used electrochemical lithiation to form the $LiMoO_2$ (detailed by Cox *et al.*), as this is also monoclinic, they believe that the rutile-like structure is maintained throughout lithiation contrary to the study by Dahn and McKinnon.[229,230,232] Thus, Huang *et al*. propose $Li_{0.67}MoO_2$ and $Li_{1.0}MoO_2$ are formed during lithiation yet do not suggest a structure for the $Li_{0.67}MoO_2$. As such, there is no evidence presented to rule out a change to an orthorhombic structure as presented by Dahn and McKinnon (Figure 1.7). However, a coulometric titration also showed that from MoO_2 to $Li_{0.33}MoO_2$ there is evidence for a solid solution mixing, which actually concurs with Dahn and McKinnon's work.

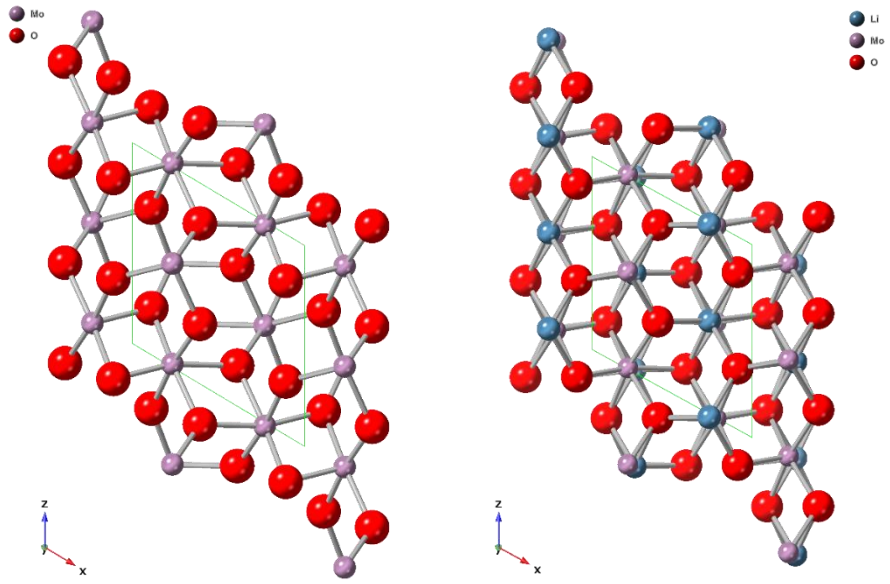

Figure 1.6 –Crystal structures from [010] plane of MoO_2 (left) and $LiMoO_2$ (right) as presented by Cox et al. via neutron diffraction experiments. [229]

From this point on, focus moved onto the conversion mechanism of MoO_2 in order to achieve the higher theoretical capacity. As such the first paper on MoO_2 as an intercalation material in 25 years was presented by Kumar Sen *et al.*[233] This showed CV profiles with four redox peaks during Li-ion insertion and only two during extraction, and claimed that Li-ion insertion is a four-step process in which there is a multi-phase transition from monoclinic to orthorhombic to monoclinic, as confirmed by *ex-situ* XRD. EIS measured at various points during cycling, showed an increase in resistance with the phase transitions during Li-ion insertion, but during extraction, there is no clear trend in resistance across the voltages. After this, Kim *et al.* further confirmed the Li-ion intercalation process via *ex-situ* XRD and first principle calculations.[227] XRD showed a double phase change during cycling and first principle calculations revealed that the orthorhombic phase was stable near x= 0.5. The energy difference between the phases is less than 0.1 eV, suggesting an ease of transition during the Li-ion storage process.

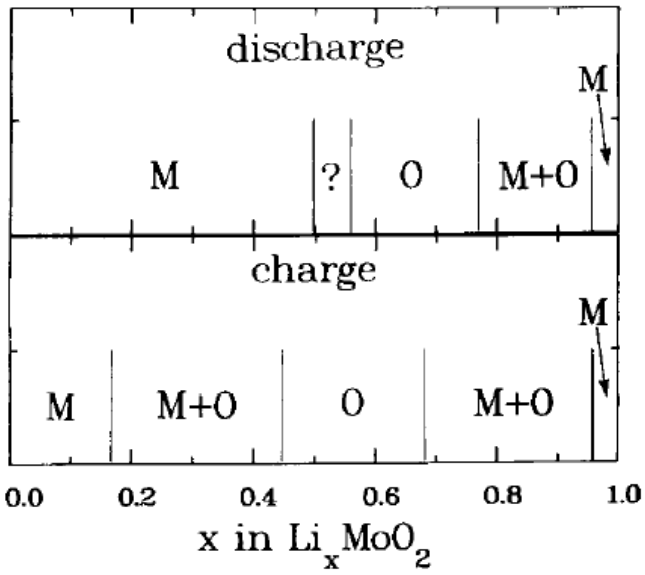

Figure 1.7 – Expected phases of Li_xMoO_2 between x=0-1 for charge and discharge, where M refers to a monoclinic phase and O refers to an orthorhombic phase. Reprinted from Solid State Ionics, 23, Dahn and McKinnon, Structure and Electrochemistry of Li_xMoO_2, 1-7, Copyright (1987), with permission from Elsevier. [230]

Zhu *et al.* suggested that a 2D-MoO_2 structure does not undergo a two-phase change during Li-ion storage, with *in-operando* XRD data only shifting and no other phases formed during cycling.[234] There is peak shift indicative of a lattice expansion, which is shown to be a 14 % expansion, which occurs along the b- and c-axis. The a-axis has a 1 % shrinkage; this is along the tunnel in the structure, where the tunnels are describing spaces in the [100] plane. This

was further confirmed by *in-operando* Raman spectra, and the authors link this ease of access through the tunnel structure with the suppression of the orthorhombic phase change thus, the material shows pseudocapacitive like properties. This is in agreement with a study by Kim *et al*. where micron-sized MoO_2 crystallites undergo the expected monoclinic-orthorhombic-monoclinic transition, as confirmed by *ex-situ* XRD.[235] However, nano-sized MoO_2 particles show a suppressed phase change and appear to store charge via a pseudocapacitive-like mechanism. No phase change was seen in the *ex-situ* XRD, the voltage profiles were sloping and there is a small peak voltage separation, all of which are pseudocapacitive characteristics. To add to this, a computational study of a MoO_2 sheet calculated a far higher theoretical capacity than has been previously acknowledged due to a capacitive-like storage. Zhou and Geng, showed that the 2D MoO_2 sheet is stable under standard conditions and that Li-ions could be adsorbed at four different sites.[236] Further to this, they showed an ease of diffusion across the sheet, however only via specific pathways, but shows no need for additional energy input to allow this. Up to 12 Li-ions were shown to be stored on the MoO_2 sheet, thus leading to a specific capacity of 2513 $mAhg^{-1}$.

Another notable result is from a study of nano-rods by Liu *et al.* who explored them as intercalation only anode materials.[237] This study shows long-term cycling, which is rare for this material, where they report a capacity of 147 $mAhg^{-1}$ after 2000 cycles at 1C. Rate sweeps with capability up to 50 C were also reported, resulting in capacities of 125 $mAhg^{-1}$. These results were attributed to the favourable insertion only mechanism, which was shown to be highly reversible via *ex-situ* XRD. Furthermore, the rate capability was linked to the high conductivity of the material and the resistances recorded in EIS showed little increase with cycling.

It should be noted that there are multiple studies on lithiated MoO_2 as a cathode in various forms.[232,238,239] During Li-ion insertion and extraction various phases of Li_xMoO_2 may be formed, and Barker *et al*. note these structures are related with an *R*3*m* hexagonal structure.[238] This is confirmed by Mikhailova *et al*. via *in-situ* synchrotron measurements.[239] It is difficult to know whether these structures are relevant to MoO_2 as an anode as are tested at higher voltages (2.1-3.6 V).

1.8.3.2 Conversion Mechanism for Storing Li-ion in MoO_2 at <1.0 V.

In 1978, Murphy *et al.* not only showed information on a lithium intercalation reaction but also showed evidence of a conversion reaction.[228] When exploring Li-ion insertion into a

selection of rutile type materials a displacement reaction took place, [24,47,240] for MoO_2 when four Li-ions were inserted Mo and LiO_2 was formed. The conversion reaction is more thoroughly described by Ku *et al*. where they look at the barriers in place to achieve a conversion reaction and the role of thermal activation.[241] They note that a number of studies are unable to access the conversion mechanism for MoO_2, as appeared to be the case at room temperature. When they conduct their electrochemical tests at 120 °C, the *ex-situ* XRD and XPS show evidence of a complete conversion taking place. They go on to show that thermochemical activation only needs to take place during the first cycle to allow for structural rearrangement.

Zhang *et al*. determined that the conversion process is only partially achieved initially, until the activation process (discussed in 1.8.3.3) is complete, after approx. 30 cycles, where a full conversion mechanism is observed.[242] This is seen as a growth in intensity of Mo peaks in the *in-situ* XRD pattern. During the activation, the capacity increases until it reaches a stable value of 720 $mAhg^{-1}$ at 30 cycles (at 0.1 Ag^{-1}), then the capacity shows a gradual drop upon cycling. At 30 cycles, *ex-situ* XRD pattern shows Li_2O but no longer shows $Li_{0.98}MoO_2$ suggesting a movement from an intercalation to a conversion mechanism. Interestingly, Zhao *et al.* show very similar electrochemical properties to this study, although they claim that a conversion mechanism is not used.[243] This is because the activation process was not complete when the authors took post mortem characterisation. Guo *et al.* explores this further and points out that Mo and LiO_2 may not be clearly seen in XRD at 0.01 V as will be in an amorphous form or will form as nano-crystallites in the structure.[244] They also observe the activation process, here up to 20 cycles where they reach a reversible capacity of 840 $mAhg^{-1}$ at C/20.

Shon *et al*. found that mesoporous MoO_2 did not store lithium via the expected conversion reaction.[245] The *ex-situ* XRD patterns at different voltages of cycling showed no phase change, nor did other phases form, only peak shift suggesting lattice expansion to accommodate lithium. After lithiation, high resolution TEM showed the presence of SEI, a crystalline and an amorphous phase, where the amorphous phase had grown between the crystalline domains. XAFS and X-ray adsorption near edge spectroscopy (XANES) showed no evidence to support the expected conversion mechanism as molybdenum was reported abnormally in a +1 state and coordination shells of MoO_2 were recorded with no evidence of metallic Mo. They suggest that Li rich phase begins to develop between the Li_xMoO_2 crystalline domains. Electron energy loss spectroscopy (EELS) data supports this as the crystalline region showed an Li edge characteristic of Li_xMoO_2, and the amorphous region

corresponded to metallic Li edge. This material reports high capacities equating to storage of 6.24 Li, the authors believe this mechanism allows for a higher Li-ion number and postulate that this is due to its highly ordered mesoporous structure.

In addition to this study, Xia *et al*. also claim that their 2D MoO_2 sheets undergo a similar mechanism.[246] It should be noted that this is a composite structure, however the authors treat the material as a pure MoO_2 sheet in modelling. They show that 2D MoO_2 is stable, and that Li-ions have a strong affinity to the material, with an adsorption energy of -1.40 eV. Furthermore, their calculations show lower energy barriers for Li-ions to diffuse along the surface than in the channels, hence the potential for improved properties from a 2D material. The authors go on to show high capacities produced experimentally, 1875 $mAhg^{-1}$ initially at 100 mAg^{-1}. Furthermore, the material can be cycled to 10 Ag^{-1} and thus CV scans were used to prove the Li-ion storage mechanism depended on capacitive-like storage. *Ex-situ* XPS and XRD studies are used to prove that this material does not undergo a conversion reaction, as no evidence was seen for metallic Mo. However, similar to Shon *et al*., evidence for amorphous Li metal was reported, where they believe metallic Li would surround the sheets.[245] Xia *et al.* proposed that the 2D structure they created allows for this mechanism, which cannot occur in bulk MoO_2, which would likely mean that this would not have been evident in the Shon *et al.* study. Thus, it is unclear why some materials experience the conversion mechanism, where others do not.

1.8.3.3 A Note on the Activation Process

An activation process only appears to take place when MoO_2 is cycled in the wider voltage range of 0.01-3.0 V. Many studies refer to this process when an increase in capacity is seen over the first 30 or so cycles, although only a couple investigate further. Zhang *et al*. presented *in-situ* XRD patterns that showed a phase restructuring during the activation process (Figure 1.8).[242] They find that MoO_2 changes from monoclinic $P2_1/c$ to monoclinic $P2_1/n$, and this change then allows for a conversion process from the monoclinic $P2_1/n$ to take place. A study by Liang *et al*. supports this, and they create MoO_2 with a $P2_1/c$ and a $P2_1/n$ space group via different synthesis routes.[247] The $P2_1/n$ MoO_2 shows high capacity but large capacity loss and *ex-situ* XRD shows the material has become amorphous suggesting a conversion process. The $P2_1/c$ MoO_2 shows lower capacities, but improved stability over the small number of cycles recorded and *ex-situ* XRD showed evidence of amorphisation (at 0.01 V) and various Li_xMoO_2 phases, however MoO_2 peaks remained after cycling. This suggests that the material has not completed an activation process to allow for a full conversion.

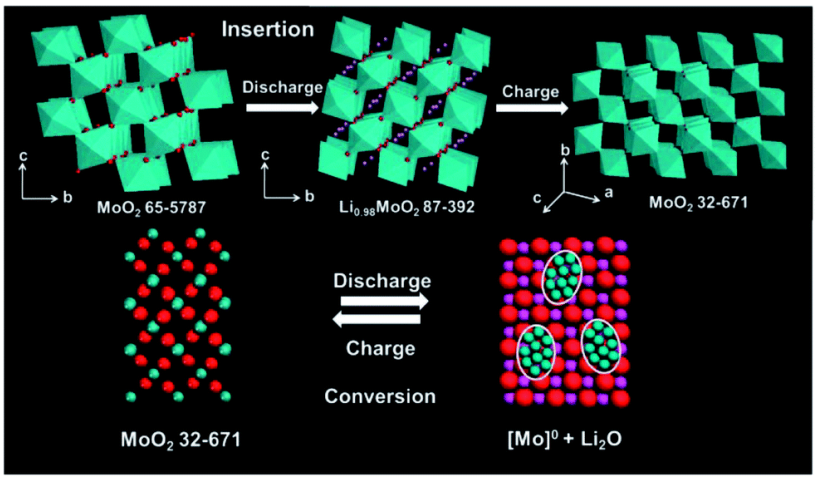

Figure 1.8 – Crystal structures of MoO_2 and lithiated forms during the activation process.[242] *Republished with permission of Royal Society of Chemistry from Journal of Materials A, Zhang et al., 2, 2014; permission conveyed through Copyright Clearance Center, Inc.*

Besnardiere *et al.* describe the activation process as a local rearrangement of electrode components to yield better percolation.[248] This study shows that the activation process only takes place in nano-particles smaller than 10 nm in size. Guo *et al*. reach similar conclusions and propose that there is an activation barrier in place, which prevents MoO_2 from undergoing the conversion reaction.[244] They use DFT studies to show that $LiMoO_2$ has an energy gap in its electronic structure, which substantially reduces its conductivity and therefore the kinetics become poorer after the intercalation step. This means that the material only has the ability to partially convert to Mo and LiO_2. As parts are converted back from Mo and LiO_2 to MoO_2, they lose their crystallinity as seen in *ex-situ* XRD. This transformation to an amorphous-like structure weakens Mo-O band strength and enhances the kinetics, which in turn allows more of the material to undergo the conversion reaction. This occurs until activation is complete and a full conversion mechanism can take place. To overcome the activation process, Ku *et al.* suggest a first cycle thermoelectrochemical activation at elevated temperatures to overcome the kinetic barriers in place. [241] They show that after this the structural rearrangement is complete, the material can make use of the conversion reaction in full, and cycling can continue at room temperature.

1.8.3.4 Amorphous MoO_2 for Li-ion Storage

Manthiram and Tang report that amorphous MoO_2 does not follow the same electrochemical mechanism as the crystalline phases.[249] The charge/discharge profiles show no plateaus suggesting a continuous single phase with lithiation. A capacity of 220 $mAhg^{-1}$ is achieved, equating to 1.1 Li insertion between 1.0 and 3.0 V. Further work by Ku *et al.* presents

amorphous MoO_2 as capable of high capacity and high rate cycling.[250] Their amorphous material was superior to the crystalline form as produces a capacity of 810 $mAhg^{-1}$ compared to 125 $mAhg^{-1}$ (at 100 mA g^{-1}). Initially, it was considered that the amorphous phase was storing Li ions via the conversion mechanism as this capacity fits the theoretical from a $4e^-$ reaction. The high rate capability of the material and the linear charge plot also seen in Manthiram and Tang's report, seemed to suggest otherwise.[249] Via EXAFS and XPS they confirmed the lack of metallic Mo or LiO_2, and no evidence of Mo-O bond cleavage. To allow for a four Li-ion storage without formation of metallic Mo, it was suggested that some of the electron density would be held in the oxygen centres. This is shown by a change in oxygen binding energy with lithiation and a Mo valance just higher than zero in XANES tests. Furthermore, ^{7}Li NMR studies were run to understand the Li-ion kinetics, which showed that there was a delocalisation of electrons and rapid movement of Li-ions to a rate in the order of 10^{-4} s. The properties are linked to structural defects in amorphous structures to allow for open Li-ion pathways.

1.8.3.5 The use of Nano-Structuring to Improve the Electrochemical Capability of MoO_2

Even in the first full cell made with MoO_2 in 1987, particle milling was used to reduce particle size. It was suggested that the large particles showed slow ionic diffusion and that lithium would insert radially into particles and thus only the outer layers would be able to be accessed due to the slow kinetics.[231] Thus, more recent research uses various techniques to nanostructure MoO_2 to improve its electrochemical properties.[200]

Work of Besnardiere *et al.* mainly focused on synthesis of various sized nanoparticles of MoO_2.[248] They presented the electrochemical properties of 30, 17 and 9 nm-sized particles. Interestingly only the smallest particles seem to undergo an activation process leading to a capacity of 600 $mAhg^{-1}$ (at C/10) compared to approximately 300 $mAhg^{-1}$ from the other particles. Other studies look to compare nano and micro-particles rather than a range of nano-sized particles. A study by Guo *et al*. compared ultrafine nanorods to bulk MoO_2, and they also saw a dependence of size on the activation process.[244] They studied the barriers involved in the activation process (discussed above) and found that the $LiMoO_2$ material has reduced electronic conductivity and poorer kinetics. Therefore, in a bulk material, this becomes extremely limiting and the material cannot achieve a full conversion reaction if at all. Nano-structuring improved the kinetics by reducing ion transport distances, having increased defects and weaker M-O bonds. With the weaker bonding allowing for improved conversion mechanism efficiency as evidenced by Raman in a complementary study.[241]

Furthermore, Kim *et al*. show nano-particles that access a higher capacity of 209 $mAhg^{-1}$ compared to 160 $mAhg^{-1}$ from the micro-particles (in a 1.0-3.0 V range).[227] They comment that the particle size is a key determinant to achieve its theoretical capacity. However, upon further cycling they find that the nano-particles show much higher instability, retaining 62% of their initial capacity over 50 cycles, compared to 80% in the micro-particles.

A study by Liu *et al*. created nano-plates and compared these to a bulk MoO_2 (a commercial material), where the nano-plates showed an initial capacity of 240 $mAhg^{-1}$ and only 158 for the bulk MoO_2 (at 1C, 1.0-2.5 V).[237] The nano-plates also showed superior rate results, the authors note that the bulk material is diffusion limited and thus the full use of the material is low. Further to these works, the Dunn group investigated nano- vs micro-particles with regards to pseudocapacitive properties.[235] They found that the nano-particles suppressed the phase transition during Li-ion intercalation (>1.0 V), and only showed lattice expansion due to the unfavourable phase nucleation in confined space, whereas the micro-particles showed the expected monoclinic-orthorhombic-monoclinic transition. Thus, the improved kinetics from a pseudocapacitive-like mechanism allowed for an improved rate performance. They do note that the nano-MoO_2 is particularly susceptible to surface oxidation, and this does not allow the material to perform as a high-power material; to improve this they form a carbon composite, as is discussed below.

Christiansen *et al*. conducted an in-depth study on the structural changes seen in MoO_2 when the size is reduced.[251] They use a combinatorial approach to discern the structure of nano-MoO_2. They find that the nanostructured material has a high concentration of defects that manifest themselves in a variety of ways, thus changing the atomic structure throughout the material. From pair distribution function (PDF) analysis, it is evident that in the nano-MoO_2 has disorder in local and long-range structure from the expected distorted rutile. This study proposes known defect structures of Magneli shear, De Wollf and interwoven models cannot account for this. The situation is complex, as the authors present evidence that all of these defects may be present and that no single model is able to encapsulate the observed defects. Furthermore, they also show that their crystalline material (also nano, 50-150 nm) also shows defects, yet the defect concentration is lower and therefore does not affect the average structure, seen in PDF profile. Interestingly they note that defects have been shown to alter the physical properties of the materials and thus suggest a link between this and the improved electrochemical properties seen in nano-MoO_2. Furthermore, Christiansen *et al*. propose the interwoven model for the nanostructured material; this is akin to a distorted NiAs structure. Cox *et al.* showed that lithiated MoO_2 also takes on a NiAs structure and thus,

may allow for less volume expansion and structural change during lithium intercalation, leading to the improved electrochemical performance seen in nano-MoO_2.[229]

1.8.3.6 Other Methods to Improve the Electrochemical Properties of MoO_2

Heat-treatment is often used as a preparative step to produce MoO_2 and some studies suggest this heat-treatment step is key to producing the electrochemical properties. Liu *et al*. examined this by studying an as-synthesised and heat–treated (at 500°C) MoO_2.[252] The as-synthesised material shows initial lithiation capacity of 720 $mAhg^{-1}$ at C/10 but shows a fast decline over the 30 cycles presented, whereas the heat-treated material possesses a capacity of 760 $mAhg^{-1}$ after 30 cycles. This group also repeated this in a MoO_2/carbon material, showing similar results yet still with no explanation on why this is.[253] Zhou *et al*. also presented a study on as-synthesised and annealed MoO_2/carbon fibres,[254] and proposed that improved properties come from a large number of defect sites and high specific surface, although they give no direct evidence for this. The only other study which appears to make comment on the effect of heat-treatment is that of Besnardiere *et al*. where it is noted that calcination improves the capacity yet cleans the MoO_2 which leads to dissolution into the electrolyte in the cell and thus more instability.[255]

Another method used to improve electrochemical properties of MoO_2 is pre-lithiation, as presented by Zhang *et al*. where lithiated nano-rods showed consistent stable cycling data (up to 15 cycles) where the pure MoO_2 seemed to fluctuate significantly.[256] Furthermore*, ex-situ* XRD after cycling showed that the pre-lithiated material maintained higher crystallinity. The authors proposed that the pre-lithiation reduces the volume expansion as the structure is already expanded and thus improves electrode stability.

1.8.4 Comparison of Electrochemical Properties of Pure MoO_2 as an Anode for Li-ion Batteries.

The comparison of available literature on pure MoO_2 is presented in Table 1.5. A variety of methods can be used to synthesise MoO_2 and as such a variety of morphologies were achieved. It is apparent that the literature lacks high rate cycling for MoO_2 materials with only a handful of studies looking at rates greater than 5 C (>4000 mAg^{-1}). This may be due to the inherent poor rate capability of MoO_2 due to the slow kinetics of the conversion process. Thus, any studies with higher rates tested are likely to have achieved a material that can store Li-ions via intercalation only or a pseudocapacitive process. Further to this, the long-term cycle ability of MoO_2 is barely presented, a small number of studies cycling for longer

than 100 cycles. Notably there is only a single study, which presents cycles in the thousands. Again, this is attributed to the pulverisation that takes place in due to the conversion reaction. Yet, even if only the intercalation mechanism is accessed, an expansion of up to 14% may be expected, leading to strain too.[234]

Table 1.5 - Comparison of electrochemical properties of various MoO_2 materials from the literature, showing the limited work in MoO_2 at high rate or long-term cycling.

Morphology	Synthesis	Initial Capacity ($mAhg^{-1}$)	Initial Current (mAg^{-1} *)	Capacity at *y* ($mAhg^{-1}$)	Current *y* (mAg^{-1} *)	Capacity at x ($mAhg^{-1}$)	Cycle x	Current at x (mAg^{-1} *)	Ref/year
Nano-spheres	Hydro	796	100	-	-	~375	20	100	[247]/2005
Plates	Rheological	484	100	-	-	478	20	100	[247]/2005
Nano-grains	Thermal Reduction	318	5 $mAcm^{-2}$	-	-	320	20	5 $mAcm^{-2}$	[257]/2008
Tremella	Hydro	538	0.5 $mAcm^{-2}$	350	5.0 $mAcm^{-2}$	300	20	0.5 $mAcm^{-2}$	[258]/2008
Mesoporous network	Templated WC + HT	630	C/20	90	1C	750	30	C/20	[259]/2009
Monolith	WC+HT	506	200	-	-	719	20	200	[260]/2011
Spheres	Hydro	445	1 C	~230	8C	300	200	1C	[261]/2011
Amorphous NP	WC+HT	810	100	705	5000	810	50	100	[250]/2012
Micro-capsules	Solvo	624	1C	300	5C	~600	50	1C	[243]/2012
Nano-rods	Templated WC + HT	521	C/20	260	1C	830	30	C/20	[244]/2012
Nano-flowers	Hydro	674	100	-	-	380	20	100	[262]/2013
Yolk-shell spheres	Hydro +HT	793	50	450	2000	662	50	500	[263]/2013
NP	WC+HT	543	100	8	2000	73	50	100	[264]/2013
NP	Hydro +HT	720	C/10	255	1C	750	30	C/10	[252]/2013
Porous nano-tubes	Thermal reduction	400	500	530	1000	720	70	100	[242]/2014
Hollow spheres	Hydro	675	100	-	-	359	50	100	[265]/2014
Film	Magnetron Sputtering	883	400	330	1600	762	100	400	[266]/2014
NP	WC+HT	600	C/10	-	-	~10	50	C/10	[248]/2015
Porous spheres	Hydro+ HT	887	100	391	2000	709	60	100	[267]/2015
Nano-plates	Hydro + HT	240	1C	125	50C	147	2000	1C	[237]/2015
Porous framework	Templated WC + HT	1814	0.1C	-	-	~1600	50	0.1C	[245]/2016
NP	WC+ HT	800	100	-	-	150	120	100	[268]/2016
Yolk-shell spheres	Solvo + HT	1095	100	438	4000	993	150	100	[269]/2019

*Unless stated otherwise.

1.8.5 Li-ion Storage Mechanism in MoO_2/Carbon Composites.

From the studies discussed so far it is evident that the mechanism for Li-ion storage in MoO_2 is complex and varies on the material. As the variety of composites is vast, once again the Li-ion storage mechanism is thoroughly explored.

The conversion mechanism is analysed by Tang *et al*. for MoO_2/reduced graphene oxide (RGO) composite.[270] The CV profiles showed evidence of a full conversion reaction, with the higher capacities to confirm this. Scanning transmission electron microscopy selected area electron diffraction (STEM-SAED) analysis showed that after charging, the composite became nanoporous as MoO_2 was converted to Mo metal nanoparticles, in a reversible process. Interestingly, they showed for pure MoO_2 nanoparticles this was not the case. After charging, only parts of the material were converted to Mo metal and much of it remained as $LiMoO_2$. This is substantiated in other studies on a variety of MoO_2/carbon composites.[253,271–273] Of which, Patil *et al*. note that the irreversible conversion in pure MoO_2 forms clusters of Mo metal which aggregate and can no longer participate in the conversion reaction leading to poor capacity. [273] Mo metal aggregation prevention is also seen in a study by Petnikota *et al*. which outlined the need for specific carbon content to allow this.[274] They created two MoO_2/graphene oxide (GO) composites with carbon content of 22 and 43 wt%. The 43 wt% composite showed stability with cycling, whereas the 22 wt% composite showed an initial activation process, causing an increase in capacity then an irreversible aggregation of metallic Mo. They noted that the higher carbon content gives more sites for the MoO_2 to be anchored to and hence reduces the metallic Mo aggregation. For comparison, the composite from Patil *et al*. only had 4 wt% carbon, and showed improvement from pure MoO_2 but also experienced the increase and decrease in capacity over cycles.[273] Also a study by Gao *et al*. suggests MoO_2 content less than 56 wt% is preferred for best stability via carbon absorption of volume expansion.[275]

Petnikota *et al*. go on to probe the Li-ion mechanism of the composites further, showing that the Li-ion storage mechanism is highly dependent on current density.[274] At low current density (100 mAg^{-1}) the material does not rely on the lithium intercalation mechanism however appears to rely on conversion and pseudocapacitive storage properties, whereas at higher current density (1000 mAg^{-1}) the material relies on the Li-ion intercalation and pseudocapacitive mechanism. This is evident in the CV profiles and *ex-situ* XRD confirms this. For high current densities, the material retains its crystallinity after cycling, but at low current density the material becomes amorphous. A report by Fu *et al*. adds to the understanding of

how electrochemical mechanisms are affected by rate.[276] The authors begin with a comparison of a MoO_2/GO composite with bulk MoO_2 (produced via the same synthesis route), where the bulk MoO_2 is limited electrochemically as it is unable to access the conversion mechanism. They found that even with a change in rate or with more cycles that this did not change, and only the intercalation reaction was accessed. In addition, this was shown to be irreversible, giving rise to high-capacity fade. Notably under the same conditions, the composite shows evidence of storing lithium via intercalation, conversion, and capacitance. They also report that with increasing cycle number the tendency toward the conversion reaction increases and as expected, the highest current densities show strong polarisation and therefore shifts in the voltage of the redox peaks in the CV. At the high current densities there is very little evidence for capacitive contribution. The study proceeds to show that the conversion reaction dominates at low current density and cannot be accessed to the same level at high current density, as would be expected due to the kinetics behind these mechanisms (Figure 1.9). E*x-situ* XRD is used after cycling to confirm this, showing that the low current densities lead to amorphisation of the material whereas at increased current density the peaks for the crystalline phase were observed. This clarifies the study by Petnikota *et al*. These findings are important as they show that MoO_2/GO composite can use three different storage mechanisms synergistically or independently depending on the electrochemical testing method. In addition, this further explains the poor rate response from MoO_2 is a move to intercalation dominated mechanism thus the theoretical capacity is capped at 209 $mAhg^{-1}$. The work by Fu *et al*. and Petnikota *et al*. helps to explain the anomalous and contradictory results seen in other papers.[274,276]

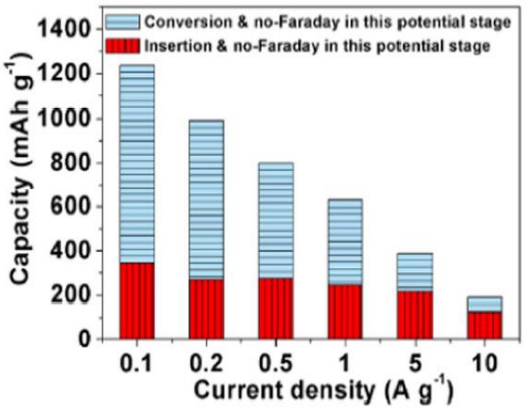

Figure 1.9 –A comparison of capacity from conversion or intercalation mechanism at different current densities for a MoO_2/GO composite presented by Fu et al. [276] *© The Electrochemical Society. Reproduced by permission of IOP Publishing Ltd. All rights reserved*

Some studies propose that there is no presence of the conversion reaction in the materials they have synthesised and tested. Yet propose little reason for this and lay out no evidence for other mechanisms.[275,277,278] However, as well as the generally accepted intercalation and conversion mechanisms discussed here, other mechanisms have been described in the literature.[245,246] Yao *et al*. found that from *in-situ* XRD that there is no evidence for the conversion mechanism in their MoO_2/C material, and a $Li_{0.98}MoO_2$ phase is maintained on full lithiation.[279] Furthermore, *in-situ* STEM-EELS showed that Li metal formed in the interphases between Li_xMoO_2. The authors go on to note that this allows for enhanced electrochemical properties as metallic Li improves conductivity. Another mechanism is shown in a MoO_2/graphene composite with oxygen vacancies, created by Zhou *et al*.[280] They probe this mechanism via XANES, EXAFS and XRD and find that the presence of oxygen vacancies causes unstable weaker Mo-O bonds which allows for the MoO_6 octahedra to break down to form MoO_4 tetrahedra (Li_2MoO_4). This process appears to be reversible with some loss in crystallisation, thus they link this with a gain in capacity up to 30 cycles. They believe the majority of the MoO_2 is irreversibly converted to Li_2MoO_4 and thus the capacity fades from here. They conclude that this mechanism is unique to the material they have created due to its structure and abundance of oxygen vacancies.

From these studies, it is apparent that the type of composite, carbon content and the synthesis of the materials can vastly affect the electrochemical properties. Besnardiere *et al*. studied carbon/MoO_2 core shell spheres, where they look at the effect of preparative method on the materials.[255] They comment on the capacity improvements that can be gained via heat-treatment, yet the 'cleaning' of the MoO_2 leads to faster dissolution. Thus, the presence of carbon does not boost capacity, as the lone carbon shells were tested and showed minimal capacity, but that the carbon prevents dissolution of the material. Liu *et al*. created carbon coated hollow MoO_2 spheres and note that the composite performed better than the pristine material due to the robust carbon coating, which reduces electrode pulverisation.[265] The restriction enforced by the coating forces the material to expand inward to the hollow space rather than outward which reduces electrode destruction. The carbon coating here acts as a durable framework to improve the cyclability. Further work by this group produced the same type of composite via a different synthesis method producing a material with further improved capacities showing that synthesis method is key to producing materials with desirable properties. [281]

Computational studies help to underpin the improvement in properties from MoO_2/carbon composites. [282,283] MoO_2/graphene composites showed improved conductivity due to Van

Der Waals interactions. Furthermore, the composites diffusion barriers were reduced compared to pure MoO_2 showing improved ion mobility. The ion storage between layers of MoO_2 and graphite allows storage of up to 8 lithium ions compared to the 4 in pure MoO_2, further aided by a reduced structural exapansion.[282] Yet these computational studies they comment on MoO_2 sheets on graphene sheets, thus may not be representative of experimental work, unless equivalent materials are able to be made.[282,283]

1.8.5.1 Comparison of Electrochemical Properties of MoO_2/Carbon Composites as an Anode for Li-ion Batteries.

The literature available on MoO_2 carbon composites spans many types of carbons, morphologies, and synthesis routes, and as such a comparison of the literature is summarised in Table 1.6. Although papers discussed above have suggested that specific carbon content is key for superior properties, when looking at the wider literature this does not appear the case as the carbon content ranges and yet properties can be similar. Nor is it clear whether a specific type of carbon yields preferred properties. It is evident that the capacities here are far superior to those seen in Table 1.4 for pure MoO_2 and forming a composite significantly improves the materials electrochemical properties. In general, the composites are also tested at much higher rates, yet studies at the highest rates are still lacking, and there are only a handful of studies which report rates over 10C (> 8000 mAg^{-1}, assuming only MoO_2 theoretical capacity is used). Furthermore, long-term testing is more common with many studies reporting over 100 cycles. The materials' stability can be vastly improved through compositing. After 1500 cycles, a MoO_2/ N-doped carbon composite still reported 570 $mAhg^{-1}$ (at 2 Ag^{-1}),[284] and similar is seen for a study that reports 456 $mAhg^{-1}$ over 1800 cycles at 5 Ag^{-1} for a MoO_2 carbon core composite.[285] These materials have shown capacities at extremely high current densities in a select few studies; at 10 Ag^{-1}, 198 $mAhg^{-1}$ was achieved, in another case, at 50 Ag^{-1} a capacity of 250 $mAhg^{-1}$ achieved, with the highest capacity appearing to be 835 $mAhg^{-1}$ at 20C.[246,270,286] However, such high rates appear to be anomalous, with the majority of studies testing up to 5 Ag^{-1}, where capacities over 700 $mAhg^{-1}$ have been achieved.[287,288] Considering these high capacities one would expect further rate testing unless the material becomes severely limited as has been seen in pure MoO_2.

Table 1.6 –Comparison of MoO_2/Carbon composites with same abbreviations used in previous tables.

Carbon Type	Morphology of MoO_2	C (%)	Synthesis Route	Initial Capacity ($mAhg^{-1}$)	Initial Current (mAg^{-1} *)	Capacity at *y* ($mAhg^{-1}$)	Current *y* (mAg^{-1} *)	Capacity at *x* ($mAhg^{-1}$)	Cycle *x*	Current at *x* (mAg^{-1}*)	Ref/ year
Semi-graphitised	Rods	36	Polymerisation +HT	1040	C/10	-	-	700	20	C/10	[289]/2007
Coating	Nano-spheres	6	Hydro + HT	570	1C	410	3C	513	30	1C	[290]/2010
Fibres	NP	14	WC+ HT	596	200	356	1000	327	20	1000	[291]/2010
Coating	Nano-fibres	11	Electrospin +HT	923	50	430	200	763	100	50	[292]/2011
Coating	NP	15	Hydro +HT	543	200	554	400	629	50	200	[293]/2011
Graphene	Rods	11	WC+HT	342	1000	407	2000	597	70	1000	[278]/2011
Graphene	NP	10	WC+ Hydro +HT	429	100	~400	500	1009	60	100	[294]/2012
Graphene	NP	22	WC+ HT	640	200	380	2000	480	100	1000	[295]/2012
Graphene	NP	33	Hydro	703	540	460	2045	530	1000	540	[271]/2012
Amorphous	Micro-spheres	3	WC+ HT	225	0.1C	210	5C	~175	30	1C	[277]/2012
MWCNT	Nano-flowers	18	Hydro	1243	100	408	1000	1143	200	100	[262]/2013
CNT	NP	20	Microwave	1384	90	570	1800	-	-	-	[296]/2013
Mesoporous	Micro-particles	37	WC+ HT	784	50	401	2000	668	50	100	[264] /2013
Porous	Hollow spheres	55	WC+ HT	574	50	-	-	619	80	50	[275]/2014
Amorphous	Hollow spheres	15	Hydro+HT	376	100	455	1000	677	80	100	[265]/2014
GO	NP	NS	WC +Solvo	779	100	507	500	524	30	100	[297]/2014
3D Graphene	NP	NS	CVD+ Hydro+ HT	921	50	537	1000	987	150	200	[298]/2014
RGO	Nano-belts	8	Hydro + WC+HT	974	60	250	50,000	~800	750	1000	[270]/2015
Sheets	Nano-sheets	18	Hydro +HT	1045	100	706	5000	1051	100	500	[287]/2015
Graphene	Micro-sphere	34	WC+ HT	1296	C/10	390	5C	1330	100	C/10	[299]/2015
Coating	Hollow spheres	12	Hydro +HT	910	0.5C	470	3C	~800	100	C/2	[281]/2015
Exfoliated GO	NP	43	GTR +HT	713	100	424	1000	878	100	100	[274]/2016
Nano-fibres	NP	11	Electrospin + solvo+ HT	859	200	453	2000	839	200	200	[300]/2016
Amorphous	Hollow spheres	22	Solvo+ HT	839	100	573	2000	560	100	1000	[301]/2016
RGO	Nano-plates	NS	WC+ HT	964	100	460	900	800	120	100	[268]/2016
Polydopamine	Hollow spheres	73	WC+HT	1139	500	433	4000	580	200	500	[302]/2016
N-doped wires	NP	14	WC+HT	646	500	200	5000	570	1500	2000	[284]/2016

Aerogel	NP	36	WC+HT	318	200	331	1000	490	120	200	[272]/2016
Graphene	NP	22	WC+ HT	1075	100	375	5000	1127	100	100	[303]/2017
N doped CNTs	Nano-rods	22	WC+ HT	686	100	726	5000	868	100	2000	[288]/2017
Carbon fibres	NP	NS	Hydro +HT	944	0.5C	540	1C	1117	50	0.5C	[254]/2017
Graphene	Hollow spheres	28	Solvo +HT	1109	0.1C	478	5C	414	1000	2C	[304]/2018
Amorphous	Flowers	55	WC+ HT	1898	100	578	5000	947	200	1000	[305]/2018
N-doped	Sphere	16	WC+ HT	1114	0.2C	835	20C	1138	130	0.2C	[286]/2018
Polypyrrole	2D sheets	35	Polymerisation + hydro +HT	1875	100	198	10,000	489	1050	1000	[246]/2018
RGO sheets	NP	4	Solid state+ hydro	1205	0.1 C	753	3C	1205	100	0.1C	[273]/2018
N, S-doped RGO	Nano-dots	NS	Hydro +HT	949	200	425	5000	1250	100	200	[306]/2018
Coating	NP	40	WC+ HT	1051	100	701	2000	952	100	100	[307]/2019
MOF derived	Nano-rods	3	Hydro + Reduction	1006	100	710	5000	787	300	1000	[308]/2019
Nano-fiber	NP	78	Electrospin + HT	1854	100	425	2000	1055	100	100	[309]/2019
Combined dots	NP	20	Hydro +HT	1007	100	911	1000	854	300	500	[214]/2019
RGO	Nano-sheets	63	Hydro +HT	1001	100	~800	1000	999	100	100	[310]/2019
SWCNT	Nano-sheets	20	Exfoliation	546	100	851	800	1085	170	100	[311]/2019
N-doped	Hydrangeas	26	Hydro +HT	899	100	406	2000	708	100	100	[312]/2019
Coating	Hollow Spheres	NS	WC+ HT	1085	500	774	500	1094	100	500	[313]/2019
Porous	Micro-rods	44	Sol Gel + HT	722	50	314	2000	167	1000	1000	[314]/2020
Core	Spheres	20	WC+HT	918	500	735	2000	456	1800	5000	[285]/2020
Amorphous	Micro-flower	39	Hydro +HT	842	200	510	4000	480	1000	1000	[279]/2020
N-doped	NP	29	WC+HT	1207	100	~200	5000	912	250	100	[315]/2021
RGO	Nano-rods	12	WC+Hydro+HT	1544	100	~700	1000	1078	200	100	[316]/2021
Nano-fibres	Nano-crystals	18	Electrospin +HT	752	200	432	2000	750	200	200	[317]/2021
Glucose derived	NP	24	sol-gel+ HT	928	100	210	1000	~400	60	100	[318]/2021
Carbon Black	Sheets	20	WC+HT	733	100	350	1000	275	60	100	[319]/2021

*Unless stated otherwise.

1.8.6 MoO_2 Composite Materials Beyond Carbon.

Carbon has been a key composite material due to ease of synthesis and cost, yet other materials potentially offer a better match for MoO_2 and further improved properties and Mo_2X materials have received some attention in this area.

Multiple studies on MoO_2/Mo_2C materials have shown improved electrochemical properties versus pure MoO_2. [320,321] A study by Zhang *et al.* showed that the Mo_2C does not contribute electrochemically but supports the stability of the MoO_2.[320] They note that the tight binding of Mo_2C, its high conductivity and the reduction in grain boundary resistance allow this composite to have a stabilising effect. Devina *et al*. report a similar stabilising effect, where they showed that Mo_2C was crucial in supressing the volume expansion during cycling in the MoO_2.[321] Cross sectional SEM showed a larger increase in the electrode volume for the composite without the Mo_2C. Furthermore, the Mo_2C containing composite showed initial capacities of 558 mAg^{-1} compared to 299 $mAhg^{-1}$ for a MoO_2/RGO composite (50 mAg^{-1}). This work does not appear to challenge that of simplistic MoO_2/carbon materials, however, the study by Zhang *et al*. does show capacities at the high end of what is reported for the carbon composites.[320] Other Mo_2X materials reported are in the form of Mo_2N as presented by Liu *et al*.[322] Hollow MoO_2 was coated with Mo_2N via a NH_3 nitridation and showed superior cycle stability compared to bare MoO_2. The composite produced 815 $mAhg^{-1}$ after 100 cycles at 100 mAg^{-1} vs only 396 $mAhg^{-1}$ from the bare MoO_2. The composite material still shows an activation step in the first 20 cycles, suggesting the expected MoO_2 Li-ion storage mechanism is maintained. Furthermore, the composite achieves a capacity of 415 $mAhg^{-1}$ at high rates (5 Ag^{-1}), which is linked to the porous structure, and the conductive Mo_2N coating.

Another heteroatom based Mo material is MoS_2 which in its own right is a promising electrode material.[323] Thus, a composite between MoO_2 and MoS_2 may produce some interesting electrochemical properties. Xu *et al.* created two composites with 91 % and 85 % MoS_2 content.[324] The composites showed initial capacities of 1167 and 849 respectively at 100 mAg^{-1} where pure MoS_2 showed 870 $mAhg^{-1}$. Although initially the MoS_2 appears to perform similarly to the 85% composite, the capacity fades quickly and there is a stabilising synergistic effect by forming the composite. Furthermore, both composites show improved rate performance over pure MoS_2 and MoO_2; with the 91 % composite showing the highest capacities at all rates. They suggest that the unique 3D architecture of the particles with fixed conductive MoO_2 improve the structural stability of MoS_2 and thus reduces the volume change seen in the MoS_2. A subsequent study includes a MoO_2/MoS_2 with different

structures, both with ~10 % MoS_2 content.[325] Both composite materials produced improved capacities compared to the pure counterparts, with a capacity at 1213 $mAhg^1$ is achieved at 100 mAg^{-1}, and 326 $mAhg^{-1}$ at elevated current density of 2000 mAg^{-1}. Lu *et al.* explored MoS_2 composites where they present a MoO_2 /MoS_2/carbon nano tubes (CNT) composite with improved stability.[326] They find that the use of CNTs for the composite improves its conductivity to 3.85 x 10^{-2} Scm^{-1} versus 1.32 x 10^{-2} Scm^{-1}, which results in a stable capacity of 320 $mAhg^{-1}$ at 1000 cycles (at 5 Ag^{-1}). The *in operando* XRD studies show that the conversion reaction only takes place in MoS_2 and is suppressed in MoO_2 which shows a good reversibility of its intercalation reaction, which is linked to the long-term stability. These materials' long-term capacities are notable, since very few studies show such materials cycled long term nor at a capacity this high. A study by Yang *et al.* showed a similar material, also bolstered by carbon; they find the addition of carbon improves the capacities from 443 to 840 $mAhg^{-1}$ after 200 cycles at 0.5 Ag^{-1}.[327]

Qin *et al*. investigated MoO_2/$MoSe_2$/N-doped carbon composite, which has good rate capability.[328] They found a capacity of 311 $mAhg^{-1}$ at 5.0 Ag^{-1}, with nearly a full recovery when returned to a low rate. A Si/MoO_2/C composite has also been described where the MoO_2 is a shell on Si to mitigate expansion and carbon is another outer shell to mitigate MoO_2 expansion.[319] With both Si and MoO_2 being high-capacity materials a reversible capacity of 1172 $mAhg^{-1}$ was achieved at 1.0 Ag^{-1} over 100 cycles. The authors showed the need for all the materials in combination as each separately show large degradation.

Oxide-oxide composites are also an area of interest. Jegal *et al*. created a mixed valence MoO_x composite with CNTs comprised of both MoO_2 and MoO_3 phases.[296] They showed that this mixture allowed a higher capacity to be achieved due to the higher theoretical capacity of the MoO_3. Improved lithium kinetics in this material results in a capacity of 900 $mAhg^{-1}$ at 90 mAg^{-1} and good rate capability. Rong *et al.* present a similar material and similar electrochemical results where a capacity of 930 $mAhg^1$ is achieved at 0.1 Ag^{-1}.[329] A different type of oxide-oxide composite was created by Duan *et al*. in the form of MoO_2/Mo_4O_{11}.[330] They show that the composite is able to complete the activation process within the first cycle, allowing for a quick transition to a conversion mechanism, whereas pristine MoO_2 is shown to take 20 cycles to complete the process. They postulate that this fast transition allows the structural integrity and no amorphisation occurs over the long activation process, thus giving higher stability from the composite versus the pristine MoO_2. A different approach was presented by Wang *et al*. where various MoO_x materials were synthesised, where a MoO_2/Mo composite showed the best results.[269] The composite showed improved

stabilities and produced capacities of 570 $mAhg^{-1}$ at 4.0 Ag^{-1}. The rate capability is linked to fast Li-ion diffusion and lower resistance, shown in EIS studies, plus the Dunn method showed a 92 % capacitive contribution at 1.0 mVs^{-1}. The improved results are linked to the increased metallic Mo availability which can contribute to a reversible conversion process and lower material resistivity.

These composites do not show significant improvement from the MoO_2/C composites, yet when considering designing electrodes for application specific properties, combining different electrochemically active materials becomes more attractive.

1.9 Research Objectives

The importance of batteries for moving to a sustainable, more technologically advanced future is clear. Development of novel materials for anodes also looks to be the best opportunity to boost energy density within the battery. As such, understanding and developing these materials is key.

The research reviewed above highlights the complexity of understanding Li-ion storage in selected metal oxide materials. However, key themes from this research highlights that synthesis is an important parameter to yield desired properties of a material. For Nb_2O_5 the 'memory of solids' is a known concept and is clearly seen when investigating the electrochemical response as there appears to be many contrasting studies on certain polymorphs of Nb_2O_5, in particular H-Nb_2O_5. Further to this, the variability in the electrochemical testing presented in the literature leaves gaps in understanding, particularly in how the materials perform over different voltage windows and in longer-term testing at high rates. The work in thesis looked to explore how heat-treatment effects the electrochemical properties of Nb_2O_5 via changing structural order or changing the material's phase. The aim of the work was to thoroughly test materials electrochemically to substantiate the high-rate capability of Nb_2O_5. Phases other than T-Nb_2O_5 were also to be synthesised and characterised to add to the limited knowledge on these polymorphs, with particular interest in whether the unique intercalation pseudocapacitive mechanism is found for the other polymorphs. In depth structural analysis was to be undertaken in order to establish whether this family of Nb_2O_5 polymorphs are structurally similar and whether phase, local or long-range order is key to producing electrochemical properties.

For MoO_2 the importance of preparative method is also seen in the literature, with heat-treatment and nano-structuring being apparently key to accessing specific ion storage capabilities. However, pure MoO_2 lacks long term cycling studies (beyond 50 cycles) and thus investigation of structural breakdown is poorly understood. The mechanism of Li-ion storage is also somewhat debated, especially with the activation process and conversion mechanism being inconsistent between different materials. Therefore, this work looked to thoroughly characterise MoO_2 electrochemically, explore the differences in physical and electrochemical properties with heat treatment and establish understanding of the activation mechanism within this system.

What is clear across the studies is that much more needs to be done to understand the mechanisms of Li-ion storage and solidify the understanding around these oxides. However, as well as adding to the understanding of these systems this work looked to propose a novel composite material system between Nb_2O_5 and MoO_2. Combining Nb_2O_5 and MoO_2 aims to exploit the promising properties of each oxide to yield a high-capacity high-rate anode material. As such, the work in this thesis looked to develop a synthesis method for the separate oxides which could be combined simply for the intimate mixing of oxides in a composite form. A selection of composites were to be developed with different ratios of the oxides to find the optimal balance between these materials, yielding the best electrochemical results. Lessons learnt from the pure oxide development and characterisation were to be implemented, with further preparative steps (heat-treatment) used to further improve the electrochemistry. The composites were to be thoroughly characterised to gain an understanding of their Li-ion storage mechanism and whether this is additive i.e., a combination of the mechanisms exhibited by the two oxides individually or occurs by a different style of storage.

Overall, the work described in this thesis aimed to provide a detailed understanding on the electrochemical properties of Nb_2O_5 and MoO_2 and how this relates to the materials physical characteristics as well as combining these materials to produce new composites with interesting properties.

2 Methods

2.1 Synthesis of Nb_2O_5, MoO_2 and Composite Oxides

A hydrothermal synthesis route was chosen, as this method of synthesis allows the formation of products at much milder conditions than would usually be needed via a solid-state route. Solvothermal synthesis can be defined as: "any heterogeneous or homogeneous chemical reaction in the presence of a solvent (whether aqueous or nonaqueous) above room temperature and at pressure greater than 1 atm, in a closed system".[331,332] The term hydrothermal applies when water is used as the solvent.

Herein the production of composite oxides is a key aim, and a synthesis route was required which was easily adaptable to produce both Nb_2O_5 and MoO_2. The addition of heat-treatment to the synthesis procedure allows further phase formation, specifically in the case of Nb_2O_5 which has multiple polymorphs.[65] The synthesis route was adapted from previous routes to achieve the production of Nb_2O_5, MoO_2 and a composite of these materials.[158,247,252,333–335]

Nb_2O_5 was synthesised via a hydrothermal synthesis at 225 °C for 72 hours. 10 g of ammonium niobate oxalate hydrate - ANOH, $NbO(C_2O_4)_2(NH_4) \cdot 5H_2O$, (Sigma Aldrich, 99.99 %) was dissolved in 30 mL of 10 %w/v oxalic acid, HO_2CCO_2H (Vickers Lab Ltd, 98%) in deionised water and charged into a 125 mL Teflon liner, within a steel autoclave. Following hydrothermal treatment, the solid product was separated via centrifugation and subsequently washed with deionised water (2 x 100 mL) then dried at 70 °C for 24 hours. The material was further dried *in vacuo* using a Büchi oven at 70 °C for 12 hours. The as-synthesised product was heat-treated in a ceramic crucible, to obtain the orthorhombic (600-800 °C) and monoclinic (1000-1300 °C) Nb_2O_5, in a box furnace (Carbolite, CWF1300) in air for 4 hours.

Monoclinic MoO_2 was synthesised via a hydrothermal synthesis at 225 °C for 72 hours. 10g of ammonium molybdate tetra hydrate, AMTH, $(NH_4)_6Mo_7O_{24} \cdot 4H_2O$, (Sigma Aldrich, 99.98 %) was dissolved in 30 mL of 10 %w/v oxalic acid in deionised water and charged into a 125 mL Teflon liner, within a steel autoclave. Following hydrothermal treatment, the solid product was separated via centrifugation, subsequently washed with deionised water (3 x 100 mL) and dried at 70 °C for 24 hours. The material was further dried *in vacuo* using a Büchi oven at 70 °C for 12 hours. Heat-treatment of the as-synthesised MoO_2 in a tube furnace

(Carbolite, Gero), at 300 °C in Ar (~5 $mLmin^{-1}$) was used to produce a secondary MoO_2 material. A MoO_2/C composite was produced via the same route however with the addition of 10% w/v of glucose ($C_6H_{12}O_6$, ACS Reagents) to the hydrothermal step.

The Nb_2O_5/MoO_2 composite oxides were produced using the same route, with proportionate amounts of Nb and Mo reagents to produce the required ratio composite. The 50:50 % composite was heat-treated after hydrothermal synthesis at 600 °C for 4 hours in Ar (~5 $mLmin^{-1}$) in a tube furnace (Carbolite, Gero) to produce a higher crystallinity material.

2.2 Physical and Chemical Characterisation

2.2.1 X-ray Diffraction

X-ray diffraction (XRD) was used to identify the materials synthesised and their crystallinity. Panalytical Aeris and Panalytical Empyrean diffractometers were used with Cu Kα1/2 sources. All materials were ground in a pestle and mortar and loaded into 16 mm diameter sample holders. 27 mm holders were used when there was sufficient sample available and holders with Si inserts were used when less sample was available. All materials were scanned from 10 to 90 °, with a 30 min scan time. In cases where higher quality X-ray data were required, 1 hr scans using an X'Pert Pro MPD (Panalytical) were used. For *in situ* heat-treatment with XRD analysis (Brucker D8 Advance, with Anton-Parr HTK900 heating stage), XRD measurements were acquired every 25 °C, between 30-800 °C at a rate of 10 $°Cmin^{-1}$. High Score Plus software (Malvern Panalytical) was used to match the XRD patterns from the available databases (Panalytical XRD database and PDF 4+). The inorganic crystal structure database (ICSD) was used for acquiring further reference data on the materials. Where required, Pawley refinement was conducted against the XRD data (GSAS II).[336]

2.2.2 Microscopy

2.2.2.1 Scanning Electron Microscopy

Scanning electron microscopy (SEM) is key to revealing particle morphology, size, and agglomeration. This becomes especially important when formulating electrode slurries and when considering how physical and electrochemical properties are linked.

Dry, ground samples were dusted onto stubs coated with adhesive carbon tabs for SEM imaging using a JEOL 7800F microscope; and the SEM electron gun was set to a voltage of 10 or 15 kV. SEM-energy dispersive X-ray spectroscopy (EDX, Oxford Instruments) mapping was performed using a 3-minute scan time and a 1080p resolution. AZtec software (Oxford Instruments) was used to analyse the maps and to produce coloured SEM-EDX maps.

2.2.2.2 Transmission Electron Microscopy

Transmission electron microscopy (TEM) is key to revealing particle morphology on the nano-scale. TEM allows for the primary particles to be described, giving more detailed information about particle shape, size roughness and presence of particle coating.

For TEM (FEI Talos), the powders were ultrasonically dispersed in methanol at a concentration of 1 $mgmL^{-1}$. 20 µL of this dispersion was pipetted onto Cu grids coated with holey carbon films (Agar Scientific), placed on filter paper and then allowed to dry under ambient conditions. A single tilt sample holder was used for TEM imaging. Scanning transmission electron microscopy (STEM) imaging and STEM-EDX was completed on the same sample set up with the same instrument, using the double tilt sample holder to reduce the background response. Velox software was used for image analysis of TEM and STEM images and AZtec software for STEM-EDX maps. For both SEM and TEM images, particle dimensions were measured using ImageJ software, where at least 150 particles were measured to create a logarithmic distribution.

2.2.3 Particle Size Analysis

Particle size analysis (PSA) was used as a complementary analysis to microscopy. Rather than measuring individual particles, PSA measures the particle size distribution over a larger sample population. Further data analysis also yields information on the materials preferred form in solution. Subsequent measurement and ultrasonication regimes can determine whether the primary particles are tightly bound as secondary particles, or freely dispersed.

PSA was carried out using dynamic light scattering (DLS, Malvern Zetasizer). 10 mg of sample was placed into 10 mL water and sonicated for 20 mins. This dispersion was then diluted at least 100-fold (depending on the sample adsorption and thus signal in the instrument) and the diluted sample was further sonicated for 5 mins. This sample was transferred into a cuvette, three scans were taken, and data averaged. DLS was only carried out on spherical

or near-spherical particles due to the approximations of the Einstein-Stokes equation.[337] The data were plotted as intensity, number and volume distributions.

2.2.4 N_2 Adsorption Analysis

N_2 adsorption/desorption analysis can give materials surface area, pore distribution and porosity. This technique has been described by Brunauer–Emmett–Teller (BET) and Barrett, Joyner, and Halenda (BJH) theories.[338] Typically, BET theory is applied to surface area where BJH is applied to pore distributions. Density functional theory (DFT) can also be applied to model and calculate the porosity of materials from the data collected.

All samples were dried at 120 °C *in vacuo* on a sample prep unit (Micrometrics) for 12 hours. Samples were then dried *in vacuo* on the instrument (Micromeritics 3flex) for 12 hours at 120 °C. A full isotherm was measured and the 3Flex software calculated key parameters using BET and BJH theories and non-local DFT (N_2 Tarazona Model).[339,340]

2.2.5 Infra-Red Spectroscopy

Infra-red (IR) spectroscopy was used here to assess the nature of surface groups on the materials which remained after synthesis. Functional groups can be identified due to the wavelength and absorption. Samples were measured (ATR-Bruker Vertex 70) with 40 background and 80 sample scans with a 4 cm^{-1} resolution over a 4500 to 500 cm^{-1} range.

2.2.6 X-ray Fluorescence Spectroscopy

X-ray fluorescence (XRF) spectroscopy was used to confirm the ratios of metal atoms in the composite materials. Samples were loaded on FluXana sample holders, covered with a Kapton film, loaded into cups and placed into the XRF sample holder units. An EZ scan was completed (Rigaku Primus IV Wavelength Dispersive XRF) on all samples with the data being compared to internal standards to identify the atomic composition. The atomic content was reported using the Nb_2O_5 and MoO_2 oxide composition.

2.2.7 Thermal Gravimetric Analysis

Thermal gravimetric analysis (TGA) was used to identify water content, surface species content and temperatures of any phase transitions in the materials. 10 mg of sample was loaded into an alumina TGA crucible and heated at 10 °Cmin^{-1} between 25 and 1000 °C in air (TGA/DSC-1, Mettler Toledo). Any samples containing Mo were analysed under N_2 to reduce sublimation of Mo.

2.2.8 X-ray Photoelectron Spectroscopy

X-ray photoelectron spectroscopy (XPS) was used to identify the oxidation states of the metals in the oxides formed. This was particularly key for the composite oxides, which may be a complex mix of oxides with mixtures of oxidation states of the metals. Furthermore, as XPS is surface sensitive, it gives an opportunity to assess surface species and how these may change with heat-treatment.

The XPS data were collected and analysed at the Photoemission Research Technology Platform, University of Warwick by Dr Marc Walker. The samples investigated were attached to electrically conductive carbon tape, mounted onto a sample bar with a layer of filter paper between the samples and the sample bar to ensure electrical isolation, before being loaded into a Kratos Axis Ultra DLD spectrometer which operates with a base pressure below 10^{-10} mbar.

The sample was illuminated using a monochromated Al Kα X-ray source ($h\nu$ = 1486.7 eV). The measurements were conducted at room temperature and at a take-off angle of 90° with respect to the surface parallel. Core level spectra were recorded using a pass energy of 20 eV (resolution approx. 0.4 eV), from an analysis area of 300 μm x 700 μm. The work function and binding energy scale of the spectrometer were calibrated using the Fermi edge and $3d_{5/2}$ peak recorded from a polycrystalline Ag sample prior to the commencement of the experiments. To prevent surface charging the surface was flooded with a beam of low energy electrons throughout the experiment and this necessitated recalibration of the binding energy scale. To achieve this, the C-C/C-H component of the C 1*s* spectrum was referenced to 284.8 eV. The data were analysed in the CasaXPS package using Shirley backgrounds. For compositional analysis, the analyser transmission function was determined using clean metallic foils to determine the detection efficiency across the full binding energy range. Mixed Gaussian-Lorentzian (Voigt) line shapes were used to analyse all regions except for the Mo 3d region. Here, in samples which exhibited screened and unscreened Mo (IV) states, an asymmetric Voigt (GL(20)T(1.5)) was used for the Mo(IV) screened components, while a modified asymmetric Lorentzian line shape (LF(1,1,35,280)) was used for the Mo(IV) unscreened, Mo(V) and Mo(VI) components. Where no screened/unscreened components were observed, Mo (IV) was fitted using the same line shape as the Mo(V) and Mo (VI) components.

2.2.9 Total Neutron Scattering

Total neutron scattering data were collected by beam line scientists Dr Helen Playford and Dr Ron Smith on the POLARIS instrument at ISIS, national neutron facility.[341] Neutron scattering is similar to that of X-ray diffraction; however, the different isotopic sensitivity allows for a different contrast. Total neutron scattering can provide information on the local order of a material via the pair distribution function (PDF). How well this correlates to the PDF of the expected structure can allow understanding of the materials structure.[342]

The samples were vacuum dried in a Büchi oven for 12 hours at 120 °C prior to loading in 8 mm diameter vanadium cans with indium wire sealing for the experiment. The samples were exposed to a 15 x 44 mm^2 neutron beam. The data were normalised by subtracting data collected from an empty can and was Fourier transformed to produce the PDF. The scattering data were converted to the PDF using GudrunN software, with a Q_{max} of 27 $Å^{-1}$ and a Lorch function being applied to the data.[343] Ideal neutron PDFs for the T-Nb_2O_5 and H-Nb_2O_5 structures were simulated from published crystal structures using PDFgui software.[69,344,345]

2.2.10 High Energy X-ray Scattering

High energy X-ray scattering were collected as a complementary method to total neutron scattering, with the aim to produce PDFs with different contrast. This is not possible from lab based XRD since the wavelength of X-rays is too short to give the high Q-range needed for good r-space resolution in the PDFs. Synchrotron X-rays, however, are generated over a large energy range and a high energy can be selected to use for PDF studies.

X-ray PDF data were collected at the I15-1 beamline at the Diamond Light Source. Samples were loaded into 0.5 mm borosilicate capillaries. Data was converted to PDF using GudrunX software, with subtraction of the empty capillary data and with a Qrange of 0.5-25 $Å^{-1}$.[343] Ideal X-ray PDFs for the T-Nb_2O_5 and H-Nb_2O_5 structures were simulated using PDFgui software.[69,344,345]

2.3 Electrochemical Characterisation

2.3.1 Anode Formulation and Casting

Anode coatings were produced by the co-dispersion of active materials with conductive carbon black (C65, Timcal) and PVDF (8 %w/v solution in 1-methylpyrrolidin-2-one (NMP)). A ratio of 70:20:10 % w/w (active material: carbon: binder) formulation was used for Nb_2O_5 materials, Nb rich composites and 50/50 composites. A ratio of 80:10:10 ratio in %w/w was used for MoO_2 and Mo rich composites. Firstly, the active material and C65 were ground using a pestle and mortar then dispersed in NMP using an ultra-sonication probe (2 × 5 min, allowing the formulation to cool between sonication to reduce solvent loss), before the PVDF solution was added. The slurry was mixed (THINKYMIXER ARE-250) at 2000 rpm (4 × 5 min, allowing the formulation to cool between sonication to reduce solvent loss). The ink was cast onto copper foil using a doctor blade at 50 µm blade gap and the electrode was subsequently dried in air at 80°C with further vacuum drying at 40°C for an hour. These electrodes were designed to be thin and highly porous to achieve high power capability.[346] Electrodes are further descried in Table A. 1.

2.3.2 Li Half Cell Production

For coin cell production (Figure 2.1), anodes (ø15 mm) and separators (ø18 mm, Celgard 2325) were cut out and dried *in vacuo* at 60 °C for 12 hours prior to cell construction. Coin cell casings were dried *in vacuo* at 60 °C prior to use or transferal to the glovebox. Cells were constructed either in a dry room (-45 °C dewpoint, Munters MDU) or in an Ar filled glove box (Inert, Pure Lab HE). The anodes were put against metallic lithium foil (0.25 mm, Pi-Kem), incorporating a separator and electrolyte (1.0 M $LiPF_6$ in 3/7 v/v ethylene carbonate: ethyl methyl carbonate with 1 % w/v vinylene carbonate (Soulbrain, PuriEL)). Coin cells were either crimped in a hydraulic crimper (at 1000 psi, MTI MSK-110) or a digital electric crimper (at 0.8 t, MTI MSK-160E) and used for galvanostatic cycling and EIS measurements.

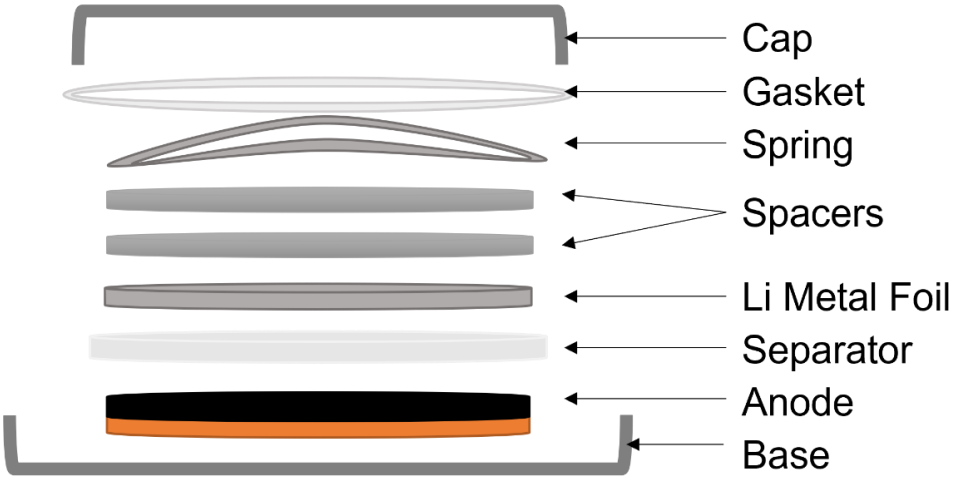

Figure 2.1 – Schematic of coin cell assembly

Swagelok cells were produced using the same anode coating as the working electrode (Section 2.3.1), with Li metal as counter and reference electrodes (Figure 2.2). The anodes were cut (ø12 mm) and dried alongside glass fibre separators (ø12.8 mm, Whatman) *in vacuo* at 60 °C prior to cell assembly. All Swagelok cell parts were dried at 60 °C and transferred to an Ar filled glovebox for assembly. Swagelok cells were tightened and parafilm (PARAFILM M) applied to the joints where the terminals and screw caps meet to prevent any electrolyte leakage or exposure to air/water. Swagelok cells were used for cyclic voltammetry (CV) testing.

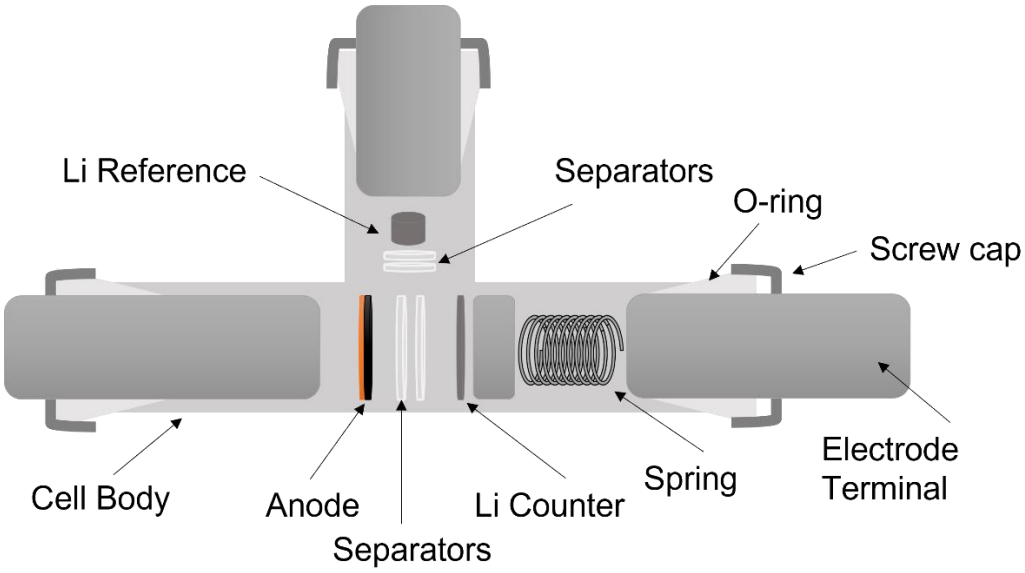

Figure 2.2 – Schematic of Swagelok cell assembly

2.3.3 Cell Testing

2.3.3.1 Galvanostatic Cycling

Coin cells were cycled on a BioLogic BCS potentiostat. All cells were rested at open circuit voltage (OCV) for 8 hrs to ensure electrolyte wetting. The cells were cycled under a galvanostatic cycling with potential limits. Voltage windows used include: 0.01-3.0 V, 0.25-3.0 V, 0.25-2.0 V and 0.9-2.0 V all versus Li/Li^+. All cells were treated to a C/20 formation cycle, where C is equal to the theoretical capacity, in the chosen voltage range before being cycled at a defined C-rate. The results were analysed using BT-Labs software (BioLogic) and differential capacity data was produced using the program. Capacity vs cycle number, capacity vs voltage (cycle profile) and differential capacity vs voltage plots were created from single cell data. However, for each material tested, under each cycling program, at least 3 cells were tested to ensure reproducibility. All numbers quoted in the text in this work were an average of at least 3 cells, with the errors quoted as the standard deviation between these results.

Under a rate sweep regime, after 8 hrs at OCV, cells were exposed to a change in rate every 5 cycles at rates: C/20, C/10, C/5, 1C, 5C, 10C, 20C, 50C, 100C, C/10, 1C. The higher rate cycles were cut removed from the regime, where the material was not able to reversibly cycle.

2.3.3.2 Cyclic Voltammetry

Cyclic voltammetry (CV) was performed on three-electrode Swagelok cells using a BioLogic VMP3 potentiostat. CV was taken every 5 cycles to understand how the Li-ion storage mechanism changed with cycling. The cells were rested at OCV for 8 hours, then subjected to a C/20 formation cycle in the chosen voltage window. Galvanostatic cycling at 1C was commenced for 5 cycles in the specific voltage range, then CV measurements were taken at 0.1 mVs^{-1} and 0.5 mVs^{-1} before cycling continued.

CV at increasing scan rate was used to analyse the materials' dependency on surface diffusion versus bulk diffusion via the Dunn method.[37] The cells were rested at OCV for 8 hrs and then cycled 5 times at 0.1 mVs^{-1} for the cell formation. The scan rate was increased to 1, 2, 3, 4, 5, 10, 20, 25, 30, 40, 50, 60, 70, 75, 80, 90 and 100 mVs^{-1} for a single cycle at each rate. The data were analysed using EC-Labs software (BioLogic) and the dependence on surface limited/capacitive mechanism is described by the power laws in equations 9-11 in Section 1.5.

2.3.3.3 Electrochemical Impedance Spectroscopy

Electrochemical impedance spectroscopy (EIS) and staircase potential EIS (SPEIS) measurements were performed on coin cells using a BioLogic VMP3 potentiostat. Prior to the SPEIS testing regime, the cells were rested at OCV for 8 hrs and were treated to a formation cycle at C/20 in the chosen voltage window, where C is the theoretical capacity of the active material. The cell was rested for 10 mins before SPEIS commenced and rested for 10 mins at each of the 20 potential steps in the voltage window. SPEIS was measured in a 10 kHz to 1 Hz frequency range. SPEIS measurement were undertaken on both lithiation and delithiation, then cycled 10 times at 1C before SPEIS was measured again. The data were plotted as impedance vs. voltage using EC-Labs software (BioLogic). The solid electrolyte interphase (SEI) and series resistance are equivalent to the high frequency response at 10 kHz. The medium frequency from 1 kHz to 10 Hz is equivalent to the interphase electronic contact and the charge transfer resistance. Finally, the resistance associated with diffusion (Warburg behaviour), is equivalent to the low frequency response at 1 Hz.[347,348]

To acquire EIS, the cells were rested at OCV for 8 hrs, then treated to a formation cycle at C/20 in the chosen voltage range. The cells were cycled up to a specific voltage (at 1C) and EIS was measured between 10 kHz and 1 Hz. The cell cycling was continued for 10 cycles before EIS was taken again. Nyquist plots were created from the data, which show real impedance vs. imaginary impedance, and were fitted to an equivalent circuit model using Zview software (Sribner) (Figure 2.3). The equivalent circuit model describes Nyquist plots with two semi-circles, where R_s is referred to as the series resistance, R_{SEI} is the SEI resistance and R_{CT} is the charge transfer (CT) resistance.[349–351] The series resistance describes any resistances associated with cell (e.g., cell body, electrodes and separators). The first semi-circle in a Nyquist plot corresponds to the SEI resistance and constant phase element (CPE), which describes the resistance caused by the presence of the SEI layer between the electrolyte and electrode. The second semi-circle describes CT resistance and CPE and refers to the resistance in the electrochemical reaction in which there may be a phase change. Finally, the diffusion tail, which here also described by a CPE, corresponding to Li-ion diffusion and takes form as a 45 ° line in a diffusion limited system (i.e., battery), but a 90 ° line in a surface limited system (i.e. capacitor).

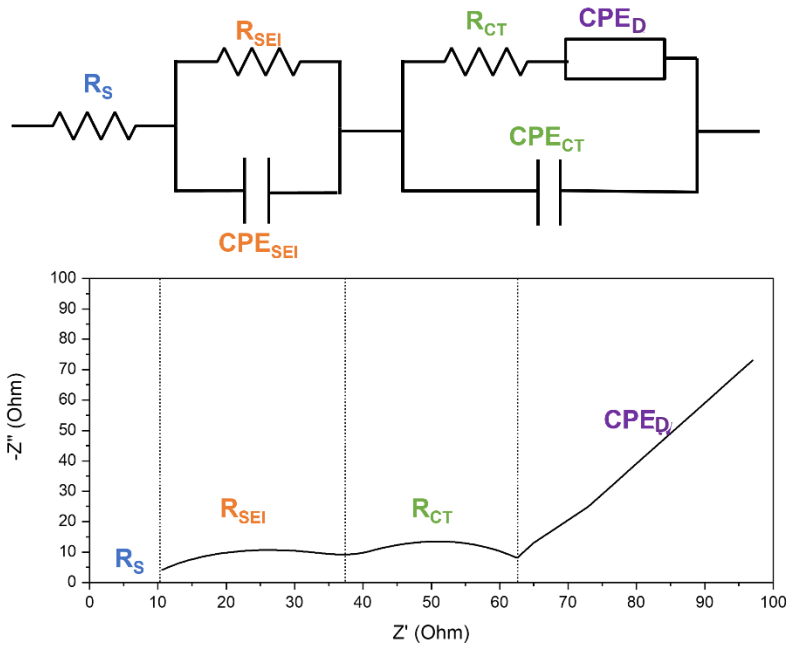

Figure 2.3 – Equivalent circuit model and equivalent typical Nyquist plot where R_s is series resistance, R_{SEI} is surface electrolyte interphase resistance, R_{CT} is charge transfer resistance and coordinating constant phase element (CPE). Were CPE_D describes the diffusion tail.

2.3.4 Ex-Situ Analysis

Ex-situ XRD on cycled electrodes was carried out to observe any structural changes of the active materials which developed during cycling. Coin cells were assembled and were studied using galvanostatic cycling as described above (Section 2.3.3.1). After cycling, the cells were transferred into an Ar filled glove box (Inert, Pure Lab HE) and disassembled using a de-crimping die in an electric crimper (at 0.8 T, MTI MSK-160E). Electrodes were separated out and electrolyte allowed to evaporate. When measuring the XRD pattern on an Aeris X-ray diffractometer (Panalytical), the electrodes were kept *in vacuo* at room temperature until analysis was undertaken. The electrodes were loaded onto a silicon insert in the XRD sample holder and scanned between 10-90 ° for 30 mins. When undergoing higher quality data collection for refinement, electrodes were loaded into an airtight XRD sample holder with a polyether ether ketone (PEEK) dome in a glovebox. These samples were loaded onto an Emperyean X-ray diffractometer (Panalytical) and scanned between 10-90 ° for an hour.

3 Niobium Pentoxide as a High-Rate Li-Ion Anode Material.

3.1 Premise

Considering the range of Nb_2O_5 polymorphs plus the concept of 'memory of solids', the literature on polymorphs other than the T-phase is limited. As these materials are affected by their crystal structure and synthesis route, there are a wide range of properties which could be achieved within this family. Often Nb_2O_5 is synthesised via a two-step synthesis, where a Nb-oxide is formed and then heat-treated to create the crystalline Nb_2O_5, where at least 500 ^oC is needed to achieve the lowest temperature phase (TT-). Yet most studies do not characterise this as-synthesised Nb-oxide before the heat-treatment step is commenced, thus it becomes difficult to understand where differences in physical properties may arise from when reporting on the same crystal phase. Not only will the characterisation of the precursors help to define physical properties but will also add to the understanding of Nb_2O_5 phase evolution. The TT- phase is known to be linked to the T-phase, with many studies classifying it as a lower crystallinity version of the phase. As some studies have shown, properties seen in the T-phase can be carried through to the TT-phase due to this relationship, so one believes that this may also be true for the precursor/ as-synthesised materials. Apart from the unique study by Lübke *et al.,* the literature is lacking study of as-synthesised phases, amorphous phases and other crystalline phases.[133] It is interesting there is a large lack of amorphous material research considering that in the area of catalysis, it is much more common, and the desired properties for both of these applications are very similar.[78,79,352] This work aims to describe a family of Nb_2O_5 materials and develop understanding into how synthesis and structure changes the electrochemical properties.

3.2 Synthesis of Nb_2O_5

A simple hydrothermal route was explored to produce Nb_2O_5. As this work looks to create composites later (Chapter 5), the adaptation of this synthesis method produce to MoO_2 (seen in Section 4.2) is key, thus a minimum temperature of 225 °C was required to allow the formation of MoO_2 in the composite materials. Figure 3.1 shows consistent X-ray diffraction (XRD) patterns for materials produced with a change in acid concentration and reaction

temperature. At 2 hours, there are impurities seen by XRD, which can be identified as unreacted ammonium niobate precursor. This XRD pattern is established as a semi-crystalline Nb_2O_5, due to the observed broad reflection peaks in the x-ray diffraction patterns as is further characterised later (Section 3.3). With both acid content and increased reaction time, the XRD patterns appear to be the same suggesting that the same material is produced despite different synthesis conditions. Whilst there appears to be little change in the XRD patterns, it is clear from transmission electron microscopy (TEM) images that an increase in acid concentration achieves higher aspect ratio nanowires (Figure 3.2a-c). At an acid concentration of 10 w/v %, there is little further difference in particle morphology with increasing reaction times after 6 hours (Figure 3.2d-h).

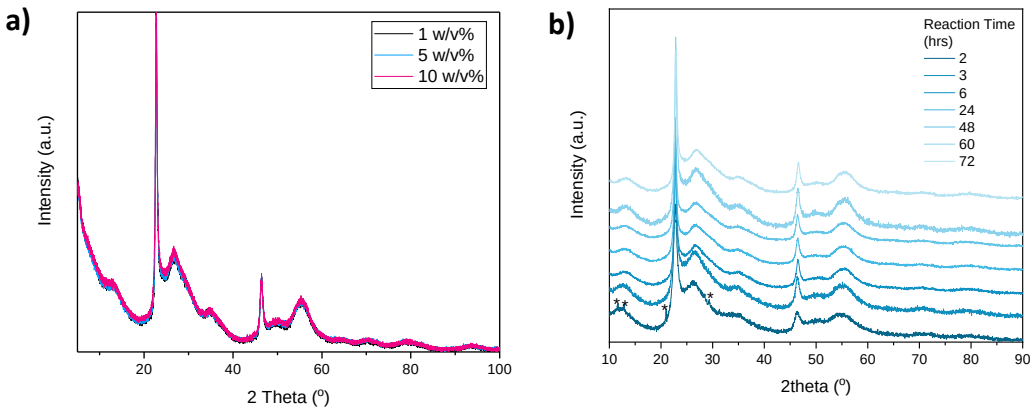

Figure 3.1 – (a) XRD pattern of niobium pentoxide synthesised with different acid concentrations at 72 hours, (b) XRD patterns of niobium pentoxide synthesised with 10 w/v% of acid but with a variety of reaction times, where '' denotes unreacted impurities.*

N_2 porosity measurements were used to further characterise the differences in the materials produced from the different synthesis conditions used (Table 3.1). All materials have the same form of hysteresis (H3) and isotherm (Type IV). [338,353] An increase in surface area is achieved between 3 and 24 hours, with all acid conditions giving high surface areas (> 200 $m^2\ g^{-1}$). With reaction time increase, the total volume in pores also increases, whilst the average pore size generally decreases. Regarding pH there appears to be no clear trend although the 10 w/v% acid concentration, at 72 hours, does appear to give the nanowires with the largest aspect ratio and highest surface area. Furthermore, these conditions are preferable for the synthesis of MoO_2, thus are used from here onwards.

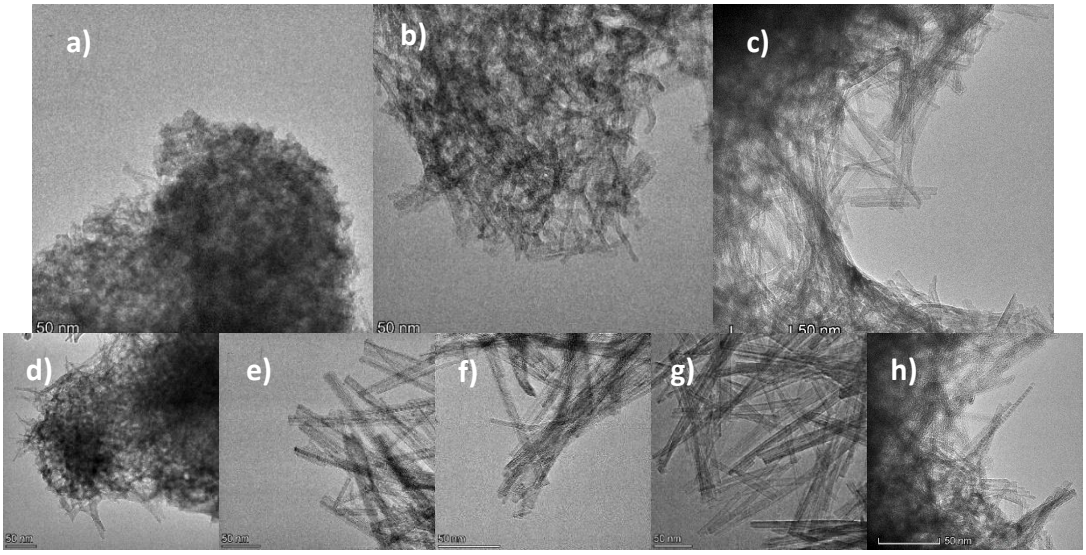

Figure 3.2 – TEM images on niobium oxide materials synthesised with 1 w/v% (a), 5 w/v% (b) and 10 w/v% (c) for 72 hours and materials synthesised with 3, 6, 24, 48, 72 hour reactions (d-h) respectively with 10 w/v% of oxalic acid.

Table 3.1 - Surface area and pore distribution values for niobium pentoxide materials under different synthesis conditions, calculated from full N_2 porosity isotherms (Figure A.1).

Oxalic Acid Concentration (w/v%)	Reaction Time (hrs)	BET Surface Area (m^2g^{-1})	DFT Total Volume in Pores (cm^3g^{-1})	BJH Adsorption Average Pore Width (nm)
1	72	263.4	0.36	5.7
5	72	264.9	0.43	7.8
10	3	206.4	0.25	6.8
10	6	244.9	0.36	8.3
10	24	260.4	0.37	7.0
10	48	260.1	0.41	7.1
10	72	278.8	0.42	6.8

3.3 Anisotropically Crystalline Nb_2O_5

The synthesis conditions yield an atypical form of niobium pentoxide, studied from this point is the Nb_2O_5 synthesised with 10 w/v% acid concentration, and 72 hours synthesis time and referend to as 'as-synthesised'. As seen in the XRD pattern, there are only two well-defined crystalline peaks (Figure 3.3). The crystalline peaks correspond well to the expected peaks from the T-Nb_2O_5 with minimal shift, indicating that this structure is linked to that of T-Nb_2O_5.

These features suggest an anisotropically crystalline material where the structure is poorly crystalline in one dimension, with more defined crystallinity in the other. If it is assumed that this phase is related to the orthorhombic phase this would suggest a preferred orientation along the [001] plane. This atypical pattern has been seen previously in literature with various explanations being proposed to the identification of the material. The identity of the material has been proposed to be a hydrated niobium oxide or niobic acid, where in some cases heat treatment could be used to form a crystalline Nb_2O_5.[77,82] Others have explained this result as a combination of a hydrated niobium oxide/niobic acid and crystalline pseudohexagonal Nb_2O_5.[334,354] Wang *et al*. identified the pattern as pseudohexagonal Nb_2O_5 with low crystallinity.[180] This structure is not well understood or well-studied, and further characterisation is needed to understand its structure and properties.

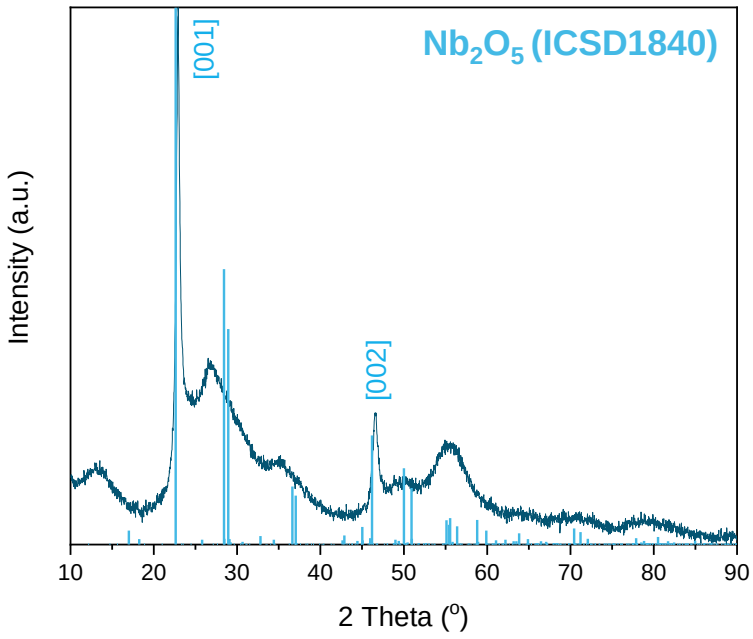

Figure 3.3 - XRD pattern of anisotropically crystalline niobium pentoxide with T-Nb_2O_5 crystal structure denoted in the blue sticks (ICSD 1840)[344].

Scanning electron microscopy (SEM) images show hierarchical 'flower-like' agglomerates of nanowires with a variety of sizes, where the smaller agglomerates look like 'hairy' spheres (Figure 3.4a, b). TEM imaging was used to understand the structure further (Figure 3.4c,d). The particles are nanowires with extremely high aspect ratios, where the widths of the particles have distribution centred at 4.0 nm. The lengths of the nanowires are hard to determine due to the nature of the complex network of particles, however from the SEM

images it can be seen that some of the wires can extend up to a micron. The morphology of the particles supports the fact that the structure is anisotropic and has a clear preferred orientation of growth as seen in the XRD pattern.

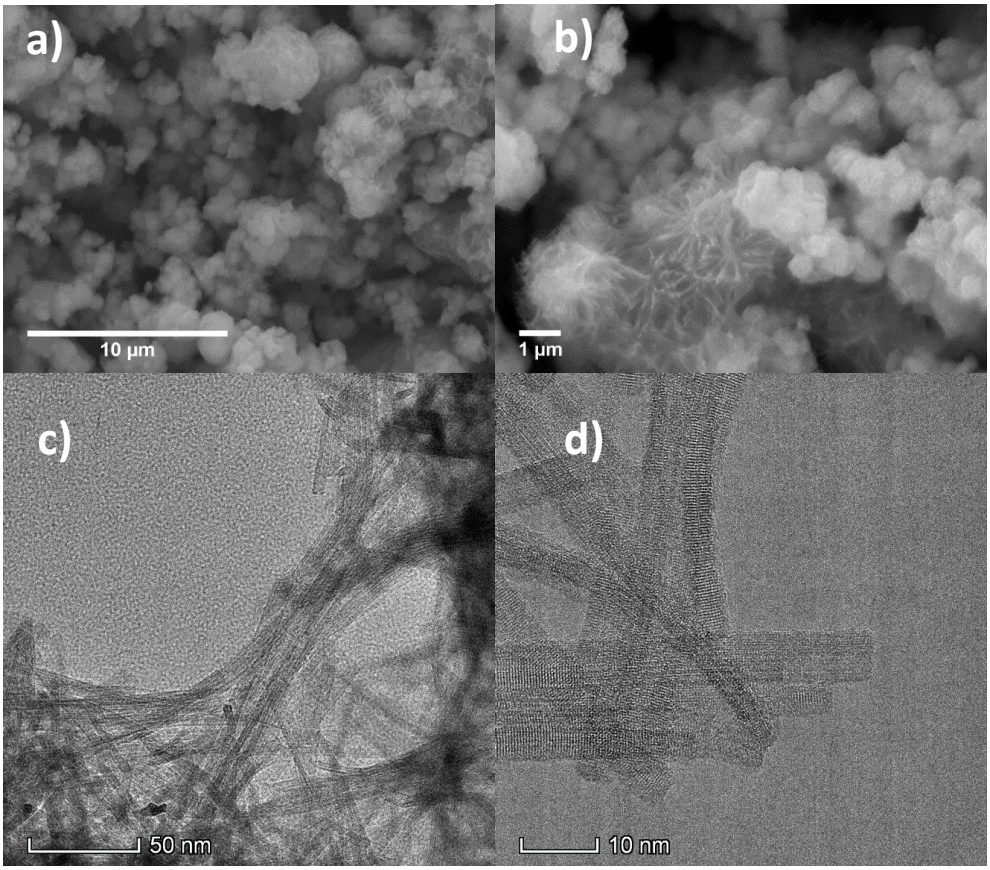

Figure 3.4 –SEM (a,b) and TEM (c,d) images of anisotropically crystalline niobium pentoxide produced via a 72 hour hydrothermal reaction at 225˚C with 10 w/v% of oxalic acid.

N_2 adsorption/desorption analysis isotherm shows a H3 hysteresis which is indicative of slit shaped pores or plate like aggregates (Figure A.8).[338,353] The isotherm is type IV - typical of a mesoporous material, supported by the pore distribution. Also apparent is micro-porosity below 2.0 nm with an average total pore size is 6.8 nm. This sample is a high surface area material with a BET surface area of 278.8 m^2g^{-1} (which is notably high for this type of material) designed for an energy storage application. Although high surface area is a favourable property for supercapacitors, it should be noted that in a battery this could compromise electrochemical performance due to the growth of a greater proportion of solid-electrolyte interphase (SEI). XPS was performed on the as-synthesised material, which showed (Figure A.2) a binding energy difference between the Nb 3d and O 1s is equal to 323.02 eV, which is indicative of Nb in the 5+ oxidation state.[355]

The TGA for the anisotropically crystalline Nb_2O_5 product shows two clear mass losses (Figure A.3). The initial mass loss can be attributed to loss of water. The second mass loss, between 200 - 400 °C, may be oxalate ions or other organics on the surface of the material from the synthesis, confirmed by infra-red (IR) spectroscopy (Figure 3.5). The change between 400 - 500 °C may be indicative of the phase change to an orthorhombic material, as this is expected between 500-700 °C when heating bulk material. After this point there appears to be no other changes in the material. The IR spectroscopy shows peaks that likely correspond with oxalic acid, carbonate or oxalate, on the surface or within the pores (Figure 3.5). There is also a broad peak at 3750-2750 cm^{-1}, which is assigned as water. Notably, all peaks reduce in intensity with heat-treatment and at 500 °C most peaks have disappeared, except for the peak corresponding to water. This may be due to the material readily reabsorbing atmospheric water to its surface due to its high surface area. These results are consistent with the TGA data, and it appears that heat-treatment 'cleans' the surface of the material.

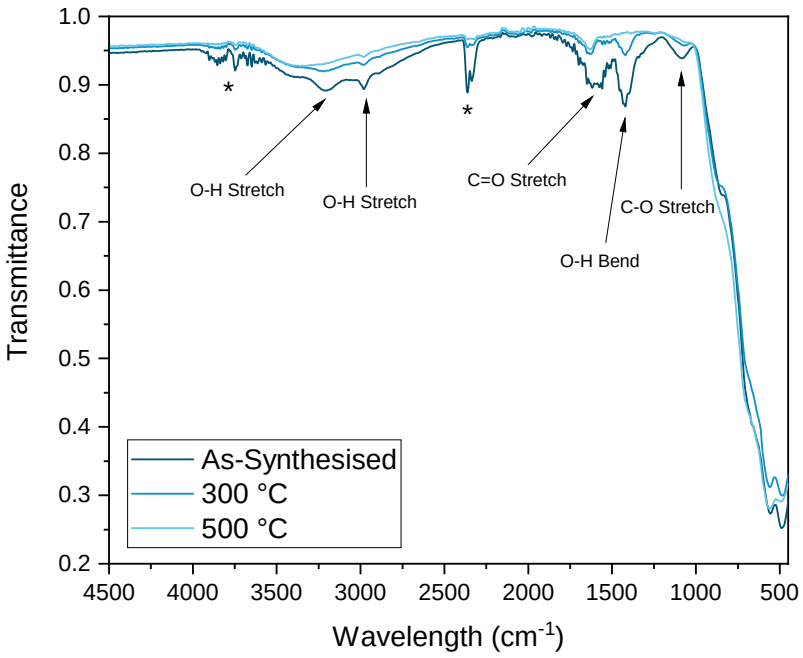

Figure 3.5 – IR spectra of anisotropically crystalline Nb_2O_5, as-synthesised and heat treated at 300 and 500 °C. key peaks are identified, stars denote response from CO_2 in the system.

Incremental heat treatment of the material was carried out in order to reveal more about the phase development in this material, with in-operando XRDs taken over the range of temperatures. The XRD patterns remain consistent and unchanging up to 480 °C (Figure 3.6), negating the idea that the as-synthesised material may be a hydrated or acid form of niobium

oxide. Therefore, one would suggest that this material is in fact an anisotropically crystalline Nb_2O_5, likely to exist with water and organic ions remaining on the surface or in the materials pores following hydrothermal synthesis route - and with a high surface area. The thermal treatment of this material shows a phase formation from 530 °C, as was expected in the TGA data. From this point, the T-Nb_2O_5 phase begins to form, appearing as sharper peaks already seen in the anisotropically crystalline Nb_2O_5 at 22.6 ° and 46.4 °, as well as the appearance of new peaks at 28.5 ° and 36.6 °.[344] Further heat-treatment of the anisotropically crystalline material reveals that at higher temperatures a further phase is formed (see Figure 3.7). This phase is matched to H-Nb_2O_5, which has a monoclinic structure.[69] From here, each different material is studied in individual sections, the focus being the as-synthesised form, the heat-treated at 600 °C and then heat-treated at 1000 °C - with a further study of materials heat-treated at 300, 500, 800 and 1300 °C.

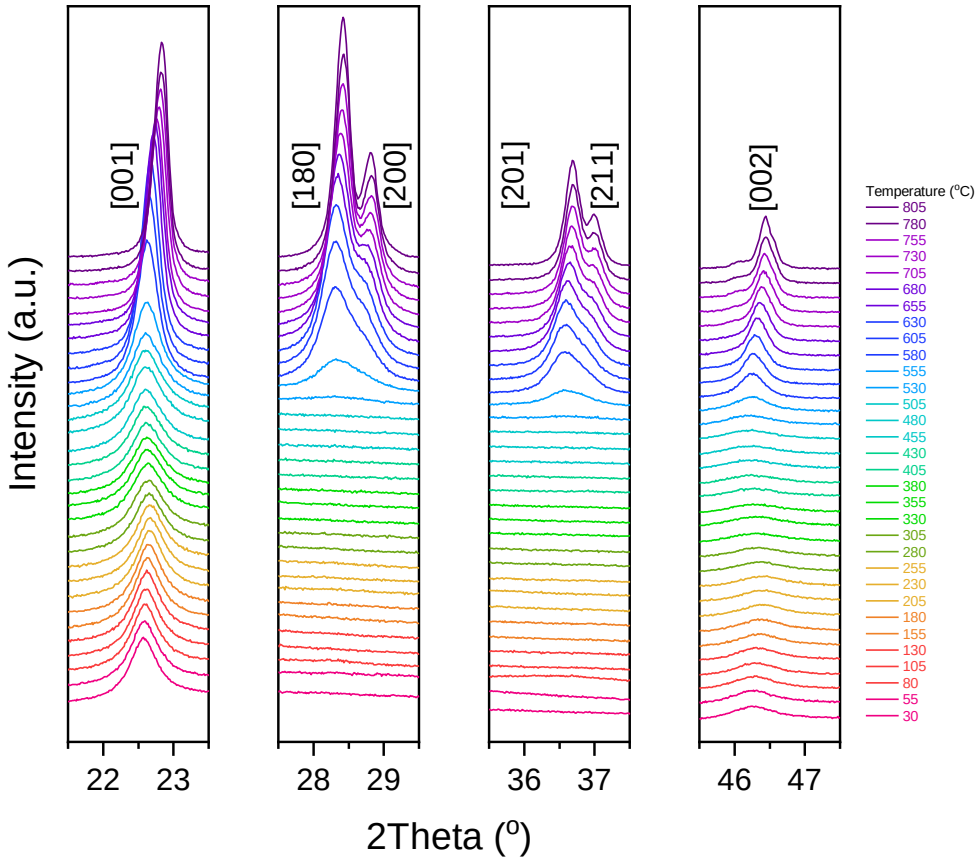

Figure 3.6 – Heat–treatment and in-situ XRD of the anisotropically crystalline material at 10 °Cmin^{-1} in air with XRD measurements taken every 25°C after a 30 min hold at this temperature, Figure highlights key regions of peak change.

3.3.1 Understanding the Structure of the Series of Niobium Pentoxides

Neutron and X-ray scattering were used to determine pair distribution functions (PDFs) to assess the structure of these materials. The PDFs show increasing long range order with heat-treatment, as expected from the improved crystallinity seen in the XRD patterns and with increasing particle size (Figure A.4 and Figure A.5). Up to 540 °C there is little order further than 15 Å, yet at 600 °C the order is improved considerably, as is seen by the crystallisation of the T-Nb_2O_5 in the XRD patterns (Figure 3.7). By 800 °C the PDF matches well with the PDF expected from the ideal T-Nb_2O_5 structure, with the neutron PDFs matching the ideal far better, compared to that of the x-ray, potentially suggesting that deviation lies with the Nb sites, as higher contrast is seen in the X-rays for heavier elements. With heat-treatment to 1000 °C, as the structure changes, changes in the PDFs are also seen but long-range order is present (Figure A.5). The PDF matches well to the PDF of H-Nb_2O_5 with just some small deviation seen, likely to be due to further crystallisation, as seen in the XRD patterns (Figure 3.7).

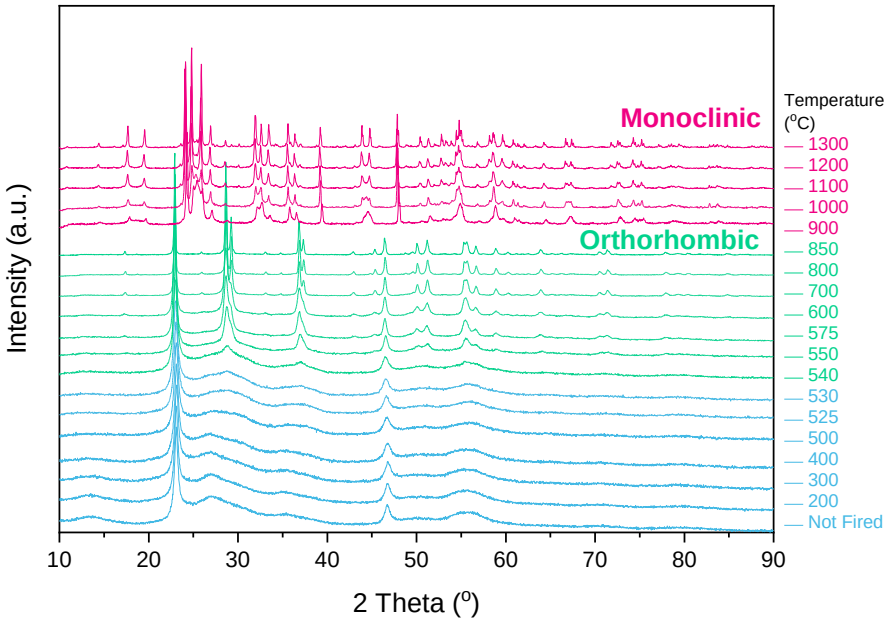

Figure 3.7 - XRD patterns of the as-synthesised material being heat treated from 200- 1300 °C at each temperature for 4 hours, with those materials indexed to the anisotropically crystalline phase in blue, T-Nb_2O_5 in green and H-Nb_2O_5 in pink.

PDFs for the local structure are shown in Figure 3.8. In the neutron PDFs there is a clear negative peak at 1 Å, this length would correspond to O-H in water (~0.96 Å) and C-H in organic surface ions at (~1.09 Å). The shift in this peak with heat-treatment to shorter lengths

suggest the cleaning of C-H containing molecules up to 540 °C, as also seen in the IR spectroscopy (Figure 3.5). Further to this, the intensity of the peak reduces with heat-treatment showing the removal of water (Figure 3.8), although the presence of water still at 540 °C may suggest this is bulk water rather than on the surface. This would agree with literature that has observed similar XRD patterns to this anisotropically crystalline form and suggest this to be a hydrated niobium oxide or niobic acid.[334,354] At 600 °C the O-H peak is diminished. The immediate local structure is similar regardless of phase, with reoccurring peaks in the neutron at 2.0, 2.8 and 3.8 Å and in the X-ray PDFs at 2.0, 3.3 and 3.8 Å. The exact position of the neutron peak at 2.0 Å deviates between materials and there appears to be broadening or potentially a second peak forming in this area. This distance is the closest Nb-O distance within the octahedra; thus, this is unsurprising that there are a range of distances experienced here depending on how the octahedra expand/contract in the structure or may be due to the presence of pentagonal bipyramids. The 3.3 and 3.8 Å distances are seen in all structures and these are Nb-Nb distances in edge-shared octahedra and stacked octahedra, respectively. Beyond this, the organisation of the octahedra look to cause the main differences between the structures, and thus the differences in long range order. The presence of pentagonal bipyramids and split occupancy Nb sites, cause further complexity within this family of materials, and it is likely that although these are expected only in the T-phase, they may also occur in the semi-crystalline form, or carry over to the monoclinic form as a defect. As such, further structural analysis is included in the corresponding sections for each material that follow below.

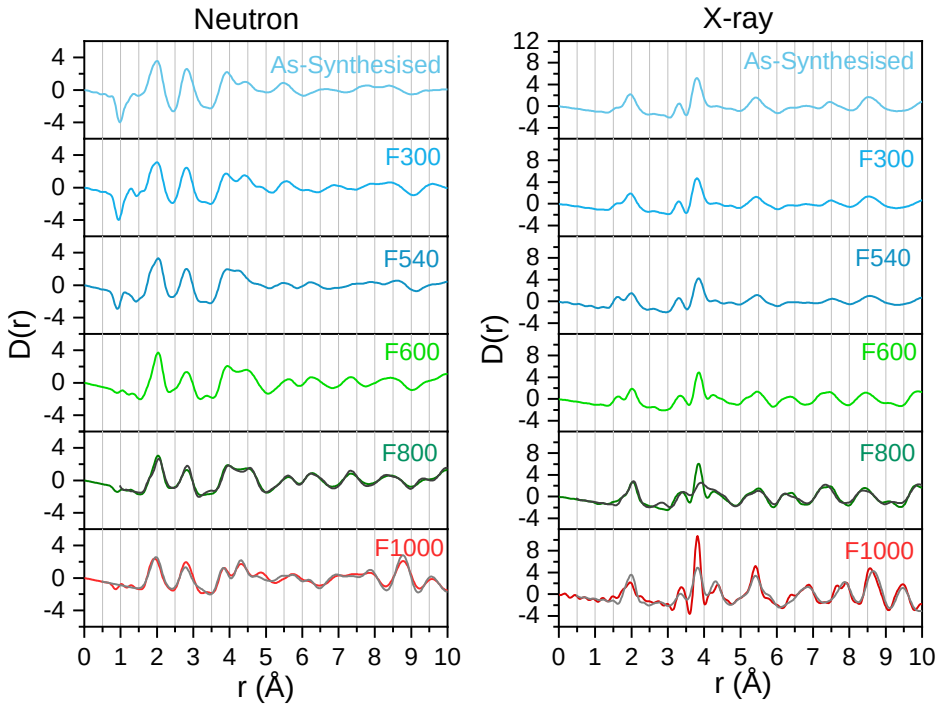

Figure 3.8 – Neutron (left) and X-ray (right) PDFs for Niobium pentoxide materials treated with increasing heat-treatment up to 1000 °C. The ideal T-Nb_2O_5 PDF is overlaid on the 800 °C PDF in black, and the ideal H-Nb_2O_5 PDF is overlaid on the 1000 °C in grey.[69,344]

3.3.2 A Series of Anisotropically Crystalline Niobium Pentoxide Materials.

The anisotropically crystalline structure is observed in the as-synthesised form, and when this material is heat-treated up to 500 °C. The XRD patterns are consistent up to 500 °C, with the particle size and morphology appearing unchanging (Figure 3.10). TEM particle counts further confirm this, where the distribution is mostly unchanged (Figure A.6). The PDF analysis suggests some improvement in long-range order with the increased temperature of heat-treatment (Figure A.4). In the X-ray PDFs, the structures of these anisotropically crystalline materials look very similar, with only some changes in peak intensity, especially for peaks at 1.6, 6.7 and 8.6 Å (Figure 3.9). The last two of these distances appear to correspond to Nb-O distances when compared to the ideal T-Nb_2O_5 partial PDFs (Figure A.7). However, in the orthorhombic structure there does not appear to be a 1.6 Å distance. Although a similar result was seen in a study of Nb_2O_5 growth where a 1.8 Å distance was associated with Nb-O distances in the octahedra, which also could not be described by a T-Nb_2O_5 model.[356] The shorter length of 1.6 Å does not easily lend itself to an Nb-O distance so

the real nature of this is unknown. When considering the neutron PDFs, the similarity between materials in peak position and intensity appears lost after 6 Å. All samples show a peak at 0.95 Å for a O-H bond corresponding to water, which is significantly reduced at 540 °C. Also peaks at 2.0, 2.8 and 3.9 Å appear relatively consistent between samples. These correspond with Nb-O and O-O distances. This appears to show that there is consistency in the forming of Nb-O octahedra yet the organisation of these differs between the samples. Further to this, as with T-Nb_2O_5, all Nb-O correlation may not be associated with octahedra with pentagonal bipyramids existing within the structure, hence the broadening of some of the peaks in the PDF patterns, as multiple similar distances may exist. Although the local order is defined, with changes in bond angles or octahedra distortion the longer-range structure cumulatively appears smeared. Furthermore, with the lack of heat-treatment here, it is unlikely that the crystals are fully developed which will lead to the PDF dampening. As such, the long-range order becomes more definite with the introduction of heat-treatment. Without further in-depth analysis the exact structure of the anisotropically crystalline form cannot be discerned.

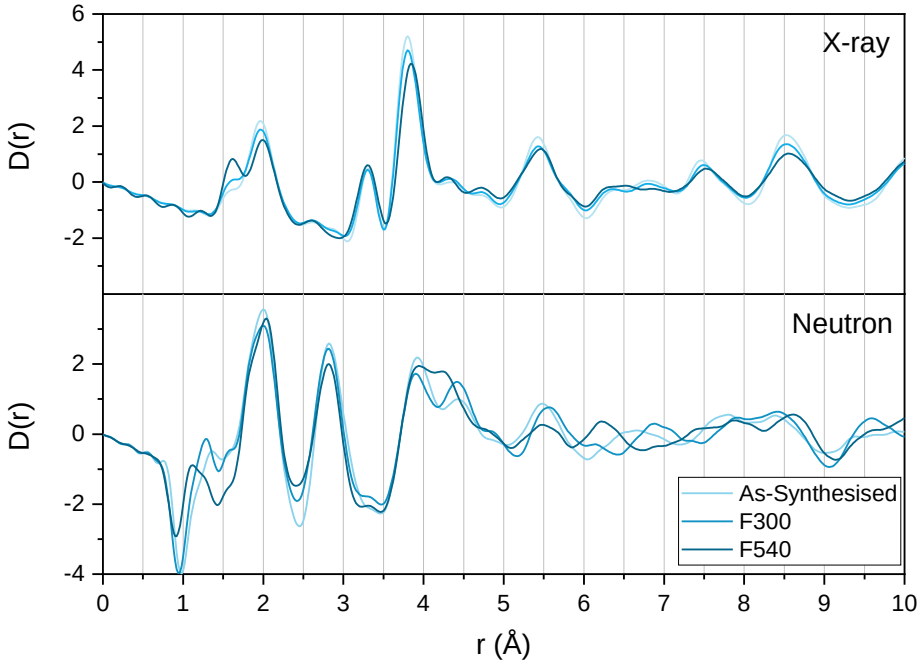

Figure 3.9 – Short range X-ray (top) and neutron (bottom) PDFs of anisotropically crystalline materials, as-synthesised and heat-treated at 300 and 540 °C.

Further physical characterisation shows the materials maintain porosity with heat-treatment (Figure A.8). However, the surface area increases with heat-treatment, with BET surface area

of 278.8, 296.5 and 321.1 m^2g^{-1} for as-synthesised, heat-treated at 300 and 500 °C materials respectively. Furthermore, although the pore distributions look similar, the 500 °C sample shows a larger volume of pores in the mesoporous range compared to the other samples. This is shown by an increase in total pore volume from 0.42, 0.51 and 0.72 cm^3g^{-1} for the respective samples. This may be linked to the losses seen in the TGA, where surface molecules may be preventing the full surface area and pores from being accessed.

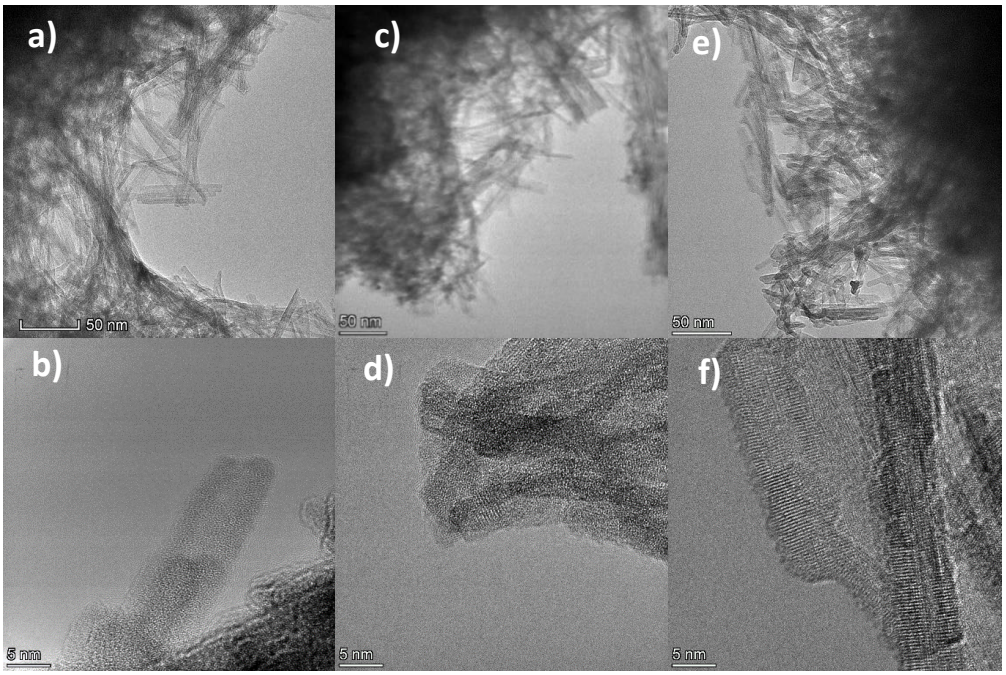

Figure 3.10 – TEM images of as-synthesised (a,b), heat treated at 300 (c,d) and 500 °C (e,f) anisotropically crystalline materials.

3.3.2.1 Electrochemical Properties of Anisotropically Crystalline Nb_2O_5.

3.3.2.1.1 Electrochemical Properties of As-Synthesised Anisotropically Crystalline Nb_2O_5.

The basic characterisation of this anisotropically crystalline material has been seen previously yet the electrochemical properties had not been reported before this work.[77,82,180,334,354] For T-Nb_2O_5, the most common voltage window used in the current literature is 1.0 – 3.0 V, to avoid an irreversible phase change at ~0.8 V, during formation cycle. However, some work suggests that a wider voltage range can be used. [133,136] As there is a mix of voltage windows used in the literature there is no guarantee that a voltage window which is appropriate for T-Nb_2O_5 would also work for the anisotropically crystalline form, thus multiple voltage windows were tested. As this material has a very high surface area, a

very low voltage cut off is avoided as this may promote the reoccurring degradation of SEI and thus electrolyte deterioration. Therefore, a moderately low voltage cut-off of 0.25 V is used. To avoid the phase formation at 0.8 V and as this is also known to be the onset voltage for SEI, a higher cut-off of 0.9 V is also tested. In summary the following windows were used: 0.25-3.0 V, 0.25-2.0 V and 0.9-2.0 V. Except for the initial few cycles this material performs similarly across all voltage windows (Figure 3.11). At 200 cycles, the average capacity is 63 ± 2.7, 65 ± 3.6 and 59 ± 0.7 $mAhg^{-1}$ for the broad, medium, and narrow windows, respectively. Furthermore, the differential capacity plots also show little difference across the voltage ranges (Figure 3.11, bottom). As such, an irreversible phase formation reported for T-Nb_2O_5 at approximately 0.8 V does not appear for this material.

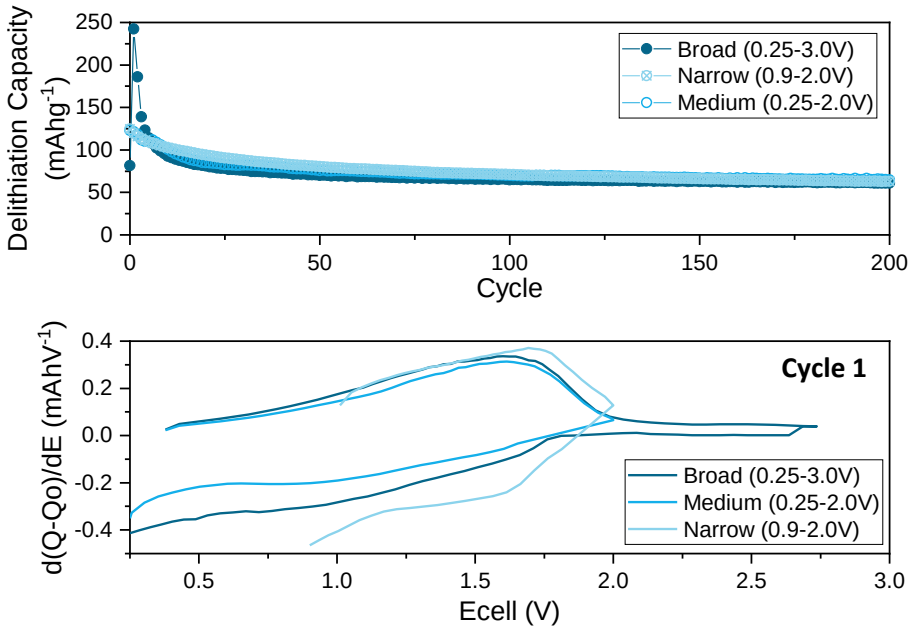

Figure 3.11 - (top) Galvanostatic cycling of as-synthesised anisotropically crystalline Nb_2O_5 in different voltage windows at 1C, and the respective differential capacity plots of cycle 1 after formation. (bottom)

The broad window shows an initial capacity (after formation) higher than the theoretical capacity of Nb_2O_5. Over lithiation has been reported for Nb_2O_5, where some Li-ions can also become trapped in the structure,[140,141] also Meng *et al*. comment on the availability of extra Li-ion storage sites in different phases being possible.[172] Thus, a higher capacity can be expected for this material as both the high surface area and structural disorder may increase the number of Li-ion sites available. After the high initial capacity, there is a large loss in capacity in the next couple of cycles, this may be due to the formation of SEI, which will be

particularly large for this material due to its surface area. Overall, there does not seem to be an obvious need to limit the voltage window of this material, thus from here the anisotropically crystalline Nb_2O_5 materials will be tested in a 0.25-3.0 V window.

This material shows the ability to be cycled to 100C with an average capacity of 18 ± 2.8 $mAhg^{-1}$ at 100C and a 96 % recovery when returned to C/10 after high-rate cycling (Figure 3.12a). Longer rate testing was performed at rates C/5, 1C and 20C (Figure 3.12b). The tests at C/5 and 1C barely differ and by 200 cycles, average capacities are 64 ± 3.6 and 63 ± 2.7 $mAhg^{-1}$, respectively. At 20C the capacity loss is more noticeable, where the average capacity at 200 cycles is 43 ± 7.6 $mAhg^{-1}$. These results show that this material is promising as a high-rate material, as it can be cycled to 100C and is stable over 200 cycles at a rate of 20C.

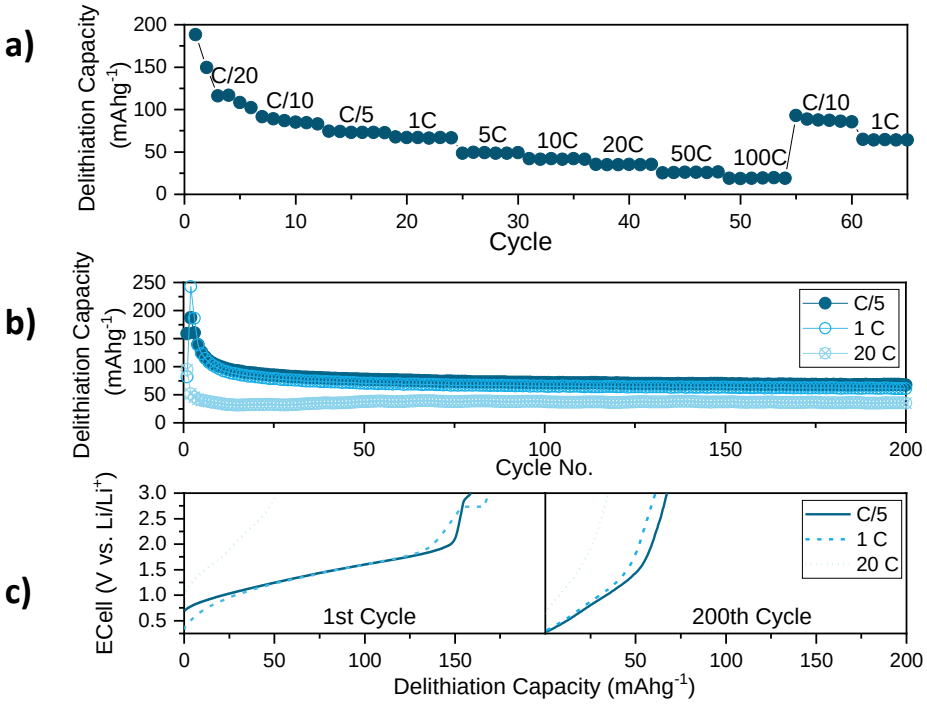

Figure 3.12 – (a) Rate sweep from C/20 to 100C with recovery to C/10, (b) Galvanostatic cycling at increasing rate over 200 cycles, (c) charge profiles at the different rates from 1st and 200th cycle, all in 0.25-3.0 V window for as-synthesised anisotropically crystalline Nb_2O_5.

The material appears to maintain its structure with cycling as shown in the *ex-situ* XRD (Figure A.9). Notably, with cycling the broad peak at 26 ° flattens out and the peak at 23 ° shows shifting and broadening. This suggests that the [001] plane is expanding to accommodate the ions and potentially losing order with continued cycling, this is also indicative of Li-ion trapping. The charge profiles at C/5 and 1C appear to be linear to ~2.0 V, where there is an inflection point (Figure 3.12c). This inflection drops in voltage to ~1.5 V

after 200 cycles. This may be indicative of a phase change in the material to facilitate storage of the Li-ions. As this material is assumed to be related to the T-Nb_2O_5, one would expect a continuous charge profile indicative of the intercalation pseudocapacitive storage mechanism. However, this suggests that the material undergoes a change to accommodate the ions, perhaps a lattice expansion as seen in the *ex-situ* XRD. Interestingly, at 20C the profile appears to be linear, thus this suggests that with higher rates the storage mechanism may change to a pure intercalation pseudocapacitive approach, via storing Li-ions in easily accessible channels. Therefore, CV tests at various scan rates were used to analyse the capacitive versus diffusion limited storage capability (Figure 3.13).

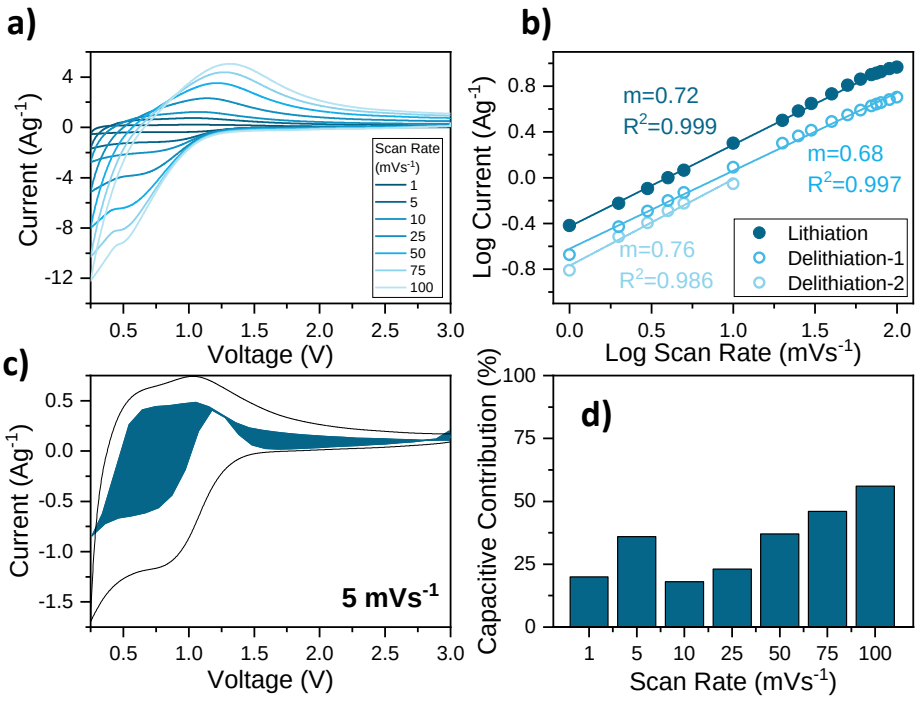

Figure 3.13 – a) CV profile of as-synthesised anisotropically crystalline Nb_2O_5 at increasing scan rate 1 to 100 mVs^{-1}, b) Log plot of current versus scan rate of redox peaks, with linear fits which have R^2 of at least 0.986, c) CV profile at 5 mVs^{-1} with shaded section as the capacitive contribution and d) the capacitive contribution at increasing scan rates.

The CV profile for this material shows a set of broad redox peaks with a second peak/shoulder in the delithiation process at low scan rates (<10 mVs^{-1}) (Figure 3.13a). The shoulder on this has been known to be due to valance variation during cycling i.e., where there is not a consistent change from one valance state to the other across all metal centres simultaneously, suggesting that a continuous valance change does not take place.[130] The

delithiation peaks combine to form a single peak at higher rates, where both peaks in the set show peak shift with increasing rate. Peak shift is expected to be due to an increase in ohmic resistance due to the insulating nature of Nb_2O_5. The log plots show gradients (b-values (Equations 9-11)) of higher than 0.5, suggesting that the Li-ion storage mechanism is not only diffusion limited but relies on a capacitive storage mechanism (Figure 3.13b). When the capacitive contribution is separated, there is a general trend to increasing capacitive contribution with increasing scan rate (Figure 3.13d). This is expected due to the fast kinetics of a pseudocapacitive storage type rather than intercalation.

In the staircase potential electrochemical impedance spectroscopy (SPEIS), the first lithiation cycle shows a decrease in impedance after 1.5 V (Figure A.11), which coincides with the redox peak position. The decrease in impedance is likely to be due to lattice expansion causing less resistive ion pathways. Once this initial change has taken place the overall impedance is reduced for the following cycles, in both delithiation and lithiation. Trapping of Li-ions initially may also aid in boosting the material's overall conductivity. The Nyquist plots show consistent results with this, with little change over cycle numbers (Figure 3.14). Only the 1st delithiation cycle shows two semi-circles, showing the formation of SEI is complete following the formation cycle, or perhaps a resistance associated with the removal of the surface species. The resistance related to charge transfer (CT) shows very little overall change from 1 to 100 cycles. Notably the diffusion tail is steeper than the expected 45 ° angle, with measurements from 20 cycles showing >50 ° phase angle, echoing that the Li-ion diffusion is similar to that of a capacitor (Figure A.12).

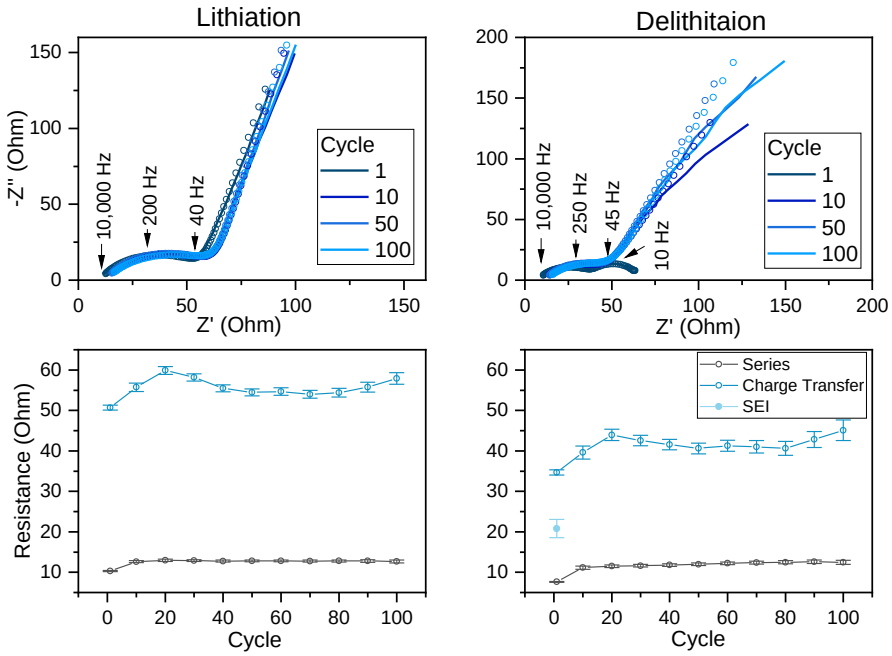

Figure 3.14 –(top) Nyquist plots for delithiation and lithiation at 2.5 V, with fitted curves overlaid (bottom) fitted resistance values for series, CT and SEI resistances for as-synthesised anisotropically crystalline Nb_2O_5.

3.3.2.1.2 Electrochemical Properties of Heat-treated Anisotropically Crystalline Nb_2O_5.

The anisotropically crystalline structure was maintained with heat-treatment to 500 °C, with some improvement in long-range order. Thus, materials heat-treated at 300 and 500 °C, were tested under a similar electrochemical regime to assess how the change in structure may affect the electrochemical properties.

At 1C, all the materials appear to behave similarly, with average capacities of 63 ± 2.7, 66 ± 2.9 and 68 ± 3.7 $mAhg^{-1}$ at 200 cycles for as-synthesised, 300 and 500 °C heat-treated materials respectively (Figure 3.15). Although the capacity here appears to be higher for the as-synthesised material, the rate sweep appears to show the difference in capacity is unlikely to be significant. On average, capacities for the respective materials are 39 ± 2.8, 46 ± 5.5 and 46 ± 10.5 $mAhg^{-1}$ at 10C and 18 ± 2.8, 21 ± 2.5 and 24 ± 6.4 $mAhg^{-1}$ at 100C. However, the coulombic efficiency is improved with heat-treatment, where the 500 °C heat-treated material reaches higher than 95 % efficiency quickest after 7 cycles (Figure A.13).

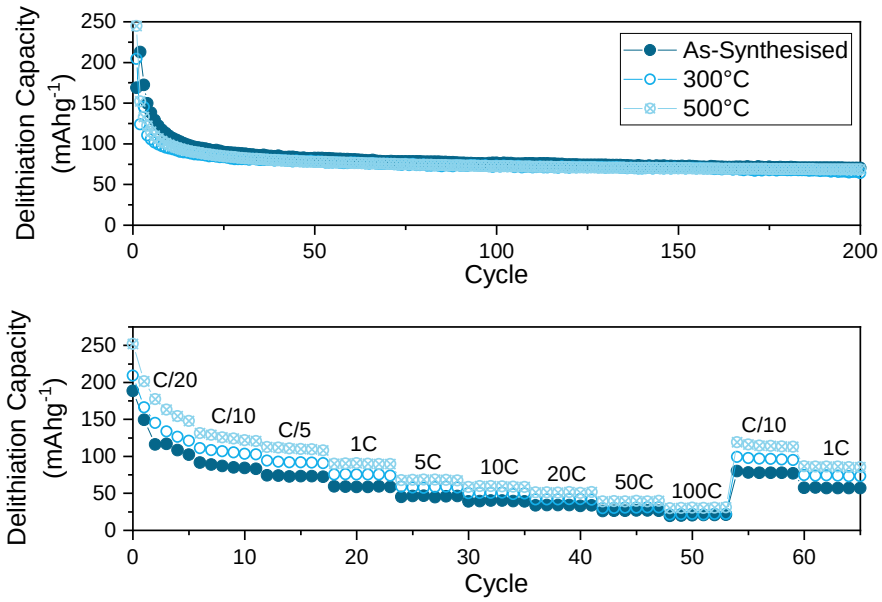

Figure 3.15 - (top) Galvanostatic cycling of anisotropically crystalline Nb_2O_5 materials at 1C between 0.25-3.0 V, (bottom) Rate sweep of anisotropically crystalline materials between C/20 and 100C, with a recovery to C/10.

Testing over longer cycles at C/5, 1C and 20C showed little improvement for the 300 °C heat-treated but more improvement for the 500 °C material (Table 3.2). One may suggest that there is little change between the results of the as-synthesised and 300 °C heat-treated materials, but a slight step up at low rates for the 500 °C, as also seen in the rate sweep. This may be due to the burn-off of surface species at elevated temperature, as seen in TGA, which can cause side reactions. These may be particularly prominent in the lower rates, as the slower insertion of Li-ions can allow for other processes to take place. Furthermore, this might be linked to the improved long-range ordering in the structure allowing the use of multiple Li-ion pathways available at these lower rates. As there is little change in the cycling performance with heat-treatment of the anisotropically crystalline materials, it is likely that the key Li-ion pathways are unchanged with the increased long-range ordering, suggesting the key pathways are accessible in this structure. Hence *ex-situ* XRD was performed for these materials to detect any structural changes with cycling. From the XRD it is apparent that the three anisotropically crystalline materials perform very similarly (Figure 3.16). All materials show a broadening of peaks and peak shift at 23 °. It appears that the as-synthesised Nb_2O_5 retains its structure better than the heat-treated counterparts, which show more considerable broadening by 50 cycles. As the main chemical difference between the material appears to be the amount of surface groups present, this may suggest that the surface

groups may aid in forming a stable SEI which can contribute to structural stability over cycling. The similar nature of these results coincides with the similar electrochemical results.

Table 3.2 – Comparison of average capacity of anisotropically crystalline Nb_2O_5 at 100 cycles at various rates in a 0.25-3.0 V voltage range and a C/20 formation cycle.

Material	Capacity at C/5 ($mAhg^{-1}$)	Capacity at 1C ($mAhg^{-1}$)	Capacity at 20C ($mAhg^{-1}$)	Figure
As-Synthesised	69 ± 3	66 ± 33	43 ± 8	Figure 3.12b
300 °C heat-treated	70 ± 1	73 ± 0.2	45 ± 6	Figure A.14
500 °C heat-treated	94 ± 2	72 ± 2	54 ± 0.5	Figure A.15

The CV profile for the material heat-treated at 300 and 500 °C appears to be very similar to that of the as-synthesised material (Figure A.16 and Figure A.17). The heat-treated materials show a reliance on capacitive type diffusion with log plot gradients at as high as 0.86 and 0.72 for heat-treated materials at 300 and 500 °C, respectively. When comparing the capacitive contribution at 5 mVs^{-1}, the percentages are 36, 43 and 32 % respectively, showing no trend with heat-treatment, however at higher rates, as expected the capacitive contribution appears to decrease. All anisotropically crystalline materials appear to rely on a mix of capacitive type and intercalation type mechanism. One would suggest that the insulating nature of this material limits it from fully exploiting the intercalation pseudocapacitive mechanism. Furthermore, this also suggests that the semi-crystalline nature of this material does not stunt its ability to use such mechanism. Again, these materials perform similarly to the as-synthesised form in the SPEIS, where the only apparent difference appears to be the resistances seen in the first lithiation cycle, where the resistance decreases with heat-treatment, due to the removal of surface species (Figure A.18 and Figure A.19). However, this difference in the first cycle, shows no effect on extended cycling of these materials. There is a continued low and stable impedance, across frequencies 10 kHz to 10 Hz for all anisotropically crystalline materials up to 100 cycles. This shows that the electrolyte and SEI system is stable, and that the Li-ion storage mechanism is reversible, as the CT region also appears unchanging.

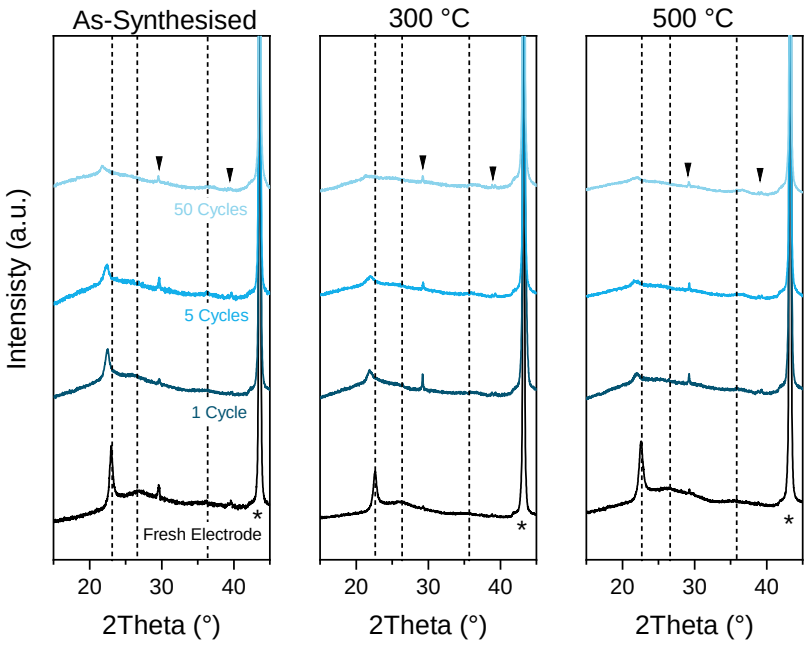

Figure 3.16 – Ex-situ XRD of as-synthesised (top), 300 °C (middle) and 500 °C (bottom) anisotropically crystalline Nb_2O_5, where Cu current collector is denoted by an Asterix, an arrow denotes a peak from the sample holder and the dotted line represent key peaks from the materials.

To summarise, all anisotropically crystalline materials appear to be physically similar. With heat-treatment there is cleaning of the surface of the material, which also comes with a small increase in surface area, as well as some improvement in long-range structural order. Electrochemically, all materials show similar trends in capacity across the different rates which is consistent with similar cycling structural change as seen in *ex-situ* XRD patterns. However, heat-treatment appears to speed up the structural degradation with cycling and has some impact of the use of the capacitive mechanism as reduction in capacitive contribution was observed. This may suggest that the surface species, which are cleaned with heat-treatment, could be preventing dissolution of the material into the electrolyte and thus material breakdown, or perhaps that there is loss of the long-range order with cycling.[248] Furthermore, the order in the [001] plane is key to achieving the intercalation pseudocapacitance and that long range order appears to increase the Li-ion sites, but these are only available via slower pathways at low rates.[37,122,124,125]

3.3.3 Characterisation of Orthorhombic Nb_2O_5 as Produced from an Anisotropically Crystalline Precursor.

As is shown in Figure 3.7, heat-treatment in the region of 550 to 850 °C, produces an orthorhombic Nb_2O_5, with increasing crystallinity as a function of temperature. At 600 °C the orthorhombic structure is clearly established, thus is the key material studied in this section. The XRD pattern shows broad features, indicating poor or nano-crystallinity (Figure 3.17, top). Furthermore, the relative peak intensities show some deviation from the expected pattern, suggesting that the anisotropic nature of crystallinity is carried through into this material from the precursor.[344] By 800 °C, the crystallinity has further improved as shown by the narrowing of the XRD peaks, thus this material will also be described here (Figure 3.17, bottom). Interestingly, although the crystallinity appears far improved, there is still the appearance of anisotropy, as the relative intensities still differ from the ideal pattern. This suggests that the heat-treatment does not remove the characteristics of the precursor material, and further characterisation will reveal whether the electrochemical properties are also carried forward. It should also be noted that XPS of the 600 °C material confirmed a +5 oxidation state or Nb with a difference in Nb to O binding energy of 322.98 eV (Figure A.21). This confirms that the oxidation state is unaffected with the formation of the T-phase.

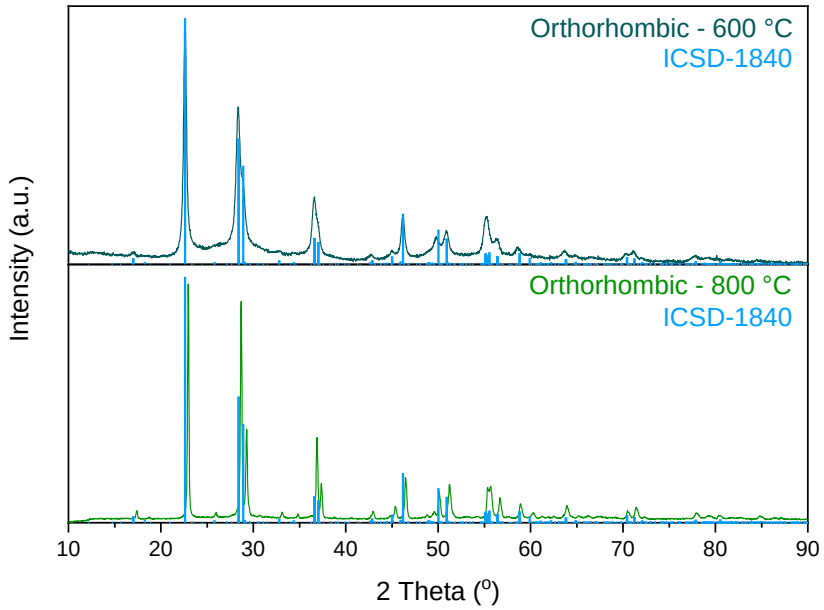

Figure 3.17 – XRD patterns of orthorhombic Nb_2O_5 created via heat-treatment of the anisotropically crystalline Nb_2O_5 at 600 (top) and 800 °C (bottom), indexed with ICSD 1840 (blue sticks).

As with the X-ray diffraction patterns, the neutron PDFs appear to match well to the ideal T-Nb_2O_5 structure at both local (Figure 3.18) and long range (Figure A.4). With the increased heat-treatment, the PDF shows more similarity to that of the ideal T-Nb_2O_5 structure. The X-ray PDF has far more deviation from the ideal, potentially suggesting the Nb atoms sit out of place compared to the expected as Nb has the higher contrast in the X-ray PDF. The 600 °C material shows additional peaks, when compared to the partial PDFs some of these correspond to O-O distances which are more intense than is expected. Peaks at 2.6, 7.5 and 9.1 Å are shifted from the ideal in position appear to be in Nb-Nb distances. These deviations still appear in the 800 °C material but to a lesser extent. Furthermore at 3.86 Å the peak is far more intense than the ideal and this is further sharpened at the 800 °C material. This may be a structural motif carried over from the anisotropically crystalline structure, as this sharp peak corresponding to an Nb- Nb distance that appears in all the materials. From this data it appears that the 600 °C heat-treated material still carries some structural similarities to the anisotropically crystalline, which do not appear in the T-Nb_2O_5 structure yet shows long range order more like the orthorhombic phase. With further heat-treatment the material looks more structurally similar to T-Nb_2O_5 with only small deviations, likely to be due to the position of Nb in the split occupancy sites and a selection of structural defects which have been reported as common in Nb_2O_5 previously.[356]

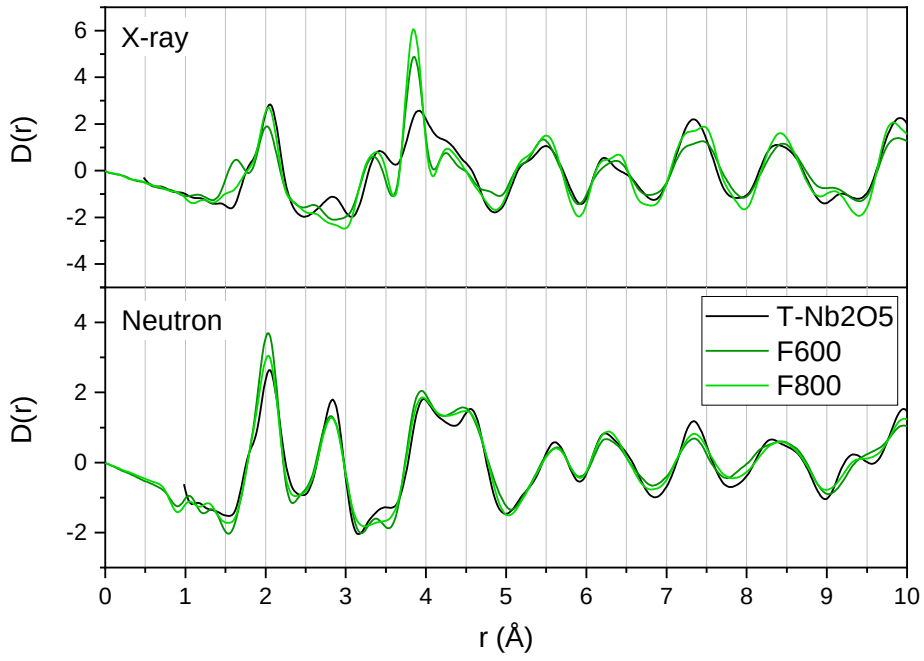

Figure 3.18 - Short range X-ray (top) and neutron (bottom) PDFs of orthorhombic materials made via heat-treated at 600 and 800 °C as compared to the ideal T-Nb_2O_5 structure.[344]

TEM images show that the morphology of the anisotropically crystalline precursor is maintained at 600 °C; however, the nanowires appear to have a much smaller aspect ratio (Figure 3.19). At 800 °C the morphology has changed to larger rectangular shaped particles. This coincides with the structural characterisation. From 500 to 600 °C, the centre of the particle width distribution increases from 11 nm to 66 nm, with an increase in width by a further 6 times from 600 to 800 °C (Figure A.6).

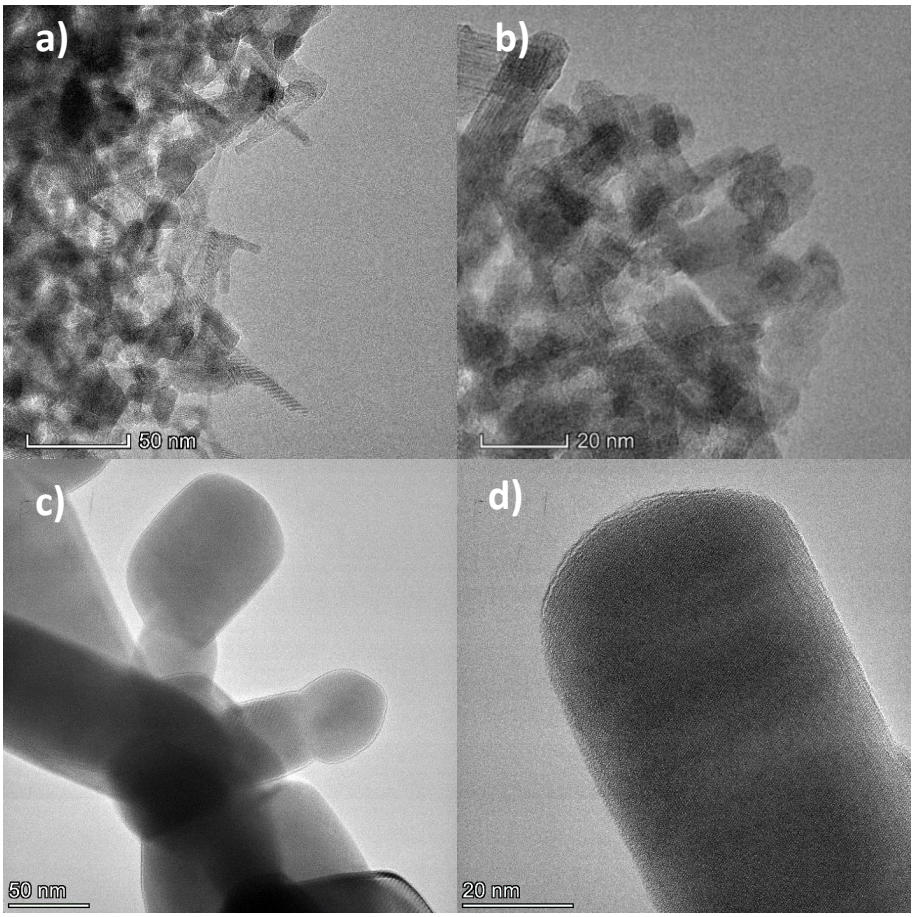

Figure 3.19 – TEM images of orthorhombic Nb_2O_5 created via heat-treatment of the anisotropically crystalline Nb_2O_5 at 600 (a,b) and 800 °C (c,d).

The 600 °C material shows the same nitrogen adsorption isotherm and hysteresis type as the anisotropically crystalline material; however, the BET surface area is smaller at 77.0 m^2g^{-1} (Figure A.20). The total pore volume is 0.31 cm^3g^{-1}, and the average pore width has increased to 21.3 nm. As the particle size has increased the majority of the porosity that was achieved from the inter-particle spacing in the network of nanowires is reduced. At 800 °C, the isotherm is flattened, and the surface area is vastly reduced to 4.8 m^2g^{-1}, with the volume in pores being negligible. This is unsurprising due to the dramatic change in morphology seen in the particles.

3.3.3.1.1 Electrochemical Properties of Orthorhombic Nb_2O_5 Produced via a 600 °C Heat-Treatment.

As with the as-synthesised material, the applied voltage window was also considered for the orthorhombic materials. Typically, a 1.0-3.0 V versus Li window is used to avoid the irreversible phase or SEI formation at approximately 0.8 V. The differential capacity plot shows this phase formation as a sharp peak at ~0.75 V, although this only appears in the formation cycle (Figure 3.20, bottom). As such, using a wider voltage window appears more favourable as both voltage windows with a lower cut-off of 0.25 V show higher capacities than the narrow window. Average capacities of 107 ± 3.4 and 101 ± 0.5 $mAhg^{-1}$ versus 64 ± 3.0 $mAhg^{-1}$ for narrowing windows respectively (at 200 cycles). Furthermore, the delithiation redox peak appears to be shifted compared to the as-synthesised material and is therefore incomplete by 2.0 V, thus this upper cut-off is inappropriate. Thus, the wide voltage range (0.25-3.0 V) will be used for the orthorhombic materials from here.

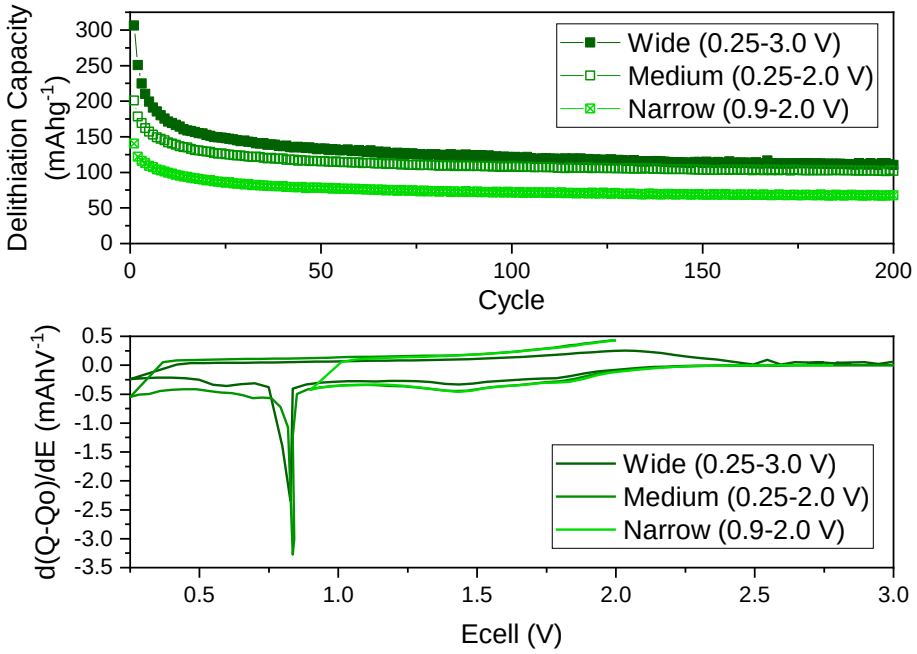

Figure 3.20 – (top) Galvanostatic cycling of orthorhombic Nb_2O_5 created at 600 °C in different voltage windows at 1C, and the respective differential capacity plots of the formation cycle. (bottom)

The redox peak seen at 0.75 V has been linked to formation of an irreversible phase formation, therefore it is studied via *ex-situ* XRD, and results are compared to cells cycled in the typical voltage range (1.0- 3.0 V), as seen in the literature (Figure 3.21). In the large voltage window, the XRD pattern is completely flattened within the 1st cycle (formation). This

suggests that the large redox peak seen at ~0.8 V, is related to a phase change to an amorphous form, rather than that of a secondary phase formation as had been previously suggested (Figure 3.21a). This explains the slightly lower capacities, as amorphous Nb_2O_5 has been shown to have poorer electrochemical proerties.[130] From the fifth cycle, a new peak at ~22 ° appears, suggesting that there may be another phase forming, however this cannot be identified, due to the lack of peaks and the low intensity of this phase. A similar event is seen in T-Nb_2O_5 with Na-ion intercalation where an 'activation' process is required to change Nb_2O_5 from only storing Na-ions at the surface to storing them within the structure.[87] This work showed amorphisation of the material in *ex-situ* XRD, which likely improves storage in the structure, however this also involves an irreversible formation of NbO and Na_2O. A similar process may be taking place here as the most intense peak in NbO is at 21 °,[357] although it becomes unclear whether NbO can contribute electrochemically or whether this change causes loss of electrochemically active material. Some work suggests that NbO is electrochemically active, although the lower capacities seen here may suggest at least some activity is lost.[358,359]

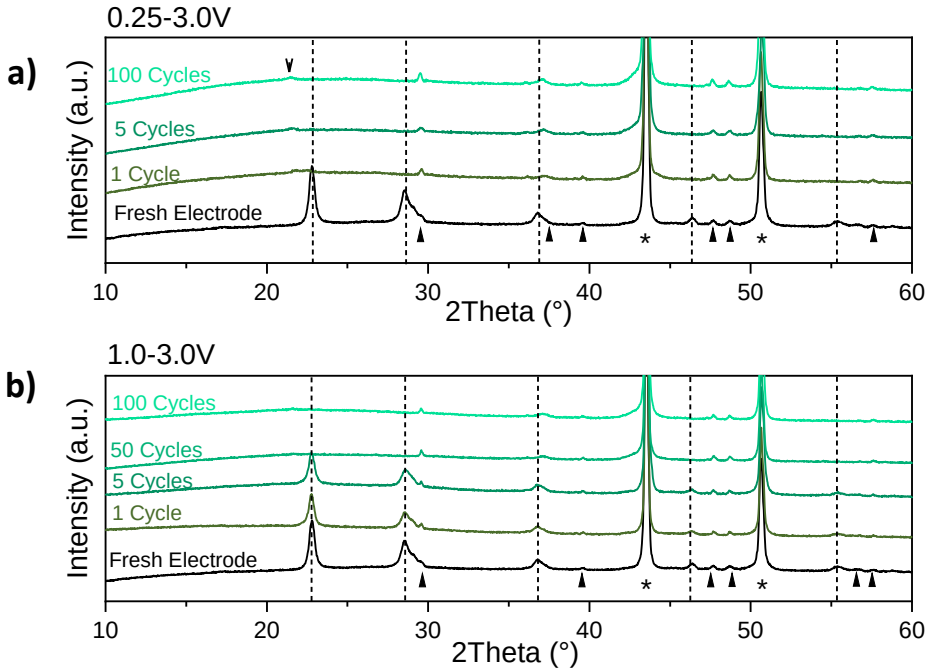

Figure 3.21 – Ex-situ XRD of electrodes of orthorhombic Nb_2O_5 prepared at 600 °C, after cycling at 1C, with a C/20 formation, for various cycle numbers in the regions of 0.25-3.0 V (a) and 1.0 – 3.0 V (b). The key T-Nb_2O_5 peaks are denoted with a dashed line, the Cu current collector peaks indexed via a star, other peaks from the sample holder are denoted with triangles (XRD pattern seen in Figure A.10), and a secondary phase is denoted with arrow.

The voltage range of 1.0 -3.0 V, which is highly cited by the literature, does not go through a phase change in the formation, however, it does appear that eventually this pattern also becomes amorphous (Figure 3.21b). By 50 cycles, the XRD pattern has also flattened out, thus it appears that even with the smaller voltage window this phase change is favourable for the material and still takes place over increased cycling. This structural rearrangement may be a result of the synthesis route used to produce this material, as previous work has shown the ability of T-Nb_2O_5 to undergo long-term cycling with good capacity retention.[172] Yet many pure Nb_2O_5 materials are not reported over long-term cycles, nor is there detailed *ex-situ* analysis, thus it is difficult to judge whether other T-Nb_2O_5 materials undergo total loss of order. The only study showing in depth analysis over long term cycling shows a tendency to rearrange to an amorphous form however this takes place over thousands of cycles.[126]

Even with these initial structural changes, the material is able to be cycled successfully up to 100C, with an average capacity of 34 ± 4.1 $mAhg^{-1}$ at this rate (Figure 3.22a). It also shows a 91% recovery when reverting to C/10 after high current density cycling. Over longer cycling there appears to be little difference between the rates, with average capacities of 112 ± 0.2, 117 ± 5.5 and 90 ± 4.3 $mAhg^{-1}$ for C/5, 1C and 20C respectively at 100 cycles. Coulombic efficiency takes some time to reach over 96%, taking at most 15 cycles at each rate. However, once the higher efficiency is achieved, this is stable across all of the C rates (Figure A.22). Although this material appears to show good rate capability, the charge profile is not as expected. A linear or near linear profile would be expected for an intercalation pseudocapacitive mechanism, but instead a broad plateau is seen between 1.5 and 2.5 V during the 1st cycle (Figure 3.22c). By the 200th cycle, this plateau appears sharper, potentially suggesting a heavier reliance on an intercalation type mechanism as cycling continues.

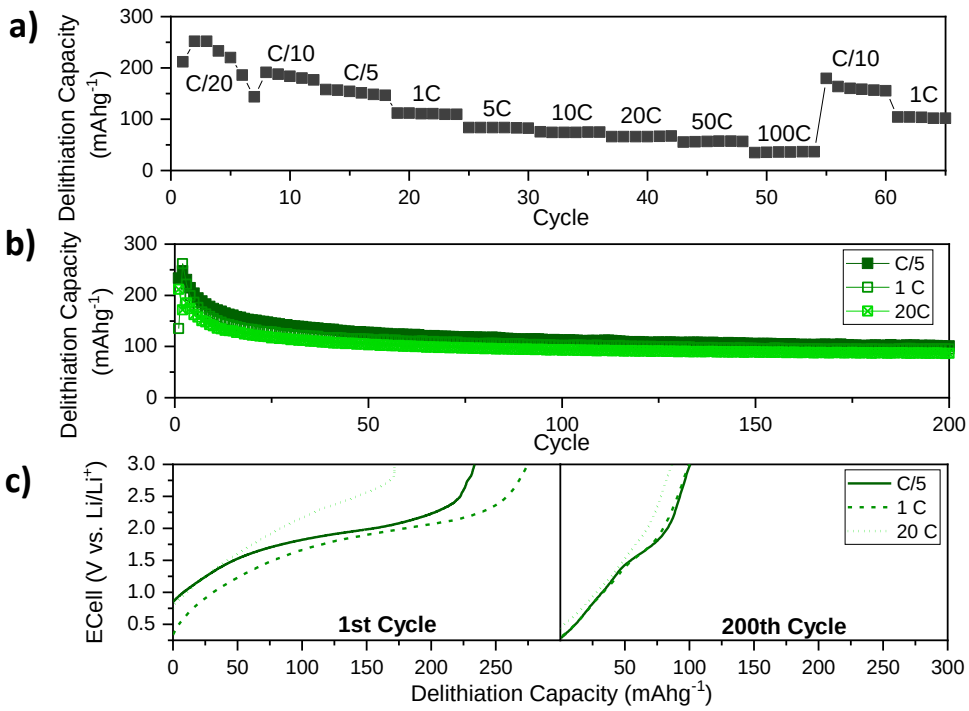

Figure 3.22 - (a) Rate sweep from C/20 to 100C with recovery to C/10, (b) Galvanostatic cycling at increasing rate over 200 cycles, (c) charge profiles at the different rates from 1st and 200th cycle, all in 0.25-3.0 V window for orthorhombic Nb_2O_5 created at 600 °C.

This material has a CV profile with a well-defined set of redox peaks (L-1 and D-2) and a second redox peak during delithiation (D-1) (Figure 3.23a). This is different to what is commonly reported in the literature, where a single set of broad redox peaks are typically seen. It has been noted that the appearance of a second peak is due to valance separation during the Li-ion storage mechanism, which is also seen in the as-synthesised material (Figure 3.11).[130] The log plot shows a shift in gradient at a scan rate of 10 mVs^{-1}, and for the lithiation process a gradient increase from 0.61 to 0.86 is seen (Figure 3.23b). For the delithiation process, this is a decrease in gradient for peak-1 from 0.88 to 0.76 and no major change for peak-2. This suggests that at higher scan rates the lithiation process becomes more reliant on a capacitive type of mechanism. Where the delithiation process has a drop in capacitive contribution above 10 mVs^{-1}; evidently, the delithiation process has the main effect on the capacitive contribution as these decreases with rate (Figure 3.23d). Previously for T-Nb_2O_5, reports of capacitive contribution as high as 91 % far surpassing what is presented here.[147,153,163] One would suggest that the poor crystallinity of this material and the initial structural changes might hinder its performance as a successful intercalation pseudocapacitive material. [125]

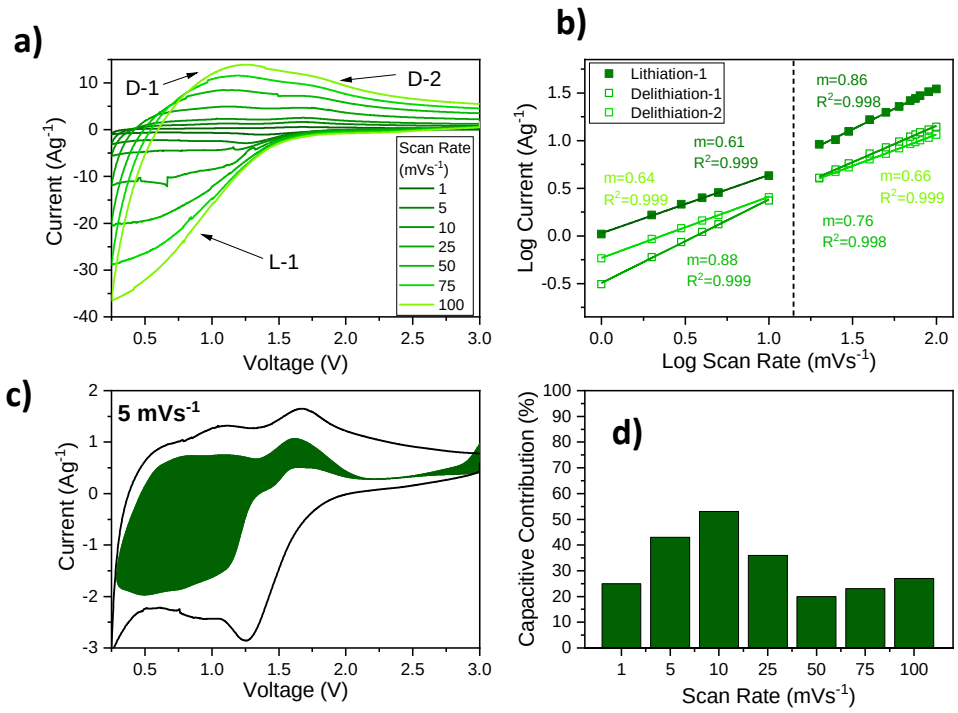

Figure 3.23 - a) CV profile of orthorhombic Nb_2O_5 created at 600 °C at increasing scan rate 1 to 100 mVs^{-1}, b) Log plot of current versus scan rate of redox peaks, with linear fits which have R^2 of at least 0.998, c) CV profile at 5 mVs^{-1} with shaded section as the capacitive contribution and d) the capacitive contribution at various scan rates.

The SPEIS results look very similar to that of the anisotropically crystalline materials, where the first lithiation cycle is different to the subsequent cycles. This cycle shows a reduction in impedance below 1.5 V for medium to low frequency, this coincides with the onset of the redox peak seen in the CV profile. After the initial cycles, a higher impedance is seen at low frequency (1Hz), which relates to solid-state diffusion above 1.5 V. This suggests that after the initial material change, the ions encounter a low and consistent CT and SEI resistance. This is clear from the Nyquist plots during the delithiation process, where the CT resistance appears to only show a small reduction with cycle number (Figure A.23). With the lithiation, like with the SPEIS, the first cycle shows a higher CT resistance which then drops dramatically, then shows a gradual decrease in resistance with cycle.

To summarise, the orthorhombic Nb_2O_5 created via heat-treatment at 600 °C shows high-rate capability with the ability to cycle to 100C and a has a high capacitive contribution. However, this material does appear to fall short of the expected capacities, which is likely to be due to the initial structural changes observed with cycling. As such, an orthorhombic Nb_2O_5 produced at 800 °C is also tested under a similar regime to assess whether the level of crystallinity of this phase influences the electrochemical properties.

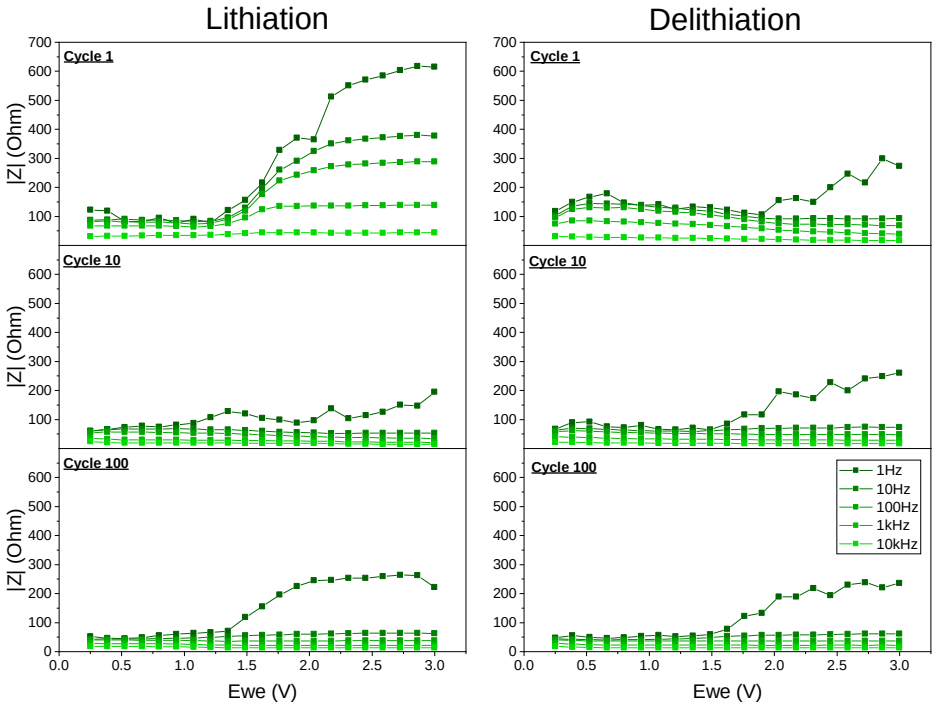

Figure 3.24 - SPEIS of orthorhombic Nb_2O_5 created at 600°C for cycles from 1 to 100 cycles in a range of 1 Hz to 10kHz.

3.3.3.1.2 Electrochemical Properties of Orthorhombic Nb_2O_5 Produced via an 800 °C Heat-Treatment.

As this material is also orthorhombic, the expected electrochemistry should be similar to the T-Nb_2O_5 produced at 600 °C. However, this material showed larger particles and a higher level of crystallinity, thus this may bring about some changes in the electrochemical performance. Notably, this material showed a huge difference in capacity between wide and narrow voltage ranges, with average capacities of 106 ± 5.6 and 15 ± 0.9 $mAhg^{-1}$ in the respective windows at 100 cycles (Figure A.24). The voltage cut-off of 2.0 V is unsuitable as the window does not allow for total delithiation (Figure 3.25). In the 0.25-3.0 V range, the capacity at formation is nearly equal to the theoretical, then there is a large drop in capacity due to SEI or secondary phase formation as with the other orthorhombic material (Figure 3.20). The large redox peak is also seen in the formation cycle here, however the voltage of this is now closer to 1.0 V (Figure 3.25, inset). As this redox process takes place at a higher voltage (i.e., 1.0 V rather than 0.7 V), the typical voltage window used in the literature (1.0 –

3.0 V) would not avoid the process. This solidifies the need for thorough electrochemical characterisation prior to implementing a long-term test regime. With the sharp redox peak comes a large loss in structure within the first cycle as shown by the *ex-situ* XRD pattern (Figure A.25). As with the other orthorhombic material, it is apparent that the T-Nb_2O_5 has lost crystallinity and a secondary phase may have formed as new peaks are observed. Again, it is difficult to positively define the formation of this material as the peaks do not appear to match to a single phase conclusively. The main suggested phase is a cubic niobium oxide (NbO, ICSD 237585), yet still leaves some peaks unidentified.[360] As with the mechanism proposed with Na-ion storage, a combination of the original Nb_2O_5, NbO and Li_2O may account for this.[87] As the magnitude of the redox peak during formation is much larger than with the previous T-Nb_2O_5 one may expect that more of the active material has undergone conversion, hence the even lower capacities seen here.

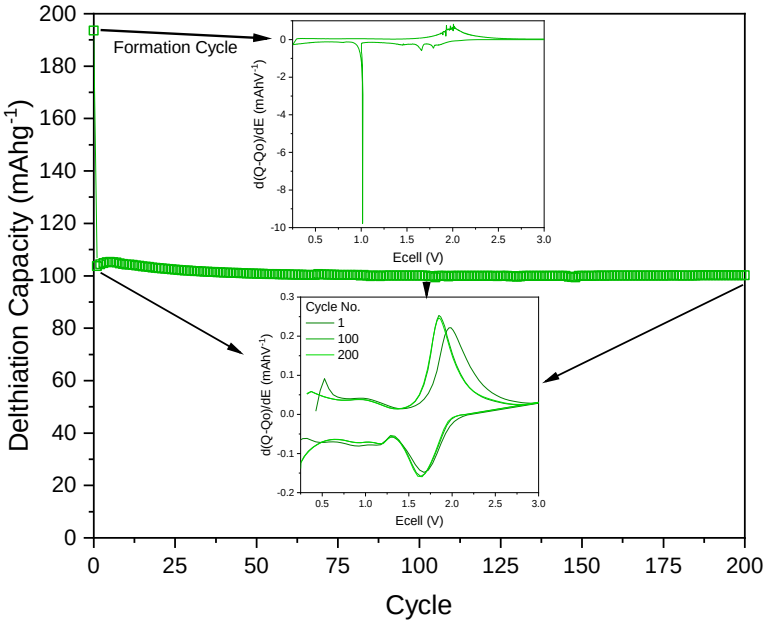

Figure 3.25 – Galvanostatic cycling at 1C in 0.25-3.0 V range of orthorhombic Nb_2O_5 created at 800 °C. Differential capacity profile of formation cycle (Inset, top), differential capacity profile of 1st, 100th and 200th cycle (Inset, bottom).

This material shows a very stable capacity; however, has a lower average capacity than the orthorhombic material created at 600 °C, with a value of 106 ± 5.7 $mAhg^{-1}$, compared to 116 ± 5.5 $mAhg^{-1}$. The differential capacity shows a well-defined redox pair between 1.25-3.0 V. This may suggest that this material stores Li-ions via a traditional intercalation mechanism rather than the expected intercalation pseudocapacitance. These profiles, almost perfectly

overlap after initial cycling showing good reversibility. Interestingly, below 1.2 V there also appears to be electrochemical activity, whereby this region shows an almost rectangular signature, suggesting an additional capacitive type of mechanism.[361]

This material shows high-rate capability, with the ability to cycle to 100C (Figure 3.26). However, this shows an unexpected response, where there is an increase in capacity from 50 to 100C. It is unclear why this is. When the material was tested further at different rates, the capacity drops off dramatically with rate. At 20C, after 200 cycles, this material exhibits an average capacity of 41 ± 2.4 $mAhg^{-1}$ which is half of the capacity recorded for the lower crystallinity orthorhombic material under the same conditions. Clearly, the extra heat-treatment improves stability yet reduces rate capability, this may suggest movement away from the intercalation pseudocapacitive mechanism expected from this material. As such the coulombic efficiency is also improved with it taking only 5 cycles to reach over 97% and remains at above 99% and stable throughout at all rates tested (Figure A.26).

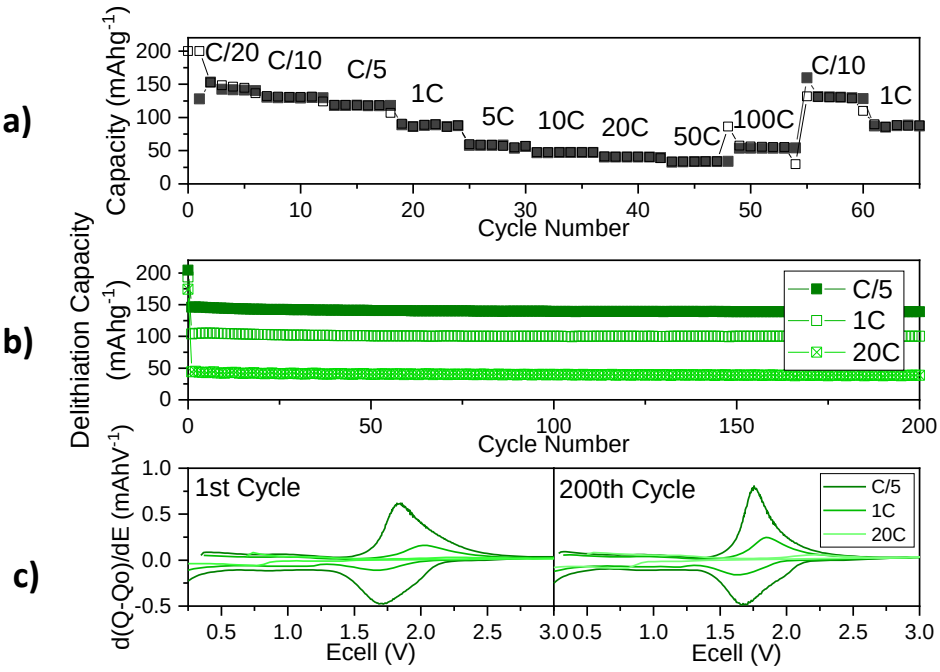

Figure 3.26 - (a) Rate sweep from C/20 to 100C with recovery to C/10 delithiation is filled squares and lithiation is empty squares, (b) Galvanostatic cycling at increasing rate over 200 cycles, (c) differential capacity profiles at the different rates from 1st and 200th cycle, all in 0.25-3.0 V window for orthorhombic Nb_2O_5 created at 800 °C.

To further evaluate this material's capability to operate by way of intercalation pseudocapacitance, the Dunn method of using CVs at different scan rates was used (Figure 3.27). CV profiles for this material are atypical, appearing rectangular, but sloping due to the internal resistance of the material. Within the profile are small peaks or shoulders, which

independently grow and retract with increasing scan rate (Figure 3.27). When the capacitive contribution is calculated, this is high and increasing with scan rate suggesting that this material uses surface limited process. On studying the differential capacity plots (Figure 3.25) and the CV profiles, there appears to be a combination of a rectangular plot in the region of 0.25 and 1.25 V, and a more traditional redox plot between 1.25 and 3.0 V. This suggests a dependence on a capacitive mechanism, below 1.25 V, and an intercalation mechanism, above 1.25 V. Multiple storage methods make take place as there are multiple active materials due to the secondary phase (NbO) produced during the formation cycle. As such, T-Nb_2O_5 undergoes intercalation pseudocapacitance and NbO, follows a traditional intercalation response. It is feasible that at lower rates Li-ions are stored via the intercalation pseudocapacitance and intercalation mechanism, in the respective materials. With increasing rate, the intercalation reaction becomes limited due to slow kinetics leading to storage, mainly via pseudocapacitance in the T-Nb_2O_5. This explains the increasing capacitive contribution seen in Figure 3.27d. However, this comes with a significant drop in capacity as the capacitive storage is limited to a smaller voltage region and quantity of active material.

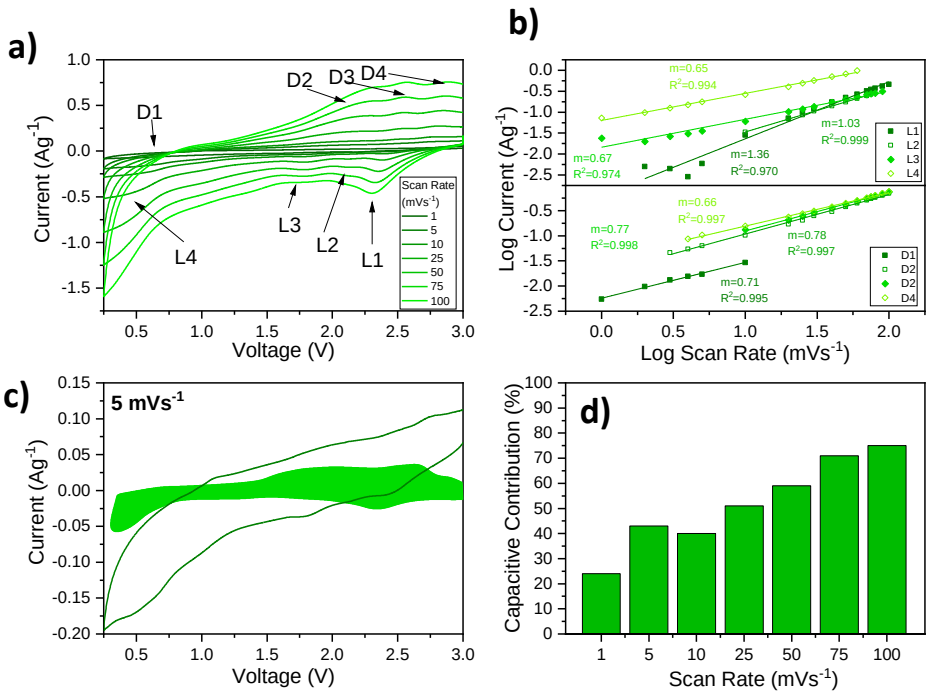

Figure 3.27 - a) CV profile of orthorhombic Nb_2O_5 created at 800 °C at increasing scan rate 1 to 100 mVs^{-1}, b) Log plot of current versus scan rate of redox peaks, with linear fits which have R^2 of at least 0.970, c) CV profile at 5 mVs^{-1} with shaded section as the capacitive contribution and d) the capacitive contribution at various scan rates.

This material shows the similar SPEIS results to the other Nb_2O_5 materials already discussed (Figure A.27). The overall impedance shows a reduction compared with the other samples, indicating that heat-treatment may reduce resistance. The Nyquist plots are also consistent with the SPEIS, with plots showing one semi-circle and a diffusion tail with a phase angle of ~27 ° showing some limitation to the diffusion in this system (Figure A.28-Figure A.29). After an initial increase in CT resistance this remains similar over cycles suggesting that the initial structural changes are associated with increased resistance.

T-Nb_2O_5 can be created from an anisotropically crystalline precursor via heat-treatment, with the extent of this treatment causing deviation from the ideal T-structure both on local and longer-range scales. However, regardless of level of crystallinity, the T-Nb_2O_5 tends to lose crystallinity upon electrochemical testing and partially converts to NbO. It appears that the more disordered structure protects from the conversion to NbO and maintains higher capacities than the more crystalline form.[129,130] However, even with the formation of a secondary material, both materials appear to remain electrochemically active and the NbO looks to stabilise the structure and improve long-term cyclability. However, this appears to sacrifice some capacity, which is noticed especially at higher rates. This section highlights the need for more thorough testing of T-Nb_2O_5 as much of the literature uses a low voltage cut-off of 1.0 V to avoid this phase formation, However, as is seen here, this may not be suitable for all T-Nb_2O_5 materials.[131,137,151,153] Further to this, much of the literature notes this secondary phase formation to be SEI, thus further work is needed to clarify the identity of the secondary phase and the reason for its formation.[136,150,152,154]

3.3.4 Characterisation of Monoclinic Nb_2O_5 as Produced via an Anisotropically Crystalline Precursor.

The monoclinic form is produced in the region of 900 to 1300 °C as shown in Figure 3.7. At 1000 °C the monoclinic structure is clearly established and is the key material studied here. The XRD pattern is matched to monoclinic Nb_2O_5 (ICSD-16605), however the relative peak intensities appear to differ from what is expected (Figure 3.28).[69] This may be due to a residual anisotropic character from the precursor, which causes skewed relative intensities within the pattern. A Pawley fit of this pattern was executed and a good fit was achieved with the lattice parameters comparing very well to that of the expected structure (Figure A.30). With increased temperature, the XRD peaks become narrower, and indicating an

improvement in crystallinity. At 1300 °C, the relative peak intensities match the expected ones far better (Figure 3.28) – suggesting a loss of dominant anisotropic crystalline character. This material will be used for comparison.

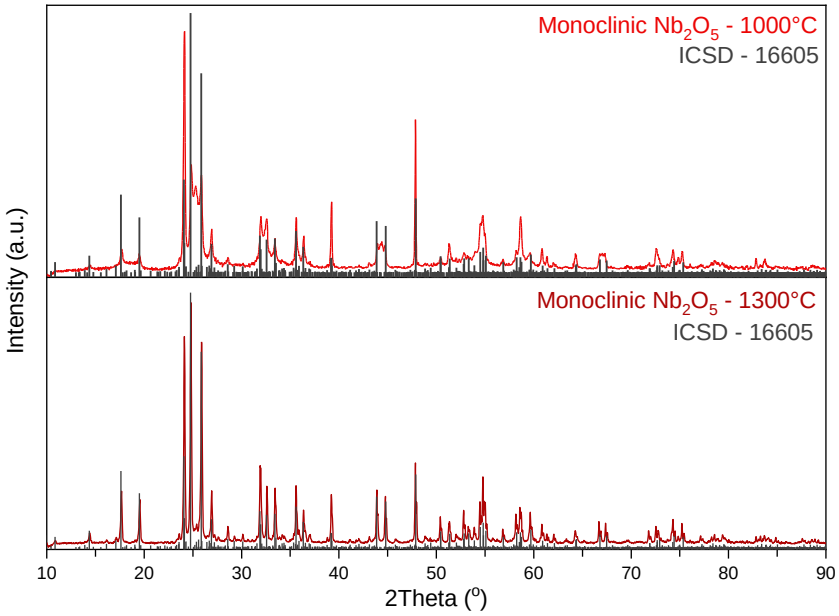

Figure 3.28 - XRD patterns of monoclinic Nb_2O_5 created via heat-treatment of the anisotropically crystalline Nb_2O_5 at 1000 (top) and 1300 °C (bottom), indexed with ICSD 16605 (black sticks).

TEM images of the monoclinic materials show that the particles have a cuboid morphology, and the particle size has increased from the lower temperature materials (Figure 3.29). The monoclinic materials have a particle width centred on 430 and 2006 nm for 1000 and 1300 °C heat-treated materials respectively (Figure A.6). The particle range is broad, with the FWHM being 298 and 1765 nm. It should be noted that the surface area of the H-Nb_2O_5 was measured (material synthesised at 1000 °C) and is negligible. With a larger particle there is no drive to form secondary particles and the material exists as large primary particles, which eliminates the large number of meso-pores seen in inter-particle spacing. XPS was also measured from the monoclinic Nb_2O_5 created at 1000 °C and confirmed no change in Nb oxidation state with this heat-treatment or phase change (Figure A.31). A difference in Nb to O binding energy of 323.06 eV was measured and thus confirms a 5+ oxidation state.

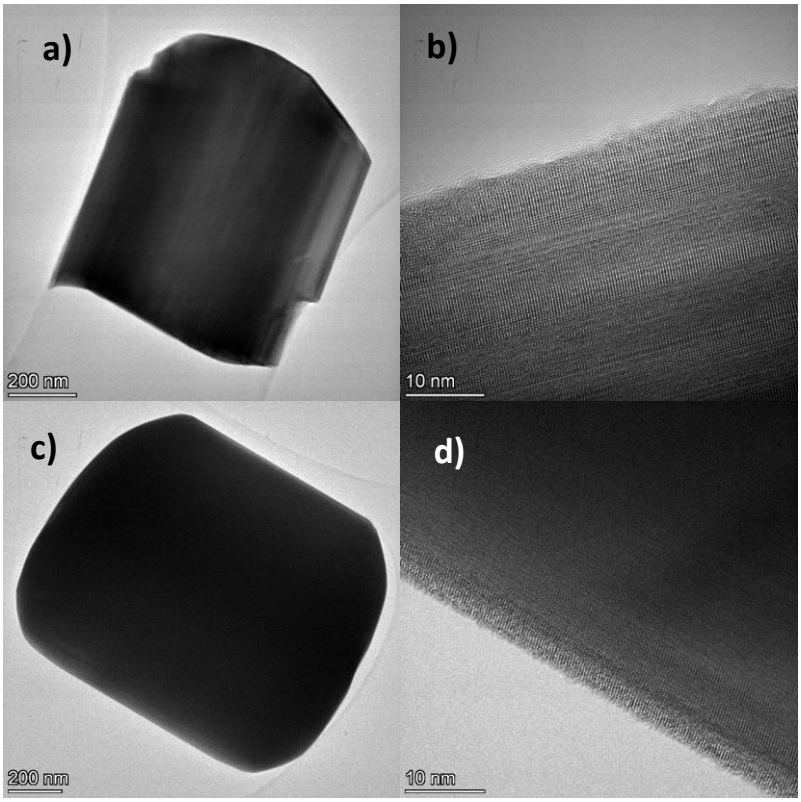

Figure 3.29 – TEM images of monoclinic Nb_2O_5 created via heat-treatment of the anisotropically crystalline Nb_2O_5 at 1000 (a,b) and 1300 °C (c,d).

Further structural analysis was carried out on the H-Nb_2O_5 formed at 1000 °C. The long-range order matches well with the expected monoclinic structure, and this is a notably better match in X-ray PDF versus neutron (Figure A.5). This potentially suggests that the Nb atoms sit in expected locations as the scattering from X-ray has higher scattering toward Nb rather than O. Some deviation is to be expected as this material is not in its highest crystallinity form, and one would expect if measurements were taken on the 1300 °C heat-treated form that this would match the ideal monoclinic PDF far better. On the local level, in both types of PDFs the sample has peaks in the same positions as the ideal however in many cases the intensities of these peaks deviate significantly. In the neutron PDF the peaks with the largest differences compared to the ideal are at 4.9, 6.2 and 7.9 Å, and these all show deviation in oxygen position to what is expected as the distances correspond to Nb-O and O-O distances. In the X-ray PDF, however, all the main peak differences appear from Nb-Nb distances. Notably the extremely sharp peak seen at 3.8 Å in the family of samples is still seen here and may be linked to some of the carried through anisotropy seen in the XRD pattern (Figure 3.28). Within both PDFs there are also peaks in the sample which are not expected in the H-Nb_2O_5 PDF and vice versa. In the neutron PDF these peaks are at 3.3 and 5.4 Å, the first of these is a small peak which appears to align with an Nb-Nb distance, which appears to be

more intense than would be predicted from the structure (Figure 3.30). The peak at 5.5 Å is not present in the sample, and this is potentially a O-O or Nb-Nb distance as seen in the partial PDFs. It is not clear why this correlation is not detected, but potentially the full local structure has not been expressed at this temperature. Similarly in the X-ray PDF there are extra peaks which cannot be accounted for in the H-structure, (6.4 and 7.6 Å) and these appear similar to the T-Nb_2O_5 and are likely due to split site occupancy. As such it appears that the H- phase is slightly underdeveloped and still carries structural motifs from the anisotropically crystalline precursor or T-phase.

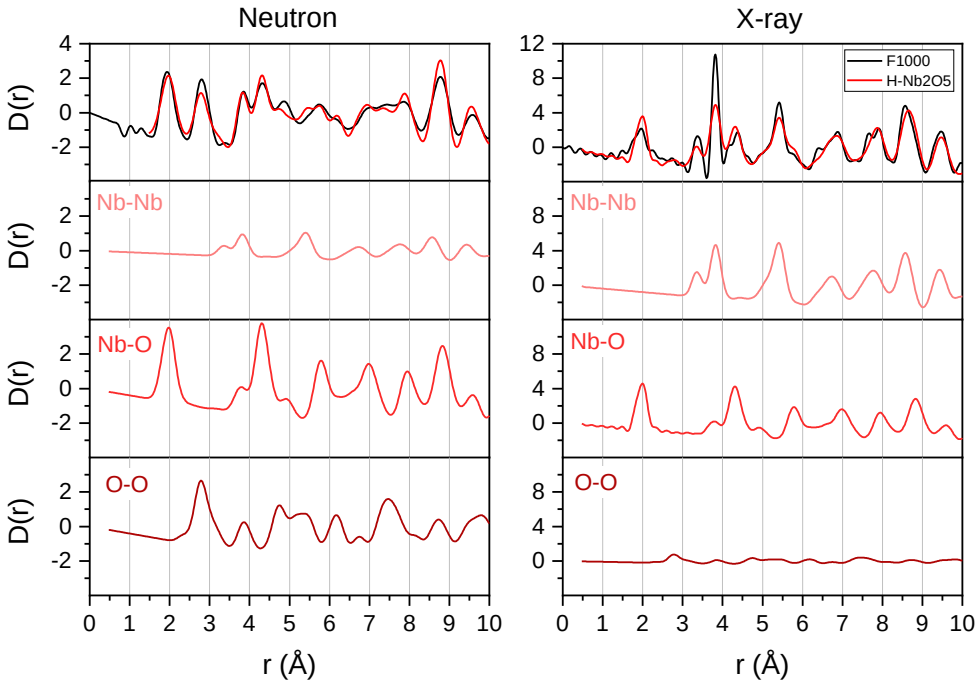

Figure 3.30 - Neutron (left) and X-ray (right) PDFs of 1000 °C heat-treated Nb_2O_5 with the ideal PDF of H-Nb_2O_5 and corresponding partials of Nb-Nb, Nb-O and O-O pairs.[69]

3.3.4.1 Electrochemical Properties of Monoclinic Nb_2O_5.

3.3.4.1.1 Electrochemical Properties of Monoclinic Nb_2O_5 Produced via a 1000 °C Heat-Treatment.

The voltage ranges tested for the previous Nb_2O_5 samples are explored again here (wide: 0.25-3.0 V, medium: 0.25-2.0 V and narrow: 0.9-2.0 V). The reversible capacity recorded for H-Nb_2O_5 produced at 1000 °C increases with narrowing voltage window. Although the initial

capacities appear similar at all voltage windows, there appears to be a far larger capacity loss over cycle for the medium and wide windows compared to the narrow one. At 100 cycles, the average capacity is 110 ± 13.8, 118 ± 6.1 and 156 ± 13.0 $mAhg^{-1}$ for wide, medium, and narrow windows, respectively. Initial capacity after formation was 226 ± 26.8, 244 ± 13.3 and 218 ± 13.0 $mAhg^{-1}$, thus this is a difference in stability as initial capacity would suggest that a wide voltage window would be preferred. The narrow window may be negating any unfavourable side reactions, hence showing an improved stability. H-Nb_2O_5 is known to store Li-ions via an intercalation mechanism with a multi-step phase transfer. This can be seen in the differential capacity plots, where there is a set of sharp redox peaks (1.5 -1.75 V) and a smaller set of broader peaks (1.1-1.3 V). For the medium and wide voltage windows, a further peak is seen at approximately 0.7 V, and no evidence of further activity above 2.0 V. Interestingly by the 100th cycle, the wide voltage range shows the differential capacity plot to have lost its shape. The medium window only shows evidence of some broad peaks, whereas the narrow range maintains the two redox pairs. As there is little change in response from the 0.25-3.0 V and 0.25-2.0 V, one would suggest that activity at low voltage may cause material destabilisation and thus 0.9-2.0 V is the chosen voltage range from here.

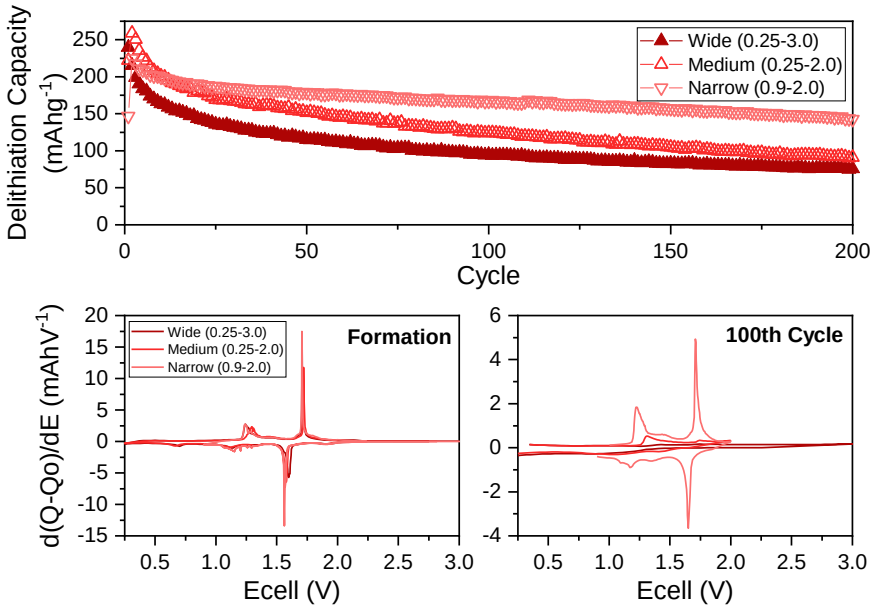

Figure 3.31 - (top) Galvanostatic cycling of H-Nb_2O_5 created at 1000 °C in different voltage windows at 1C, and the respective differential capacity plots of the formation cycle and 100th cycle. (bottom)

Interestingly, the *ex-situ* XRD shows little change in the XRD pattern between the electrodes cycled at the different voltage ranges (Figure 3.32). Notably, the structure is maintained with

increasing cycles, with no apparent formation of any other phases. By 100 cycles, there appears to be some broadening of the peaks, suggesting some breakdown in crystallinity with increasing cycling which is expected considering the multi-phase change. Evidently, there is a different electrochemical response for the wide and narrow voltage windows, and the differential capacity plots would suggest a breakdown in the Li-ion storage mechanism, thus one way also expect a breakdown in structure (Figure 3.31). Yet, the *ex-situ* XRD results suggest otherwise. It is not clear, what is causing this difference, perhaps a resistance difference in the SEI which may have formed differently due to the selected lower voltage, this emphasises the need for further characterisation of properties.

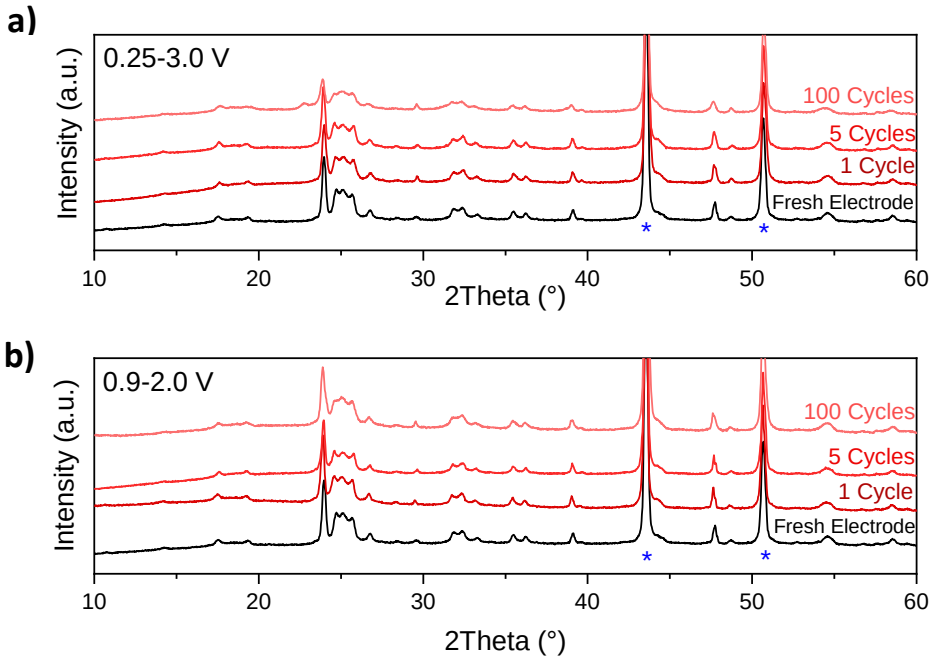

Figure 3.32 – Ex-situ XRD of cycled electrodes of H-Nb_2O_5 produced at 1000 °C at 1C, with a C/20 formation, in the range of 0.25-3.0 V (a) and 0.9-2.0 V (b). Peaks identified as Cu current collector is identified by blue stars.

Further testing shows this material is also capable of being cycled to 100C in the rate sweep displayed in Figure 3.33a, where an average capacity of 58 ± 1.8 $mAhg^{-1}$ is recorded. It is to be noted that there is not the expected step down in capacity from 50 to 100 C which may relate to the limitation of electrolyte or even Li-stripping and plating. However, there is an 80 % recovery when the rate is returned to C/10 after this high current density. When cycled over longer cycles, the results from C/5 and 1C are very similar to the point that average capacities of 147 ± 8.3 and 131 ± 13.0 $mAhg^{-1}$ are achieved at 200 cycles respectively (Figure 3.33b). At these rates, the charge profiles also look identical, with two clear plateaus, which

correspond to the two-step intercalation process (Figure 3.33c). Furthermore, these appear unchanged in shape after 200 cycles, showing good reversibility. When the rate is further increased to 20C, there is a larger step down in capacity with an average capacity of 95 ± 13.5 $mAhg^{-1}$ at 200 cycles. This is just short of half of the theoretical capacity, so shows extremely good rate capability, even over long-term cycling. In addition, this material shows over 98 % coulombic efficiency within the first 5 cycles independent of rate (Figure A.32). After this the coulombic efficiency remains high and stable throughout.

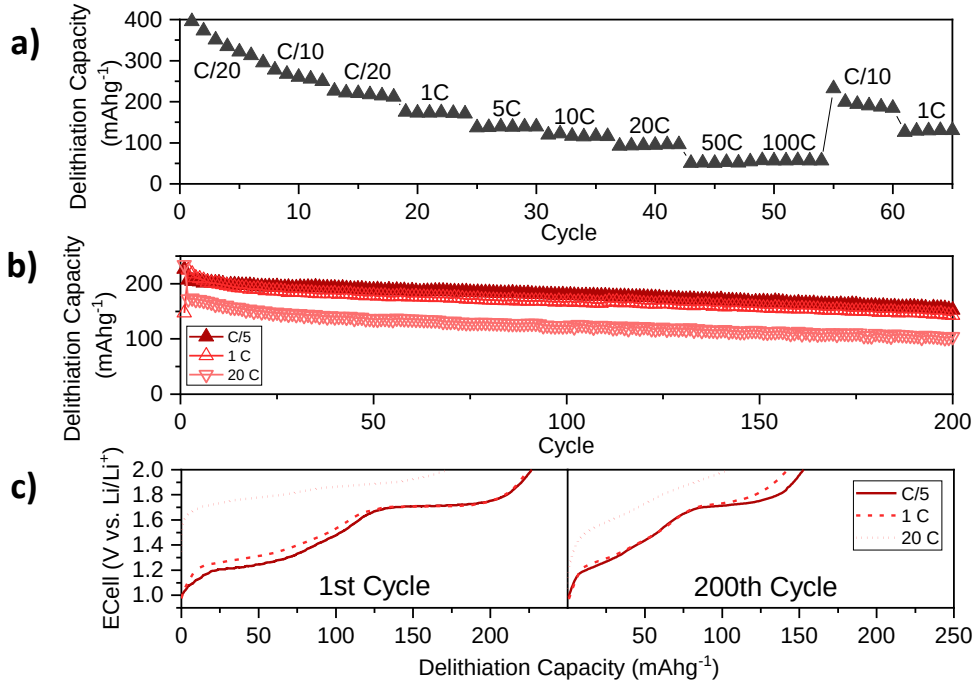

Figure 3.33 - (a) Rate sweep from C/20 to 100C with recovery to C/10, (b) Galvanostatic cycling at increasing rate over 200 cycles, (c) charge profiles at the different rates from 1st and 200th cycle, all in 0.9-2.0 V window for monoclinic Nb_2O_5 created at 1000 °C.

The CV profile of this material shows a single set of broad peaks (Figure 3.34a), this is different to the differential capacity plot where two sets of peaks are seen (Figure 3.31, bottom). This may be due to the CV scan rates, being larger than 1C, and thus with faster rate only one process can be accessed. The CV profile shows major peak shift with increasing scan rate, leading to the delithiation peak being cut-off from 10 mVs^{-1}. This calls into question the accuracy of the capacitive contribution calculations, since not only is it known that peak shift is an issue for these calculations but losing a peak from the measurement may cause over exaggeration of the capacitive contribution. Thus, one must be critical of the capacitive contributions from 10 mVs^{-1}.

Initially the impedance for this material is very high, with the largest impedances seen in both lithiation and delithiation below 1.2 V, across the frequencies. This may suggest that the second stage in the multi-stage lithiation is more resistive. However, after the initial cycle the impedance across the frequencies is decreased significantly. This initial resistivity highlights the rationale toward carbon compositing these materials in order to boost conductivity. Notably, even after the initial cycles, at 1 Hz the impedance is raised across the voltage range suggesting the continual diffusion of ions into the material at all voltages. This high impedance related to diffusion may be due to inhomogeneous ion intercalation and ion trapping sites.[123,140] Furthermore, the Nyquist plots suggests that the lithiation process is more resistive, and both the Li-ion diffusion into the material and the CT process comes with a barrier (Figure A.33). Whereas the delithiation process shows a very low resistance throughout and the diffusion tail is steeper than 45 °, suggesting fast kinetics, approaching that of a capacitive mechanism (Figure A.34). Although both EIS measurements were taken at 1.5 V it should be noted that for the lithiation, this would have been taken at the point of peak current on a redox peak, whereas due to hysteresis in the charge profile, this is not the case on delithiation, hence the large differences here. This highlights the materials limitations, as suggests a large resistance with the onset of redox change.

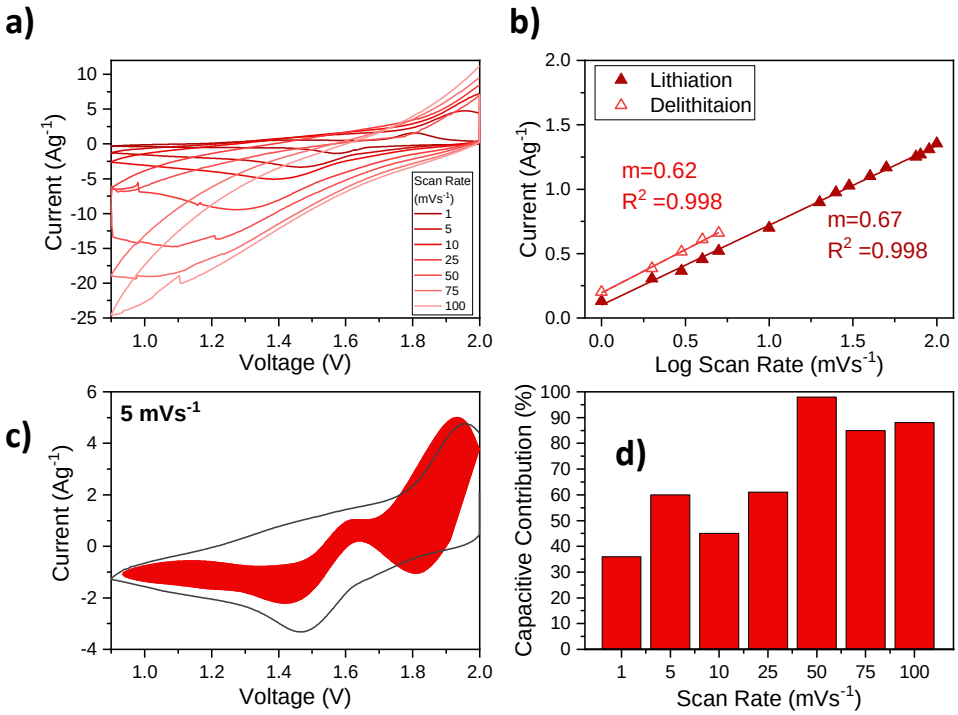

Figure 3.34 - a) CV profile of monoclinic Nb_2O_5 created at 1000 °C at increasing scan rate 1 to 100 mVs^{-1}, b) Log plot of current versus scan rate of redox peaks, with linear fits which have R^2 of at least 0.998, c) CV profile at 5 mVs^{-1} with shaded section as the capacitive contribution and d) the capacitive contribution at various scan rates.

This H-Nb_2O_5 shows good capacities and reversibility with surprising rate capability. The rate capability is much better than reported previously in the literature and this is reflected in the high capacitive contribution seen for this material. As a higher crystallinity form of the H-phase has also been produced, it will reveal whether these properties are accessible in both materials or whether this lower crystallinity form with some anisotropy is key to this.

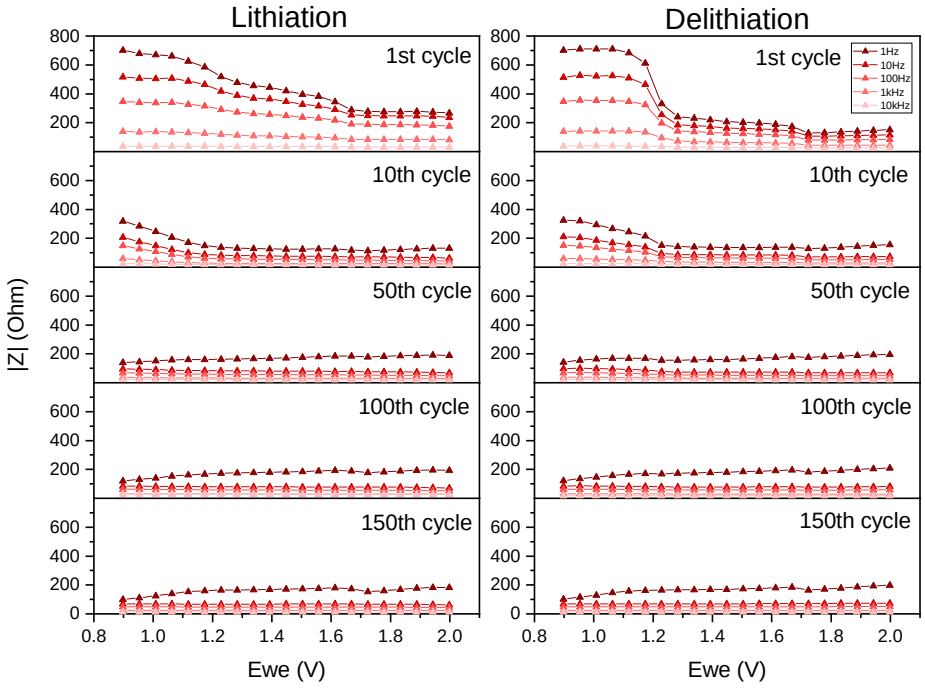

Figure 3.35 - SPEIS of H- Nb_2O_5 created at 1000°C for cycles from 1 to 150 cycles in a range of 1 Hz to 10kHz.

3.3.4.1.2 Electrochemical Properties of Monoclinic Nb_2O_5 Produced via a 1300 °C Heat-Treatment.

The monoclinic material produced at 1300 °C was also tested under a similar regime to the other samples to reflect on whether improved crystallinity has an impact upon the electrochemistry. As with the other H-Nb_2O_5 samples, it was expected that the preferred voltage range would be the narrow range of 0.9-2.0 V, however, the rate sweep tests show that the material performs best in the wide range (Figure 3.36a). Between rates C/20 and 1C, the average capacity for each voltage window is comparable, however, at the higher rates the material performs poorly in the narrow window. Even with longer testing at 1C the

material appears to perform similarly, independent of voltage window, with average capacities of 86 ± 11.3 and 73 ± 2.9 $mAhg^{-1}$ at 200 cycles for wide and narrow windows respectively (Figure 3.36b). Further to this, the differential capacity plots during formation appear almost identical for both windows, yet by cycle 1, as with the previous monoclinic Nb_2O_5 the redox peaks have largely diminished for the wide range (Figure 3.36c). After the formation cycles, the sharp redox peaks are retained in the narrow window, suggesting good reversibility. However even with the changes in redox response the wider window shows continued higher capacities at higher rates. It is not clear so far why this is the case, although the peak shift seen at high scan rates in the other monoclinic material, suggests an unsuccessful delithiation at increased current density in the narrow window.

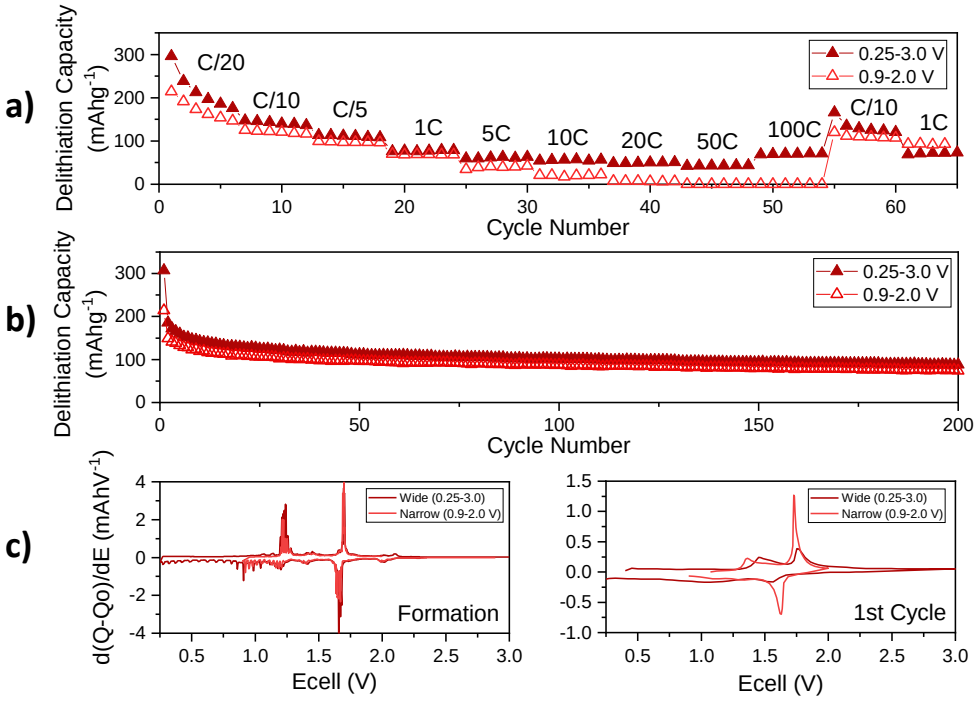

Figure 3.36 - (a) Rate sweep from C/20 to 100C with recovery to C/10, (b) Galvanostatic cycling at 1C over 200 cycles, (c) formation at C/20 and first cycle at 1C differential capacity plots for the different voltage windows for monoclinic Nb_2O_5 created at 1300 °C.

E*x-situ* XRD patterns show that structure is retained to 100 cycles for both voltage ranges, showing the continued reversibility of this phase (Figure 3.37). However, the narrow voltage range clearly allows for improved reversibility as peak broadening and formation of other materials is seen in the XRD patterns of the electrodes tested in 0.25-3.0 V by 100 cycles. This is consistent with the apparent loss in redox peaks seen in the differential capacity plot. These results are similar to those from the other monoclinic material, but here there is

obvious evidence for secondary materials forming with cycling in the wide range. However here, this does not appear to have the same level of destabilising effect on the capacity and thus one may conclude the higher crystallinity structure is key to achieving this.

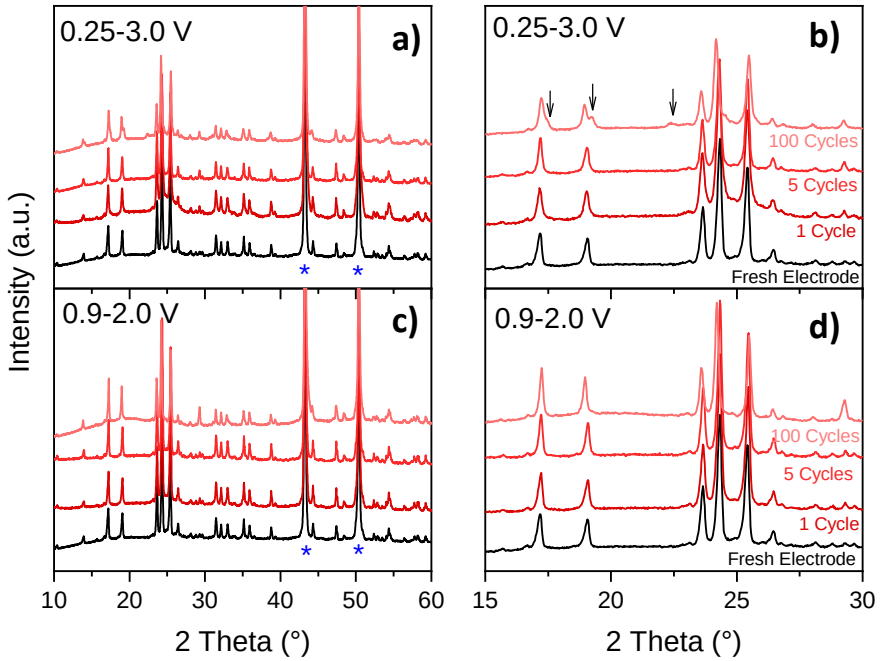

Figure 3.37 – Ex-situ XRD of cycled electrodes of H-Nb_2O_5 produced at 1300 °C at 1C, with a C/20 formation, in the range of 0.25-3.0 V (a, b) and 0.9-2.0 V (c, d). b and d are zoomed areas of corresponding patterns in a and c. Peaks identified as Cu current collector is identified by blue stars.

The *ex-situ* XRD results do not shed light on the differences seen in the voltage windows trialled. As although the XRD patterns show greatest change, with the formation of another phase present, the electrochemical response in superior. As such, different rates were tested over 200 cycles in the wide range (Figure 3.38). After the first 25 cycles all rates give a very similar capacity response with similar slow capacity loss over the 200 cycles. The average capacities at 200 cycles are 76 ± 4.3, 92 ± 2.9, 97 ± 4.6 $mAhg^{-1}$ for increasing rate from C/5 to 20C, respectively. The capacities at 1C and 20C are the same within error of each other, however the average capacity at C/5 is surprisingly lower than this. This may be due to the slow rate allowing for more side reactions taking place and thus a lower stability and lower capacity. However, the coulombic efficiency achieved does not appear to differ between rates, with all rates achieving over 98 % in the first ten cycles, and then high CE and good stability throughout the cycles. This is slower to achieve the higher efficiency than the lower crystallinity form, although this may be due to the slight differences in electrochemical conditions used (Figure A.36). The charge profile for 1C and C/5 cycling show two plateaus

in the first cycle, yet the 20C only shows one plateau. By 200 cycles the plateau is not apparent and the charge profile seems to have an inflex, this appears more like that of the intercalation pseudocapacitive type seen in the T-Nb_2O_5. This suggests a change in storage mechanism after the initial cycles and may explain the high-rate response. Therefore, this material was further tested at higher rates, 50C and 100C over 400 cycles (Figure A.35). There is more of decrease in capacity with increasing rates here, but at 200 cycles the average capacities are 73 ± 3.4 and 57 ± 16.4 $mAhg^{-1}$ for 50C and 100C, and by 400 cycles the capacities are 61 ± 5.3 and 48 ± 24.4 $mAhg^{-1}$ for respective rates. At these high current densities, there is some significant polarisation in the charge profiles, as expected from an insulating material. Furthermore, the charge profiles are near linear and thus suggest a capacitive-like storage at these rates.

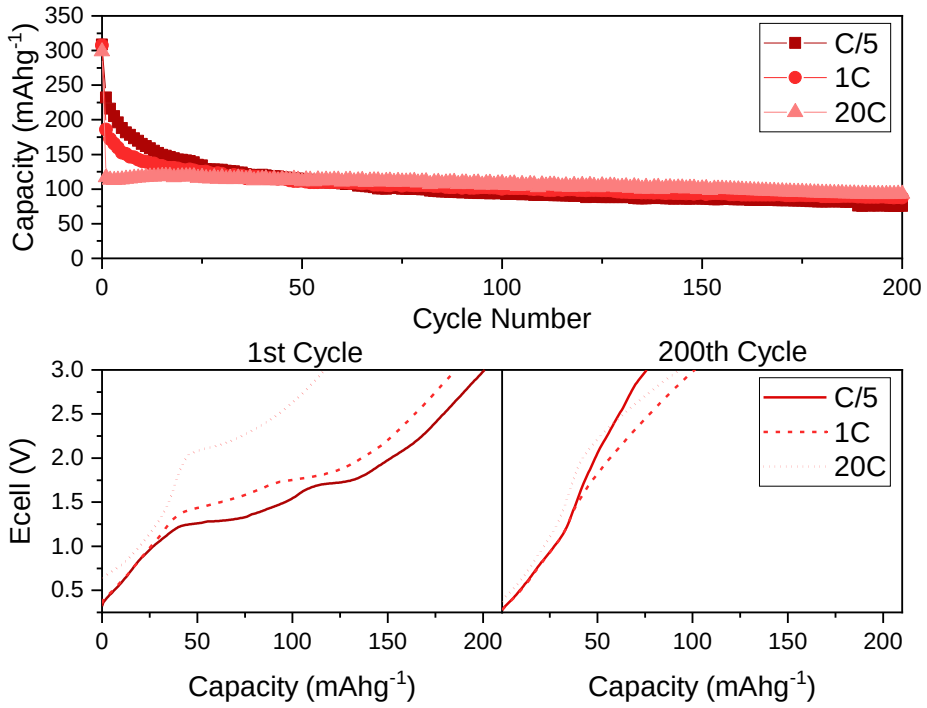

Figure 3.38- (top) Galvanostatic cycling at increasing rate over 200 cycles, (bottom) charge profiles at the different rates from 1st and 200th cycle, all in 0.25-3.0 V window for monoclinic Nb_2O_5 created at 1300 °C.

The CV profile shows three peaks in both lithiation and delithiation, where one set of peaks diminishes or combines with others at high scan rates (> 10mVs^{-1}) (Figure A.37). The log plot shows a large variation in gradient, with one peak (L-1, Figure A.37) showing a gradient greater than 1.0. This suggests that there is some key dependence on surface limited processes such as capacitive charge storage. As such the capacitive contribution was

calculated, showing 49 % at 5 mVs^{-1}. This is the same as the less crystalline H-Nb_2O_5 which had a capacitive contribution of 50 % under the same conditions.

The electrochemical impedance spectroscopy shows a reduction in impedance with cycling, suggesting the slight disordering seen in the *ex-situ* XRD is reducing resistance, specifically CT resistance (Figure 3.39 and Figure A.38). The initial SPEIS shows high impedance in the mid to high frequencies with an increase in between 0.25 – 1.25 V in both delithiation and lithiation (Figure 3.39). This coincides with the second stage of the redox process suggesting the further intercalation of lithium is resistive. This is still present in the 10th cycle, but by 50 cycles the impedance is low in frequencies 10 Hz- 10kHz. This coincides with a reduction in CT resistance in the Nyquist plots (Figure A.38). The 1Hz response, does show an increase in impedance between 3.0 -1.0 V in both lithiation and delithiation, showing the diffusion in and out of the materials does come with resistance. However, the diffusion tails do appear typical (at approximately 45 °) throughout, suggesting a stable diffusion process.

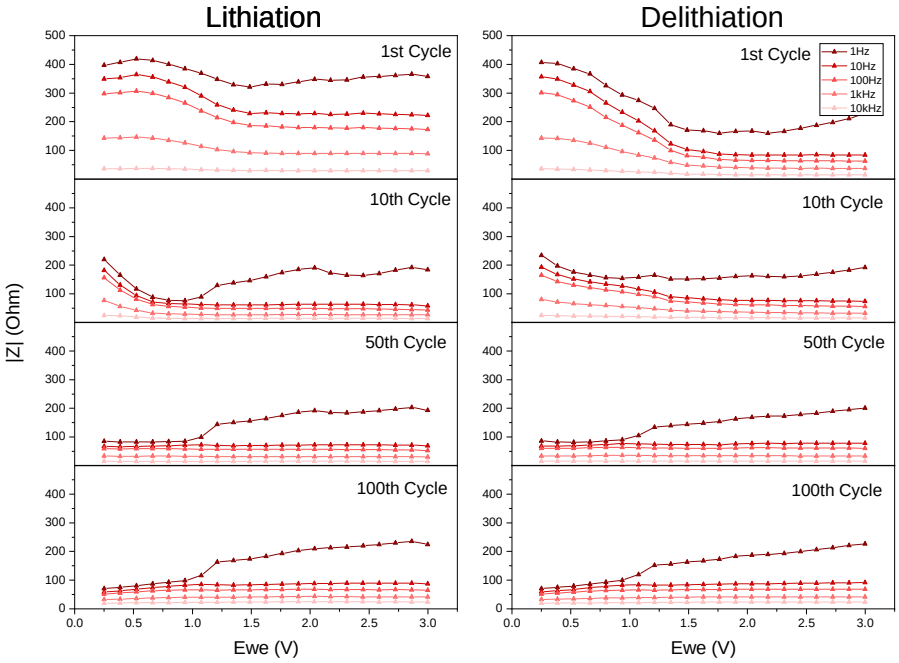

Figure 3.39 - SPEIS of H- Nb_2O_5 created at 1300°C for cycles from 1 to 150 cycles in a range of 1 Hz to 10kHz.

This highly crystalline monoclinic Nb_2O_5 shows reversibility and high-rate capability with cycling at 100C over 400 cycles. The material shows good maintenance of its structure with cycling, with minimal peak shift and broadening seen in the *ex-situ* XRD. This material

appears stable and can be cycled in a wider voltage range with little effect on long-term material integrity. Both monoclinic materials appear to be candidates for high-rate anode materials, regardless of the level of crystallinity.

3.4 A Comparison of Nb_2O_5 Materials Produced and the Associated Electrochemical Properties.

A simple hydrothermal method was used to produce Nb_2O_5 in an unusual anisotropically crystalline form. With heat-treatment crystalline phases, T- and H- are formed with various levels of crystallinity depending on the specific treatment. The as-synthesised particles are nano-wire networks with considerable surface area, with heat-treatment this decreases with the particles increasing in size and forming cuboidal particles. The same structural motifs are seen throughout the materials with increasing long-range order upon heat-treatment. Even in the apparent highly crystalline forms of the materials (800 °C T-Nb_2O_5 and 1000 °C H-Nb_2O_5) there is still deviation in PDFs compared to the ideal and obvious anisotropy within the structure due to large variations in peak sharpness. Some of the deviations come from the expected amounts of Nb in split occupancy sites when compared to what is expected form the ideal structures. These results highlight the complexity of the Nb_2O_5 structural system and the levels of disorder and defects that may be present in a seemingly ideal material.[65,356]

Electrochemically, the anisotropically crystalline structures appear to undergo intercalation pseudocapacitive storage expected of the T-Nb_2O_5, showing high-rate capability and high capacitive current contributions. The expected capacities are, however, not achieved, likely due to the reduction in accessible storage sites due to the material's disorder and the large SEI formation due to the high surface area. However, this material does appear to cycle in a larger voltage window with no stability issues, which may be expected from the phase formation seen in the T-Nb_2O_5. As such the T-Nb_2O_5 studied here does have an irreversible phase change within the first cycle, leaving a low crystallinity Nb_2O_5 and potentially NbO. Although this does not appear to affect the material's rate capability the capacities do not match the previous literature. Although a smaller voltage range could be used to prevent this change, *ex-situ* XRD suggests that this change happens over long-term cycling, even in a 1.0-3.0 V range. For the T-Nb_2O_5, the level of crystallinity appears to be a key factor, with the 600 and 800 °C materials showing a difference in the stability and capacities achieved. Yet it should be noted that even with this supposedly unfavourable phase change occurring, as the

literature suggests, these materials still show good cyclability and reasonable rate response. Surprisingly, the monoclinic phase shows the most promising results from this family of materials. Both H-Nb_2O_5 samples show very similar electrochemical responses suggesting the level of crystallinity is not a key factor for this phase. The capacities are high and most notably the capability to cycle at 100C cycling to 400 cycles. Notably, all materials show a similar impedance response, with some improvements with heat-treatment. Even though these materials show some relatively low resistances, the insulating nature of Nb_2O_5 is still an issue. This is evident from the huge redox peak shift observed in the CV profiles with increasing rate and polarisation in the charge profiles. Hence further work could be done to composite or coat these materials with a conductive material to allow for better optimisation.

When these materials are compared to the literature, the anisotropically crystalline phase compares well to the only other semi-crystalline Nb_2O_5 that has been reported and it also outperforms an amorphous Nb_2O_5 (Table 3.3). The T-Nb_2O_5 materials appear to match recent studies well at lower rates, with the reversible capacity showing some variation across reported studies. At higher rates the capacities appear lower than other reports, especially with the higher crystallinity T-Nb_2O_5, although this is consistent with the report by Hu *et al.* [131] This emphasises the effect of synthesis on material properties, as the work here shows that for T-Nb_2O_5 material a small improvement in crystallinity can significantly change the properties. With regards to the H-phase, as discussed already the literature on this is conflicted, with some studies showing the material is incapable of high-rate testing.[123,172] However, the work here reveals favourable rate capability, surpassing the studies showing good electrochemical properties for the phase. Interestingly, Song *et al*. show cycling to 80C which confirms the high rate capability observed here with capacities of 70 $mAhg^{-1}$ at 100C.[140] It can be suggested that the highly oriented precursor allows this family of materials to present high rate capability due to easily accessible non-torturous pathways available for Li diffusion.

The work presented here shows the level of complexity associated with the niobium pentoxide system, and the need for more in-depth structural analysis to fully describe these types of materials. The preliminary PDF analysis described here is only the beginning of the analysis which could be undertaken to determine fully atom-scale structures of this family of materials. Further work could look at PDF fitting and full Rietveld refinement of the neutron and X-ray scattering data in combination, however, this was beyond the scope of the current work. Moreover, to further describe these materials electrochemically *in-situ* XRD and XANES would be required to study the Li-ion storage mechanism thoroughly.

Table 3.3 – Comparison of capacities of Nb_2O_5 materials produced in this work to recent or relevant literature.

Nb_2O_5 phase	**Initial Capacity ($mAhg^{-1}$)**	**Reversible Capacity ($mAhg^{-1}$)**	**Rate**	**High-rate Capacity ($mAhg^{-1}$)**	**High Rate**	**Ref/Year**
Amorphous	150	75	0.5C	50	2.5C	[130]/2016
Anisotropically crystalline T-	225	63	1C	48	20C	This work
Semi Crystalline R-	145	143	2.5C	43	50C	[133]/2016
TT-	178	158	1C	86	20C	[157]/2020
T- (600 °C)	238	117	1C	90	20C	This work
T- (800 °C)	115	106	1C	42	20C	This work
T-	117	85	1C	33	25C	[131]/2020
T-	170	120	5C	127	50C	[137]/2019
T-	205	175	0.5C	118	25C	[153]/2019
H-	217	160	1C	115	20C	This work
H-	151	100	1C	68	25C	[131]/2020
H-	150	65	10C	50	80C	[140]/2020

4 Molybdenum Dioxide as a High-Capacity Li-Ion Storage Material.

4.1 Premise

Molybdenum dioxide (MoO_2) is investigated as a Li-ion battery anode material due to its electronic conductivity and high theorical capacity.[207] It is generally accepted that MoO_2 has the ability to undergo a four-electron transfer giving an 838 $mAhg^{-1}$ theoretical capacity. This comes from two lithium insertion mechanisms: an intercalation mechanism of one electron above 1.0 V (equation 13), and a further conversion reaction below 1.0 V (equation 14).[228]

$$MoO_2 + xLi^+ \rightarrow Li_xMoO_2 \qquad [13]$$

$$Li_xMoO_2 + (4 - \mathrm{x})\mathrm{Li}^+ \rightarrow Mo + 2Li_2O \qquad [14]$$

The conversion mechanism leads to irreversible reactions and electrode pulverisation meaning experimentally, the high capacities have not been achieved and the material has poor stability over long-term cycling. MoO_2 has been investigated as an intercalation material, having a capacity of 209 $mAhg^{-1}$ which avoids pulverisation issues by not resorting to a conversion mode of interaction with Li. This can be achieved by cycling above 1.0 V and has been shown to achieve 147 $mAhg^{-1}$ specific capacity after 2000 cycles at 1C.[237] When it comes to accessing the full electrochemical potential of MoO_2, an activation process is needed to achieve the highest capacities. This can be achieved via thermal activation, or can take place during the initial cycles, and allows for a structural rearrangement of the material to enable the conversion process.[241,242] However, some studies question whether the conversion mechanism even takes place, and suggests that Li rich phases form or large expansions of layers to incorporate many Li-ions.[236,245]

Stabilisation is required to enable exploitation of the promising properties from MoO_2. Heat-treatment has been shown to improve the electrochemical properties, yet with little investigation into how exactly this is brought about, or articulation as to the rationale for doing this.[252,253,255] Additionally, forming composites with carbon materials is a preferred method to improve the electrochemistry, due to addition of a conductive matrix. However, MoO_2 should be intrinsically conductive, thus it is proposed that the addition of carbon networks improves electrode integrity with conversion taking place.

4.2 Exploration of Synthesis of MoO_2

A simple hydrothermal synthesis route was used to produce MoO_2 using ammonium molybdate tetrahydrate (AMTH) and oxalic acid as precursors. The initial development of the synthesis method varied the temperature and acid concentration: temperatures of 200 and 225 °C and oxalic acid concentrations of 1, 5 and 10 %w/v were trialled, with a fixed synthesis time of 72 hours. The phase matched XRD patterns show that 200 °C is inadequate for successful synthesis of MoO_2, with only the 10 %w/v content reaction showing synthesis of MoO_2, however still amongst other material (Figure 4.1). At an elevated temperature of 225 °C, MoO_2 can be synthesised with 5 or 10 %w/v. A higher acid content is required to reduce the precursor from Mo (VI) to Mo (IV) to form MoO_2, hence 1 %w/v is unsuitable. MoO_2 formed via 5 or 10 %w/v acid concentration have similar XRD patterns, assigned to monoclinic MoO_2. Further characterisation is needed to discern the difference between these products. Microscopy images show the 10 %w/v product to have more consistent particle morphology than the 5 %w/v material (Figure A.39b-e). This was further confirmed using particle size analysis, where the 10 %w/v product shows a single distribution, regardless of data presentation, whereas the 5 %w/v product shows multiple distributions in the number and volume data (Figure A.39a). Therefore, the synthesis at 225 °C with 10 %w/v was preferred due to better particle consistency.

Regarding synthesis time, the XRD patterns at 3 and 6 hours shows an unsuccessful synthesis, as MoO_2 as a single phase is not formed (Figure A.40). At least 12 hours is required to produce MoO_2, from 12 to 72 hours, there appears to be no improvement in crystallinity as all the XRD patterns look similar and show broad peaks. The TEM images of these materials appear to show all materials have the same morphology, clusters of ellipsoidal particles, which all look of similar size (Figure 4.2). Particle size analysis (PSA) was used for further characterisation, where the 12- and 72-hour products appear similar, with the 24-hour product appearing anomalous with multiple particle distributions. One would propose that synthesis above 12 hours is appropriate to create MoO_2 successfully. However, the aim is to combine the synthesis of MoO_2 with Nb_2O_5, thus the 72-hour material is taken forward as this showed improved performance for Nb_2O_5 (Section 0).

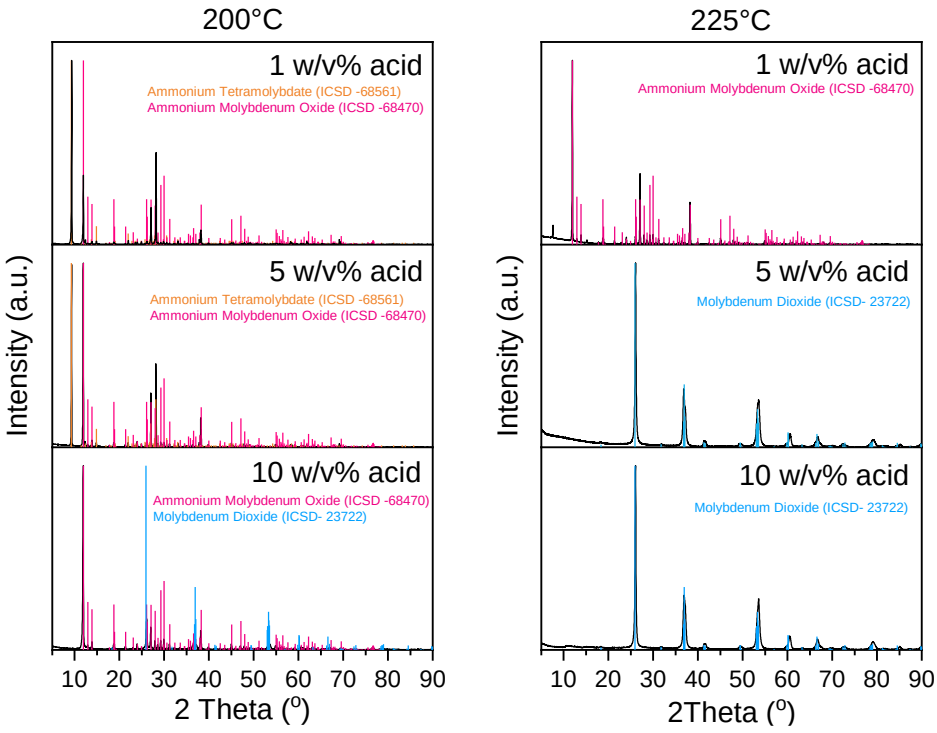

Figure 4.1 – XRD patterns of synthesis products created at 200 °C (left) and 225 °C with various oxalic acid concentrations all synthesised for 72 hours. The patterns are indexed to AMTH (ICSD-68561), ammonium molybdenum oxide (ICSD-68470) and MoO_2 (ICSD-23722). [362–364]

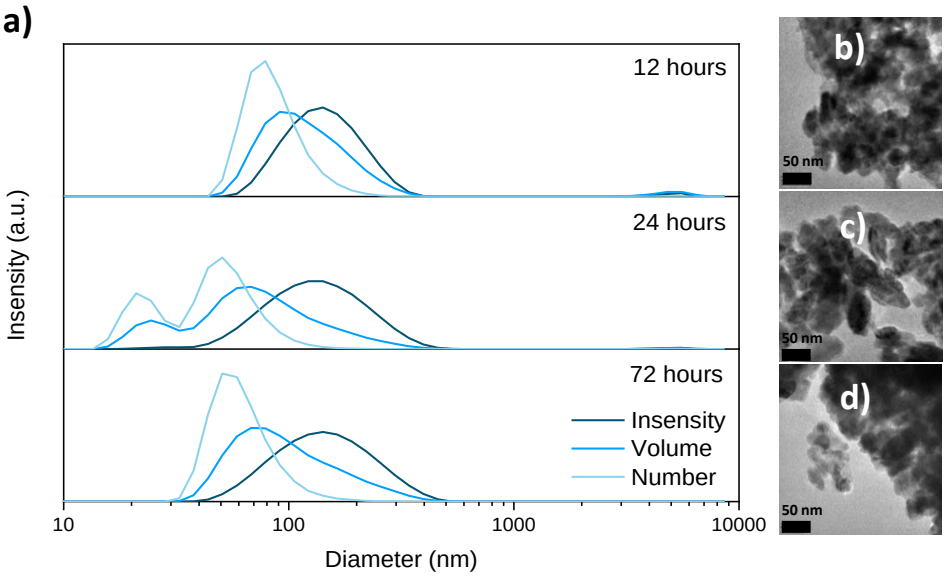

Figure 4.2 – a) Particle size analysis of MoO_2 created via synthesis at 225°C with 10 w/v% at increasing synthesis time. (b-d) Corresponding TEM images of products of 12-hour (b), 24-hour (c) and 72-hour (d) reactions.

4.3 Characterisation of MoO_2

The synthesis conditions chosen to prepare MoO_2 are 225 °C, 10 %w/v acid and 72-hour synthesis time. The XRD pattern is assigned to monoclinic MoO_2, and the particles are regular ellipsoids (Figure 4.3). These particles have a particle size distribution centred on 55 nm (number distribution) (Figure 4.2a). This is larger than the particle width measured from TEM counts, of 21 nm, and this may be due to the morphology of the particles and the assumptions made in PSA calculations (Figure A.41). This material has a BET surface area of 25.4 m^2g^{-1} with an average pore width of 22 nm (Figure A.44). From the average pore size and with most of the pore volume being above 10 nm, one would suggest that most of the porosity comes from inter-particle spacing. Therefore, the porosity within these particles is limited. The TGA of the as-synthesised MoO_2 was carried out; an initial loss of 2.4 % can be attributed to surface water (Figure A.45). A second loss in the range of 200-400 °C, is likely to be residual organic ions on the surface from the synthesis, also seen in the hydrothermally synthesised Nb_2O_5 (Section 3.3.2). From 400 to 750 °C, there are no change, suggesting a pure MoO_2 is achieved, with no residual surface ions. At 850 °C there is a large loss which can be attributed to the disproportionation to MoO_3 and Mo.[365]

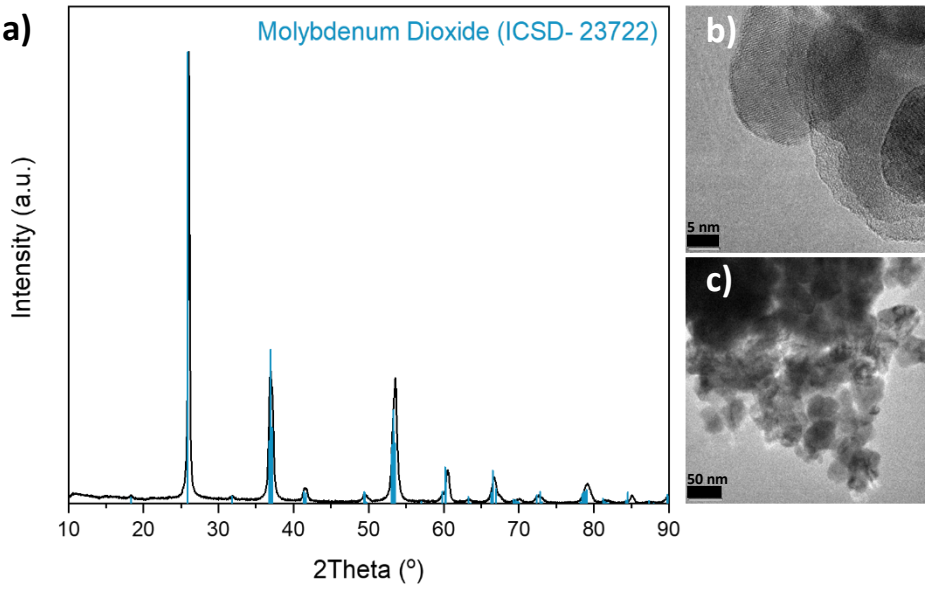

Figure 4.3 – (a) XRD pattern of as-synthesised MoO_2 assigned to monoclinic MoO_2 (ICSD-23722) denoted by blue sticks.[364] (b,c) TEM images of as-synthesised MoO_2. (Figure A. 42)

With heat-treatment MoO_2, cannot be retained at higher temperatures (Figure 4.4). XRD of the products from heat-treatment at 500 and 600 °C show a secondary phase forming. This is assigned to Mo_4O_{11} (ICSD-201573).[366] Even in an Ar atmosphere the oxidisation process has begun. Therefore, only the material heat-treated at 300 °C can be considered for further testing. The XRD pattern recorded for the MoO_2 heat-treated at 300 °C shows no change from the as-synthesised MoO_2. Further to this, the particles appear like the as-synthesised MoO_2, with agglomerates of ellipsoid shaped particles (Figure 4.5). There also appears to be no change in particle width. The heat-treated material showed a particle distribution centred on 20 nm, where the as-synthesised shows a distribution centre of 22 nm (Figure A.41).

Interestingly, what appears to be the main difference between the as-synthesised and heat-treated MoO_2 is the surface area. Although the isotherm and hysteresis type appear similar, the BET surface area is reduced from 25.4 to 5.9 m^2g^{-1} (Figure A.44). Furthermore, the pore distribution is shifted and has a larger mesoporous region, with the pore size average increasing from 22.0 to 33.8 nm (Table A. 3). It is unclear what causes this change as from the microscopy and PSA the particle size and morphology appear unchanged.

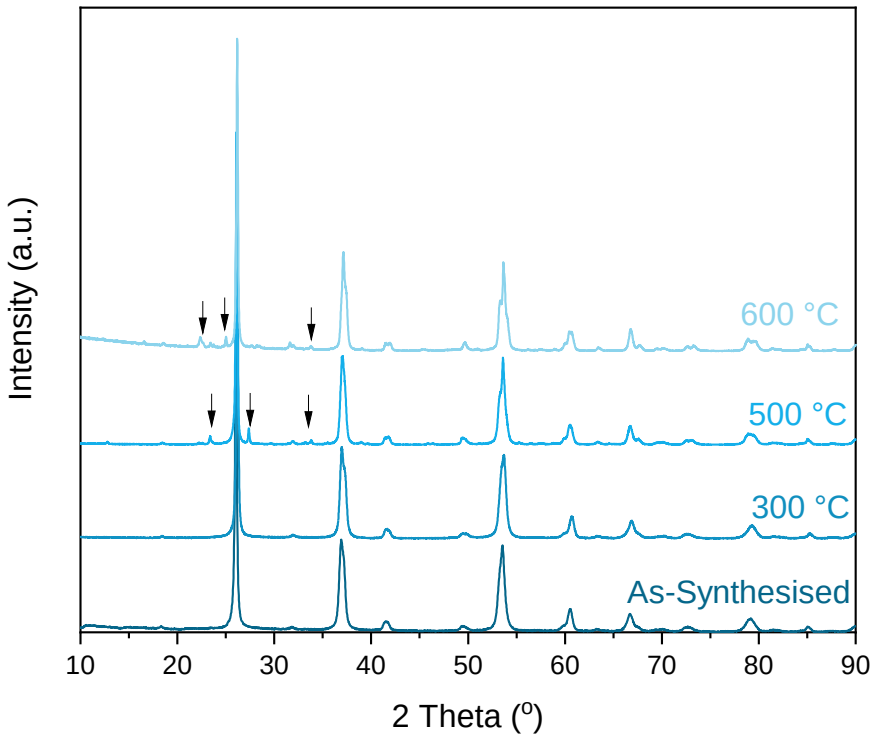

Figure 4.4 – XRD patterns of MoO_2 heat-treated at increasing temperatures under Ar, arrows denote the formation of the Mo_4O_{11} phase.[366]

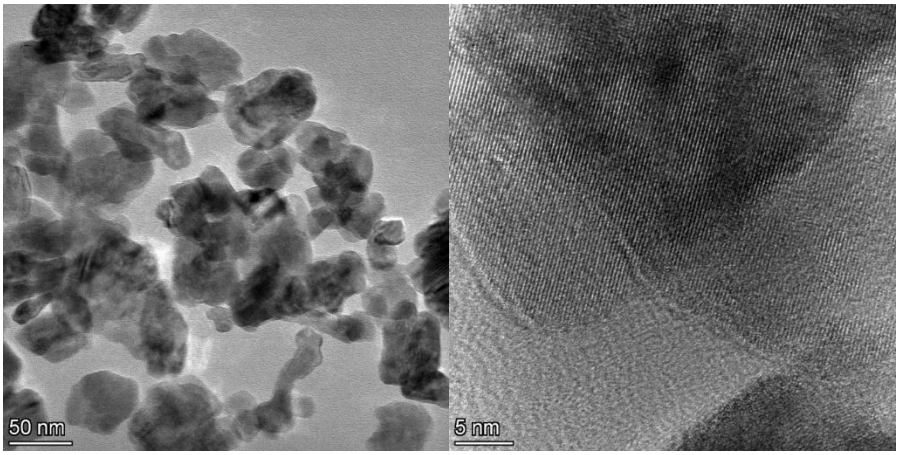

Figure 4.5 – TEM images of MoO_2 heat-treated at 300 °C, (Figure A.43).

Fitting of the Mo 3d XPS spectrum is complex due to spin-orbit splitting as described by Goodenough (Figure 4.6).[48] Although Mo in MoO_2 should only be in oxidation state (IV), states (IV) and (VI) are observed, thus MoO_3 may sit on the surface of the material.[205] Further to this, heat-treatment of this material in absence of oxygen shows self-oxidation at higher temperature, which is concurrent with the presence of MoO_3 (Figure 4.4). Mo (VI) makes up 42% of the molybdenum region which may suggest more than just a surface coating, however, the nature of XPS means that the measurements are dominated by surface species. Therefore, it cannot be ruled out that this is an oxidised surface. It should be also noted that the XPS data shows evidence of metal carbon bonds (denoted as metal carbide) as well as an ammonium type of nitrogen bonding. One would expect these to be organic ions left on the surface of the material due to the nature of the hydrothermal synthesis.

XPS confirms that with heat-treatment there is very little change in the composition of the material (Figure 4.7). Mo (VI) is still seen in this material, as well as the presence of organic ions on the surface represented by the metal carbide and N-H fitting. Evidently, to completely remove surface oxide a higher temperature and more reducing conditions may be needed, furthermore a higher temperature is required to completely remove the organics on the surface. As with the TGA, it appears that the complete removal of organics would occur at 500 °C. Yet, issues are evident when heat-treating to this temperature, and use of a reducing atmosphere when heat-treating the material may drastically affect the materials characteristics. Therefore, further tests were performed on this material as it provides a good comparative study between as-synthesised and heat-treated material, which the literature is somewhat lacking in.[252–255]

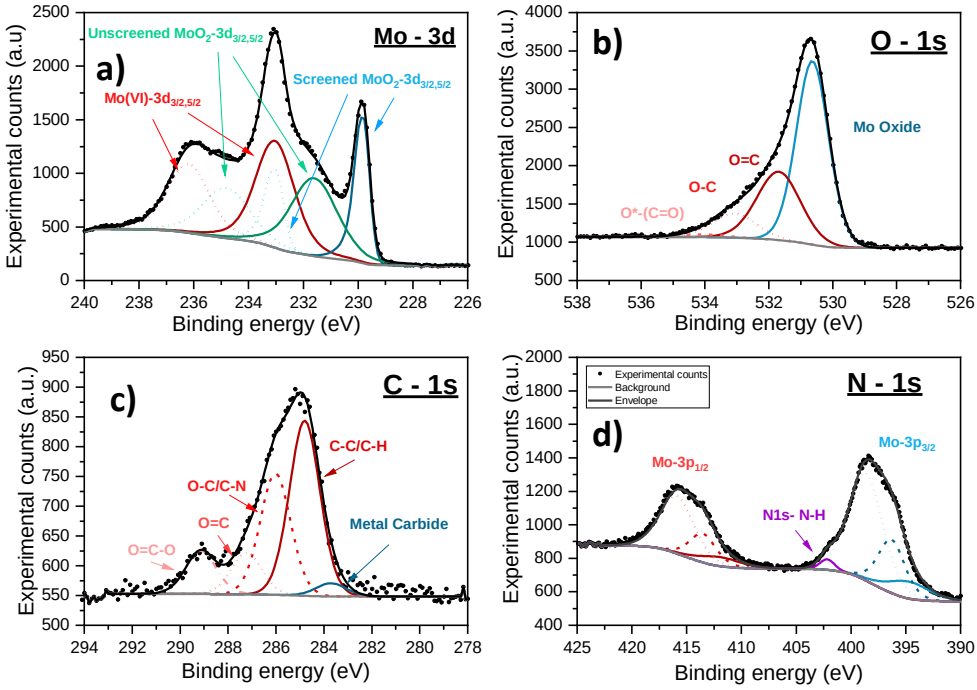

Figure 4.6 – High resolution XPS spectra of the Mo 3d region (a), O 1s region (b), C 1s region (c) and N 1s region (d) for as-synthesised MoO_2.

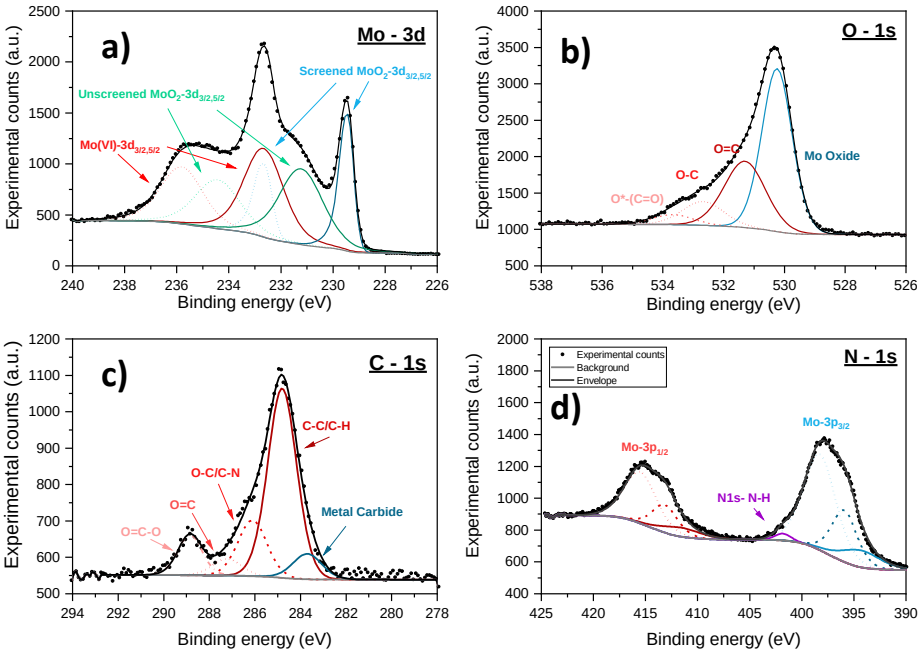

Figure 4.7 - High resolution XPS spectra of the Mo 3d region (a), O 1s region (b), C 1s region (c) and N 1s region (d) for heat-treated MoO_2.

The IR spectra shows the expected MoO_2 peaks at 1076, 941, 863, 719 and 603 cm^{-1} (Figure 4.8), with some shift compared to those complied and reported by Dukstiene *et al*.[367] The presence of a peak at 719 cm^{-1} and the shift to lower frequency of the 1076 cm^{-1} peak- compared to the standard 1014 cm^{-1} - suggests crystallinity in the structure. The peaks at 863 and 603 cm^{-1} are identified as short and medium length Mo-O bonds respectively, and thus the change in frequencies from those reported may suggest some change in bond length from the expected crystalline structure. This is unsurprising as nanoparticles of MoO_2 are produced. Interestingly, upon heat-treatment all MoO_2 peaks remain, yet the absorption is reduced. As there is no change observed in the XRD patterns is unlikely that this is a significant structural change, however surface changes cannot be ruled out. Other than peaks identified as MoO_2, there appears to be many weak peaks which correspond to some water remaining in or on the material - as well as potential organic molecules - which is concurrent with the XPS. Notably, there are larger peaks at 3400 and 1500 cm^{-1} which correspond N-H or N-O for the respective peaks. Further to this, these peaks vastly reduce in intensity with heat-treatment, suggesting that these are cleaned from the surface with heat-treatment. Yet, the full removal of these molecules is not achieved at this temperature as there is still a nitrogen response seen in the XPS.

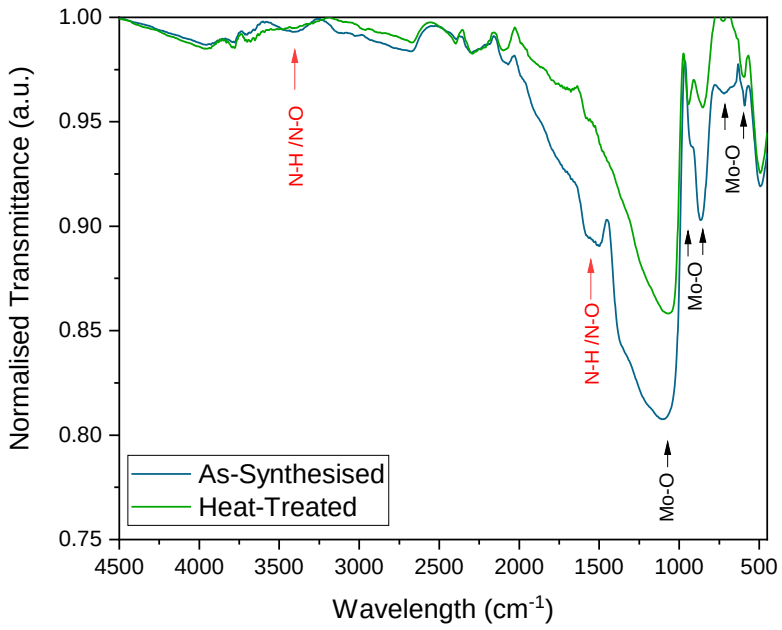

Figure 4.8 – IR spectra of as-synthesised (blue) and heat-treated at 300 °C MoO2 (green), the data are smoothed to clarify the peaks measured.

4.3.1 Electrochemical Characterisation of MoO_2 as an Anode for Li-Ion Half Cells

4.3.1.1 As-Synthesised MoO_2 Electrochemical Testing

MoO_2 can store Li-ions via two reversible mechanisms: intercalation and conversion.[207] Above 1.0 V there is a multi-phase intercalation reaction and below 1.0 V, there is a conversion reaction, and pseudocapacitance can be also expected. Therefore, a wide voltage range of 0.01-3.0 V was tested to take advantage of all mechanisms and thus access the high theoretical capacity. A second voltage window of 0.9-2.0 V was used to study the intercalation reaction only, as seen by the two pairs of redox peaks in the differential capacity plot in Figure 4.9b. The wide voltage range shows a period of activation between the 1st and 5th cycle where the capacity increases from 273 to 419 mAhg^{-1} where capacity is largely varied between cells prior to activation (Figure 4.9a). This activation process happens quickly as often takes up to 30 cycles for completion.[242–244] However, it is likely that the poor crystallinity of this material and the nanostructure allows for a lower Mo-O bond energy compared to a highly crystalline structure and thus a faster activation.[242,244,248] However, even at the activation peak the capacity is far lower than the theoretical. After the activation is complete, the capacity reduces rapidly until 50 cycles where the capacity plateaus and only shows a minimal loss of up to 200 cycles. The differential capacity plots show all loss of profile shape, with no notable redox peaks, from 1 to 100 cycles at the wide voltage window, (Figure 4.9b) suggesting that the reaction is not reversible, and that the activation may have caused structural degradation – this will be discussed further below.

For the narrow voltage window, the average capacity of the 1st cycle is 128 ± 10.7 mAhg^{-1}, which still has not achieved the theoretical capacity of 209 mAhg^{-1}. There is a fast capacity loss followed by a plateau, and by 100 cycles both voltage windows achieve an identical capacity. However, the redox peaks are present in the differential capacity plot after 100 cycles (Figure 4.9b). This suggests that even without the conversion reaction, the intercalation procedure is not fully reversible as there is nearly a 50 % loss in capacity over 100 cycles. This may be due to Li- trapping in the structure or disordering of the structure with the multi-phase intercalation reaction taking place.[234]

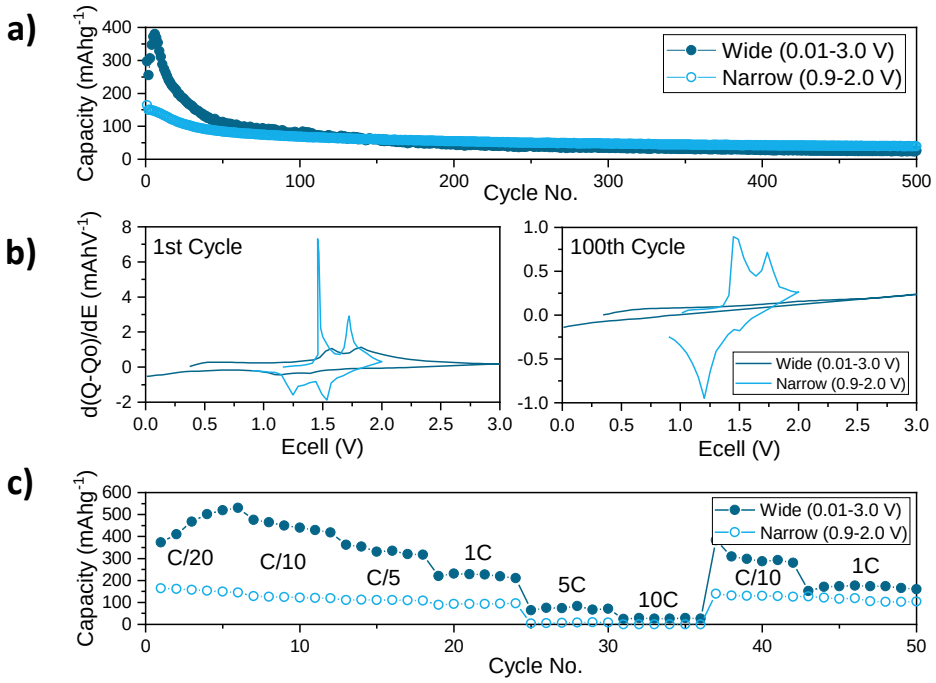

Figure 4.9 - a) Galvanostatic cycling at 1C for 200 cycles at voltage windows 0.01-3.0 V and 0.9-2.0 V for as-synthesised MoO2. b) Differential capacity profiles of the 1st and 100th cycle for the wide and narrow voltage window. c) Rate Sweep from C/20 to 20C, with recovery to C/10 at different voltage windows.

During the rate sweep, at C/20, the capacity is close to the theoretical for both voltage windows (Figure 4.9c). The high capacity is maintained to C/5, but as the rate is increased from here, the step down in capacity is much larger. As for recovery at C/10 the narrow window achieves over 90% capacity recovery, where in the wide window there is only 67% recovery. This material can only cycle to 10 C without failure, and it favours a lower C-rate. To achieve the high capacities which MoO_2 is famed for, a wider voltage range should be used, although further stabilisation of this material is needed.

When the as-synthesised MoO_2 was further tested at different rates - the first cycles appear to be very similar - with average 1st cycle capacity of 324, 333 and 331 mAhg^{-1} for C/5, 1C and 5C, respectively (Figure 4.10). All these results show poor reproducibility, as the initial cycles can deviate from cell to cell largely, standard deviations of over 25 mAhg^{-1}. However, the capacity trend is clear across all cells: an activation process between cycle 1 and 5, followed by a fast decrease in capacity to approximately 50 cycles. The gradient of capacity loss becomes steeper with increasing rate, suggesting the higher rate destabilises the material more quickly. The charge profiles change dramatically for all rates between 1 and 100 cycles; at 100 cycles the plateaus have completely disappeared, and the profile is almost linear

(Figure 4.10, bottom). This may suggest that both the conversion and intercalation mechanisms can no longer take place and that the remaining capacity is achieved via pseudocapacitance only. Interestingly, although this material appeared to perform better at lower rates, over the long-term cycling the rate appears to show little effect on the stability and thus capacity.

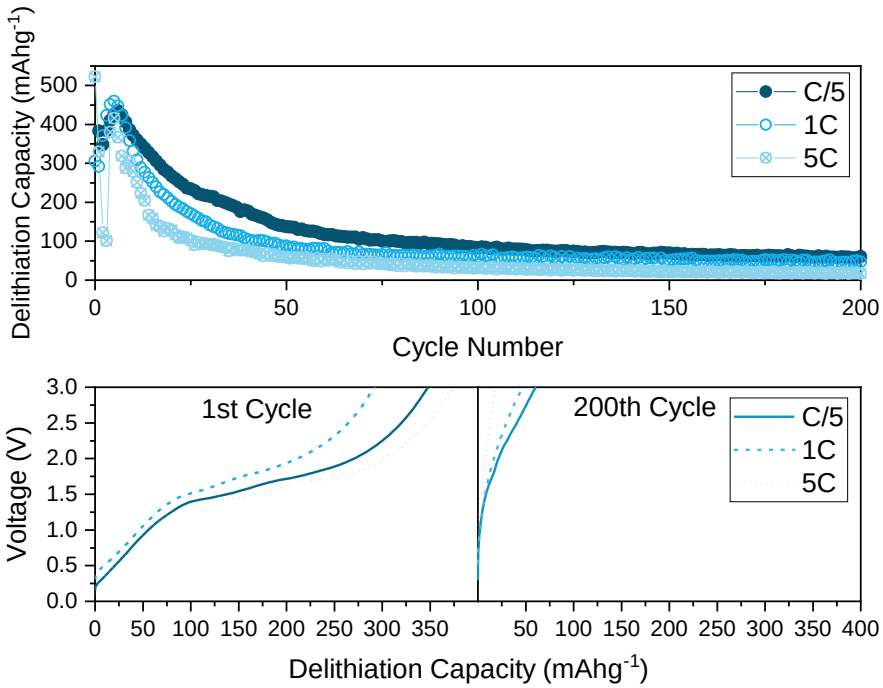

Figure 4.10 – (top) Galvanostatic cycling at increasing rate between 0.01-3.0 V for as-synthesised MoO_2. (Bottom) Corresponding charge profile of 1st and 100th cycle at increasing rate.

Ex-situ XRD patterns of the electrodes, show no change after the 1st cycle, yet within 10 cycles, there is a secondary phase formation (Figure 4.11). With cycling, the MoO_2 peaks do show shift and broadening compared to the fresh electrode pattern. Notably at 10 cycles, small new peaks have formed, these can be assigned to $Li_{0.98}MoO_2$, and lithium oxides, Li_2O and Li_2O_2 (ICSD 25530 and 257372).[368,369] It is difficult to say with certainty that these are the true products as the peaks are small and show some shift from the ideal structure, especially for the $Li_{0.98}MoO_2$ peaks. This suggests that the lithiation process is not fully reversible and some material remains in the lithiated form. This will lead to loss of MoO_2 inventory and therefore loss of overall capacity. By 50 cycles, capacity is vastly reduced, and the redox peaks are diminished, this may be expected to come with a structural decomposition, as seen by XRD peak broadening and secondary phases. In addition, there is little evidence of an irreversible conversion mechanism except small lithium oxide peaks, as previous literature has shown full amorphisation of MoO_2 and presence of metallic Mo with successful

conversion mechanisms. The differential capacity plots show clearly that the conversion mechanism takes place by the presence of a redox peak below 0.5 V. This increases in size with activation, but at 4 cycles the peak begins to decrease in intensity (Figure A.47). As the conversion mechanism becomes unfavourable, it is unclear what causes this as there is no obvious structural change observed, only secondary phase formation (Figure 4.11). However, there is a change in the redox peaks in the range of 1.0 – 2.5 V, which coincides with activation, where the two sets of peaks form one broad set of peaks (Figure A.47). Further to this, the *ex-situ* XRD suggests that the intercalation is only partially reversible, hence the further loss in capacity is expected.

Further electrochemical analysis, cyclic voltammetry (CV), shows the two pairs of redox peaks indicative of the intercalation yet, no clear peak for conversion (Figure 4.12a). This may be due to the activation process not taking place as the kinetics are too slow in comparison to the scan rate used. As the scan rate increases, the two redox peaks merge and show a broadening and voltage shift. This suggests an increase in resistance within the material with increasing current density, and thus the multi-phase intercalation mechanism can no longer take place. However, the remaining broad peaks suggests a single-phase intercalation with material expansion, therefore there is potential for an intercalation pseudocapacitive type mechanism to take place. Between 1 and 10 mVs^{-1} the two-redox pairs are clear and the lithiation process appears to be less limited by diffusion compared to the delithiation process as the log plot gradients are 0.80 and 0.60 compared to 0.54 and 0.58 respectively (Figure 4.12b). After 10 mVs^{-1}, the redox peaks begin to merge, and the peaks show large voltage shift. This increase in ohmic resistance is also seen by a reduction in gradient for the log current peaks. All the gradients reduce to below 0.5; this shows an extremely limited and resistive process. This may explain the lack of rate capability seen by this material at high rates. When the capacitive contribution is separated, there is an increase up to 10 mVs^{-1}, then after this, it is then reduced up to 100 mVs^{-1} (Figure 4.12d). However, this material demonstrates a clear pseudocapacitive mechanism regardless of rate; consistent with the linear charge profiles after 100 cycles (Figure 4.10). This explains that even when the intercalation reaction breaks down the material is still achieving some capacity via capacitive behaviour.

Staircase Potential Electrochemical Impedance Spectroscopy (SPEIS) was carried out on the material to further analyse the resistive processes during electrochemical reactions (Figure 4.13). The first lithiation shows a reduction in impedance from 3.0 V to 1.5 V, where it remains low. This suggests that the insertion of Li-ions into the structure is a resistive

process, but this resistance is mitigated with the phase change to intercalate the ions. Alternatively, with Li-ion extraction the resistance is relatively low throughout but shows a further decrease from 2.0 V, suggesting that the extraction is a favourable process. This is counter to the results from the CV scans, where the delithiation process appears to be diffusion limited. With increasing cycles, the impedance is increasing across the voltages at all frequencies. This is unsurprising as there is a drastic capacity loss and structural degradation, which likely comes with an energy barrier or some type of resistance.

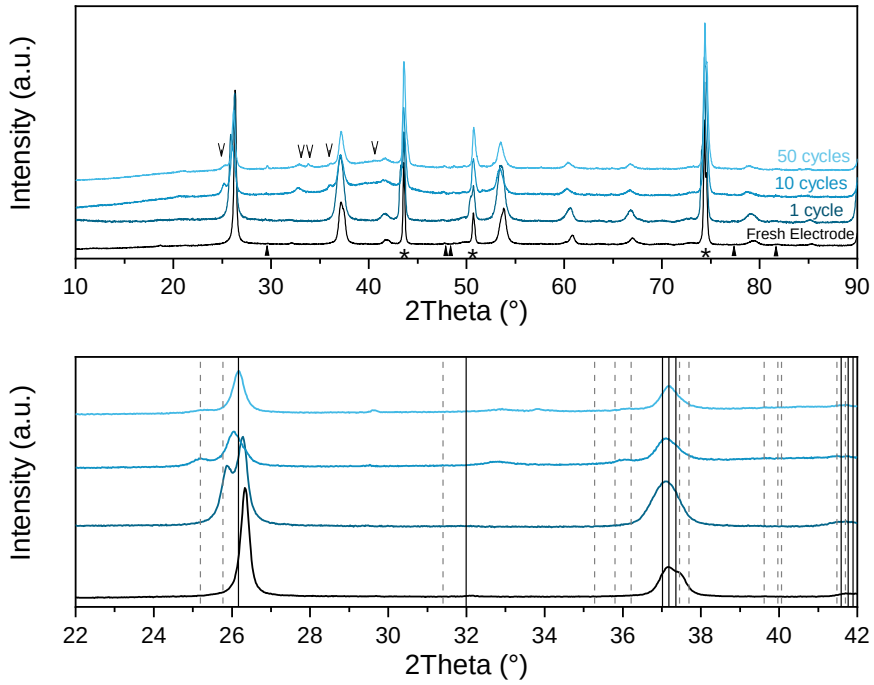

Figure 4.11 – Ex-situ XRD patterns of as-synthesised MoO_2 cycled between 0.01-3.0 V at 1C. (Top) full XRD pattern for fresh, 1, 5, and 50 cycled electrodes, where the Cu current collector is denoted by stars, triangles denote peaks from the sample holder, and arrows denote new phases forming. (Bottom) Zoomed in region of XRD patterns between 22 and 42°, where MoO_2 pattern is denoted by black lines (ICSD 23722), $Li_{0.98}MoO_2$ is marked by grey dashed lines (ICSD 204180). [229,366]

This hydrothermally produced MoO_2 appears to lack stability which drastically effects its electrochemical properties, in particular cycling stability. The conversion mechanism is unfavourable after a short activation and as such the theoretical capacity becomes limited to only 209 $mAhg^{-1}$ through the intercalation mechanism. However, this appears to have poor reversibility with *ex-situ* XRD analysis showing structural disordering and multiple phase formation. This material requires further stabilisation to realise its potential, hence a heat-treated form is tested as this has previously been noted to be a successful method to achieve electrochemical stability.[252–254]

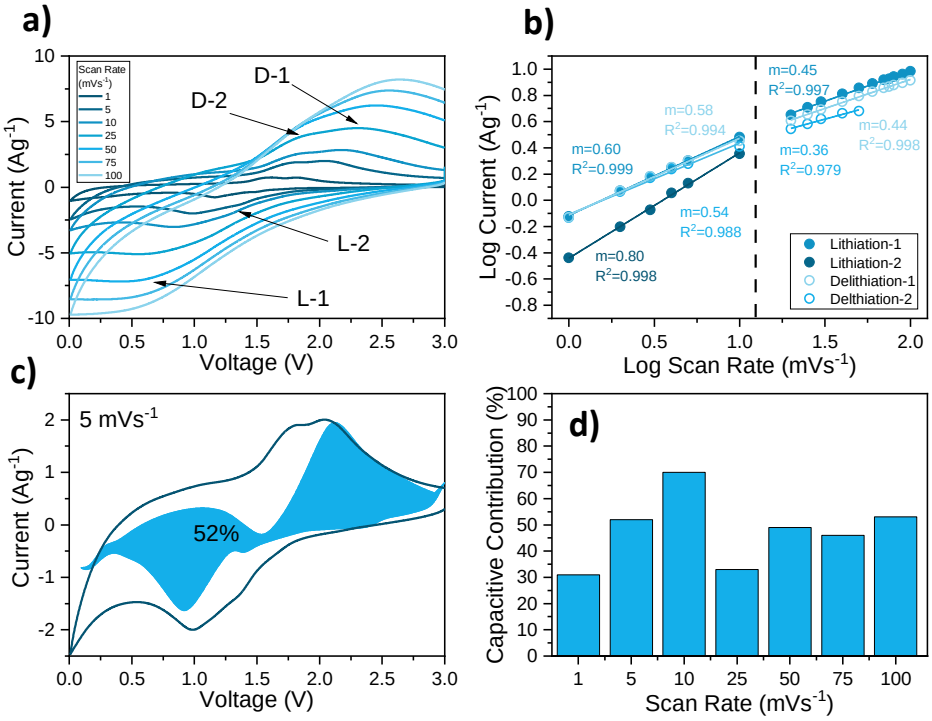

Figure 4.12 – a) CV profile at increasing scan rates, arrows point to current peaks for lithiation (L) and delithiation (D). b) Log plot of peak currents with linear fits with R^2 of at least 0.979. c) CV profile at 5 mVs^{-1} with the shaded area as the capacitive contribution. d) Capacitive contribution at increasing scan rate, all for as-synthesised MoO_2.

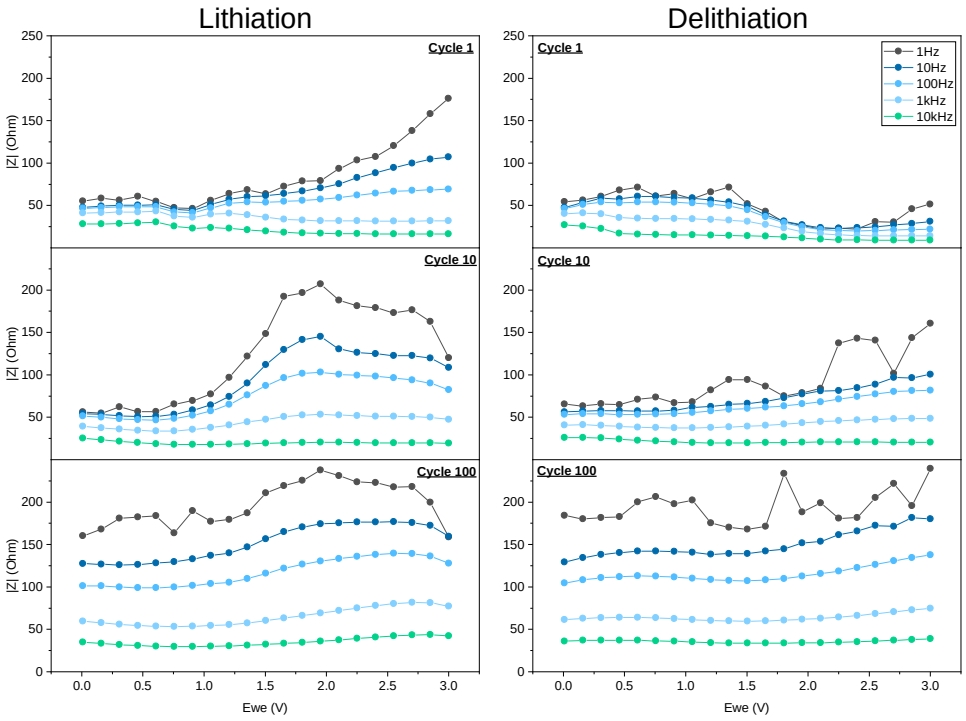

Figure 4.13 – SPEIS of as-synthesised MoO_2 at cycles 1, 10 and 100 for lithiation (left), delithiation (right).

4.3.1.2 Electrochemical Properties of MoO_2 Heat-treated at 300 °C

As with the as-synthesised MoO_2 two voltage windows were explored to take advantage of the different Li-ion storage mechanisms. This material shows a short initial activation reaching its highest capacity within 5 cycles, with an average peak capacity of 622 ± 15 $mAhg^{-1}$ (Figure 4.14a). After activation, there is a fast loss in capacity up to approximately 25 cycles, where an average capacity of 380 ± 19 $mAhg^{-1}$ is recorded. Strangely, after this there appears to be a second increase in capacity up to 75 cycles then a steeper capacity loss to 200 cycles from there. The differential capacity plot has a redox peak attributed to the conversion reaction <0.25 V in the initial cycle and at the 100th cycle, thus this suggests that the activation process does not change the occurrence of this reaction (Figure 4.14b). However, the redox peaks associated with the intercalation reaction become far broader by the 100th cycle suggesting a lack of reversibility in the process. Alternatively, in the narrow voltage range, the capacity appears stable throughout and the differential capacity plots show that the redox peaks are maintained. The capacity is expected to be lower in this voltage range as there is now a theoretical capacity of 209 $mAhg^{-1}$ attributed to the intercalation reaction only. This material appears to match this theoretical capacity well with an average of 168 ± 2.3 $mAhg^{-1}$ initially at 1C, and thus at a lower rate, may meet this. This shows that this material may be a good intercalation only material, although the preferred higher capacities cannot be achieved in this way. Regarding rate capability, the wide range shows higher capacities at all rates, with higher relative steps down in capacity at increasing rate. The higher capacities appear to be maintained at lower rates, but as the rate is increased to 1C, this is lost. A similar trend is seen in the narrow window however shifted to 5C; this material may be rate limited. Indeed, this is expected when the conversion reaction is used due to the very slow kinetics of this reaction, yet when the intercalation reaction is used only, one may expect an improved rate capability. This limited rate performance may not only be due to the material itself but may also be a call to an optimised electrolyte system with a higher salt concentration to reduce ion depletion at these higher rates. To assess this, further rate tests are completed.

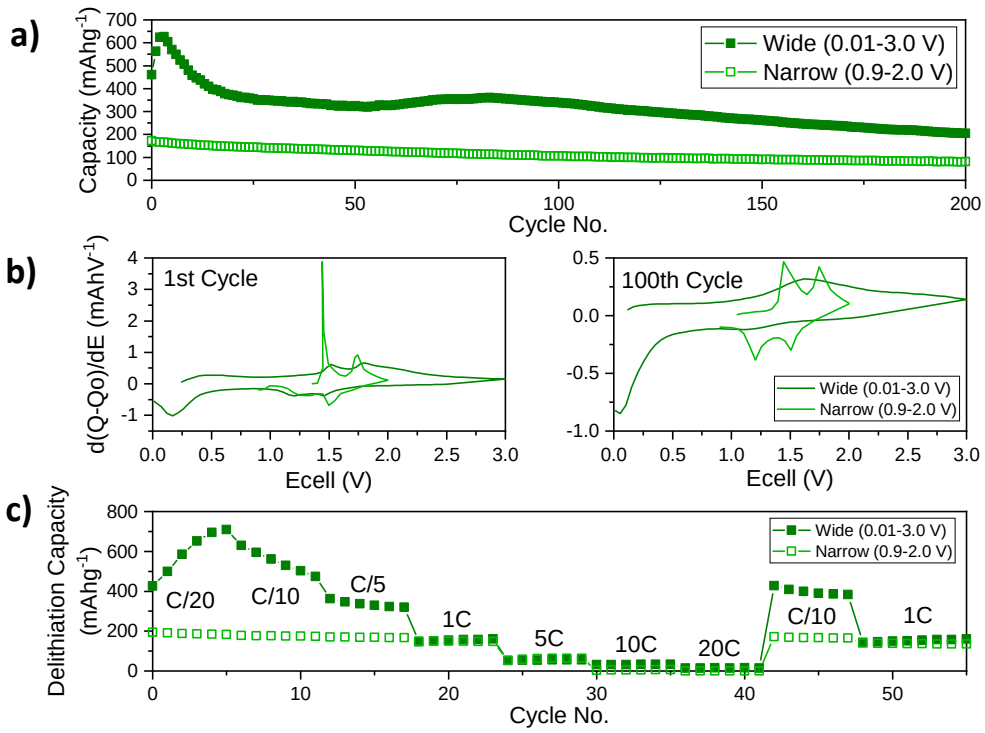

Figure 4.14 - a) Galvanostatic cycling at 1C for 200 cycles at voltage windows 0.01-3.0 V and 0.9-2.0 V for heat-treated MoO_2. b) Differential capacity profiles of the 1st and 100th cycle for the wide and narrow voltage window. c) Rate Sweep from C/20 to 20C, with recovery to C/10 at different voltage windows.

The same trend in capacity over cycle life is seen at all rates, with a slight delay on the activation process seen at C/5 (Figure 4.15). The peak capacities are 687, 622 and 557 for cycle rates C/5, 1C and 5C respectively, clearly higher capacities can be achieved at a lower rate. The results for the 1C and 5C appear very similar, with the C/5 showing higher capacities throughout, by 200 cycles the average capacity is 402 ± 4, 228 ± 20 and 220 ± 22 $mAhg^{-1}$, at increasing rate. The differential capacity plots show that initially at all rates a redox peak corresponding to the conversion reaction is seen. However, the two pairs of redox peaks corresponding to the intercalation reaction can only be seen at C/5 and 1C. At 5C there is a single set of broad peaks, this may suggest that the multi-phase change expected from the intercalation reaction no longer takes place and that there is only an expansion in the material, thus retaining a single-phase. This may suggest that the kinetics of the intercalation reaction are slow and thus are favoured in the lower rates. By 200 cycles, the intercalation redox pairs have diminished considerably at all rates, this may be due to the structural breakdown, and thus the material is no longer the appropriate phase required for the multi-phase reaction. It is evident that the conversion reaction does still take place at 200 cycles

for tests at C/5, this peak is no longer visible at higher rates, therefore may be attributed to the capacity differences at this point.

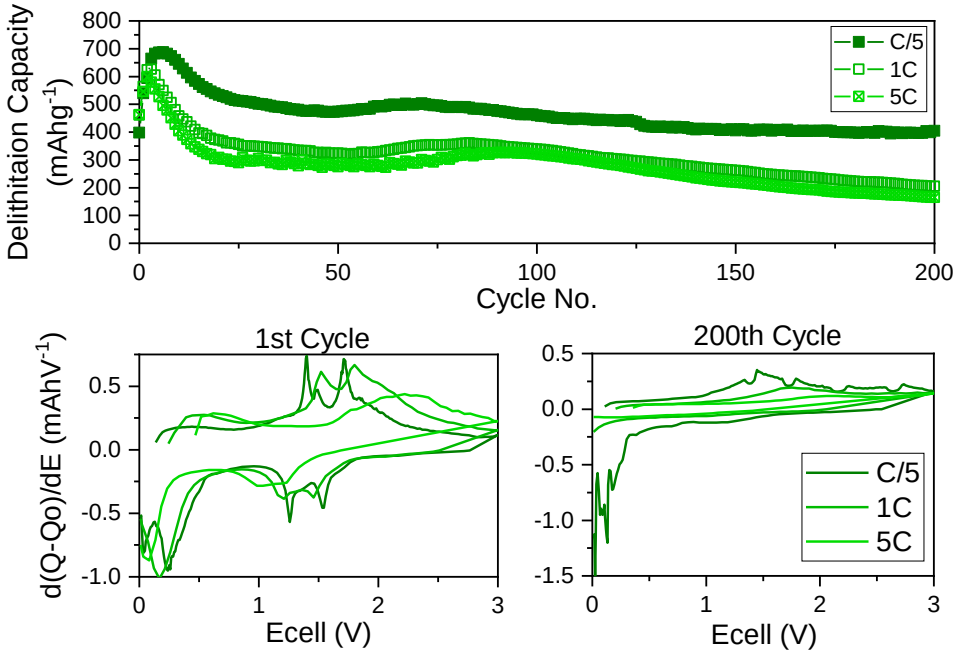

Figure 4.15 - (top) Galvanostatic cycling at increasing rate between 0.01-3.0 V for heat-treated MoO_2. (bottom) corresponding differential capacity plots of 1st and 200th cycle at increasing rate.

The mechanism is further explored via *ex-situ* XRD after cycling (Figure 4.16), where change in peak position and sharpness and secondary phase formation is seen. Within the first cycle the monoclinic MoO_2 structure breaks down where there is peak broadening and loss of intensity. However, by the 5th cycle, the structure appears to have recovered, with a small shift to lower 2-theta values. Yet the peaks at ~37° and ~54° which both appear to be sets of peaks originally only return as a single peak, this suggests a shift to a similar structure, however with a change in symmetry. This may be evidenced by a change in the symmetry from $P2_1/c$ to $P2_1/n$ as was proposed by Zhang *et al*. during the conversion process.[242] This suggests that the material undergoes structural rearrangement during activation and thus improves capacities during this stage. One would suggest that this proposed change is unlikely and the publication in which it is proposed lacks clear evidence to prove it, not only is the $P2_1/n$ phase uncommonly cited but the phase database (PDF 4+) notes that the $P2_1/c$ phase was a better fit to the MoO_2 phase and thus should be considered a replacement for this phase. To add to this, these two phases appear indistinguishable as a fit for the MoO_2

created here due to the broad nature of the peaks (Figure A.48). Therefore, the changes seen within the first five cycles must have an alternate cause.

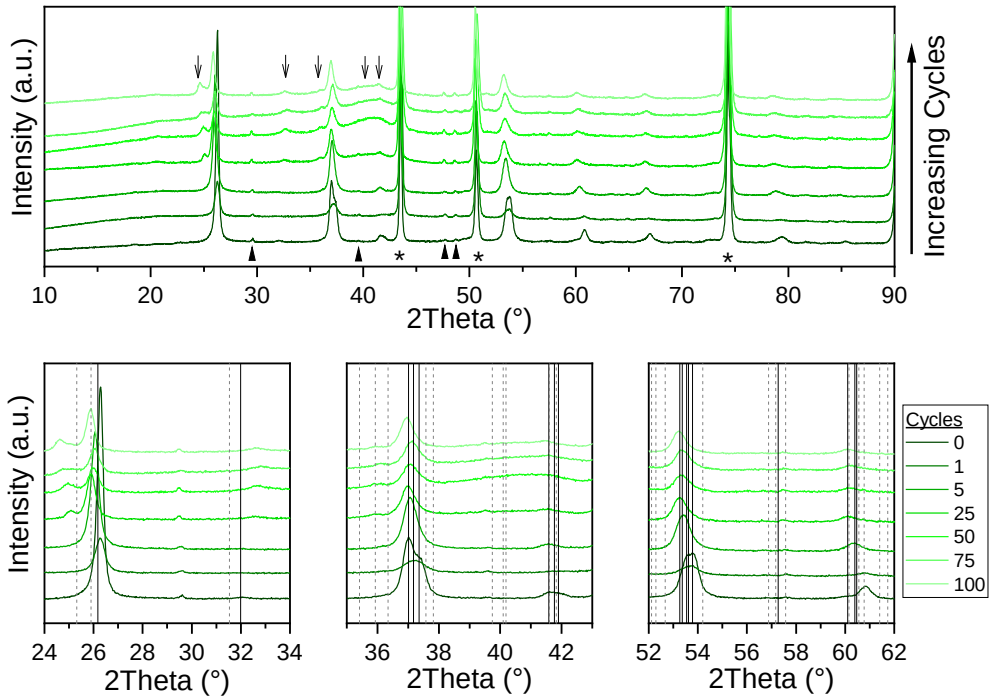

Figure 4.16 – Ex-situ XRD of heat-treated MoO_2 electrodes after cycling at 1C in 0.01-3.0 V range for various cycle numbers, where 0 cycles is a fresh electrode. The stars denote the Cu current collector, triangle show peaks from the sample holder and arrows show formation of new phases. (Bottom) Zoomed areas of key peak changes in ranges of 24-34, 35-41 and 52-62 °. The black lines index MoO_2 (ICSD 23722), $Li_{0.98}MoO_2$ is marked by grey dashed lines (ICSD 204180). [229,366]

There is no doubt that this may be a structural rearrangement as much of the literature suggests, but the exact nature of this is still unclear. One would like to suggest that this rearrangement comes in the form of a change to a tetragonal structure and thus the successive crystallisation of this phase. Figure 4.17 shows Pawley fit of the fresh MoO_2 electrode and *ex-situ* XRD pattern of a cycled electrode fitted both with the monoclinic and tetragonal forms of MoO_2 (P21/c and P42/mnm respectively) (Figure 4.18). For the fresh electrode the tetragonal structure does not fit to the low intensity peaks at 18 and 31°. After cycling, these peaks are no longer observed and thus may suggest a transition to the tetragonal phase. Yet one must not dismiss that these peaks are just too low intensity to be detected, thus the data from the cycled electrode was fitted to both structures. Although, both models fit the data from the cycled electrode well one would suggest that the tetragonal structure is most appropriate. This is because the monoclinic structure negatively fits the peak at 18° as the structure cannot fit to the lack of peak at this point. Furthermore,

in the monoclinic structure, there are many peaks which are bunched together, which manifests itself as split peaks, yet this is not apparent in the cycled electrode and although the peaks are broad, the shape suggest a lack of multiple peaks in the same region. Therefore, this would also suggest that the activation process is due to a structural rearrangement to the tetragonal MoO_2.

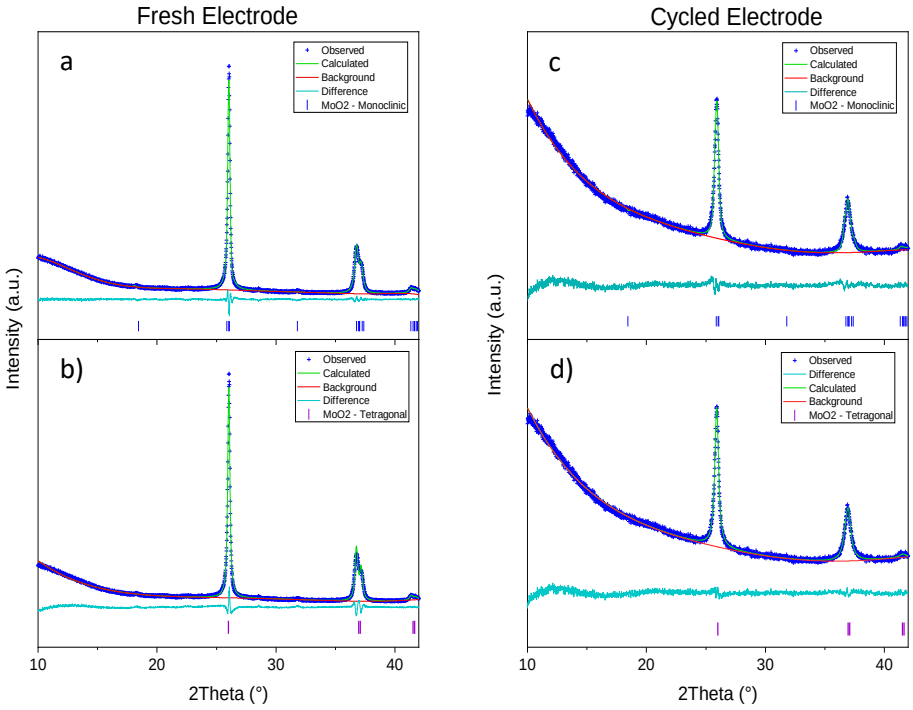

Figure 4.17 – Pawley fit of monoclinic (P21/c) and tetragonal (P42/mnm) MoO_2 to XRD patterns of electrodes of heat-treated MoO_2 pre- (a,b) and post- cycling (c,d) ran on a Panalytical Empyrean in a 10-90° range, where 10-42° is fitted to avoid Cu peaks from the current collector within the fit. Fitted patterns correspond to ICSD: 99741 and 23722 for tetragonal and monoclinic respectively. [370,371] *The cycled electrode underwent a C/20 formation cycle and 4 cycles at 1C (0.01-3.0 V), before the electrode was extracted for analysis. Fitting parameters in Table A. 4.*

After 5 cycles, the peaks gradually broaden and further shift (Figure 4.16). At 25 cycles, a new peak arises at ~25° this may be due to $Li_{0.98}MoO_2$, which forms during the intercalation process, thus may not be truly reversible. Although the low intensity nature and shifted peaks does call into question the accuracy of this phase match. According to the cycling data, there is a second activation at ~75 cycles, where a small increase in capacity is seen again (Figure 4.15). Yet, the *ex-situ* XRD pattern remains largely unchanged after 50 cycles. At ~41 ° there does appear to be an amorphous feature forming after 50 cycles, which may be linked to amorphous metallic molybdenum formation, as this is the position of Mo metal's most

intense XRD peak. Yet it is hard to assure this as it is only based on the formation of one broad peak. If this is the formation of clusters of metallic Mo, as mentioned in the literature previously,[242–244] this may reduce the resistance due to its metallic conductivity and hence the slight increase in capacity.

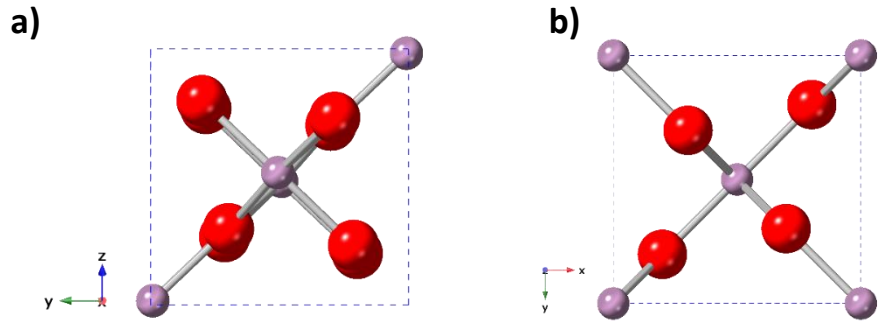

Figure 4.18 – a) monoclinic MoO_2 structure (ICSD 23722) visualised along a-axis, b) tetragonal MoO_2 structure (ICSD 99741) visualised along c-axis. Mo is represented a purple spheres and O as red spheres, with blue dotted line to show the unit cell.

CV was also used to further discern the Li-ion storage process here; the initial cycle shows two sets of clear redox peaks in the 1.0-2.75 V range indicative of the Li-ion intercalation process (Figure 4.19). This has two sets of peaks due to the multi-phase change to achieve this, monoclinic to orthorhombic to monoclinic. The is also a large peak at ~0.2 V which is indicative of the conversion process, which is surprising as one would expect the development of the conversion process to be achieved after the activation process, however this suggests that the conversion process is achievable from the start. However, at 5 cycles, there is an increase in the conversion peak suggesting that the activation process does develop this mechanism and the increase in capacity likely comes from extra storage via conversion. This also coincides with the potential phase change to tetragonal MoO_2 seen in Figure 4.16, thus, likely this phase allows for ease of conversion compared to the original monoclinic MoO_2 form. From 5 cycles, the loss of the two sets of redox peaks for lithium intercalation becomes apparent, and only one broad peak is seen in this region. This may suggest that after the change in phase during activation a multi-phase change is no longer responsible for Li-ion intercalation, and it is now likely that the structure expands to allow Li-ion storage in an intercalation pseudocapacitive-like mechanism. Furthermore, from cycle 5 the conversion reaction peak begins to shrink, and after 25 cycles, it has majorly decreased. This coincides with the capacity loss seen after the activation process, thus it is clear that the conversion process is majorly responsible for the higher capacities. Yet, the mechanism is

unstable as does not appear to continue after 25 cycles, also this is at the point where new peaks form within the XRD. This may suggest that the lack of reversibility in the mechanism is compromising the ability to use the conversion reaction as the less MoO_2 is available for conversion. Interestingly, even though the conversion mechanism does not appear to take place, the capacity is still far higher than the theoretical capacity for the intercalation only process, perhaps the CV scan rate is too fast to observe this. At 50 cycles, an average capacity is 352 ± 23 $mAhg^{-1}$ at 1C, and 452 ± 14 $mAhg^{-1}$ at a lower rate of C/5. Thus, for the lower rate, this could be attributed to just over 2-electron transfer, this may suggest that the tetragonal phase can store more ions via this different mechanism than is expected from monoclinic MoO_2. After 100 cycles the capacity appears to decline far faster, the reason for this is unclear, however this is obviously mirrored in the CV where there appears to be flattening of the profile.

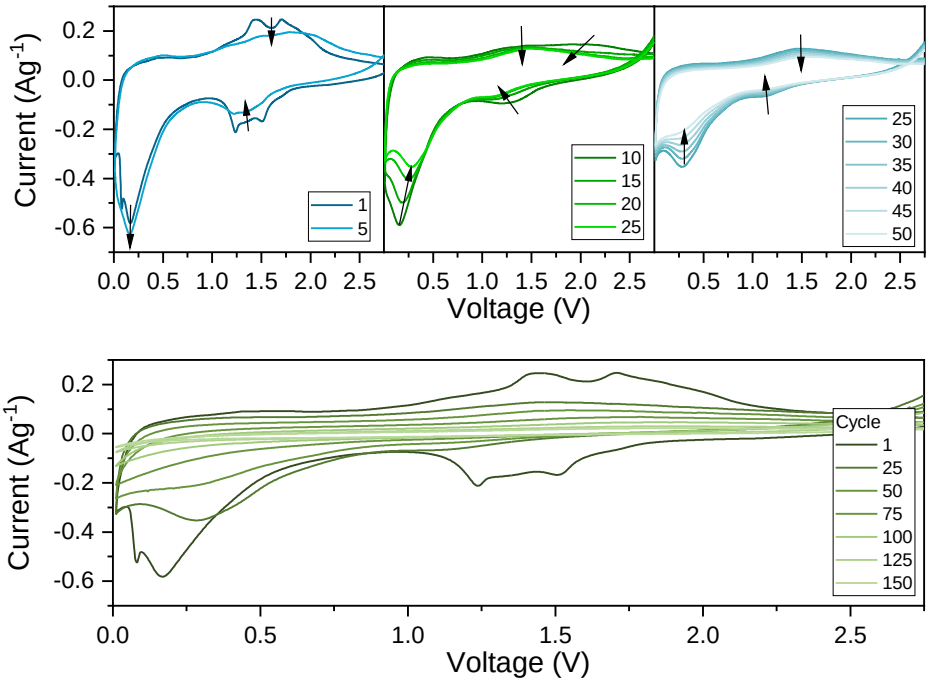

Figure 4.19 – CV profiles taken at 0.1 mVs^{-1} every 5 cycles at 1C between 0.01-3.0 V for 150 cycles, where the top graphs show profiles at cycle 1 to 50 and bottom graph shows a profiles every 25 cycles from 1 to 150 cycles.

CV was also collected at various scan rates to evaluate the reliance on a surface diffusion versus bulk diffusion mechanism. The scan rates were too high to access the conversion reaction, due to the slow kinetics of this mechanism (Figure 4.20a). However, the two pairs of redox peaks attributed to the intercalation reaction are present, yet with increase in scan

rate these merge and shift. The log plots show that there is some reliance on a surface diffusion mechanism as all gradients are higher than 0.5, however delithiation has lower gradients suggesting a bulk diffusion mechanism (Figure 4.20b). When the capacitive contribution is calculated, there is no clear trend with increasing scan rate, however the capacitive contribution is high throughout, with an average of 55 %, and this supports the idea that this material may be using a pseudocapacitive intercalation type mechanism (Figure 4.20d).[37–39] Although MoO_2 is not expected to be an intrinsic pseudocapacitive material, the nanostructured particles and the material's inherent conductivity would easily allow it to behave as an extrinsic pseudocapacitor.[40,235] However, one might consider that if the transition between monoclinic to tetragonal MoO_2 upon activation can be substantiated then it should be further researched into whether this form of MoO_2 may be an intrinsic pseudocapacitor.

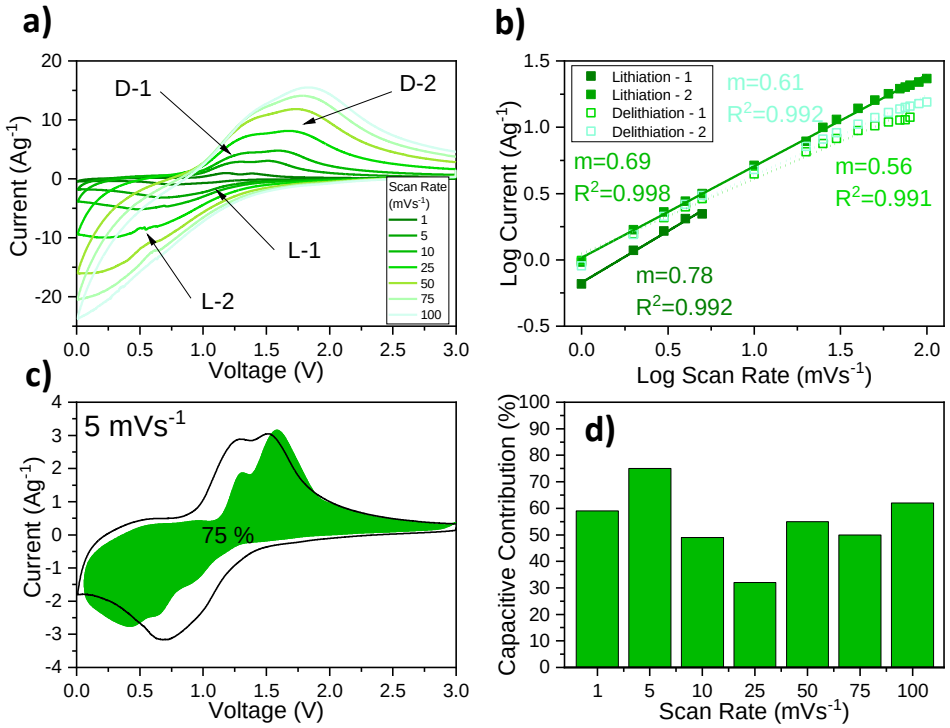

Figure 4.20 - a) CV profile at increasing scan rates of heat-treated MoO_2, arrows point to current peaks for lithiation (L) and delithiation (D). b) Log plot of peak currents with linear fits with R^2 of at least 0.992. c) CV profile at 5 mVs^{-1} with the shaded area as the capacitive contribution. d) Capacitive contribution at increasing scan rate.

SPEIS can be used to characterise the changes in impedance in the system with cycling, where Figure 4.21 shows an increase in resistance with cycle number. The initial impedance is low where the 1st lithiation there is a decrease in impedance from 3.0 to 1.0 V, showing that the Li-ion intercalation reduces the resistance of the system. Then there is another increase in

resistance below 1.0 V, which is expected as with the conversion process there is a large change within the material which can be resistive. This also shows an impedance increase at the highest frequency suggesting that the conversion reaction causes changes in the surface electrolyte interphase (SEI) system, as may be expected due to the disruptive nature of the process, this may also be destabilisation in the electrolyte system at such low voltage. For delithiation, there is the highest impedance between 0.01 and 1.5 V, again due to the conversion reaction and onset of the deintercalation. With further cycling, the impedance is increasing across the frequencies and at lower voltages there is a disruption in the electrolyte and SEI system, which may lead to the destabilisation of the material. Evidently, the loss in capacity seen with increased cycling coincides with the increase in resistance; this is likely due to material restructuring and degrading. The impedance during delithiation appears lower, even with cycling, compared to lithiation, this may be because the conversion back to MoO_2 is favourable and therefore comes with less energy barrier and resistance. Between 50 and 75 cycles, there is an increase in capacity with cycling, yet the cause of this is unclear, with the SPEIS also showing no notable change. Although the *ex-situ* XRD suggests the conversion reaction is not fully reversible, leading to metallic Mo and Li_2O forming, the potential improvement in conductivity due to this is not observed with a reduction in impedance.[242–244,269] However, this may not be a large enough improvement in conductivity to observe in the SPEIS versus the resistive mechanism of lithiation, furthermore work has also suggested that the clusters of metallic Mo can become isolated due to the electrode pulverisation over cycling, and therefore no longer contribute to the conductive network.[273,274]

To summarise, the heat-treated MoO_2 appears to be stabilised via the extra preparative step, which leads to higher capacities being accessed. The material undergoes an activation process, which causes structural rearrangement. This causes a shift from a two-stage phase change during intercalation to a single-phase lattice expansion and thus, accommodates two Li-ions where before only one ion was stored during intercalation. The presence of a lattice expansion with an intercalation pseudocapacitive mechanism appears probable as this material has a high capacitive contribution and reports have suggested that more than one Li-ion may be stored within the material's layers.[234,236,245,246] As with many of the MoO_2 materials in literature this material suffers from great capacity loss with continued cycling, yet by 200 cycles 402 ± 4.2 $mAhg^{-1}$ is achieved at C/5, which is just short of half of the theoretical capacity. This work evidences a structural rearrangement during the activation and suggests a phase change to a tetragonal structure, which has not been seen previously.

Furthermore, as with previous works it appears that the conversion mechanism is unsustainable over cycling, causing formation of metallic Mo, which only temporarily benefits the system. [242,244,269] Evidently, there appears to be mechanistic similarities between heat-treated and as-synthesised MoO_2, this adds to the narrative that preparation method is a key factor when determining material properties. However, further stabilisation is required to allow a fully reversible ion storage mechanism, therefore MoO_2/Carbon compositing is explored.

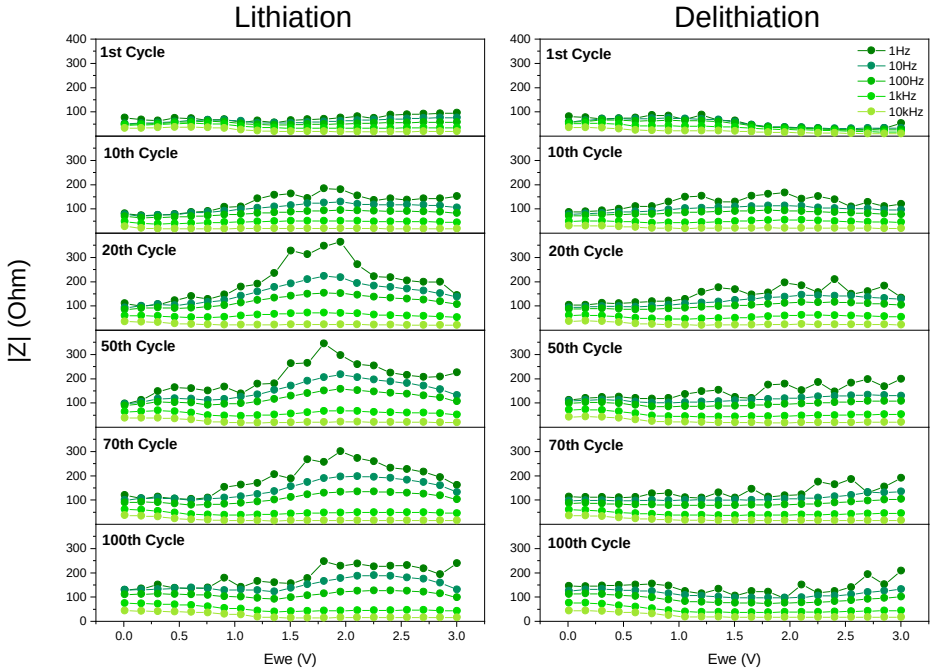

Figure 4.21 - SPEIS of heat-treated MoO_2 at cycles 1 to 100 at 1C for lithiation (left) and delithiation (right).

4.4 Characterisation of a MoO_2/Carbon Composite

As further stabilisation of MoO_2 is required, compositing with carbon is a useful method as carbon coatings or matrices can mitigate electrode pulverisation. The heat-treated MoO_2 material has shown promising properties yet lacks the ability to maintain high capacities. The same synthesis process was used with the simple addition of glucose as a carbon source to the hydrothermal vessel. Heat-treatment will subsequently convert the polymeric glucose to carbon. A similar testing regime was carried out upon this material as with the materials above. The XRD pattern of the carbon composite appears to be no different from that of the

heat-treated MoO_2. This suggests that the addition of the carbon precursor has little effect on the material formation (Figure 4.22). The lack of extra peaks in the XRD may suggest that it is an amorphous carbon that has formed. TGA analysis shows that there is only 2% of carbon in the system (Figure A.49). The carbon content is low considering the amount of glucose added to the hydrothermal reaction. This may suggest that the heat-treatment temperature is inadequate to achieve full carbon conversion, or there was poor polymerisation of glucose during the hydrothermal reaction. Also, due to only a small addition of carbon, N_2 adsorption measurements show a small increase in surface area to 20.4 m^2g^{-1} for this material (Table A. 3).

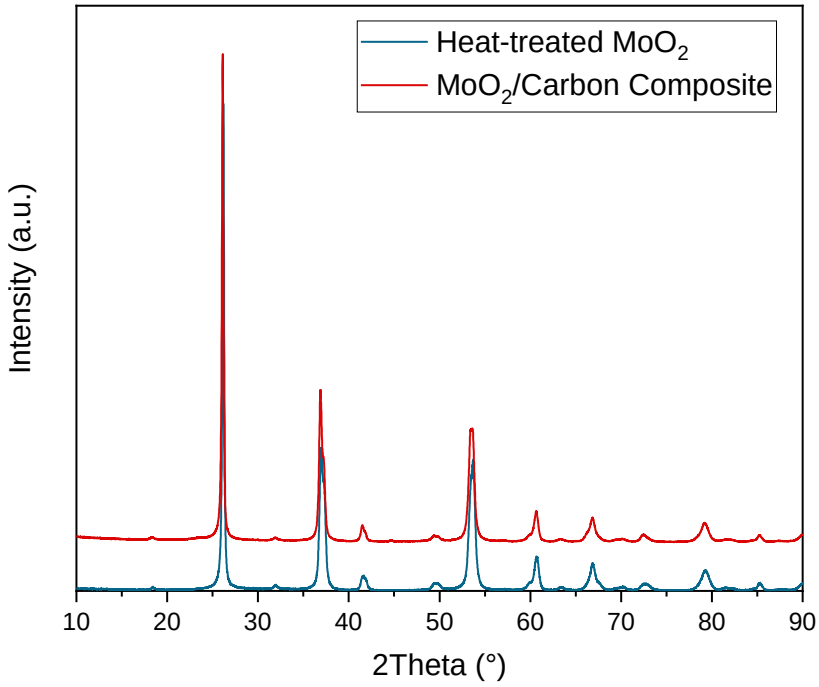

Figure 4.22 – XRD pattern of heat-treated MoO_2 and MoO_2/Carbon composite created via the same route with the addition of glucose to the hydrothermal step.

The microscopy images show similar particles to that of the pure MoO_2 materials: irregular agglomerates of near elliptical primary particles (Figure 4.23). Image particle counting gives a broad particle width distribution centred on 167 nm (Figure A.41). The TEM images and EDX mapping confirm carbon mainly resides between the agglomerates of MoO_2; thus, it appears that this acts as a webbing matrix between particles (Figure 4.23d, e).

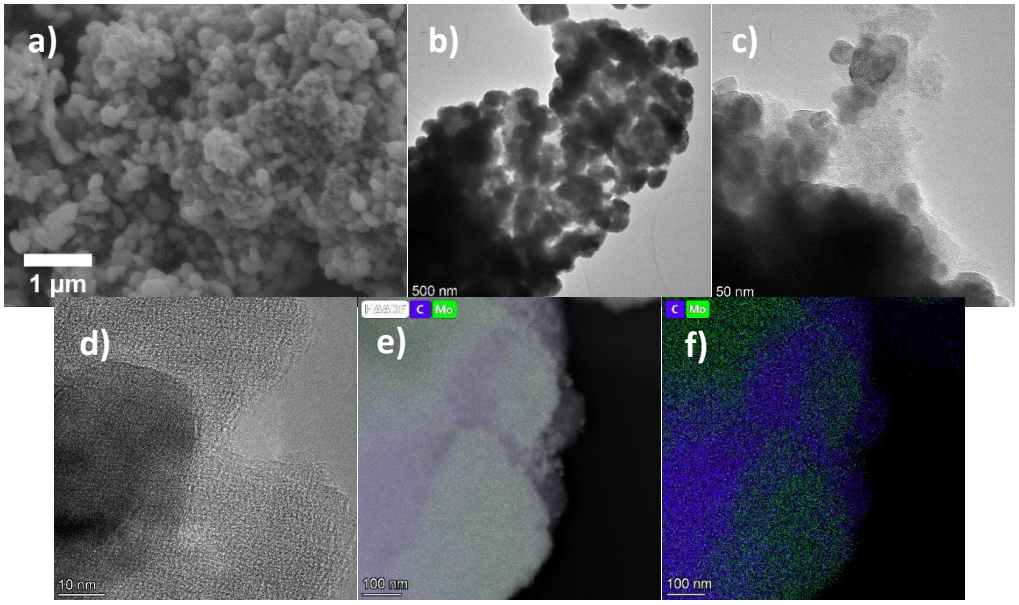

Figure 4.23 – SEM (a) and TEM images, (Figure A.50) (b-d) of MoO_2 carbon composite and STEM-EDX map where Mo is in green and C is purple (e,f) with overlaid bright field image in e.

4.4.1 Electrochemical Characterisation of MoO_2/C Composite as Li-ion Anode.

This composite is exposed to a similar electrochemical testing regime as with the other MoO_2 materials. In the narrow voltage range the initial cycle only shows an average capacity of 120 ± 9.6 $mAhg^{-1}$ at 1C, which drops to only 48 ± 1.0$mAhg^{-1}$ after 200 cycles (Figure 4.24a). Although this is low, the Li-ion storage mechanism does appear to be reversible, as the differential capacity plots show evidence that two sets of redox peaks remain at 200 cycles (Figure 4.24b). The wide voltage range shows much higher capacities with a maximum of 513 $mAhg^{-1}$ at approximately 10 cycles at peak activation of the material. Although this is also lower than the theoretical, an average capacity of 307 ± 17$mAhg^{-1}$ can still be gained after 200 cycles. It is evident that this material may also undergo a similar change as with the heat-treated MoO_2, as the differential capacity profile broadens and only shows one set of redox peaks at 200 cycles (Figure 4.24b). Regarding the rate sweep, there appears to be a very small step down in capacity on the narrow voltage range, showing that the intercalation reaction can still be achieved at high rates (Figure 4.24c). As with the other MoO_2 materials, in the wide range, there is little change in capacity at low rates. After 1C, the change in capacity becomes larger. The material still shows a 91 % recovery when the rate is returned to C/10, after cycling at these high rates. Further rate tests show little difference between rates C/5 and 1C. Both have similar capacity fading and average capacities of 527 and 507 $mAhg^{-1}$ at

10 cycles and 388 and 307 $mAhg^{-1}$ at 200 cycles (Figure A.51). Here, large cell to cell variation is still seen prior to activation where standard deviations of greater than 30 $mAhg^{-1}$ are calculated, whereas post activation these are dropped to approximately 15 $mAhg^{-1}$ (depending on exact cycle number). The differential plots also appear similar at these rates, with two clear sets of redox peaks in the first cycle, plus a redox peak at low voltage corresponding to conversion. Furthermore, after 200 cycles, a broad single set of peaks alongside the conversion peak are still observed. Alternatively, at the higher rate of 5C, there appears to be no clear conversion redox peaks in the differential plots shown, and although the capacity also follows the same trend, the results are lower.

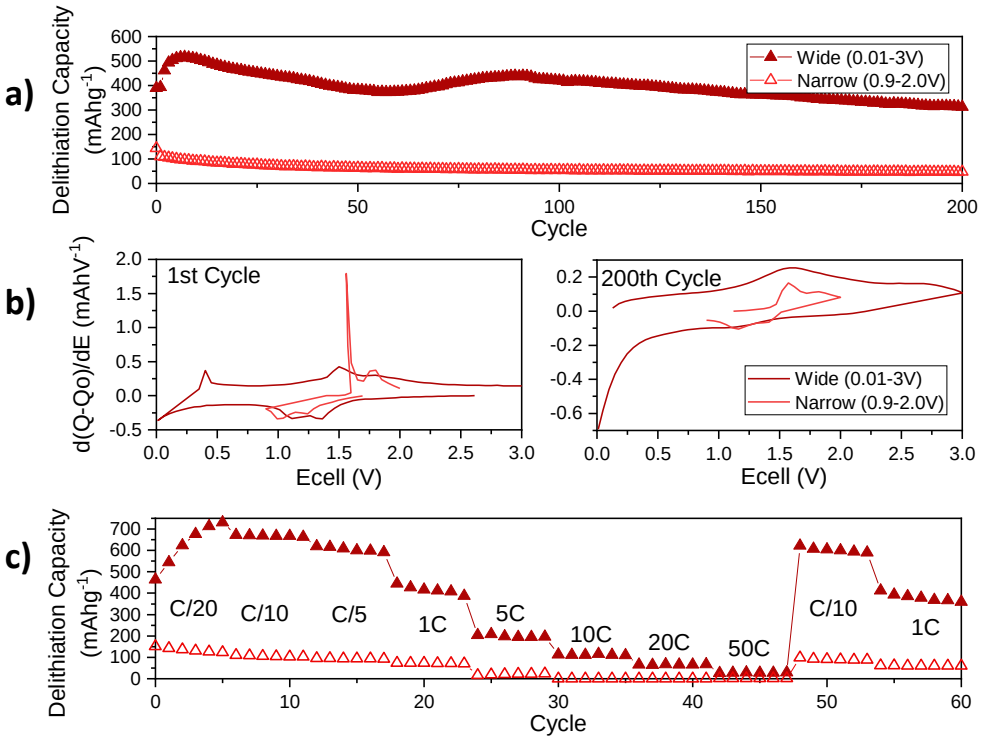

Figure 4.24 - a) Galvanostatic cycling at 1C for 200 cycles at voltage windows 0.01-3.0 V and 0.9-2.0 V for MoO_2/C composite. b) Differential capacity profiles of the 1st and 100th cycle for the wide and narrow voltage window. c) Rate Sweep from C/20 to 20C, with recovery to C/10 at different voltage windows.

As with the heat-treated MoO_2, the CV profile for this material has two sets of broad peaks in the region of 1.0-2.0 V, plus a single peak at approximately 0.2 V (Figure A.52). From the 1st cycle to 50th, the conversion peak appears to shrink. This shows that with cycling, the conversion reaction becomes less favourable or inaccessible, which may be attributed to a change or degradation in material. Interestingly, unlike the pure MoO_2 (heat-treated), there is not an increase in conversion peak with the activation process. This is supported by the *ex-*

situ XRD where the composite material shows peak broadening from the first cycle (Figure 4.25), whereas the pure MoO2 material shows a broadening then narrowing with the activation process (Figure 4.22). Furthermore, this corresponds with the difference in duration of the activation, which takes longer in this composite material (Figure 4.24). As for the peaks attributed to the intercalation mechanism, these broaden with cycling, until about 25 cycles where there only appears to be one set of broad peaks remaining and the presence of the second set has diminished, which also occurs in the other MoO_2 materials. Although the electrochemical testing draws parallels between all the MoO_2 materials presented, there are some differences in the *ex-situ* XRD results (Figure 4.25). Notably, there is immediate structural change with the XRD peaks broadening and losing intensity from the 1st cycle. Yet there does appear to be the formation of $Li_{0.98}MoO_2$, from the 10th cycle. At 100 cycles, there is the development of an amorphous feature at ~41 ° due to formation of amorphous metallic molybdenum. Both have been observed previously. The mechanism used here appears to form a lower degree of crystallinity or amorphous structure far more quickly than that of the pure MoO_2, yet also produces similar capacity results. In the pure MoO_2, the *ex-situ* XRD shows a clear MoO_2 structure yet here the structure has fully broken down. Evidently MoO_2 is a material which is able to achieve capacities with various states of crystallinity, which is confirmed by work that shows good results from amorphous forms of MoO_2.[249,250]

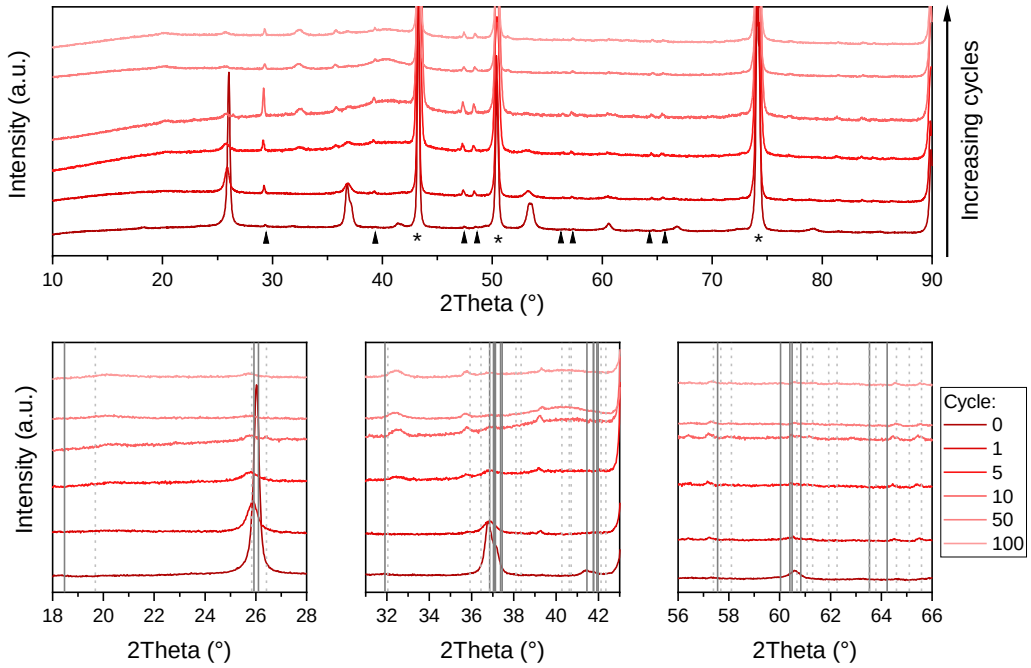

Figure 4.25 - Ex-situ XRD of heat-treated MoO_2 electrodes after cycling at 1C in 0.01-3.0 V range for various cycle numbers, where 0 cycles is a fresh electrode. The stars denote the Cu current collector and triangle show peaks from the sample holder. (Bottom) Zoomed areas of key peak changes in ranges of 18-28, 31-43 and 56-66 °. The grey lines denote monoclinic MoO_2 (ICSD 23722), $Li_{0.98}MoO_2$ is marked by light grey dashed lines (ICSD 204180). [229,366]

There is also some deviation between this MoO_2/C composite and the pure materials when it comes to considering the surface versus bulk diffusion limitations (Figure A.53). The two sets of peaks for the interaction reaction are visible and as the scan rate increases, these become one set of broad peaks, which shift as the rate is further increased. The log plot of the peaks shows the delithiation process to be generally bulk diffusion limited, whereas for lithiation, the gradient is much steeper suggesting a dominant surface limited process. When the capacitive contribution is calculated, there is a general increase with increasing scan rate, suggesting a change to a capacitive storage mechanism. Finally, SPEIS shows a trend which is almost identical to that of the other MoO_2 materials. In fact, the overall impedance of the composite was higher than both pure MoO_2 materials. This suggests that the carbon here does not improve the conductivity as MoO_2 is already a conductive medium. Furthermore, the increased resistivity here may be due to the structural breakdown as highlighted by the *ex-situ* XRD.

Overall, the MoO_2/C composite achieves high capacities in the 0.01-3.0 V voltage window, although capacities still do not reach that of the theoretical. However, capacity retention of

60 % (between cycle 10 and 200) across various rates shows great promise for a MoO_2 containing material, traditionally known for poor stability. This material appears to store lithium via conversion, intercalation, and a capacitive mechanism. The conversion reaction becomes less evident with cycling, as the redox peak reduces in the CV, likely due to structural breakdown as evidenced in the *ex-situ* XRD. Although good capacities are maintained after 100 cycles, it appears that the structure has lost almost all crystallinity at this point, and thus a change in the mechanistic process is unsurprising. In the literature, carbon compositing has been shown to stabilise the MoO_2 and boost the rate capability of the material.[262,270,284–287,308,316] Unfortunately, this material does not live up to these promises where carbon composites achieve over 1000 $mAhg^{-1}$.

4.5 Comparison of MoO_2 Materials

Considering their similar synthesis route and similar physical characterisation, all three MoO_2 materials presented here have different electrochemical properties. As such, this work highlights the complexity of Li-ion storge mechanisms seen in MoO_2 and its ability to store ions via intercalation, conversion and pseudocapacitive routes. The as-synthesised MoO_2 struggles to reach its theoretical capacity, even with an activation process. It appears that the conversion mechanism becomes unfavourable after activation and the intercalation mechanism is only partially reversible. Where this material achieves 69 $mAhg^{-1}$ at 100 cycles at 1 C, other work achieves 300 $mAhg^{-1}$ after 200 cycles at 1C from a hydrothermally synthesised MoO_2.[261]

Evidently heat-treatment is key in producing a MoO_2 with reasonable electrochemical properties, as vast improvements are seen especially in the coulombic efficiency (Figure A.55), even with a relatively low increase in temperature. Figure 4.26 shows that the heat-treatment allows for stabilisation cycling and gives a dramatic increase in capacity retention. Although, when it comes to physical characterisation, only the IR spectrum showed notable changes with the heat-treatment. Both materials show an activation process within the first 10 cycles, with a conversion mechanism recorded via CV or differential capacity plots. The electrochemical mechanism of these materials appears remarkably similar, with *ex-situ* XRD showing similar patterns with the as-synthesised material, the degradation appears to be sped up. It is likely that surface cleaning via heat-treatment can promote stability, as the surface molecules can cause side reactions during electrochemical cycling and prevent the formation of a stable SEI. Notably, the heat-treated MoO_2 shows evidence that structural rearrangement occurs during activation and a change from a monoclinic to tetragonal MoO_2

could be established. It appears that the other MoO_2 materials may also undergo this transition, yet it is less apparent due to structural breakdown and secondary phase formation. Overall, the literature has lacked thorough characterisation of the activation mechanism and further work is needed to substantiate what is presented here.

When considering the heat-treated materials capability compared to the literature, a study by Koziej *et al.* showed comparable results, under similar conditions, reporting 300 $mAhg^{-1}$ at 200 cycles at 1C.[261] Other, more recent long-term studies, show superior results to this work albeit at lower current densities (Table 4.1). However, the heat-treated MoO_2 appears to achieve a good rate capability; at 5C, this material can achieve 220 $mAhg^{-1}$ even after 200 cycles and shows very little capacity loss compared to tests at 1C. Most studies only show high-rate testing within a rate sweep with no long-term results; thus, the results appear higher and thus only comparable to initial capacities (Table 4.1). Although, Zhao *et al*. do show 50 cycles at 5 C achieving a capacity of 300 $mAhg^{-1}$, this is similar to the results presented here, 277 $mAhg^{-1}$ under the same conditions.[243]

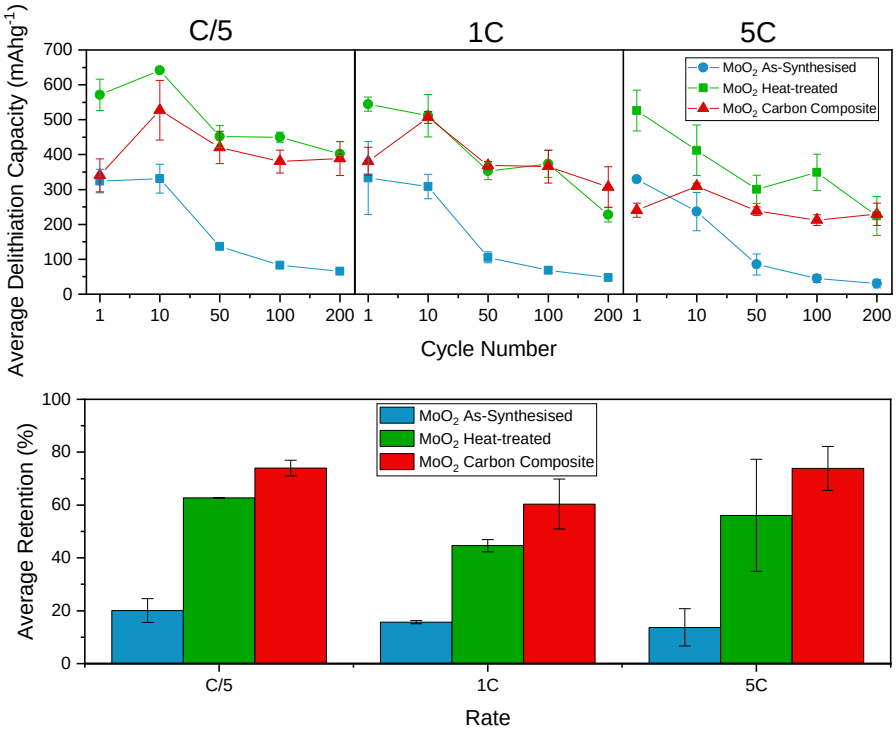

Figure 4.26 – Comparison of as-synthesised, heat-treated MoO_2 and MoO_2/C composite, (top) capacity over cycle at different rates, (bottom) capacity retention between 10 and 200 cycles at different rates.

The stabilisation of MoO_2 is an ongoing area of study where carbon compositing has achieved this to an extent in the literature, and here it is clear that the simple incorporation of a low

amount of carbon also improves stability (Figure 4.26). Notably the capacity retention is improved; this was calculated after activation (at 10 cycles) to give a better representation of retention of the higher capacities the materials achieve. The carbon composite shows improved retention over all rates; this is also outside of error for C/5 and 1C so can be considered a notable change. This suggests that the carbon is stabilising the MoO_2, yet the apparent 'scaffolding' is not seen here as there is no capacity gain from the addition of carbon. When considering previously published MoO_2 carbon composite initial capacities at low current densities have surpassed the theoretical.[262,270,284–287,308,316]Hence the capacities produced by the MoO_2/C composite here are poor in comparison (Table 4.1).

Although these materials cannot be presented as improvements upon the literature, the exploration of the electrochemical properties presented is an important step toward thoroughly characterising the Li-ion mechanism. MoO_2 requires further study due to the nuance of the electrochemical mechanism and the potential for a stable, high capacity, conductive anode material. Due to the complexity of the Li-ion interaction with MoO_2, many studies have missed important details surrounding this or appear to present contradictory results compared to other studies. Hence, more studies require in depth electrochemical testing and *ex-situ* post-mortem XRD with cycling to solidify the understanding around the storage mechanism. Further to this, the correlation between synthesis route and electrochemical properties should also be considered to allow for future materials optimisation.

Table 4.1 – Comparison of capacities achieved by MoO_2 when compared to the literature where heat-treated is denoted as HT.

Material	**Low-rate initial capacity ($mAhg^{-1}$)**	**Low rate (Ag^{-1})**	**Low-rate reversible capacity ($mAhg^{-1}$)**	**Cycles**	**High-rate capacity ($mAhg^{-1}$)**	**High rate (Ag^{-1})**	**Ref**
As-synthesised MoO_2	333	0.84	70	100	45	4.2	This work
Heat-treated MoO_2	545	0.84	374	100	349	4.2	This work
MoO_2 (no HT)	445	0.38	300	200	~320	1.5	[261]/2011
MoO_2 (no HT)	608	0.84	624	50	~300	4.2	[243]/2012
Amorphous MoO_2	810	0.1	~800	50	700	5.0	[250]/2012
MoO_2 (no HT)	564	0.1	1085	170	-	-	[311]/2019
MoO_2 (HT)	1096	0.1	1192	100	438	4.0	[269]/2019
MoO_2/C composite	381	0.84	366	100	212	4.2	This work
MoO_2/ N-doped CNTs	646	0.5	840	500	700	2.0	[284]/2016
MoO_2/C composite	918	0.5	916	100	734	2.0	[285]/2020
MoO_2/rGO	1544	0.1	~850	300	~700	1.0	[316]/2021

5 Novel Niobium Pentoxide/Molybdenum Dioxide Composite Materials.

5.1 Premise

As individual oxides, MoO_2 and Nb_2O_5 have been explored thoroughly in this work so far, due to the interesting electrochemical properties they present. However, both oxides also suffer from some unfavourable characteristics. For Nb_2O_5 its insulating properties and MoO_2 lacks stability. The ability to combine these oxides in a composite form aims to exploit the promising properties of the materials and thus negating the less preferable properties. Composites have often been used in the literature previously to boost the electrochemical properties of the main active material via the growth of a second separate material alongside the original.[83,207] Crucially this is not forming a mixed oxide but is growing one material on or within another. For battery applications, most commonly this is undertaken with carbon materials to boost the conductivity and stability of the active materials.[84,200] However, forming a composite out of these two promising oxide materials, may look to further improve the properties, beyond that of forming composites with carbon.

The synthesis of MoO_2 and Nb_2O_5 explored in the previous chapters was developed to not only generate the pure oxides, but to also allow for an easy combination of synthesis to create composite materials. Hence, a hydrothermal synthesis containing ammonium molybdate tetrahydrate, ammonium niobate oxalate hydrate and oxalic acid was undertaken to create an 'as-synthesised' composite material. Further heat-treatment was also investigated using a 4-hour treatment, in an argon atmosphere for the 50 % composite. Composites with ratios of Nb_2O_5:MoO_2 of 10:90, 20:80, 50:50, 80:20 and 90:10, are synthesised, characterised, and tested electrochemically here. This chapter is split into Nb_2O_5-rich and MoO_2-rich composites, to allow ease of comparison to the respective pure material. As the 50:50 composite fits into neither of these sections, this will be addressed separately at the end of this section.

Note – when Nb_2O_5 or MoO_2 is referred to, this is the as-synthesised forms of these materials unless stated otherwise.

5.2 Nb_2O_5-Rich Composite Materials

5.2.1 Characterisation of Nb_2O_5-Rich Materials.

Both Nb_2O_5-rich composites show a similar XRD pattern to that of the as-synthesised Nb_2O_5, with the two sharp peaks at ~22 and 45 ° and broad diffraction features in other regions (Figure 5.1). This suggests that even with the addition of the MoO_2 reagent that the Nb_2O_5 still manifests itself as an anisotropically crystalline structure. The 10 % Mo composite XRD pattern shows little change from the pure Nb_2O_5, perhaps with slight sharpening of the broader peaks. This suggests that at this level Mo may have doped or substituted into the Nb_2O_5 structure. The disordered structure of the as-synthesised Nb_2O_5 may also promote doping into the structure, but additional analysis is needed to fully understand this. For the 20 % Mo composite, the XRD pattern has multiple sharp peaks in addition to the familiar semi-crystalline Nb_2O_5 pattern. These peaks are identified as monoclinic MoO_2, with some of these showing small shifts from the expected. This shows that the synthesis of the composite is successful as the two phases remain distinct and a mixed phase is not formed.

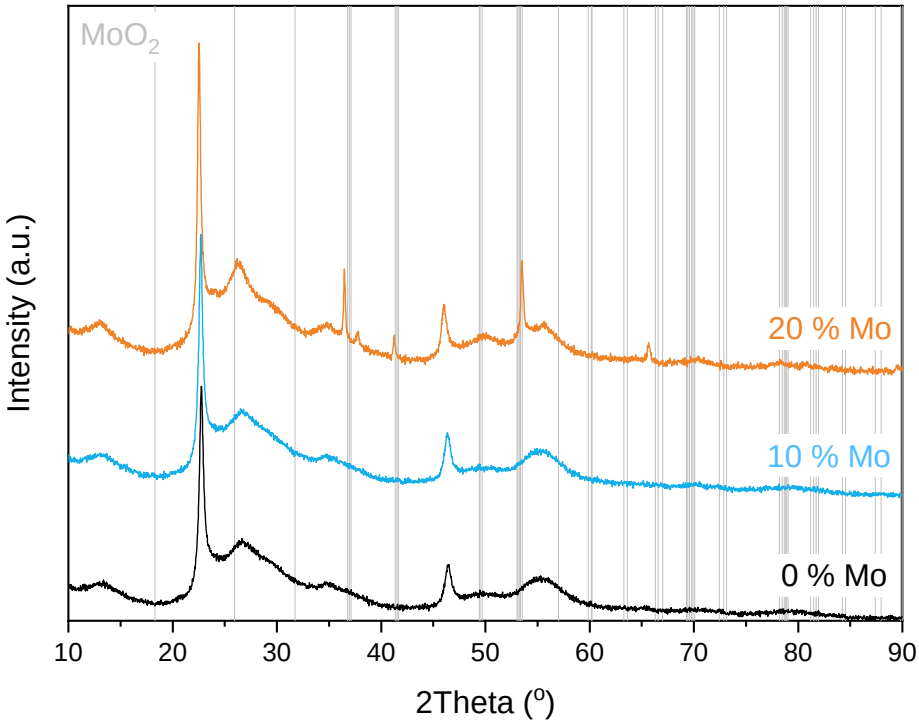

Figure 5.1 – XRD patterns of Nb2O5-rich composites and 'as-synthesised' Nb_2O_5, with grey drop lines marking the appearance of peaks, which are identified as monoclinic MoO_2 (ICSD-23722).[364]

TGA analysis shows that the 10 % composite follows a similar mass loss to pure Nb_2O_5, up to 300 °C (Figure A.56). However, unlike pure Nb_2O_5 there is a loss at ~800 °C indicative of a loss of Mo via a disproportionation and sublimation reaction. For the 20 % composite, this loss starts earlier at 750 °C and is equivalent to 11.3 % mass loss, showing an increase in Mo content in the material. The composition of the composites is confirmed using XRF, with the 10 % Mo composite having the desired composition at 89.65 % Nb (Table A.5). The 20 % composite shows slightly higher Mo content than the synthesis aimed for with 75.23 % Nb. The variation between batches is low, and particularly small in the 20 % composite at 0.63 % standard deviation, showing a reproducible synthesis route.

Microscopy images show the composites to have a similar morphology to Nb_2O_5 where the nano-wires are consistent with the anisotropically crystalline nature of the XRD patterns (Figure 5.2). The 10 % material does not have particles of any other morphologies, which supports the proposal that Mo is doped or substituted into the Nb_2O_5 structure. The 20 % composite also shows the networks of nanowires decorated with nano-spheres (Figure A.570). These particles appear to have a textured surface and are much denser than the nano-wires (Figure 5.2e, f). EDX mapping confirms the nano-spheres to be Mo only, hence the separate MoO_2 phase in the XRD pattern (Figure 5.3g,h). SEM-EDX image maps show that the 10 % composite has a homogenous mixture of metals across the material (Figure A.57d). STEM-EDX shows the same result, these are consistent with the XRD pattern (Figure 5.3a-d).

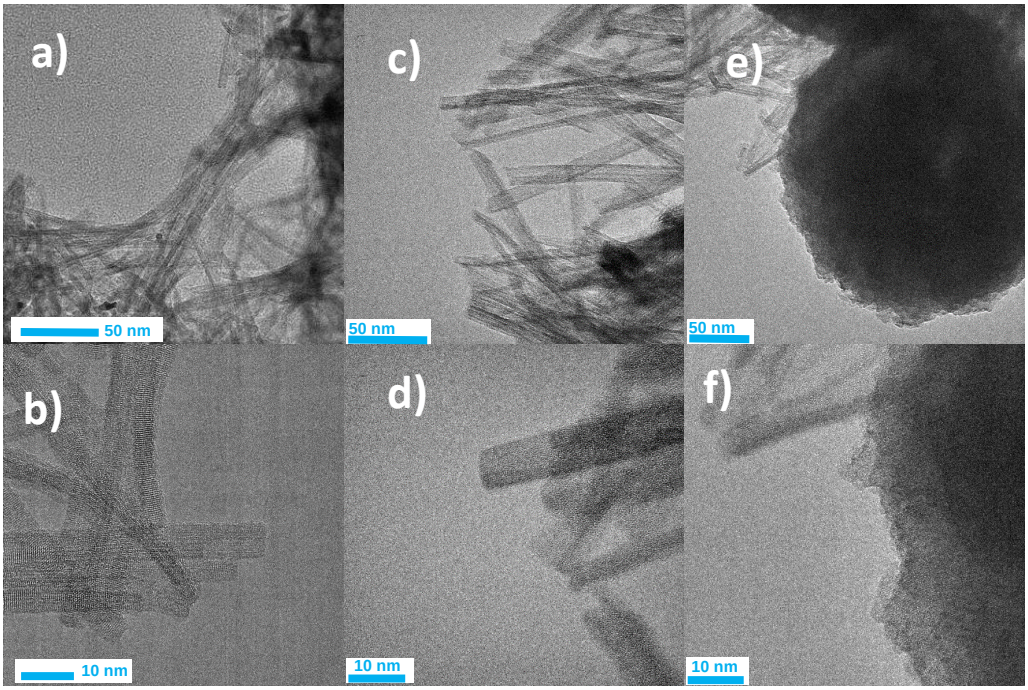

Figure 5.2 – TEM images of (a, b) as-synthesised Nb_2O_5, (c, d) 10 % Mo composite, (e, f) 20 % Mo composite. Further images can be found in Figure A.58 and Figure A.59.

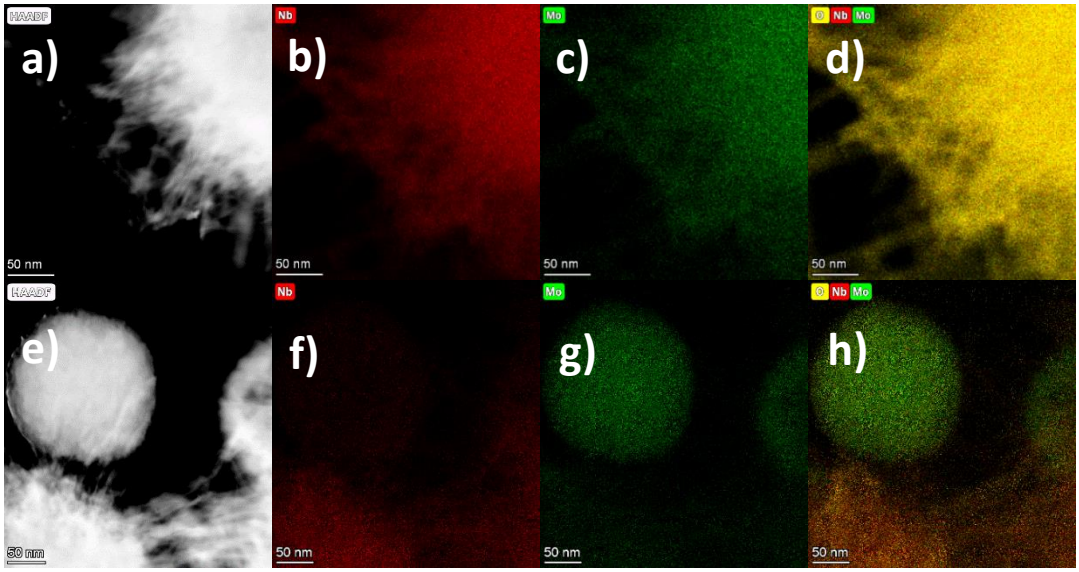

Figure 5.3 – STEM-EDX mapping of 10 % Mo composite (a-d) and 20 % Mo composite (e-h). from left to right, HAADF image, Nb Map (Nb is red), Mo Map (Mo is green) and Nb, Mo, O map.

N_2 adsorption analysis shows a retention of isotherm and hysteresis type with increasing molybdenum content (Figure A.60). Both composite materials show a drop in surface area compared to the pure Nb_2O_5 (Table 5.1). The pore distribution is similar across the materials; however, the 10 % Mo material has a larger volume of pores in the micro-pore region.

Table 5.1 – Key parameters calculated from full N_2 adsorption isotherms (Figure A.60) of the Nb_2O_5 materials.

Material	BET Surface Area (m^2g^{-1})	DFT Total Volume in Pores (cm^3g^{-1})	BJH Adsorption Average Pore Width (nm)
NbO_x (0%)	278.8	0.42	6.8
10 % Mo	180.0	0.23	6.9
20% Mo	160.9	0.24	7.3

XPS reveal that upon mixing with Mo, Nb_2O_5 is no longer only in the +5 oxidation state as with the pure materials (Figure 5.4 and Figure 5.5). Some of the Nb is in a +4 oxidation state, such as that of NbO_2. This may change the available redox sites for the electrochemistry to take place. The MoO_2 is also over oxidised as it exists in more states than +4, i.e., the +6 state is also identified. There was difficulty in confirming the other state of Mo which appears to fit to a +5 state. This may be due to doping of Mo into the Nb_2O_5 structure, which pushes Mo into a +5-oxidation state to match that of Nb +5. This may further explain the mixed valency of Nb to accommodate this doping. The hydrothermal synthesis leads to surface species containing both carbon and nitrogen, as seen previously on the pure oxides. The XPS gave a Mo percentage of 15 and 26 % for the 10 and 20 % composites respectively. This is slightly

higher than that calculated from XRF, however a difference is expected as XPS is surface sensitive.

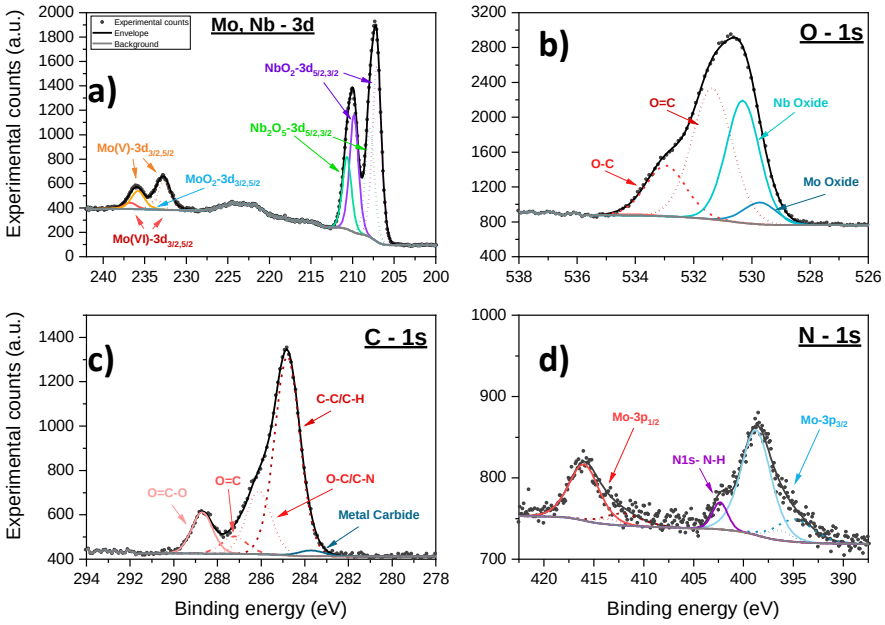

Figure 5.4 – High resolution XPS spectra of the Mo and Nb 3d region (a), O 1s region (b), C 1s region (c) and N 1s region (d) for 10 % Mo containing composite. Full scan in Figure A.61.

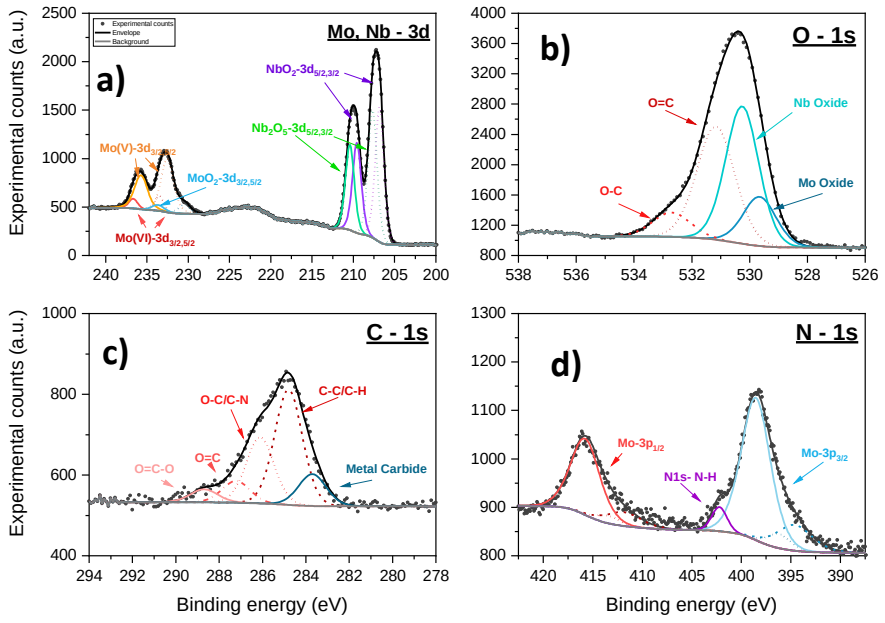

Figure 5.5 - High resolution XPS spectra of the Mo and Nb 3d region (a), O 1s region (b), C 1s region (c) and N 1s region (d) for 20 % Mo containing composite. Full scan in Figure A.61.

5.2.2 Electrochemical Characterisation of Nb_2O_5-Rich Composites

These composite electrodes were formulated in the same ratios as was chosen for the pure Nb_2O_5, thus a 70:20:10 ratio of AM:C65: PVDF was used, and thin electrodes with a wet coating thickness of 50 µm on copper were created. Theoretical capacities were calculated as a weighted summation of the theoretical capacity of Nb_2O_5 and MoO_2, e.g., for 10 % composite, 263 $mAhg^{-1}$.

5.2.2.1 Electrochemical Characterisation of 10 % Mo Containing Composite

In the literature, MoO_2 materials have been tested between 0.01 – 3.0 V and 1.0 - 3.0 V, the latter is also seen for Nb_2O_5. For Nb_2O_5 a voltage cut-off of 1.0 V had been used in the literature to avoid a large solid electrolyte interphase (SEI) formation, yet in this work it is apparent that this cut-off is unnecessary for the as-synthesised Nb_2O_5. Cycling above 1.0 V is also used for MoO_2 to avoid the conversion process i.e., where Li_xMoO_2 converts to Mo and Li_2O. As with the pure Nb_2O_5, this material has a high surface area, thus may lead to SEI instability and electrolyte degradation at low voltages, so a voltage cut-off of 0.25 V was trialled. Thus, for the composite materials three windows of: 0.01-3.0 V (wide), 0.25-3.0 V (medium) and 0.9-2.0 V (narrow), were tested. These voltage ranges appear to encapsulate the intercalation mechanism completely, even with the narrow range showing a full set of broad redox peaks. The medium and narrow windows show very similar results, whereas the wide window shows a higher capacity by comparison (Figure 5.6a). The average capacity is 97 ± 12.4, 51 ± 0.1 and 43 ± 0.6 $mAhg^{-1}$ for wide, medium, and narrow ranges respectively at 200 cycles. Although all results show far lower capacities than the theoretical (263 $mAhg^{-1}$), the Li-ion storage mechanism is reversible as the differential capacity plots keep their shapes to 200 cycles (Figure 5.6b). The rate sweep continues the capacity trend across the voltage windows, with the wide window showing a higher capacity across all rates. Notably, all voltage windows allow cycling to 100C without failure, although the narrow range returns a negligible capacity. Furthermore, a 99 % recovery is achieved after high current cycling between both C/10 steps in the wide voltage range. Thus, a wide voltage window will be implemented in testing from now on.

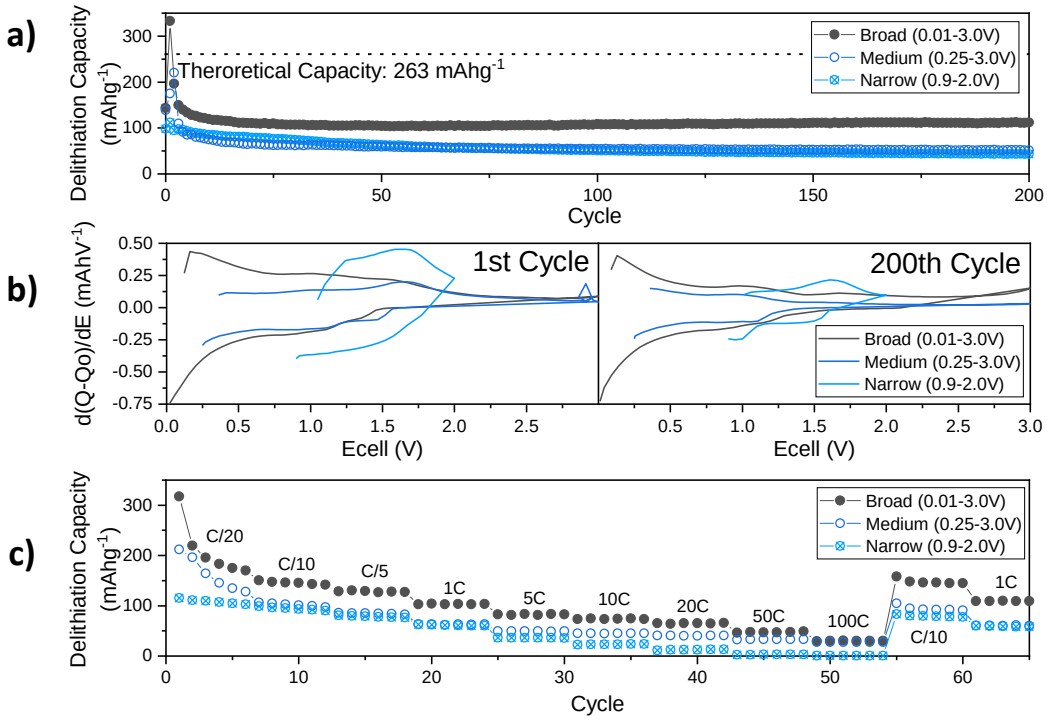

Figure 5.6 – (a) Galvanostatic cycling of 10 % Mo composite at 1 C at various voltage windows, with a C/20 formation cycle. (b) Corresponding differential capacity plots at the 1st (left) and 200th cycle(right). (c) Rate sweep from C/20 to 100C at different voltage windows.

At different rates this material appears to show a similar trend in capacity (Figure 5.7). The initial loss is solid electrolyte interphase (SEI) formation due to the high surface area of this material. There is only a very small drop in capacity from C/5 to 20C, and at the 100th cycle the capacities are 126 ± 3.4 and 88 ± 6.7 $mAhg^{-1}$ respectively. By 200 cycles, there is a larger loss in the capacity at 20C suggesting a slowing of the Li-ion diffusion. At 20C, there are plateaus in the 1st cycle charge profile, although it is unclear why this is as it appears anomalous to the other profiles (Figure 5.7, bottom). At the other rates there is a broadening of an inflection in the profiles. The coulombic efficiency (CE) decreases with rate, for C/5 it is 98 % and above, and is maintained after 20 cycles, whereas at 1C it is 97 % and at 20C it is only 95 % (Figure A.62).

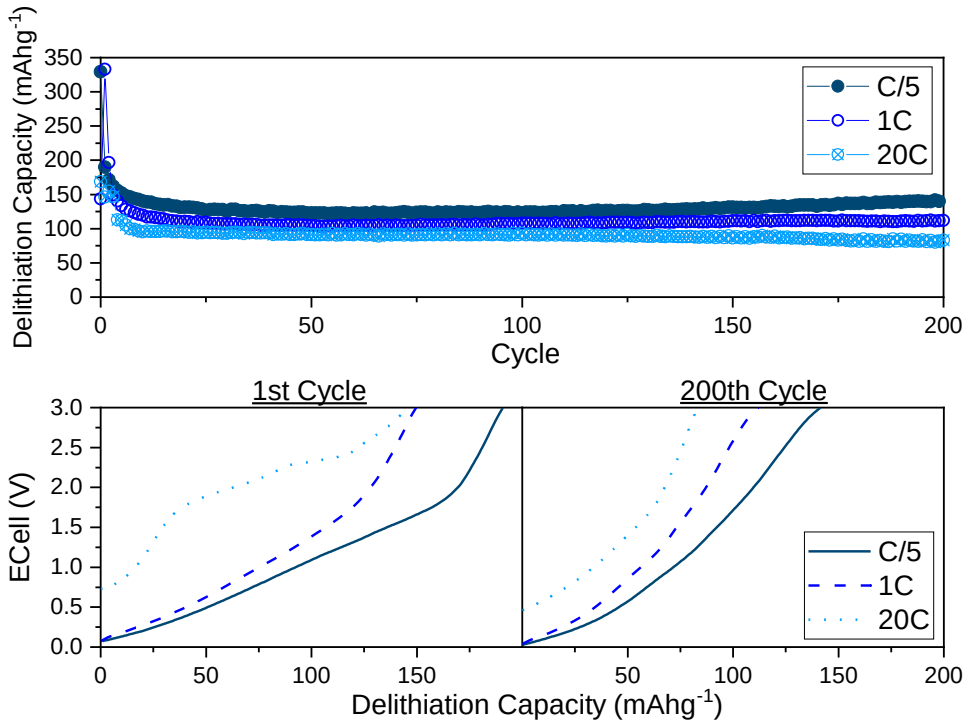

Figure 5.7 – (top) Galvanostatic cycling between 0.01-3.0 V at various rates, (bottom) charging profiles at various rates at 1st and 200th cycle, for the 10 % Mo composite.

Cyclic voltammetry (CV) at increasing scan rates is used to further understand the electrochemical properties of the composite material. The CV profile has one clear lithiation peak and two delithiation peaks, which begin to merge as the scan rate is increased (Figure 5.8a). All peaks show a voltage shift with increasing scan rate, due to the internal resistance in the material causing polarisation. The log plot shows gradients of 0.77, 0.84 and 0.91 for delithiation peak-1, 2 and lithiation peak-1 respectively (as labelled in Figure 5.8b). These gradients all show a high capacitive dependence as they are close to 1.0. When the CV data is further analysed, a maximum capacitive contribution is seen at 10 mVs^{-1}, with 54 % capacitive current, showing that more than half of the measured current comes from a capacitive type of storage. This confirms the maintenance of high-rate properties from pure Nb_2O_5. Although the CV profiles are similar to the as-synthesised Nb_2O_5 (Section 3.3.2.1.1), there does appear to be some limit to the surface diffusion, as the capacitive contribution does not increase with scan rate.

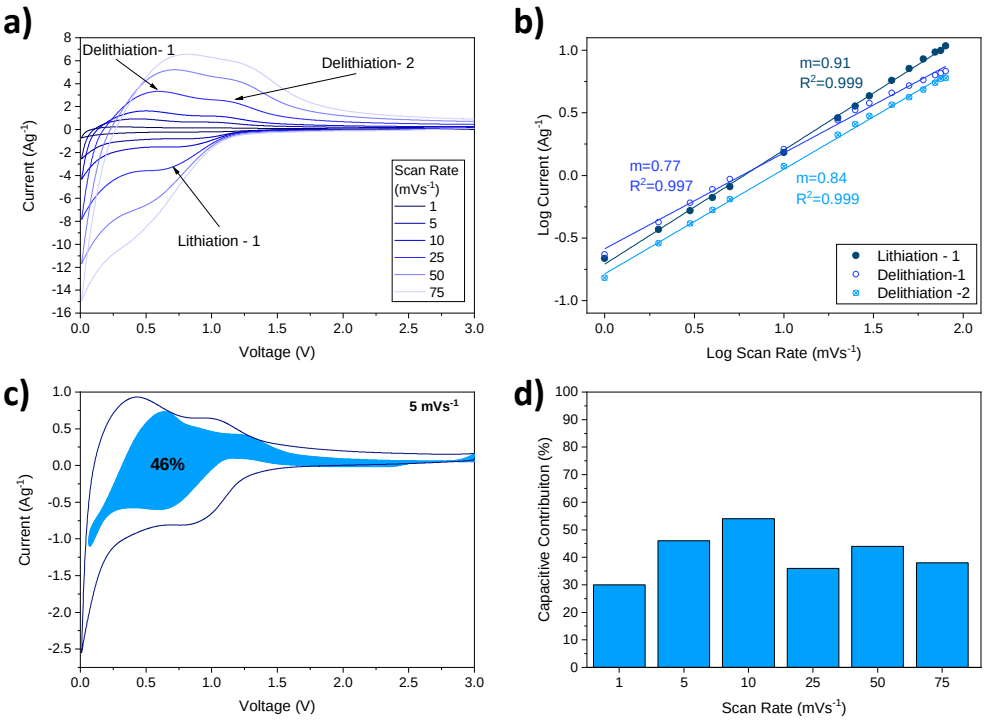

Figure 5.8 – a) CV profiles of 10 % Mo composite materials at increasing scan rate from 1.0 – 75 mVs^{-1}. b) Log plot of peak currents, versus scan rate, fitted with a linear function where R^2 is greater than 0.997 on all lines. c) CV profile at 5 mVs^{-1} with filled area representing the capacitive contribution. d) Chart of percentage capacitive contribution at increasing scan rate from 1.0 to 75 mVs^{-1}.

Staircase potential electrochemical impedance spectroscopy (SPEIS) shows a low and stable impedance at all mid to high frequencies (10 Hz to 10 kHz), after the initial cycle (Figure 5.9). Initially there is a drop in impedance after 1.5 V during lithiation, corresponding to the onset of the redox peak seen in the CV profiles (Figure 5.8a). Once Li-ions are inserted into the material, the resistance is reduced - this corresponds with the fact that lithiation enhances the poor conductivity seen in Nb_2O_5 materials.[80] After this, the resistance stays low and stable throughout the cycles, except at the low frequency response corresponding to Li-ion diffusion. In all instances, there is a higher impedance for the 1 Hz response between 1.0 and 3.0 V. This could equate with lithium diffusion within the electrode, and the tortuous pathways that ions may experience. In comparison to the pure as-synthesised Nb_2O_5, the impedance is largely reduced across the cycle numbers and thus suggests that the addition of Mo doping is boosting the conductivity of the material. In the Nyquist plots, the diffusion tail shows a typical 45 ° angle for a diffusion-limited type material during delithiation, whereas during the lithiation this is a steeper line suggesting a capacitive type of diffusion (Figure A.63). This appears consistent with the CV signatures, which suggests a continuous intercalation mechanism with a two-phase mechanism upon delithiation. In addition, the

charge transfer (CT) resistance is higher for lithiation, thus may be indicative of an expansion needed to accommodate the Li-ions, yet upon de-insertion a less resistive two-phase step occurs.

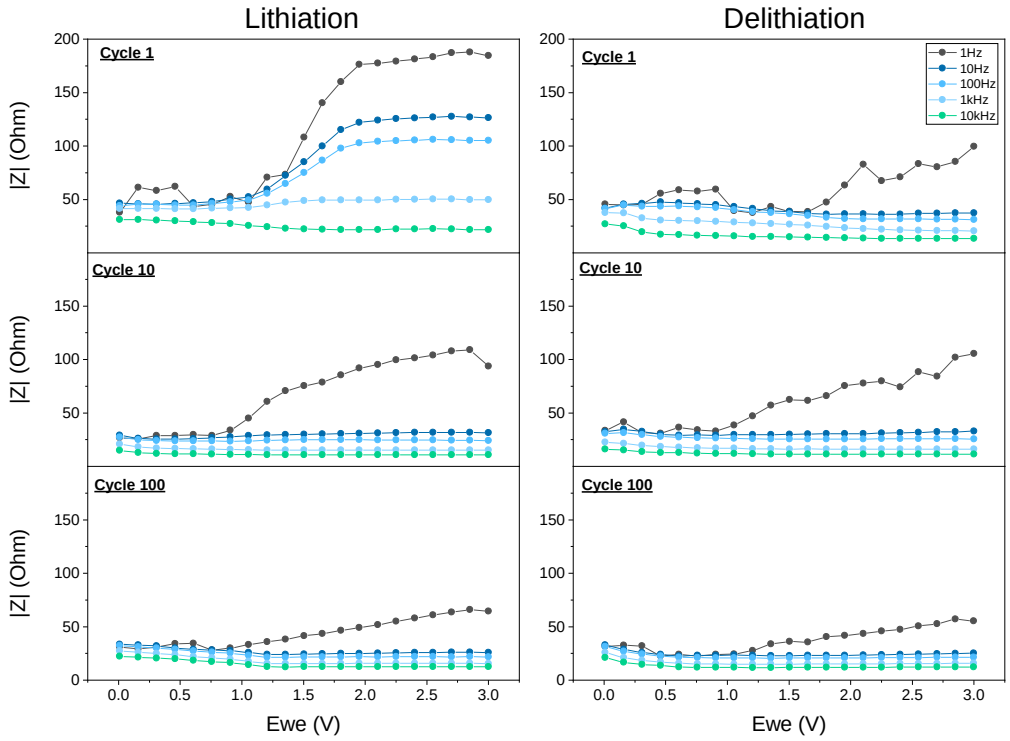

Figure 5.9 – SPEIS profiles of 10 % Mo composite material for increasing cycles from 1 to 100 (top to bottom) for lithiation and delithiation (left and right respectively).

In summary, an Nb_2O_5/MoO_2 material was synthesised, where Mo appears to be doped or substituted into the structure at 10 %. As such, this material performs similarly to the as-synthesised Nb_2O_5 with maintenance of good rate capability. This suggests that the Mo in the structure does not impede the fast Li-ion kinetics. Yet at C/5 the capacity is boosted after 10 cycles (in comparison to the pure counterpart), which may suggest that at slow rates the Mo may add to the electrochemical redox activity. This may come from the availability of more active sites due to the Mo content. Additionally, the doping can significantly lower resistances. On the other hand, there appears to be a limit to the material's ability to rely on capacitive mechanisms, as disorder may lead to more tortuous pathways. It is challenging to characterise definitively whether Mo is doped or substituted into the material and how this changes the electrochemical properties.

5.2.2.2 Electrochemical characterisation of 20% Mo containing composite

Equivalent electrochemical tests were carried out on the 20 % Mo in Nb_2O_5 composite. The wide voltage range has the highest capacities, with the other ranges showing little difference between them (Figure 5.10a). By 200 cycles the average capacities are 108 ± 12.5, 60 ± 3.0 and 44 ± 0.9 $mAhg^{-1}$ for wide, medium, and narrow ranges, respectively. There is good reversibility as even at 200 cycles, the differential capacity profiles maintain their shapes (Figure 5.10b).

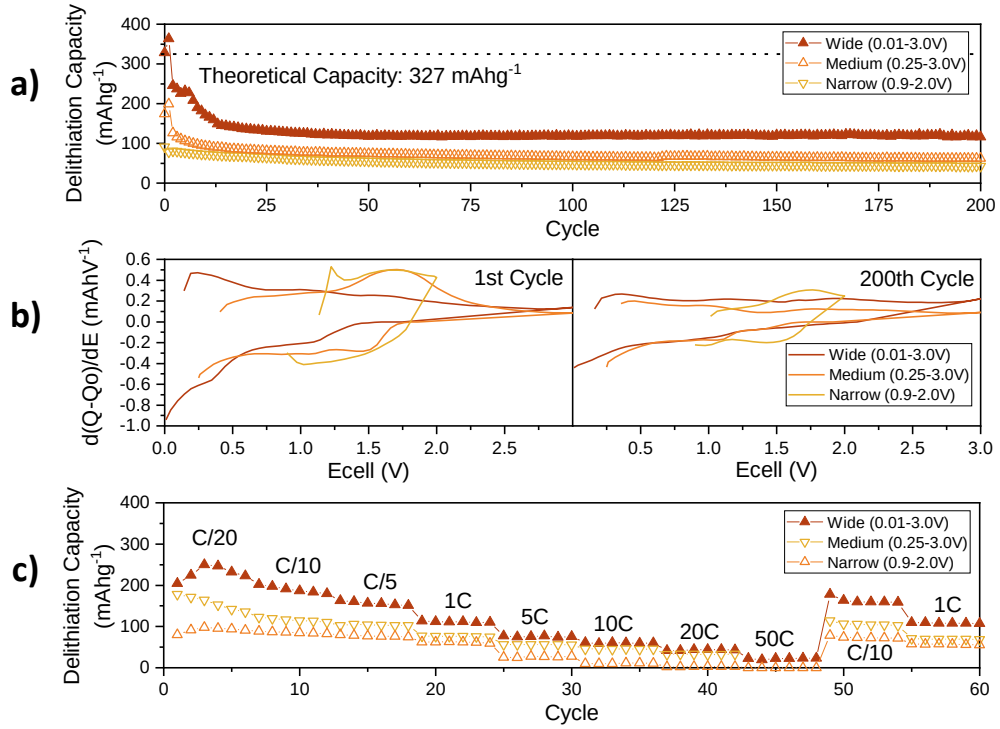

Figure 5.10 - (a) Galvanostatic cycling of 20 % Mo composite at 1 C at various voltage windows, with a C/20 formation cycle. (b) Corresponding differential capacity plots at the 1st (left) and 200th cycle(right). (c) Rate sweep from C/20 to 100C at different voltage windows.

Regarding rate capability, this material can only be cycled to 50C, and by 100C, cell failure occurs (Figure 5.10c). This shows that with increasing Mo content, some of the rate capability is lost. Again, the wide range shows higher capacities across the rates, with a recovery of 88 % after high-rate cycling. Over 200 cycles, between C/5 and 5C the trend in capacity is similar and there is only a small drop in capacity between the rates (Figure 5.11). However, when increasing to 20C, there is a huge capacity drop, and so this material becomes performance-limited at higher current densities. By 200 cycles average capacities of 146 ± 0.5, 108 ± 12.5 and 79 ± 13.4 $mAhg^{-1}$ are delivered at rates C/5, 1C and 5C, respectively. The charge profiles

are linear up to 2.0 V for all rates initially, suggesting an intercalation pseudocapacitive mechanism, as expected from Nb_2O_5. Yet at 200 cycles, there appears to be an inflection in the profile at 1C and 5C, potentially suggesting a movement away from the continuous mechanism at higher rates. This may result in the limited rate capability observed in this material. Regarding coulombic efficiency, this material achieves over 99 % efficiency after the first 30 cycles at C/5, the time to reach high efficiency is reduced with higher rate testing (Figure A.64).

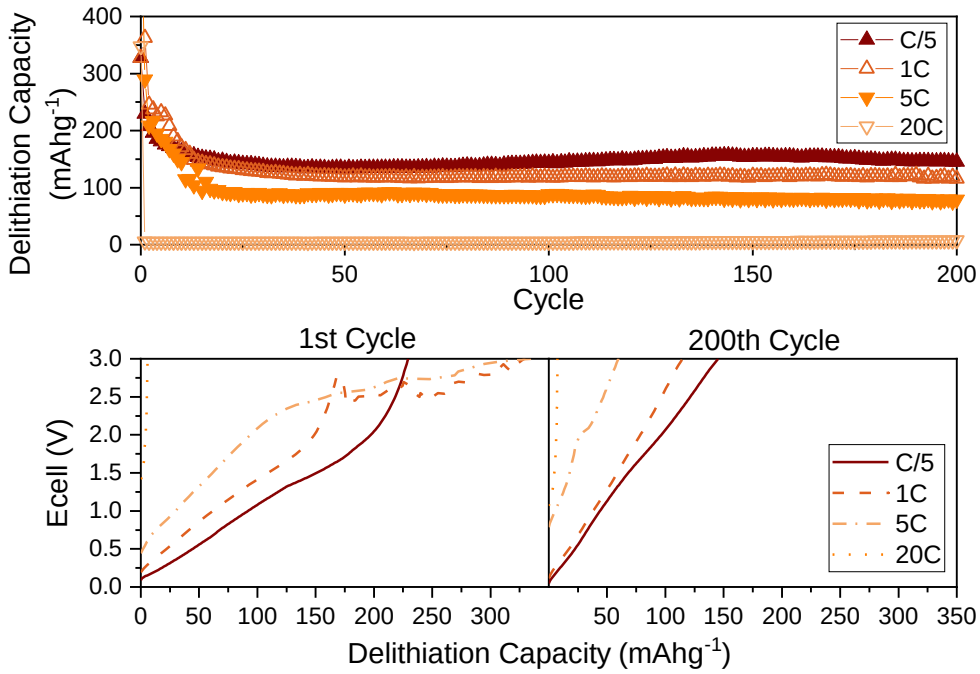

Figure 5.11 - (top) Galvanostatic cycling of 20 % Mo content material between 0.01-3.0 V at various rates, (bottom) charging profiles at various rates at 1st and 200th cycle.

The limit to the rate capability of this material is explored via CV at increasing scan rates. A similar CV profile is seen to that of the pure Nb_2O_5 and 10 % Mo doped material (Figure A.65a). However, with increasing scan rate the peak seperation appears to be much larger suggesting an internal resitance. The log plot of the peak currents shows linear gradients of 0.74, 0.58 and 0.63 for lithiation-1, delithatiation -1 and -2 resepecively (Figure A.65b). As seen previously, the lithiation process is more similar to that of a capacitive mechanism than the corresponding delithiation, as the gradient is much higher than 0.5. This difference in kinetic response may be seen due to the single broad redox peak in lithiation, suggesting a continous redox change, yet two peaks during delithiation. Perhaps delithation requires removal of Li from the surface, then the bulk hence the two states of redox and lower

capacitive character of one of the peaks. When the capacitive contribution is calculated for this material it only reaches a maximum of 24%, which is relatively low. This is a big reduction in capacitive contribution compared to the 10% Mo material, suggesting that the increase in MoO_2 content inhibits the surface limited kinetics perhaps due to the way MoO_2 and Nb_2O_5 are intimatly grown.

In the SPEIS plots the initial lithiation shows a large decrease in impedance as the voltage moves below 1.0 V, this corresponds to the redox peak in the CV (see Figure 5.12). After this, the impedance is reduced over the subsequent cycles. At 1Hz, higher impedance is seen between 1.0 and 3.0 V for all plots, with this frequency corresponding to Li-ion diffusion. For lithiation at 10 and 100 cycles there is a step up in impedance across the frequencies at 0.5 V, this sits at the where the redox peak is in the CV, therefore suggesting an increased resistance within this redox process. At high frequency (10 kHz) this is also shown, suggesting that the electrolyte and SEI may be unstable. Overall, the impedance is reduced from the pure Nb_2O_5, suggesting MoO_2 is improving the overall conductivity. EIS measurements show two semi circles for both lithiation and delithiation, which correspond to SEI and CT resistances (Figure A.66). These resistances do not seem to follow a trend for the delithiation. However, for lithiation, the SEI resistance constantly increases, suggesting a continuous SEI re-formation.

To summarise, a Nb_2O_5/MoO_2 composite with 20 % Mo content was successfully synthesised, where MoO_2 nanospheres decorate the Nb_2O_5 nanowire networks. This material shows a boost in capacity at low rates in comparison to pure Nb_2O_5. This is particularly notable at C/5, where not only is there an increase in capacity, but the capacity retention has also drastically improved. However, the rate capability of this composite is stunted, and it can no longer be cycled higher than 50C in a rate sweep, with the response at 20C over longer term cycling becoming negligible. The lack of capacitive contribution is further evidence to the limit on rate. It appears that there may be a more complex situation at play with this material, as the impedance spectroscopy shows high SEI resistance and instability. This may suggest structural breakdown with increasing cycling, even though the overall resistance has been reduced by the presence of MoO_2 as a conductive additive. This composite does not give enough of a beneficial capacity improvement versus rate capability to warrant further exploration.

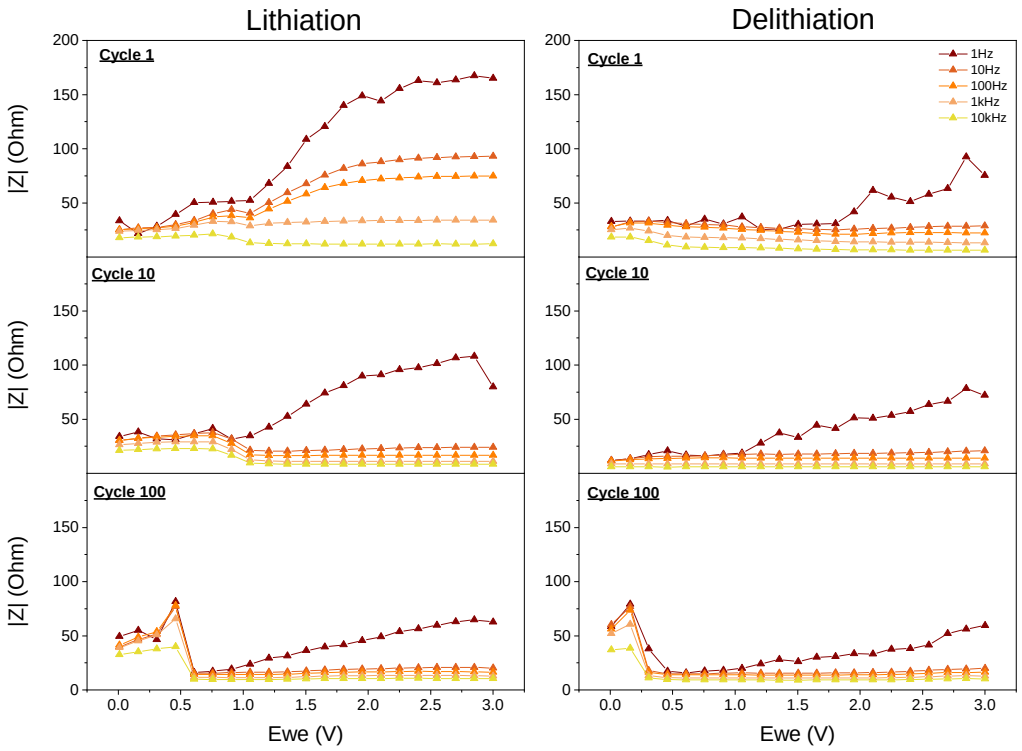

Figure 5.12 - SPEIS profiles of 20 % Mo composite material for increasing cycles from 1 to 100 (top to bottom) for lithiation and delithiation (left and right respectively).

5.2.3 Comparison of the Nb_2O_5-Rich Composite Materials

The Mo appears to dope/substitute up to 10 % into a semi-crystalline Nb_2O_5, where XRD and EDX mapping show no formation of a secondary phase. The XPS also shows both metals in a range of oxidation states, which suggests doping occurs for both composites. Yet, with an increase in Mo content, measured at 24 % using XRF, MoO_2 is formed as a separate phase and manifests as nano-spheres. Electrochemically, the addition of Mo into the materials reduces overall impedance, likely to be achieved by boosting the materials' conductivity. This is promising as is one of the key aims in forming these composite materials. Further to this there is a boost in capacity seen (up to 1C) with the addition of Mo. However, as might be expected, there is a drop in rate capability, this is particularly obvious in the 20 % Mo composite as at 20C, it contributes negligible capacity.

These materials cannot be directly compared with literature as they are novel, and no similar materials were found. However, Table 5.2 shows a brief comparison to other Nb_2O_5 materials. When compared to the pure Nb_2O_5 produced here, discussed in chapter 3, the

composites show improvement. In comparison to a similar semi-crystalline Nb_2O_5, the 10 % composite performs comparably at high rate,[133] and far surpasses a recent study by Hu *et al*. on T and TT- Nb_2O_5 under similar conditions.[131] However, the composite material is compromised at lower rates, where the capacity does not match those reported in literature. The 20 % composite gets closer to the capacities reported at lower rates yet has a much poorer rate capability. There appears to be some benefit of introducing Mo into the Nb_2O_5 system, yet much further investigation is needed here. Furthermore, Mo content should be tested to try to find an optimum amount for improving conductivity without drastic rate reduction. Considering the levels in which the electrochemical properties of pure Nb_2O_5 can be changed with heat-treatment, there is an opportunity to study how this may also affect these materials.

Table 5.2 – Comparison of reversible capacities of high Nb content composites with published Nb_2O_5 materials.

Material	**Synthesis**	**Capacity at low rate ($mAhg^{-1}$)**	**Low Rate**	**Capacity at high rate ($mAhg^{-1}$)**	**High Rate**	**Ref**
Anisotropically Crystalline Nb_2O_5	Hydrothermal	82	1C	43	20C	This work
10 % Mo Nb_2O_5 composite	Hydrothermal	99	1C	88	20C	This work
20 % Mo Nb_2O_5 composite	Hydrothermal	114	1C	85	5C	This work
Semi-Crystalline Nb_2O_5	Continuous Hydrothermal	143	2.5C	74	25C	[133]
TT-Nb_2O_5	Thermal Oxidation	110	1C	19	25C	[131]
T-Nb_2O_5	Thermal Oxidation	105	1C	33	25C	[131]

5.3 MoO_2-Rich Composite Materials

5.3.1 Characterisation of MoO_2-Rich Composite Materials

The successful production of MoO_2 in both composite materials is seen by the monoclinic MoO_2 peaks in the XRD pattern (Figure 5.13). The 10 % Nb composite shows very little difference in its XRD pattern compared to pure MoO_2, with two small peaks arising at 22 and 46 °, which may be attributed to the formation of a Nb oxide. This suggests that the 10 % Nb content is either largely in an amorphous or nano crystal form or doped into the MoO_2

structure. Whereas at 20 % Nb, the amorphous features seen in the as-synthesised Nb_2O_5 become apparent, with key peaks at ~22 and 46 ° being present.

The composition of the composite materials is confirmed via XRF (Table 5.3). The 10 % material shows a slightly higher Nb content than expected, however the synthesis process appears to be reproducible. The 20 % Nb material shows elemental percentages closer to the expected yet has a higher deviation between batches of material. The TGA of the composite material has a very similar profile to that of MoO_2; however, the large loss from 800 °C differs between the materials (Figure A.67). This loss is associated with sublimation of Mo, which may vary due to the ease of oxidation of MoO_2 within the materials. All materials show an initial loss of water, followed by a small loss between 200-400 °C, which has been associated with organic ions on the surface residing from the hydrothermal synthesis.

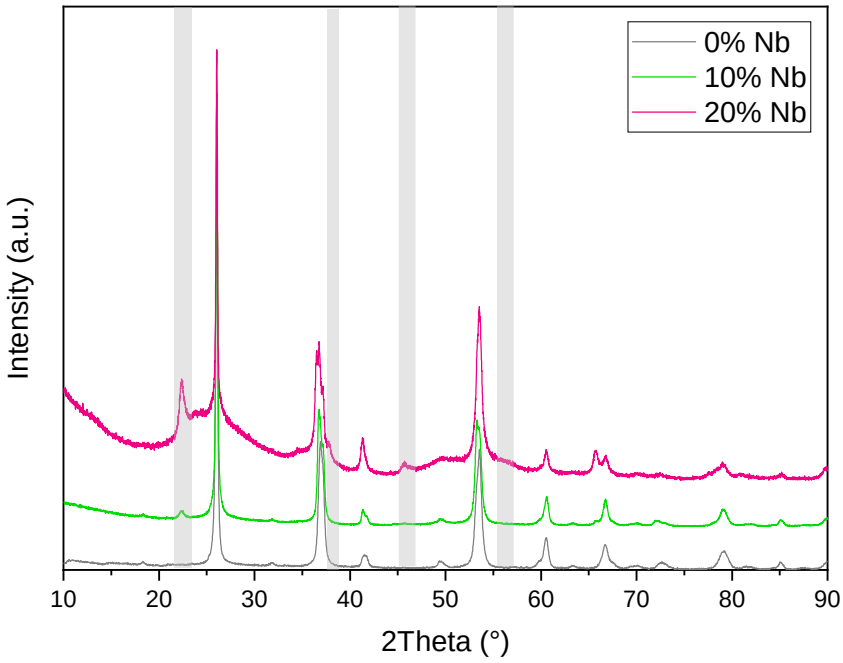

Figure 5.13 - XRD patterns of MoO_2-rich composites and pure MoO_2, with grey shading marking the appearance of peaks of the anisotropically crystalline Nb_2O_5.

Both materials are a collection of agglomerated nanoparticles, as seen by the SEM images; and do not look dissimilar to the pure MoO_2 in either size or morphology (Figure A.68). However, TEM images show that this is not the case; the pure MoO_2 particles are 'rice grain' shaped and much larger than the composite material (Figure 5.14). Both composites take on a more rectangular shape, similar to that of the as-synthesised Nb_2O_5 nano-wires and appear

to be of similar dimensions to this. The SEM-EDX maps show an homogeneous mixture of Mo and Nb across the materials (Figure A.68d,e) yet the STEM-EDX gives a more detailed picture of the elemental mapping (Figure 5.15). In the 10 % Nb composite most of the sample appears to be a homogeneous mix of Mo and Nb, however there are small areas dominated by Nb only. This may suggest that the material is beyond its doping limit, and thus the Nb may also be forming as an oxide also, this agrees with the XRD pattern (Figure 5.13). When the Nb content is increased to 20 %, the elemental separation is more apparent, as the two oxides appear separately in the XRD pattern.

Table 5.3 - Results of XRF analysis of MoO_2-rich composite materials.

Composite	Oxide Component	Quantity (atomic %, of metal atom)	Standard deviation between batches (%)
10% Nb Composite	Nb_2O_5	12.92	0.25
	MoO_2	87.08	
20% Nb Composite	Nb_2O_5	21.60	1.39
	MoO_2	78.40	

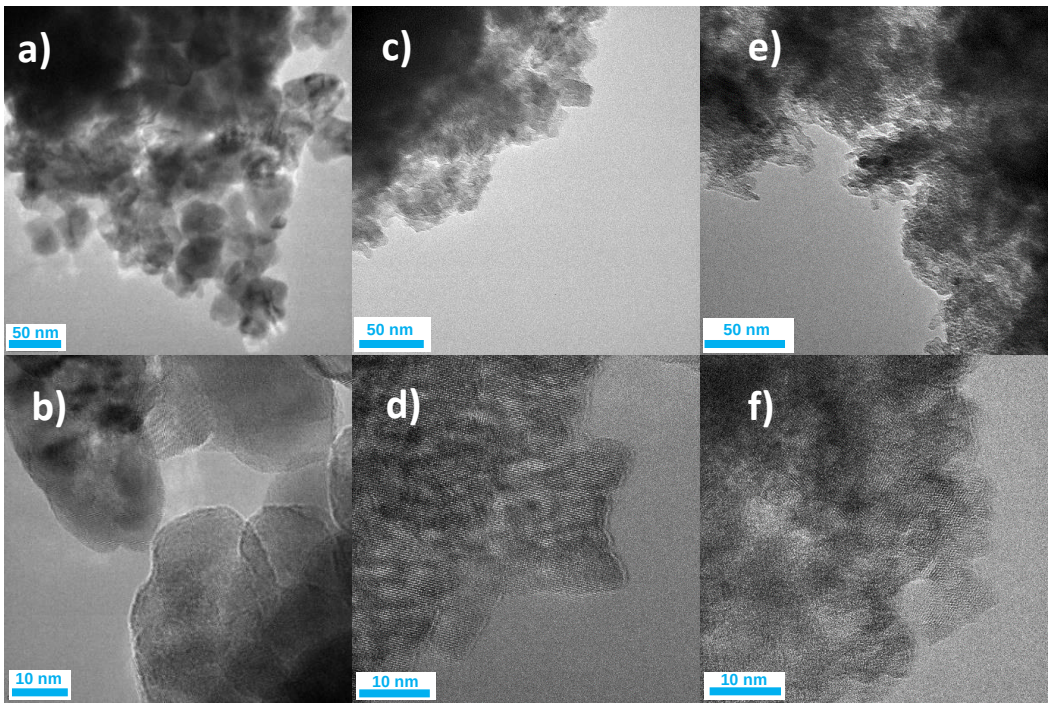

Figure 5.14 - TEM images of (a, b) MoO_2, (c, d) 10 % Nb composite, (e, f) 20 % Nb composite. A selection of images is shown in Figure A.69 and Figure A.70

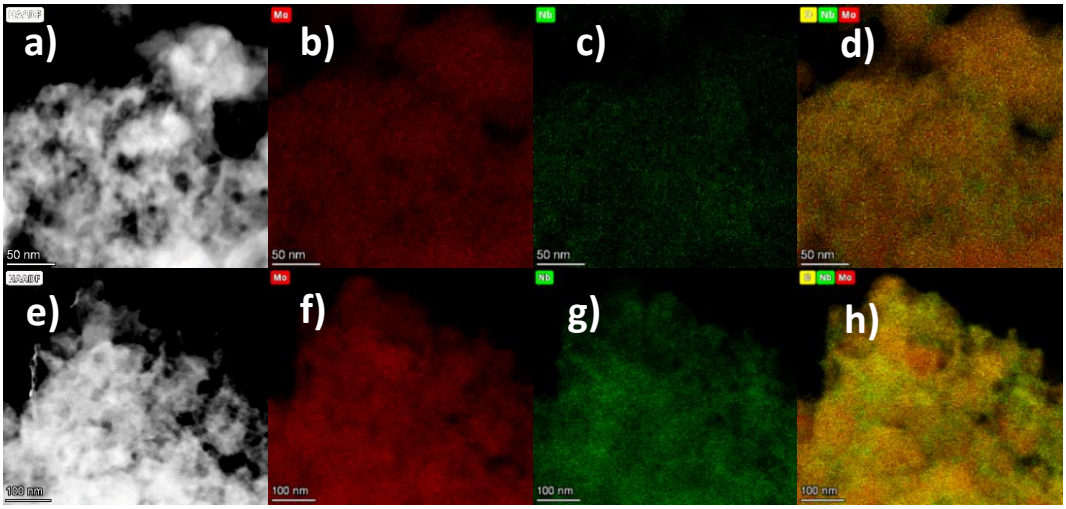

Figure 5.15 - STEM-EDX mapping of 10 % Nb composite (a-d) and 20 % Nb composite (e-h). From left to right, HAADF image, Mo Map (Mo in red), Nb Map (Nb in green) and Nb, Mo, O map.

The use of electron microscopy has made it clear that the size and morphology of the composite materials differs from pure MoO_2, thus, the particle size was examined. The particle width was measured from the TEM images, MoO_2 has a large particle size of 30 nm (mean) compared to 5.5 and 3.5 nm (mean width) for 10 and 20 % Nb composites respectively (Figure A.71). This is similar to the as-synthesised Nb_2O_5, with a particle width 3.5 nm. The particle size was further scrutinised using particle size measurements (Figure A. 72). One should note that the assumptions surrounding particle size calculations mean that this method is most accurate for spherical particles. Thus, the measurements on MoO_2 will be a better representation than that of the composites. MoO_2 has a particle size distribution centred around 50 nm (number distribution), which is slightly higher than the TEM count estimate. The 10 % and 20 % composite show a distribution centred on 70 and 75 nm respectively. This is far from the expected size from the TEM imaging; and suggests that secondary particles are formed here. This is supported by SEM imaging, which appears to show the composites to be very similar to MoO_2 in size (Figure A.68).

Further physical characterisation of these composites was carried out via N_2 adsorption. All materials have the same type of isotherm and hysteresis (Figure A.73), pore distributions also being similar. With higher Nb content, the surface area and pore volume increases, and the average pore width decreases (Table 5.4). The 20 % Nb composite has almost double the surface area of pure MoO_2; this is likely due to the reduction in particle size and the formation of nano-wires of Nb_2O_5 in the material.

Table 5.4 - Key parameters calculated from full N_2 adsorption isotherms of the MoO_2 heavy materials.

Material	BET Surface Area (m^2g^{-1})	DFT Total Volume in Pores (cm^3g^{-1})	BJH Adsorption Average Pore Width (nm)
MoO_2 (0%)	25.4	0.09	22.0
10 % Nb	36.0	0.12	16.4
20% Nb	56.2	0.16	13.2

XPS reveals that the 10 % Nb composite shows the unscreened and screened MoO_2 states as would be expected and some Mo in the +6 state suggesting oxidation at the surface (Figure 5.16).[205] Furthermore, Nb appears in a +5 oxidation state, however the difference in binding energy between the Nb 3d and O 1s is 323.79 eV, which sits on the borderline between +5 and +4, suggesting a slightly reduced state.[355] This looks like a simple mixture of the pure oxides, as it does not deviate from the results seen in the pure materials. As for the 20 % composite, the Nb also appears in the same state, however there is deviation in the Mo states here (Figure 5.17

Figure 5.17). The Mo appears to fit another +4 types of state, separate from those expected. This may suggest some change in the MoO_2, although the exact nature of this is unclear. Unlike the Nb heavy materials, it is not obvious that doping is taking place from the XPS results. These composites also have surface species as seen from metal carbon and nitrogen bonding, likely to be a remnant from the hydrothermal synthesis. The XPS reveals that the Nb content is 16 and 31 % for the 10 and 20 % composites, respectively. This is much higher than that shown by the XRF measurements (Table 5.3), which may be due to the XPS being surface dominated rather than a bulk measurement.

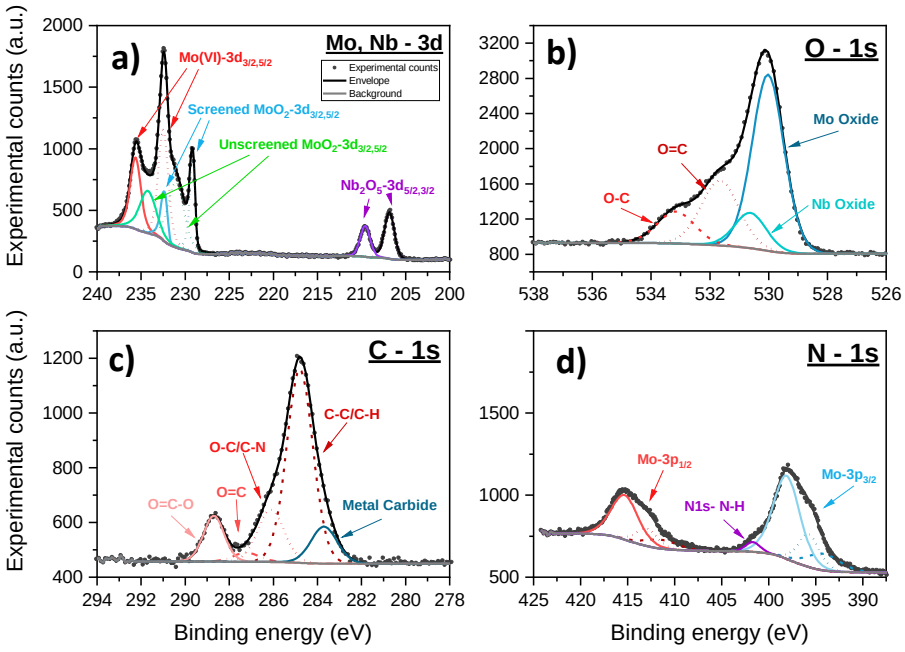

Figure 5.16 - High resolution XPS spectra of the Mo and Nb 3d region (a), O 1s region (b), C 1s region (c) and N 1s region (d) for 20 % Nb containing composite. Full scan in Figure A.74.

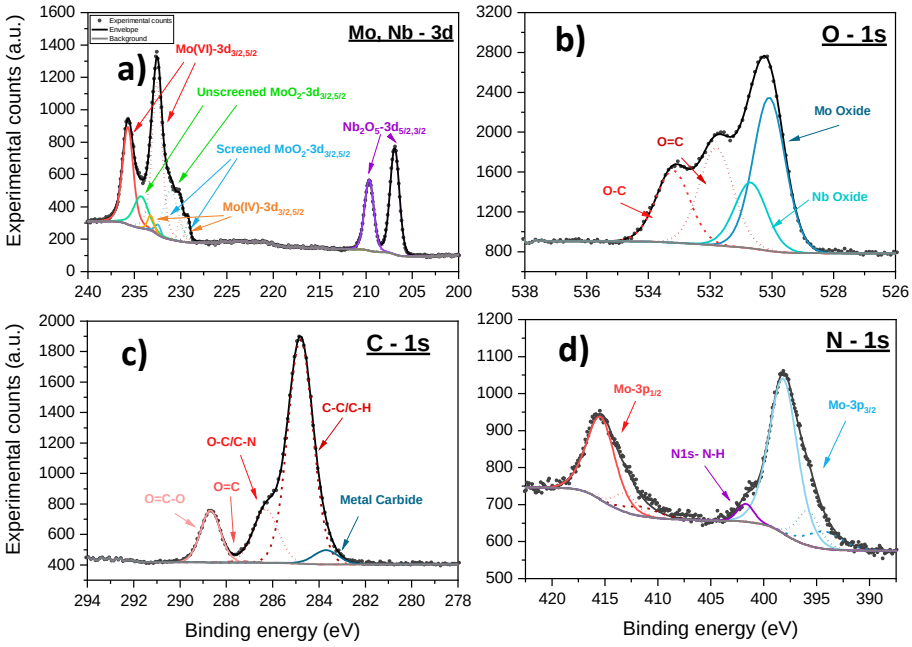

Figure 5.17 - High resolution XPS spectra of the Mo and Nb 3d region (a), O 1s region (b), C 1s region (c) and N 1s region (d) for 20 % Nb containing composite. Full scan in Figure A.74.

5.3.2 Electrochemical Characterisation of MoO_2 Rich Composites

An 80:20:10 ratio of AM: C65: PVDF was used for the formulation of the MoO_2-rich composites, as this was used for pure MoO_2. Thin electrodes were made as with the other materials in the aim to enhance their rate performance, thus a wet coating thickness of 50 µm on copper were created. As with the other composites, theoretical capacities were calculated as a weighted summation of the theoretical capacities of Nb_2O_5 and MoO_2.

5.3.2.1 Electrochemical Characterisation of 10% Nb Containing Composite

The preferred voltage window for MoO_2 falls into windows above and below ~1.0 V depending on the use of the conversion reaction. Thus, two ranges of 0.01-3.0 and 0.9-2.0 V were investigated, to be consistent with the other works presented here. As expected, the wide range shows a higher initial capacity however, this fades quickly in the first 15 cycles to a capacity lower than that of the narrow range (Figure 5.18a). Subsequently, between 75 and 100 cycles there is an increase in capacity, giving an average capacity of 137 ± 16 $mAhg^{-1}$ at 200 cycles. In this region, the material behaves similarly to pure MoO_2, where the increase is linked to a lowered resistance in the material via formation of metallic Mo, although this assumes the same mechanisms take place within the composite.

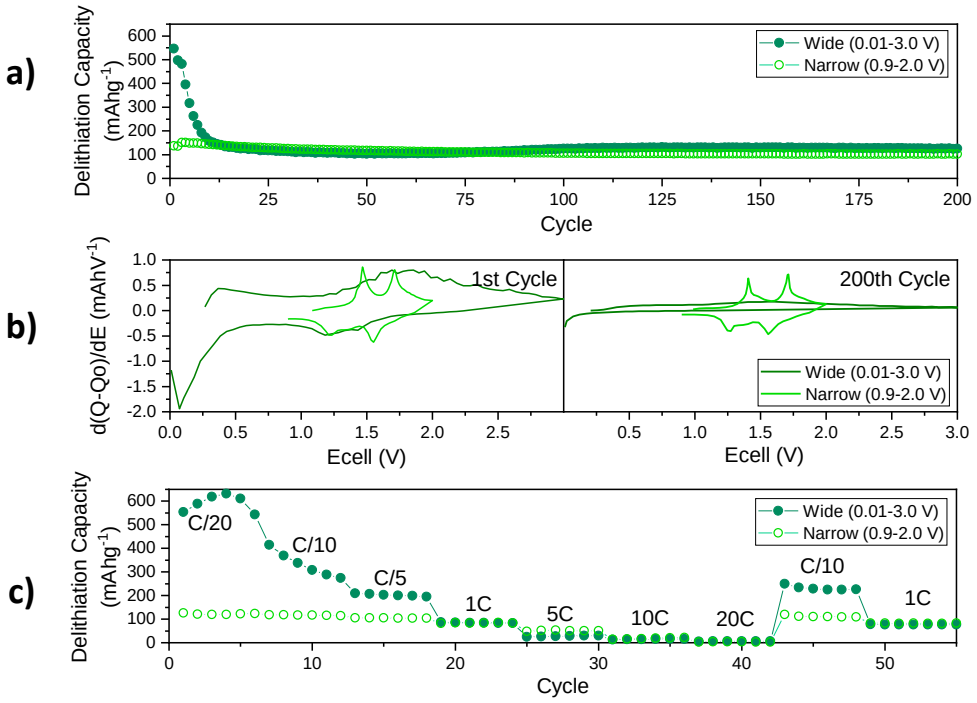

Figure 5.18 – (a) Galvanostatic cycling of 10 % Nb composite at 1 C at various voltage windows, with a C/20 formation cycle. (b) Corresponding differential capacity plots at the 1st (left) and 200th cycle(right). (c) Rate sweep from C/20 to 100C at different voltage windows.

In the narrow voltage range, there is a steady loss in capacity over cycles leaving an average capacity of 97 ± 5.1 $mAhg^{-1}$ at 200 cycles. In this range the Li-ion storage mechanism appears stable and reversible, as evidenced by the maintenance of the two redox pairs in the differential capacity plots (Figure 5.18b). The differential capacity plot for the wide range shows evidence of the conversion reaction taking place initially, alongside a set of broad peaks. Yet by 200 cycles the profile has lost these peaks, indicating a reduction in electrochemical activity. In the wide range, the coulombic efficiency takes 20 cycles to increase to over 98 % (Figure A.75) but takes much longer to sustainably achieve over 99 %. This is likely to be due to the large loss in capacity seen in this material, as this is not observed in the narrow range - the coulombic efficiency achieves over 98 % after only 5 cycles.

Ex-situ XRD reveals that the Li-ion intercalation process is reversible in the 0.9-2.0 V range, as the MoO_2 peaks are retained to 20 cycles with minimal broadening and shift (Figure 5.19b). With cycling there is shift in peaks at 25, 36 and 52°, which correspond to [110] planes, to lower angles, hence an expansion occurs within these planes to accommodate the ions. The only Nb_2O_5 peak in the pattern is also maintained, although appears to be broadening with cycling, suggesting formation of an amorphous form. This agrees with the maintenance of redox peaks seen in the differential capacity plots (Figure 5.18b). In the wide voltage range, the *ex-situ* XRD patterns also show shifting and slight broadening of the MoO_2 peaks, yet here the Nb_2O_5 peak disappears after the first cycle suggesting immediate loss of crystallinity or structural degradation (Figure 5.19a). This has been seen in the pure Nb_2O_5 (orthorhombic phase) previously. Notably, in the pure MoO_2 the activation of the material comes with a structural rearrangement from monoclinic to tetragonal. It is difficult to assess whether this has also taken place here, as the main indicators are loss of peaks at 18 and 32 °, and apparent peak shape change in places due to the reduction in number of peaks grouped together. As the 18 and 32 ° peaks show low intensity, they are not even seen in the fresh electrode, thus cannot be used as a structural marker. Yet there appears to be some peak shape change, which is most obvious at 37 °, however this is also seen in the narrow range. Therefore, it is difficult to know whether the structural rearrangement to tetragonal MoO_2 takes place here. It is not certain that all MoO_2 materials will undergo the same structural change as many properties may affect this, particle size being one of them, which has drastically changed in the composite compared to pure MoO_2.[227,244,248,251] The capacity loss seen in the initial 20 cycles in the 0.01-3.0 V range can be attributed to the conversion reaction becoming inaccessible. Yet, the *ex-situ* XRD patterns do not show dramatic

structural change, which may suggest only a subtle structural change, such as lattice expansion or disordering, may prevent the conversion reaction.

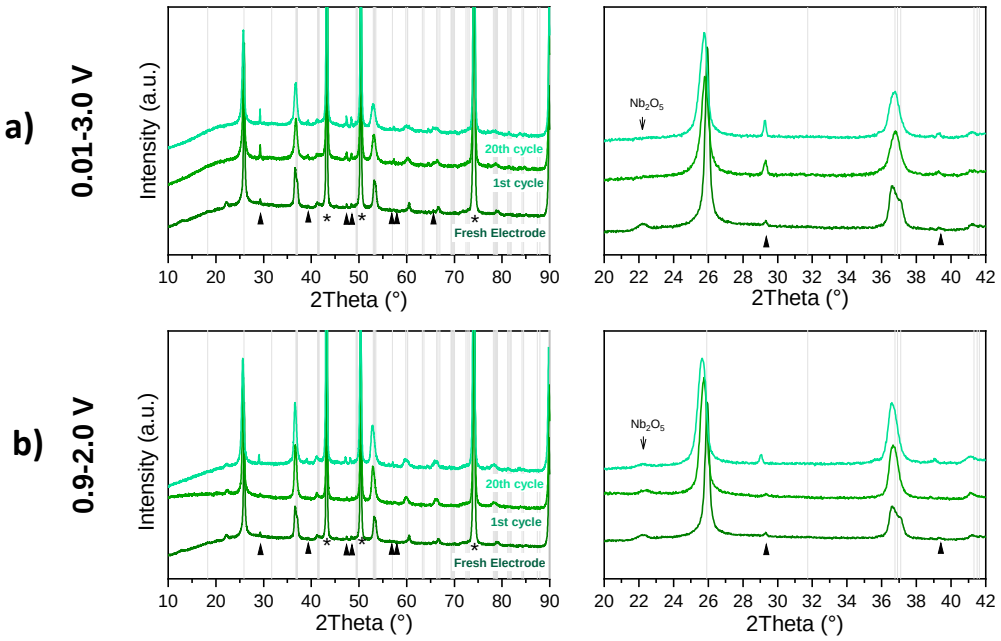

*Figure 5.19 – Ex-situ XRD patterns of 10 % Nb in MoO_2 composite cycled at 1C in a 0.01-3.0 V (a) and 0.9-2.0 V (b) range. The monoclinic MoO_2 is marked as grey lines, with peak attributed to Nb_2O_5 is labelled. Cu current collector peaks are denoted by *, other peaks from the sample holder are denoted by triangles.*

Regarding rate capability, during the rate sweep, there seems to be an activation process in the wide voltage window at C/20 (Figure 5.18c). This may be due to the reduced rate allowing for the structural rearrangement expected, owing to the slow kinetics of this process. This may also be why in the *ex-situ* XRD a structural change from conversion was not apparent as tests were ran at 1C, where this may not be able to take place. The wide range shows higher capacities at low rate, however, has poor rate capability and matches the narrow range at 1C. Both voltage ranges show good recovery to C/10, with retentions of 77 and 89 % for wide and narrow ranges, respectively. It is unclear what voltage range is most suitable, therefore the composite was tested in both ranges at different rates over 200 cycles.

In the 0.01-3.0 V range, a similar response is seen across the rates, where the material undergoes an activation process in the first few cycles (Figure 5.20). There is a slight improvement in these peak capacities with reduced rate. From here the capacity plateaus, except for 1C, which appears anomalous with a capacity gain between 75 and 100 cycles.

The differential capacity plots show initially two sets of redox peaks corresponding to the multi-phase intercalation reaction, plus a peak for the conversion at <0.5 V (Figure 5.20, bottom). At 5C there is no conversion redox peak, likely to be due to the slow kinetics of this. However, the material still shows activation and high capacities thus the conversion reaction does take place, but it may not be to the same magnitude as with other rates. By 200 cycles, there is still evidence of the conversion process at C/5 and 1C. At all rates there is a broad set of peaks above 1.0 V, this may be due to the intercalation mechanism changing to a single-phase process. These differential capacity plots are similar to those of pure MoO_2, suggesting that the Nb_2O_5 does not have a large effect on the system at this level.

In the 0.9-2.0 V tests, the differential capacity plots show two sets of redox peaks at all rates (Figure 5.21, bottom). This corresponds to the two-phase intercalation reaction: monoclinic to orthorhombic to monoclinic. Yet at 5C, there is clear polarisation at this rate, and the resistance experienced here is seen as fluctuations in the capacity over cycling. The intercalation process is significantly limited at higher rates by the multi-stage process. The change in mechanism seen in the wide voltage window, alongside the subtle structural change is important when it comes to high-rate cycling. The continuous intercalation process seen in the wide range (following activation) has faster kinetics, as the rate capability is far improved. In the narrow range at high rate (5C) the capacity appears to fluctuate and is a lot lower than the capacity achieved in the wide range: 58 versus 113 $mAhg^{-1}$ respectively at 200 cycles. This suggests that although the high capacities that are desired from a wider window are not achieved, there is merit to cycling in the wider range to access a faster continuous lithiation process.

Further electrochemical studies of this material reveal more about its rate cyclability. The CV profile of this composite appears to have no well-defined peaks, but multiple broad shoulders can be identified, with four of these features on both lithiation and delithiation (Figure A.76a). Most of these shoulders flatten out with increasing scan rates to the point where the profile becomes rectangular above 50 mVs^{-1}. This causes some atypical patterns in the peak current plot, as such it appears that there is some reliance on a capacitive mechanism although it is difficult to accept the calculated capacitive contributions due to the strange shape of the CV profile.

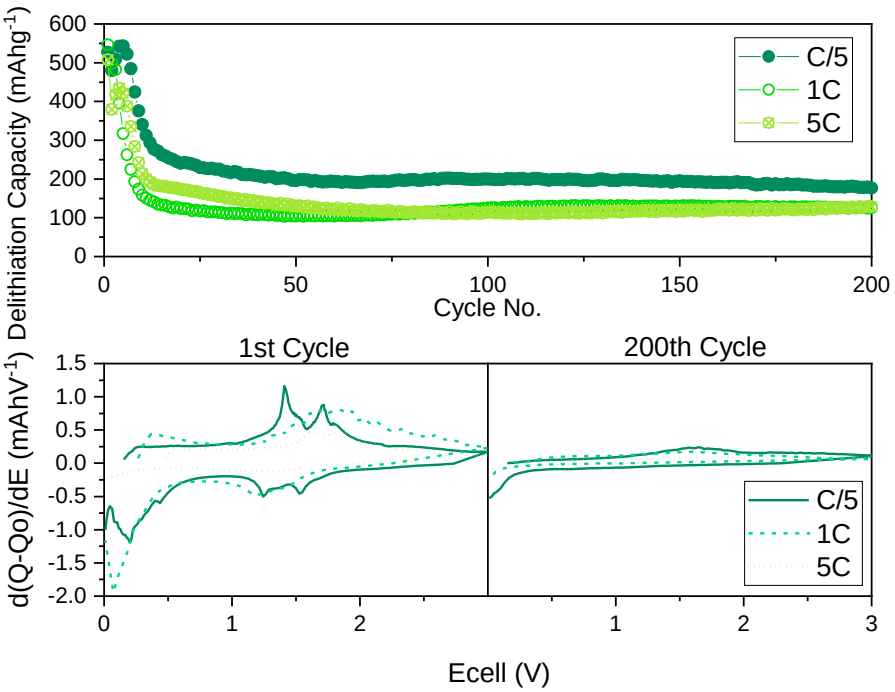

Figure 5.20 - (top) Galvanostatic cycling between 0.01-3.0 V of 10 % Nb composite at various rates, (bottom) differential capacity plot at various rates at 1st and 200th cycle.

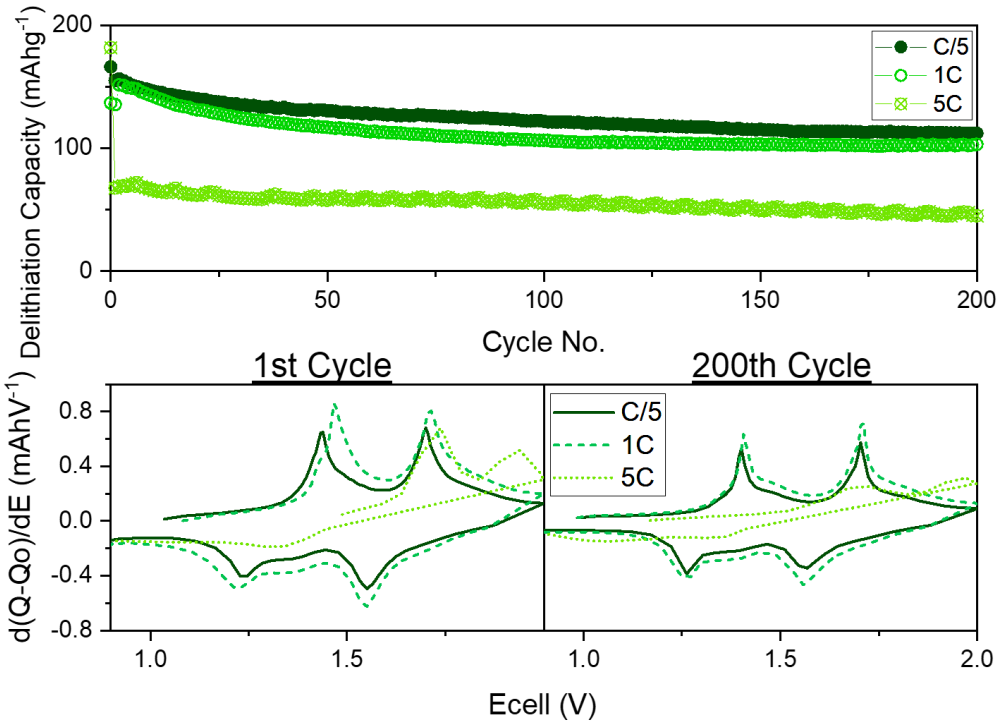

Figure 5.21 - (top) Galvanostatic cycling between 0.9-2.0 V of 10 % Nb composite at various rates, (bottom) differential capacity plot at various rates at 1st and 200th cycle.

SPEIS was used to characterise this material further, where the impedance increases from the first cycle (Figure A.77). During the initial lithiation the resistance increases from 2.0 to 0.5 V across all frequencies, which also corresponds to the onset of the plateau in the charging profile. This suggests that the Li-ion intercalation comes with an associated resistance, which may be expected due to the two-phase mechanism. This is seen similarly in the initial delithiation. However, this trend does not continue into the other cycles, where there appears to be impedance increases below 0.5 V, which may be linked to the conversion reaction. This change is also seen at high frequency (10 KHz), suggesting breakdown and reformation of SEI, with the conversion process and/or a degradation of electrolyte at this low voltage. The low frequency response appears to fluctuate at the 10 and 100th cycles, and no clear pattern is seen here (perhaps a longer relaxation time between measurements is required to clarify this). As the SPEIS appeared inconsistent, EIS was carried out at the preferred voltages used in MoO_2: EIS at 2.75 and 0.5 V were tested and 0.5 V showed repeatable and stable results. For both lithiation and delithiation a single semi-circle and shallow diffusion tail were seen (Figure 5.22). This suggests that the diffusion of ions is extremely limited as the diffusion tail sits at a smaller angle than 45°, hence cannot be fully described as semi-infinite diffusion.[372] Furthermore, the CT resistance increases with cycling, and notably there is a large increase between 10 and 20 cycles during lithiation, which corresponds, to the large drop off in capacity (Figure 5.20). Therefore, the material appears to have a resistive charge transfer mechanism which may be affected by structural changes with cycling.

To summarise, a composite of MoO_2/Nb_2O_5 was created with 10 % Nb content. This material behaves preferentially as an intercalation only material, as reasonable capacities compared to the theoretical were achieved, and the material showed a high level of reversibility. Yet when aiming to use the multiple storage mechanisms, large losses and poor capacity retention is seen. Overall, the rate capability is poor, and this is evidenced via the low capacitive contribution calculated for this material. This material shows some advantage over pure MoO_2, as there is a boost in capacity, which is seen over all rates. This capacity improvement may be due to the addition of Nb_2O_5 or the reduction in particle size and thus an increase in Li-ion sites. In the wide range, the composite appears to behave similarly to pure MoO_2 but with improved structural stability, evidenced by the lack of other phases formed in the *ex-situ* XRD. However, it is unlikely that this material will compare well against previous literature (discussed later in section 5.3.3) and may also require heat-treatment to reach better stability as with the pure MoO_2.

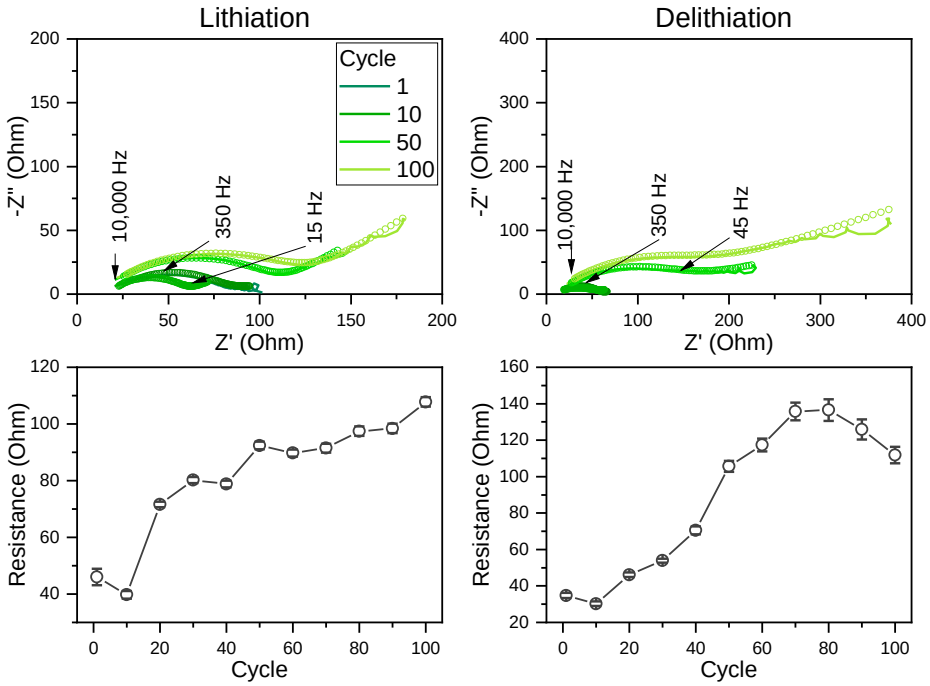

Figure 5.22 - Nyquist plots of 10 % Nb composite taken at 0.5 V during lithiation and delithiation (left and right respectively), with fitted curves (circles) and below their corresponding, fitted CT resistance values.

5.3.2.2 Electrochemical Characterisation of 20 % Nb Containing Composite

The same electrochemical testing regime was used to characterise the composite with 20 % Nb content in MoO_2. The wide voltage range shows an initial high capacity, which decreases immediately to match a similar capacity to the narrow voltage window (Figure 5.23a). This is vastly lower than the theoretical capacity of 710 $mAhg^{-1}$ for the wide range. The capacity response in the narrow range is far more stable and just shows a steady loss with cycling. By 200 cycles average capacities of 76 ± 7.0 and 64 ± 7.7 $mAhg^{-1}$ are achieved for wide and narrow voltages respectively. These results are poor and may suggest that the addition of Nb_2O_5 at this level is not having the stabilising effect on MoO_2 that is desired. Yet the coulombic efficiency is good, showing a greater than 99 % efficiency after 25 cycles for both ranges (Figure A.78). This material shows poor reversibility in the wide range as the differential capacity profile is completely diminished after 200 cycles with no clear shape (Figure 5.23b). There does seem to be improved reversibility in the narrow range where the profile shape is maintained, and two sets of broad peaks are still apparent at 200 cycles. When comparing the voltage windows over various rates, the wide range shows a fast-fading

high capacity at C/20, from here the capacity drops with increasing rate, by 5C the capacity is low. The capacity response is similar in the narrow range, suggesting that 0.01-3.0 V range does not improve the electrochemistry. This may be due to the conversion reaction being irreversible.

Cycling at different rates over 200 cycles revealed that rate has little effect on electrochemical performance in the wide voltage range (Figure A.79). There is a similar trend in capacity over cycle number at all rates and the all charge profiles show a sloping plateau, suggesting a solid solution reaction takes place.[122] In the narrow range, the capacity is much more stable with an increasing capacity loss with increasing rate (Figure 5.24). The reduction in capacity with increasing rate is small and suggests that it performs better as an intercalation only material. At 100 cycles the average capacities are 77 ± 16, 73 ± 7.7 and 52 ± 13 $mAhg^{-1}$ for C/5, 1C and 5C respectively. However, the large loss in capacity comes from here where the average capacity at 200 cycles is 69 ± 19, 64 ± 12 and 34 ± 0.5 $mAhg^{-1}$ at each rate respectively. The charge profiles are near linear for all rates, with small features in the profiles, most notable at C/5. This potentially suggests a mix of capacitive type storage mechanism from Nb_2O_5, hence the linearity, and a battery type intercalation, seen via the features corresponding to the two redox peaks of MoO_2. This is further explored by CV measurements at increasing scan rates.

The CV profile is broad and has multiple features in the delithiation process, but only two, clearly defined peaks during lithiation (Figure 5.25a). The number of features during delithiation may be due to the two redox peaks expected from the MoO_2 and the peak expected from the Nb_2O_5, which can sometimes be seen as two due to mixed valency in the material. The lack of peak symmetry and unequal peak numbers in the profiles demonstrates that the delithiation is not the reverse of the lithiation process. When these peaks are displayed as a log plot, the lithiation and delithiation peak-1 appears to have a steep gradient, suggesting a fully capacitive mechanism, thus one would suggest these peaks might be linked to Nb_2O_5 (Figure 5.25b). The other gradients are similar: 0.56, 0.52, 0.52 and 0.57 for lithiation-2, delithiation-2, -3 and -4 respectively for log plots of redox peak currents in the CV profiles (Figure 5.25a,b). These are typical of a diffusion-limited process, thus are likely to be linked to the Li-ion storage from MoO_2. This suggests that both oxides are behaving independently of one another, and separately responding in their expect way. Furthermore, the capacitive contribution calculated for this material is low and may only be coming from the Nb_2O_5, hence the low percentage contribution (Figure 5.25d).

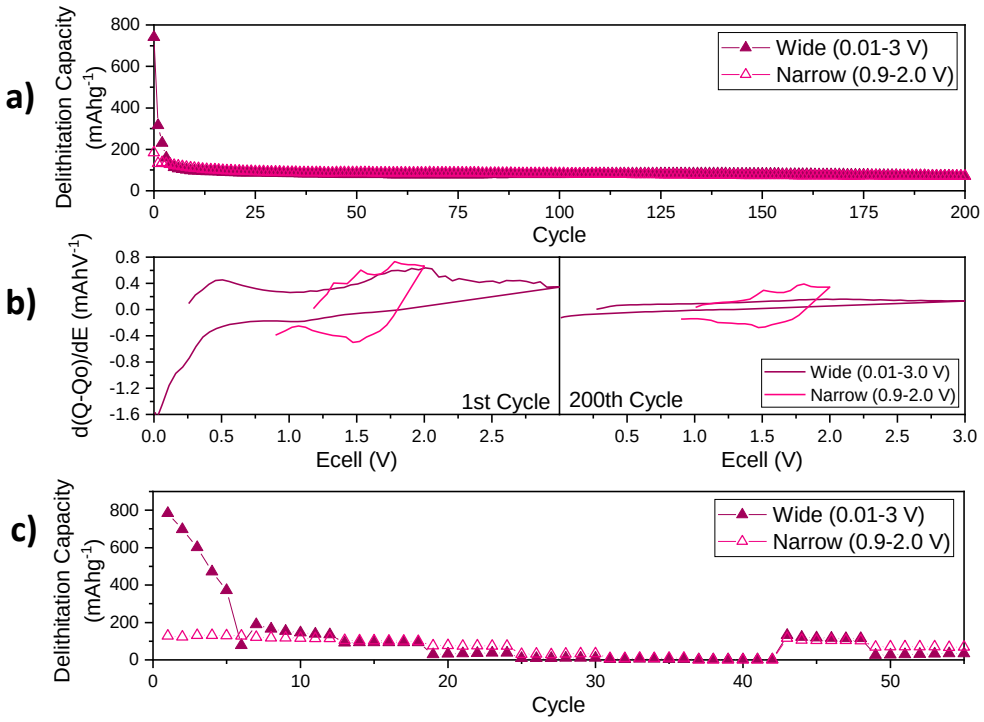

Figure 5.23 - (a) Galvanostatic cycling of 20 % Nb composite at 1 C at various voltage windows, with a C/20 formation cycle. (b) Corresponding differential capacity plots at the 1st (left) and 200th cycle(right). (c) Rate sweep from C/20 to 100C at different voltage windows.

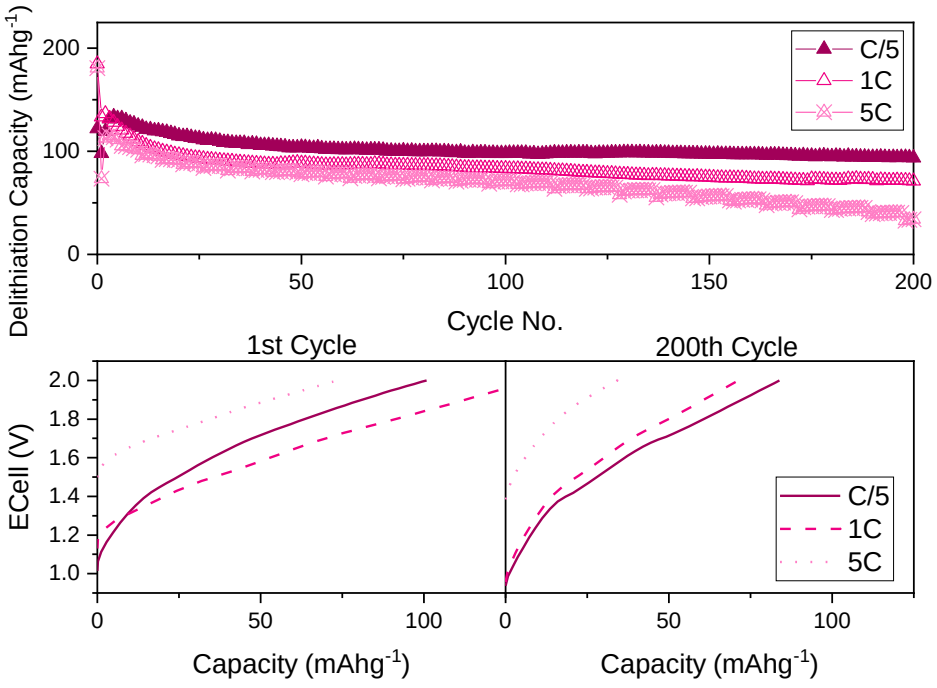

Figure 5.24 - (top) Galvanostatic cycling between 0.9-2.0 V of 20 % Nb composite at various rates, (bottom) charging profiles at various rates at 1st and 200th cycle.

SPEIS shows that the initial impedance is low, and all frequencies behave similarly (Figure 5.26). In lithiation, there is an initial reduction in impedance from 3.0 to 2.0 V then an increase again to 0.5 V. This broadly equates to the expected redox peaks positions for MoO_2. During delithiation, the impedance increases up to 3.0 V across all frequencies, suggesting an increased resistance to remove the final Li-ions from the structure. By cycle 10, this has changed, and the overall impedance has increased in both lithiation and delithiation. During lithiation, the impedance is constant until 2.0 V then it begins to reduce until 0.01 V at all frequencies, this is seen similarly at delithiation. The lack of change in impedance at lower voltages confirms this material's inability to undergo any conversion reaction. The continuous changing nature of the impedances over voltage suggests a continuous change in the material to accommodate the Li-ions. Throughout, the high frequency response is constant suggesting a stable electrolyte SEI system. Overall, the impedance is relatively high especially in comparison to other MoO_2 pure and rich materials. EIS measurements also show increase in resistance with cycling (Figure A.80). Furthermore, the diffusion tail is approx. 45° for lithiation, however is much shallower in the delithiation plots; this suggests that the diffusion is severely limited. This is also evidenced by the CV profiles where there appears to be a more complex process taking place for delithiation compared to lithiation.

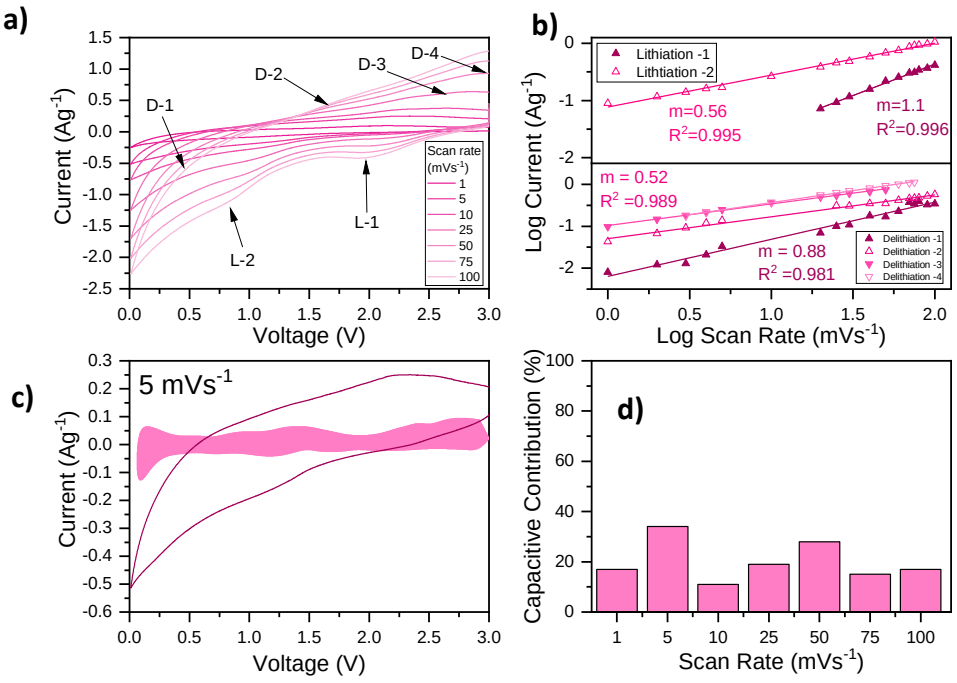

Figure 5.25 - a) CV profiles of 20 % Nb composite materials at increasing scan rate from 1.0 – 100 mVs^{-1}. b) Log plot of peak currents, versus scan rate, fitted with a linear function where R^2 is greater than 0.981 on all lines for lithiation and delithiation peaks (top and bottom respectively). c) CV profile at 5 mVs^{-1} with filled area representing the capacitive contribution. d) Chart of percentage capacitive contribution at increasing scan rate from 1.0 to 100 mVs^{-1}.

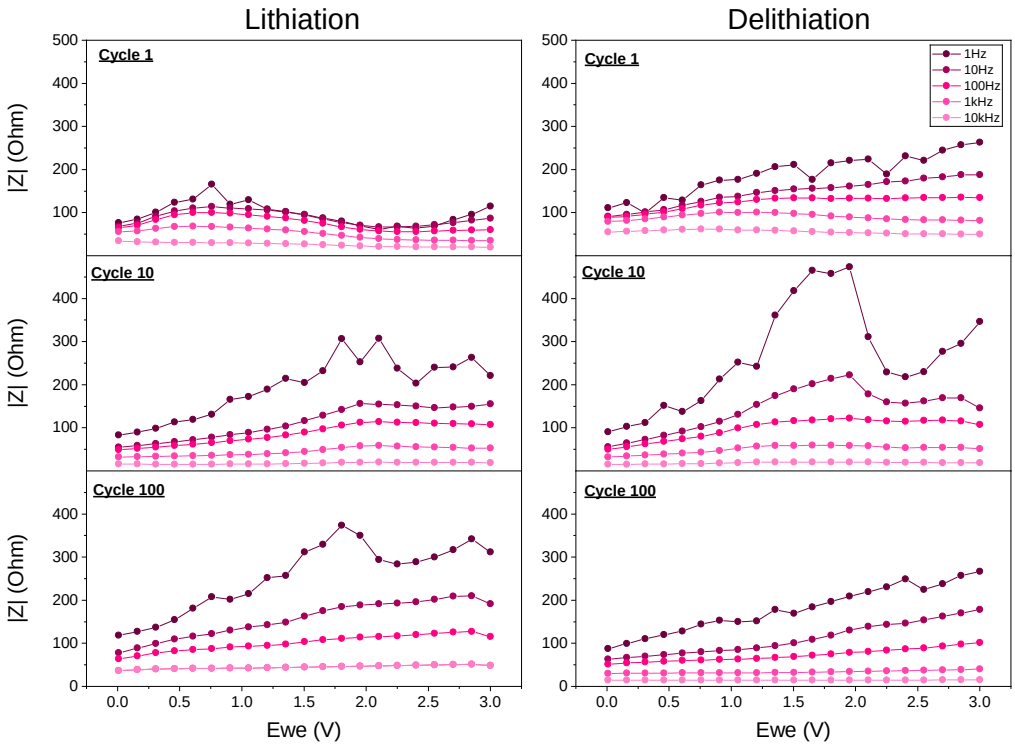

Figure 5.26 - SPEIS profiles of 20 % Nb composite material for increasing cycles from 1 to 100 (top to bottom) for lithiation and delithiation (left and right respectively).

In conclusion, a composite of MoO_2/Nb_2O_5 was successfully created with 20 % Nb content, in the form of an intimate mix of nanoparticles. The electrochemical properties reported show this as an intercalation only material. Within a wide voltage range the material suffers a large irreversible capacity loss and poor stability with increasing cycles. The resistances reported are high and the delithiation process is severely limited. EIS shows limited diffusion, which is concurrent with the analysis of the CV data, and links to the poor rate capability and cyclability. Unfortunately, in comparison to pure MoO_2 (as-synthesised), there appears to be no benefits to forming this composite.

5.3.3 Comparison of Properties Reported for the MoO_2-Rich Composite Materials

The 10 % composite has too high a Nb content to consist purely of Nb doped MoO_2 - and a niobium oxide is also formed at low levels alongside this. It appears that the 10 % Nb composite shows a better level of improvement compared to pure MoO_2. The 10 % composite achieves an average capacity of 137 $mAhg^{-1}$ (in 0.01-3.0V) and 97 $mAhg^{-1}$ (0.9-2.0 V) at 200 cycles. MoO_2 only achieves 48 and 57 $mAhg^{-1}$ and the 20 % composite achieves 76 and 64 $mAhg^{-1}$ respectively under the same conditions. The capacities are boosted over all

rates tested, and similar resistances within the material are maintained. As with MoO_2, these materials vastly underperform compared to their theoretical abilities. This suggests that the destructive mechanisms seen in MoO_2 are maintained in these materials.

These materials cannot be compared meaningfully with the literature as these are novel and have not been reported previously. When looking to recent literature, one issue is that most recent papers are on MoO_2/carbon composites. Furthermore, many papers report a heat-treatment step during synthesis which has been shown to be significant in improving electrochemical properties. The composite materials have a higher capacity at low rates compared to the as-synthesised MoO_2, leading to the capacities being closer to what is published (Table 5.5). At high rates the composites surpass the studies presented here (with no heat-treatment step in the synthesis). Although the 10 % composite appears to match work by Wang *et al*. at high rate, the low rate capacities fall largely short of the reported 1072 $mAhg^{-1}$ at 1C.[269] Work by Liu *et al*. uses a narrower voltage range than typical and thus can be compared to the results produced in the 0.9-2.0 V range explored here.[237] Again, the composites have lower capacities at the low rates, but come closer to literature at 5C, showing an improvement likely due to the formation of a composite with a high-rate capability material. As has been seen with pure MoO_2 a simple heat-treatment step may allow for improvements in these materials and thus warrants further study.

Table 5.5 - Comparison of initial capacities of Mo heavy composites with MoO_2 materials from the literature.

Material	**Synthesis**	**Low-rate Capacity ($mAhg^{-1}$)**	**Low Rate**	**High-rate Capacity ($mAhg^{-1}$)**	**High Rate**	**Ref**
MoO_2	Hydrothermal	324	C/5	330	5C	This work
10 % Nb MoO_2 composite	Hydrothermal	462	C/5	463	5C	This work
20 % Nb MoO_2 composite	Hydrothermal	599	C/5	353	5C	This work
MoO_2	Solvothermal	445	1C	~320	4C	[261]
MoO_2	Solvothermal	608	1C	300	5C	[243]
MoO_2	Magnetron Sputtered	860	C/2	330	4C	[266]
MoO_2	Hydrothermal + Heat-treatment	240	1C	178	5C	[237]
MoO_2	Hydrothermal + Heat-treatment	1072	~1C	438	~4C	[269]

5.4 50/50 Nb_2O_5/MoO_2 Composite Materials

5.4.1 Characterisation of 50/50 Nb_2O_5/MoO_2 Composite.

The 50 % Nb/Mo composite has an XRD pattern which looks to be a sum of the Nb_2O_5 and MoO_2 patterns (Figure 5.27). It maintains the semi-crystalline appearance of Nb_2O_5 within the pattern and the sharp peaks of MoO_2. There appears to be slight peak shifting in the Nb_2O_5 peaks in the pattern in comparison to the pure form. This may suggest doping, which is unsurprising as this was a possibility for the Nb-rich composites (5.2.1), although in those cases the shift in the XRD pattern was not apparent. XRF was used to confirm the ratios of metal oxides within the material; this was calculated as 44.65 atm % Nb_2O_5 and 55.31 atm % for MoO_2. This has a slightly higher MoO_2 percentage than was expected; however, this synthesis process shows good reproducibility with only a 0.21 % standard deviation in the percentages between batches. In the TGA profile the 50% composite showed a similar pattern to MoO_2, however with a larger weight loss from 800 to 900 °C, this may suggest that the MoO_2 in this composite is more reactive and thus is more readily lost (Figure A.81). It shows an initial loss, of water then a loss of weight between 150 and 400 °C, due to loss of surface species, an artefact of the hydrothermal method.

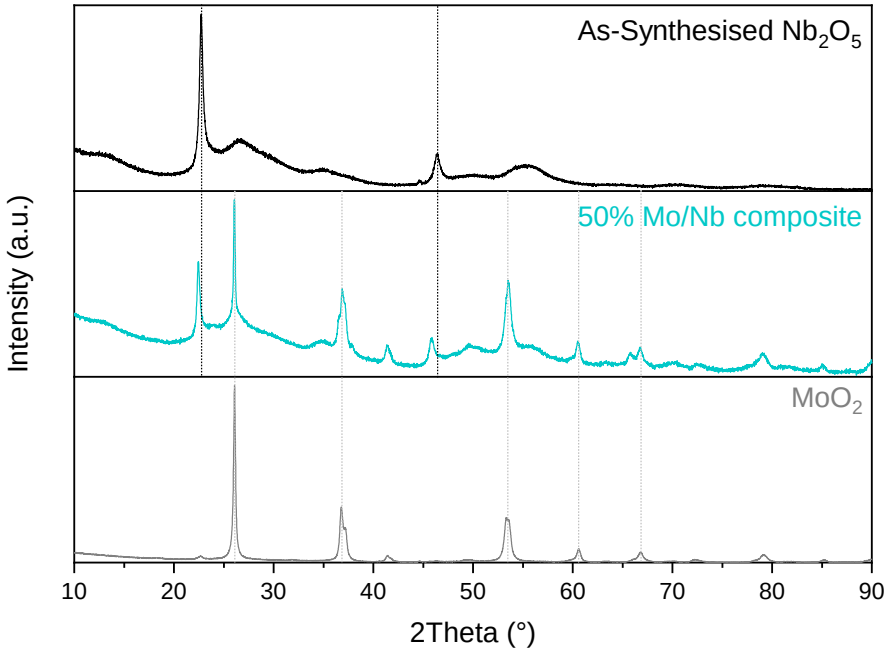

Figure 5.27 – XRD pattern of the 50/50 Nb_2O_5/MoO_2 composite (turquoise), with patterns of MoO_2 (grey) and Nb_2O_5 (black) for comparison. Dotted lines are used to show key peaks common across pure and composite samples.

The SEM images show this composite to be a network of nano-wires decorated with nano-spheres (Figure 5.28a). The TEM images show that the spheres are secondary particles made from nano-rods with small aspect ratios. The EDX mapping makes it clear that the wires are Nb dominant, and the spheres are Mo dominant (Figure 5.29). From the STEM-EDX, it appears that the nano-wire networks are a mix of Nb and Mo oxide, whereas the spheres appear to be Mo only. Thus, this suggests a Mo doped Nb_2O_5 nano-wire network decorated in MoO_2 nano-spheres.

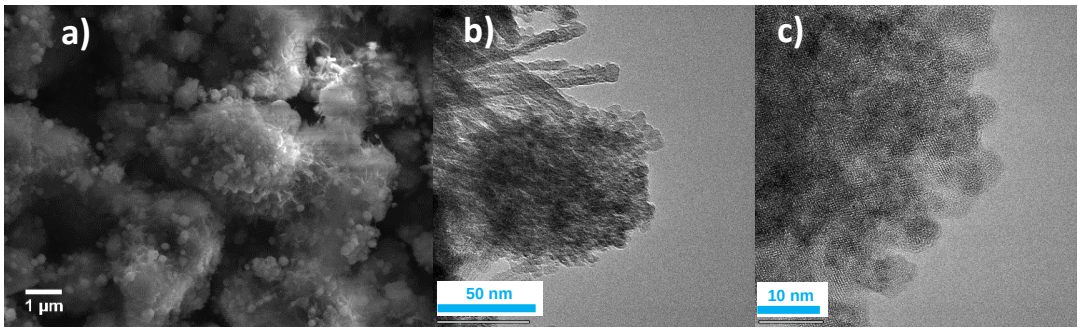

Figure 5.28 – a) SEM image, b,c) TEM images of the 50 % composite. Further images are in Figure A.82.

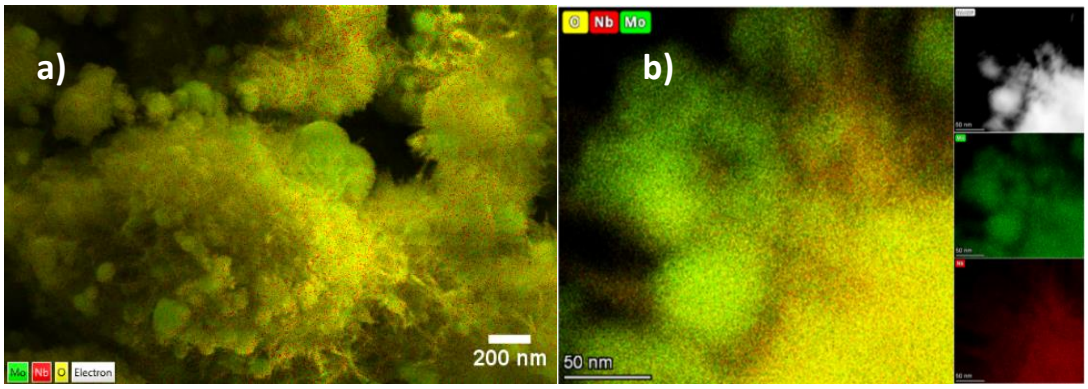

Figure 5.29 – a) SEM-EDX Map, b) STEM-EDX Map, with HAADF image, Mo map and Nb map (top to bottom stacked), of 50 % composite material. Red represents Nb, Green represents Mo and Yellow represents oxygen.

The N_2 adsorption/desorption isotherm shows that the 50 % composite has the same type of isotherm and hysteresis as Nb_2O_5, which is still very similar to MoO_2 (Figure A.83). Moreover, the pore distribution is more like Nb_2O_5, as the composite also shows pores in the micro-pore region (below 1.0 nm). The composite has a BET surface area of 93.7 m^2g^{-1}, which is approximately a third of the as-synthesised Nb_2O_5. The DFT pore volume is 0.18 cm^3g^{-1} and BJH adsorption pore width of 10.1 nm.

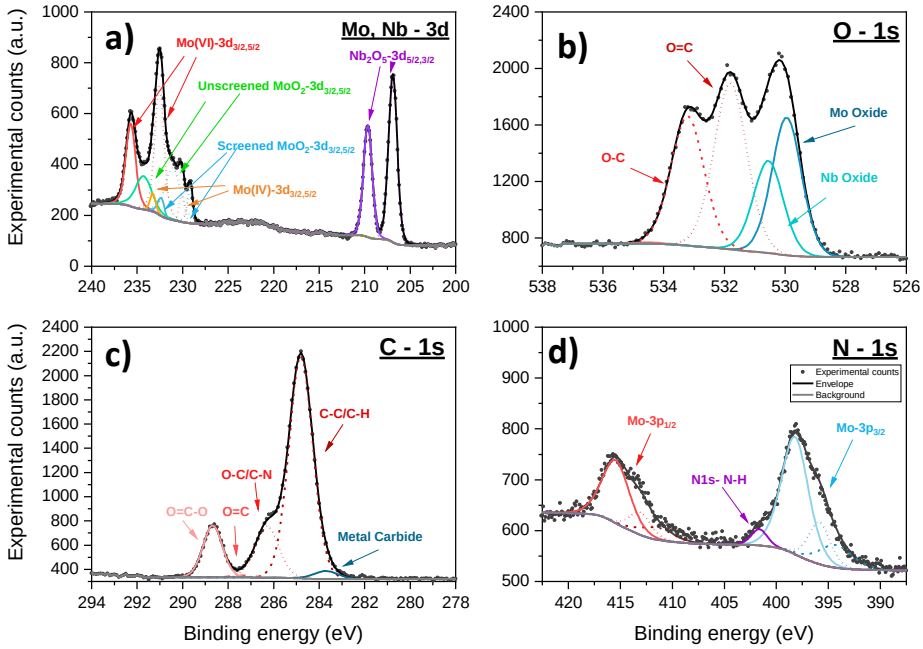

Figure 5.30 - High resolution XPS spectra of the Mo and Nb 3d region (a), O 1s region (b), C 1s region (c) and N 1s region (d) for 50 % composite. Full scan in Figure A.84 - Full XPS survey of 50 % composite oxides, as-synthesised and heat-treated (top and bottom respectively).Figure A.84.

In this composite Nb exists in a +5 oxidation state, however the difference in binding energy between the Nb 3d and O 1s is 323.65 eV, thus suggesting a slightly reduced state (Figure 5.30).[355] For Mo, the screened and unscreened states of the +4 oxidation are seen and the +6 state of the oxidised surfaces. Additionally, there is another +4-type state, as seen with the 20 % Nb composite, which suggests a secondary +4 environment, yet the nature of this is unclear. Here there is evidence of surface species with the presence of metal carbon and nitrogen bonding. These results show a 41 to 59 % of Nb and Mo content, respectively, this is slightly higher, with respect to Mo than the XRF results however deviations between bulk and surface measurements are to be expected.

5.4.1.1 Electrochemical Characterisation of 50 % Composite.

As with the other composites, it is important to explore voltage windows for the material to optimise its electrochemical performance. As this material contains both Nb_2O_5 and MoO_2 in almost equal quantities, voltage ranges investigated for both materials are tested here: 0.01-3.0 V, 0.25-3.0 V and 0.9-2.0V.

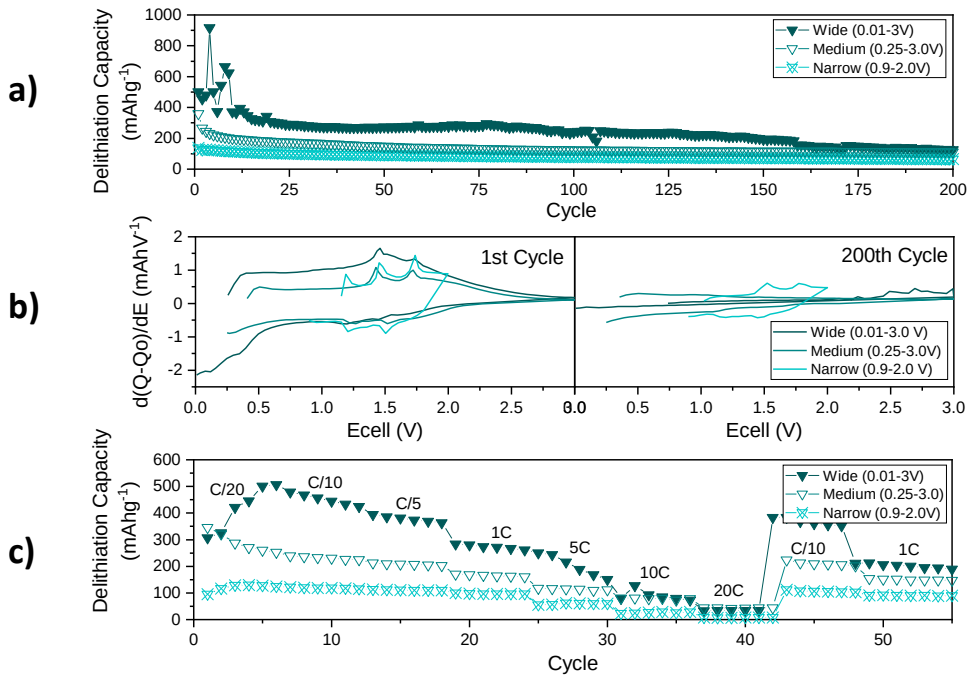

Figure 5.31 - (a) Galvanostatic cycling of 50 % composite at 1 C at various voltage windows, with a C/20 formation cycle. (b) Corresponding differential capacity plots at the 1st (left) and 200th cycle(right). (c) Rate sweep from C/20 to 100C at different voltage windows.

The wide range shows a high capacity after a short activation, this surpasses the theoretical capacity of MoO_2, suggesting more active Li-ion sites are available than expected (Figure 5.31a). Unlike for MoO_2, the activation process shows a fluctuation in capacity. Subsequently, there is a large capacity loss until approx. 15 cycles. The capacity then plateaus until the 100th cycle, where it begins to gradually drop. This suggests instability in the material as there are two stages of capacity loss. However, it should be noted that at 100 cycles the average capacity is 230 ± 26 $mAhg^{-1}$, which currently surpasses all other composites presented here so far, under the same conditions. In the other voltage ranges, the capacity is stable over cycling with a gradual loss, with average capacities of 106 ± 8.5 and 69 ± 4.4 $mAhg^{-1}$ after 200 cycles, at medium and narrow voltage windows respectively. The differential capacity plots in the 1st cycle show that the material exhibits a broad rectangular shaped profile with redox peaks (Figure 5.31b). All ranges cover the two sets of redox peaks indicative of the two-phase intercalation reaction in MoO_2. The wide range also shows a redox peak for conversion reaction of MoO_2. The medium range may also allow some conversion to take place as the peak appears to be forming from 0.5 – 0.01 V. By 200 cycles, only the narrow voltage range shows a maintained differential capacity profile, suggesting good reversibility of lithiation/delithiation. Regarding coulombic efficiency, the wide range shows large amounts of fluctuation during activation, where the efficiency is exceeding 100 %, due to the nature

of the activation process (Figure A.85). By 20 cycles the efficiency is stable and greater than 98 % but does show more fluctuation at the points in which there is large capacity losses. The other two voltage windows show good efficiency throughout after the initial few cycles.

Regarding C-rate, the material appears to cope well up to 1C, however, escalating the rate results in more loss of capacity (Figure 5.31c). The recovery after high-rate cycling is good in all windows; 88, 90 and 92 % recovery on return to C/10 for wide, medium, and narrow windows respectively. The narrow range does appear to show a better rate capability as the recovery is the highest and the step down in capacity with increasing rates is low. Ultimately, the wide range seems to produce the better capacity, although there is an issue with stability. When tested over a longer term in a wide voltage range a similar trend in capacity is seen, however at C/5 there is no initial activation (Figure 5.32). This is unexpected, as the slower rate would allow for the slow kinetics of a structural change to take place, and it is unclear why this has happened. After the initial 25 cycles, the capacity plateaus at all rates, with average capacities of 337 ± 0.9, 230 ± 26 and 150 ± 10 $mAhg^{-1}$ at 100 cycles for C/5, 1C and 5C respectively. From 125 cycles capacity loss begins to be evident again, by 200 cycles the capacities are vastly reduced. Thus, the charge profiles are linear and show large polarisation suggesting an internal resistance. The charge profiles have changed compared to the 1st cycle where a sloping plateau suggests a solid solution, then a two-phase reaction. The coulombic efficiency shows more fluctuation with increased rate and increased cycling suggesting instability in this material particularly at these higher rates (Figure A.86).

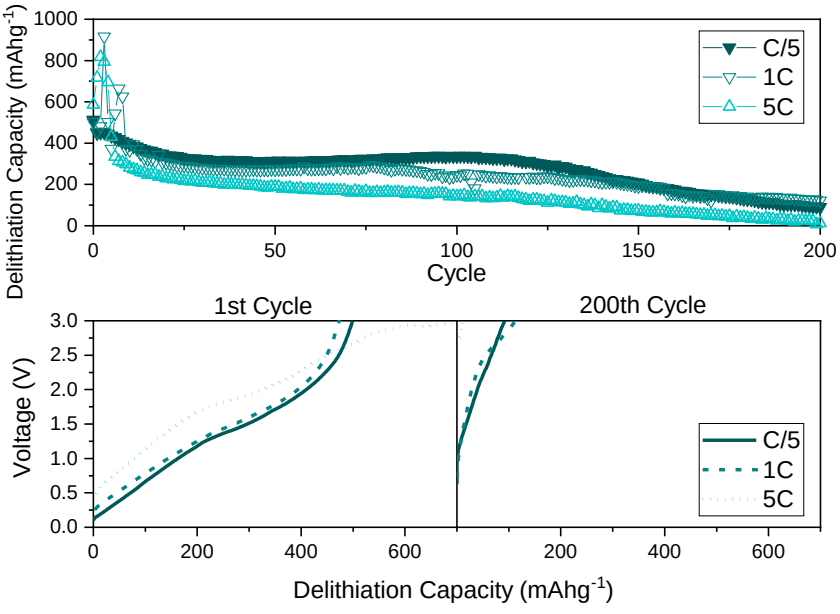

Figure 5.32 - (top) Galvanostatic cycling between 0.01-3.0 V of 50 % composite at various rates, (bottom) charging profiles at various rates at 1st and 200th cycle.

The medium and narrow voltage ranges showed a better rate functionality with smaller changes in capacity, the 0.25-3.0 V range was also investigated as a higher capacity could be achieved here (Figure 5.33). Here all rates perform similarly, with little difference in capacity, at cycle 10 average capacities of 220 ± 8.4, 206 ± 8.8 and 205 ± 13 $mAhg^{-1}$ for C/5, 1C and 5C respectively. By 200 cycles the average capacities are 138 ± 11, 106 ± 8.5 and 95 ± 0.6 $mAhg^{-1}$, the capacity difference between 1C and 5C is small, suggesting some potential as a high-rate intercalation material. Notably, the average capacity at 5C at 200 cycles in this range is nearly six times higher than the capacity measured in the wide range. There is a big change in the differential capacity plots between 1 and 200 cycles (Figure 5.33, bottom). In the first cycle, the redox peaks for MoO_2 intercalation are sharp and there is also a suggestion of conversion at <0.5 V, other than this the shape is rectangular and broad, likely due to the capacitive type of mechanism of Nb_2O_5.[37,122] At 200 cycles, the profile has no sharp peaks and is composed of multiple broad peaks and is rectangular below 1.5 V. This suggests the intercalation mechanism from MoO_2 becomes inaccessible, or the shift to an intercalation pseudocapacitive type mechanism as with Nb_2O_5. Notably there is no evidence of polarisation as with the wide window, and thus suggests that the slightly higher cut-off of 0.25 V versus 0.01 V helps with the stability of this material.

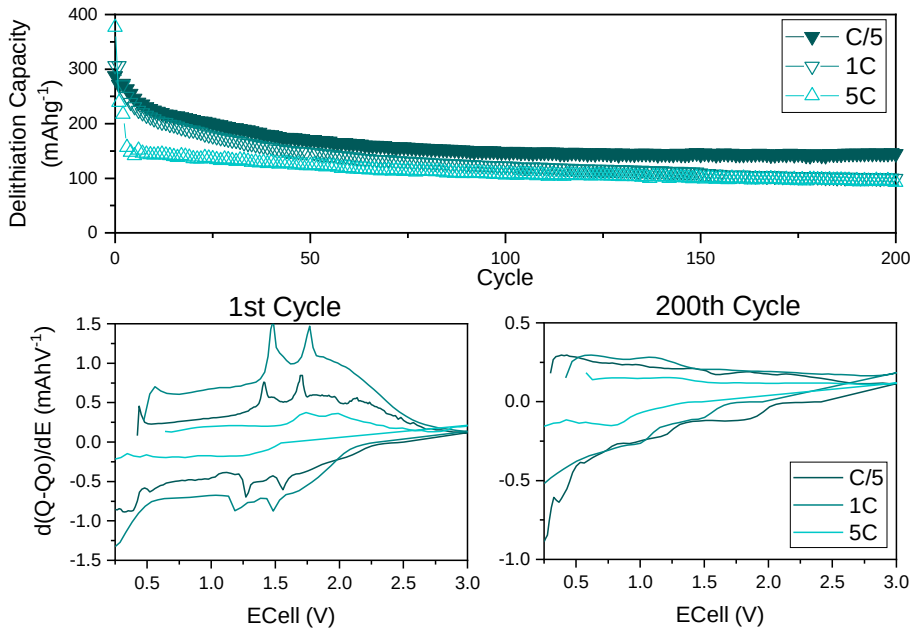

Figure 5.33 - (top) Galvanostatic cycling between 0.25-3.0 V of 50 % composite at various rates, (bottom) charging profiles at various rates at 1st and 200th cycle.

The effect of cycling on the structure was observed via *ex-situ* XRD (Figure 5.34). As the largest changes occur in the wide voltage range, this was chosen as the focus of the study. Within the first cycle, (here the formation cycle) the crystalline peaks of Nb_2O_5 have disappeared, suggesting a tend toward the amorphous form of this material. This is seen previously with the T-Nb_2O_5, where there is a dramatic structural change in the first cycle (Section 3.3.3.1.1). Regarding the MoO_2 part of this material, the MoO_2 peaks show a small shift and broadening with cycling. This suggests a break down in the structure and a need for expansion to accommodate the Li-ions. It is unclear whether this MoO_2 is in a monoclinic or tetragonal form, as discussed in the MoO_2 (Section 4.3.1.2). Unlike with pure MoO_2, $Li_{0.98}MoO_2$ is not formed as a side product here, suggesting improved reversibility in the Li-ion intercalation reaction. However, there is formation of other peaks, such as a broad peak at 40.5 °, which could be matched to Mo metal. Some of the other small peaks match Li_2O, but in both cases, due to the low intensity and lack of peaks this is not definitive. This could be indicative of an irreversible conversion reaction, hence the large capacity losses observed. From 10 cycles onwards there is a second amorphous peak forming at 62.5 °, the nature of this cannot be identified. Evidently there is structural break down, irreversible change of phase, loss of active material, all which ultimately lead to the poor stability seen here.

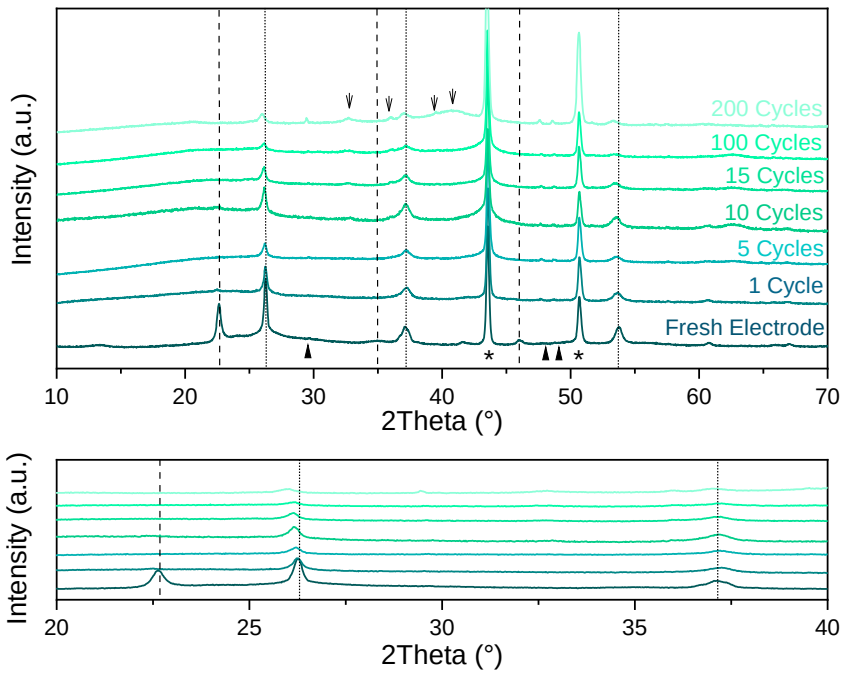

Figure 5.34 – Ex-Situ XRD pattern of 50% composite electrode after cycling in the 0.01-3.0 V range at 1C with a C/20 formation cycle. Key MoO_2 peaks are denoted with black dotted lines, Nb_2O_5 indexed with dashed line. The Cu current collector is denoted by '' and other peaks from the sample holder denoted but the triangles. Arrows highlight new peaks formed. The bottom pattern is a section of interest from the main XRD pattern shown above.*

CV measurements at increasing scan rates were used to further characterise this material (Figure A.87). The CV shape has some small peak like features, like that seen in the MoO_2 heavy composites studied above (5.3.2). The log plots of the redox peaks do not appear to fit well linearly. There is a mix of high log plot gradients and those close to 0.5, as with the 20 % Nb in MoO_2 composite (Figure 5.25). Again, this suggests that the MoO_2 part of the material is diffusion limited, where the Nb_2O_5 part of the material is only surface limited.

SPEIS was used to further investigate the capacity losses seen in this material (Figure 5.35). The initial cycles show low impedance for mid to high frequency response, corresponding to the CT and SEI resistances. The low frequency response shows increased impedance in the range 1.5 to 3.0 V, this corresponds to solid-state Li-ion diffusion and hence there must be an initial resistance of ions diffusing into the material. A similar observation is seen for the delithiation process, and this is maintained to 100 cycles. This suggests that the activation process does not affect the long-term impedance. After 100 cycles there is a step up in impedance across all frequencies. The largest change comes in the range of 1 Hz to 100 Hz, suggesting a change in the diffusion and CT impedance. This is likely to be due to a structural change in the material. At 180 cycles there is another large increase in impedance with a shift in the voltage range of the highest impedance. At this point there is increased impedance below 1.0 V. This suggests further strain on the material when trying to insert more Li-ions in and out of the structure. The structural break down and formation of secondary materials increases the resistance in the system to the point whereby Li-ions cannot move in or out of the material effectively. Furthermore, the irreversible conversion mechanism likely causes electrode pulverisation leading to material becoming electronically isolated, hence the high resistance. EIS also shows similar results, with an increasing CT resistance with cycling (Figure A.88). Notably, the first cycle shows high resistance in EIS, this may be due to the material initially experiencing strain to accommodate the ions. Furthermore, in the case of Nb_2O_5, the insulating nature is reduced after the first Li-ion intercalation, hence a reduction in resistance after this.

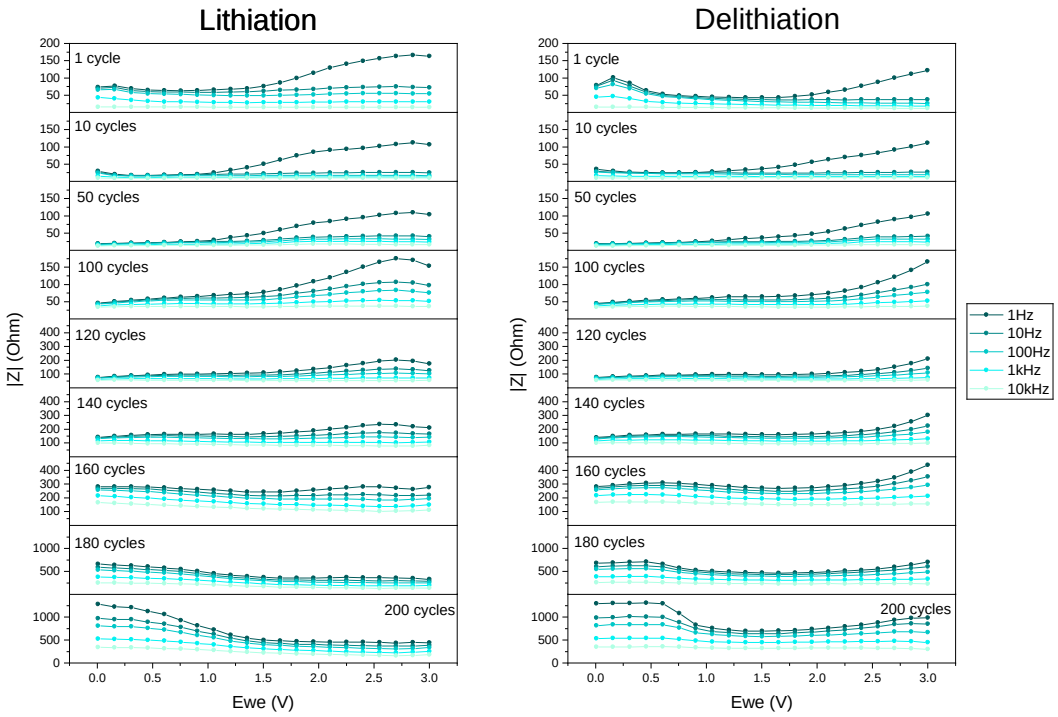

Figure 5.35 - SPEIS profiles of 50 % composite material for increasing cycles from 1 to 200 (top to bottom) for lithiation and delithiation (left and right respectively). note that the y axis changes at 120 and 180 cycles.

To summarise this material, a composite of MoO_2 and Nb_2O_5 was produced with near equal proportion of oxides. The material consists of an intimate mixture of Nb_2O_5 nanowires decorated with MoO_2 secondary nano-spheres. The electrochemical properties are promising, with high capacities at wide voltage range and apparent low resistance in the first 100 cycles. Unfortunately, this material lacks stability, especially when cycling in a wide voltage range, showing two stages of capacity loss. Narrowing the voltage window appears to improve the stability of the material, likely to be due to lack of access to the destructive conversion mechanism. When this is compared to the as-synthesised pure Nb_2O_5 and MoO_2, this composite shows an improvement in electrochemistry. With improvement in stability this material looks to be a great opportunity to create a high-capacity, high-rate material.

5.4.2 Characterisation of Heat-Treated 50 % Composite.

As the 50 % composite showed the most promising results, heat-treatment was investigated to improve the electrochemical stability of the material. One of the heat-treated materials was then taken forward for electrochemical characterisation. When the 50 % composite was

heat-treated up to 600 °C, the XRD pattern shows very little change (Figure 5.36). There appears to be no formation of new phases, but there is sharpening of the peaks, and flattening of the amorphous regions. This suggests an improvement in crystallinity however, there is no obvious formation of T-Nb_2O_5 as would be expected at 600 °C. The main peaks present in the T-phase are already seen in the semi-crystalline form at ~22 and 46 °. However other intense peaks at ~28 ° do not appear. This suggests that the Nb_2O_5 has suppressed crystallinity and may still be semi-crystalline even with heat-treatment. This may be due to the presence of the MoO_2 particles inhibiting the growth of the T-Nb_2O_5 phase, thus this composite may be exhibiting Zener pinning.[373,374] To analyse this further, the material was further heat-treated, at 800 °C, the XRD pattern changes dramatically, where there still appears to be peaks from the monoclinic MoO_2 and Nb_2O_5 remaining, but a $Mo_{13}O_{33}$ phase has formed. Thus, from these the materials, those heat-treated between 300 and 600 °C appear to be preferred candidates for electrochemical testing.

XRF is used to confirm that the ratios of the oxides do not change upon heat-treatment of the material. The 600 °C heat-treated material had ratios of Nb of 44.8 atm%, with 55.2 atm% of Mo, with a small deviation of 0.4 % between batches. The change in atm% of the elements with heat treatment is within error, suggesting the heat treatment produces no change in bulk elemental ratio.

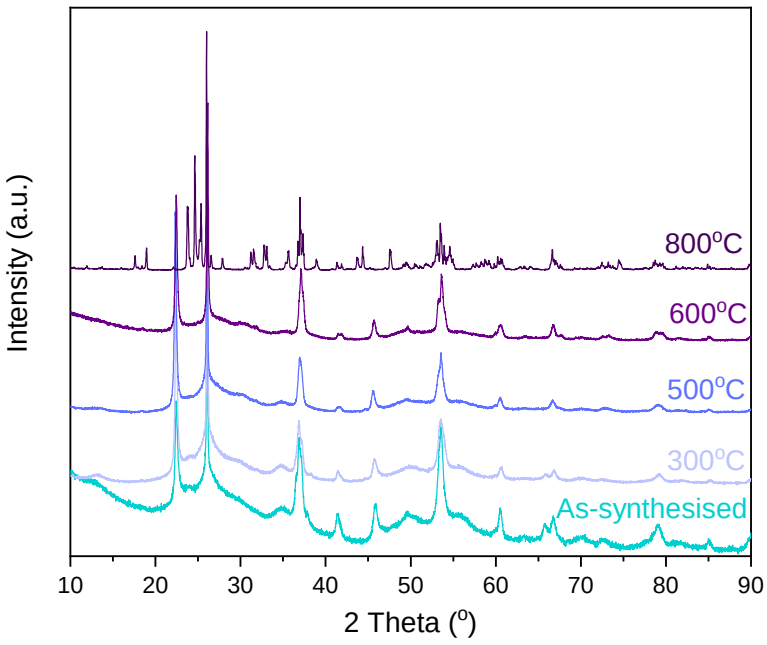

Figure 5.36 - XRD patterns of 50 % composite, left and right respectively, at increasing temperatures of heat-treatment to 800 °C, heated for 4 hours in Ar.

The particles show little change in morphology with increased temperature of heat-treatment, as the SEM images show the same nano-wire networks, decorated with nanoparticles at all temperatures (Figure 5.37a-d). TEM images show that at 600 °C, the MoO_2 particles appear to have lost some texture, where primary particles have fused (Figure 5.37e-h). In EDX mapping it appears that with increase in heat-treatment the MoO_2 particle congregate, this may be in part due to the particle fusing and is particularly evident at the images at 500 °C (Figure 5.37c, g). However, not only are the primary particles fusing together but, in some cases, where the secondary particles which are in close contact, these begin to fuse too, creating a selection of particles with an increased particle size. Regarding the Nb_2O_5 particles, the morphology does not show any changes with increasing temperature, unlike with the pure Nb_2O_5 where the nano-wire aspect ratio reduces. This is consistent with the lack of T-Nb_2O_5 phase formation in the XRD pattern suggesting these materials exist in the same form, and the presence of MoO_2 at this quantity suppresses crystallisation due to Zenner pinning. The 600 °C heat-treated composite was studied further as the treatment has not drastically changed the material from the as-synthesised form in structure or morphology.

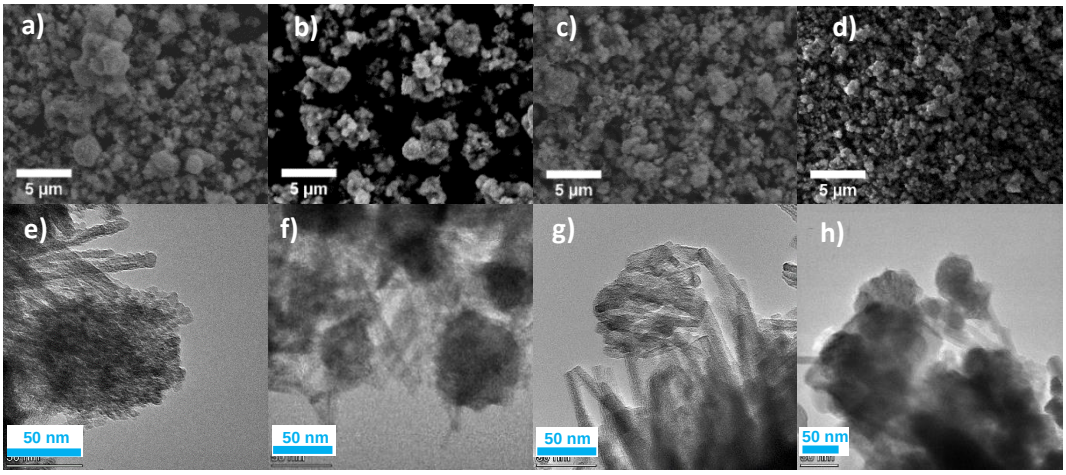

Figure 5.37 – (a-d) SEM images and (e-h) TEM images of 50 % composite heat treated at increasing temperatures, as-synthesised, 300, 500, 600 °C left to right respectively. Further images of 600 °C heat-treated material can be seen in Figure A.89.

N_2 adsorption shows a maintenance of isotherm and hysteresis type after heat-treatment at 600 °C (Figure A. 90). However, the surface area is reduced from 93.7 m^2g^{-1} to 29.5 m^2g^{-1}. The DFT pore volume is 0.33 cm^3g^{-1} and BJH adsorption pore width of 37.1 nm. This has increased from the as-synthesised material, suggesting that some of the porosity may have been between MoO_2 primary particles, and as these began to fuse, the porosity is moved into larger spaces within the matrix of particles.

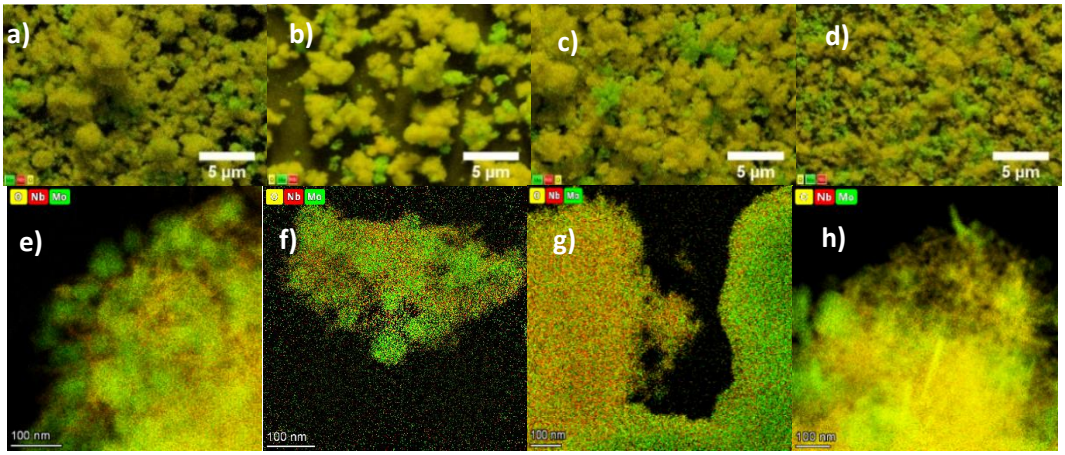

Figure 5.38 – (a-d) SEM-EDX maps and (e-f) STEM-EDX maps of 50 % composite heat treated at increasing temperatures, as-synthesised, 300, 500, 600 °C left to right respectively.

The XPS results are also similar to that of the as-synthesised 50 % composite, however with the lack of the extra Mo +4 environment (Figure 5.39). This may be due to the crystallinity improvement in MoO_2 causing the Mo to be in the expected +4 screened and unscreened states only. However, there is no reduction in the Mo +6 percentage with heat-treatment, and this suggests that to remove this oxidised surface a reducing atmosphere would be required. The Nb state is unchanged as it sits in a slightly reduced +5 state with a Nb 3d – O 1s difference of 323.65 eV.[355] Notably, with heat-treatment there is a reduction in carbon content, suggesting that some surface species have been removed with heating.

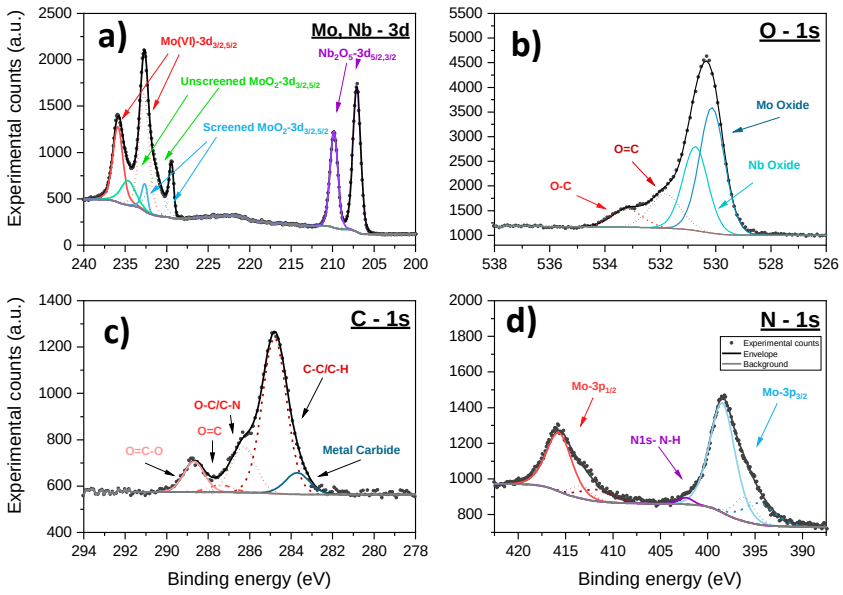

Figure 5.39 - High resolution XPS spectra of the Mo and Nb 3d region (a), O 1s region (b), C 1s region (c) and N 1s region (d) for 50 % heat-treated composite. Full scan in Figure A.84.

5.4.2.1 Electrochemical Characterisation of 600 °C Heat-Treated 50 % Composite

The heat-treated form is tested under a similar electrochemical regime as its as-synthesised counterpart. The wide voltage range gives the highest capacities, although capacity changes within the first 100 cycles before stabilising (Figure 5.40a). There is an initial loss in capacity before a subsequent increase between 10 and 30 cycles; this appears to be the activation process typical of MoO_2.[244] After this there is another loss in capacity until 60 cycles, where the capacity increases again, this has a multi-stage activation process, further characterisation of this is discussed below. At 200 cycles, an average capacity of 514 ± 10 $mAhg^{-1}$ is recorded, which is matching the theoretical capacity. The medium voltage range shows a loss of capacity within the first 20 cycles, then plateaus with a small loss over cycles. The narrow range shows a low but stable capacity throughout. At these ranges the average capacities recorded after 200 cycles are 181 ± 3.3 and 81 ± 13 $mAhg^{-1}$ respectively. The medium range gives good capacity response compared to the theoretical capacity for this range, yet the narrow range is much lower. However, the narrow range produces a reversible process as the differential capacity plot maintains its shape after 200 cycles (Figure 5.40b). For the wider ranges, the differential capacity plots lose the two sets of redox peaks and only a broad profile remains. This may suggest a movement away from the multi-phase intercalation reaction of MoO_2. The conversion reaction is apparent in the wide voltage range, although at 200 cycles there is no longer a redox peak for this, only a sloping profile under 0.5 V.

Regarding rate, the wide voltage range maintains the highest capacities at all rates with minimal losses up from C/20 to 1C (Figure 5.40c). In all ranges the recovery to C/10 is good, with a recovery of 94 and 93 % for medium and narrow ranges. In the wide range, the recovery is higher than 100 %, this is due to the activation process. A range of 0.01-3.0 V is preferable for this material, giving both good rate capability and high capacities. When tested over 200 cycles, there is a drop in capacity as the rate is increased (Figure 5.41). The trend in capacity with cycle number remains at 5C but at 20C the hump shape of the activation process appears flattened, and the second activation is not obvious. At 100 cycles, the average capacities are 480 ± 19, 492 ± 17, 301 ± 24 and 165 ± 8.8 $mAhg^{-1}$ for C/5, 1C, 5C and 20C respectively. The capacity of C/5 and 1C are similar and with cell-to-cell deviation, the capacities fall within error of one another across the 200 cycles. All charge profiles appear near linear, with a slight bend at ~1.0 V, which may suggest a phase transition. This type of slope, with lack of clear plateau suggests a solid-solution mechanism. Although there is quite

a large loss between 1C and 20C, the capacities achieved at 20C surpass all other materials discussed in this work under these conditions. There does appear to be some polarisation at this rate, suggesting further work could be done to improve the resistance at high rates. This can also be seen in the coulombic efficiency of this material which is high after the first 10 cycles (at rates C/5 to 20C). Yet the efficiency struggles to reach above 99% for the lower rates where an efficiency average is 97.2 and 98.2 % for C/5 and 1C, respectively (Figure A.91).

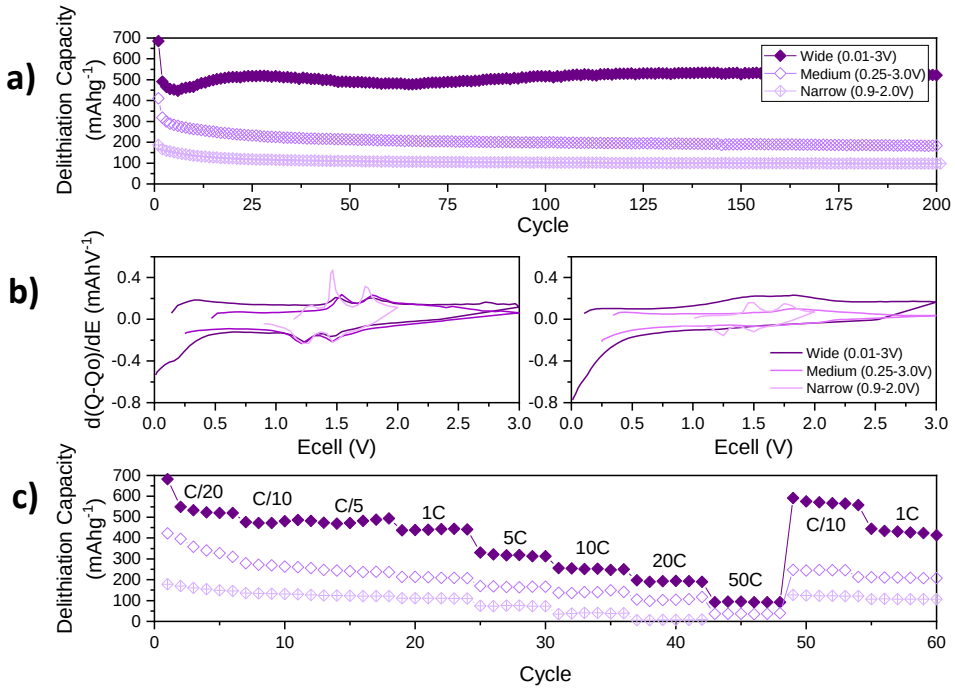

Figure 5.40 - (a) Galvanostatic cycling of the heat-treated 50 % composite at 1 C at various voltage windows, with a C/20 formation cycle. (b) Corresponding differential capacity plots at the 1st (left) and 200th cycle(right). (c) Rate sweep from C/20 to 100C at different voltage windows.

This material was further tested at higher rates over 400 cycles to address the true rate capability (Figure 5.42). As seen previously there is a large step down in capacity between 5C and 20C, yet from 20C to 100 C there is little change. Notably, at 50 and 100 C there is a prominent activation process seen as a large peak in capacity, which is delayed at 100C. This feature is unusual as at the slow rates the activation shows only a small capacity increase and takes place over many more cycles. Although this has been seen before in pure MoO_2 materials.[242,244,247] Evidently, rate is an important factor when considering electrochemical mechanism, as here the structural rearrangement related to the activation process happens in a different way to that at lower rates. Importantly, average capacities of 148 ± 9.9 and 112 ± 15 $mAhg^{-1}$ are recorded at 200 cycles for 50 and 100 C rates respectively. The charge

profiles at this rate show notable polarisation, yet this is reduced after the activation, hence the structural rearrangement reduces the internal resistance in the material. These profiles are linear, suggesting a capacitive mechanism, and at this rate it is likely that the Nb_2O_5 is the major storage material as is known for its intercalation pseudocapacitance. Yet these high capacities suggest that the MoO_2 is key to achieving this, likely due to it acting as a conductive network.

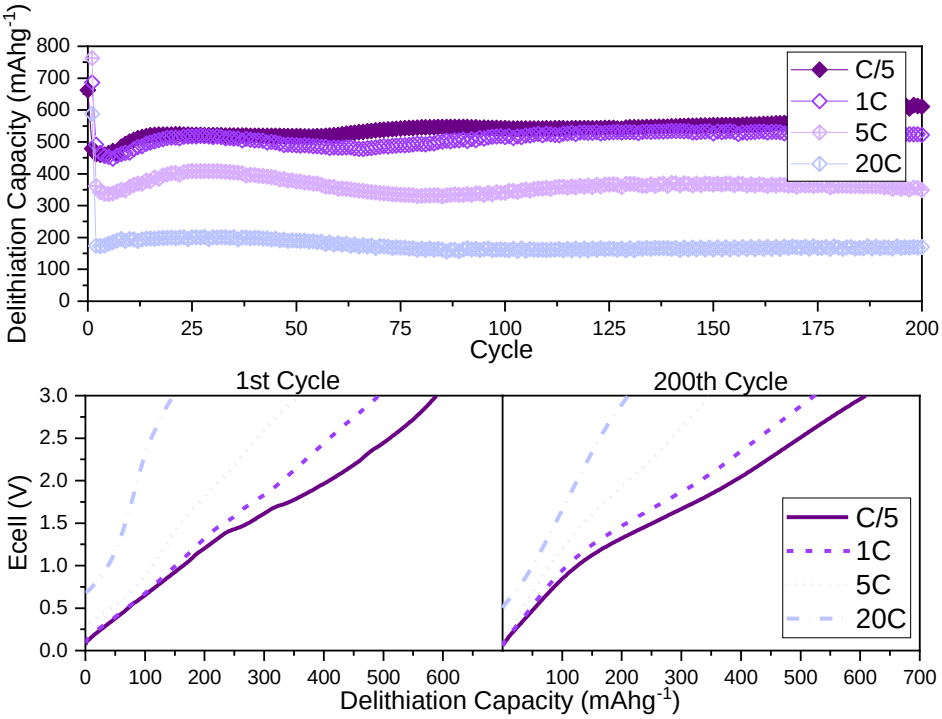

Figure 5.41 - (top) Galvanostatic cycling between 0.01-3.0 V of Heat-treated 50 % composite at various rates, (bottom) charging profiles at various rates at 1st and 200th cycle.

To further understand this complex material, cyclic voltammetry is used to help identify the mechanism of Li-ion storage (Figure 5.43). The CV presents three pairs of redox peaks: during lithiation at 1.5, 1.25 and 0.2 V and during delithiation at 0.1, 1.5 and 1.8 V. There appears to be some hysteresis in the CV profile, particularly apparent in the pairs 1.25/1.5 V and 1.5/1.8 V, this may suggest that the delithiation process is more energy demanding than the lithiation process. These peaks correspond to the multi-phase Li-ion intercalation step, where the MoO_2 changes from monoclinic to orthorhombic to monoclinic.[230] Furthermore, these pairs appear to have shoulders on the peaks initially during the lithiation process, suggesting a potentially more complex phase change than in delithiation. This multistep process may reduce the energy required for lithiation. The peak at 0.2 V is indicative of the conversion reaction; this peak grows until cycle 25 where it begins to retract again, this is

evidence for the increasing capacity in the first 30 cycles (Figure 5.43b). This activation process is linked to a structural rearrangement of MoO_2 material, which may allow for an easier conversion reaction. After the 25 cycles this redox peak begins to retract, suggesting that the conversion reaction is no longer taking place in full, this may be due to an irreversible conversion causing a clustering of Mo metal, thus reducing the MoO_2 content.[242,244,274] Alternatively, this may be due to the conversion becoming unfavourable compared to other storage methods. At the same time as the activation process, the other redox peaks begin to flatten out, to the point where at 25 cycles, there appears to be one set of broad peaks in place at 1.5 /1.75 V (Figure 5.43). This shows a shift away from the multi-step phase change Li-ion intercalation. It is possible that after activation, the evolved MoO_2 can take on Li-ions with little change in the structure, hence a single-phase process. Notably, all these peaks appear to be overlaid on a broad rectangular profile, this is likely to come from the Nb_2O_5 part of this material, known for its capacitive type of response. From 60-100 cycles there appears to be a second increase in capacity (Figure 5.40), however there is no obvious change in the CV profile that coincides with this and thus it is difficult to explain.

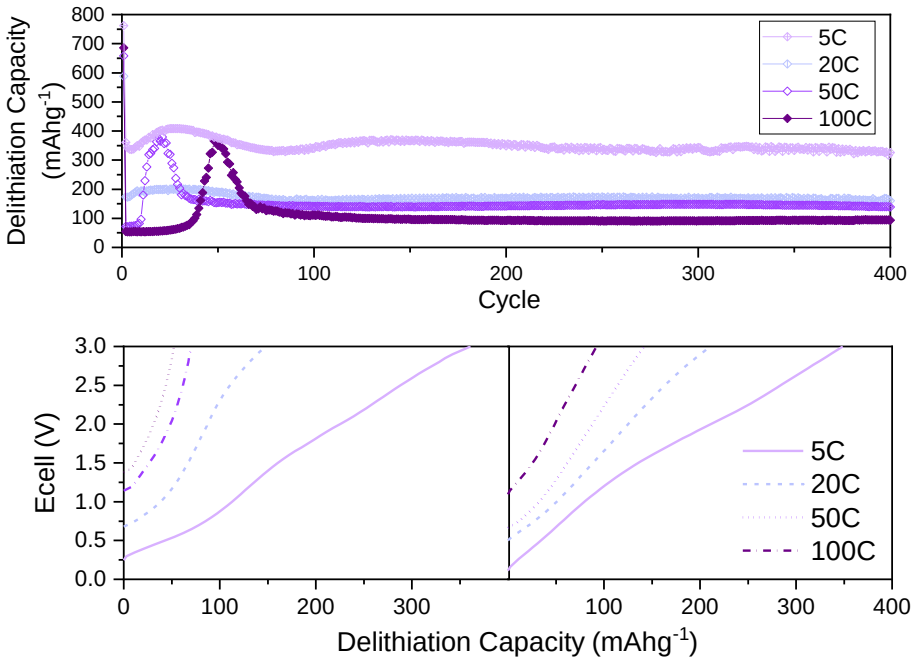

Figure 5.42 - (top) High rate galvanostatic cycling between 0.01-3.0 V of Heat-treated 50 % composite at rates greater than 5C, (bottom) charging profiles at various rates at 1st and 200th cycle.

The *ex-situ* XRD shows a very familiar pattern for the fresh electrodes with the addition of Cu peaks from the current collector (Figure 5.44). After the first cycle, the crystalline peaks associated with the semi-crystalline Nb_2O_5, completely flatten, suggesting that the formation

cycle allows a change from semi-crystalline to completely amorphous Nb_2O_5 whereas the MoO_2 peaks remain. The MoO_2 peaks reduce in intensity with cycling, however at 100 cycles; there is still evidence of the most prominent peaks at 26 and 38 °. The peaks show minimal shift with cycling and lack of apparent peak splitting as seen from changes in the presence of peaks which are overlapping, as evident by the peaks at 53-54 °. This is important as suggests that the MoO_2 remains monoclinic and is not transformed into the tetragonal form, as suggested for pure MoO_2. This is of particular interest as the as-synthesised 50 % composite and the MoO_2-rich materials studied via this method appear to follow a similar pattern to the pure MoO_2, which is not the case here. This may give a reason behind the particularly impressive capacities and retention seen for this material, but this does not give an explanation to the activation process seen here, as no structural rearrangement is observed. The impressive electrochemistry could be further linked to the structural stability as by 100 cycles there is no formation of any extra materials as in previous MoO_2 containing materials. This would suggest that the MoO_2 is stabilised in this material, and the fusion of the MoO_2 particles within the stable Nb_2O_5 network is key. Finally, as with the CV results, the *ex situ* XRD appears to give no explanation to the increase in capacity at approximately 70 cycles, as there is no obvious change in the XRD patterns at this point (Figure 5.44).

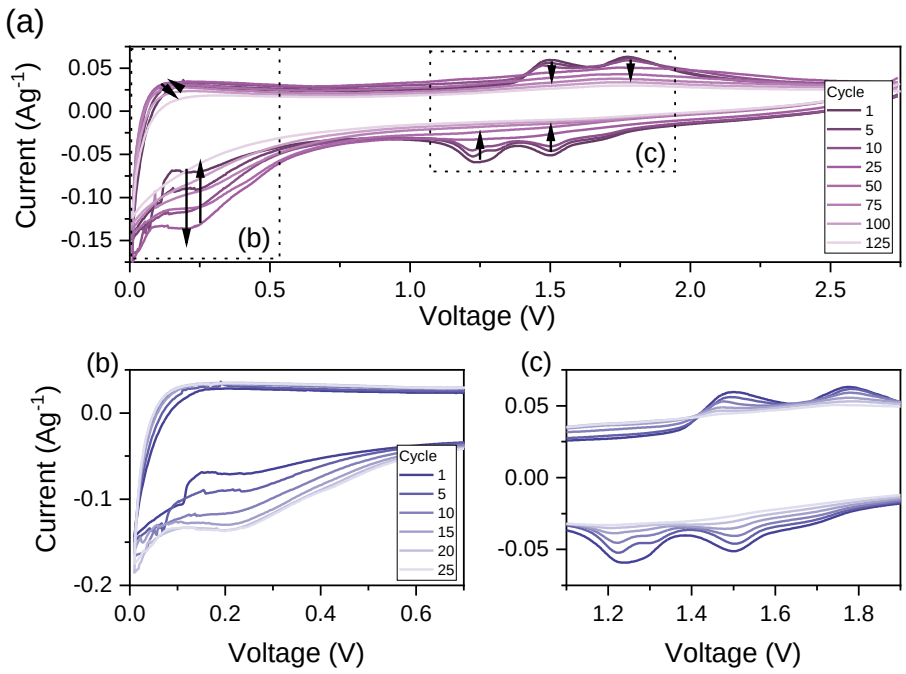

Figure 5.43 – (a) Cyclic voltammograms of heat-treated 50 % composite material at 0.1 mVs^{-1} taken between galvanostatic cycling between 1- 125 cycles at 1C. (b,c) Cyclic voltammograms taken at 0.1 mVs^{-1} every 5 cycles between 1 and 25 cycles at 1C.

To establish the extent of a capacitive storage mechanism used by this material, CV at different scan rates were collected and analysed (Figure 5.45). At low scan rates (<25 mVs^{-1}) there is two pairs of redox peaks in the profiles, and then at increased scan rate, this becomes one set of broad peaks. For all scan rates there is no defined peak for the conversion mechanism, which suggests that this may require slow rates to be favourable. The peak current plots show that all redox processes do show reliance on a surface limited process as the gradients are all above 0.6 (Figure 5.45b). The change from two redox pairs to one also comes with a drop in capacitive contribution; this may suggest that there is a change in storage mechanism at higher rates, which is very limited (Figure 5.45d). The highest capacitive contribution is 61% at 10 mVs^{-1}which is particularly high and suggests than there may be capacitive storage occurring in both materials simultaneously. Furthermore, although a drop in capacitive contribution is seen at 25 mVs^{-1} this does increase again when moving to the highest rates, which shows a shift to reliance on a capacitive storage mechanism once again. This is consistent with the rate data which shows a good rate capability. This drop in capacitive contribution at higher rates is surprising as this material has a good capability to cycle at 50 and 100C. At these rates there was a change in the activation process, which was key to produce higher capacities. It is unlikely that the activation process has been completed in these tests, thus the capacitive contribution may be lower due to this.

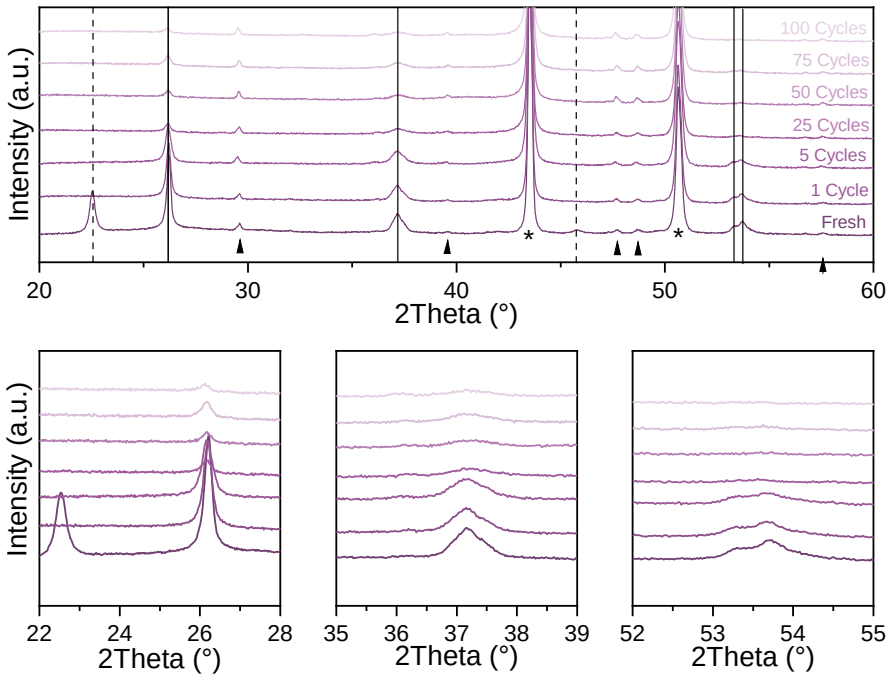

*Figure 5.44 – Ex-situ XRD of heat-treated 50% composite electrodes, fresh and cycled between 1-100 cycles at 1C in a 0.01-3.0V voltage range. Lines denote peaks of monoclinic MoO_2, dotted lines denote T-Nb_2O_5 peaks and * represent the peaks indexed to Cu current collector and triangles denote peaks from the sample holder.*

SPEIS shows the initial lithiation to have high impedance, which is reduced as Li-ions are inserted (Figure 5.46). After the first cycle, the impedance is lower, even with increasing cycles. During delithiation there is an increased impedance in the range of 0.01-0.5 V, and this is in all frequency regions, thus suggests a full structural change from the conversion process in MoO_2. Interestingly, although the CV profile suggests the lack of conversion after 25 cycles, this pattern continues into 50 cycles. By 70 cycles the increase in impedance in this range is reduced, and thus may link with the second increase in capacity that is seen. As for lithiation, up to 50 cycles there is some increase in impedance below 2.0 V in the medium range frequencies. This shows that there is an increased CT resistance in this range, likely from a phase change/expansion. After 50 cycles, the increase in impedance is above 2.0 V, this suggests that with the reduction in crystallinity of MoO_2, the CT resistance changes, likely due to a change in expansion needed for the material to accommodate ions.

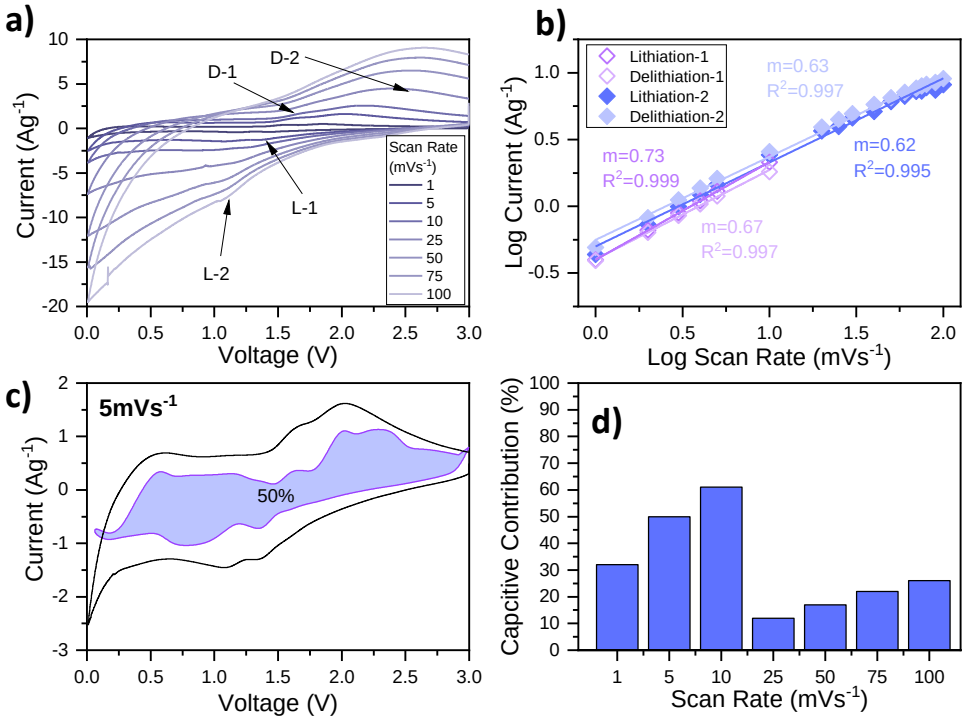

Figure 5.45 - a) CV profiles of heat-treated 50 % composite materials at increasing scan rate from 1.0 – 100 mVs^{-1}. b) Log plot of peak currents, versus scan rate, fitted with a linear function where R^2 is greater than 0.995 on all lines. c) CV profile at 5.0 mVs^{-1} with filled area representing the capacitive contribution. d) Chart of percentage capacitive contribution at increasing scan rate from 1.0 to 100 mVs^{-1}.

The Nyquist plots show a single semi-circle with a shallow diffusion tail (Figure A.92). The initial resistance is high and drops dramatically by 10 cycles, as seen in the SPEIS too. The material shows an initial loss of crystallinity in the Nb_2O_5 component, which may equate to the reduction in resistance, as typically Nb_2O_5 is insulating. The EIS measured during lithiation is stable after the first 10 cycles, and the changes seen in the SPEIS are not observed here. For delithiation the CT resistance is at its lowest at 30 cycles, this equates to the point at which activation is complete. From here, the CT resistance is increasing with cycle. The SPEIS studies show a more well-rounded over-view of the impedance involved in the ion storage for this material than EIS.

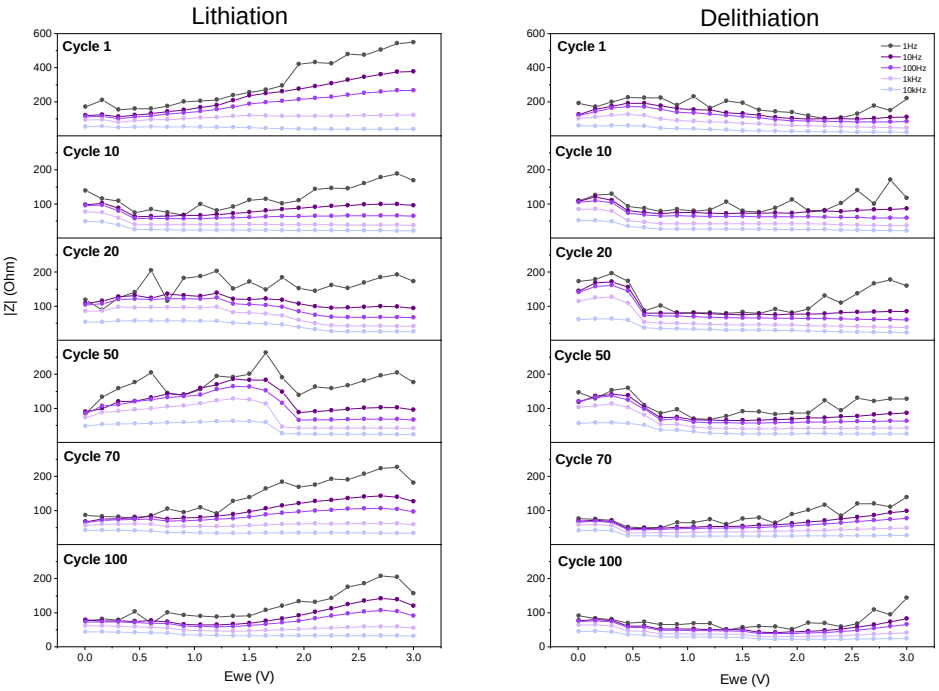

Figure 5.46 - SPEIS profiles of heat-treated 50 % composite material for increasing cycles from 1 to 100 (top to bottom) for lithiation and delithiation (left and right respectively). Note that the y axis changes after 1 cycle.

To summarise, this composite is a mixture of MoO_2 and semi-crystalline Nb_2O_5. This material produces capacities at the theoretical of the sum of its parts. With an average capacity of 514 $mAhg^{-1}$ even after 200 cycles at 1C. This material appears to undergo an activation process within the first 30 cycles, where there is only a small increase capacity seen. The cause of this is unclear as the material's structure appears stable and lacks change after the initial loss of crystallinity seen in the Nb_2O_5 only. From the CV profiles the material appears to store Li-ions using intercalation and conversion via the MoO_2, and there is an overall rectangular shape which suggests capacitive storage. This is further confirmed by capacitive contribution calculations. As such, this material shows excellent rate capability with cycling at 100C, likely due to the synergy of the high rate Nb_2O_5 and conductive MoO_2. When compared to the as-synthesised form the heat-treatment allows for stabilisation of the electrochemical response as the as-synthesised 50 % composite begins to lose all its capacity after 100 cycles. Both materials appear to have structural similarities in the *ex-situ* XRD, yet the difference comes with the lattice expansion and associated peak shift, which is apparent in the as-synthesised material but not in the heat-treated form. This simple heat-treatment step has led to a vast improvement in electrochemical properties, due to improved structural

rigidity in MoO_2 as seen via the lack of change in *ex situ* XRD patterns. Further studies should be taken to optimise this composite and take advantage of the full range of properties. There is a need for full understanding of the complex electrochemical mechanisms to optimise this material. Thus, *In-situ* XRD and XPS studies would be recommended as this can reveal how each oxide is acting in the composite.

5.5 Composite Materials Summary

A variety of MoO_2/Nb_2O_5 composites were synthesised with various ratios. Both composites at 10 % content may be composed of doped oxides. The morphology of the oxides appears to be generally maintained through the selection, with the main changes observed in the primary particles of MoO_2.

All composites were thoroughly tested electrochemically, where the most promising composite was heat-treated. Although the composites appeared to be a mixture of the individual oxides, the electrochemical properties reveal that the situation is more complex than this. As expected, the high niobium content composites appear to behave similarly to Nb_2O_5, yet the MoO_2 in the composites is contributing electrochemically as a reduction in impedance is observed and an unfortunate loss of high-rate capability. As with these materials the Mo-rich composites also behaved like that of the pure MoO_2. These composites showed poor stability, although did give an improvement in a narrower voltage window which may suggest an application as an intercalation only anode. The 50 % composite appeared to combine aspects of both oxides, yet the heat-treated form of this showed vast improvement in stability.

When compared, all composites show improvements from the pure forms under specific conditions, which shows proof of concept for the formation of composites from Nb_2O_5/MoO_2. Figure 5.47 shows the measured capacities of these materials at different rates. Regarding as-synthesised materials, the composites show improvement over pure Nb_2O_5 generally. The as-synthesised composites appear to form a near volcano plot, with the 50 % composite showing improvement from pure Nb_2O_5 and MoO_2, at all rates up to 100 cycles. The MoO_2 heavy composites do not follow this in some cases as show a decrease in capacity from pure MoO_2. By 200 cycles the materials show little difference in capacity, showing the need for further stabilisation as there is a lack of improvement from the pure counterparts. The 50 % heat-treated material shows similar capacities to the as-synthesised

form initially, yet this material's poor stability leads to the heat-treated form surpassing its capacities at longer cycling. There is a pay off between capacity and stability here, as the composites will have a lower capacity compared to MoO_2, due to the lower theoretical capacity of Nb_2O_5, yet the composites' stabilities appear far improved from MoO_2. These results show great promise for this composite system and call for further investigation. The results on the heat-treated 50 % composite warrants further heat-treatment studies for these materials. Future work could optimise the composite, through tuning of oxide ratios and exploration of the heat-treatment step. Overall, this looks to be a promising way to exploit and combine the properties of two promising anode materials in one material.

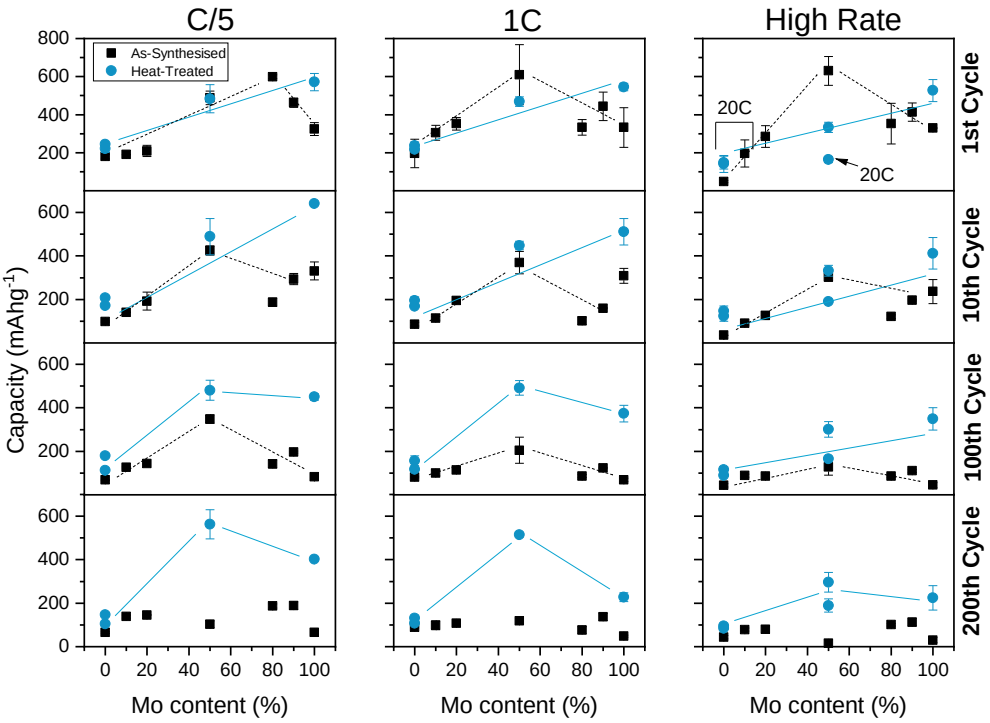

Figure 5.47 – Comparison of delithiation capacity at increasing cycle (top to bottom) after a C/20 formation in the materials preferred voltage range at rates of C/5, 1C and 5C, with those at a higher rate of 20C marked upon the 1st cycle graph. The as-synthesised materials are black squares and heat-treated materials in blue, colour coded lines are used as a guide. The heat-treated Nb_2O_5 materials here are 600 °C and 1000 °C treated materials.

6 Conclusions

The purpose of this work was to produce a Li-ion battery anode material with high capacity and capable of high-rate cycling. As such, two different oxides were investigated: MoO_2 for high capacity and Nb_2O_5 for high-rate capability, with the goal to combine them to produce composite materials that might offer an optimised combination of properties.

A family of Nb_2O_5 materials were synthesised hydrothermally and subsequently heat-treated under different conditions to produce various polymorphs. An anisotropically crystalline Nb_2O_5 was produced from the initial hydrothermal synthesis step. Although Nb_2O_5 in this form had been described before in the literature, no work had been previously published on the material's electrochemical properties, nor was its structure understood. It was apparent that the anisotropically crystalline Nb_2O_5 was structurally similar to T-Nb_2O_5, with powder X-ray diffraction (XRD) patterns suggesting this structure was crystalline in one direction but disordered in the others. Pair distribution function (PDF) analysis of the anisotropically crystalline Nb_2O_5 revealed a similar local structure to T- and H-Nb_2O_5, but the long-range structure deviated from these crystalline forms. Electrochemically, the anisotropically crystalline Nb_2O_5 materials could be cycled to 100C with a capacity of ~25 $mAhg^{-1}$ and when cycled for 200 cycles at 20C, a ~45 $mAhg^{-1}$ capacity could still be achieved. This material shows evidence of using the same intercalation pseudocapacitance mechanism as T-Nb_2O_5, where the disorder in the structure appears to be slowing some of the diffusion pathways or restricting active sites, resulting in capacities that are lower than expected.

T-Nb_2O_5 was obtained by heat treating the as-synthesised anisotropically crystalline Nb_2O_5 at 600 °C, with a higher crystallinity form produced at 800 °C. The T-Nb_2O_5 produced at 600 °C had an XRD pattern near to that of the ideal, yet PDF analysis revealed that there was long range disorder and short-range distances that are not seen in the ideal T-Nb_2O_5 structure. The 800 °C heat-treated form was more crystalline, and this structure matched the ideal PDF more closely, yet there were still small deviations. This suggested that the anisotropic character of the precursor was still present in this structure. This emphasises the complexity of the Nb_2O_5 system.

Electrochemically, the T-Nb_2O_5 materials showed some differences from what has been published. Notably, the formation cycle showed a large irreversible phase change (~0.8 V), which does not appear to be solid electrolyte interphase (SEI) formation as the literature

suggests. This irreversible change appears to be activation of the material where amorphous-Nb_2O_5 and NbO are produced. This has been studied previously with Na-ion technology, where the activation is key to achieving bulk ion intercalation. Typically, previous studies have cycled T-Nb_2O_5 between 1.0-3.0 V, avoiding this activation process. Yet, the work in this thesis has indicated that this voltage window may not be suitable in all cases as here the activation process takes place at 1.0 V in the 800 °C material. The 600 °C material seems to still follow an intercalation pseudocapacitive process, showing high-rate capability (35 $mAhg^{-1}$ at 100C) and long-term rate capability (83 $mAhg^{-1}$ after 200 cycles at 20C). Yet the 800 °C material operate by a traditional intercalation mechanism, which although stunts its rate capability (40 $mAhg^{-1}$ after 200 cycles at 20C) it is more stable with much higher retentions achieved. This work highlights the need for thorough electrochemical characterisation as even for materials of the same polymorph, the electrochemical properties can vary dramatically.

Finally, within the Nb_2O_5 family, H-Nb_2O_5 can be produced via 1000 °C heat-treatment, with further crystallisation at 1300 °C. The H-Nb_2O_5 still showed evidence of structural motifs seen in the anisotropically crystalline precursor in XRD and PDF analysis. This clarifies the importance of the memory of solids concept, where preparative method is a key factor for determining the structure formed. The H-Nb_2O_5 far surpassed expectations electrochemically, showing high-rate capability (50 $mAhg^{-1}$ achieved at 400 cycles at 100C). This suggests that the anisotropically crystalline character remaining in the structure may provide non-torturous pathways for fast ion diffusion. The material shows a two-phase intercalation mechanism, which is highly reversible with minimal structural degradation after cycling (seen from *ex-situ* XRD). Overall, the Nb_2O_5 family of materials all show interesting electrochemical properties, of which the rate capability is most notable.

MoO_2 materials were also produced using a simple hydrothermal route. Clusters of monoclinic MoO_2 nanoparticles were produced which could be further heat-treated up to 300 °C in Ar without a formation of additional phases. The differences between the as-synthesised and heat-treated MoO_2 is a cleaning of surface molecules and some particles fusing together within agglomerates. The as-synthesised MoO_2 showed high initial capacities, with a short activation process. Subsequently, the capacity proceeds to drop drastically showing the material's poor stability. Impedance in this material was initially low, due to its conductive nature, yet this increased dramatically with cycling, suggesting that the electrode instability also leads to resistance. These issues have been seen before in the literature with many studies only performing a short number of cycles, as the conversion

mechanism and structural rearrangement during the activation causes electrode pulverisation and active material isolation.

Surprisingly, with heat-treatment, the electrochemical stability of MoO_2 could be improved significantly. Although the heat-treated MoO_2 appears very similar physically (in particle size and morphology) to that of the as-synthesised form, it showed much improved capacities over longer cycling. 400 $mAhg^{-1}$ was achieved after 200 cycles at C/5 compared to only 65 $mAhg^{-1}$ for the as-synthesised MoO_2 under the same conditions. The heat-treated MoO_2 showed a reversible intercalation and conversion reaction, with evidence of capacitive storage also being at play. Investigation into the activation process of MoO_2 showed that the material changed symmetry from a monoclinic to a tetragonal form during activation. This may be a reason for the improvement seen between the two materials as the change to a tetragonal form may allow for a more stable electrochemical response. A MoO_2/C composite was also synthesised, with the intention of further improving the stability. This material showed little improvement from the pure heat-treated MoO_2. Overall, the MoO_2 materials presented here appear to fall short of that presented in the literature. The heat-treated form shows good high-rate capacities, inline or surpassing other pure MoO_2, however, the low-rate capacities are lower than expected. The work here presents longer, more thorough high-rate testing and in-depth mechanistic characterisation compared to much of the literature, so adds to the knowledge on MoO_2 as an anode.

A selection of composite materials were produced with varying ratios of Nb_2O_5 and MoO_2 via a simple hydrothermal route. The aim of developing the composite oxides was to achieve the high-rate capability of Nb_2O_5 and combine this with the higher capacities of MoO_2. This was hoped to boost the conductivity of Nb_2O_5 and allow further stabilisation of MoO_2. The Nb-rich composites appear similar to the as-synthesised Nb_2O_5 in structure and particle morphology. The 10 % Mo material may have Mo substituted into the Nb_2O_5 structure rather than forming a composite. Electrochemically, the Nb-rich composites behave similarly to the as-synthesised Nb_2O_5, yet with the increasing Mo content, the rate capability dropped, even though the impedance decreased due to the improved conductivity. On the opposite end of the series, the Mo-rich composites were found to be a collection of MoO_2 nano-particles and Nb_2O_5 nano-wires. These showed some improvement in capacity and electrochemical stability compared to the as-synthesised MoO_2, yet still fell short of expected capacities. The Mo-rich composites appear to perform with more favourable electrochemical properties in a narrow voltage window where the material undergoes intercalation only, however this limits the capacities due to a reduced number of ions which are stored.

Most notably the 50/50 Nb_2O_5/MoO_2 composite showed the best electrochemical properties, with the heat-treatment of this material giving further improvement. The 50/50 composite stored Li-ions via a combination of mechanisms and showed capacities of 340 $mAhg^{-1}$ after 100 cycles at C/5. However, after 100 cycles the material loses stability, the capacity drops, and the impedance increases dramatically. Heat-treatment allows the material to be stabilised with capacities of 515 $mAhg^{-1}$ after 200 cycles at 1C. This material also showed impressive rate capability with capacities of 110 $mAhg^{-1}$ after 200 cycles at 100C. This composite appears to sit in the optimum combination of the oxides to achieve the preferred properties. Therefore, this work has presented a novel composite oxide material with high capacities and high-rate capability, realising the aims of this project.

7 Future Works

This work began to uncover the structural complexity of the Nb_2O_5 family and how the polymorphs are related to each other. The data collected could be further analysed via modelling to reveal the true structural form and deliver detailed structural information on these materials. Full modelling of PDFs would allow a proper understanding of deviation from average crystal structure seen here. Further characterisation of the structural conversion which takes place during the initial cycle for T-Nb_2O_5 is needed to assess the limitations of the material and whether a wider voltage range could be used. Furthermore, H-Nb_2O_5 showed high-rate capability, which has not been seen to this extent for the pure polymorph, yet it is still limited by poor conductivity. Further work would establish a conductive composite with this material.

The electrochemical mechanisms that MoO_2 operates by, and the nature of the activation process is already highly debated in the literature. Here, activation where monoclinic MoO_2 changes to tetragonal MoO_2 was proposed. This should be probed further to establish whether tetragonal MoO_2 has preferred electrochemical properties and *in-situ* analysis could clarify this activation process. Furthermore, the work here has solidified the notion that heat-treatment improves the stability of MoO_2, yet the exact nature of this could not be discerned. This warrants a further in-depth study via surface analysis and structural assessment to determine subtle differences.

The composite materials proposed and produced here are novel and show promise. The 50:50 composite showed high capacities and high-rate capability after heat-treatment. Therefore, further improvements could be made with the Nb-rich and Mo-rich composites via a similar route. This could lead to a selection of composites where the ratios of the oxides could be tuned for a specific application. Ultimately, to allow for these materials to be considered commercially, further electrochemical testing would be required, with higher mass loading electrodes and crucially, testing in a full cell set up.

8 References

1 Olof Ramström, *The royal swedish academy of sciences*, 2019, 0–13.

2 M. S. Whittingham, *Nano Lett*, 2020, **20**, 8435–8437.

3 M. S. Whittingham, *J Power Sources*, 2020, **473**, 228574.

4 Department for Environmental Food and Rural Affairs and Department for Transport, *UK plan for tackling roadside nitrogen dioxide concentrations: An overview*, London, 2017.

5 Department for Transport, *Road To Zero.*, 2018.

6 A. Yoshino, *Angewandte Chemie - International Edition*, 2012, **51**, 5798–5800.

7 A. Yoshino, *Development of the Lithium-Ion Battery and Recent Technological Trends*, Elsevier, 2014.

8 J. Theerthagiri, S. J. Lee, P. Shanmugam and M. Y. Choi, *Basic principles in energy conversion and storage*, Elsevier Inc., 2020.

9 C. P. Grey and D. S. Hall, *Nat Commun*, 2020, **11**, 2–5.

10 R. Alcántara, P. Lavela, C. Pérez-Vicente and J. L. Tirado, *Lithium-Ion Batteries: Advanced Materials and Technologies*, 2016, 97–146.

11 J. B. Goodenough, *Chem Mater*, 2014, **26**, 820–829.

12 C. Liu, F. Li, L.-P. Ma and H.-M. Cheng, *Advanced Materials*, 2010, **22**, E28–E62.

13 J. B. Goodenough and Y. Kim, *Chemistry of Materials*, 2010, **22**, 587–603.

14 M. S. Whittingham, *Chem Rev*, 2004, **104**, 4271–4301.

15 J. P. Pender, G. Jha, D. H. Youn, J. M. Ziegler, I. Andoni, E. J. Choi, A. Heller, B. S. Dunn, P. S. Weiss, R. M. Penner and C. B. Mullins, *ACS Nano*, 2020, **14**, 1243–1295.

16 J. Asenbauer, T. Eisenmann, M. Kuenzel, A. Kazzazi, Z. Chen and D. Bresser, *Sustain Energy Fuels*, 2020, **4**, 5387–5416.

17 A. Wang, S. Kadam, H. Li, S. Shi and Y. Qi, *Computational Materials*, 2018, **4**, 1–26.

18 M. Armand and J.-M. Tarascon, *Nature*, 2001, **414**, 359–367.

19 M. Ghassemi, M. Kamvar and R. Steinberger-Wilckens, in *Fundamentals of Heat and Fluid Flow in High Temperature Fuel Cells*, Elsevier, 2020, pp. 75–99.

20 Y. Gogotsi and R. M. Penner, *ACS Nano*, 2018, **12**, 2081–2083.

21 M. R. Lukatskaya, B. Dunn and Y. Gogotsi, *Nat Commun*, 2016, **7**, 1–13.

22 R. C. Massé, C. Liu, Y. Li, L. Mai and G. Cao, *Natl Sci Rev*, 2017, **4**, 26–53.

23 N. Sick, O. Krätzig, G. G. Eshetu and E. Figgemeier, *J Energy Storage*, 2021, **43**, 103231.

24 M. Armand and J.-M. Tarascon, *Nature*, 2008, **451**, 652–657.

25 B. E. Conway, *Proceedings of the International Power Sources Symposium*, 1991, 319–327.

26 P. Simon, Y. Gogotsi and B. Dunn, *Science (1979)*, 2014, **343**, 1210–1211.

27 D. P. Dubal, O. Ayyad, V. Ruiz and P. Gómez-Romero, *Chem. Soc. Rev.*, 2015, **44**, 1777–1790.

28 W. Zuo, R. Li, C. Zhou, Y. Li, J. Xia and J. Liu, *Advanced Science*, 2017, **4**, 1–21.

29 Z. Lin, E. Goikolea, A. Balducci, K. Naoi, P. L. Taberna, M. Salanne, G. Yushin and P. Simon, *Materials Today*, 2018, **21**, 419–436.

30 L. Guan, L. Yu and G. Z. Chen, *Electrochim Acta*, 2016, **206**, 464–478.

31 Y. Liu, S. P. Jiang and Z. Shao, *Mater Today Adv*, 2020, **7**, 100072.

32 C. Costentin, T. R. Porter and J. M. Savéant, *ACS Appl Mater Interfaces*, 2017, **9**, 8649–8658.

33 B. E. Conway, *Electrochemical Supercapacitors*, Springer US, Boston, MA, 1999, vol. 1.

34 R. Kötz and M. Carlen, *Electrochim Acta*, 2000, **45**, 2483–2498.

35 V. Augustyn, P. Simon and B. Dunn, *Energy Environ Sci*, 2014, **7**, 1597.

36 C. Choi, D. S. Ashby, D. M. Butts, R. H. DeBlock, Q. Wei, J. Lau and B. Dunn, *Nat Rev Mater*, 2020, **5**, 5–19.

37 V. Augustyn, J. Come, M. A. Lowe, J. W. Kim, P. L. Taberna, S. H. Tolbert, H. D. Abruña, P. Simon and B. Dunn, *Nat Mater*, 2013, **12**, 518–522.

38 J. Xie, P. Yang, Y. Wang, T. Qi, Y. Lei and C. M. Li, *J Power Sources*, 2018, **401**, 213–223.

39 H. Lindström, S. Södergren, A. Solbrand, H. Rensmo, J. Hjelm, A. Hagfeldt and S. E. Lindquist, *Journal of Physical Chemistry B*, 1997, **101**, 7717–7722.

40 V. Augustyn, P. Simon and B. Dunn, *Energy Environ Sci*, 2014, **7**, 1597.

41 M. V. Reddy, G. V. Subba Rao and B. V. R. Chowdari, *Chem Rev*, 2013, **113**, 5364–5457.

42 M. Lübke, 2018, 73–73.

43 S. Boyd and V. Augustyn, *Inorg Chem Front*, 2018, **5**, 999–1015.

44 C. Dong, W. Dong, X. Lin, Y. Zhao, R. Li and F. Huang, *EnergyChem*, 2020, **2**, 100045.

45 R. S. Devan, R. A. Patil, J. H. Lin and Y. R. Ma, *Adv Funct Mater*, 2012, **22**, 3326–3370.

46 C.-Q. Yi, J.-P. Zou, H.-Z. Yang and X. Leng, *Trans Nonferrous Met Soc China*, 2018, **28**, 1980–2001.

47 P. Poizot, S. Laruelle, S. Grugeon, L. Dupont and J. Tarascon, *Nature*, 2000, **407**, 496–499.

48 J. B. Goodenough, *Prog Solid State Chem*, 1971, **5**, 145–399.

49 J. Lu, Z. Chen, F. Pan, Y. Cui and K. Amine, *Electrochemical Energy Reviews*, 2018, **1**, 35–53.

50 C. Lin, C. Yang, S. Lin and J. Li, *Materials Technology*, 2015, **30**, A192–A202.

51 S. Lou, Y. Zhao, J. Wang, G. Yin, C. Du and X. Sun, *Small*, 2019, **15**, 1–44.

52 Z. Su, J. Liu, M. Li, Y. Zhu, S. Qian, M. Weng, J. Zheng, Y. Zhong, F. Pan and S. Zhang, *Electrochemical Energy Reviews*, 2020, **3**, 286–343.

53 L. Mao, X. Zhao, Q. Cheng, G. Yang, F. Liao, L. Chen, P. He and S. Chen, *Sustain Energy Fuels*, 2021, **5**, 5061–5113.

54 K. J. Griffith, Y. Harada, S. Egusa, R. M. Ribas, R. S. Monteiro, R. B. Von Dreele, A. K. Cheetham, R. J. Cava, C. P. Grey and J. B. Goodenough, *Chemistry of Materials*, 2021, **33**, 4–18.

55 J. W. Kim, V. Augustyn and B. Dunn, *Adv Energy Mater*, 2012, **2**, 141–148.

56 K. Brezesinski, J. Wang, J. Haetge, C. Reitz, S. O. Steinmueller, S. H. Tolbert, B. M. Smarsly, B. Dunn and T. Brezesinski, *J Am Chem Soc*, 2010, **132**, 6982–6990.

57 M. Winter and R. J. Brodd, *Chem Rev*, 2004, **104**, 4245–4269.

58 N. A. Chernova, M. Roppolo, A. C. Dillon and M. S. Whittingham, *J Mater Chem*, 2009, **19**, 2526.

59 M. A. Azam, N. E. Safie, A. S. Ahmad, N. A. Yuza and N. S. A. Zulkifli, *J Energy Storage*, 2021, **33**, 102096.

60 M. A. Kebede, *Curr Opin Electrochem*, 2020, **21**, 182–187.

61 M. Wang, T. Chen, T. Liao, X. Zhang, B. Zhu, H. Tang and C. Dai, *RSC Adv*, 2020, **11**, 1200–1221.

62 H. Wang, H. Huang, C. Niu and A. L. Rogach, *Small*, 2015, **11**, 1364–1383.

63 P. Shen, B. Zhang, Y. Wang, X. Liu, C. Yu, T. Xu, S. S. Mofarah, Y. Yu, Y. Liu, H. Sun and H. Arandiyan, *Nanoscale niobium oxides anode for electrochemical lithium and sodium storage: a review of recent improvements*, Springer Berlin Heidelberg, 2021, vol. 11.

64 C. P. Koçer, K. J. Griffith, C. P. Grey and A. J. Morris, *Phys Rev B*, 2019, **99**, 1–11.

65 C. Nico, T. Monteiro and M. P. F. Graça, *Prog Mater Sci*, 2016, **80**, 1–37.

66 V. G. Brauer, *Z Anorg Allg Chem*, 1941, **248**, 1–31.

67 H. Schäfer, R. Gruehn and F. Schulte, *Angewandte Chemie International Edition in English*, 1966, **5**, 40–52.

68 J. L. Waring, R. S. Roth and H. S. Parker, *J Res Natl Bur Stand A Phys Chem*, 1973, **77A**, 705.

69 B. M. Gatehouse and A. D. Wadsley, *Acta Crystallogr*, 1964, **17**, 1545–1554.

70 E. I. Ko and J. G. Weissman, *Catal Today*, 1990, **8**, 27–36.

71 R. Brayner and F. Bozon-Verduraz, *Physical Chemistry Chemical Physics*, 2003, **5**, 1457–1466.

72 B. Pilarek, A. J. Pelczarska and I. Szczygieł, *J Therm Anal Calorim*, 2017, **130**, 77–83.

73 C. Arico, S. Ouendi, P. L. Taberna, P. Roussel, P. Simon and C. Lethien, *ACS Nano*, 2019, **13**, 5826–5832.

74 V. G. F. Hüttig, E. Zeidler and E. Franz, *Z Anorg Allg Chem*, 1937, **231**, 104.

75 A. M. Raba, J. Bautista-Ruíz and M. R. Joya, *Materials Research*, 2016, **19**, 1381–1387.

76 M. R. N. Soares, S. Leite, C. Nico, M. Peres, A. J. S. Fernandes, M. P. F. Graça, M. Matos, R. Monteiro, T. Monteiro and F. M. Costa, *J Eur Ceram Soc*, 2011, **31**, 501–506.

77 W. Fan, Q. Zhang, W. Deng and Y. Wang, *Chemistry of Materials*, 2013, **25**, 3277–3287.

78 K. Skrodczky, M. M. Antunes, X. Han, S. Santangelo, G. Scholz, A. A. Valente, N. Pinna and P. A. Russo, *Commun Chem*, 2019, **2**, 1–11.

79 T. Fuchigami, M. Kuroda, S. Nakamura, M. Haneda and K. I. Kakimoto, *Nanotechnology*, 2020, **31**, 325705.

80 B. Orel, M. Maček, J. Grdadolnik and A. Meden, *Journal of Solid State Electrochemistry*, 1998, **2**, 221–236.

81 L. Yan, X. Rui, G. Chen, W. Xu, G. Zou and H. Luo, *Nanoscale*, 2016, **8**, 8443–8465.

82 W. Dong, F. Pan, Y. Wang, S. Xiao, K. Wu, G. Q. Xu and W. Chen, *Appl Surf Sci*, 2017, **392**, 514–522.

83 Q. Deng, Y. Fu, C. Zhu and Y. Yu, *Small*, 2019, **15**, 1–26.

84 H. Ding, Z. Song, H. Zhang and X. Li, *Mater Today Nano*, 2020, **11**, 100082.

85 J. Liao, W. Ni, C. Wang and J. Ma, *Chem Eng J*, 2020, **391**, 123489.

86 E. Lim, J. Changshin, M. S. Kim, M. H. Kim, J. Chun, H. Kim, J. Park, K. C. Roh, K. Kang, S. Yoon and J. Lee, *Adv Funct Mater*, 2016, **26**, 3711–3719.

87 H. Kim, E. Lim, C. Jo, G. Yoon, J. Hwang, S. Jeong, J. Lee and K. Kang, *Nano Energy*, 2015, **16**, 62–70.

88 L. Yan, G. Chen, S. Sarker, S. Richins, H. Wang, W. Xu, X. Rui and H. Luo, *ACS Appl Mater Interfaces*, 2016, **8**, 22213–22219.

89 J. Ni, W. Wang, C. Wu, H. Liang, J. Maier, Y. Yu and L. Li, *Advanced Materials*, 2017, **29**, 1–6.

90 L. Yang, Y. E. Zhu, J. Sheng, F. Li, B. Tang, Y. Zhang and Z. Zhou, *Small*, 2017, **13**, 6–11.

91 Z. Chen, W. Chen, H. Wang, Z. Xiao and F. Yu, *Nanoscale*, 2020, **12**, 18673–18681.

92 N. Li, F. Zhang and Y. Tang, *J Mater Chem A Mater*, 2018, **6**, 17889–17895.

93 F. Idrees, J. Hou, C. Cao, F. K. Butt, I. Shakir, M. Tahir and F. Idrees, *Electrochim Acta*, 2016, **216**, 332–338.

94 B. H. Deng, T. Y. Lei, W. H. Zhu, L. Xiao and J. P. Liu, *Adv Funct Mater*, 2018, **28**, 1–11.

95 S. Hemmati, G. Li, X. Wang, Y. Ding, Y. Pei, A. Yu and Z. Chen, *Nano Energy*, 2019, **56**, 118–126.

96 W. Hu, S. Zhang, W. Zhang, M. Wang and F. Feng, *Journal of Nanoparticle Research*, 2020, **22**, 1–11.

97 H. Li, J. Chen, B. Yang, K. Wang, X. Zhang, T. Zhang, L. Zhang, W. Liu and X. Yan, *Electrochim Acta*, 2019, **299**, 163–172.

98 J. Zhang, H. Zhang, Y. Zhang, J. Zhang, H. He, X. Zhang, J. J. Shim and S. Zhang, *Electrochim Acta*, 2019, **313**, 532–543.

99 R. Vicentini, D. M. Soares, W. Nunes, B. Freitas, L. Costa, L. M. Da Silva and H. Zanin, *J Power Sources*, 2019, **434**, 226737.

100 R. Vicentini, W. Nunes, B. G. A. Freitas, L. M. Da Silva, D. M. Soares, R. Cesar, C. B. Rodella and H. Zanin, *Energy Storage Mater*, 2019, **22**, 311–322.

101 S. Ahmed and M. Rafat, *Mater Res Express*, 2018, **5**, 35512.

102 Z. Tong, S. Liu, Y. Zhou, J. Zhao, Y. Wu, Y. Wang and Y. Li, *Energy Storage Mater*, 2018, **13**, 223–232.

103 Y. Wu, X. Fan, R. R. Gaddam, Q. Zhao, D. Yang, X. Sun, C. Wang and X. S. Zhao, *J Power Sources*, 2018, **408**, 82–90.

104 Y. Yang and J. Zhao, *Advanced Science*, 2021, **8**, 1–24.

105 B. Babu and M. M. Shaijumon, *Electrochim Acta*, 2020, **345**, 136208.

106 K. J. Griffith, K. M. Wiaderek, G. Cibin, L. E. Marbella and C. P. Grey, *Nature*, 2018, **559**, 556–563.

107 C. P. Koçer, K. J. Griffith, C. P. Grey and A. J. Morris, *Chemistry of Materials*, 2020, **32**, 3980–3989.

108 Y. Kim, Q. Jacquet, K. J. Griffith, J. Lee, S. Dey, B. L. D. Rinkel and C. P. Grey, *J Electrochem Soc*, 2021, **168**, 010525.

109 X. Ma, P. Chen, M. Qian, D. Wu, J. Du, X. Chen, R. Dai, M. Sha, Z. Zi and J. Dai, *J Alloys Compd*, 2021, **864**, 158379.

110 J. Cheng, F. Lu and X. Kuang, *Mater Adv*, 2021, **2**, 6272–6277.

111 H. Zhang, X. Zhang, H. Li, Y. Gao, J. Yan, K. Zhu, K. Ye, K. Cheng, G. Wang and D. Cao, *J Colloid Interface Sci*, 2021, **583**, 652–660.

112 M. Liang, Y. Huang, Y. Lin, G. Liang, C. Huang, L. Chen, J. Li, Q. Feng, C. Lin and Z. Huang, *J Mater Sci Technol*, 2021, **83**, 66–74.

113 B. Reichman and A. J. Bard, *Journal of Electrochemical Society*, 1981, **128**, 344–346.

114 N. Kumagai, K. Tanno, T. Nakajima and N. Watanabe, *Electrochim Acta*, 1983, **28**, 17–22.

115 T. Ohzuku, K. Sawai and T. Hirai, *J Power Sources*, 1987, **19**, 287–299.

116 N. Kumagai, Y. Koishikawa, S. Komaba and N. Koshiba, *J Electrochem Soc*, 1999, **146**, 3203–3210.

117 N. Kumagai, I. Ishiyama and K. Tanno, *J Power Sources*, 1987, **20**, 193–198.

118 R. Kodama, Y. Terada, I. Nakai and S. Komaba, *J Electrochem Soc*, 2006, 9–14.

119 N. Kumagai, Y. Tateshita, Y. Takatsuka, M. Baba, T. Ikeda and K. Tanno, *J Power Sources*, 1995, **54**, 175–179.

120 A. Le Viet, M. V Reddy, R. Jose, B. V. R. Chowdari and S. Ramakrishna, *Journal of Physical Chemistry C*, 2010, **114**, 664–671.

121 M. V. Reddy, R. Jose, A. Le Viet, K. I. Ozoemena, B. V. R. Chowdari and S. Ramakrishna, *Electrochim Acta*, 2014, **128**, 198–202.

122 J. Come, V. Augustyn, J. W. Kim, P. Rozier, P.-L. Taberna, P. Gogotsi, J. W. Long, B. Dunn and P. Simon, *J Electrochem Soc*, 2014, **161**, A718–A725.

123 K. J. Griffith, A. C. Forse, J. M. Griffin and C. P. Grey, *J Am Chem Soc*, 2016, **138**, 8888–8899.

124 A. A. Lubimtsev, P. R. C. Kent, B. G. Sumpter and P. Ganesh, *J Mater Chem A Mater*, 2013, **1**, 14951.

125 D. Chen, J. H. Wang, T. F. Chou, B. Zhao, M. A. El-Sayed and M. Liu, *J Am Chem Soc*, 2017, **139**, 7071–7081.

126 I. Andoni, J. M. Ziegler, G. Jha, C. A. Gadre, H. Flores-Zuleta, S. Dai, S. Qiao, M. Xu, V. T. Chen, X. Pan and R. M. Penner, *ACS Appl Energy Mater*, 2021, **4**, 6542–6552.

127 R. J. Cava, *J Electrochem Soc*, 1983, **130**, 2345.

128 L. Kong, X. Cao, J. Wang, W. Qiao, L. Ling and D. Long, *J Power Sources*, 2016, **309**, 42–49.

129 J. Liao, R. Tan, Z. Kuang, C. Cui, Z. Wei, X. Deng, Z. Yan, Y. Feng, F. Li, C. Wang and J. Ma, *Chinese Chemical Letters*, 2018, **29**, 1785–1790.

130 S. Li, Q. Xu, E. Uchaker, X. Cao and G. Cao, *CrystEngComm*, 2016, **18**, 2532–2540.

131 Z. Hu, Q. He, Z. Liu, X. Liu, M. Qin, B. Wen, W. Shi, Y. Zhao, Q. Li and L. Mai, *Sci Bull (Beijing)*, 2020, **65**, 1154–1162.

132 H. Ding, Z. Song, K. Feng, H. Zhang, H. Zhang and X. Li, *J Solid State Chem*, 2021, **299**, 122136.

133 M. Lübke, A. Sumboja, I. D. Johnson, D. J. L. Brett, P. R. Shearing, Z. Liu and J. A. Darr, *Electrochim Acta*, 2016, **192**, 363–369.

134 S. Q. Guo, X. Zhang, Z. Zhou, G. D. Gao and L. Liu, *J Mater Chem A Mater*, 2014, **2**, 9236–9243.

135 C. Huang, J. Fu, H. Song, X. Li, X. Peng, B. Gao, X. Zhang and P. K. Chu, *RSC Adv*, 2016, **6**, 90489–90493.

136 L. Lou, X. Kong, T. Zhu, J. Lin, S. Liang, F. Liu, G. Cao and A. Pan, *Sci China Mater*, 2019, **62**, 465–473.

137 Y. Yoo and Y. C. Kang, *J Alloys Compd*, 2019, **776**, 722–730.

138 E. C. Wheeler-Jones, M. J. Loveridge and R. I. Walton, *Electrochim Acta*, 2021, **392**, 138964.

139 D. Liang, L. Hu, L. Wang, L. Liu, S. Liang, L. Yang, N. Zhou and C. Liang, *ChemNanoMat*, 2020, **6**, 73–78.

140 Z. Song, H. Li, W. Liu, H. H. Zhang, J. Yan, Y. Tang, J. Huang, H. H. Zhang and X. Li, *Adv Mater*, 2020, **32**, 1–9.

141 M. Wei, K. Wei, M. Ichihara and H. Zhou, *Electrochem commun*, 2008, **10**, 980–983.

142 M. Liu, C. Yan and Y. Zhang, *Sci Rep*, 2015, **5**, 8326.

143 X. Wang, C. Yan, J. Yan, A. Sumboja and P. S. Lee, *Nano Energy*, 2015, **11**, 765–772.

144 S. Liu, J. Zhou, Z. Cai, G. Fang, A. Pan and S. Liang, *Nanotechnology*, 2016, **27**, 1–6.

145 J. Zhai, Y. Wu, X. Zhao and Q. Yang, *J Alloys Compd*, 2017, **715**, 275–283.

146 G. Liu, B. Jin, K. Bao, H. Xie, J. Guo, X. Ji, R. Zhang and Q. Jiang, *Int J Hydrogen Energy*, 2017, **42**, 6065–6071.

147 J. Y. Cheong, J. W. Jung, D. Y. Youn, C. Kim, S. Yu, S. H. Cho, K. R. Yoon and I. D. Kim, *J Power Sources*, 2017, **360**, 434–442.

148 S. Lou, X. Cheng, L. Wang, J. Gao, Q. Li, Y. Ma, Y. Gao, P. Zuo, C. Du and G. Yin, *J Power Sources*, 2017, **361**, 80–86.

149 Y. G. Sun, J. Y. Piao, L. L. Hu, D. S. Bin, X. J. Lin, S. Y. Duan, A. M. Cao and L. J. Wan, *J Am Chem Soc*, 2018, **140**, 9070–9073.

150 W. Wu, J. Huang, J. Li, L. Zhou, L. Cao, Y. Cheng, Y. He and Q. Li, *Electrochim Acta*, 2019, **298**, 449–458.

151 K. Kim, J. Hwang, H. Seo, H. S. Kim and J. H. Kim, *J Mater Sci*, 2019, **54**, 2493–2500.

152 P. Venkatachalam, T. Kesavan, G. Maduraiveeran, M. Kundu and M. Sasidharan, *Mater Res Express*, 2019, **6**, 35502.

153 S. Fu, Q. Yu, Z. Liu, P. Hu, Q. Chen, S. Feng, L. Mai and L. Zhou, *J Mater Chem A Mater*, 2019, **7**, 11234–11240.

154 X. Qu, B. Xing, G. Huang, H. Zhao, Z. Jiang, C. Zhang, S. W. Hong and Y. Cao, *Journal of Materials Science: Materials in Electronics*, 2021, **32**, 875–885.

155 X. Liu, G. Liu, H. Chen, J. Ma and R. Zhang, *Journal of Physics and Chemistry of Solids*, 2017, **111**, 8–11.

156 X. Liu, G. Liu, Y. Liu, R. Sun, J. Ma, J. Guo and M. Hu, *Dalton Transactions*, 2017, **46**, 10935–10940.

157 Y. Zhou, K. Liu, Y. Zhou, J. hua Ni, A. chun Dou, M. ru Su and Y. jian Liu, *J Cent South Univ*, 2020, **27**, 3625–3636.

158 H. Lu, K. Xiang, N. Bai, W. Zhou, S. Wang and H. Chen, *Mater Lett*, 2016, **167**, 106–108.

159 C. Shi, K. Xiang, Y. Zhu, W. Zhou, X. Chen and H. Chen, *Ceram Int*, 2017, **43**, 12388–12395.

160 H. Park, D. Lee and T. Song, *J Power Sources*, 2019, **414**, 377–382.

161 W. Zhang, P. Shen, L. Qian, Y. Wang, H. Arandiyan, H. Mahmoud, X. Liu, J. Wang, X. Wang, Y. Liu, H. Sun and Y. Yu, *ACS Appl Energy Mater*, 2021, **4**, 4551–4560.

162 W. van den Bergh, H. N. Lokupitiya, N. A. Vest, B. Reid, S. Guldin and M. Stefik, *Adv Funct Mater*, 2021, **31**, 1–11.

163 S. Zhang, G. Liu, W. Qiao, J. Wang and L. Ling, *J Colloid Interface Sci*, 2020, **562**, 193–203.

164 S. Li, Y. Cui, R. Kang, B. Zou, D. H. L. Ng, S. A. El-Khodary, X. Liu, J. Qiu, J. Lian and H. Li, *Chemical Communications*, 2021, **57**, 8182–8185.

165 Ö. Budak, M. Geißler, D. Becker, A. Kruth, A. Quade, R. Haberkorn, G. Kickelbick, B. J. M. Etzold and V. Presser, *ACS Appl Energy Mater*, 2020, **3**, 4275–4285.

166 S. Li, C. N. Schmidt, Q. Xu, X. Cao and G. Cao, *ChemNanoMat*, 2016, **2**, 675–680.

167 Z. Liu, W. Dong, J. Wang, C. Dong, Y. Lin, I. W. Chen and F. Huang, *iScience*, 2020, **23**, 100767.

168 C. Kim, H. J. Cho, K. R. Yoon, J. Y. Cheong, S. H. Cho, J. W. Jung, S. W. Song and I. D. Kim, *ACS Appl Mater Interfaces*, 2021, **13**, 587–596.

169 S. Deng, H. Zhu, G. Wang, M. Luo, S. Shen, C. Ai, L. Yang, S. Lin, Q. Zhang, L. Gu, B. Liu, Y. Zhang, Q. Liu, G. Pan, Q. Xiong, X. Wang, X. Xia and J. Tu, *Nat Commun*, 2020, **11**, 1–11.

170 H. Li and H. Zhou, *Chem Commun*, 2012, **48**, 1201–1217.

171 J. Lin, Y. Yuan, Q. Su, A. Pan, S. Dinesh, C. Peng, G. Cao and S. Liang, *Electrochim Acta*, 2018, **292**, 63–71.

172 J. Meng, Q. He, L. Xu, X. Zhang, F. Liu, X. Wang, Q. Li, X. Xu, G. Zhang, C. Niu, Z. Xiao, Z. Liu, Z. Zhu, Y. Zhao and L. Mai, *Adv Energy Mater*, 2019, **9**, 1–11.

173 H. Sun, L. Mei, J. Liang, Z. Zhao, C. Lee, H. Fei, M. Ding, J. Lau, M. Li, C. Wang, X. Xu, G. Hao, B. Papandrea, I. Shakir, B. Dunn, Y. Huang and X. Duan, *Science (1979)*, 2017, **356**, 599–604.

174 G. Zhao, L. Zhang, C. Li, H. Huang, X. Sun and K. Sun, *Chemical Engineering Journal*, 2017, **328**, 844–852.

175 F. Yang, W. Li, Y. Rui and B. Tang, *ChemElectroChem*, 2018, **5**, 3468–3477.

176 H. Yu, L. Xu, H. Wang, H. Jiang and C. Li, *Electrochim Acta*, 2019, **295**, 829–834.

177 E. Lim, H. Kim, C. Jo, J. Chun, K. Ku, S. Kim, H. I. Lee, I. S. Nam, S. Yoon, K. Kang and J. Lee, *ACS Nano*, 2014, **8**, 8968–8978.

178 L. P. Wang, L. Yu, R. Satish, J. Zhu, Q. Yan, M. Srinivasan and Z. Xu, *RSC Adv*, 2014, **4**, 37389.

179 E. Lim, C. Jo, H. Kim, M. H. Kim, Y. Mun, J. Chun, Y. Ye, J. Hwang, K. S. Ha, K. C. Roh, S. Yoon and J. Lee, *ACS Nano*, 2015, **9**, 7497–7505.

180 X. Wang, G. Li, R. Tjandra, X. Fan, X. Xiao and A. Yu, *RSC Adv.*, 2015, **5**, 41179–41185.

181 P. Arunkumar, A. G. Ashish, B. Babu, S. Sarang, A. Suresh, C. H. Sharma, M. Thalakulam and M. M. Shaijumon, *RSC Adv*, 2015, **5**, 59997–60004.

182 L. Wang, B. Ruan, J. Xu, H. K. Liu and J. Ma, *RSC Adv*, 2015, **5**, 36104–36107.

183 M. Y. Song, N. R. Kim, H. J. Yoon, S. Y. Cho, H. J. Jin and Y. S. Yun, *ACS Appl Mater Interfaces*, 2017, **9**, 2267–2274.

184 G. Luo, H. Li, D. Zhang, L. Gao and T. Lin, *Electrochim Acta*, 2017, **235**, 175–181.

185 G. Y. Zeng, H. Wang, J. Guo, L. M. Cha, Y. H. Dou and J. M. Ma, *Chinese Chemical Letters*, 2017, **28**, 755–758.

186 H. Yang, H. Xu, L. Wang, L. Zhang, Y. Huang and X. Hu, *Chemistry - A European Journal*, 2017, **23**, 4203–4209.

187 Q. Deng, M. Li, J. Wang, K. Jiang and Z. Hu, *Nanotechnology*, 2018, **29**, 185401.

188 D. Li, J. Shi, H. Liu, C. Liu, G. Dong, H. Zhang, Y. Yang, G. Lu and H. Wang, *Sustain Energy Fuels*, 2019, 1055–1065.

189 V. Ojha, K. Kato, M. A. Kabbani, G. Babu and P. M. Ajayan, *Chemistry Select*, 2019, **4**, 1098–1102.

190 Y. Lian, D. Wang, S. Hou, C. Ban, J. Zhao and H. Zhang, *Electrochim Acta*, 2020, **330**, 135204.

191 J. Hu, J. Li, K. Wang and H. Xia, *Electrochim Acta*, 2020, **331**, 135364.

192 S. Zhu, P. Xu, J. Liu and J. Sun, *Electrochim Acta*, 2020, **331**, 135268.

193 C. Shi, K. Xiang, Y. Zhu, X. Chen, W. Zhou and H. Chen, *Electrochim Acta*, 2017, **246**, 1088–1096.

194 C. Shi, K. Xiang, Y. Zhu, X. Chen, W. Zhou and H. Chen, *Ceram Int*, 2017, **43**, 6232–6238.

195 D. Cao, Z. Yao, J. Liu, J. Zhang and C. Li, *Energy Storage Mater*, 2018, **11**, 152–160.

196 Z. Chen, H. Li, X. Lu, L. Wu, J. Jiang and S. Jiang, *ChemElectroChem*, 2018, **5**, 1516–1524.

197 K. Kim and J. H. Kim, *J Mater Chem A Mater*, 2018, **6**, 13321–13330.

198 G. Li, X. Wang, Z. Chen, X. Ma and Y. Lu, *Electrochim Acta*, 2013, **102**, 351–357.

199 Y. Bando, Y. Kato and T. Takada, *Bull. Int. Chem. Res.*, 1976, **54**, 330–334.

200 X. Hu, W. Zhang, X. Liu, Y. Mei and Y. Huang, *Chem. Soc. Rev.*, 2015, **44**, 2376–2404.

201 A. Magnéli, G. Andersson and G. Sundkvist, *Acta Chem Scand*, 1955, 9, 1378–1381.

202 A. Magnéli, G. A. Son, B. Blomberg and L. Kihlborg, *Anal. Chem.*, 1952, **24**, 1998.

203 D. B. Rogers, R. D. Shannon, A. W. Sleight and J. L. Gillson, *Inorg Chem*, 1969, **8**, 841–849.

204 B. Marinder and A. Magneli, *Acta Chem. Scand*, 1957, 11, 1635–1640.

205 D. O. Scanlon, G. W. Watson, D. J. Payne, G. R. Atkinson, R. G. Egdell and D. S. L. Law, *Journal of Physical Chemistry C*, 2010, **114**, 4636–4645.

206 T. Qin, Q. Wang, D. Yue, H. Liu, Y. Zheng, Y. Han and C. Gao, *J Alloys Compd*, 2020, **814**, 152336.

207 K. Tang, S. A. Farooqi, X. Wang and C. Yan, *ChemSusChem*, 2019, 12, 755–771.

208 B. Mendoza-Sánchez, T. Brousse, C. Ramirez-Castro, V. Nicolosi and P. S. Grant, *Electrochim Acta*, 2013, **91**, 253–260.

209 H.-S. S. Kim, J. B. Cook, H. Lin, J. S. S. Ko, S. H. H. Tolbert, V. Ozolins and B. Dunn, *Nat Mater*, 2016, **16**, 454–460.

210 R. Liang, H. Cao and D. Qian, *Chemical Communications*, 2011, **47**, 10305.

211 Y. C. Rao, S. Yu, X. Gu and X. M. Duan, *Appl Surf Sci*, 2019, **479**, 64–69.

212 S. Bao, S. hua Luo, S. xue Yan, Z. yuan Wang, Q. Wang, J. Feng, Y. ling Wang and T. feng Yi, *Electrochim Acta*, 2019, **307**, 293–301.

213 H. Kim, S. Son, W. I. Choi, G. O. Park, Y. Kim, H. Kim, M. Jeong, H. S. Lee, J. M. Kim and W. S. Yoon, *J Power Sources*, 2018, **397**, 113–123.

214 M. Qing, Y. Meng, Y. Wang, X. Li, C. Zhou, Y. Liang, Z. Zhang, Q. Liu, Y. Guo and D. Xiao, *Electrochim Acta*, 2019, **319**, 740–752.

215 F. Zeng, L. Yang, Y. Pan, M. Xu, H. Liu, M. Yu, M. Guo and C. Yuan, *Electrochim Acta*, 2019, **325**, 134903.

216 E. Zhou, C. Wang, Q. Zhao, Z. Li, M. Shao, X. Deng, X. Liu and X. Xu, *Ceram Int*, 2016, **42**, 2198–2203.

217 X. Mu, X. Liu, K. Zhang, J. Li, J. Zhou, E. Xie and Z. Zhang, *Electronic Materials Letters*, 2016, **12**, 296–300.

218 R. Thangappan, M. Arivanandhan, S. Kalaiselvam, R. Jayavel and Y. Hayakawa, *J Inorg Organomet Polym Mater*, 2018, **28**, 50–62.

219 P. Ou, Q. Zhou, J. Li, W. Chen, J. Huang, L. Yang, J. Liao and M. Sheng, *Mater Res Express*, 2019, **6**, 95044.

220 K. Wu, J. Zhao, X. Zhang, H. Zhou and M. Wu, *J Taiwan Inst Chem Eng*, 2019, **102**, 212–217.

221 D. Van Pham, R. A. Patil, C. C. Yang, W. C. Yeh, Y. Liou and Y. R. Ma, *Nano Energy*, 2018, **47**, 105–114.

222 H. Si, L. Sun, Y. Zhang, L. Wu, Y. Zhang and Y. Zhang, *Dalton Transactions*, 2020, **49**, 1637–1645.

223 Y. Li, F. Tang, R. Wang, C. Wang and J. Liu, *ACS Appl Mater Interfaces*, 2016, **8**, 30232–30238.

224 D. Mandal, P. Routh, A. K. Mahato and A. K. Nandi, *J Mater Chem A Mater*, 2019, **7**, 17547–17560.

225 A. A. Bolzan, B. J. Kennedy and C. J. Howard, *Aust J Chem*, 1995, **48**, 1473–1477.

226 W. H. Baur, *Acta Crystallogr*, 1956, **9**, 515–520.

227 A. Kim, E. Park, H. Lee and H. Kim, *J Alloys Compd*, 2016, **681**, 301–306.

228 D. W. Murphy, F. J. Di Salvo, J. N. Carides and J. V. Waszczak, *Mater Res Bull*, 1978, **13**, 1395–1402.

229 D. E. Cox, R. J. Cava, D. B. McWhan and D. W. Murphy, *Journal of Physics and Chemistry of Solids*, 1982, **43**, 657–666.

230 J. R. Dahn and W. R. McKinnon, *Solid State Ion*, 1987, **23**, 1–7.

231 J. Auborn and Y. Barberio, *Journal of Electrochemical Society*, 1987, 638.

232 C. -K. Huang, S. Crouch-Baker and R. A. Huggins, *J Electrochem Soc*, 1988, **135**, 408–412.

233 U. Kumar Sen, A. Shaligram and S. Mitra, *ACS Appl Mater Interfaces*, 2014, **6**, 14311–14319.

234 Y. Zhu, X. Ji, S. Cheng, Z. Y. Chern, J. Jia, L. Yang, H. Luo, J. Yu, X. Peng, J. Wang, W. Zhou and M. Liu, *ACS Nano*, 2019, **13**, 9091–9099.

235 H.-S. Kim, J. B. Cook, S. H. Tolbert and B. Dunn, *J Electrochem Soc*, 2015, **162**, A5083–A5090.

236 Y. Zhou and C. Geng, *Nanotechnology*, 2017, **28**, 105402.

237 X. Liu, J. Yang, W. Hou, J. Wang and Y. Nuli, *ChemSusChem*, 2015, **8**, 2621–2624.

238 J. Barker, M. Y. Saidi and J. L. Swoyer, *Electrochemical and Solid-State Letters*, 2003, **6**, 6–11.

239 D. Mikhailova, N. N. Bramnik, K. G. Bramnik, P. Reichel, S. Oswald, A. Senyshyn, D. M. Trots and H. Ehrenberg, *Chemistry of Materials*, 2011, **23**, 3429–3441.

240 P. G. Bruce, B. Scrosati and J. M. Tarascon, *Angewandte Chemie - International Edition*, 2008, 47, 2930–2946.

241 J. H. Ku, Y. S. Jung, K. T. Lee, C. H. Kim and S. M. Oh, *J Electrochem Soc*, 2009, **156**, A688.

242 H. J. Zhang, J. Shu, K. X. Wang, X. T. Chen, Y. M. Jiang, X. Wei and J. S. Chen, *J Mater Chem A Mater*, 2014, **2**, 80–86.

243 X. Zhao, M. Cao, B. Liu, Y. Tian and C. Hu, *J Mater Chem*, 2012, **22**, 13334–13340.

244 B. Guo, X. Fang, B. Li, Y. Shi, C. Ouyang, Y. S. Hu, Z. Wang, G. D. Stucky and L. Chen, *Chem Mater*, 2012, **24**, 457–463.

245 J. K. Shon, H. S. Lee, G. O. Park, J. Yoon, E. Park, G. S. Park, S. S. Kong, M. Jin, J. M. Choi, H. Chang, S. Doo, J. M. Kim, W. S. Yoon, C. Pak, H. Kim and G. D. Stucky, *Nat Commun*, 2016, **7**, 1–9.

246 C. Xia, Y. Zhou, D. B. Velusamy, A. A. Farah, P. Li, Q. Jiang, I. N. Odeh, Z. Wang, X. Zhang and H. N. Alshareef, *Nano Lett*, 2018, **18**, 1506–1515.

247 Y. Liang, S. Yang, Z. Yi, J. Sun and Y. Zhou, *Mater Chem Phys*, 2005, **93**, 395–398.

248 J. Besnardiere, C. Surcin, V. Buissette, T. Le Mercier, M. Morcrette, D. Portehault and S. Cassaignon, *Particle & Particle Systems Characterization*, 2015, **32**, 251–257.

249 A. Manthiram, *J Electrochem Soc*, 1996, **143**, L143.

250 J. H. Ku, J. H. Ryu, S. H. Kim, O. H. Han and S. M. Oh, *Adv Funct Mater*, 2012, **22**, 3658–3664.

251 T. L. Christiansen, E. D. Bøjesen, M. Juelsholt, J. Etheridge and K. M. Ø. Jensen, *ACS Nano*, 2019, **13**, 8725–8735.

252 Y. Liu, H. Zhang, P. Ouyang and Z. Li, *Electrochim Acta*, 2013, **102**, 429–435.

253 Y. Liu, H. Zhang, P. Ouyang, W. Chen and Z. Li, *Mater Res Bull*, 2014, **50**, 95–102.

254 E. Zhou, C. Wang, M. Shao, X. Deng and X. Xu, *Ceram Int*, 2017, **43**, 760–765.

255 J. Besnardiere, X. Petrissans, C. Surcin, V. Buissette, T. Le Mercier, M. Morcrette, D. Portehault and S. Cassaignon, *RSC Adv*, 2014, **4**, 21208–21215.

256 X. Zhang, X. Zeng, M. Yang and Y. Qi, *Eur J Inorg Chem*, 2014, 352–356.

257 L. C. Yang, Q. S. Gao, Y. Tang, Y. P. Wu and R. Holze, *J Power Sources*, 2008, **179**, 357–360.

258 L. C. Yang, Q. S. Gao, Y. H. Zhang, Y. Tang and Y. P. Wu, *Electrochem commun*, 2008, **10**, 118–122.

259 Y. Shi, B. Guo, S. A. Corr, Q. Shi, Y. S. Hu, K. R. Heier, L. Chen, R. Seshadri and G. D. Stucky, *Nano Lett*, 2009, **9**, 4215–4220.

260 Y. Sun, X. Hu, J. C. Yu, Q. Li, W. Luo, L. Yuan, W. Zhang and Y. Huang, *Energy Environ Sci*, 2011, **4**, 2870–2877.

261 D. Koziej, M. D. Rossell, B. Ludi, A. Hintennach, P. Novák, J. D. Grunwaldt and M. Niederberger, *Small*, 2011, **7**, 377–387.

262 A. Bhaskar, M. Deepa and T. Narasinga Rao, *ACS Appl Mater Interfaces*, 2013, **5**, 2555–2566.

263 X. Zhang, X. Song, S. Gao, Y. Xu, X. Cheng, H. Zhao and L. Huo, *J Mater Chem A Mater*, 2013, **1**, 6858–6864.

264 L. Zeng, C. Zheng, C. Deng, X. Ding and M. Wei, *ACS Appl Mater Interfaces*, 2013, **5**, 2182–2187.

265 X. Liu, W. Ji, J. Liang, L. Peng and W. Hou, *Physical Chemistry Chemical Physics*, 2014, **16**, 20570–20577.

266 Y. Liu, H. Zhang, P. Ouyang, W. Chen, Y. Wang and Z. Li, *J Mater Chem A Mater*, 2014, **2**, 4714–4721.

267 W. Zhai, Y. Xu, X. Cheng, S. Gao, X. Zhang, H. Zhao and L. Huo, *Mater Lett*, 2015, **145**, 287–290.

268 C. Zhang, P. Zhang, J. Dai, H. Zhang, A. Xie and Y. Shen, *Ceram Int*, 2016, **42**, 3618–3624.

269 W. Wang, G. Shi, H. Cai, C. Zhao, J. Wu, Y. Yu, J. Hu, Z. Fang, J. Yan and B. Liu, *J Alloys Compd*, 2019, **792**, 191–202.

270 W. Tang, C. X. Peng, C. T. Nai, J. Su, Y. P. Liu, M. V. V. Reddy, M. Lin and K. P. Loh, *Small*, 2015, **11**, 2446–2453.

271 A. Bhaskar, M. Deepa, T. N. Rao and U. V. Varadaraju, *J Power Sources*, 2012, **216**, 169–178.

272 Y. Che, X. Zhu, J. Li, J. Sun, Y. Liu, C. Jin and C. Dong, *RSC Adv*, 2016, **6**, 106230–106236.

273 S. B. Patil, B. Kishore, V. Reddy and N. Ganganagappa, *ChemistrySelect*, 2018, **3**, 13289–13296.

274 S. Petnikota, K. W. Teo, L. Chen, A. Sim, S. K. Marka, M. V. Reddy, V. V. S. S. Srikanth, S. Adams and B. V. R. Chowdari, *ACS Appl Mater Interfaces*, 2016, **8**, 10884–10896.

275 H. Gao, C. L. Liu, Y. Liu, Z. H. Liu and W. S. Dong, *Mater Chem Phys*, 2014, **147**, 218–224.

276 H. Fu, Z. Xu, T. Wang, K. Li, X. Shen, J. Li and J. Huang, *J Electrochem Soc*, 2018, **165**, A439–A447.

277 W. Cho, J. H. Song, J. H. Kim, G. Jeong, E. Y. Lee and Y. J. Kim, *J Appl Electrochem*, 2012, **42**, 909–915.

278 Y. Sun, X. Hu, W. Luo and Y. Huang, *ACS Nano*, 2011, **5**, 7100–7107.

279 Y. Yao, Z. Chen, R. Yu, Q. Chen, J. Zhu, X. Hong, L. Zhou, J. Wu and L. Mai, *ACS Appl Mater Interfaces*, 2020, **12**, 40648–40654.

280 Y. Zhou, H. Xie, C. Wang, Q. He, Q. Liu, Z. Muhammad, Y. A. Haleem, Y. Sang, S. Chen and L. Song, *Journal of Physical Chemistry C*, 2017, **121**, 15589–15596.

281 X. Liu, D. Wu, W. Ji and W. Hou, *J Mater Chem A Mater*, 2015, **3**, 968–972.

282 J. Ma, J. Fu, M. Niu and R. Quhe, *Carbon N Y*, 2019, **147**, 357–363.

283 Q. Zhang, D. Zhu, X. Li and Y. Zhang, *RSC Adv*, 2020, **10**, 43312–43318.

284 L. C. Yang, W. Sun, Z. W. Zhong, J. W. Liu, Q. S. Gao, R. Z. Hu and M. Zhu, *J Power Sources*, 2016, **306**, 78–84.

285 C. Wang, L. Sun, B. Tian, Y. Cheng and L. Wang, *Energy and Environmental Materials*, 2020, 1–8.

286 Y. Yun, Z. Shi, J. Shao, Q. Qu, Y. Gao, Z. Chen, Y. Chen and H. Zheng, *ChemNanoMat*, 2018, **4**, 1247–1253.

287 J. Ni, Y. Zhao, L. Li and L. Mai, *Nano Energy*, 2015, **11**, 129–135.

288 S. Wang, Y. Zhao, C. Li, X. Zhang and Y. Chen, *J Alloys Compd*, 2017, **695**, 1285–1293.

289 X. Ji, P. Subramanya Herle, Y. Rho and L. F. Nazar, *Chemistry of Materials*, 2007, **19**, 374–383.

290 Z. Wang, J. S. Chen, T. Zhu, S. Madhavi and X. W. Lou, *Chemical Communications*, 2010, **46**, 6906–6908.

291 Q. Gao, L. Yang, X. Lu, J. Mao, Y. Zhang, Y. Wu and Y. Tang, *J Mater Chem*, 2010, **20**, 2807–2812.

292 W. Luo, X. Hu, Y. Sun and Y. Huang, *Physical Chemistry Chemical Physics*, 2011, **13**, 16735–16740.

293 L. Zhou, H. Bin Wu, Z. Wang and X. W. Lou, *ACS Appl Mater Interfaces*, 2011, **3**, 4853–4857.

294 Q. Tang, Z. Shan, L. Wang and X. Qin, *Electrochim Acta*, 2012, **79**, 148–153.

295 K. H. Seng, G. D. Du, L. Li, Z. X. Chen, H. K. Liu and Z. P. Guo, *J Mater Chem*, 2012, **22**, 16072–16077.

296 J. P. Jegal, H. K. Kim, J. S. Kim and K. B. Kim, *J Electroceram*, 2013, **31**, 218–223.

297 S. Hu, F. Yin, E. Uchaker, W. Chen, M. Zhang, J. Zhou, Y. Qi and G. Cao, *Journal of Physical Chemistry C*, 2014, **118**, 24890–24897.

298 Z. X. Huang, Y. Wang, Y. G. Zhu, Y. Shi, J. I. Wong and H. Y. Yang, *Nanoscale*, 2014, **6**, 9839–9845.

299 K. Palanisamy, Y. Kim, H. Kim, J. M. Kim and W. S. Yoon, *J Power Sources*, 2015, **275**, 351–361.

300 X. Liu, H. Xu, Y. Huang and X. Hu, *Physical Chemistry Chemical Physics*, 2016, **18**, 19832–19837.

301 L. Zeng, X. Huang, X. Chen, C. Zheng, R. Liu, G. Chen, Q. Qian, Q. Chen and M. Wei, *RSC Adv*, 2016, **6**, 105558–105564.

302 Y. Wang, L. Yu, X. Wen and D. Lou, *Angew. Chem.*, 2016, **128**, 14888–14892.

303 Z. Xu, K. Yao, H. Fu, X. Shen, X. Duan, L. Cao, J. Huang and H. Wang, *Global Challenges*, 2017, **1**, 1700050.

304 P. Wang, Y. Zhang, Y. Yin, L. Fan, N. Zhang and K. Sun, *Chemical Engineering Journal*, 2018, **334**, 257–263.

305 L. Sun, C. Wang, X. Wang and L. Wang, *Small*, 2018, **14**, 1–8.

306 J. Pei, H. Geng, H. Ang, L. Zhang, H. Wei, X. Cao, J. Zheng and H. Gu, *Nanotechnology*, 2018, **29**, 295404.

307 X. Zhang, J. G. Wang, W. Hua, H. Liu and B. Wei, *J Alloys Compd*, 2019, **787**, 301–308.

308 W. Zhang, B. Wang, H. Luo, F. Jin, T. Ruan and D. Wang, *J Alloys Compd*, 2019, **803**, 664–670.

309 K. Zhang, X. Chen, G. Gao, Z. Wu, J. Xiang, X. Li and G. Guan, *RSC Adv*, 2019, **9**, 37556–37561.

310 Y. Feng and H. Liu, *Nanotechnology*, 2019, **30**, 315602.

311 J. B. Boland, A. Harvey, R. Tian, D. Hanlon, V. Vega-Mayoral, B. Szydlowska, A. Griffin, T. Stimpel-Lindner, S. Jaskaniec, V. Nicolosi, G. Duesberg and J. N. Coleman, *Nanoscale Adv*, 2019, **1**, 1560–1570.

312 H. Sun, Y. Zhang, H. Liu, X. Zhang and J. G. Wang, *J Alloys Compd*, 2019, **787**, 45–52.

313 T. Rasheed, F. Nabeel, A. Naveed, S. Majeed and T. A. Sherazi, *Mater Today Commun*, 2019, **21**, 100694.

314 J. Huo, Y. Xue, Y. Liu, Y. Ren and G. Yue, *Journal of Electroanalytical Chemistry*, 2020, **857**, 113751.

315 H. Wang, X. Jiang, Y. Wang, X. Yang, Y. Chai, Z. Yu, M. Xu and R. Yuan, *Powder Technol*, 2021, **377**, 281–288.

316 Y. Feng and H. Liu, *Appl Surf Sci*, 2021, **538**, 147992.

317 X. Zhang, M. Gao, W. Wang, B. Liu and X. Li, *Polymers (Basel)*, 2021, **13**, 1–13.

318 G. S. Zakharova, L. Singer, Z. A. Fattakhova, S. Wegener, E. Thauer, Q. Zhu, E. V. Shalaeva and R. Klingeler, *J Alloys Compd*, 2021, **863**, 158353.

319 D. Wu, F. Ge, S. Xing, W. Ji and L. Peng, *Ionics (Kiel)*, 2021, **27**, 4713–4720.

320 H. J. Zhang, K. X. Wang, X. Y. Wu, Y. M. Jiang, Y. B. Zhai, C. Wang, X. Wei and J. S. Chen, *Adv Funct Mater*, 2014, **24**, 3399–3404.

321 W. Devina, J. Hwang and J. Kim, *Chem Eng J*, 2018, **345**, 1–12.

322 J. Liu, S. Tang, Y. Lu, G. Cai, S. Liang, W. Wang and X. Chen, *Energy Environ Sci*, 2013, **6**, 2691–2697.

323 T. Stephenson, Z. Li, B. Olsen and D. Mitlin, *Energy Environ Sci*, 2014, **7**, 209–231.

324 Z. Xu, T. Wang, L. Kong, K. Yao, H. Fu, K. Li, L. Cao, J. Huang and Q. Zhang, *Part Part Syst Charact*, 2017, **34**, 1600223.

325 Z. Xu, H. Wang, Z. Li, A. Kohandehghan, J. Ding, J. Chen, K. Cui and D. Mitlin, *J Phys Chem C*, 2014, **118**, 18387–18396.

326 H. Lu, K. Tian, L. Bu, X. Huang, X. Li, Y. Zhao, F. Wang, J. Bai, L. Gao and J. Zhao, *Journal of Energy Chemistry*, 2021, **55**, 449–458.

327 W. Yang, L. Han, X. Liu, L. Hong and M. Wei, *J Colloid Interface Sci*, 2021, **588**, 804–812.

328 Z. Qin, X. Liu, Z. Huang, R. Sun, Z. Li, H. Fan and S. Lu, *Acta Metallurgica Sinica (English Letters)*, 2021, **34**, 425–434.

329 Z. Rong, C. Fang, Z. Zhang, W. Miao, X. Li, J. Liang, W. Yang, Y. Wang, X. Guo, Y. Jung and X. Dong, *Journal of Materiomics*, 2021, **7**, 498–507.

330 L. Duan and X. Li, *Synth Met*, 2021, **272**, 116672.

331 M. Yoshimura and K. Byrappa, *J Mater Sci*, 2008, **43**, 2085–2103.

332 K. Byrappa and M. Yoshimura, in *Handbook of Hydrothermal Technology*, Noyes Publications, 2001, pp. 1–52.

333 J. -M Jehng and I. E. Wachs, *Journal of Raman Spectroscopy*, 1991, **22**, 83–89.

334 T. Fuchigami and K. Kakimoto, *J Mater Res*, 2017, **32**, 3326–3332.

335 B. Basavalingu and J. Tareen, *Curr Sci*, 1991, **61**, 473–475.

336 B. H. Toby and R. B. Von Dreele, *J Appl Crystallogr*, 2013, **46**, 544–549.

337 Malvern Panalytical Ltd., *Technical Note MRK656-01*, 2018, 1–8.

338 F. Rouquerol, J. Rouquerol, K. S. W. Sing, P. Llewellyn and G. Maurin, *Adsorption by powders and porous solids*, Academic Press, London, 2014.

339 C. Lastoskie, K. E. Gubbins and N. Quirke, *J. Phys. Chem*, 1993, **97**, 4786–4796.

340 P. Tarazona, U. Marini Bettolo Marconi, R. Evans and H. H. Wills, *Mol Phys*, 1987, **60**, 573–595.

341 R. I. Smith, S. Hull, M. G. Tucker, H. Y. Playford, D. J. McPhail, S. P. Waller and S. T. Norberg, *Review of Scientific Instruments*, 2019, **90**, 115101.

342 H. Y. Playford, M. G. Tucker and C. L. Bull, *J Appl Crystallogr*, 2017, **50**, 87–95.

343 A. K. Soper, *GudrunN and GudrunX: Programs for Correcting Raw Neutron and X-ray Diffraction Data to Differential Scattering Cross Section*, 2011.

344 K. Kato and S. Tamura, *Acta Crystallogr B*, 1975, **31**, 673–677.

345 C. L. Farrow, P. Juhas, J. W. Liu, D. Bryndin, E. S. Boin, J. Bloch, T. Proffen and S. J. L. Billinge, *Journal of Physics Condensed Matter*, 2007, **19**, 335219.

346 M. J. Lain, J. Brandon and E. Kendrick, *Batteries*, 2019, **5**, 1–11.

347 Q. Huang, M. J. Loveridge, R. Genieser, M. J. Lain and R. Bhagat, *Sci Rep*, 2018, **8**, 1–9.

348 D. K. Kang and H. C. Shin, *Journal of Solid State Electrochemistry*, 2007, **11**, 1405–1410.

349 W. Choi, H. C. Shin, J. M. Kim, J. Y. Choi and W. S. Yoon, *Journal of Electrochemical Science and Technology*, 2020, **11**, 1–13.

350 M. E. Orazem and B. Tribollet, in *Electrochemical Impedance Spectroscopy*, John Wiley& Sons, Inc., 2008, pp. 154–162.

351 E. Barsoukou and J. R. Macdonald, in *Impedance Spectroscopy*, Kluwer Academic Publishers, Boston, Third., 2006, pp. 1–16.

352 H. T. Kreissl, M. M. J. Li, Y. K. Peng, K. Nakagawa, T. J. N. Hooper, J. V. Hanna, A. Shepherd, T. S. Wu, Y. L. Soo and S. C. E. Tsang, *J Am Chem Soc*, 2017, **139**, 12670–12680.

353 E. A. Boucher, *J Mater Sci*, 1976, **11**, 1734–1750.

354 R. F. Ali, A. H. Nazemi and B. D. Gates, *Cryst Growth Des*, 2017, **17**, 4637–4646.

355 V. V. Atuchin, I. E. Kalabin, V. G. Kesler and N. V. Pervukhina, *J Electron Spectros Relat Phenomena*, 2005, **142**, 129–134.

356 O. Aalling-Frederiksen, M. Juelsholt, A. S. Anker and K. M. Ø. Jensen, *Nanoscale*, 2021, **13**, 8087–8097.

357 A. Miura, T. Takei, N. Kumada, S. Wada, E. Magome, C. Moriyoshi and Y. Kuroiwa, *Inorg Chem*, 2013, **52**, 9699–9701.

358 J. Li, W. W. Liu, H. M. Zhou, Z. Z. Liu, B. R. Chen and W. J. Sun, *Rare Metals*, 2018, **37**, 118–122.

359 H. D. Asfaw, C. W. Tai, L. Nyholm and K. Edström, *ChemNanoMat*, 2017, **3**, 646–655.

360 A. Miura, T. Takei, N. Kumada, S. Wada, E. Magome, C. Moriyoshi and Y. Kuroiwa, *Inorg Chem*, 2013, **52**, 9699–9701.

361 B. E. Conway and W. G. Pell, *Journal of Solid State Electrochemistry*, 2003, **7**, 637–644.

362 K. J. Range, K. Bauer and U. Klement, *Acta Crystallogr C*, 1990, **46**, 2007–2009.

363 R. Benchrifa, M. Leblanc and R. De Pape, *ChemInform*, 1990, **21**, 593–601.

364 B. G. Brandt, a. C. Skapski, E. Thom, E. Stoll, G. Eriksson, R. Blinc, S. Paušak, L. Ehrenberg and J. Dumanović, *Acta Chem Scand*, 1967, 21, 661–672.

365 M. Kumar Trivedi, *International Journal of Materials Science and Applications*, 2015, **4**, 354.

366 M. Ghedira, H. Vincent, M. Marezio, J. Marcus and G. Furcaudot, *J Solid State Chem*, 1985, **56**, 66–73.

367 N. Dukstiene, D. Sinkeviciute and A. Guobiene, *Central European Journal of Chemistry*, 2012, **10**, 1106–1118.

368 H. Föppl, *ZAAC - Journal of Inorganic and General Chemistry*, 1957, **291**, 12–50.

369 A. Watanabe, G. Kobayashi, N. Matsui, M. Yonemura, A. Kubota, K. Suzuki, M. Hirayama and R. Kanno, *Electrochemistry*, 2017, **85**, 88–92.

370 G. A. Seisenbaeva, M. Sundberg, M. Nygren, L. Dubrovinsky and V. G. Kessler, *Mater Chem Phys*, 2004, **87**, 142–148.

371 B. G. Brandt, Stockholm University, 1971.

372 M. Schönleber, C. Uhlmann, P. Braun, A. Weber and E. Ivers-Tiffée, *Electrochim Acta*, 2017, **243**, 250–259.

373 C. Zener, *J Appl Phys*, 1949, **20**, 950–953.

374 L. A. ODell, S. L. P. Savin, A. V Chadwick and M. E. Smith, *J. Phys. Chem. C*, 2007, **111**, 13740–13746.

375 W. L. Bragg, *Philosophical Magazine*, 1914, 355–360.

9 Appendix

Table A. 1- Average electrode properties for electrodes used in this work

Material family	Material	Formulation	Active Material Mass Loading ($mgcm^{-2}$)	Total Coating Density ($mgcm^{-3}$)	Calculated porosity (%)
Nb_2O_5	Anisotropically Crystalline	70:20:10	1.1 ±0.3	520	85
	Orthorhombic	70:20:10	0.9 ±0.1	470	87
	Monoclinic	70:20:10	0.6 ±0.3	350	90
MoO_2	As Synthesised	80:10:10	2.9 ±0.5	800	85
	Heat-treated	80:10:10	1.4 ±0.06	600	89
	MoO_2/Carbon composite	80:10:10	0.8 ±0.03	370	92
Nb_2O_5/MoO_2 composites	Nb Rich	70:20:10	1 .2 ±0.2	520	90
	Mo Rich		2.4 ±0.5	850	77
	50/50 mix	70:20:10	1.7 ±0.3	680	84

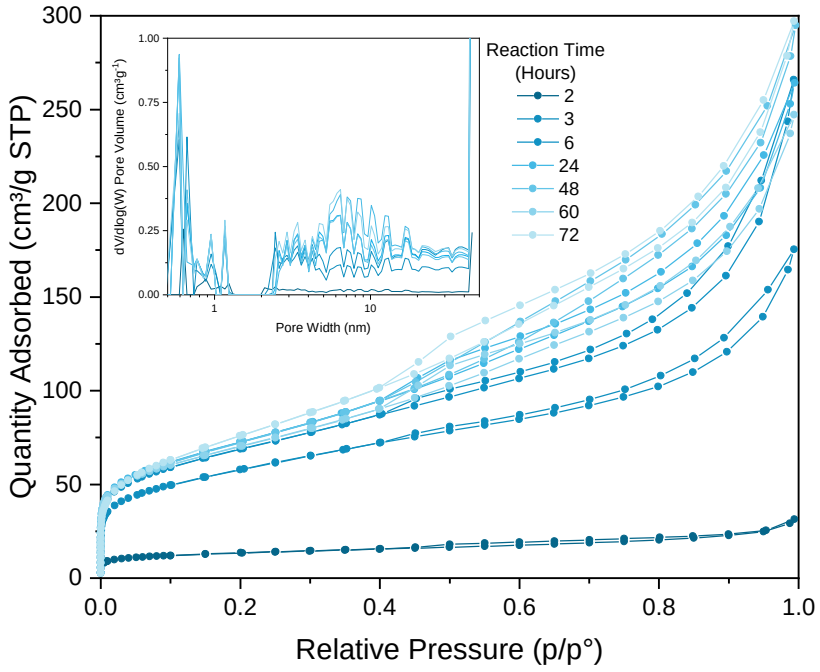

Figure A.1 – N_2 Porosity isotherm for Nb_2O_5 synthesised at increasing reaction times. Inset is the pore volume distribution of respective samples.

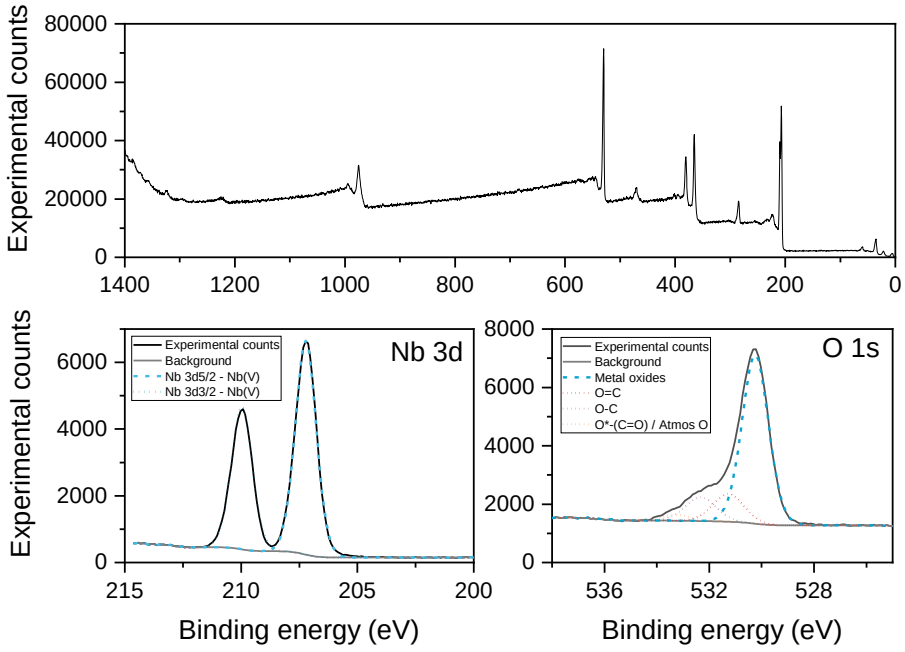

Figure A.2– XPS of as-synthesised anisotropically crystalline material, showing the Nb 3d and O 1s.

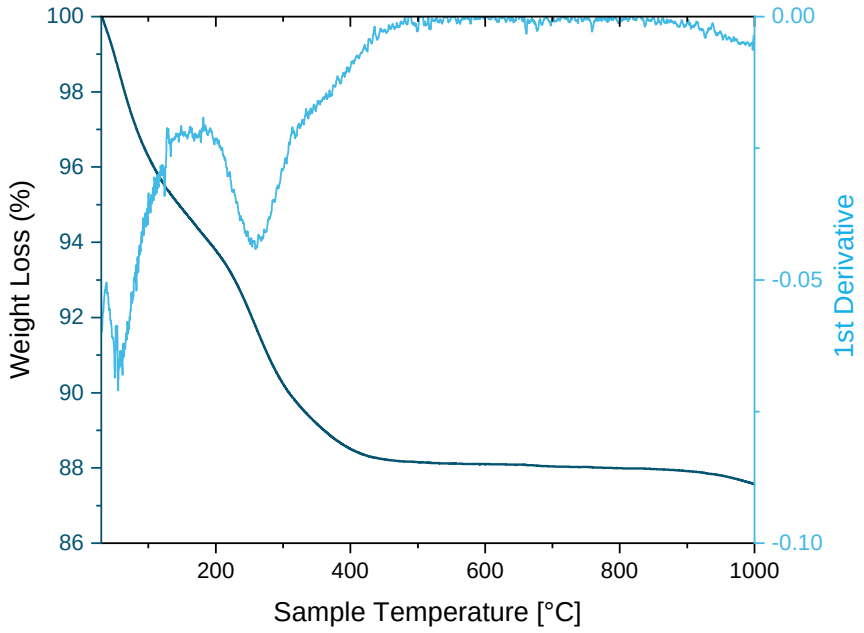

Figure A.3 - TGA and first derivative curve (light blue) of the anisotropically crystalline Nb_2O_5 30 to 1000 °C in N_2 at a ramp rate of 10 °C per min.

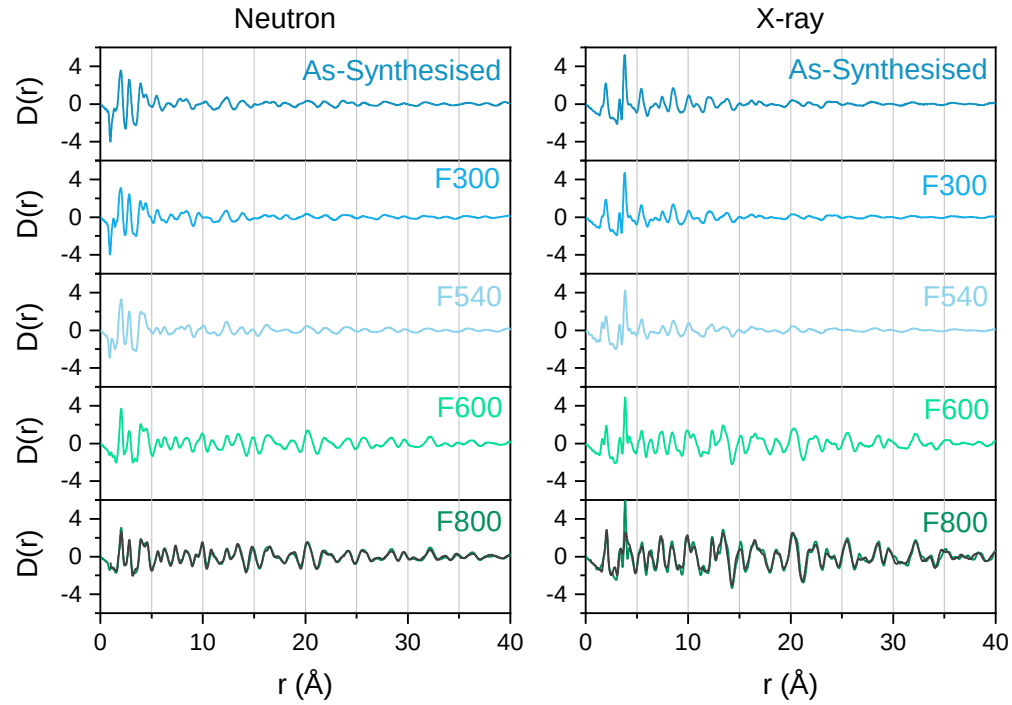

Figure A.4 – Full neutron (left) and X-ray (right) PDFs for niobium pentoxides with increasing heat-treatment to 800 °C.

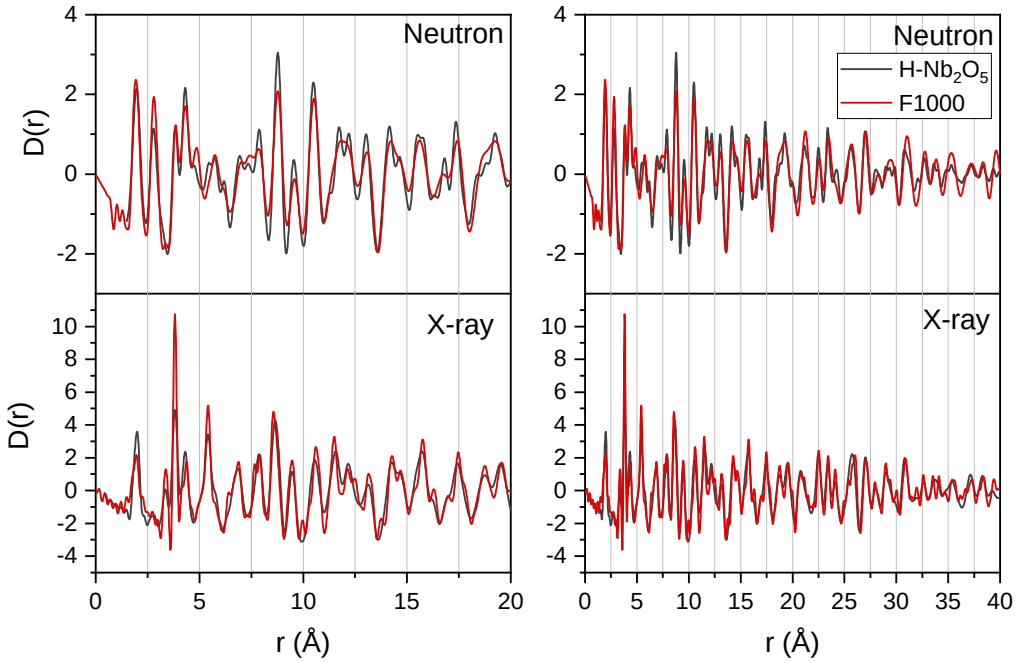

Figure A.5 – Local (left) and full (right) neutron (top) and X-ray (bottom) PDFs for niobium pentoxide heat-treatment to 1000 °C, overlaid with the ideal H-Nb_2O_5 PDFs in black.[69]

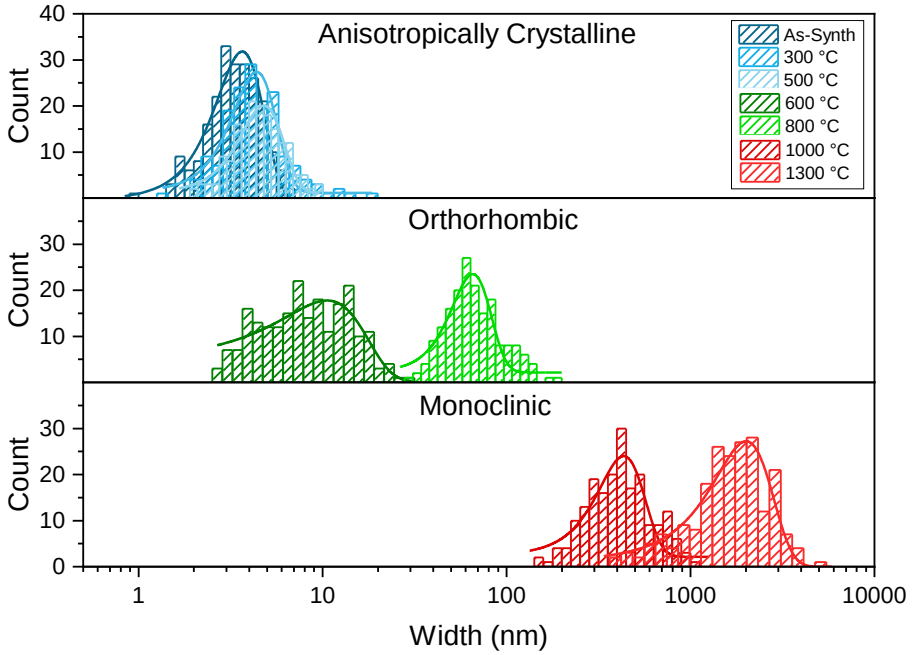

Figure A.6 – Particle width measurements of all Nb_2O_5 materials with various heat-treatment temperatures, split via the crystal structure of the material anisotropically crystalline, orthorhombic, and monoclinic (top-bottom).

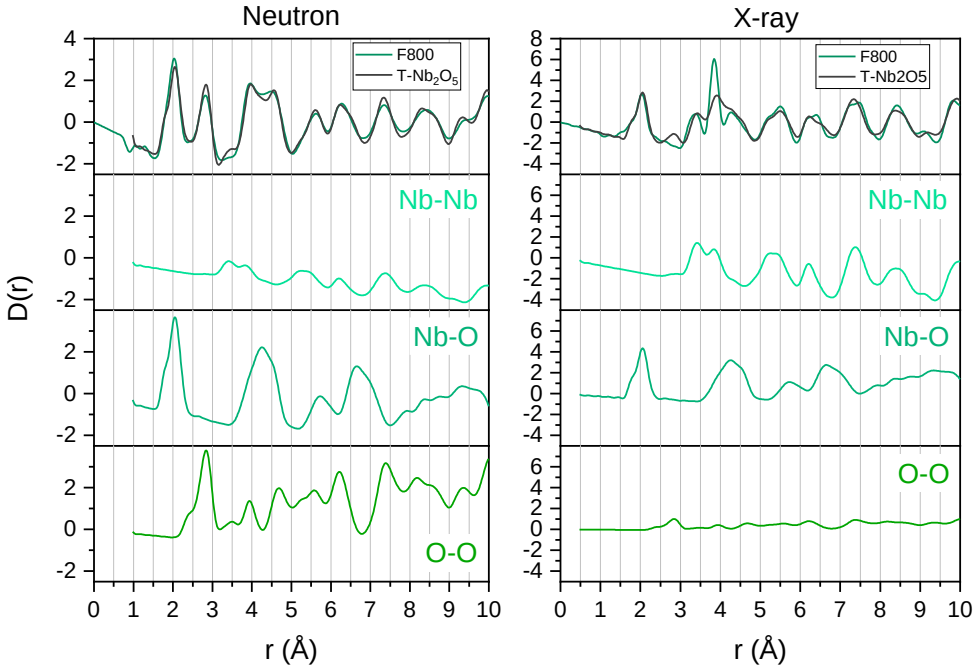

Figure A.7– Neutron (left) and X-ray (right) PDFs of 800 °C heat-treated Nb_2O_5 with the ideal PDF of T-Nb_2O_5 and corresponding partials of Nb-Nb, Nb-O and O-O pairs.[344]

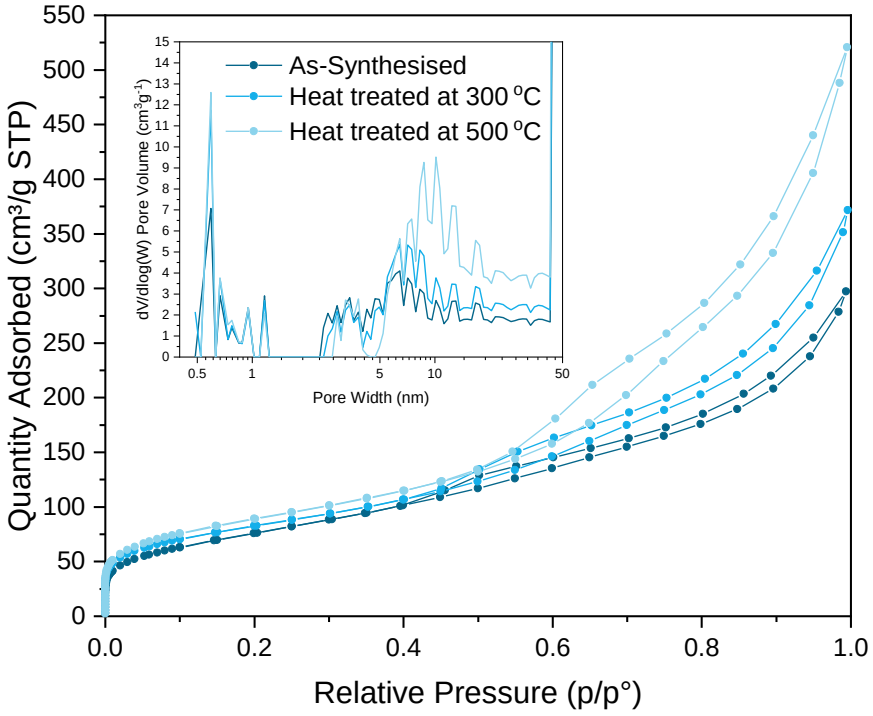

Figure A.8 - N_2 Porosity isotherm for anisotropically crystalline Nb_2O_5 (Inset) Pore volume distribution of respective samples.

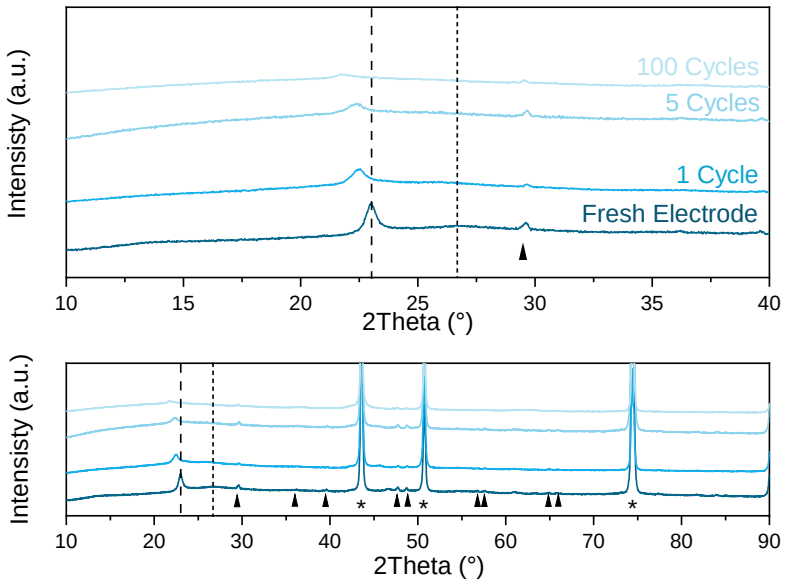

Figure A.9 - Ex-situ XRD of as-synthesised anisotropically crystalline Nb_2O_5 at increasing cycles, with Cu peaks denoted with Asterix and sample holder peaks noted by arrows (bottom). Zoomed area of XRD showing main peaks of the material, with crystalline peak noted by the dashed line and amorphous peak denoted by dotted line (top).

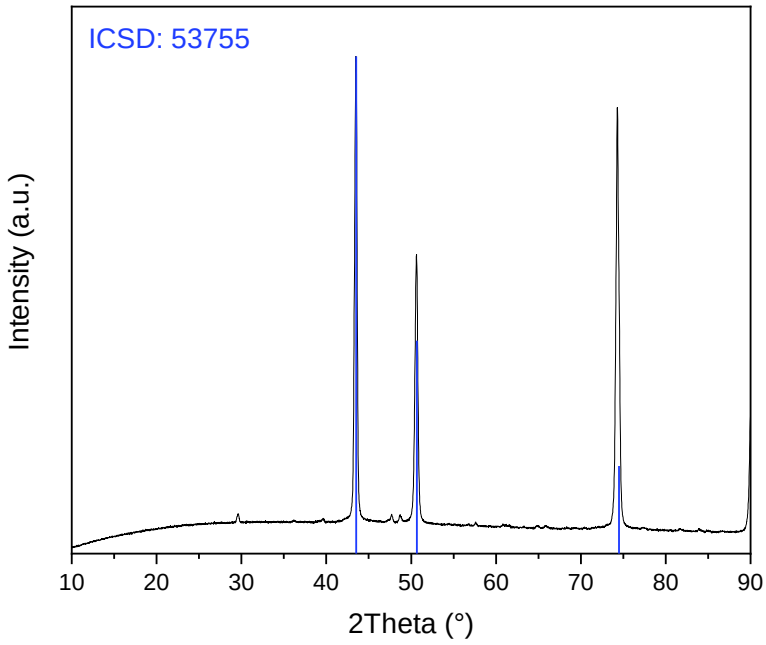

Figure A.10 – X-ray diffraction pattern of copper current collector used for electrode creation on a silicon sample holder, indexed with ICSD 53755, (blue sticks). [375]

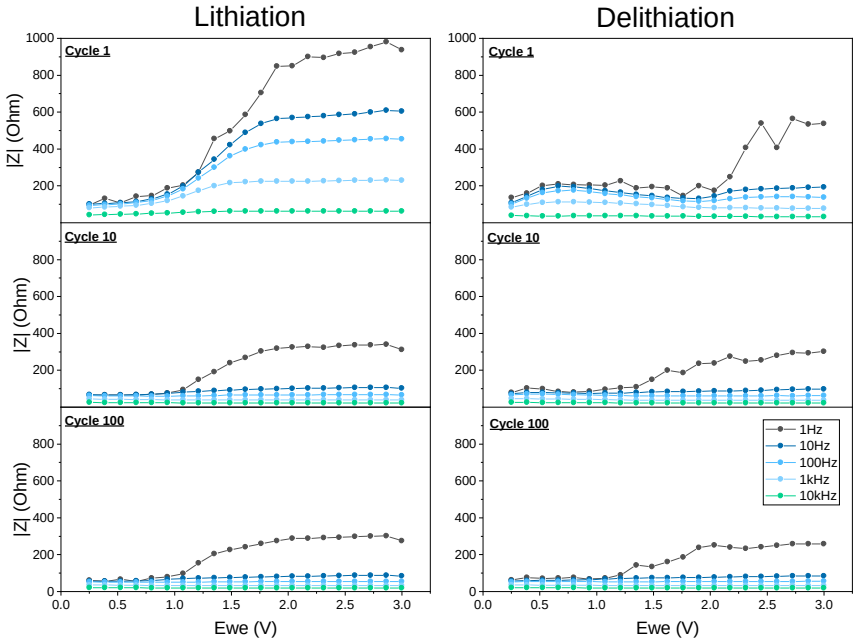

Figure A.11 - SPEIS for cycles from 1 to 100 cycles in a range of 1 Hz to 10kHz for as-synthesised anisotropically crystalline Nb_2O_5.

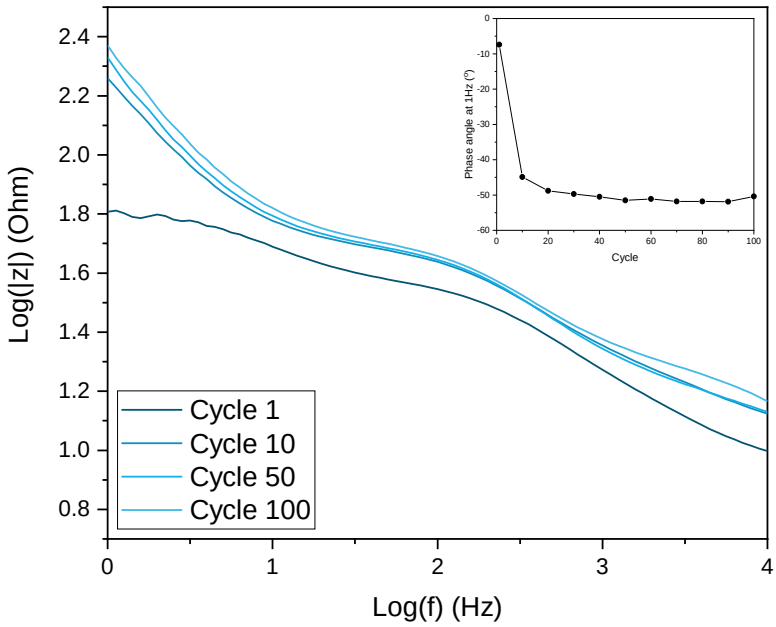

Figure A.12 – Magnitude Bode plot for EIS taken at 2.5 V voltage on delithiation cycle at cycle 1, 10, 50, 100 for as-synthesised Nb_2O_5. (Inset) Phase angle at 1 Hz versus cycle number.

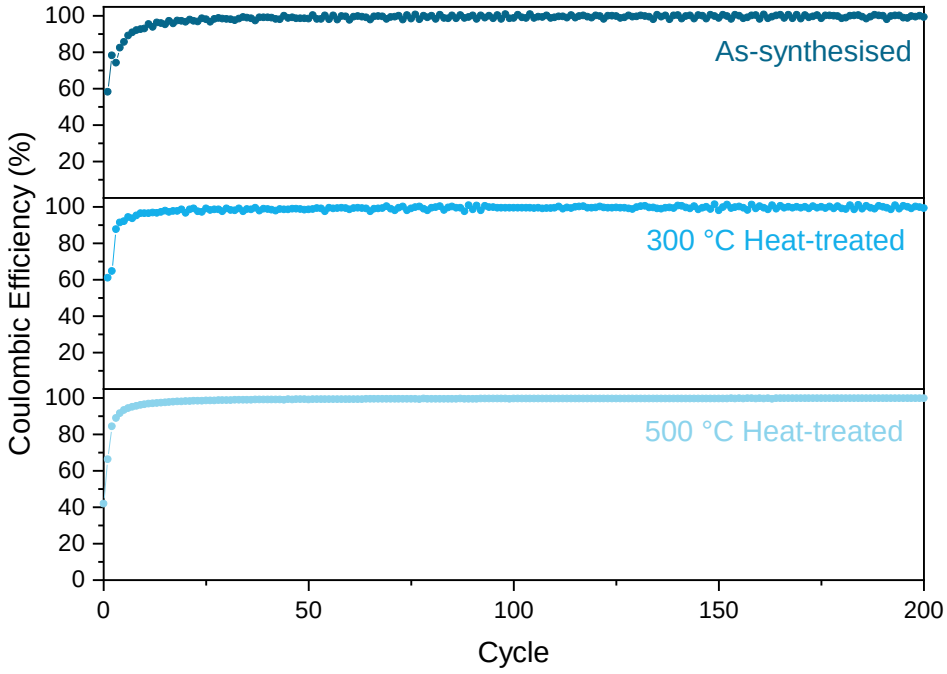

Figure A.13 – Coulombic efficiency of anisotropically crystalline materials cycled between 0.25-3.0V at 1C after a C/20 formation cycle.

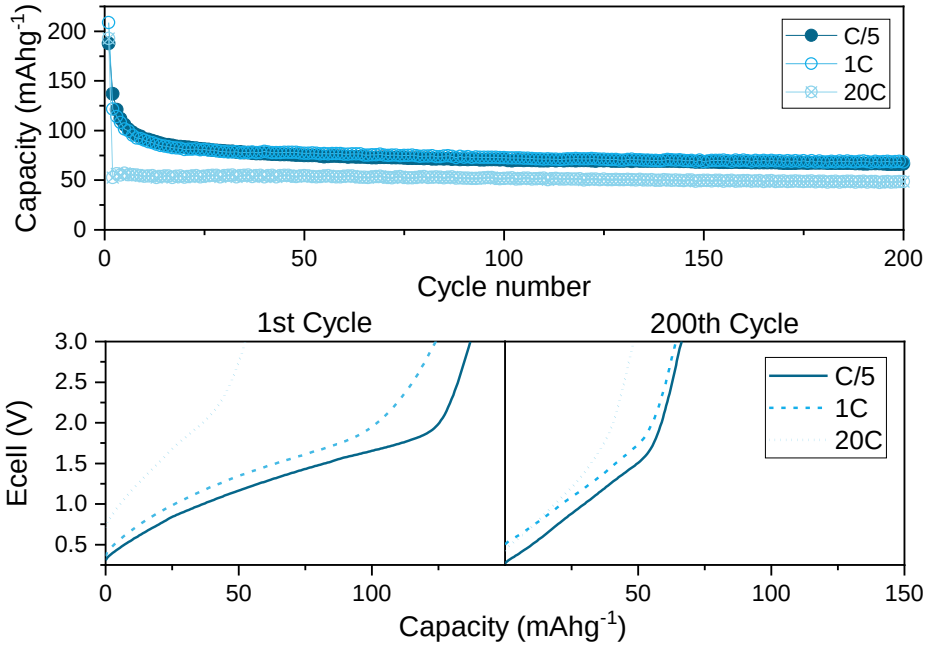

Figure A.14 – (top) Galvanostatic cycling at increasing rate over 200 cycles, (Bottom) charge profiles at the different rates from 1st and 200th cycle, all in 0.25-3.0 V window for 300 °C heat-treated anisotropically crystalline Nb_2O_5.

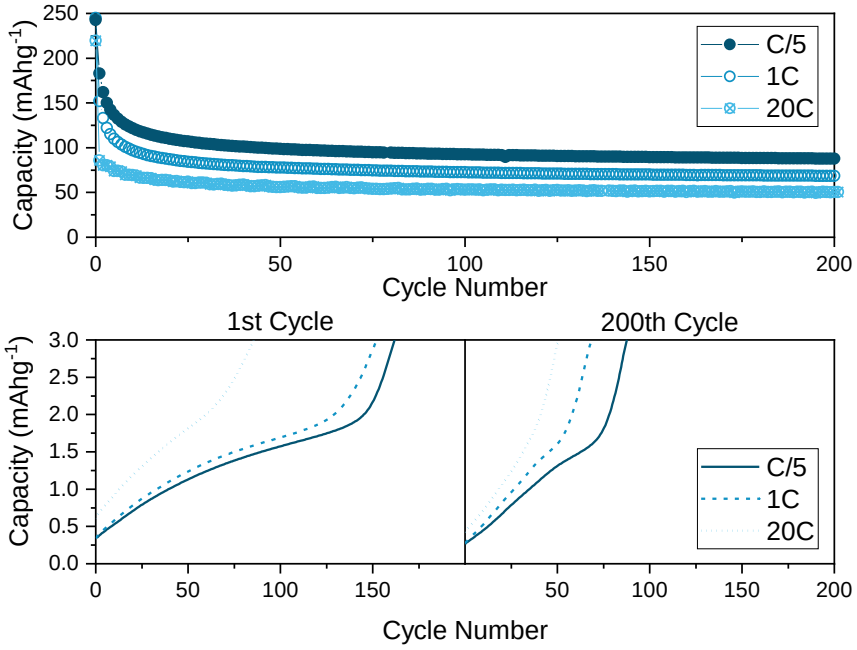

Figure A.15 - (top) Galvanostatic cycling at increasing rate over 200 cycles, (Bottom) charge profiles at the different rates from 1st and 200th cycle, all in 0.25-3.0 V window for 500 °C heat-treated anisotropically crystalline Nb_2O_5.

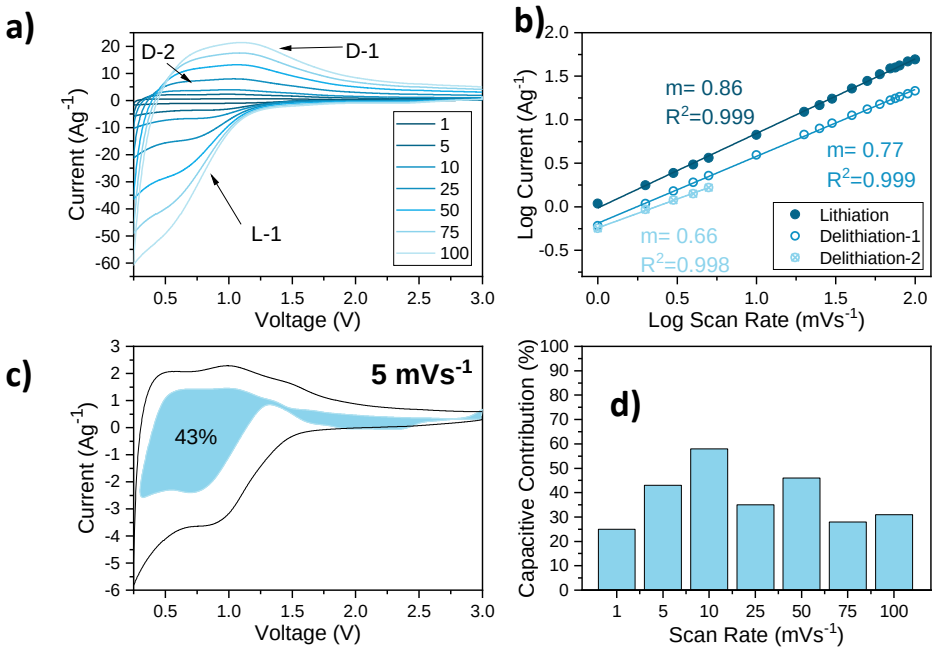

Figure A.16 - a) CV profile of anisotropically crystalline Nb_2O_5 heat-treated at 300°C at increasing scan rate 1 to 100 mVs^{-1}, b) Log plot of current versus scan rate of redox peaks, with linear fits which have R^2 of at least 0.998, c) CV profile at 5 mVs^{-1} with shaded section as the capacitive contribution and d) the capacitive contribution at various scan rates.

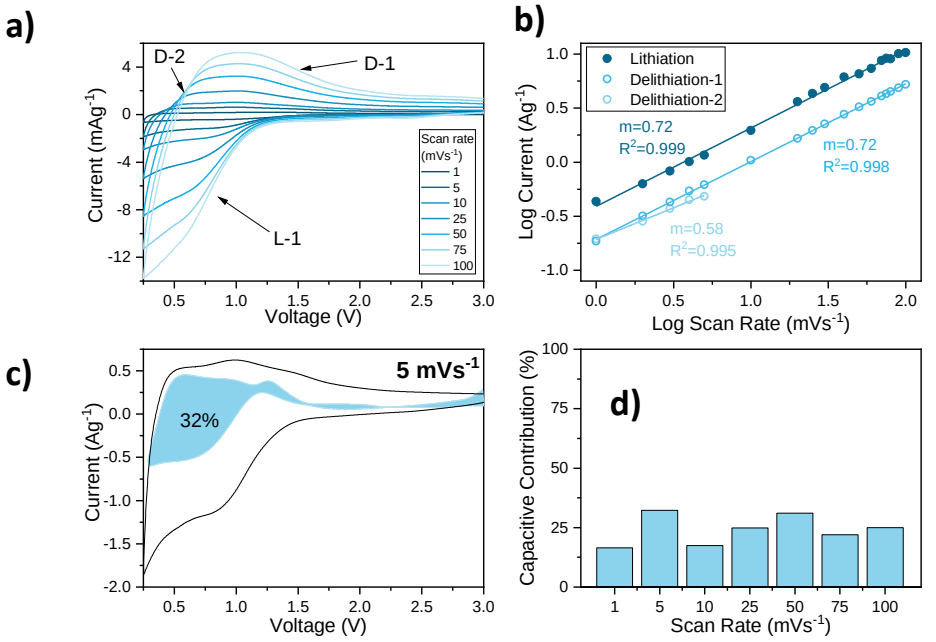

Figure A.17 - a) CV profile of anisotropically crystalline Nb_2O_5 heat-treated at 500°C at increasing scan rate 1 to 100 mVs^{-1}, b) Log plot of current versus scan rate of redox peaks, with linear fits which have R^2 of at least 0.986, c) CV profile at 5 mVs^{-1} with shaded section as the capacitive contribution and d) the capacitive contribution at various scan rates.

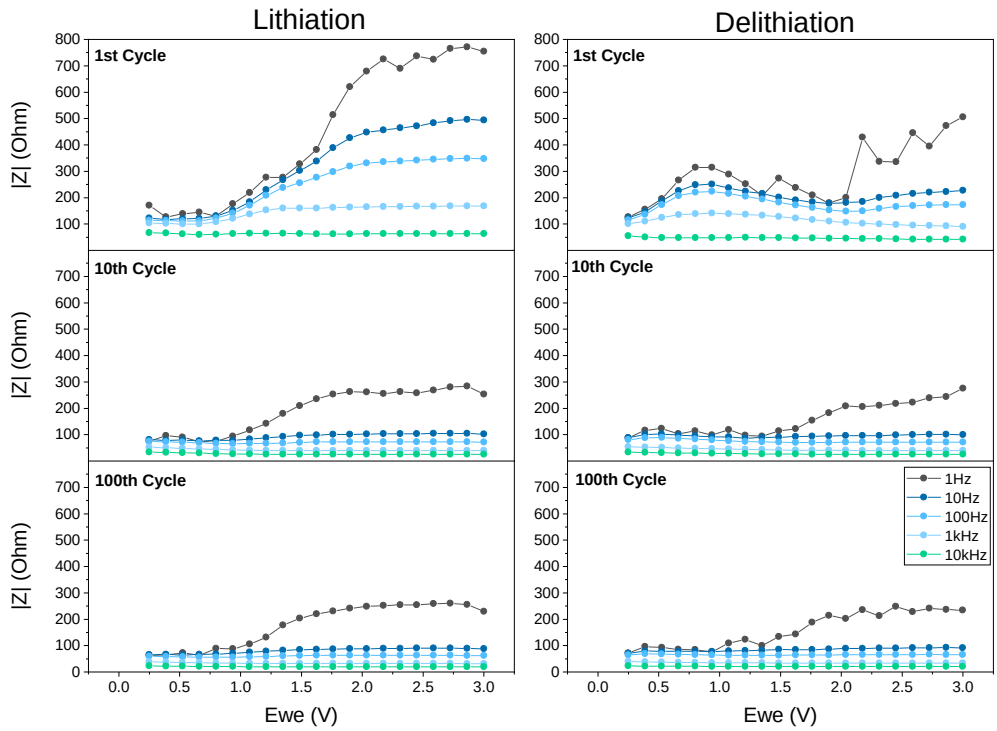

Figure A.18 – SPEIS of anisotropically crystalline Nb_2O_5 heat-treated to 300 °C for cycles from 1 to 100 cycles in a range of 1 Hz to 10kHz.

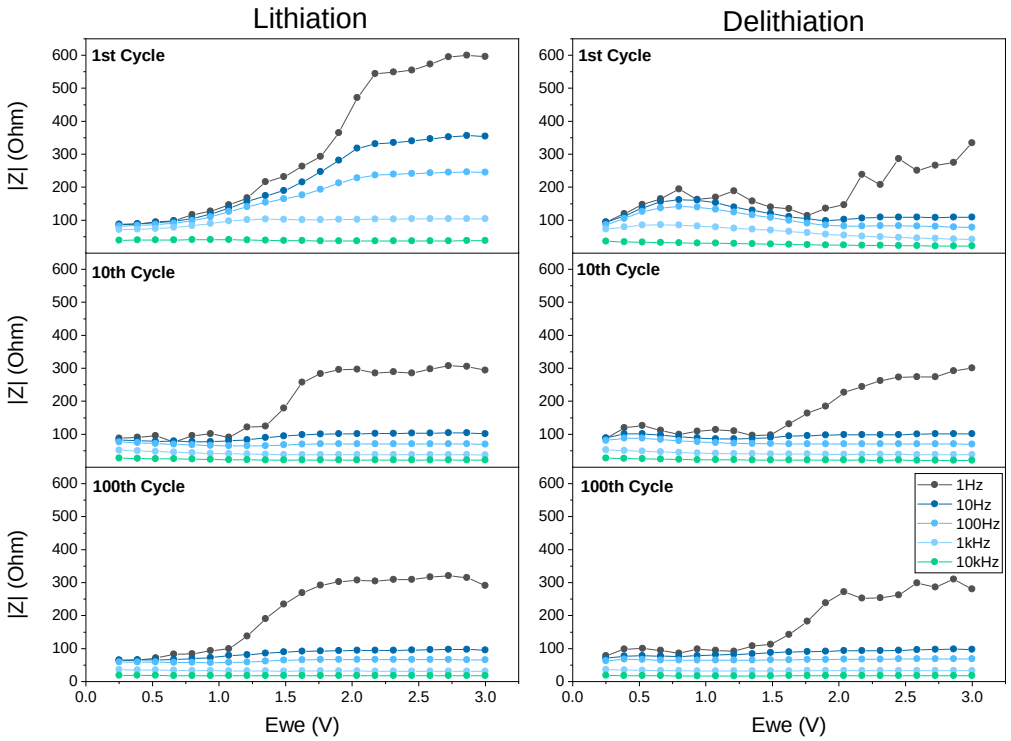

Figure A.19 - SPEIS of anisotropically crystalline Nb_2O_5 heat-treated to 500 °C for cycles from 1 to 100 cycles in a range of 1 Hz to 10kHz.

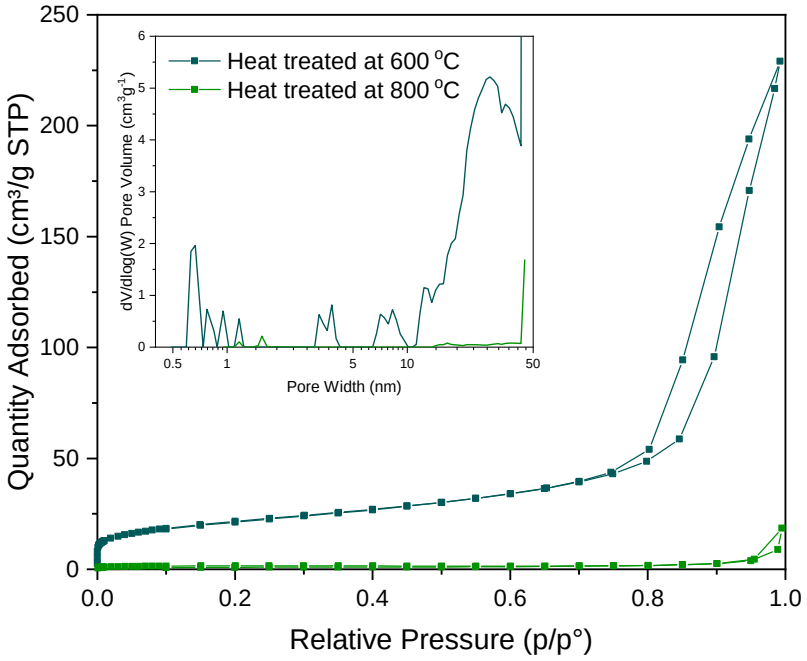

Figure A.20 - N_2 Porosity isotherm for orthorhombic Nb_2O_5 Inset is the pore volume distribution of respective samples.

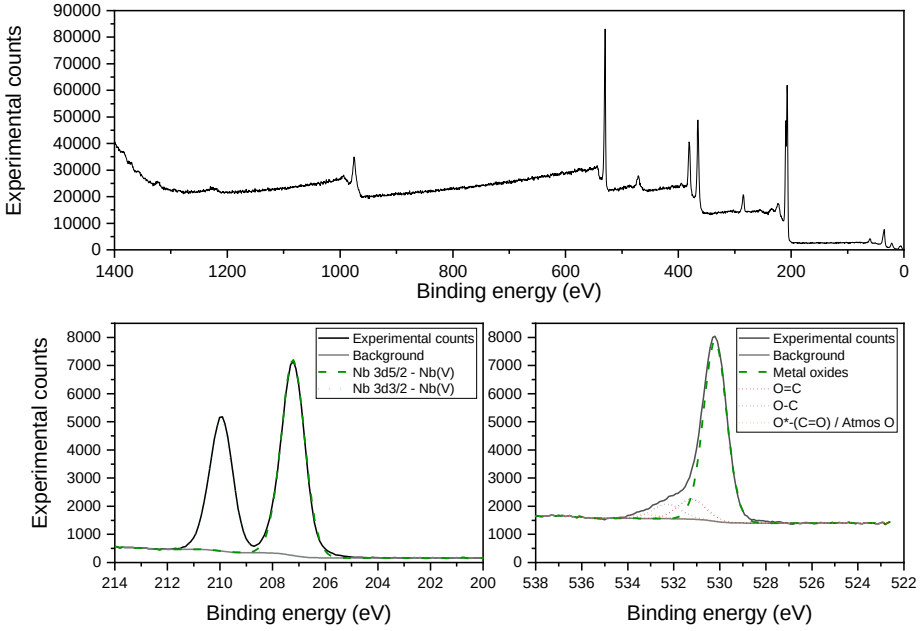

Figure A.21 - XPS of orthorhombic Nb_2O_5 material synthesised via an anisotropically crystalline precursor heat-treated at 600 °C, showing the Nb 3d and O 1s regions

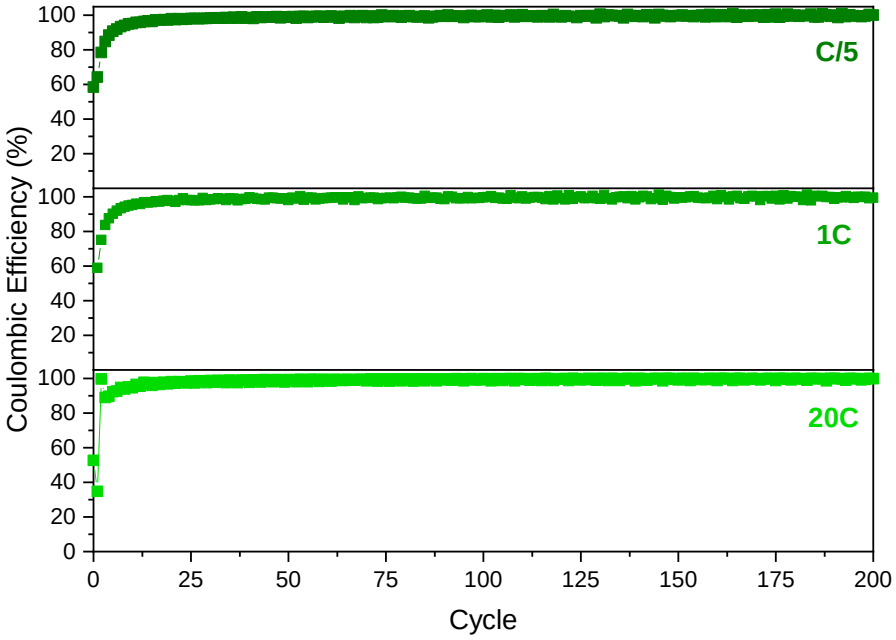

Figure A.22 - Coulombic efficiency of orthorhombic Nb_2O_5 produced at 600 °C cycled between 0.25-3.0V at different rates, C/5, 1C and 20C (top to bottom) after a C/20 formation cycle.

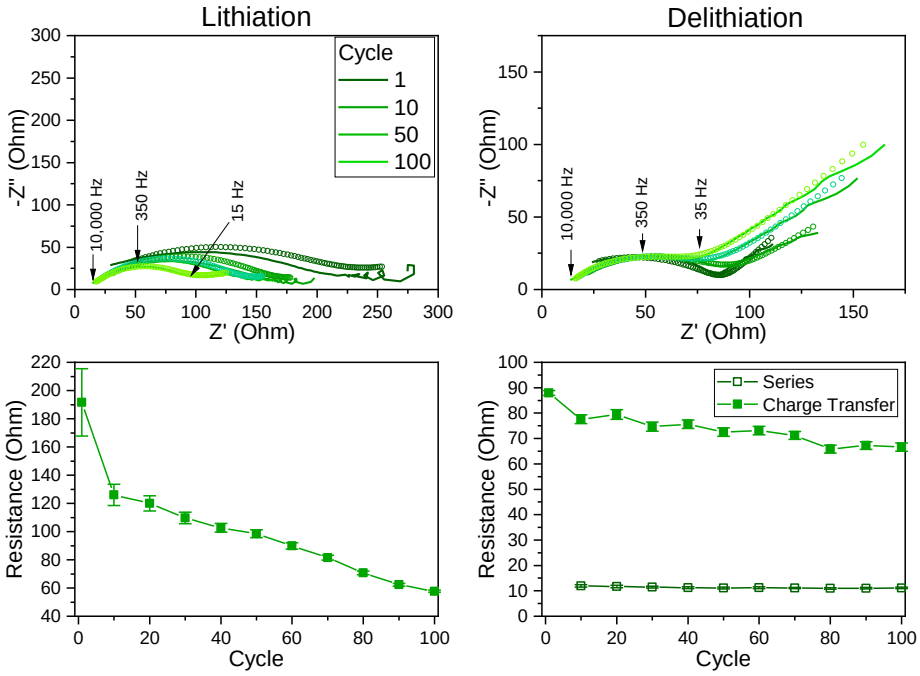

Figure A.23 - (top) Nyquist plots for delithiation and lithiation at 2.5 V, with fitted curves overlaid (bottom) fitted resistance values for series, charge transfer and SEI resistances for orthorhombic Nb_2O_5 created at 600°C.

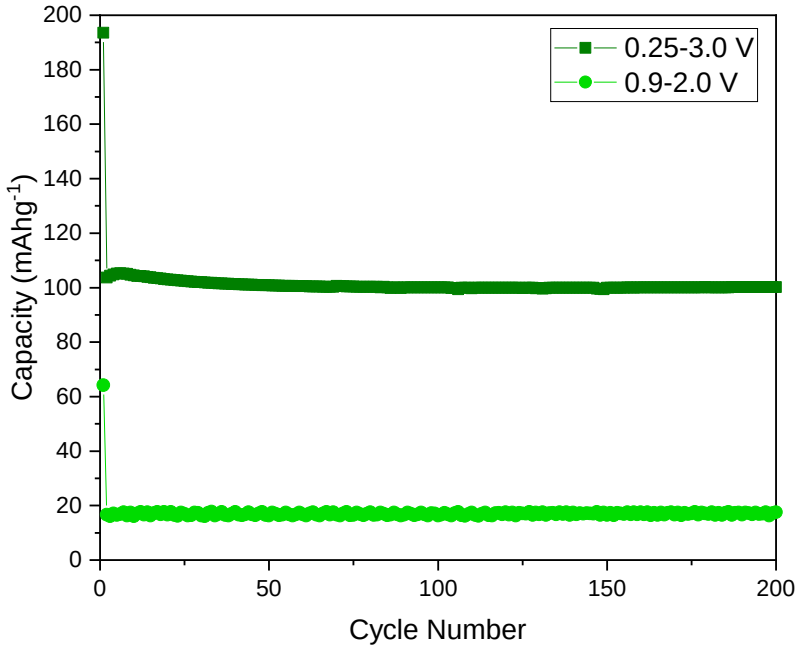

Figure A.24 – Galvanostatic cycling at 1C in wide and narrow voltage ranges, 0.25-3.0 V and 0.9-2.0 V respectively, with a C/20 formation cycle.

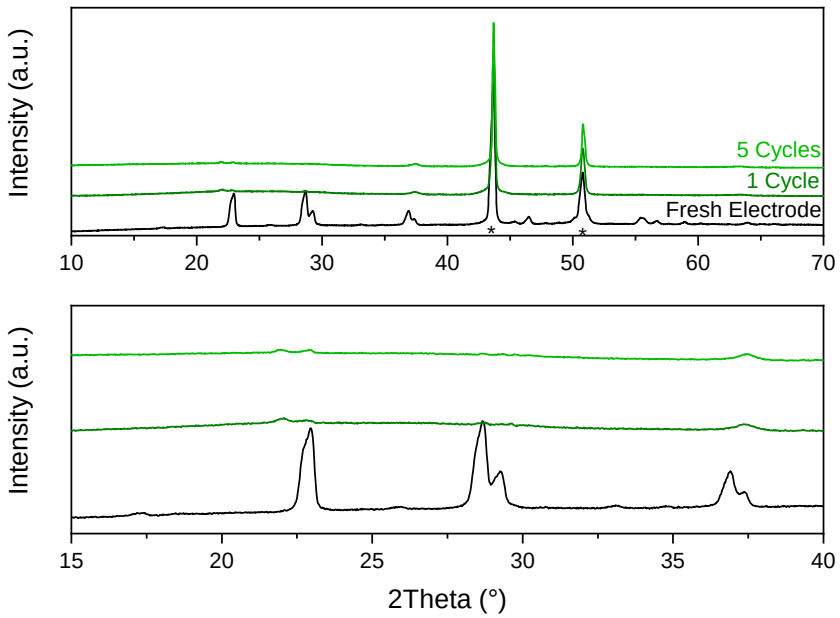

Figure A.25 – Ex-situ XRD of orthorhombic Nb_2O_5 produced at 800 °C, electrodes after cycling at 1C in 0.25-3.0V range in Li half-cell. (bottom) Corresponding XRD pattern in zoomed range. Stars denote peaks for Cu current collector.

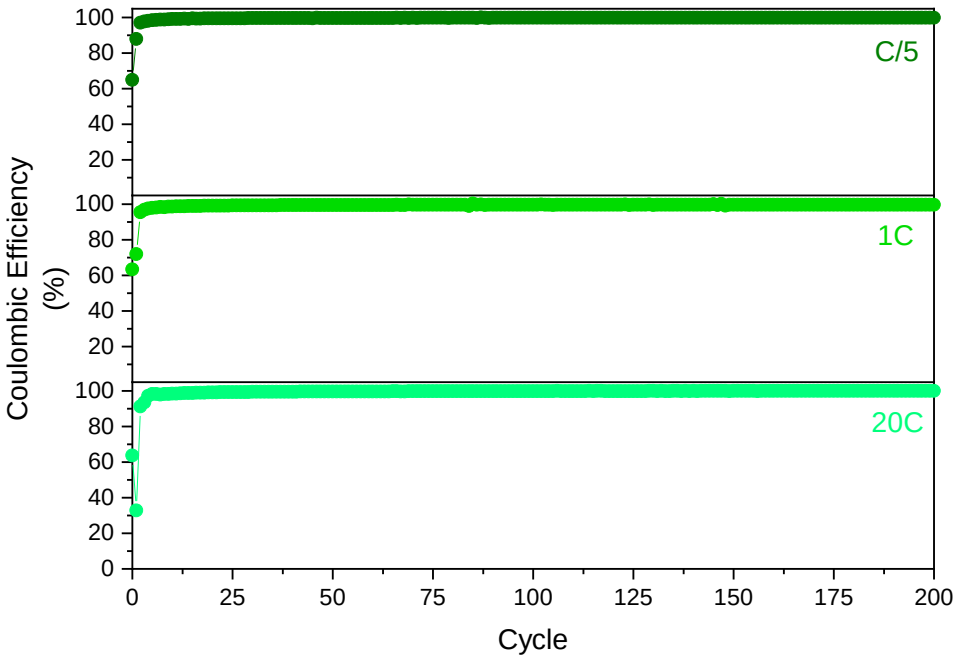

Figure A.26 - Coulombic efficiency of orthorhombic Nb_2O_5 produced at 800 °C cycled between 0.25-3.0V at different rates, C/5, 1C and 20C (top to bottom) after a C/20 formation cycle.

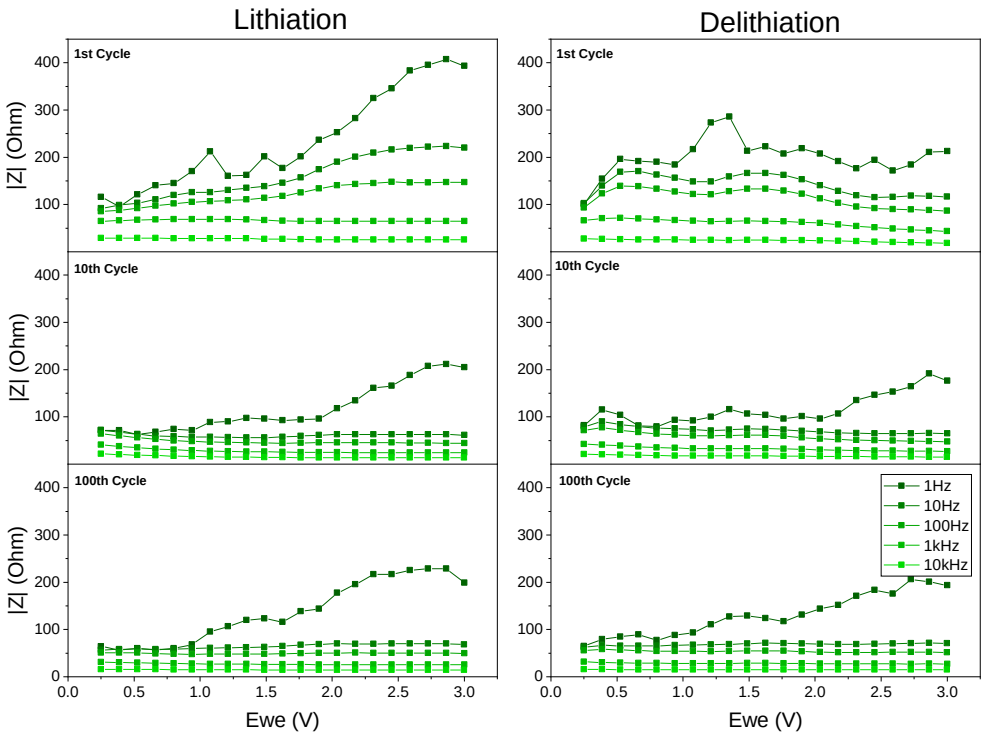

Figure A.27 - SPEIS of T- Nb_2O_5 created at 800°C for cycles from 1 to 100 cycles in a range of 1 Hz to 10kHz.

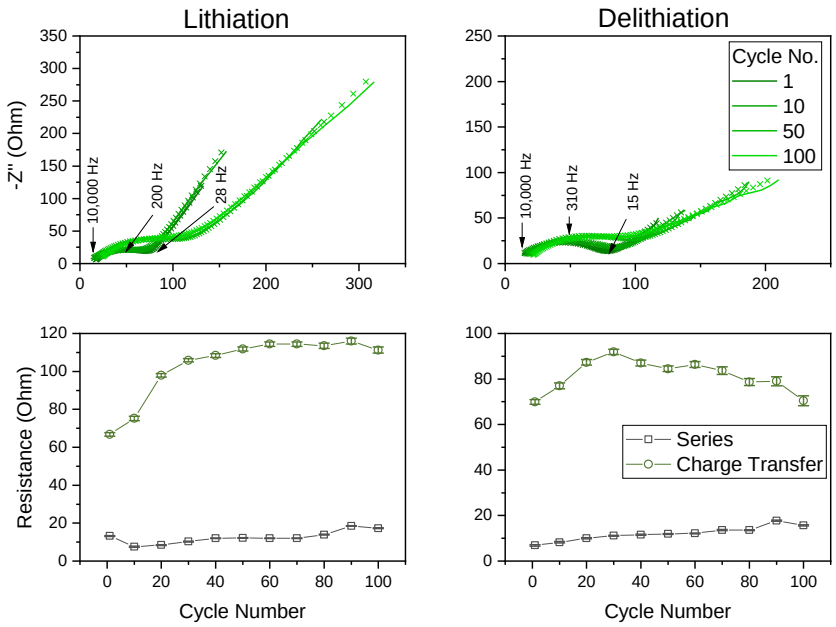

Figure A.28 - top) Nyquist plots for delithiation and lithiation at 2.5 V, with fitted curves overlaid (bottom) fitted resistance values for series, charge transfer for orthorhombic Nb_2O_5 created at 800°C.

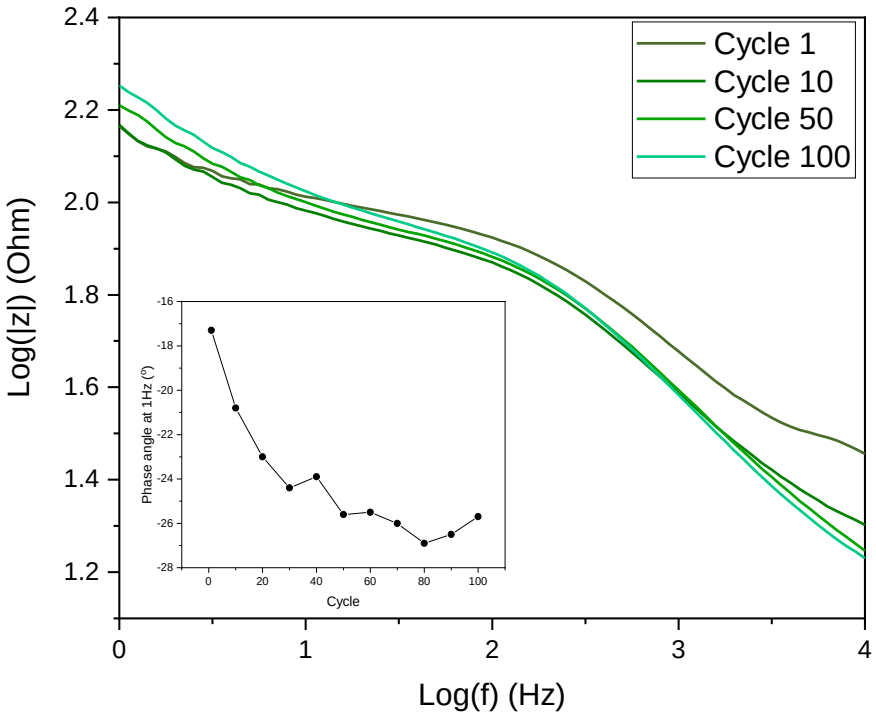

Figure A.29 - Magnitude Bode plot for EIS taken at 2.5 V voltage on delithiation cycle at cycle 1, 10, 50, 100 for 800 °C Orthorhombic Nb_2O_5. (Inset) Phase angle at 1 Hz versus cycle number.

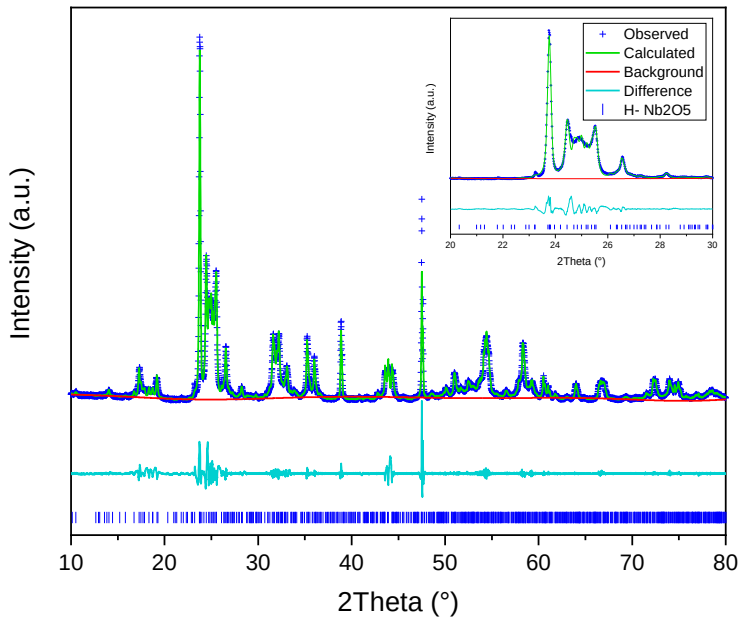

Figure A.30 - Pawley fit of XRD pattern of monoclinic Nb_2O_5 material to ICSD 16605-crystal structure. The XRD pattern was taken using a Cu Kα1/2 source Panalytical Empyrean, and the GSAS II software was used for the Pawley fit.[336] *This figure is seen in supporting information from Wheeler-Jones et al.*[138]

Table A. 2 - Comparison of lattice parameters of Pawley fitted H-Nb_2O_5 and expected values from ICSD 16605

	a (Å)	b (Å)	c (Å)	β (°)	Volume (Å^3)
Expected (16605)	21.16	3.822	19.35	119.83	1357.56
Fitted	21.163068 (0.003667)	3.824716 (0.000138)	19.330697 (0.003130)	119.8498 (0.0055)	1357.099 (0.067)

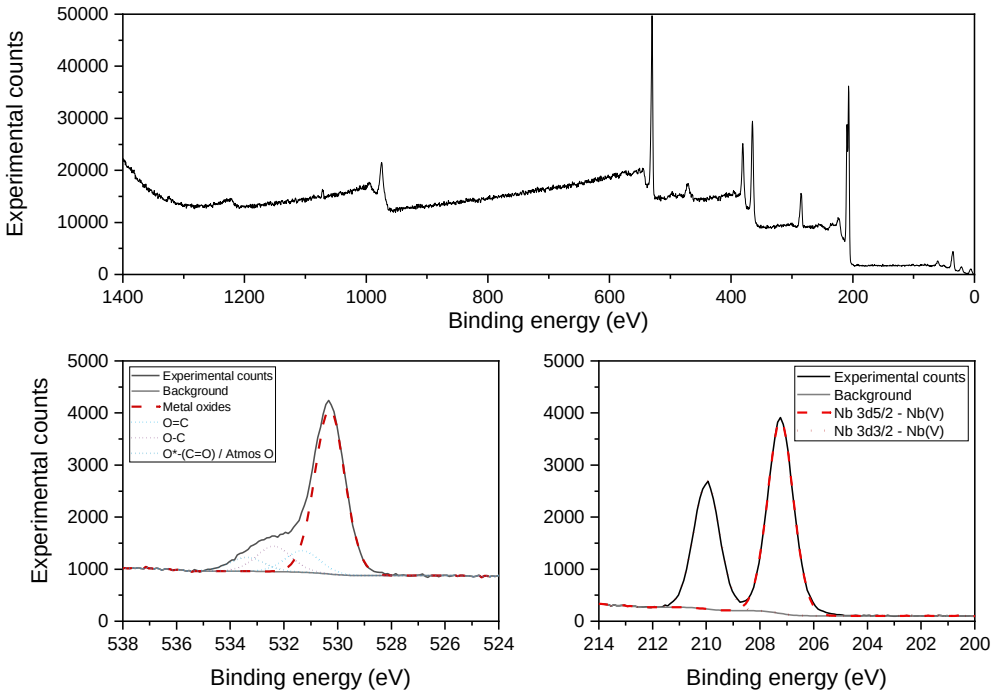

Figure A.31 - XPS of monoclinic Nb_2O_5 material synthesised via an anisotropically crystalline precursor heat-treated at 1000 °C, showing the Nb 3d and O 1s regions.

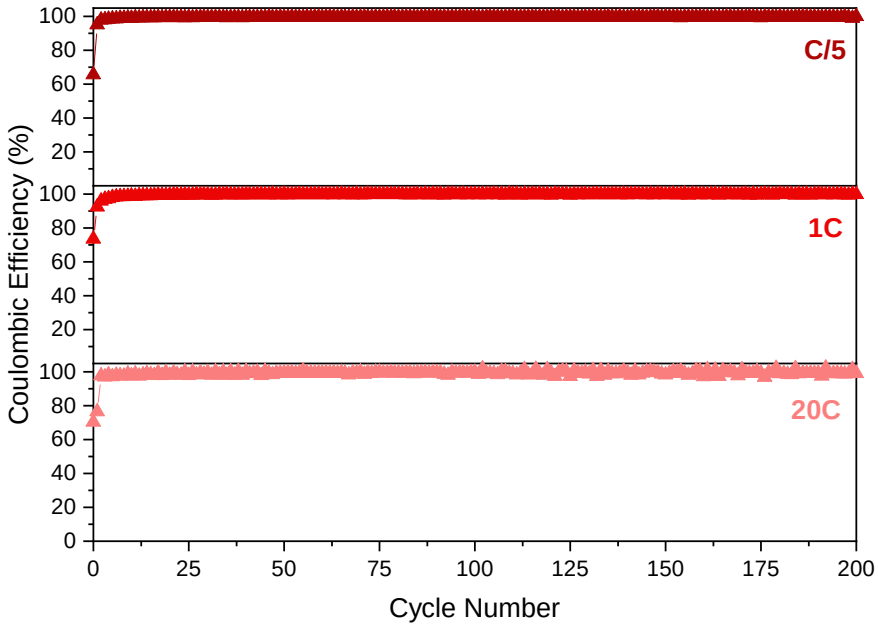

Figure A.32 - Coulombic efficiency of monoclinic Nb_2O_5 produced at 1000 °C cycled between 0.9-2.0V at different rates, C/5, 1C and 20C (top to bottom) after a C/20 formation cycle.

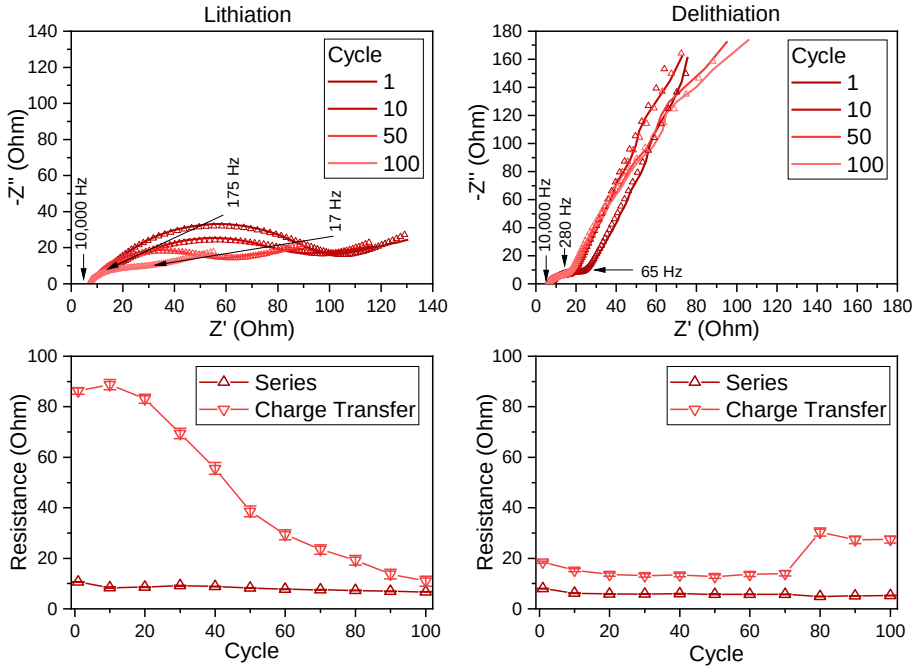

Figure A.33 - (Top) Nyquist plots for delithiation and lithiation at 1.5 V, with fitted curves overlaid. (Bottom) Fitted resistance values for series and charge transfer resistances for monoclinic Nb_2O_5 created at 1000 °C.

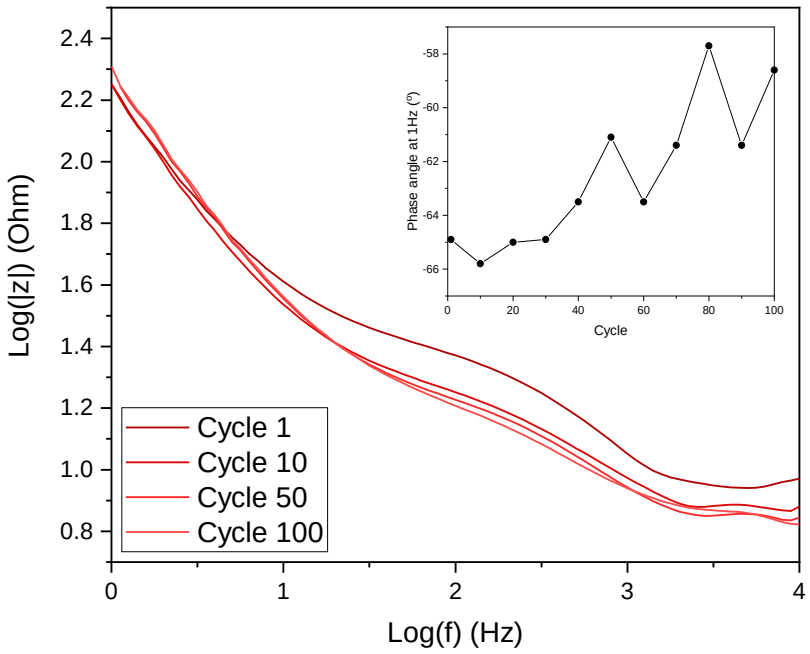

Figure A.34 - Magnitude Bode plot for EIS taken at 1.5 V voltage on delithiation cycle at cycle 1, 10, 50, 100 for 1000 °C monoclinic Nb_2O_5. (Inset) Phase angle at 1 Hz versus cycle number.

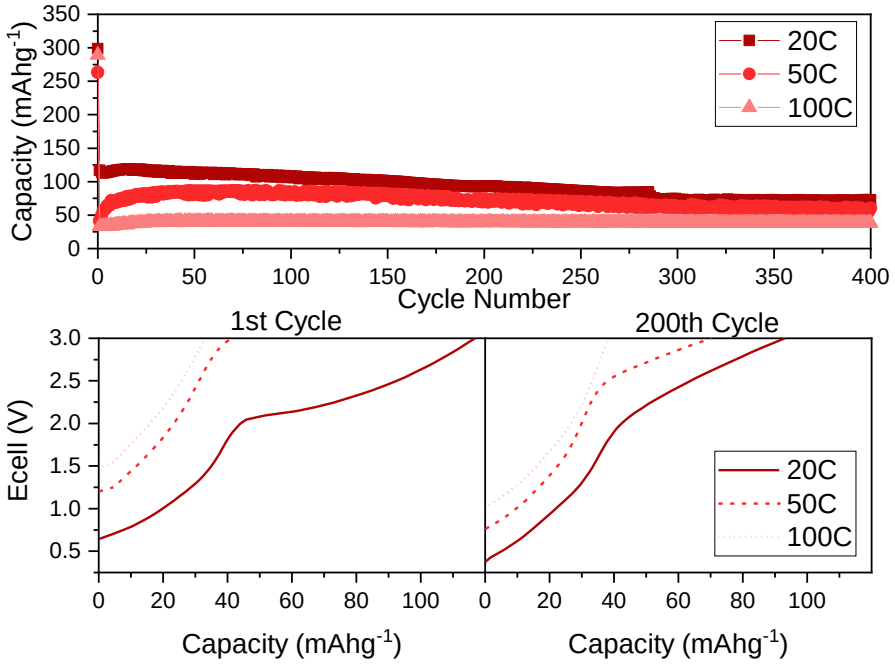

Figure A.35 - (top) Galvanostatic cycling at increasing rate over 400 cycles, (bottom) charge profiles at the different rates from 1st and 200th cycle, all in 0.25-3.0 V window for monoclinic Nb_2O_5 created at 1300 °C.

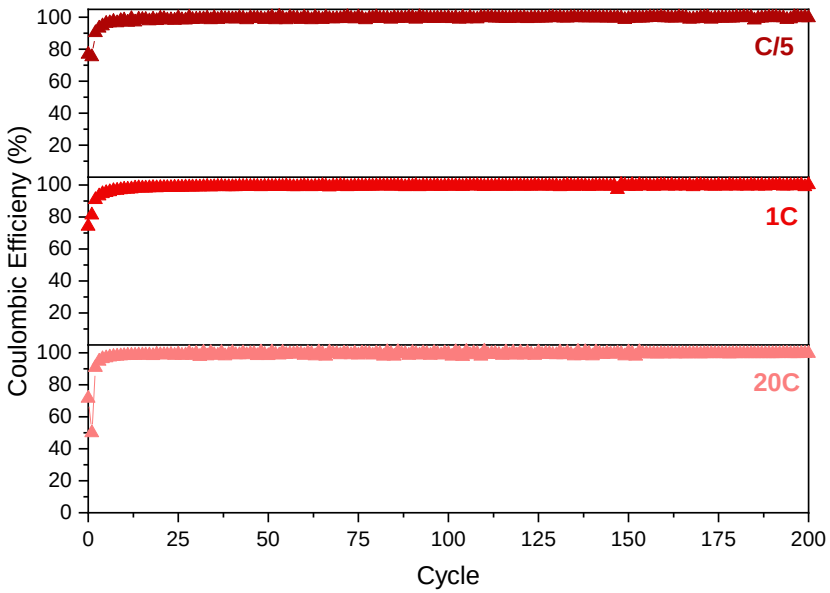

Figure A.36 - Coulombic efficiency of monoclinic Nb_2O_5 produced at 1300 °C cycled between 0.25-3.0V at different rates, C/5, 1C and 20C (top to bottom) after a C/20 formation cycle.

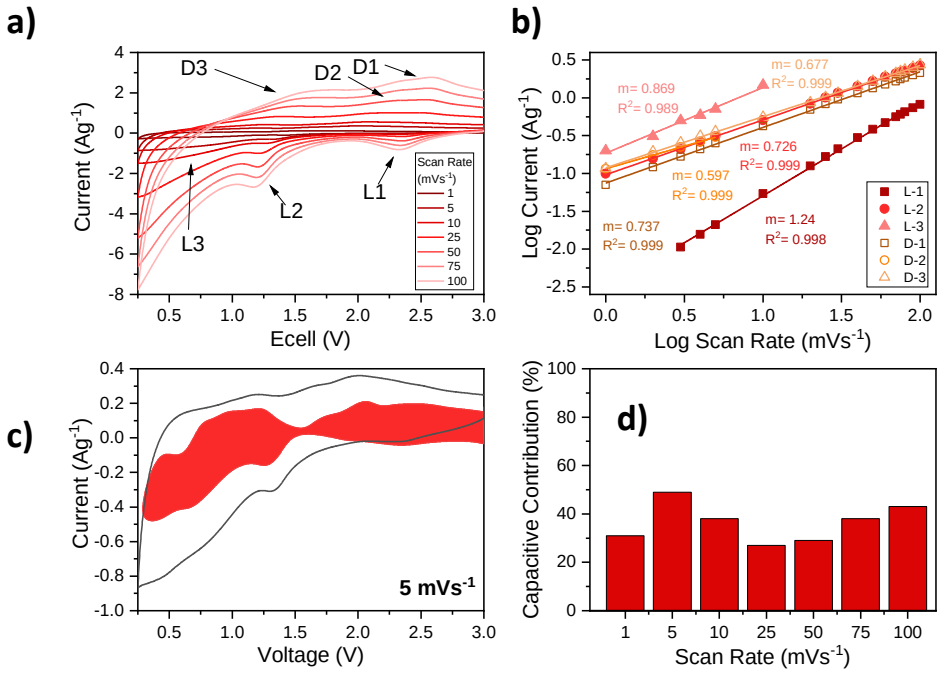

Figure A.37 - a) CV profile of monoclinic Nb_2O_5 created at 1300 °C at increasing scan rate 1 to 100 mVs^{-1}, b) Log plot of current versus scan rate of redox peaks, with linear fits which have R^2 of at least 0.998, c) CV profile at 5 mVs^{-1} with shaded section as the capacitive contribution and d) the capacitive contribution at various scan rates.

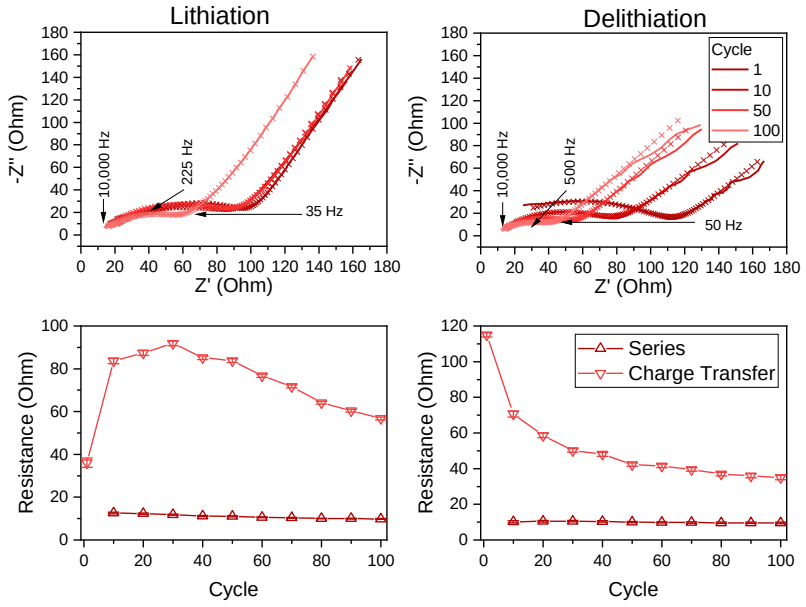

Figure A.38 – (Top) Nyquist plots for delithiation and lithiation at 1.5 V, with fitted curves overlaid. (Bottom) Fitted resistance values for series and charge transfer resistances for monoclinic Nb_2O_5 created at 1300 °C.

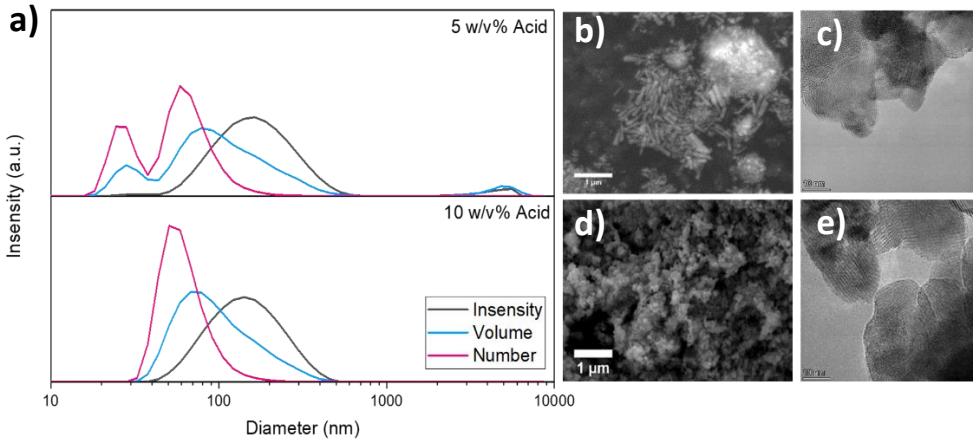

Figure A.39 - a) Particle size analysis of MoO_2 created via synthesis at 225°C for 72 hours with 5 w/v% (top) and 10 w/v% (bottom). SEM and TEM images of MoO_2 synthesised at 225 °C for 72 hours with 5 w/v% (b,c) and 10w/v% (d,e).

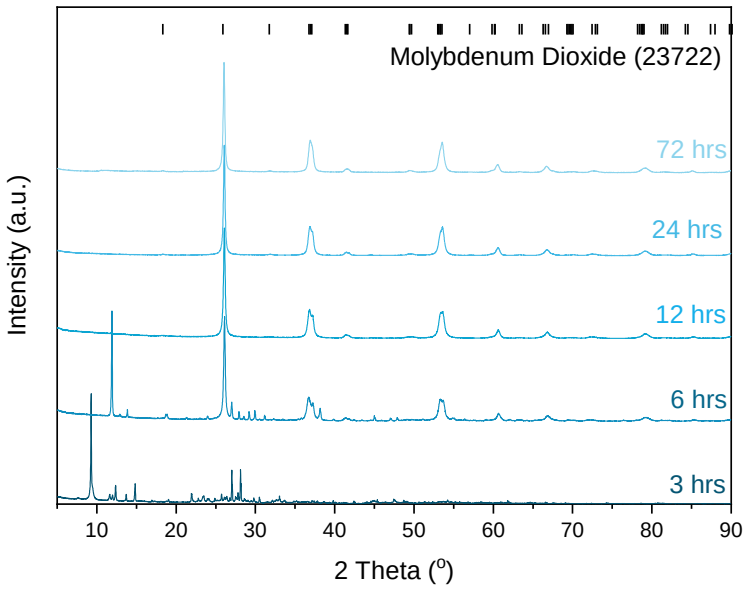

Figure A.40 - XRD patterns of products synthesised at 225 °C with 10 w/v% with increasing synthesis times from 3 to 72 hours.

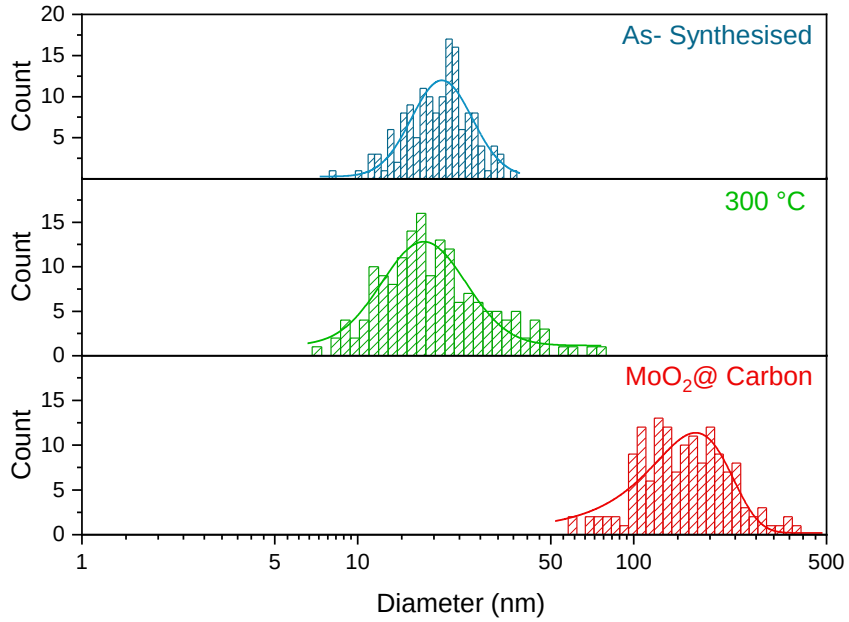

Figure A.41 – Particle width from TEM images of the as-synthesised, heat-treated MoO_2 and MoO_2@Carbon composite, with Gaussian fits to the log histograms.

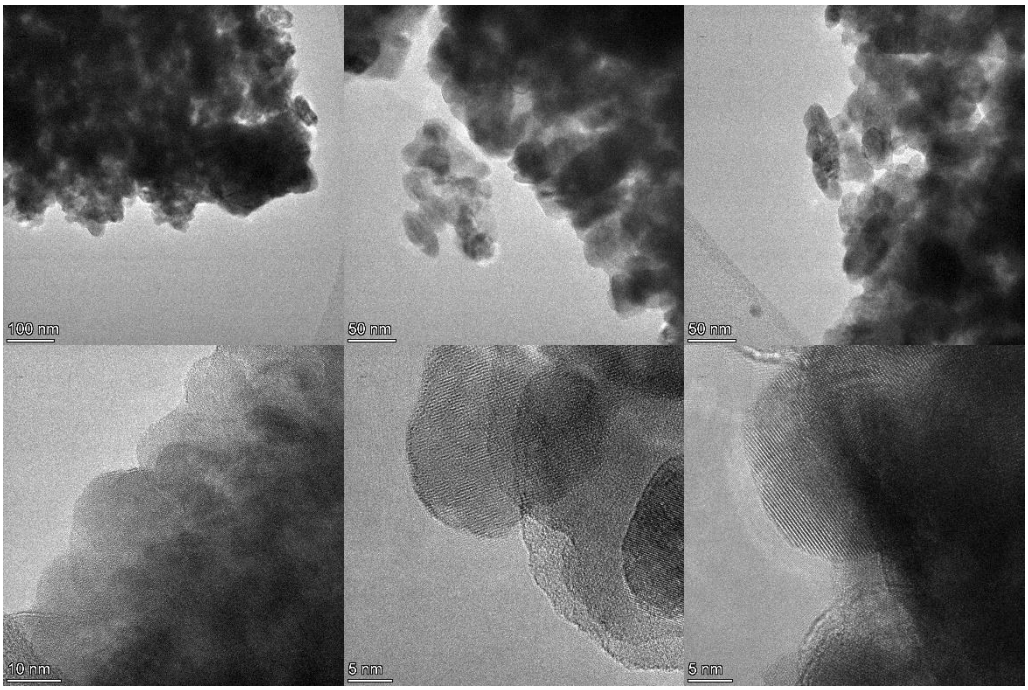

Figure A. 42 – TEM images of as-synthesised MoO_2

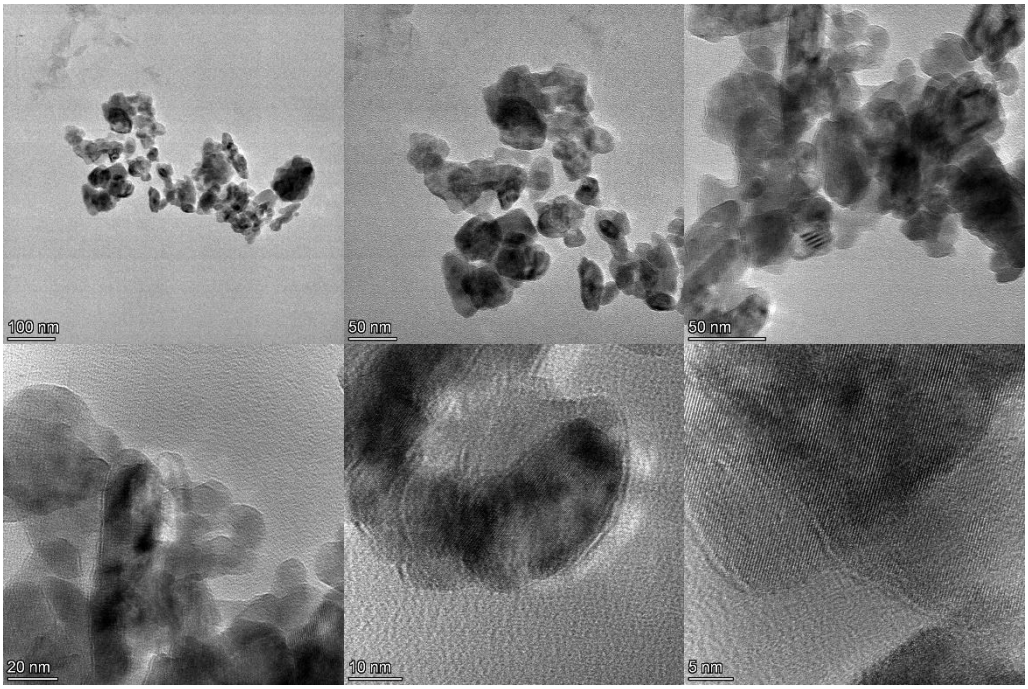

Figure A.43 – TEM images of Heat-treated MoO_2 (300 °C)

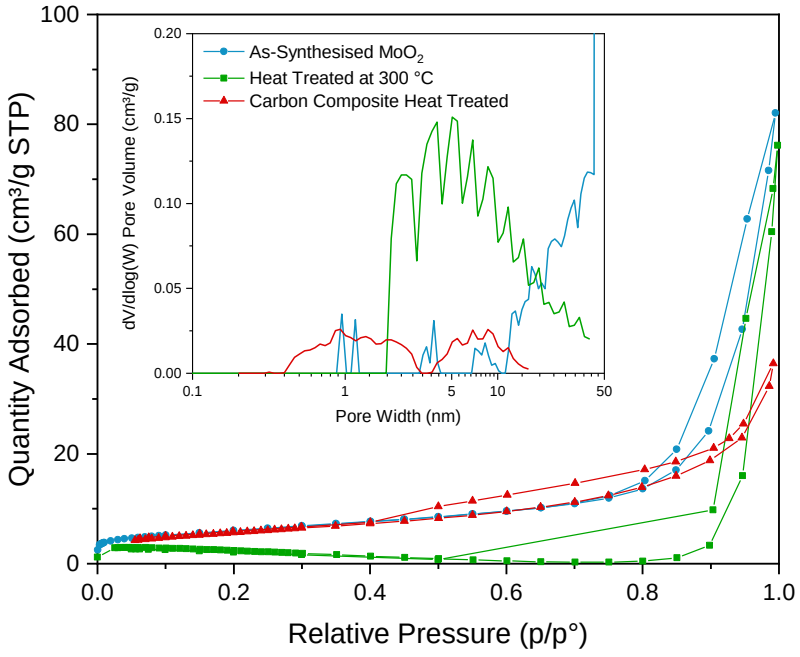

Figure A.44 - Full isotherm of N_2 adsorption/desorption of the as-synthesised MoO_2, heat-treated MoO_2 and MoO_2/Carbon composite with the corresponding log pore distribution inset.

Table A. 3- Calculated parameters from N_2 adsorption isotherms of as-synthesised MoO_2, heat-treated MoO_2 and MoO_2/ carbon composite, as seen in Figure A.44.

Material	BET Surface Area (m^2g^{-1})	DFT Total Volume in Pores (cm^3g^{-1})	BJH Adsorption Average Pore Width (nm)
As-Synthesised MoO_2	25.4	0.09	22.0
Heat-Treated MoO_2	5.87	0.11	33.8
MoO_2/Carbon composite	20.4	0.06	11.7

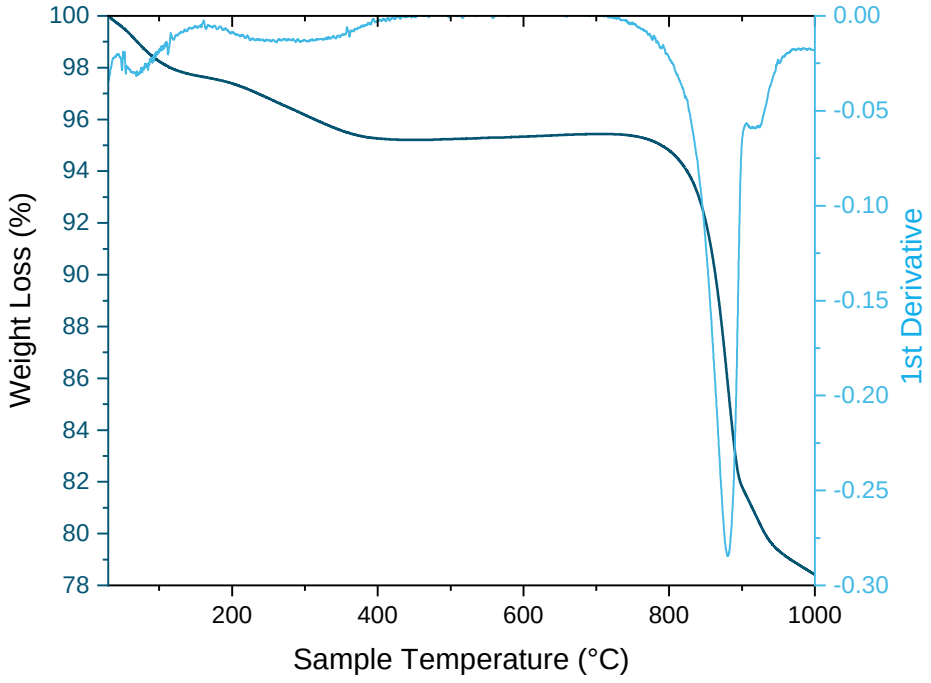

Figure A.45 - TGA and 1st derivative of as-synthesised MoO_2, between 30 and 1000 °C at 10 °Cs^{-1} in N_2.

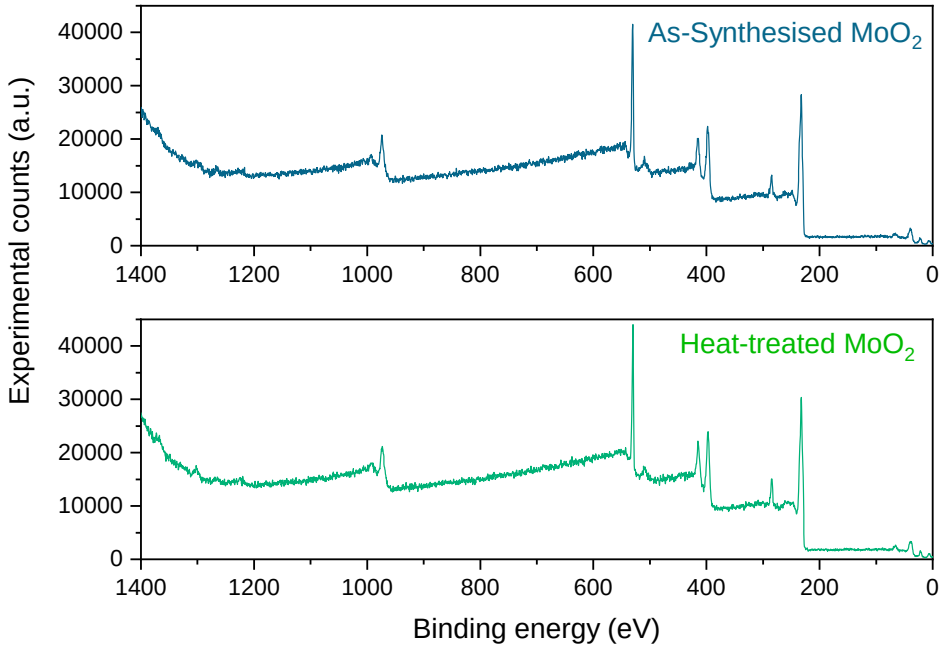

Figure A.46 – Survey XPS spectrum of as-synthesised MoO_2 (top) and heat-treated MoO_2 (bottom).

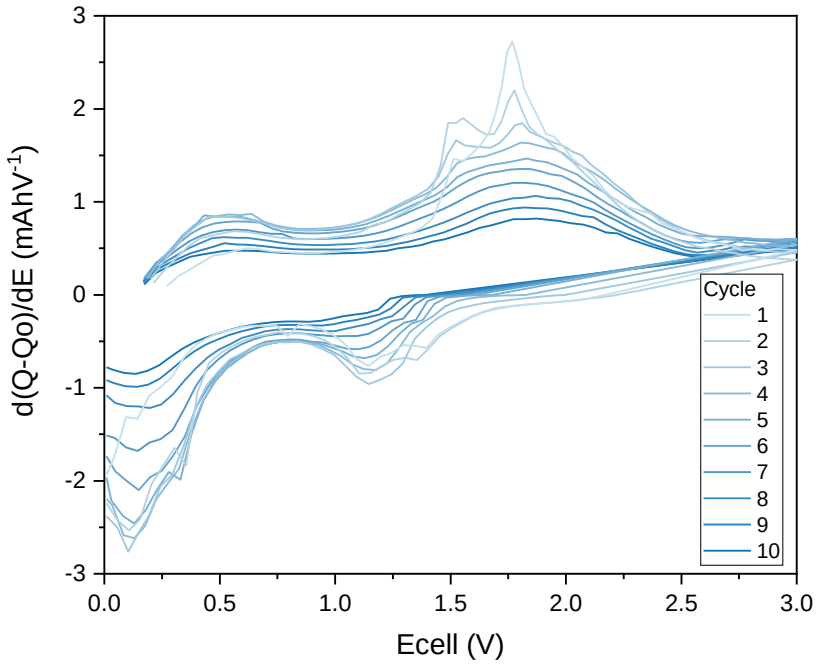

Figure A.47 - Differential capacity plots of the initial 10 cycles, after formation, of the as-synthesised MoO_2 cycled between 0.01-3.0 V at 1C.

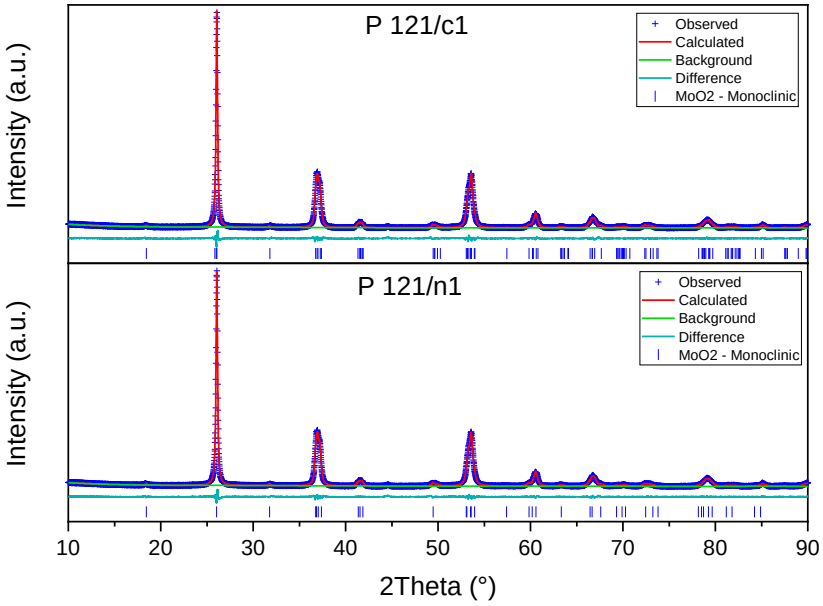

Figure A.48 – Pawley fit of P121/c1 (top) and P121/n1 (bottom) to heat-treated MoO_2 XRD powder pattern. Where both phases show a good fit where the lattice parameters are close to the ideal.

Table A. 4 – Pawley Fit parameters for fresh and cycled electrodes of heat-treated MoO_2 fit to P121/c1 and P121/mnm structures.

		a (Å)	b (Å)	c (Å)	Beta (°)	Volume (Å³)
P121/c1	**Initial (CIF values)**	5.59454	4.86366	5.65151	121.110	131.660
Fresh	**Pawley Fit**	5.561387 (0.004328)	4.83379 (0.000244)	5.499025 (0.00430)	118.4777 (0.0092)	129.941 (0.018)
Cycled	**Pawley Fit**	5.589928 (0.016272)	4.864316 (0.000342)	5.655229 (0.014893)	121.1808 (0.0280)	131.558 (0.035)
		a (Å)	**b (Å)**	**c (Å)**	**Beta (°)**	**Volume (Å³)**
P121/mnm	**Initial (CIF Values)**	4.85800	4.85800	2.82630	90	66.70
Fresh	**Pawley Fit**	4.833818 (0.000162)	4.833818 (0.000162)	2.830723 (0.000146)	90	66.142 (0.005)
Cycled	**Pawley Fit**	4.858428 (0.000307)	4.858428 (0.000307)	2.826165 (0.000938)	90	66.71 (0.020)

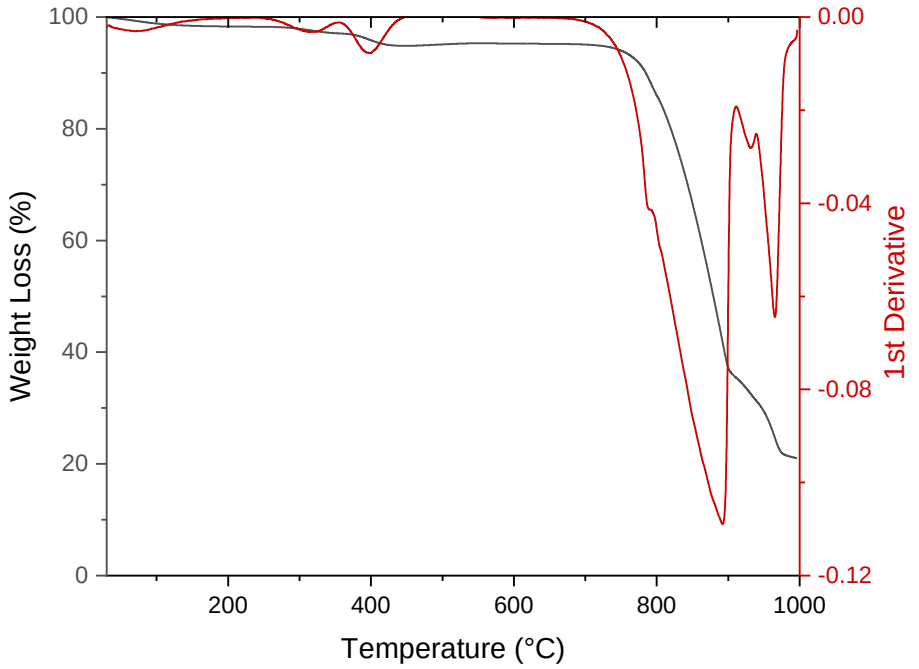

Figure A.49- TGA of MoO_2/C composite in O_2 between 30 and 1000 °C at a ramp rate of 10 °C/min, with overlaid 1st derivative of the TGA data.

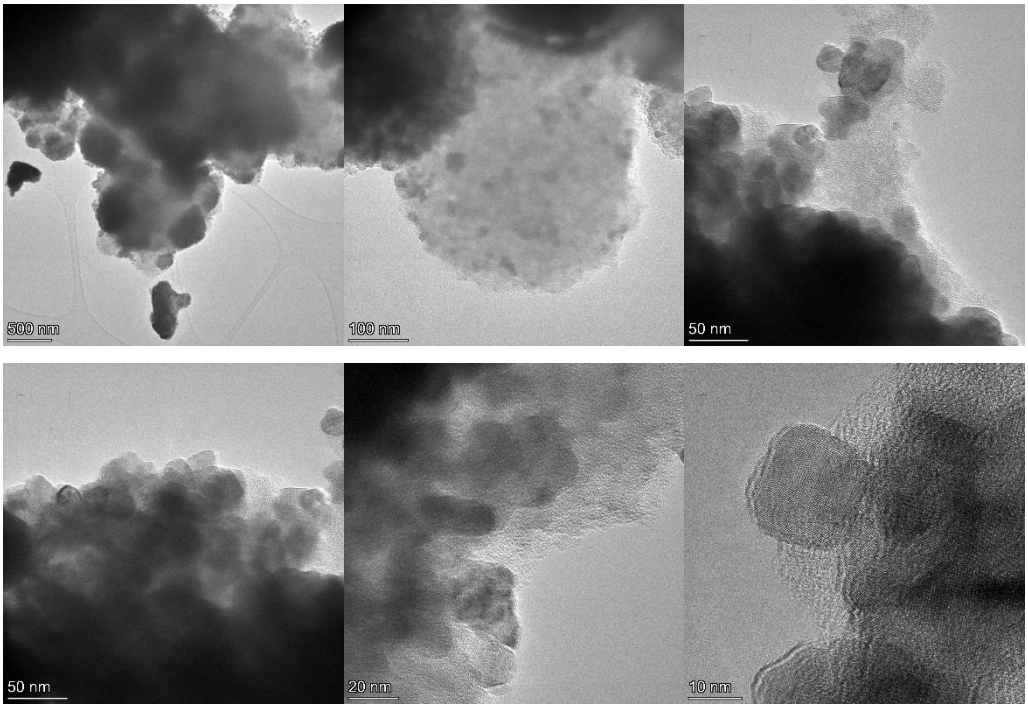

Figure A.50 – TEM images of MoO_2/C composite.

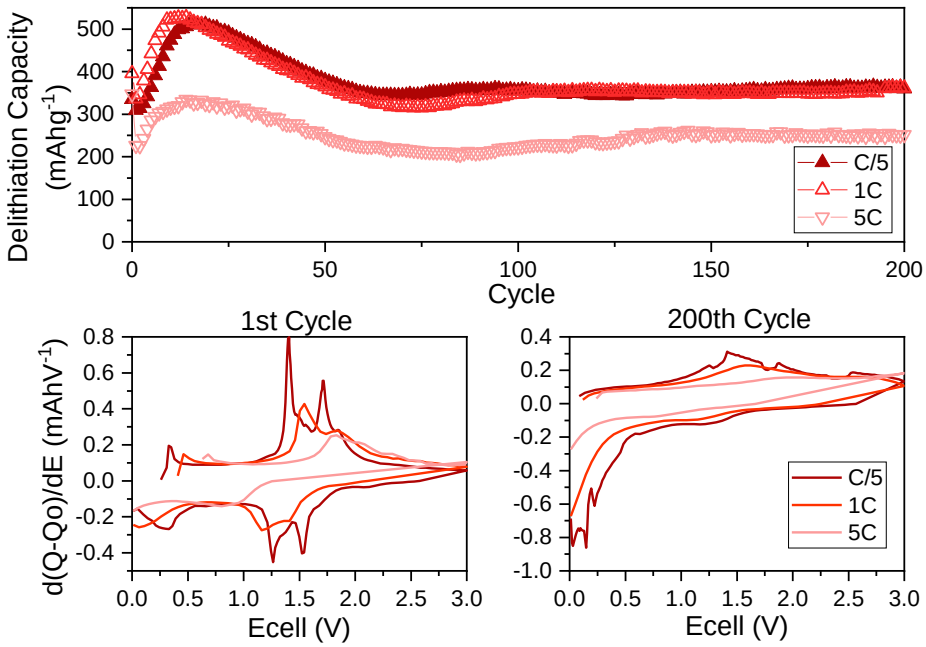

Figure A.51 - (top) Galvanostatic cycling at increasing rate between 0.01-3.0 V for MoO_2/C composite. (bottom) corresponding differential capacity plots of 1st and 200th cycle at increasing rate.

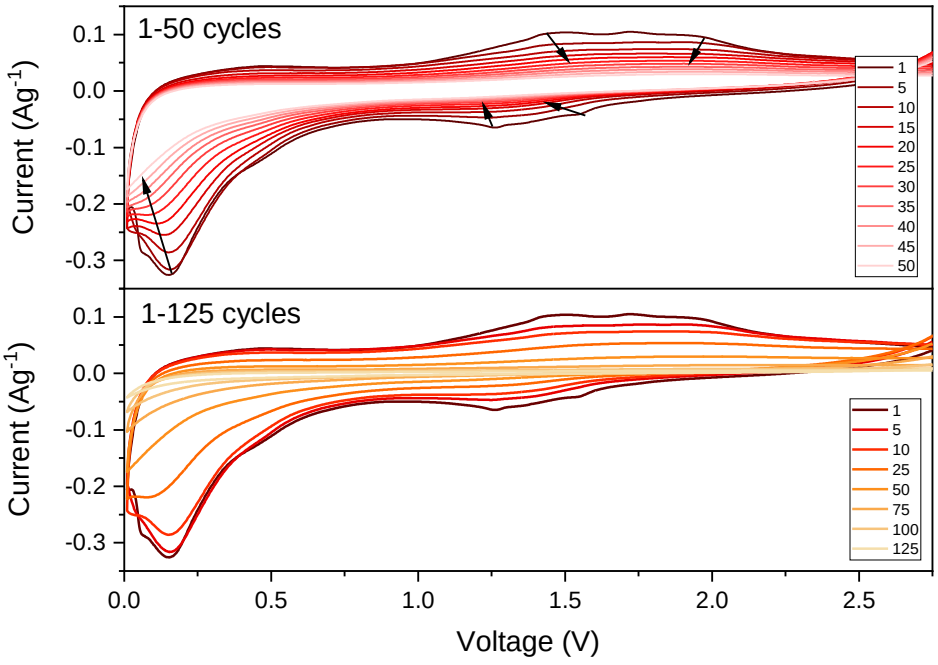

Figure A.52 - CV profiles measured at 0.1 mVs^{-1} every 5 cycles at 1C, where the top graph shows all CV's measured between 1 and 50 cycles and the bottom graph shows key profiles between 1 and 125 cycles

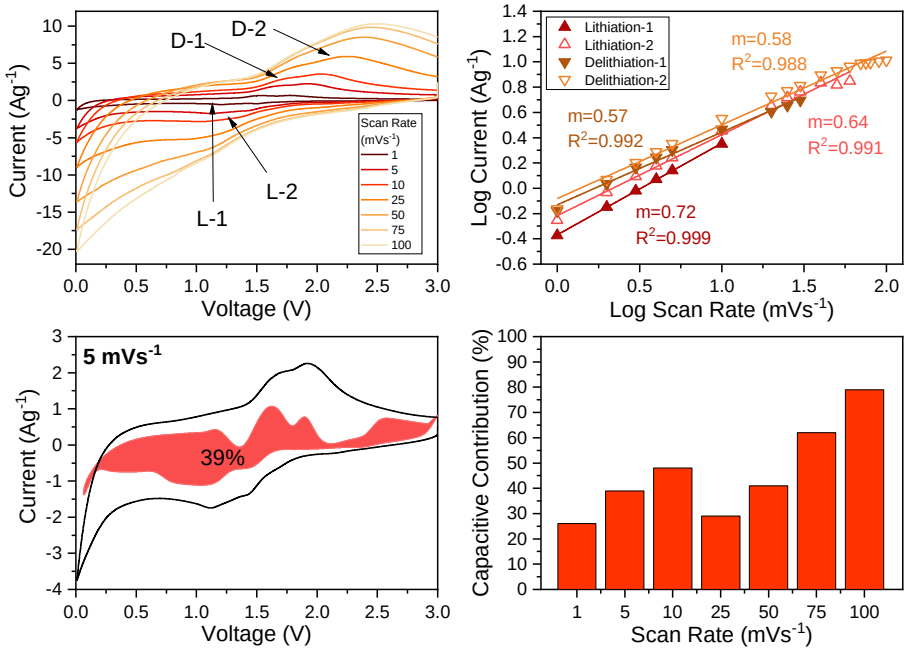

Figure A.53 - a) CV profile at increasing scan rates of MoO_2/C composite, arrows point to current peaks for lithiation (L) and delithiation (D). b) Log plot of peak currents with linear fits with R^2 of at least 0.992. c) CV profile at 5 mVs^{-1} with the shaded area as the capacitive contribution. d) Capacitive contribution at increasing scan rate.

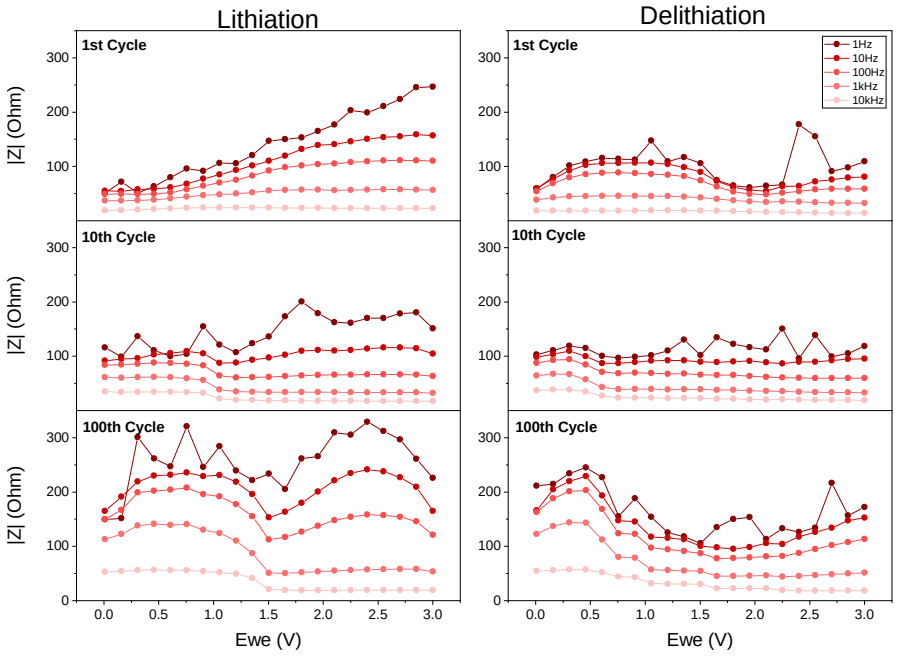

Figure A. 54 - SPEIS of MoO_2/C composite at cycles 1, 10 and 100 at 1C for lithiation (left) and delithiation (right).

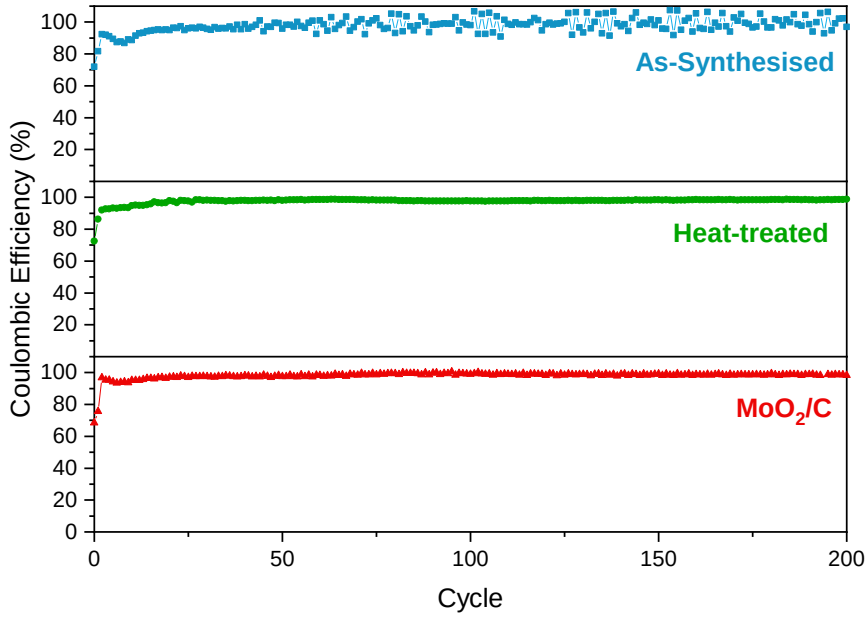

Figure A.55 – coulombic efficiency of galvanostatic cycling at 1C in the range 0.01-3.0 V with a C/20 formation cycle over 200 cycles for MoO_2 materials

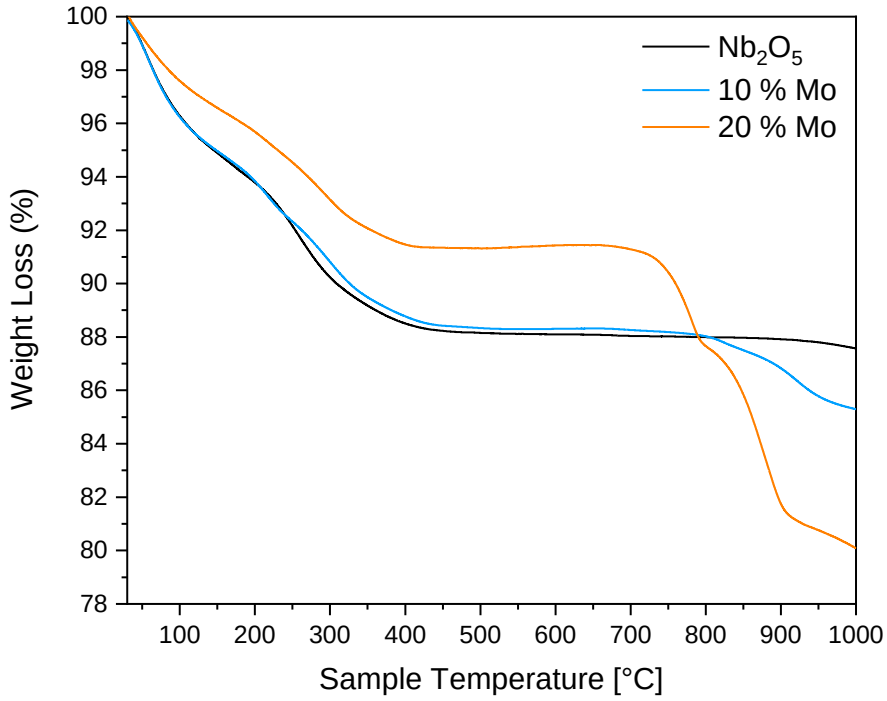

Figure A.56 - TGA in N_2 at 10 °Cmin $^{-1}$ for Nb_2O_5-rich composites and 'as-synthesised' Nb_2O_5.

Table A.5 - Results of XRF analysis of Nb_2O_5-rich composite materials.

Composite	Oxide Component	Quantity (atomic %, of metal atom)	Standard deviation between batches (%)
10% Mo Composite	Nb_2O_5	89.65	2.05
	MoO_2	10.35	
20% Mo Composite	Nb_2O_5	75.23	0.63
	MoO_2	24.32	

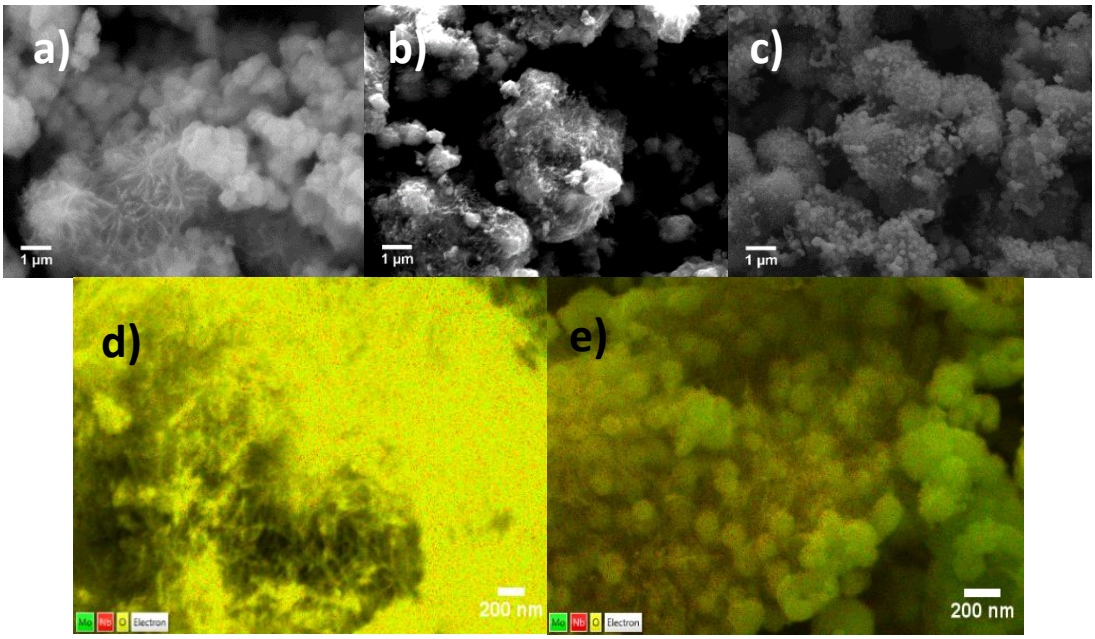

Figure A.57– a-c) SEM images of as-synthesised Nb_2O_5, 10 % Mo and 20 % Mo composites respectively. d,e) SEM-EDX image maps of 10 and 20 % Mo composites respectively, where Mo is green, Nb is red, and O is yellow.

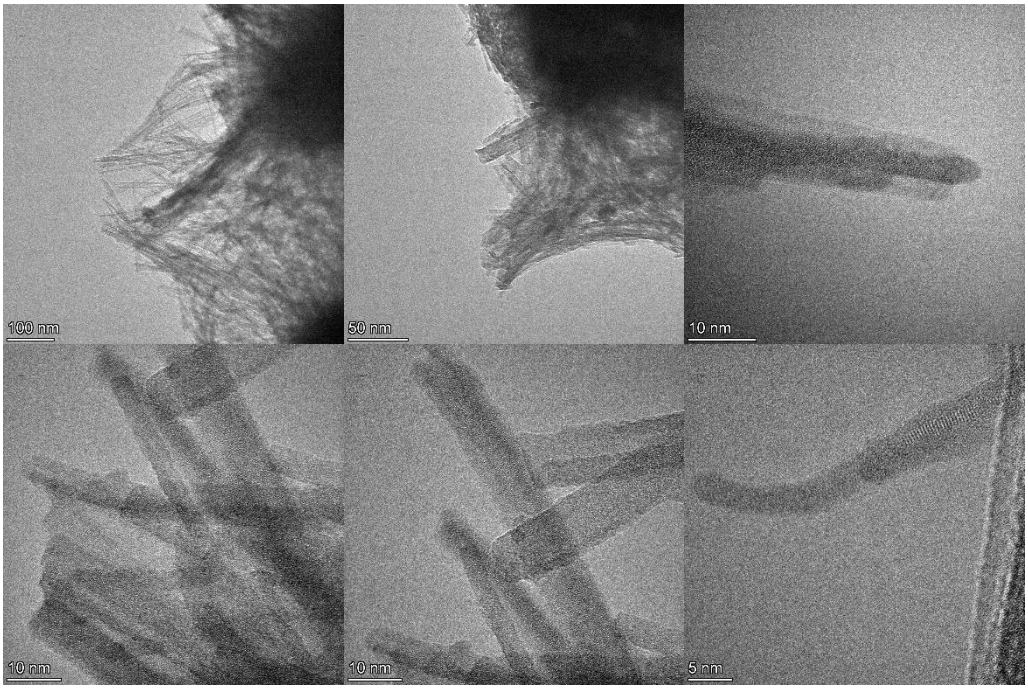

Figure A.58 – Selection of TEM images of 10 % Mo in Nb_2O_5 composite.

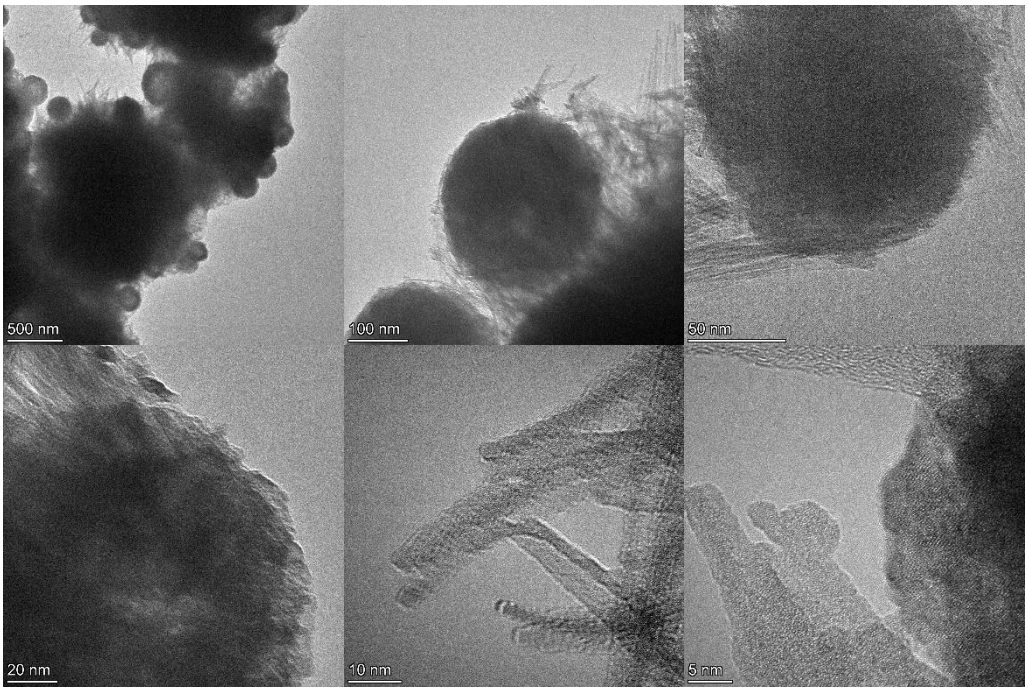

Figure A.59 - Selection of TEM images of 20 % Mo in Nb_2O_5 composite.

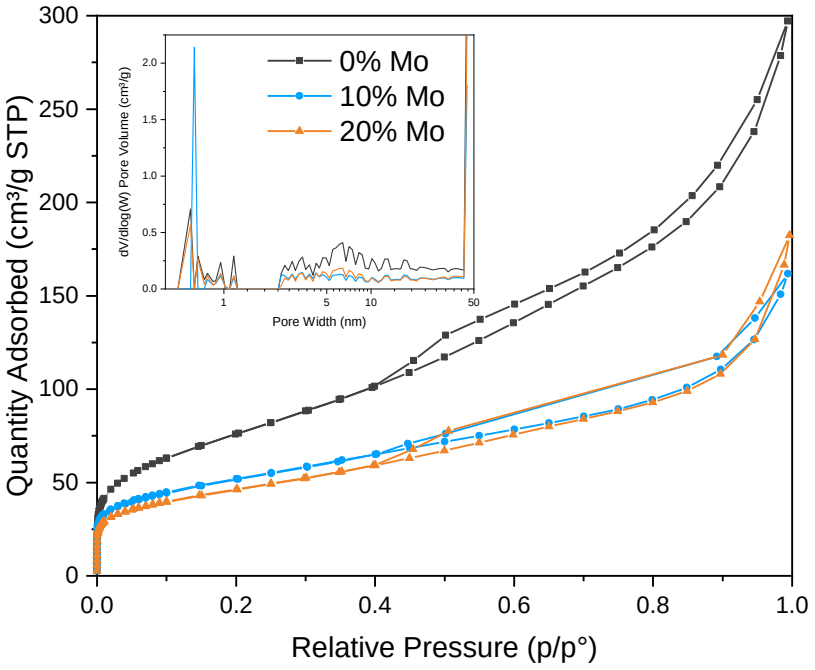

Figure A.60 - N_2 adsorption isotherms of Nb_2O_5 heavy composite materials, (inset) Pore distribution plot calculated from the isotherms.

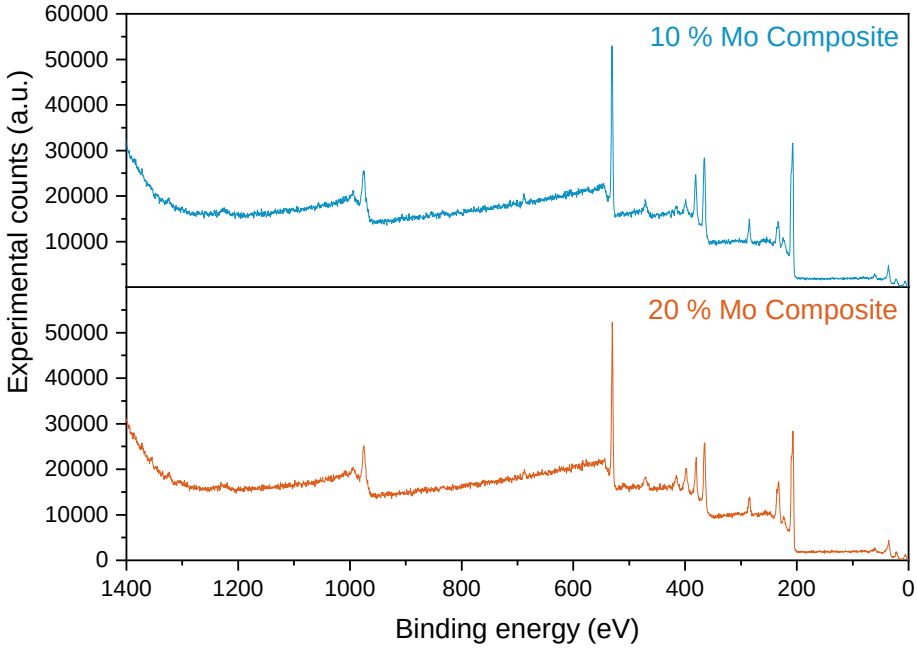

Figure A.61 – Full XPS survey of 10 and 20 % Mo content composite oxides (top and bottom respectively).

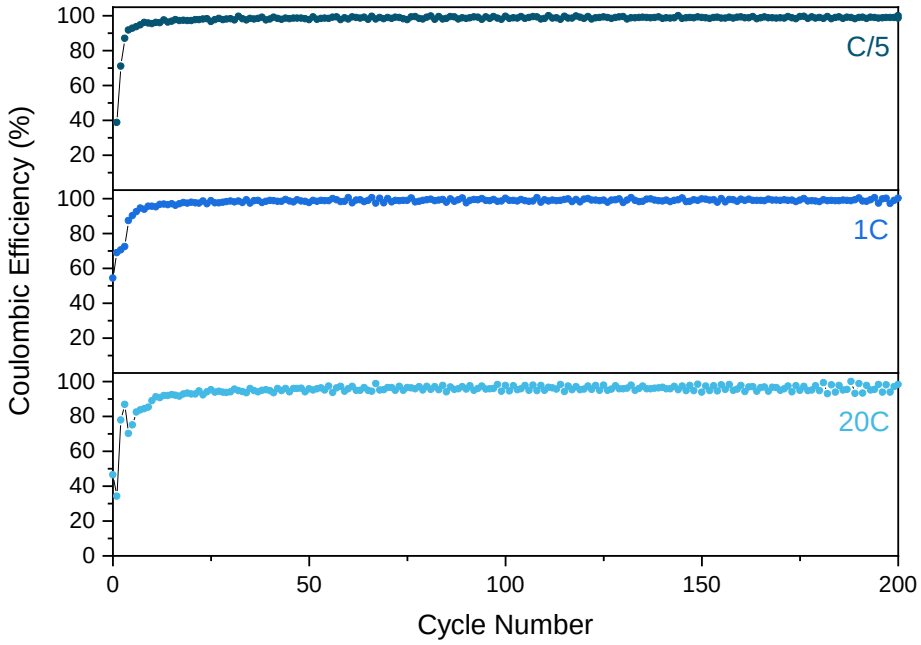

Figure A.62 – Coulombic efficiency of 10 % Mo in Nb_2O_5 composite material at increasing rates C/5, 1C and 20 C, top to bottom respectively in a voltage range of 0.01-3.0 V and a formation at C/20.

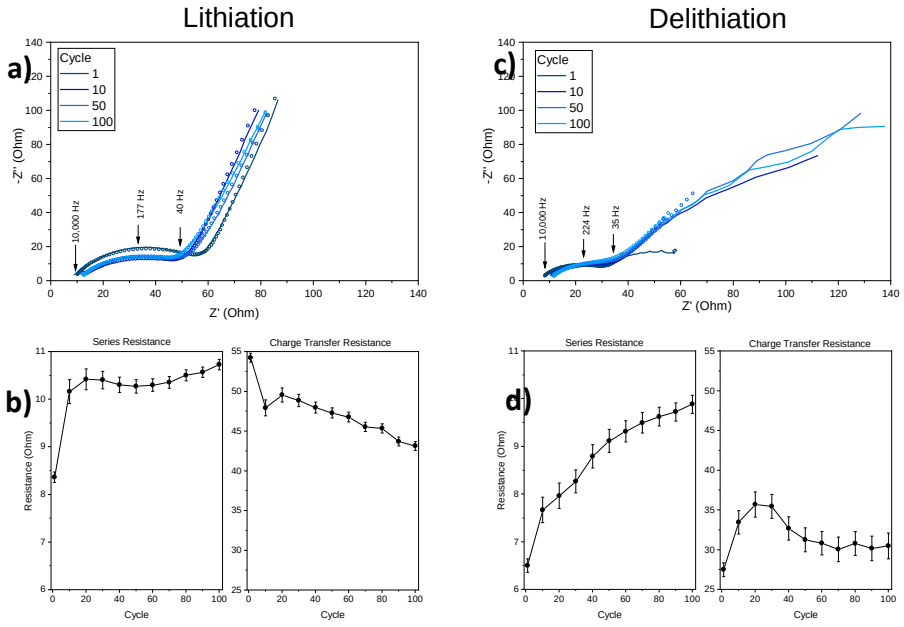

Figure A.63 - Nyquist plots of 10 % Mo composite taken at 0.5 V during Lithiation (a) and delithiation (c) at increasing cycles (lines) with fitted data (circles). Fitted resistance values with increasing cycles for series and charge transfer for lithiation (b) and delithiation (d).

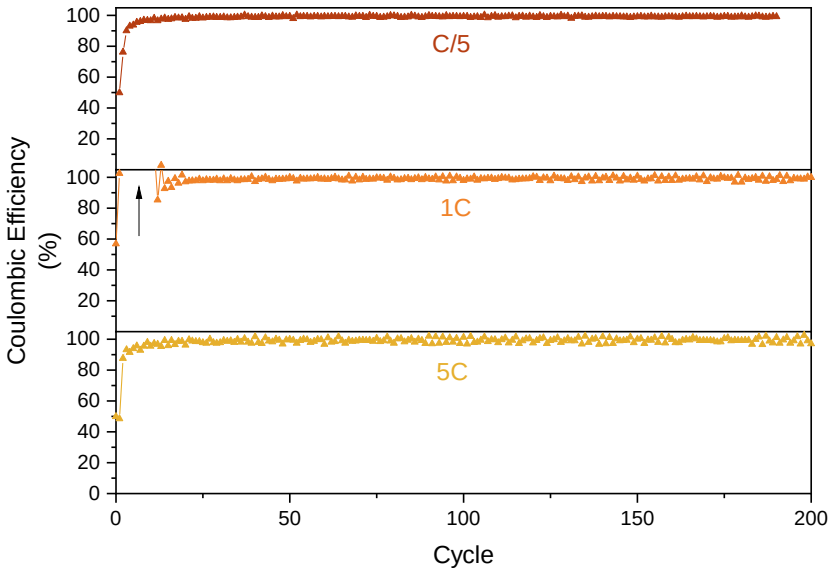

Figure A.64 - Coulombic efficiency of 20 % Mo in Nb_2O_5 composite material at increasing rates C/5, 1C and 20 C, top to bottom respectively in a voltage range of 0.01-3.0 V and a formation at C/20. Arrow points out anomalous region where CE vastly exceeds 100 %.

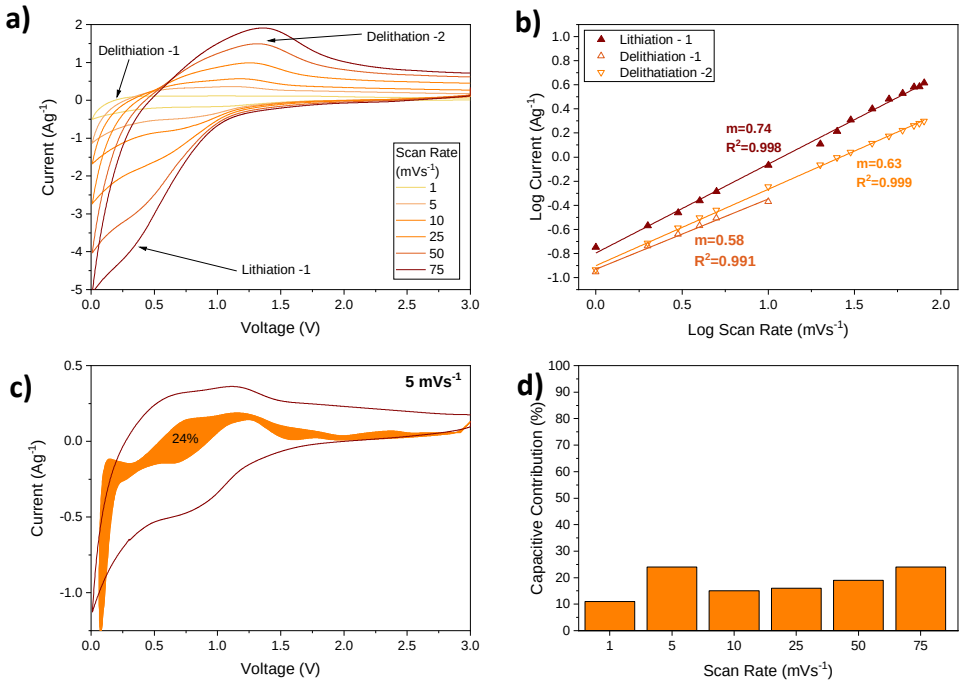

Figure A.65- a) CV profiles of 20 % Mo composite materials at increasing scan rate from 1.0 – 75 mVs^{-1}. b) Log plot of peak currents, versus scan rate, fitted with a linear function where R^2 is greater than 0.991 on all lines. c) CV profile at 5 mVs^{-1} with filled area representing the capacitive contribution. d) Chart of percentage capacitive contribution at increasing scan rate from 1.0 to 75 mVs^{-1}.

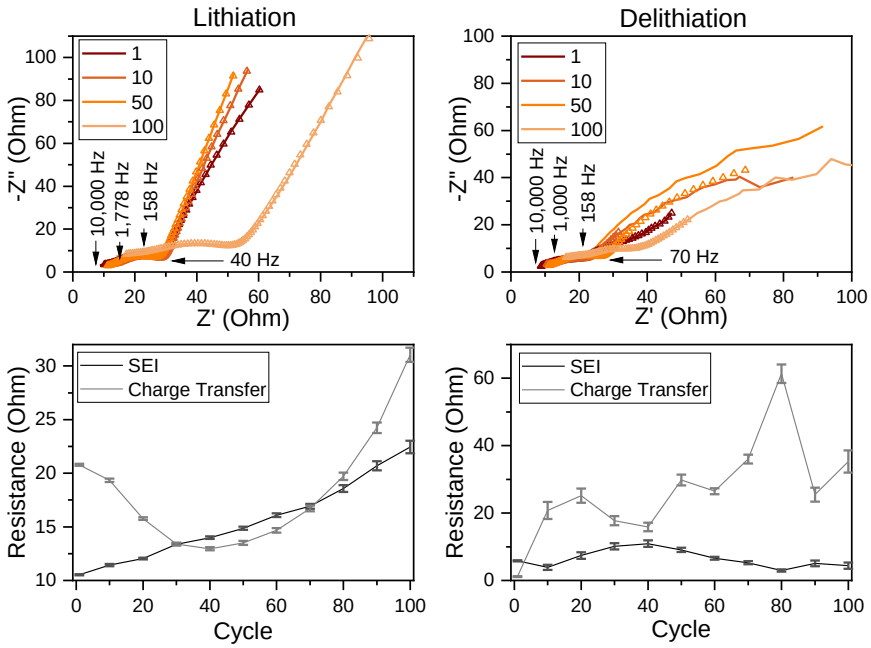

Figure A.66 - Nyquist plots of 20 % Mo composite taken at 0.75 V during Lithiation and delithiation (left and right respectively) and below their corresponding fitted resistance values for SEI and charge transfer resistance over cycle.

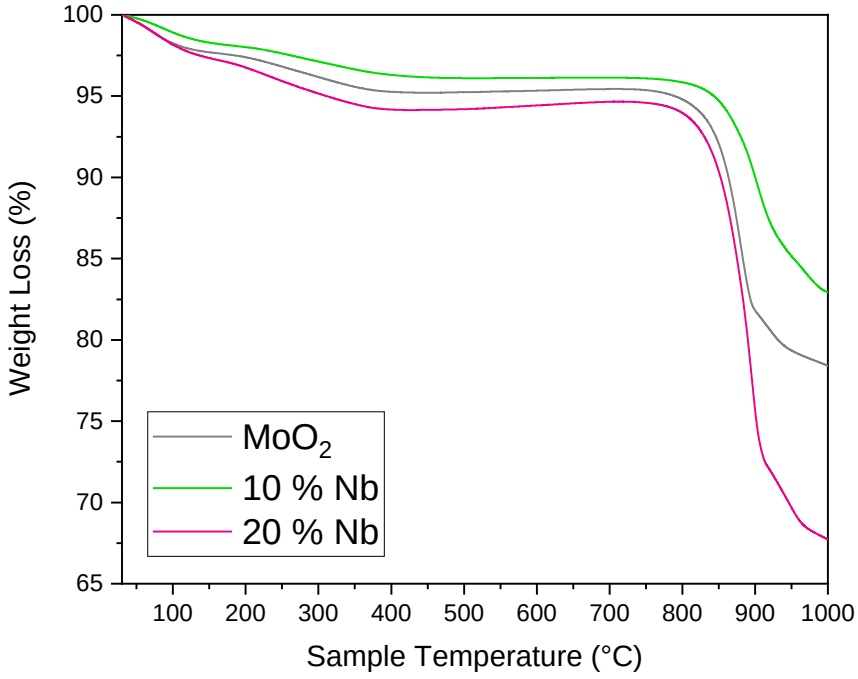

Figure A.67 - TGA in N_2 at 10 °Cmin $^{-1}$ for MoO_2-rich composites and pure MoO_2.

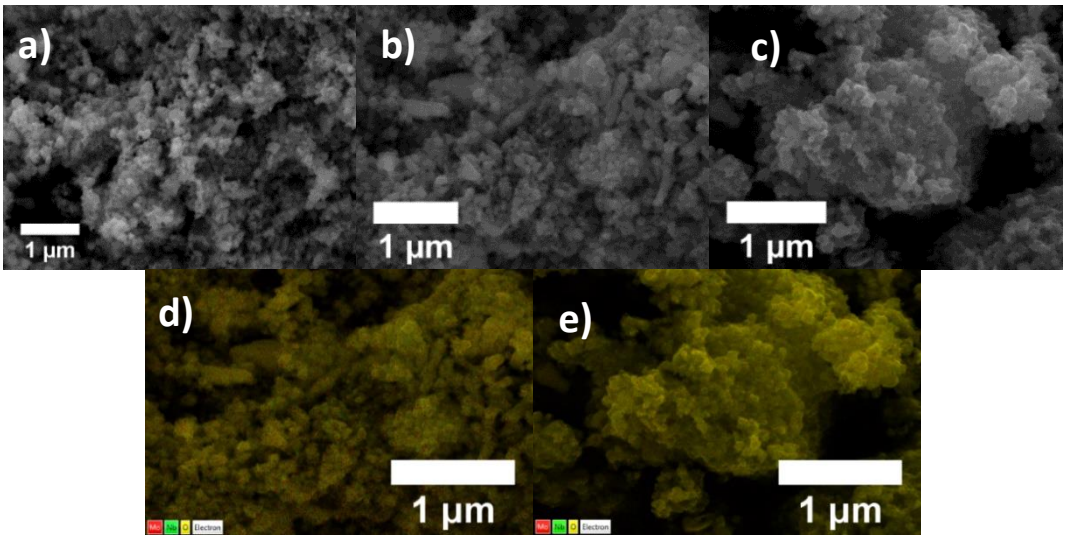

Figure A.68 - a-c) SEM images of MoO_2, 10 % Nb and 20 % Nb composites respectively. d,e) SEM-EDX image maps of 10 and 20 % Nb composites respectively, where Mo is red, Nb is green, and O is yellow.

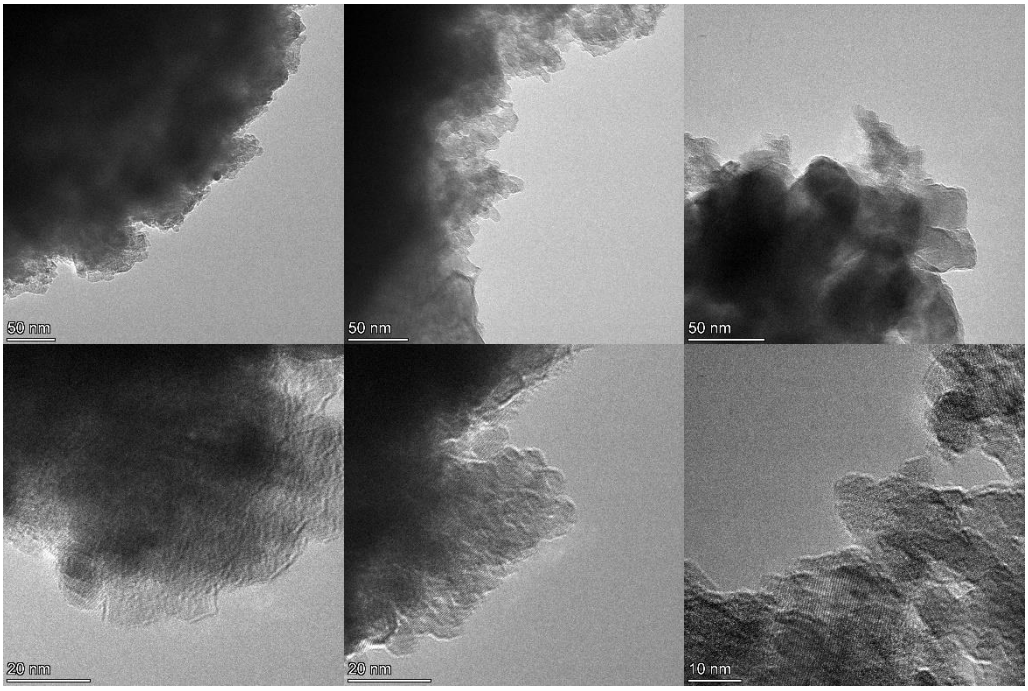

Figure A.69 – A selection of TEM images of 10 % Nb in MoO_2 composite.

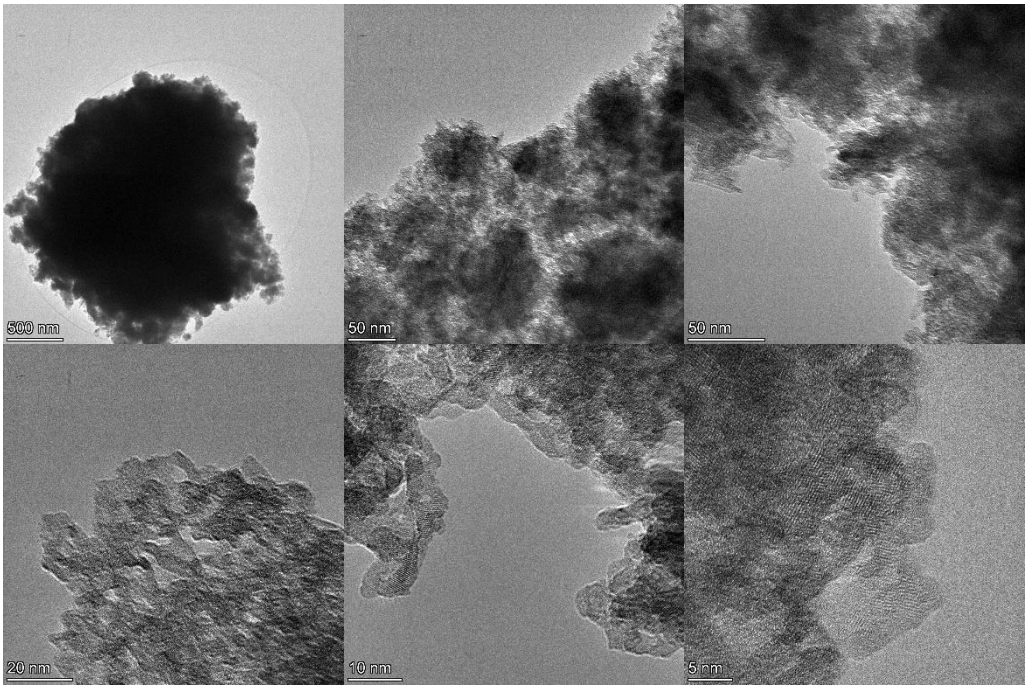

Figure A.70 – A selection of TEM images of 20 % Nb in MoO_2 composite.

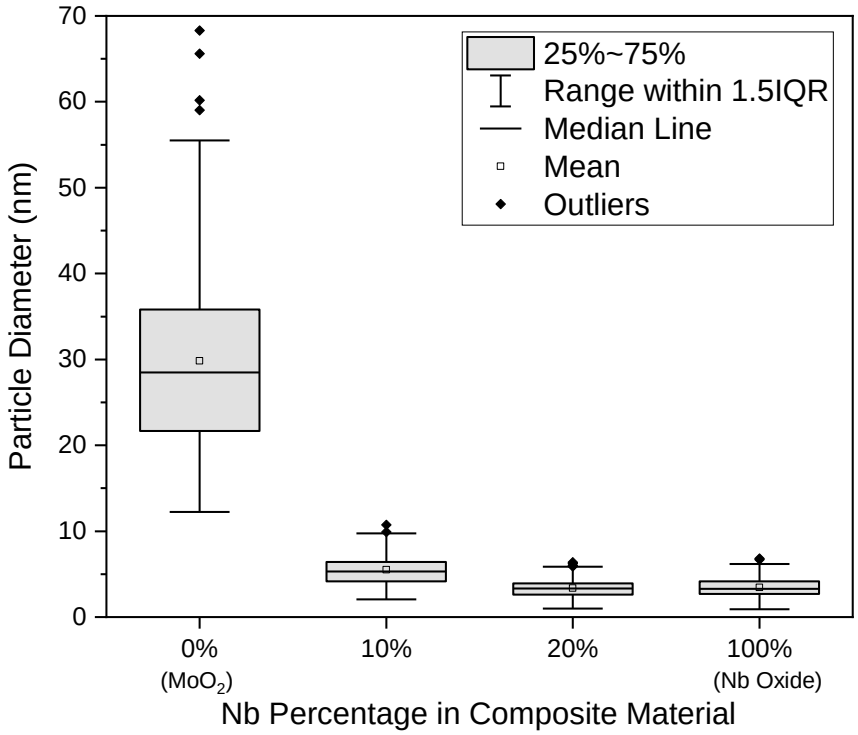

Figure A.71 - Box and whisker plots of particle widths as measured from TEM images of MoO_2 heavy composite materials with comparison to pure MoO_2 and as-synthesised Nb_2O_5.

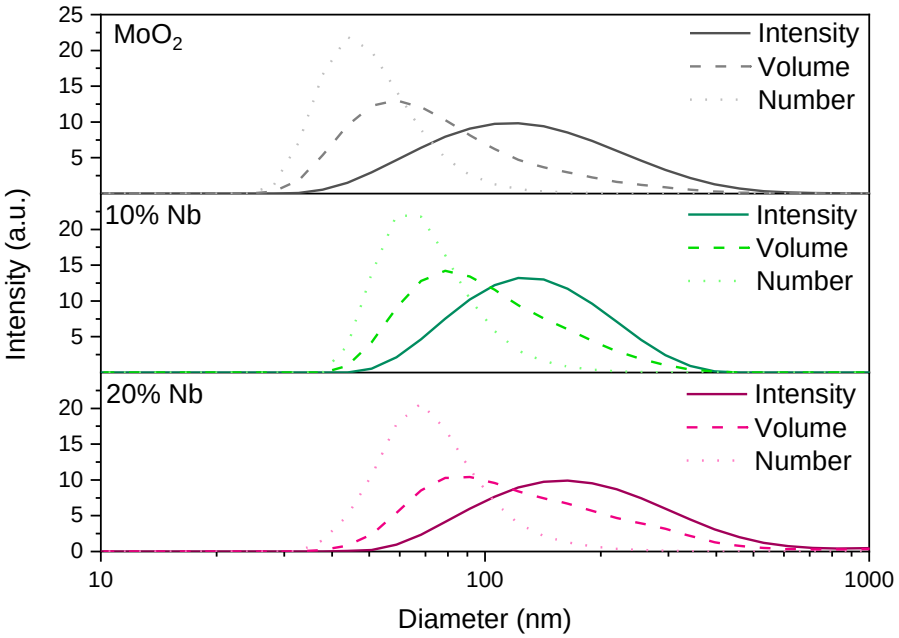

Figure A. 72 - Particle diameter of MoO_2 (grey) and composite materials 10 and 20 % Nb (green and pink respectively) as measured with a zeta sizer and displayed are intensity, volume, and number distribution.

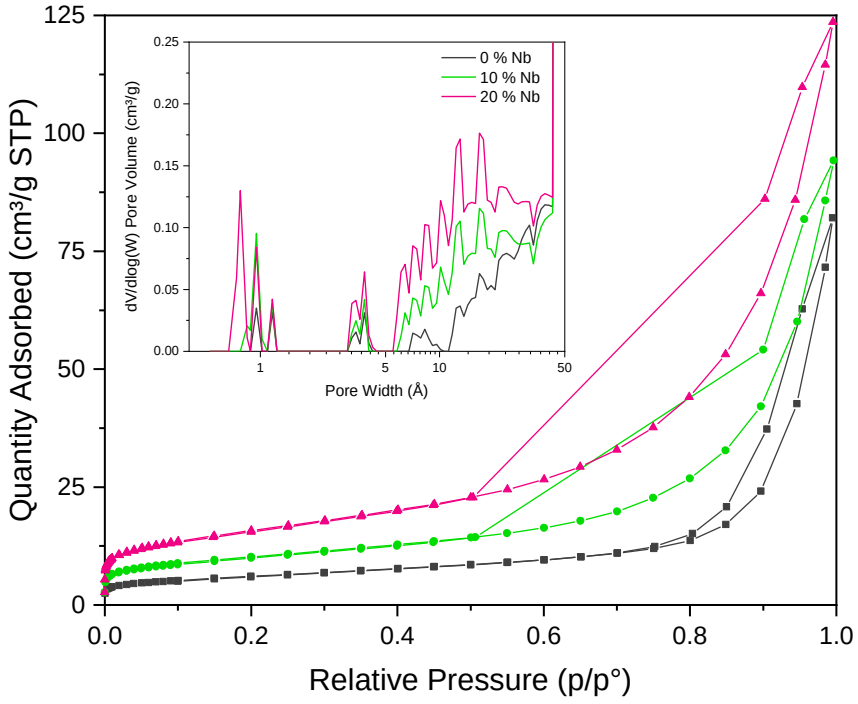

Figure A.73 - N_2 adsorption isotherms of MoO_2-rich composites and MoO_2. (inset) Pore distribution plot calculated from the isotherms.

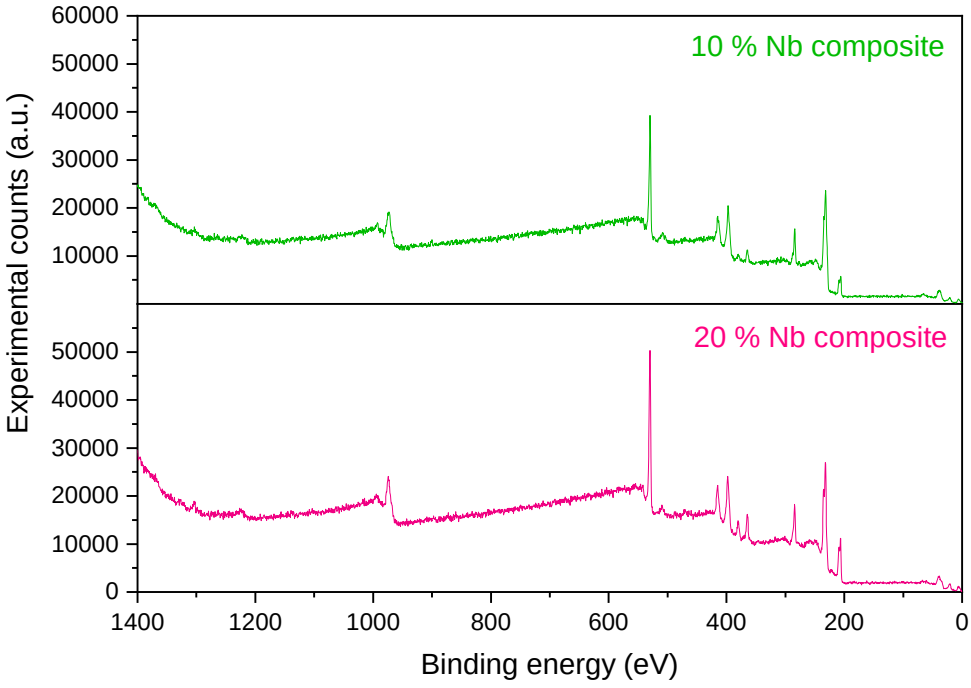

Figure A.74 - Full XPS survey of 10 and 20 % Nb content composite oxides (top and bottom respectively).

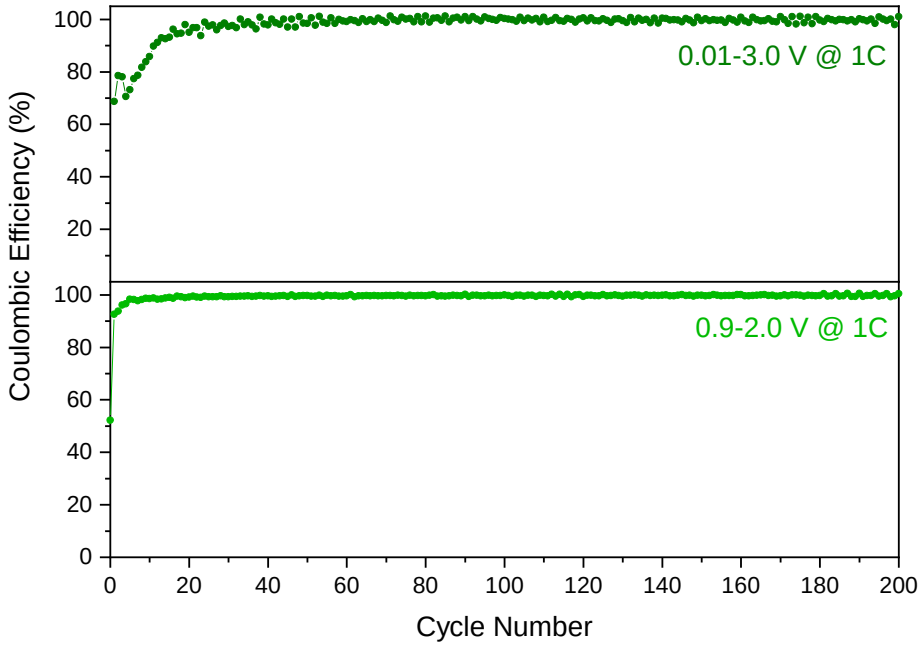

Figure A.75 - Coulombic efficiency of 10 % Nb content in MoO_2 composite in wide and narrow voltage windows, top and bottom respectively, at 1C rate after a C/20 formation cycle.

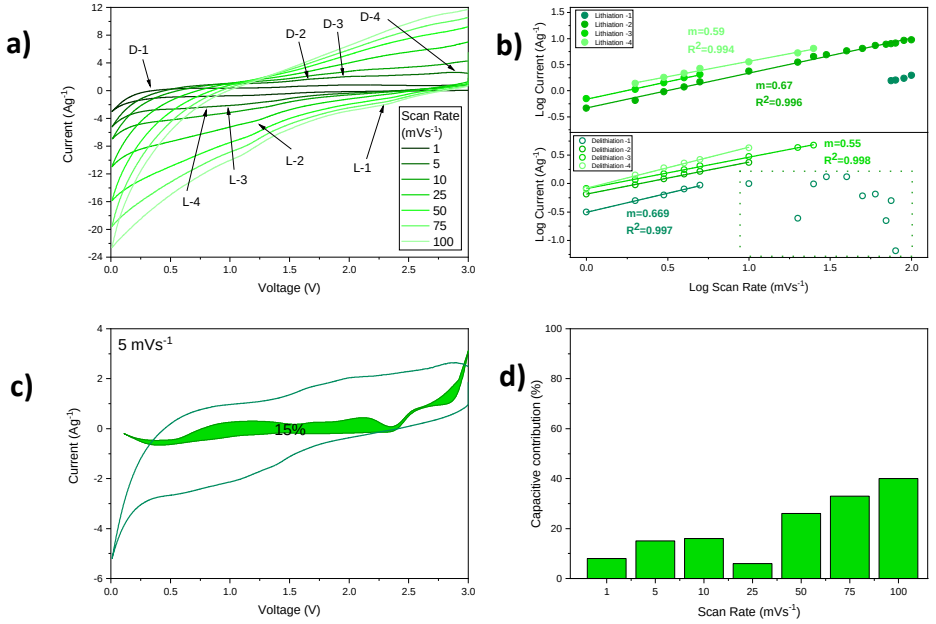

Figure A.76 - a) CV profiles of 10 % Nb composite materials at increasing scan rate from 1.0 – 100 mVs^{-1}. b) Log plot of peak currents, versus scan rate, fitted with a linear function where R^2 is greater than 0.993 on all lines for lithiation and delithiation peaks (top and bottom respectively). c) CV profile at 5 mVs^{-1} with filled area representing the capacitive contribution. d) Chart of percentage capacitive contribution at increasing scan rate from 1.0 to 100 mVs^{-1}.

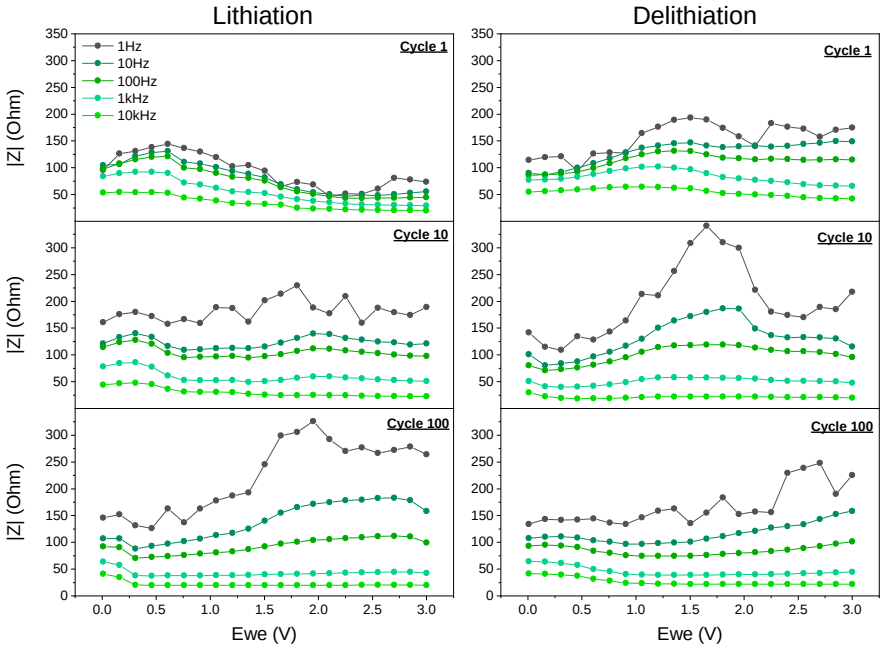

Figure A.77 - SPEIS profiles of 10 % Nb composite material for increasing cycles from 1 to 100 (top to bottom) or lithiation and delithiation (left and right respectively).

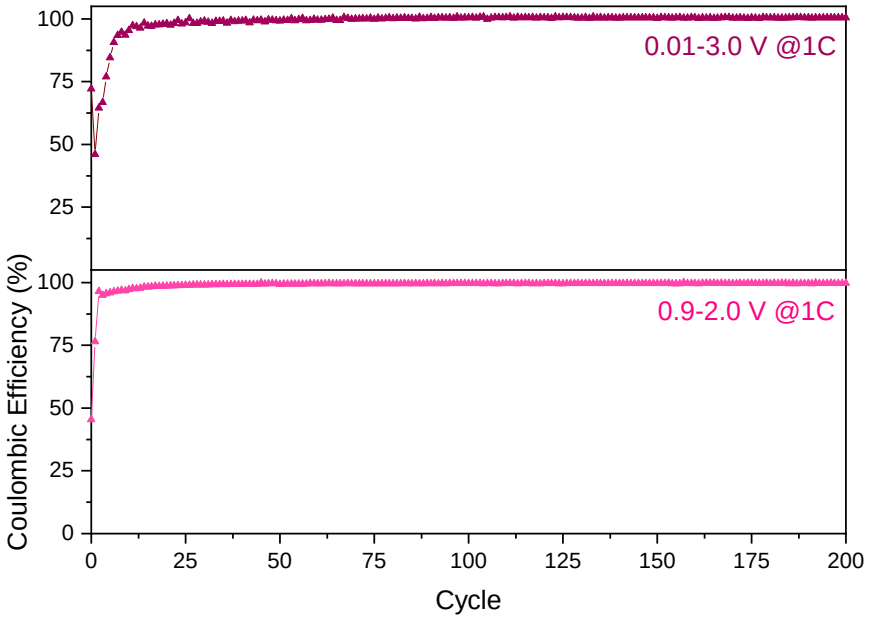

Figure A.78 – Coulombic efficiency of 20% Nb content in MoO_2 composite in wide and narrow voltage windows, top and bottom respectively, at 1C rate after a C/20 formation cycle.

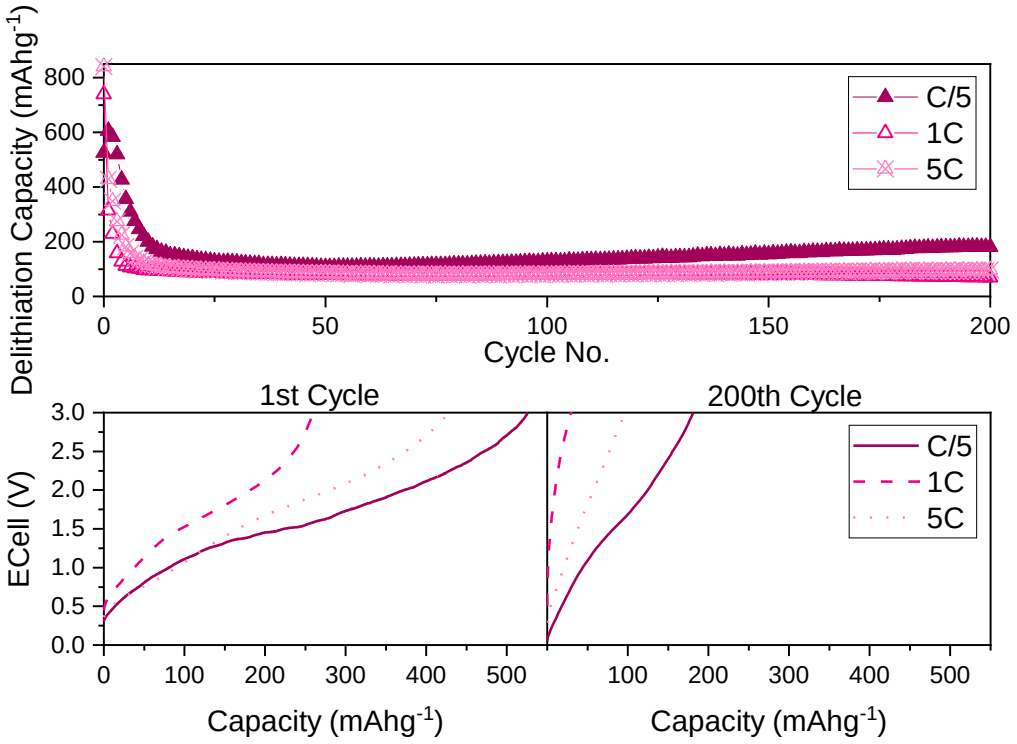

Figure A.79 - (top) Galvanostatic cycling between 0.01-3.0 V of 20 % Nb composite at various rates, (bottom) charging profiles at various rates at 1st and 200th cycle.

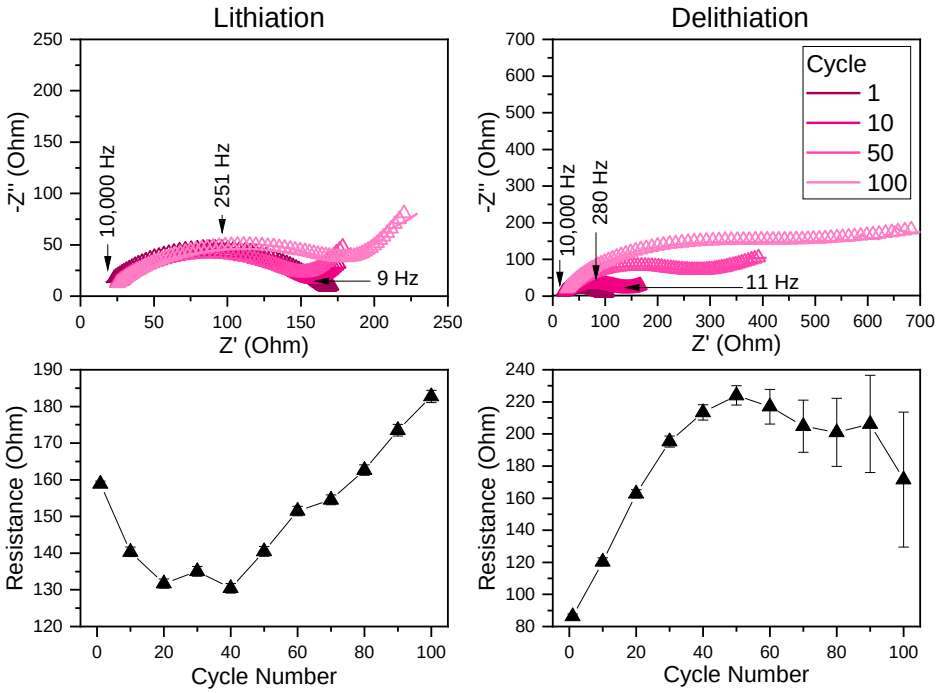

Figure A.80 - Nyquist plots of 20 % Nb composite taken at 0.5 V during lithiation and delithiation (left and right respectively), with fitted curves (circles) and below their corresponding, fitted resistance values for charge transfer resistance over cycle.

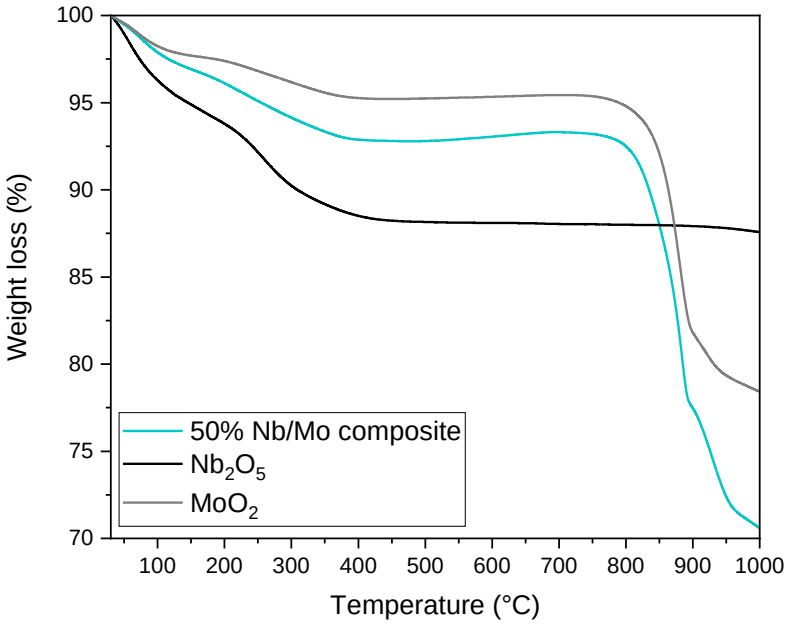

Figure A.81 - TGA in N_2 at 10 °Cmin^{-1} for 50/50 Nb/Mo composite with TGA of Nb_2O_5 and MoO_2 for comparison.

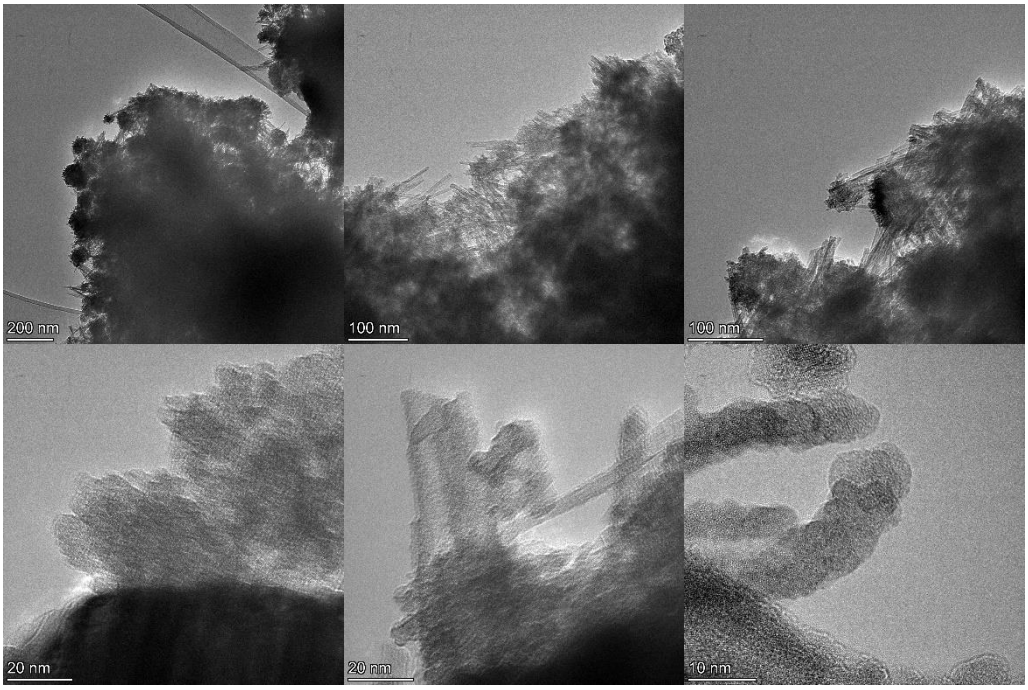

Figure A.82 – A selection of TEM images of 50 % composite.

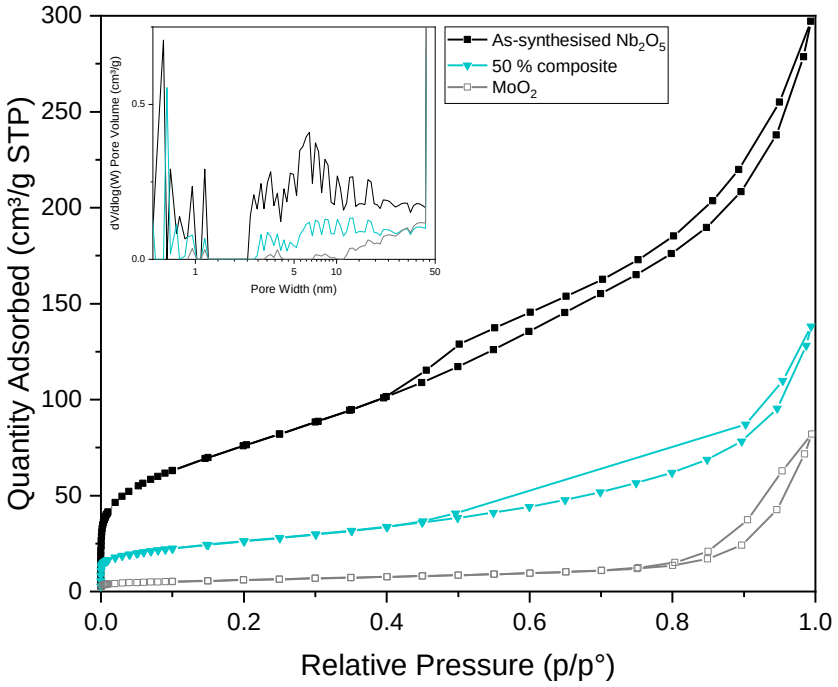

Figure A.83 - N_2 adsorption isotherms of 50 % composite, Nb_2O_5 and MoO_2. (Inset) Pore distribution plot calculated from the isotherms.

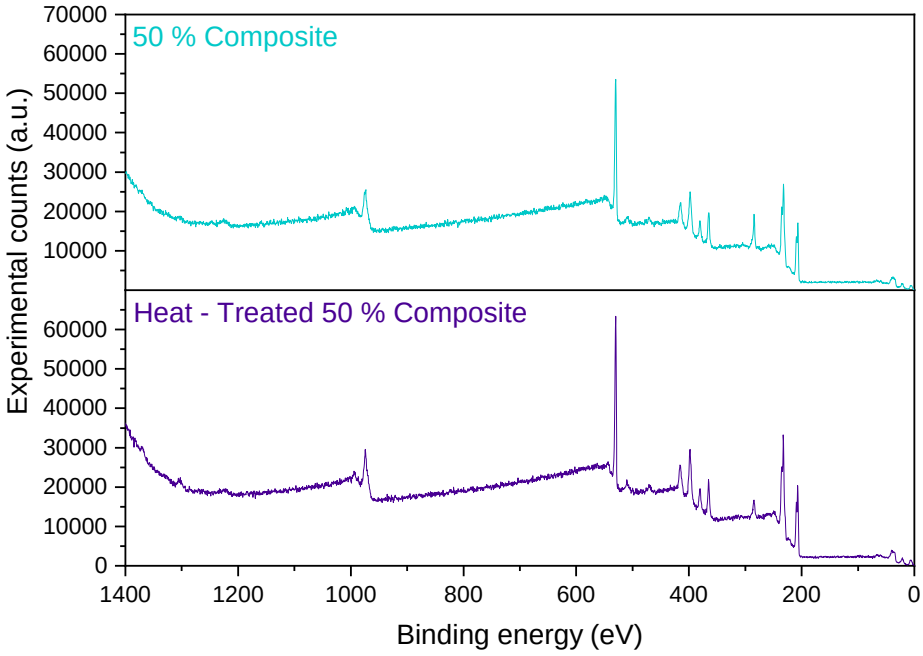

Figure A.84 - Full XPS survey of 50 % composite oxides, as-synthesised and heat-treated (top and bottom respectively).

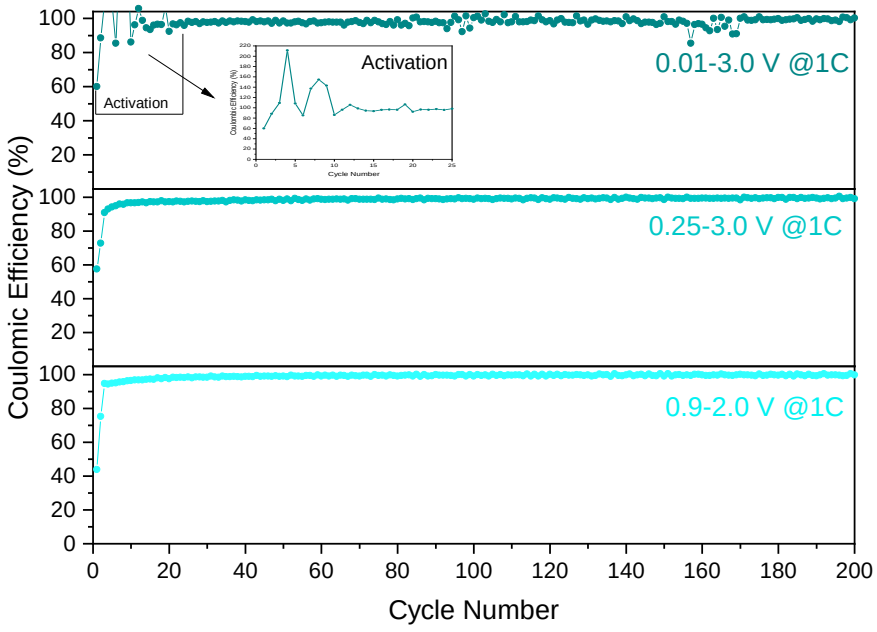

Figure A.85 - Coulombic efficiency of 50% Nb content in MoO_2 composite in wide, medium, and narrow voltage windows, top to bottom respectively, at 1C rate after a C/20 formation cycle. Activation region which exceeds 100 % is inset.

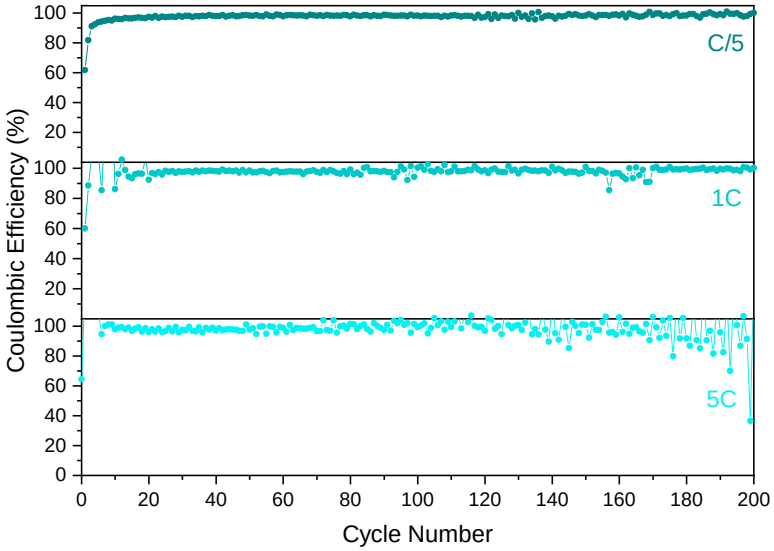

Figure A.86 - Coulombic efficiency of 50% Nb content in MoO_2 composite at C/5, 1C and 5C, top to bottom respectively, in a 0.01-3.0 V range with a C/20 formation cycle.

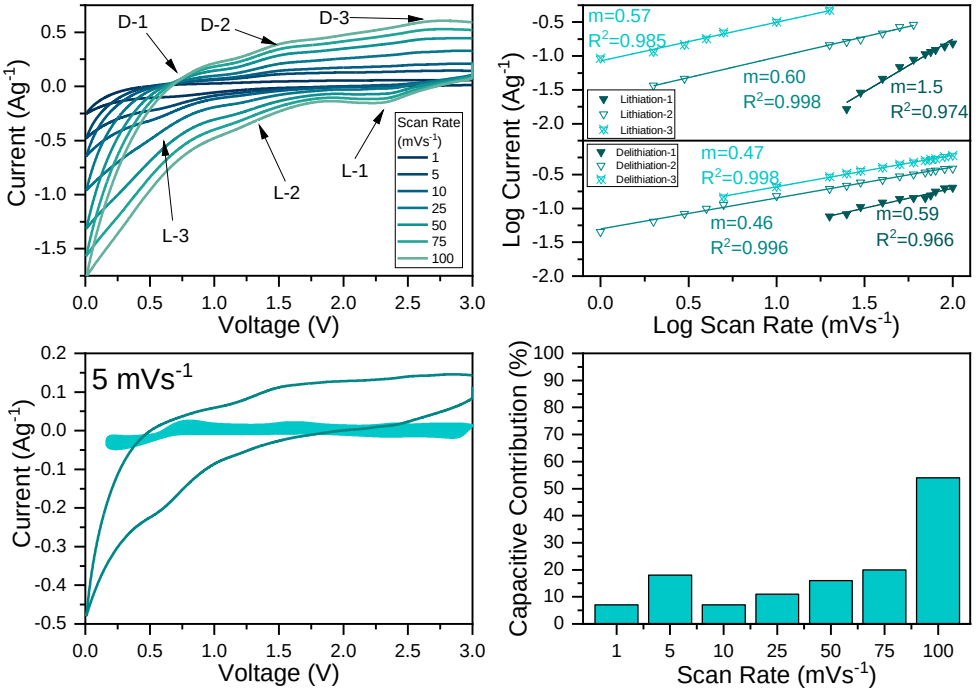

Figure A.87 - a) CV profiles of 50 % composite materials at increasing scan rate from 1.0 – 100 mVs^{-1}. b) Log plot of peak currents, versus scan rate, fitted with a linear function where R^2 is greater than 0.966 on all lines. c) CV profile at 5.0 mVs^{-1} with filled area representing the capacitive contribution. d) Chart of percentage capacitive contribution at increasing scan rate from 1.0 to 100 mVs^{-1}.

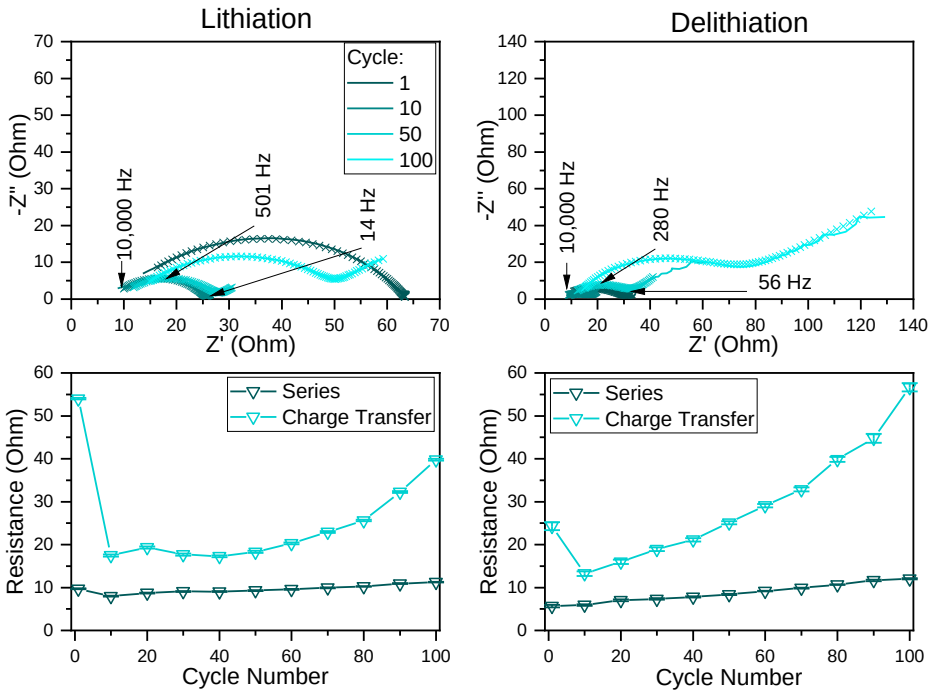

Figure A.88 - Nyquist plots of 50 % composite taken at 0.5 V during lithiation and delithiation (left and right respectively), with fitted curves (circles) and below their corresponding, fitted resistance values for charge transfer resistance over cycle.

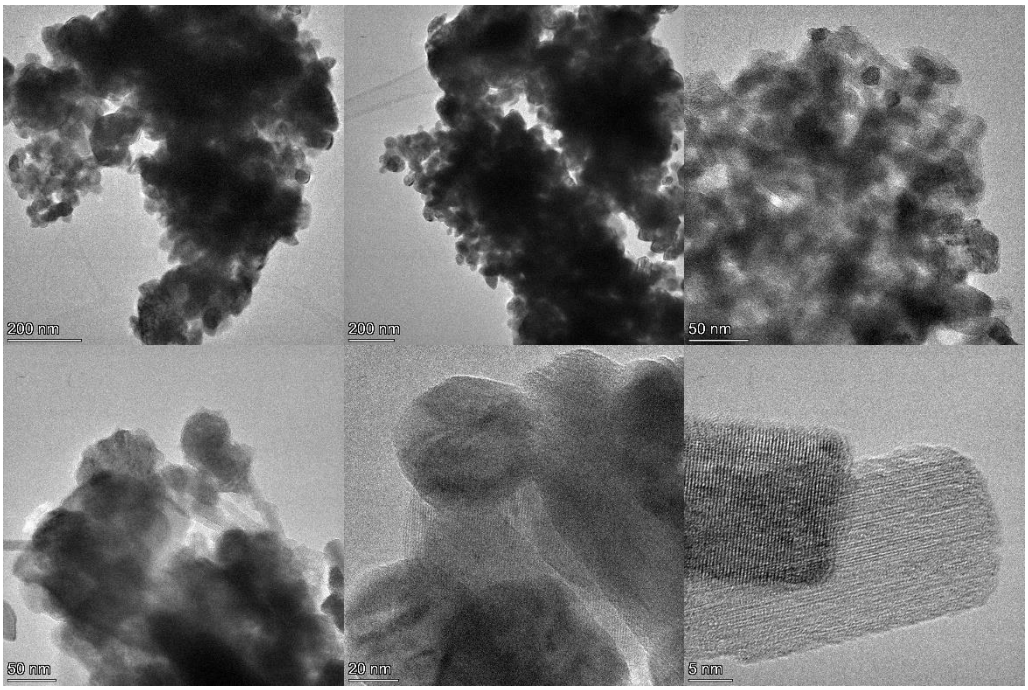

Figure A.89 – A selection of TEM images of heat-treated 50% composite.

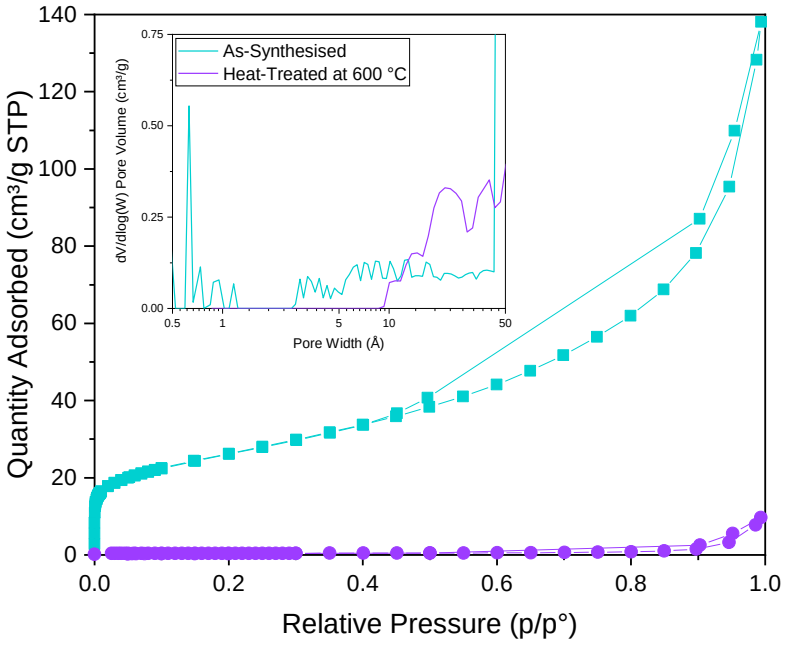

Figure A. 90 - N_2 adsorption isotherms of 50 % composite, as-synthesised and heat-treated to 600 °C. (Inset) Pore distribution plot calculated from the isotherms.

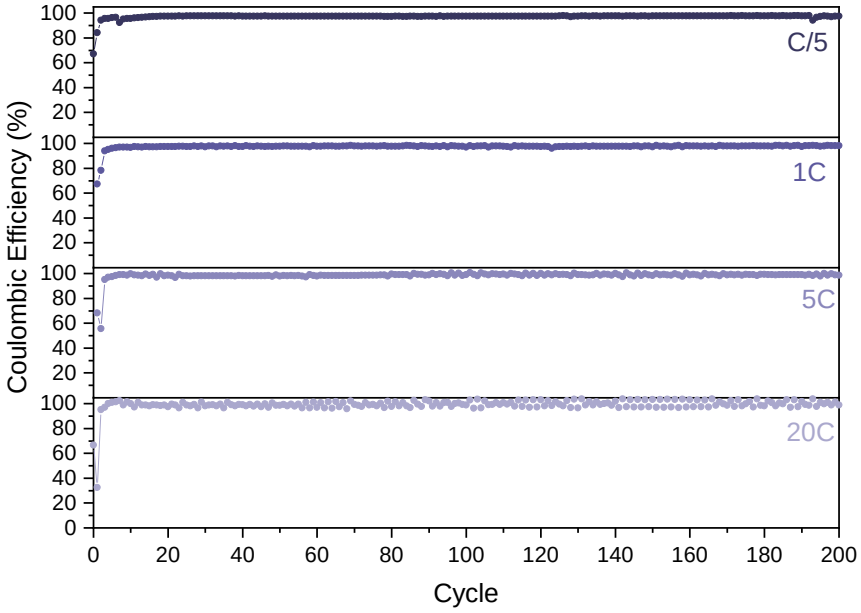

Figure A.91 - Coulombic efficiency of heat-treated 50% Nb content in MoO_2 composite at C/5, 1C, 5C and 20C, top to bottom respectively, in a 0.01-3.0 V range with a C/20 formation cycle.

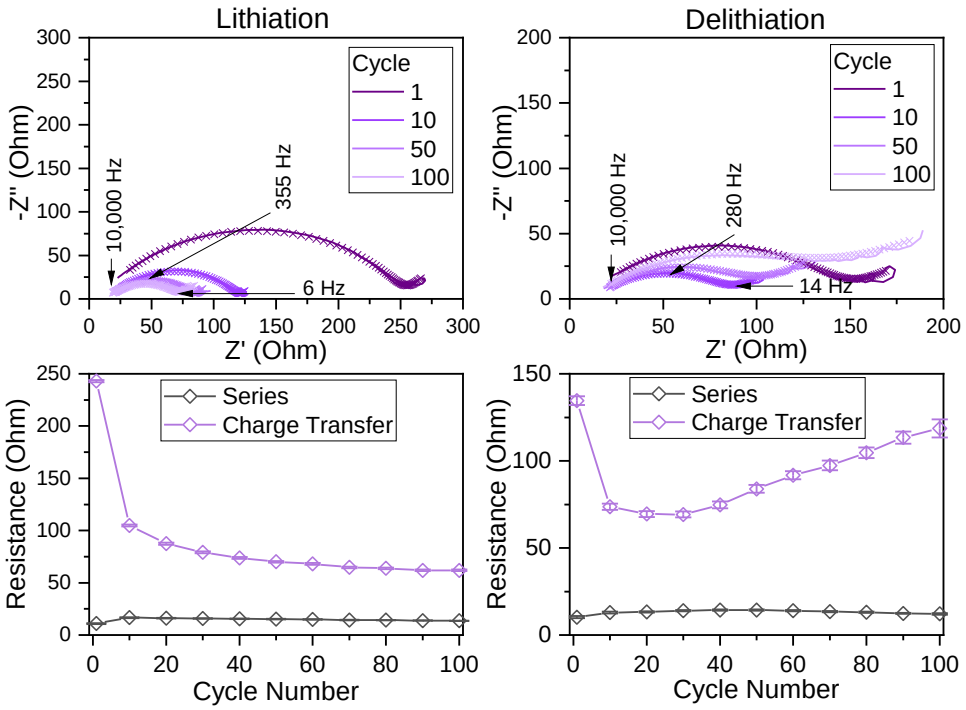

Figure A.92 - Nyquist plots of heat-treated 50 % composite taken at 0.5 V during lithiation and delithiation (left and right respectively), with fitted curves (Crosses) and below their corresponding, fitted resistance values for charge transfer resistance over cycle.